

ALCATOR DCT PROPOSAL

B. Blackwell, M. Greenwald, D. Gwinn, B. Lipschultz,
E. Marmor, D. B. Montgomery, R. Parker, P. Politzer,
M. Porkolab, J. Schultz, S. Wolfe

Plasma Fusion Center
Massachusetts Institute of Technology
Cambridge, MA 02139

October 1983

This work was supported by the U.S. Department of Energy Contract No. DE-AC02-78ET51013. Reproduction, translation, publication, use and disposal, in whole or in part by or for the United States government is permitted.

MASSACHUSETTS INSTITUTE OF TECHNOLOGY

PLASMA FUSION CENTER

ALCATOR DCT PROPOSAL

OCTOBER, 1983

Submitted to

OFFICE OF FUSION ENERGY

U. S. DEPARTMENT OF ENERGY

WASHINGTON, D. C. 20545



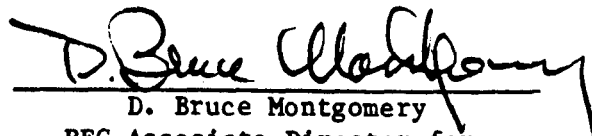
Ronald C. Davidson
Director, Plasma Fusion Center

George H. Dummer
Director

Office of Sponsored Programs



Ronald R. Parker
PFC Associate Director for
Confinement Experiments



D. Bruce Montgomery
PFC Associate Director for
Engineering Systems

ALCATOR DCT PROPOSAL

B. Blackwell, M. Greenwald, D. Gwinn, B. Lipschultz, E. Marmor,
B. Montgomery, R. Parker, P. Politzer, M. Porkolab, J. Schultz, S. Wolfe

Plasma Fusion Center
Massachusetts Institute of Technology
Cambridge, MA 02139

September 22, 1983

Acknowledgements

Many people have contributed to the development of the Alcator DCT concept and the preparation of this document. The following specific contributions are gratefully acknowledged: P. Bonoli and B. Lloyd have provided material in support of LH heating and current drive plans; D. Blackfield and B. Koester have contributed to the ICRF heating concept; D. Pappas has done computations concerning requirements for neutron shielding; R. Granetz and P. Pribyl have aided in MHD equilibrium and stability computations; M. Besen, H. Becker, E. Bobrov and R. Thome have carried out engineering analysis and made useful contributions to the design; D. Griffin and J. Rose have provided material for RF and AC power systems design; N. Diatchenko and A. Chernomordik have skillfully produced most of the engineering drawings and technical illustrations, respectively.

The highly competent, professional and tireless efforts of L. Pfeifer, B. Ogar, L. McKnight, A. Kotsopoulos, D. Marble and L. Funari in preparing the manuscript are most appreciatively acknowledged.

TABLE OF CONTENTS

1.	INTRODUCTION	
1.1.	Introduction.....	1-1
1.1.1.	Background.....	1-1
1.1.2.	Alcator DCT Objectives.....	1-3
1.1.2.1.	Plasma Physics Issues.....	1-6
1.1.2.2.	Plasma Engineering Issues.....	1-9
1.1.2.3.	Long Pulse Tokamak Technology Issues.....	1-13
1.2.	Alcator DCT Description.....	1-16
1.2.1.	General Considerations.....	1-16
1.2.2.	Alcator DCT Specifications and Expected Parameters	1-17
1.2.2.1.	Plasma Geometry.....	1-19
1.2.2.2.	Magnetic Field Strength.....	1-19
1.2.2.3.	Magnetics Technology.....	1-20
1.2.2.4.	RF Systems.....	1-21
1.2.2.5.	Plasma Parameters.....	1-22
1.3.	Programmatic Role.....	1-23
1.3.1.	Role Within the Toroidal Confinement Program Plan	1-23
1.3.2.	Relationship to TFCD.....	1-28
1.3.3.	Relationship to Other Experiments.....	1-29
1.3.3.1.	Existing Copper Devices and their Upgrades.....	1-29
1.3.3.2.	Comparison to Tore Supra.....	1-32

2.	PLASMA PHYSICS CONSIDERATIONS	
2.1.	Introduction.....	2-1
2.2.	Plasma Regimes.....	2-2
2.2.1.	Introduction.....	2-2
2.2.2.	Ohmic Plasma Parameters.....	2-4
2.2.3.	High Power Heating Simulations.....	2-10
2.2.4.	Shaped Plasmas.....	2-18
2.2.5.	Time Evolution.....	2-24
2.2.6.	Summary.....	2-30
2.3.	MHD Configurations.....	2-37
2.3.1.	General Considerations.....	2-37
2.3.2.	Divertor Configurations.....	2-38
2.3.3.	The Alcator DCT Divertor.....	2-41
2.3.4.	Plasma Shaping.....	2-44
2.3.5.	Beta Dependent Equilibrium Effects.....	2-44
2.3.6.	Stability Limits.....	2-49
2.3.7.	The Vertical ($n=0$) Instability.....	2-51
2.4.	RF Current Drive.....	2-53
2.4.1.	Introduction.....	2-53
2.4.2.	Frequency Selection.....	2-54
2.4.3.	Accessibility.....	2-58
2.4.4.	Brambilla Spectrum.....	2-63
2.4.5.	Current Drive Efficiency.....	2-65
2.4.6.	Ray Tracing.....	2-67
2.4.7.	Code Simulations.....	2-72
2.5.	RF Heating.....	2-83
2.5.1.	Lower Hybrid Heating.....	2-83

2.5.2.	ICRF Heating Physics.....	2-86
2.5.2.1.	Introduction.....	2-86
2.5.2.2.	The Dispersion Relation.....	2-86
2.5.2.3.	Predictions of a 1-D Four Wave Slab Model.....	2-88
2.5.2.4.	Predictions of a 2-D Fokker-Planck Code..	2-92
2.5.2.5.	Summary of ICRF Physics.....	2-94
3.	PLASMA ENGINEERING	
3.1.	Introduction.....	3-1
3.2.	Pellet Injection.....	3-2
3.2.1.	Introduction.....	3-2
3.2.2.	Requirements.....	3-3
3.3.	Particle and Impurity Control Techniques.....	3-5
3.3.1.	Introduction.....	3-5
3.3.2.	Pumped Limiter.....	3-6
3.3.3.	Internal Poloidal Divertor.....	3-8
3.3.4.	External Poloidal Divertor.....	3-10
3.3.5.	Heat Deposition Calculation.....	3-13
3.3.6.	Edge Plasma Parameters.....	3-18
3.3.7.	Heat Removal Components.....	3-21
3.3.8.	Heat Removal and Impurity Control Summary.....	3-25
3.4.	RF Systems and Couplers.....	3-31
3.4.1.	Lower Hybrid System.....	3-31
3.4.1.1.	General.....	3-31
3.4.1.2.	Lower Hybrid Coupler.....	3-33
3.4.2.	The Alcator DCT ICRF System.....	3-40
3.4.2.1.	General.....	3-40
3.4.2.2.	Tuning and Matching.....	3-42

	3.4.3.3. Antenna.....	3-44
	3.4.2.4. Transmission System.....	3-46
	3.4.2.5. Advanced Coupler Design.....	3-46
4.	ALCATOR DCT POINT DESIGN	
	4.1. Introduction.....	4-1
	4.2. Overall Machine Description.....	4-2
	4.3. Magnetic System Concept Selection.....	4-11
	4.3.1. Toroidal Field Coils.....	4-11
	4.3.1.1. Conductor Choice.....	4-11
	4.3.1.2. Winding Pack Design.....	4-16
	4.3.1.3. Structural Approach and Stress Analysis.....	4-23
	4.3.1.4. Protection.....	4-36
	4.3.2. Poloidal Field System.....	4-38
	4.3.2.1. Conductor Selection.....	4-44
	4.3.2.2. Current and Voltage Level Selections.....	4-51
	4.3.2.3. PF Coil Loads and Structural Approach.....	4-53
	4.3.3. Cryogenic Considerations.....	4-56
	4.3.3.1. Design Approaches.....	4-56
	4.3.3.2. Cryogenic Refrigeration System and Loss Inventory.....	4-58
5.	VACUUM VESSEL, COOLING SYSTEM, and VACUUM PUMPING	
	5.1. Vacuum Vessel.....	5-1
	5.2. Vessel Cooling System.....	5-10
	5.3. Vessel Vacuum Pumping System.....	5-14
6.	ALCATOR DCT DIAGNOSTICS	
	6.1. Introduction.....	6-1
	6.2. Fully Developed Diagnostic Systems.....	6-1

6.3.	Diagnostic Systems in Development.....	6-9
6.4.	Special Steady-State Diagnostics Issues.....	6-12
6.5.	Summary.....	6-13
7.	DATA ACQUISITION and CONTROL	
7.1.	Data Handling.....	7-1
7.1.1.	System Description.....	7-2
7.1.2.	Data Acquisition Hardware - CAMAC.....	7-4
7.1.3.	Computers.....	7-5
7.1.4.	Back-End Network.....	7-6
7.1.5.	Local Area Network.....	7-7
7.1.6.	Data Display System.....	7-8
7.1.7.	Data System Software.....	7-9
7.2.	Automated Control System.....	7-10
8.	FACILITIES	
8.1.	Siting and Building Layout.....	8-1
8.1.1.	Overall Site Description.....	8-1
8.1.2.	Shielding Requirements of the Experimental Cell...	8-3
8.1.3.	Experimental Cell and Power Equipment Area Description.....	8-5
8.1.4.	Support Areas.....	8-6
8.2.	Power Systems.....	8-6
8.2.1.	Prime Power.....	8-6
8.2.2.	Magnet Power Supplies.....	8-9
8.2.3.	RF Power System.....	8-12
8.2.3.1.	Lower Hybrid System.....	8-12
8.2.3.2.	ICRF.....	8-15

9. ALCATOR DCT RESEARCH and DEVELOPMENT ACTIVITIES

10. COST, SCHEDULE and PROJECT MANAGEMENT

10.1. Cost.....	10-1
10.1.1. Costing Basis for Fabrication and Purchased Components	10-1
10.1.1.1. Torodial Field Coils and Intercoil Structure.....	10-4
10.1.1.2. Poloidal Field Coils and PF Cryostats.....	10-6
10.1.1.3. Magnet Vacuum Cryostat.....	10-8
10.1.1.4. Refrigeration.....	10-8
10.1.1.5. Vacuum Chamber Torus and Vacuum Pumping.....	10-9
10.1.1.6. Collector Plates and Heat Shields.....	10-10
10.1.1.7. Site Modifications.....	10-11
10.1.1.8. Power and Control.....	10-12
10.1.1.9. RF Modifications.....	10-13
10.1.1.10. Alcatraz DCT Research and Development Activities.....	10-15
10.1.2. Composite Labor Costs for Engineering, Installation, and Project Management.....	10-16
10.2. Schedule.....	10-19
10.3. Funding Profiles.....	10-22
10.4. Project Management.....	10-25
10.4.1. Management Plan.....	10-25
10.4.2. Project Organization.....	10-28

APPENDICES

A.	DESCRIPTION OF THE LOWER HYBRID CURRENT DRIVE CODE	
B.	HEAT LOAD ANALYSIS	
B.1.	Thermal Hydraulics of the Collector Plate.....	B-1
B.2.	Disruption Characteristics and Lifetime Analysis.....	B-4
C.	EDDY CURRENT EFFECTS	
C.1.	Disruption Induced Eddy Currents.....	C-1
C.2.	Startup Induced Eddy Currents.....	C-13
D.	HIGH POWER RF INDUCED IMPURITY GENERATION IN TOKAMAK EXPERIMENTS	
D.1.	Introduction.....	D-1
D.2.	TFR.....	D-1
D.3.	Alcator C.....	D-4
D.4.	PLT.....	D-10
E.	ENHANCEMENTS	
E.1.	RF Systems.....	E-1
E.1.1.	Enhanced Lower Hybrid Current Drive System.....	E-1
E.1.2.	Enhanced ICRF Systems.....	E-3
E.1.3.	ECRH Option.....	E-3
E.2.	Beta Enhancement with Extreme Shaping.....	E-4
E.3.	Internal Coils for Divertors and Shaping.....	E-7
F.	REACTOR RELEVANCE	
F.1.	Magnetic Field.....	F-2
F.2.	Aspect Ratio.....	F-3
F.3.	Beta.....	F-5
F.4.	Long Pulse Capability.....	F-7
F.5.	Lower Hybrid Current Drive.....	F-7

CHAPTER 1

INTRODUCTION

1.1. Introduction

1.1.1. Background

The last decade of tokamak research has seen continuous and often remarkable progress in the approach of tokamak plasmas to the reactor regime. For example, $n\tau_E$ values in excess of those required for breakeven have been achieved in Alcator C and FT (Frascati tokamak), temperatures in excess of the minimum necessary for ignition have been attained on PLT and PDX, and β -values in excess of the minimum required for practical design of a tokamak reactor have been achieved in D-III. Preliminary results from TFTR suggest that the confinement will be adequate to allow the goal of scientific breakeven to be achieved in the middle of this decade.

Taken together, these results imply that the tokamak is nearing the end of the scientific feasibility stage of its evolution toward the goal of a practical fusion reactor. According to DOE policy, the concept is thus entering a product definition phase, in which it must be established that the tokamak can result in an attractive, practical fusion reactor. While further improvement in confinement at high- β and fusion relevant temperatures must still be demonstrated (and these are, in fact, major goals of D-III and TFTR, respectively), the central task confronting the tokamak program is to show that certain issues related to the development of the tokamak to a practical reactor can be resolved.

Many of these issues can be classified as having to do with extension of the pulse length. Owing to considerations of thermal fatigue and first-wall maintenance a generally accepted value for the minimum length

of pulse of a tokamak reactor is about 10^4 s. In contrast, all currently operating tokamak experiments have pulses which last only 1 s or less under conditions of reactor-relevant density. It is interesting to note that the issue of extension of pulse length has been recognized within the national tokamak program at least since the late 1970's. Nevertheless, during the past five years there has been no significant increase of the pulse length in tokamak experiments in either the U.S. or the international community. This is so even though the transformer volt-seconds and the toroidal field pulse capability in many experiments are adequate to allow pulses of several seconds. The limitation in pulse length in present-day devices is due not only to constraints imposed by the magnetic systems but also to factors such as duration of auxiliary heating pulse, capacity of cooling systems and lack of long-pulse impurity control methods. Existing facilities simply do not have the capability to extend pulse length beyond original design values without extensive (and expensive) modifications.

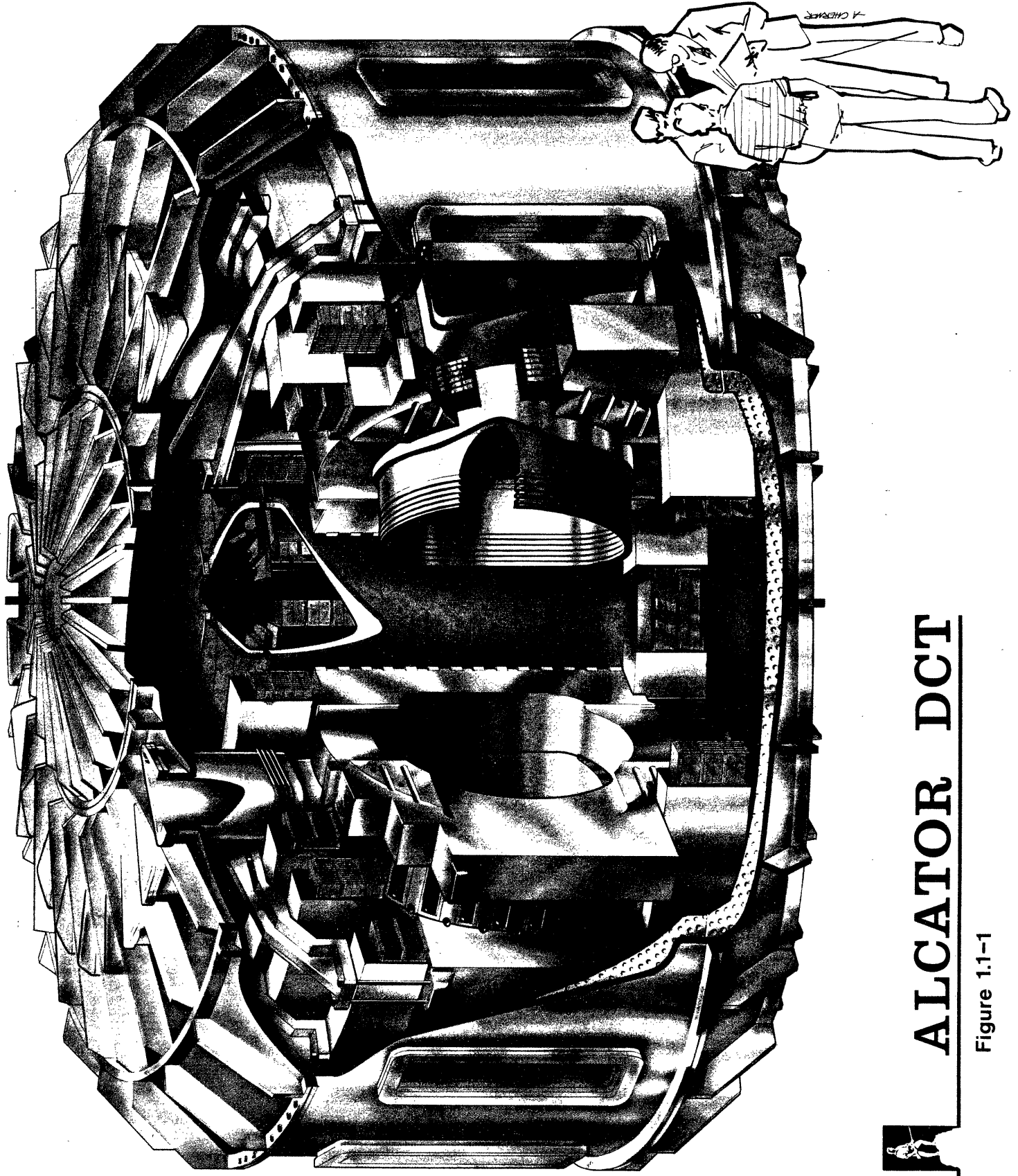
These considerations have motivated the proposed Alcator DCT device, a superconducting tokamak with major radius of 2.0 m, minor radius of 0.4 m and an axial toroidal field of 7 T. Both poloidal field (PF) and toroidal field (TF) magnets are entirely superconducting and can be operated at full performance continuously. The PF system permits plasma currents of at least 1 MA ($q = 3$, circular), allows elongations of 1.4 and produces a single-null divertor configuration with external coils. The baseline auxiliary heating package provides 4 MW of CW power at lower hybrid (LH) frequency, and 5 MW of CW power in the ion cyclotron frequency range. The LH power can be used either to heat electrons or to drive current, a feature which allows the possibility of true steady-state operation. An

isometric view of the proposed Alcator DCT is presented in Figure 1.1-1. A more detailed machine description follows in Section 1.2.

Extension of the pulse length to a duration greater than 100 s in a medium-scale experiment such as the proposed Alcator DCT represents a crucial step in the product definition stage of the tokamak concept. Successful accomplishment of the mission and achievement of the objectives will provide essential information for the tokamak engineering device and greatly enhance the potential of the pulsed tokamak as a practical reactor. Even more significant would be the attainment of a true steady-state in a tokamak operating with plasma parameters close to the reactor regime. Several important engineering advantages accrue from steady-state operation and this concept would lead to a substantially more attractive reactor.

1.1.2. Alcator DCT Objectives

The major purpose of the Alcator DCT program is to demonstrate long-pulse to steady-state operation of a tokamak with reactor level parameters. In this context, "long-pulse" means in excess of 100 s, and "reactor level parameters" implies densities of about 10^{20} m^{-3} and peak temperatures of at least 5 keV. In carrying out this mission, the Alcator DCT program will make important contributions in three distinct areas: plasma physics, plasma engineering and tokamak technology. This multi-faceted program is in contrast to those of present-day tokamaks whose major objectives are determined solely by plasma physics considerations. While such issues are certainly important to the evolution of a tokamak pulse, other issues which are at the interface between plasma physics and



ALCATOR DCT

Figure 1.1-1



engineering and technology are equally important.

The Alcator DCT design is based on many concepts which have been produced by the Development and Technology Program of OFE over the past several years. Because it is dependent on advanced technologies either developed or under development, it is more closely tied to D and T programs than any previous tokamak. This dependence could provide a new opportunity to strengthen both programs through a joint focus on a near-term advanced technology confinement experiment.

The breadth of the Alcator DCT program is reflected in the following set of programmatic objectives:

- Investigation and optimization of the time-evolution of high-performance tokamak discharges for pulse length well in excess of the resistive diffusion time.
- Development of methods of shape and profile control to optimize stability and performance under steady-state conditions.
- Development and evaluation of methods of non-inductive current drive and RF heating techniques appropriate for reactor level plasmas.
- Development of plasma edge, particle and impurity control methods required for long-pulse to steady-state operation with reactor level plasmas.
- Demonstration of fully-integrated, high-performance superconducting toroidal field (Nb_3Sn) and poloidal field (NbTi) systems.

- Development and evaluation of high heat flux and RF components appropriate for reactor applications.

The first two objectives are related mainly to plasma physics; the middle two to plasma engineering and the last two to tokamak technology. The issues which must be addressed in achieving these objectives and the approach which has been adopted in Alcator DCT are discussed in the remainder of this section.

1.1.2.1. Plasma Physics Issues

It is well known that a tokamak discharge cannot be considered to be in the steady-state until the passage of a few skin times τ_S where $\tau_S = \mu_0 \sigma a^2 / 4$. This time, which is essentially the time required for relaxation between two equilibria, is in the range 10-100 s for plasmas with multi-keV temperature and minor radius of the order of 1 m. In a typical tokamak scenario, a low temperature ohmic plasma is heated by an auxiliary heating pulse, a process which comes to thermal equilibrium on the energy transport time scale which is 1 s or less. The discharge is then in a flux-conserved state which will relax on the τ_S time scale to a new ohmic equilibrium. The fundamental physics questions are concerned with gross stability and effects on transport during this transient phase. The same considerations apply to controlling the current density profile by tailoring the spatial deposition of the auxiliary heating power.

An even longer time scale is involved in the case of non-inductive current drive. Here the relevant time is the L/R time $\tau_{L/R}$, which is about 2-3 times τ_S . The typical scenario in this case involves replacing the inductively-established current by one driven by non-inductive means.

As in the ohmic case, a pulse duration of 10-100 s is required before the new time-independent equilibrium can be established.

The Alcator DCT is ideally suited for investigation of these issues. Since both toroidal and poloidal field systems are superconducting, and since both the auxiliary heating and heat removal systems are designed for CW operation, there is no limit on pulse length imposed by thermal constraints. Thus true steady-state is possible in the non-inductively driven current mode. In the inductively driven case, pulse length limitations exist due to the finite value of the poloidal flux. It is interesting to note that the ratio of pulse length to skin time is given by

$$\frac{\tau_{\text{pulse}}}{\tau_{\text{skin}}} = \frac{\sigma_0 q_0}{\bar{\sigma}} \frac{\phi_P}{\phi_T}$$

where σ_0 and q_0 are, respectively, the conductivity and safety factor on axis, $\bar{\sigma}$ is a (weighted) volume-averaged conductivity, ϕ_P is the poloidal flux available for flat-top and ϕ_T is the toroidal flux in the plasma cross-section. For Alcator DCT, $\phi_P/\phi_T = 8.6$; for Tore Supra[†] $\phi_P/\phi_T = 2$ and for all other tokamaks presently operating or designed for operation during the 1980's, $\phi_P/\phi_T \lesssim 1$. Thus, Alcator DCT is uniquely suited to study long-pulse resistive relaxation phenomena.

Additional important physics issues are concerned with the development and optimization of techniques for non-inductive current drive.

[†]However, for Tore Supra, thermal limitations in the EF system constrain the pulse length at full performance to a maximum of 30 s, a value somewhat less than the expected skin time.

The only proven technique for RF generation of significant current is by lower hybrid waves. In particular, in the Alcator C experiments, RF currents of the order of 200 kA have been driven at average densities of $\bar{n} \approx 8 \times 10^{13} \text{ cm}^{-3}$ with injected power levels up to 1 MW. The key issue is efficiency, and the main factors which affect it are choice of frequency and plasma dielectric constant; design of the radiating grill, including use of phase control; and radial profile of the plasma electron temperature. Theoretical predictions suggest that optimization of the above factors should result in an efficiency of LHCD which is adequate for a reactor operating with Q in the range 10-20 (see Appendix F). The steady-state feature of such a reactor would appear to offset the relatively modest increase in recirculating power.

From the initial stages, the Alcator DCT design has been motivated by considerations of lower hybrid current drive optimization. The relatively high field on axis permits LHCD operation at reactor density ($\bar{n} = 10^{14} \text{ cm}^{-3}$) without serious degradation in efficiency. The wide ports accommodate arrays with up to 16 waveguides, resulting in spectra which are close to optimum. The introduction of a divertor should be useful both in controlling the production of impurities and permitting high edge temperature, thereby minimizing collisional absorption. Based upon the experimental and theoretical experience gained from the Alcator C experiment it is expected that CW currents in the range 0.5-1 MA will be generated in Alcator DCT with densities approaching $1 \times 10^{14} \text{ cm}^{-3}$.

In addition to the established lower hybrid technique, advanced forms of current drive will also be pursued, especially as they are proven feasible in small experiments. For example, current drive by the fast

wave branch of the lower hybrid modes should be tested on PLT and possibly Alcator C in the next few years. Should the results be encouraging, a more definitive test would be planned for Alcator DCT.

1.1.2.2. Plasma Engineering Issues

The term plasma engineering refers to the process of engineering design in which the role of the plasma occurs in a predictable way through established principles of plasma physics. The plasma can therefore be characterized, at least conceptually, by a set of input-output relationships insofar as interaction with other systems is concerned. For example, in the magnetic design of a divertor, the plasma is well described by MHD equilibrium theory and this description is adequate to determine the placement of coils in order to produce a desired magnetic configuration. Similarly, in the design of an RF coupler, the plasma can be characterized as a nonuniform, anisotropic dielectric for the purpose of calculation of the antenna impedance.

From the viewpoint of extending the tokamak pulse length, specification and control of the plasma edge parameters is one of the most important plasma engineering issues. Implicit in this conclusion is the assumption that effective edge control can be used to inhibit impurity generation. Apart from desorption mechanisms, impurities are produced primarily by melting or sputtering of material in contact with the plasma; it follows that edge control methods such as limiting the heat flux or softening the energy spectrum of the incident particle flux will reduce the impurity generation rate and thereby provide an effective means of impurity control. Of course, for a given generation rate, other means such as plasma

screening or RF pumping may also be effective in minimizing the net impurity concentration in the main plasma.

A key issue in this area is the degree to which the plasma outflux can be confidently predicted and controlled. Ideally, the heat outflux should be spread over as large an area as possible to minimize the power density; however, a number of physics phenomena can work counter to this strategy:

- Non-uniform plasma transport, D_{\perp} , $\chi_{\perp}(\theta)$
- Parameter dependent equilibria (β , $\ell_i/2$ variation)
- Equilibrium field coil misalignment and deflections
- Error fields due to current feed points
- Toroidal field ripple

Since energy scrapeoff widths are small (few mm-few cm) any of the above effects can lead to highly localized heat deposition. With the present state of understanding large margins must be designed for, perhaps as large as 5-10, especially in the case in which the large area, relatively low power density approach is followed. Clearly, much more understanding and experience must be gained in this area in order to proceed with confidence in the TFCD/ETR/Reactor sequence.

Control of edge plasma temperature and its maintenance at a sufficiently low value to control the sputtering rate is an essential aspect of long pulse impurity control. Several innovative approaches to this problem have been suggested: radiating cold-plasma mantel, stochastic magnetic limiter, expanded boundary magnetic limiter and the highly-recycling divertor. The first two techniques have yet to be demonstrated

on short-pulse devices; the latter two have been successfully demonstrated on a short-pulse basis on D-III (expanded boundary), and PDX and ASDEX (recycling divertor) and appear to have promise for successful application to a very long pulse tokamak. A proposed impurity control method can only be considered reactor-qualified when it has been used to produce an acceptable impurity level after all plasma physics and plasma engineering time scales have been exceeded by the pulse length.

The primary approach to edge control in Alcator DCT is a single-null, external coil divertor. With the present state of understanding of the impurity control problem, a divertor seems to be the prudent choice at this time. Further, the external coil configuration appears to be the most attractive form from the reactor viewpoint and a successful demonstration in Alcator DCT would qualify this approach for reactor use. By removing the baffles, the transition from a fully-baffled high-recycling divertor to an expanded boundary configuration can be studied. In addition, the pumped limiter concept is being carried along for use in Alcator DCT as a tokamak improvement, since it potentially offers a simpler approach to edge control. However, the obvious risks in the pumped limiter approach mitigate against adopting it as the primary method of impurity control.

While use of a divertor in a tokamak is mainly for the purpose of edge control, operation in a diverted configuration has implications on many physics, engineering and technology issues. In the plasma physics area, confinement, especially at high β , is likely to be significantly affected, as recent experience on ASDEX has shown; in the plasma engineering area, fueling and RF coupler design are impacted; and in the tokamak

technology area, the choice of wall materials and cooling techniques, and the design of the entire magnetic system and supporting structure are profoundly influenced by the divertor and its associated hardware. It is noteworthy that Alcator DCT will be the only tokamak in the U.S. program operating in the late 1980's which will be in a position to address those issues which are related to operation in a fully-diverted mode.

An issue related to edge control is plasma fueling. Experience on Alcator C has revealed that the density profile is relatively broad in the case of gas-puffing and peaked for pellet fueling. Specifically, if we take the form $n = n_0(1-r^2/a^2)^m$, we find $m \approx 0.5$ for the gas-puff and $m \approx 2$ for pellets. Consequently, for a given average density, the density in the vicinity of the edge is substantially lower in the pellet-fueled case. The two methods can therefore be used in combination to provide additional control in the edge region.

Unlike Alcator C, in which a four-shot pneumatic injector is adequate for fueling purposes, the Alcator DCT will require quasi-continuous injector operation. Two designs, both from ORNL, show promise for this purpose. A centrifugal injector has been operating for some time and seems capable of producing the pellet sizes, velocities and repetition rates necessary for Alcator DCT ohmic operation. Further work would be necessary to increase the velocity to that required for the RF heated plasma. An advanced pneumatic injector is under development and should have specifications similar to the centrifugal device.

The problems in pellet fueling RF heated plasmas in Alcator DCT are the same as those faced by other large devices. A good deal of community-wide effort has been put into understanding the interaction between the

ablating pellet and non-thermal particles. There should be a beneficial interaction between experiments on Alcator DCT and the general program. In this country, pellet injector technology has been developed primarily at ORNL. We would hope that the collaboration which has been so productive on Alcator C would continue on Alcator DCT.

1.1.2.3. Long Pulse Tokamak Technology Issues

Superconducting Magnetics - A superconducting tokamak will have a number of engineering features which are qualitatively different than in a copper tokamak. For example, the coils are constructed from very different materials and are far more sensitive to very low levels of energy disturbance relative to the energies stored in the magnetic system. The need for a liquid helium environment gives rise to a number of additional vacuum barriers with their inevitable impact on the electromagnetic characteristics of the tokamak. Almost every detail at the level of the coil current and cooling interconnections in a superconducting system involves entirely different technologies than in a copper system.

The reliability of an operating tokamak clearly depends on the reliability of the subsystems. It is generally extremely difficult to reach and repair many components in a conventional tokamak, and certainly even more difficult in a superconducting machine. Copper tokamaks have had a long evolutionary history of progressively larger steps, with previous steps contributing successful solutions as well as an elimination of less successful engineering designs. It was this rich background that allowed the world tokamak programs to make the single step from PLT to TFTR or JFT-2 to JT-60. Even in the most aggressive reactor development program,

the need for an intermediate size superconducting tokamak is imperative.

High Heat Flux Components - The most obvious area where technology issues must be addressed inside the vacuum envelope is that of limiter and divertor plates which must simultaneously handle high heat and particle fluxes with minimal detrimental effect to the plasma. Suitable materials and configurations must be found which have the following properties:

- Capability of handling $0.5 - 4 \text{ MW/m}^2$ on a steady-state basis.
- Exhibit unity recycling coefficient with $\Gamma \gtrsim 10^{16} \text{ cm}^{-2} \text{ s}^{-1}$ for a time on the order of 10 s.
- Contain only low- to medium- Z elements which will have minimum impact on plasma energy balance.
- Exhibit sputtering rates which produce acceptable erosion rate and plasma impurity level.

In addition, the material must be compatible with the vacuum and maintenance requirements of the device, and have good mechanical and thermal shock properties.

It is very unlikely that a single material can satisfy all of the above constraints in an optimum way. Instead, continuously graded materials or a composite, such as SiC-coated graphite brazed to a Cu base, offer more potential. Present Development and Technology programs support R&D aimed at finding attractive first wall components given specifications which are derived from plasma engineering considerations; only in situ use in long-pulse tokamaks operating with reactor level parameters can qualify a candidate for reactor applications.

RF Development - Included in the RF technology area is the entire RF system from source to coupler. As in the case of high heat flux compo-

nents, the coupler specification is determined primarily from plasma physics considerations. Contributions which can be considered to be primarily of a technological nature are: development of sources in selected frequency ranges (ECH, ICRH, LHH, . . .) and substantial power levels (~ 1 MW per tube); development of specialized high power components such as circulators, arc protection devices and RF power transport systems; development of reactor relevant vacuum barriers and antennas which are compatible with vacuum requirements and have high power-handling capability including the capacity for CW operation. Many of these elements clearly require the availability of a long-pulse device operating at near-reactor parameters for qualification to the TFCD/ETR stage.

The Alcator DCT device and the associated experimental program is extremely well suited to address the technology issues discussed in this section. The advanced superconducting TF and OH magnets will provide not only important fabrication experience but also enable an evaluation of the difficulties inherent in integration of the superconducting magnet system into the tokamak operating environment, including the effects of major disruptions. The expected heat and particle fluxes on limiter/divertor plates and first wall are comparable with those anticipated in a reactor; hence the performance of new materials and techniques can readily be evaluated and qualified for applications in the TFCD/ETR/DEMO sequence. In the RF area, the power densities expected at the antenna are characteristic of those expected in a reactor, as are the selected frequency ranges. In addition, the divertor configuration will impose certain constraints on the coupling problem which will force reactor-relevant approaches. Of course, it is recognized that in all of the technology areas, the Alcator DCT will permit only partial simulation of the reactor

environment; high-fluence interactions with 14 MeV neutrons must await the TFCD or, more probably, ETR.

1.2. Alcator DCT Description

1.2.1. General Considerations

The machine parameters and specifications of Alcator DCT have been determined by many, sometimes conflicting, boundary conditions. The fundamental constraints arise from the requirement that the device be capable of providing critical information needed in the areas of long-pulse physics, engineering and technology for the next major tokamak device, TFCD. It must also, however, be capable of exploring and developing advanced tokamak features such as quasi-steady-state and true steady-state operation, and simplified methods of impurity control. In addition, the device must be flexible with regard to shaping capability, permitting operation with desirable cross-sections such as ellipse and dee, and with advanced shapes such as the bean.

From an institutional viewpoint, any proposed toroidal device must satisfy the following constraints: 1) it must have an intellectual and technical challenge which is appropriate for an educational institution of high quality such as M.I.T., 2) it must build upon the scientific and technical expertise established within the Alcator Program, and 3) it must be of a scale which is within the capability of the resources of the Plasma Fusion Center.

The above programmatic and institutional considerations have led to the proposal of the Alcator DCT device, a tokamak of medium size, major radius $R = 2$ m, of moderately high toroidal field, $B_T = 7$ T, and with

fully superconducting toroidal and poloidal field magnetic systems. It is dedicated to the study and resolution of the long-pulse issues of plasma physics, plasma engineering and tokamak technology. The Alcator DCT program is of high intellectual challenge and builds in an optimum way on the expertise developed in the Alcator Program, specifically in areas of high field, high power density tokamak operation, RF heating and current drive, and advanced magnet design and development. It also uses existing equipment and facilities with as little modification as possible, in order to take advantage of savings in both cost and construction time.

1.2.2. Alcator DCT Specifications and Expected Parameters

Table 1.2-1 presents the major specifications of the Alcator DCT device, as well as the expected plasma parameters. The considerations which have led to the design choices and the rationale for the expected plasma performance are discussed in the remainder of this section.

TABLE 1.2-1

Alcator DCT Specifications and Parameters

A. Plasma Geometry

Major Radius	2.0 m
Minor Radius	0.4 m
Elongation (minimum)	1.4 at 1.0 MA
Triangularity (minimum)	0.2
Current	1.4 MA at $q=2.0$ and $\kappa=1.0$

B. Magnetics

Field on Axis	7 T
Ripple on Axis	0.04%
Max Field at Coil	10 T
TF Conductor	Cabled Nb ₃ Sn
TF Stored Energy	550 MJ
PF Conductor	Cabled NbTi
PF Stored Energy	120 MJ
Flux Change	35 Wb (double swing)

C. RF Systems

Lower Hybrid Range	4 MW CW at 4.6 GHz
Ion Cyclotron Range	5 MW CW at 180-215 MHz (7 MW at 10 sec pulse)

D. Anticipated Range of Plasma Parameters

Average Density	$0.5 - 2.5 \times 10^{20} \text{ m}^{-3}$
Peak Temperature	9 keV
Maximum Average Pressure	2 atmospheres
RF Driven Current	$> 0.5 \text{ MA @ } \bar{n}=7 \times 10^{19} \text{ m}^{-3}$
Pulse Time	$> 100 \text{ sec}$
$\epsilon\beta_p$	> 0.5
β	$> 1\% \text{ @ } 7 \text{ T}$

E. Plasma Edge

Power Density (Average)	$> 0.2 \text{ MW/m}^2$ at plasma surface
Edge Control	Divertor (external coil) Pumped Limiter
Fueling Method	Steady-state Pellet Injection Gas Puff

1.2.2.1. Plasma Geometry

The size of the Alcator DCT plasma is determined by two opposing considerations. On one hand, it is important to maintain the rather large value of flux linked by the OH transformer solenoid (17.5 Wb) in order to allow very long-pulse (100 seconds) studies even without RF current drive. The rapid decrease in flux for small reduction of the major radius sets an effective lower limit on R. On the other hand, an increase in major radius leads to a significant increase in the cost of the system, and in the power required, particularly for RF current drive. One of the premises of the baseline Alcator DCT design is that initial RF power levels be limited to present levels in order to use existing equipment.

Coupled with the choice of major radius is the selection of minor radius, or aspect ratio. The nominal aspect ratio of 5 results from two main factors: 1) it allows more effective utilization of the available RF power for heating by taking advantage of neo-Alcator confinement scaling (should it persist), and 2) it provides the opportunity for expanding the overall tokamak database to include the entire range of aspect ratios envisioned for possible reactors. The aspect ratio of 5 also permits relatively high field at the plasma, $B_T = 7$ T, compared to the field at the coil which is constrained to be 10 T by stress considerations. The many advantages of the relatively high field at the plasma are given in Section 1.2.2.2.

1.2.2.2. Magnetic Field Strength

The 10 T field at the coil is typical of design values for future superconducting TF magnets, and will therefore allow accumulation of

practical experience at this level. The aspect ratio of 5 is generally considered to be close to the upper bound on the range envisioned for reactors, since beyond this value the "engineering beta" is likely to degrade. Thus, the on-axis field of 7 T represents the largest practical value which can be achieved and maintained reliably with direct reactor significance. The virtues of the choice of high magnetic field are: 1) it allows operation with high plasma current and density in a machine of moderate size; 2) it permits operation with reactor-level pressure at modest β , e.g., $\bar{p} = 5$ Atm. at $\beta = 2.5\%$; 3) it allows efficient current drive by slow lower hybrid waves at reactor-relevant density and 4) it permits optimum use of existing RF equipment, namely the high power ICRF sources at 180-210 MHz.

Taken together, the dimensions and the field strength give a toroidal plasma current limit in the range 1.0-1.5 MA, which is needed for confinement of the fast particles generated by RF heating (particularly ICRF). Also, this range is sufficient to give satisfactory energy confinement scaling with those scaling laws which include a dependence on current.

1.2.2.3. Magnetics Technology

The superconducting toroidal and poloidal field coil systems are intended to be prototypical of tokamak reactors. Because of the high field at the TF coils, the only possibilities generally considered for the toroidal field conductor are either Nb₃Sn at 4.2 K, or NbTi at 1.8 K. We have chosen Nb₃Sn based on its advantages of simpler cryogenic requirements and a greater energy margin for stability against disturbances, particularly at high fields.

The Nb₃Sn conductor will be that used in the Westinghouse LCP coil and in the M.I.T. 12 Tesla test coil. The experience accumulated with this conductor is indicated by the fact that approximately 22 tonnes of this conductor have been fabricated, which is 40% of the Alcator DCT requirement. This is a full scale conductor directly usable in next-generation large machines.

The poloidal field coil systems will also be superconducting in order to maximize the capability for long-pulse operation, and to minimize the overall cost. Use of all copper PF coils would result in the consumption of more than 100 MW at full excitation. We plan to use cabled conductors, again in the form of the Westinghouse/Airco conductor for the PF systems. The lower fields at the PF coils (7 T in the OH solenoid; 5 T or less elsewhere) will permit the use of NbTi in this configuration.

1.2.2.4. RF Systems

One of the key features of Alcator DCT is the emphasis on the use of RF power as the primary heat source and for the generation of significant plasma current. The main RF programs will be ICRF heating of ions at the (second) harmonic of the ion cyclotron frequency in hydrogen plasma, and the use of power near the lower hybrid frequency for both electron heating and current drive. As indicated above, the design of Alcator DCT is predicated on using the significant RF equipment now at M.I.T. with minimal additional investment.

The ICRF program will use the FPS-17 radar transmitter tubes obtained from the Air Force. These RCA tubes can be operated at 0.5 MW each under steady-state conditions, and at 0.7 MW for up to 10 seconds. With the

replacement of the 100 kW driver tubes and the procurement of a low voltage (< 20 kV) power supply system, ten of these units will provide 5.0 MW of CW source power. The operating frequency is in the range of 180-210 MHz, covering the hydrogen harmonic cyclotron frequency for magnetic fields in the range of 6-7 Tesla.

Lower hybrid power will be provided by an upgraded version of the present Alcator C system. The power supply and modulator system need to be upgraded for continuous operation, and new water-cooled couplers must be developed. The required modifications are considered to be relatively minor. Each of the 16 klystrons has already been tested under CW conditions at the 0.25 MW level. This system will provide a source power of 4.0 MW at 4.6 GHz.

In the heating mode, the use of these systems will allow operation with average plasma pressure exceeding 2 atmospheres. We also expect to be able to generate steady-state toroidal plasma currents of at least 0.5 MA at densities above $0.7 \times 10^{20} \text{ m}^{-3}$. This equipment will also provide the power needed for studies of RF driven current ramp-up and of RF maintenance of the current during transformer recharge (quasi-steady-state operation).

1.2.2.5. Plasma Parameters

The selection of target values for the plasma parameters in Alcator DCT is based on the importance of maintaining levels of energy density and flux at the plasma surface which are large enough to be relevant for reactors. The average plasma pressure, or equivalent energy density, is expected to be in the neighborhood of 2 atmospheres, comparable to that

anticipated in several reactor studies. The average density ($1-2 \times 10^{20} \text{ m}^{-3}$) and the temperature range (up to 9 keV) are each at appropriate levels. These parameters are required in order that the results of studies on Alcator DCT, for example in RF current drive and heating, be of direct use in the design of next-generation large machines. The heat flux at the plasma surface (up to 200 kW/m^2) is sufficient to allow realistic performance testing of components for these next devices. Furthermore, these parameters together give values of $\epsilon\beta_p \gtrsim 0.5$, which put Alcator DCT in the "finite-beta" regime of plasma equilibrium.

1.3. Programmatic Role

1.3.1. Role within the Toroidal Confinement Program Plan

The Toroidal Program Planning Office has prepared a plan which outlines a program leading to the realization of an economically attractive magnetic fusion reactor. It reflects the views of the toroidal confinement community and provides a framework within which to evaluate the role of Alcator DCT.

According to the Draft Plan, the major program issues can be outlined as follows:

A. Reactor Feasibility Issues

1. Demonstration of high power multiplication in moderate reactor size.
 - 1.1 Sufficiently high $n\tau_e$ -values for ignition.
 - 1.2 Sufficiently low recirculating power.
2. Demonstration of high fusion power density with practical magnet systems.

- 2.1 Sufficiently high plasma beta value.
- 2.2 Sufficiently high ratio of field strength at the plasma to field strength at the magnet coils.

B. Reactor Development Issues

1. Demonstration of optimal plasma heating methods.
2. Control of plasma impurities and removal of fusion ash (helium).
3. Extension of pulse length to quasi-steady-state or even steady state operation.
4. Control of gross plasma transients.

C. Issues of Supporting Technology

1. Development of large superconducting-coil systems for operating tokamak devices.
2. Development of long-lived first-wall materials and components for operating tokamak devices.
3. Development of cost-effective sources for RF and beam heating.
4. Development of the nuclear-engineering aspects of fusion power.

D. Issues of Reactor Design Optimization

1. Mechanical-components cost, lifetime and maintainability.
2. Auxiliary-systems cost and complexity.

As should be clear from the material presented in this chapter, the primary purpose of Alcator DCT is to address the Reactor Development Issues of Plasma Heating, Impurity Control, Pulse Length Extension and Transient Control. This point is further underscored in Figure 1.3-1 which identifies the devices in which the Class A and B issues will be addressed, and which depicts Alcator DCT as the primary vehicle for addressing Class B issues during the latter part of this decade.

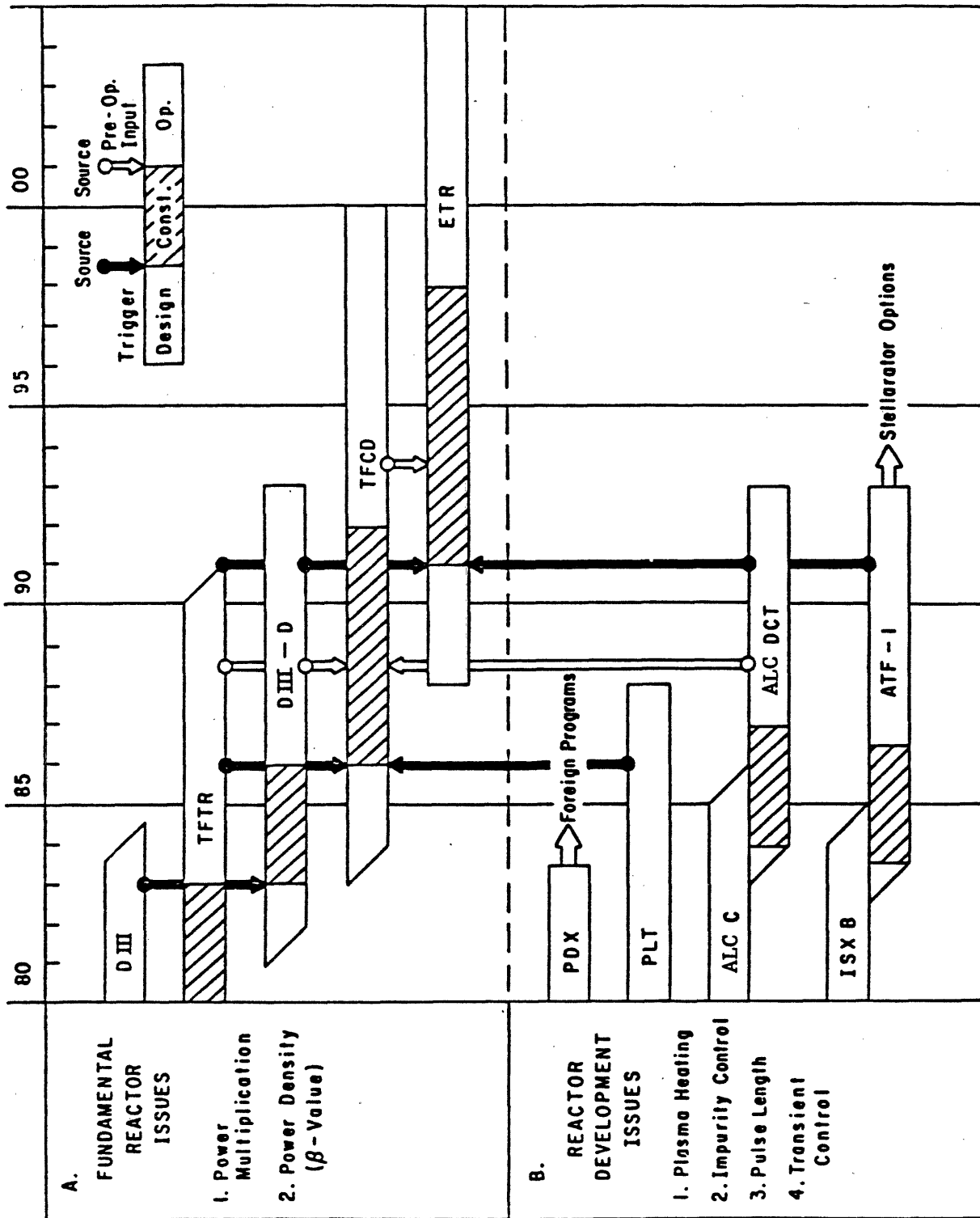


FIGURE 1.3-1 Toroidal Confinement Program Plan by Device

An additional important role of Alcator DCT is to address the Class C issues of supporting technology, especially issues C-1 and C-2.

With regard first to issue C-1, we note that plans for tokamak steps beyond TFTR generally include superconducting windings either for both the TF and PF or for the PF alone. We argue that it will be excessively risky to take that step without the benefit of an intermediate scale superconducting tokamak.

The benefit of intermediate steps has been recognized in the European fusion program, where Tore Supra will provide a superconducting technology background to be combined with JET to go forward into NET. The Soviet program through T-7 and T-15 is clearly pursuing a step-by-step build-up of superconducting background. Discussions are currently being held in Japan toward commissioning a superconducting up-grade version of JFT-2M to provide this intermediate scale experience. Alcator DCT could provide an excellent intermediate scale superconducting tokamak background for the US program.

The mirror program has recognized the value of a step-by-step introduction of superconductor technology. The recently successful MFTF Yin-Yang coil represented the third in a series of superconducting baseball coils built over a ten year period at Lawrence Livermore National Laboratory. The tokamak environment will be more difficult than the steady-state nature of the mirror, placing an even greater premium on pre-steps.

The U.S. fusion program has invested heavily in the "Large Coil Project" to gain intermediate scale experience in toroidal field magnets. This test stand approach has certain advantages, principally in accommo-

dating multiple approaches and encouraging testing beyond nominal specifications. It unfortunately has limitations in not adequately simulating a true tokamak environment and in not forcing solution of a host of integration problems.

There are also limitations in some of the coil solutions chosen in LCP. For example, because the coil specifications were very relaxed with regard to disruption simulation, many of the conductors are not sufficiently subdivided to guarantee stability under realistic disruption conditions. Peak fields in LCP are also limited to 8 Tesla. The one LCP conductor which is considered sufficiently stable and extendable to higher field is the Westinghouse/Airco Nb₃Sn conductor, which is the conductor we have chosen for Alcator DCT.

Superconducting poloidal field coil development is far behind toroidal coil development largely because nearly all available development resources have been devoted to TF development. Poloidal field conductors differ from toroidal field conductors principally in their need to be sufficiently finely divided to limit pulse field losses and to remain superconducting during PF field changes. The requirements for subdivision are in conflict with mechanical requirements in many of the proposed poloidal field conductors. A PF coil development program will clearly be required before such conductors could be reliably used in next step machines; Alcator DCT can provide an essential part of that necessary development program.

An additional opportunity for technology contributions is the C-2 issue of first-wall materials and components. For example, there is currently no proven tile or tile attachment concept capable of steady-state

heat removal, although the high heat flux program will clearly pursue this goal in a generic way. If the high-heat flux program were to take as one of its goals the production of a steady-state rated generic tile, typically 5×5 cm, then Alcator DCT would be able to adopt them directly for use. Similar interfaces could obviously be developed in the area of CW RF components and magnetics.

Alcator DCT could also provide an extended opportunity for international cooperation in technology development. For example, there is a clear indication of interest in both Japan and Europe in expanding poloidal coil development and both see Alcator DCT as a near term driver for that development. The Japanese and European programs both see advantages to supplying portions of the Alcator DCT PF system, and in participating in machine operations. Discussions have also been held on the possibility of supplying some of the toroidal field coils from overseas programs.

1.3.2. Relationship to TFCD

Alcator DCT shares many probable features of TFCD and therefore provides a suitable testbed. First wall high heat flux components and CW RF launchers are clear areas in which the TFCD requirements overlap with those of Alcator DCT. In the magnetics area, possible TFCD options vary from all superconducting, to mixed copper and superconducting TF hybrid magnets, to copper TF magnets with superconducting PF magnets. It is of particular note that the central core PF coil in all the TFCD options is quite comparable to the Alcator DCT transformer. This is largely because the aspect ratio of 5 in Alcator DCT permits a large transformer space. Development of components for Alcator DCT transformer therefore provides

a direct development for TFCD. By the same token, any early development activities for TFCD can provide upgrades for Alcator DCT which can, in turn, serve as a long-pulse qualification test bed.

The toroidal coils in Alcator DCT will utilize high current conductors which are directly extrapolable to TFCD should a superconducting TF coil option be chosen. The Alcator DCT Nb₃Sn TF conductor will also be suitable for use in a TFCD PF central core transformer should it be necessary to choose a higher field for the TFCD core, or to provide additional stability margin to meet the TFCD requirements.

The availability of a small machine like Alcator DCT to serve as a test bed and as an early confirmation of concepts can easily pay for itself many times over in a project of the scale of TFCD. The schedule relation of the two projects is shown in Figure 1.3-2, as well as the interrelation which would be possible in an area such as PF development. The development shows a parallel path in which: 1) early developments would be utilized in Alcator DCT and qualified for use as detailed design concepts for TFCD, and 2) subsequent, more optimized developments could be fed back into Alcator DCT upgrades and become TFCD component qualification tests. A similar parallel path strategy can be evolved for first wall components and CW RF systems.

1.3.3. Relationship to other Experiments

1.3.3.1. Existing Copper Devices and their Upgrades

All existing tokamak devices in the U.S. (see Figure 1.3-1) have pulse lengths of about 1 s, which is clearly too short to address the issues discussed in Section 1.1.2. Consequently, examination of the long-

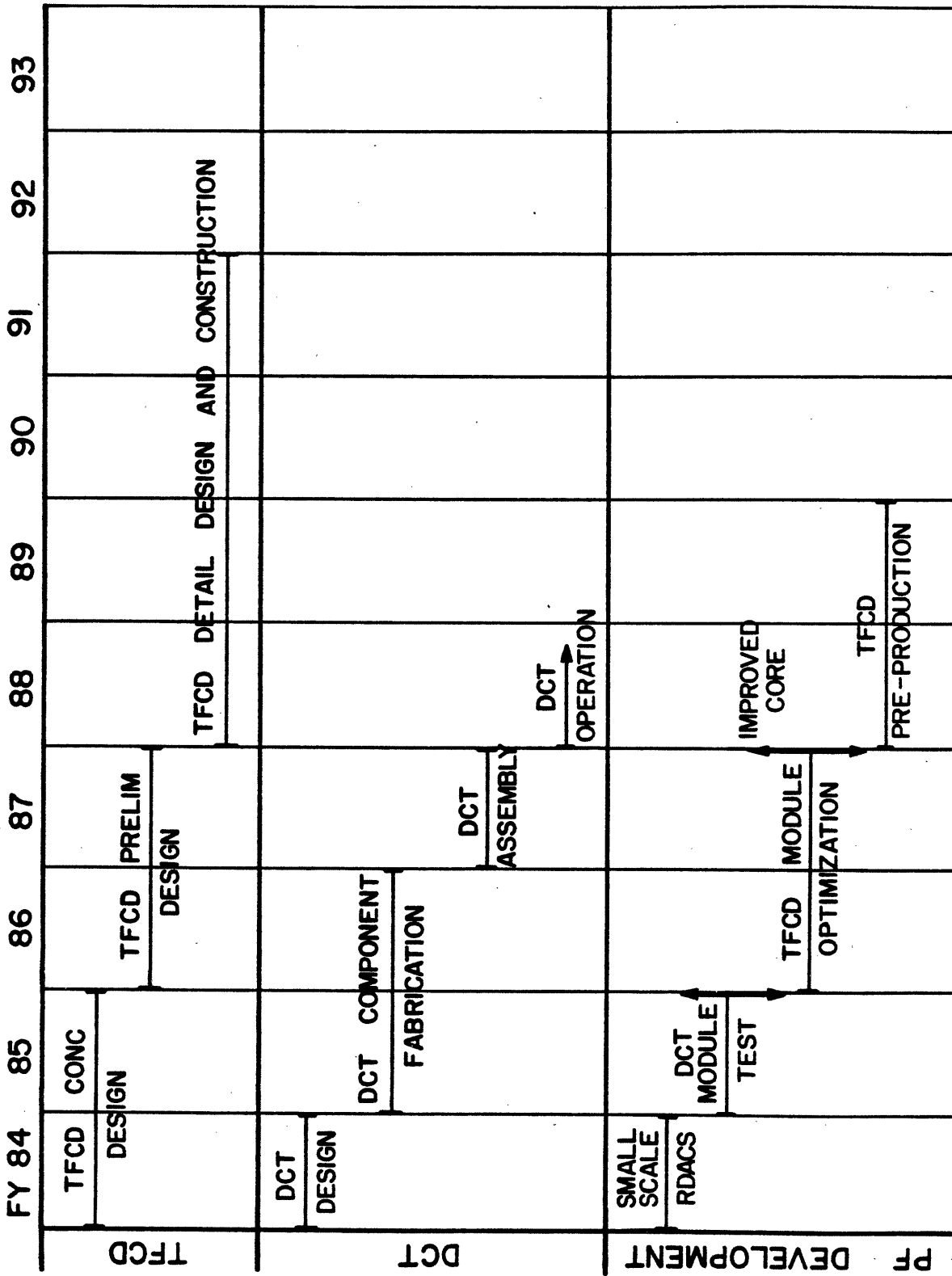


FIGURE 1.3-2 Relationship of TFC and DCT Programs

pulse issues within the context of the existing program will require, at a minimum, substantial extension of the capabilities of these facilities.

In general, the areas in which long-pulse upgrades would have to occur are: duration of the auxiliary heating pulse; capacity of the cooling systems; protection of the first-wall; and increase of the transformer volt-seconds available for current flat-top. The minimal cost of such enhancements to any existing tokamak within the U.S. program, in order to achieve pulse lengths on the order of τ_S , is equal to or somewhat greater than the cost of the proposed Alcator DCT.

In addition, choosing the path of enhancing the performance of an existing copper device(s) for the purpose of pulse length extension has a number of significant disadvantages relative to proceeding with Alcator DCT:

- At best, the pulse length would be equal to one skin time, and this is achievable only with sub-optimal plasma parameters. Hence, time scales in excess of the skin time which might allow stable routes of access to optimized high performance regimes (for example, through profile control) would be prohibited. Degradation in parameters derives from the fact that the TF and possibly the PF magnet systems must be derated for long pulses, since they were originally designed for short-pulse, low duty-cycle operation.

- Development and demonstration of quasi-steady and true steady-state modes of operation by lower hybrid current drive at reactor-relevant parameters would be prohibited, owing to the low toroidal field.
- Inadequate impurity control methods, especially the lack of an appropriate divertor, may limit the pulse length and result in unoptimized regimes.
- No TFCD/ETR-relevant technology contributions nor integration experience would be gained in the superconducting magnetics area.

Except for the lack of adequate impurity control methods, the foregoing disadvantages also apply to a comparison of Alcator DCT with ASDEX-UPGRADE, to be built at Garching, FRG. It is concluded, then, that although pulse length extension in existing copper devices may be feasible, the cost to the OFE program will be at a minimum equal to that of Alcator DCT. Such extended performance devices can, at best, address only a small subset of the important issues which would be addressed by Alcator DCT.

1.3.3.2. Comparison to Tore-Supra

Finally, it is appropriate to comment on the relationship of Alcator DCT to Tore-Supra, which is the only other funded tokamak with long-pulse objectives outside of the Soviet Union. A U.S.-France workshop was held in Cadarache, France in June 1983, to examine the capability of Tore-Supra in addressing long-pulse issues and to compare the Tore-Supra approach to that taken in Alcator DCT. An extensive trip report prepared

by attending members of the Alcator DCT team is on file in OFE Headquarters, as is a report prepared jointly by OFE and non-M.I.T. personnel. In the remainder of this section, a synopsis of the comparison prepared by the M.I.T. team is presented.

A comparison of the physical characteristics of Tore Supra and Alcator DCT is provided in Table 1.3-1.

TABLE 1.3-1

Physical Characteristics of Tore-Supra and Alcator DCT

	<u>Tore-Supra</u>	<u>Alcator DCT</u>
Plasma major radius, R_0	2.25 m	2.0 m
Plasma minor radius	0.70 m	0.40 × 0.56 m
Vacuum vessel bore	1.8 m	1.1 × 1.56 m
Toroidal magnetic field ($R = R_0$)	4.5 T	7.0 T
Maximum field in conductor	9.0 T	10.0 T
Toroidal field coil mean diameter	2.6 m	1.5 × 2.0 m
TF conductor	NbTi	Nb ₃ Sn
Weight of superconductor	45 t	66 t
Total magnet weight	160 t	180 t
Total magnetic energy	600 MJ	580 MJ
Plasma current ($q = 3$)	1.7 MA	1.0 MA
Maximum discharge duration	30 s	∞
Poloidal field conductor	Cu	NbTi
Total flux swing ($R = R_0$)	21 Wb	35 Wb
Flux available for current plateau	8 Wb	25 Wb
Weight of induction coil	56 t	30 t

The toroidal field magnets for both machines are superconducting: NbTi in Tore-Supra and Nb₃Sn in Alcator DCT. Tore-Supra is larger, having 20% greater major radius, and has slightly more than twice the cross-sectional area. Alcator DCT has a higher toroidal field (7 T vs. 4.5 T) and the stored energies in the toroidal magnets are nearly the same. The poloidal field system in Tore Supra is fabricated from water-cooled copper coils and this limits the maximum pulse length to 30 s at full current, which is 1.7 MA at $q = 3$. The poloidal field system in Alcator DCT is fabricated from NbTi superconducting coils and there is no limit on pulse length. The $q = 3$ current is 1 MA for circular plasmas and the poloidal system is capable of 1.5 MA plasma current at lower q or with elongation. The transformer flux swing in Tore-Supra is 21 Wb with 8 Wb available for current flat-top and this compares with 35 Wb and 25 Wb respectively in Alcator DCT. At the same central temperature and Z_{eff} , Alcator DCT would be capable of about twice the pulse length.

Special capabilities of Tore-Supra and Alcator DCT are compared in Table 1.3-2.

TABLE 1.3-2

Capabilities of Tore-Supra and Alcator DCT

	<u>Tore-Supra</u>	<u>Alcator DCT</u>
<u>Shape</u>	Circle	Circle, Ellipse, Dee, Bean
<u>Impurity Control</u>	Poloidal pumped limiter; ergodic magnetic limiter	Poloidal divertor; toroidal pumped limiter
<u>RF Heating (CW at Source)</u>		
ICRF	9 MW [†]	5 MW
LHH and LHCD	8 MW [†]	4 MW

Tore-Supra is able to produce plasmas of circular cross-section only, whereas Alcator DCT has the capability to operate with elliptical and dee shaped plasmas with the base coil package, and bean-shaped plasmas with the addition of an internal coil. In the impurity control area, Tore-Supra is relying on conventional poloidal limiters, some of which can be pumped, and the design team is studying the use of an ergodic magnetic limiter as a backup. The Alcator DCT design features a single null poloidal divertor and a full toroidal pumped limiter as an advanced feature. The divertor can also be run in an expanded boundary mode. Finally, in the RF heating area, each device will utilize RF power at both ion cyclotron and lower hybrid frequency. The RF power in all cases has CW capability, and as is seen from Table 1.3-2, the proposed RF power level for Tore-Supra is about twice the baseline RF power planned for Alcator DCT.

[†] The RF program for Tore-Supra is in the proposal stage and, at the time of preparation of this proposal, has not been approved.

As the volume of Tore-Supra is slightly more than twice that of DCT, the ratio of pressures attained in these devices will be nearly equal to the ratio of the confinement times. Owing to the higher toroidal field, the density limit for current drive in Tore-Supra should be lower by the factor 2.5 relative to the density limit in Alcator DCT. Thus, efficient current drive should be produced in Tore-Supra at densities up to $4 \times 10^{19} \text{ m}^{-3}$ and in Alcator DCT at densities up to $1 \times 10^{20} \text{ m}^{-3}$.

There are four principle magnetics design issues which distinguish Alcator DCT from Tore-Supra:

- A toroidal field conductor approach which utilizes full scale niobium-tin conductors at 4.2 K versus subscale niobium-titanium conductors at 1.8 K.
- Non-circular TF coils with a peak field of 10 tesla, versus circular coils with a peak field of 9 tesla.
- An air-core all superconducting PF system versus an iron-core copper coil PF system (with a one coil superconducting substitution as a follow-on phase technology demonstration).
- A base line PF system designed for full performance shaping and diverting, versus a PF system designed to maintain circular plasmas.

We consider these to be important differences which have a direct bearing on next-step mainline machine design considerations. We believe that these differences, when coupled with the need to develop and maintain a national technology base, make a strong rationale for construction of Alcator DCT.

CHAPTER 2

PLASMA PHYSICS CONSIDERATIONS

2.1. Introduction

The Alcator DCT physics program is primarily concerned with issues related to long-pulse and steady-state tokamak operation. Specifically, we address the problems of transport, equilibrium and stability, divertor and edge physics, RF heating, and RF current drive in the context of very long time scales. In the following sections we present detailed discussions of each of these topics, and provide results of computer calculations for some particular cases.

These calculations have been carried out with several specialized codes designed to study specific aspects of the problem. For example, the RF current drive efficiency has been investigated using a sophisticated ray-tracing and Fokker-Planck code to deal with the RF-plasma interaction, coupled to a rather simplified transport model. The study of plasma regimes, on the other hand, employs a more detailed transport code in conjunction with an idealized RF power deposition model consistent with the ray-tracing results. This approach has permitted us to efficiently investigate the essential features of each aspect of the problem over a wide range of parameters. At the same time, we have attempted to maintain consistency among the assumptions required for each computation, keeping in mind the mutual interdependence of the effects being studied.

The relationships among these various physical processes, particularly as they result in the establishment of multiple time scales, become especially important in the study of steady and quasi-steady-state plas-

mas. For example, the evolution and control of the equilibrium cannot be considered independently of the heating and current generation processes, while the RF heating efficiency may depend on the edge physics and impurity control. In addition, the interaction between physical processes and plasma technology issues, such as heat removal and first wall materials requirements, becomes particularly strong for long pulse or continuous operation. A major feature of the Alcator DCT program lies in the ability to investigate such synergistic effects in high performance tokamak discharges.

2.2. Plasma Regimes

2.2.1. Introduction

We have investigated the anticipated operating regimes of the Alcator DCT tokamak by performing transport simulations with the BALDUR [2.2-1] and ONETWO [2.2-2] codes. This work has been carried out as part of the design process in order to estimate the accessible parameter space, assess the impact of engineering related constraints on plasma performance, and evaluate the suitability of the resulting parameter range with respect to the primary mission of the device. We have studied plasma evolution using a variety of transport models, described in detail below, to insure that the final design is capable of achieving its objectives in spite of potentially unfavorable confinement behavior associated with auxiliary heating. The effects of variations in plasma size, toroidal field, current, ripple, impurities, etc. have been investigated.

The plasma parameters of principal interest are those which directly relate to the attainment of long-pulse and quasi-steady-state conditions.

In the case of inductively maintained plasma current, the pulse length achievable with a given flux swing is determined primarily by the electron temperature and the impurity level, while the volt-seconds available are determined by the transformer capability, the plasma inductance, and the dissipation during the current rise phase. The length of the quasi-steady phase of the pulse can be evaluated from

$$t_{\text{pulse}} = \frac{\phi_{\text{pf}} - LI_p - \phi_{\text{diss}}}{V_\ell} \quad (1)$$

where $\phi_{\text{pf}} = 35$ Wb is the total flux swing provided by the poloidal field system, the plasma inductance L is approximately given by

$$L = \mu_0 R [\ln(8 R/a) - 2 + \ell_1/2], \quad (2)$$

ϕ_{diss} represents the dissipative loss integrated over the current rise phase, and V_ℓ and I_p are the quasi-steady surface voltage and plasma current respectively. The electron temperature also has a significant effect on the efficiency of non-inductive current drive, as described in Section 2.4 below.

A major topic of investigation in the Alcator DCT physics program concerns plasma shape and profile control for times long compared to the current diffusion time scale. An important aspect of this study is the maintenance and control of high pressure equilibria, for which details of the pressure and current density profile shapes can strongly influence stability with respect to kink and ballooning modes. The ability to produce long-pulse or steady-state discharges with large values of $\epsilon\beta_p$ is therefore of interest.

2.2.2. Ohmic Plasma Parameters

While Alcator DCT is essentially an RF-driven tokamak, most of the anticipated modes of operation involve an ohmic start-up and target plasma. Since the efficiency of the RF heating and current drive can depend on the target parameters, it is important to characterize this pre-injection discharge. While transport in ohmically heated plasmas is by no means well understood, several commonly used empirical models have proved relatively successful in modelling contemporary experiments. The two models we have chosen represent optimistic and pessimistic limits with respect to the present design, and so effectively bracket the expected parameter range for ohmic plasmas.

The principal difference between the two models lies in the choice of the electron thermal conductivity. The more optimistic, referred to as the "neo-Alcator" coefficient, takes into account a favorable dependence on major radius consistent with that observed in experiments on Alcator C [2.2-3] and in statistical studies of a variety of tokamaks [2.2-3, 2.2-4]. The full expression is given by

$$K_e = 5.0 \times 10^{20} r/R^2 + n_e D_b f(q) + n_e \chi_{eNC} \quad (3)$$

where D_b is the Bohm diffusion coefficient, χ_{eNC} is the neoclassical electron thermal diffusivity, and the function

$$f(q) = \begin{cases} 1 - 1/[1 + (1/q - 1)^2] & \text{for } q < 1 \\ 0 & \text{for } q > 1 \end{cases} \quad (4)$$

accounts for the time averaged effect of sawtooth activity. The leading term results in a confinement time proportional to nR^2a for electron dominated discharges, consistent with the findings on Alcator C and recent preliminary results from TFTR [2.2-5]. As a more pessimistic assumption, we have taken the more familiar INTOR expression

$$K_e = 5.0 \times 10^{17} + n_e D_b f(q) \quad (5)$$

which leads to electron confinement times proportional to na^2 . While this coefficient has been frequently used in reactor studies, we note that essentially all large scale tokamaks have obtained somewhat better ohmic confinement than that predicted by the INTOR scaling.

In each case we have modelled the ion thermal conductivity as

$$K_i = 3.0 \times K_{iNC} + n_i D_b f(q) \quad (6)$$

where K_{iNC} is the neoclassical ion thermal conductivity given by Chang and Hinton [2.2-6]. The majority ion species diffuse with a coefficient

$$D = 0.2 \times \chi_{eAN} + n_i D_b f(q) \quad (7)$$

with χ_{eAN} the anomalous electron thermal diffusivity for each case. A pinch corresponding to one times the Ware neoclassical value is used. Impurity ions are either modelled by fixed Z_{eff} profiles due to oxygen or carbon, or are allowed to transport with the same coefficients used for the hydrogenic species. The resistivity is taken to be the Spitzer value, with no trapped particle correction or bootstrap current.

Typical parameters for the ohmic plasmas are shown in the plots of central electron and ion temperature vs. density for three different

currents in Figure 2.2-1a and 2.2-1b. Values are in the 1.1 - 1.8 keV range for both models except in the case of the lowest current, for which ion conduction is a dominant loss process. This temperature range corresponds to loop voltages of roughly 1 - 2 Volts, for which pulse lengths of 15-30 sec are achievable using ohmic heating alone. These plasma parameters, aside from the long pulse length, are similar to those obtained in contemporary tokamaks with ohmic heating, and are suitable for target plasmas for RF heating and current drive experiments.

A time dependent simulation of plasma start-up, using the "neo-Alcator" transport model, is shown in Figure 2.2-2. In this case the current is raised to approximately 1 MA in 1.5 seconds, while simultaneously the density is increased by gas puffing from a "breakdown" value of $5 \times 10^{12} \text{ cm}^{-3}$ to approximately 10^{14} cm^{-3} . Several interesting effects appear in the simulation. The density profile, which becomes flat or slightly hollow during the strong gas puff, begins to show a pronounced peaking following the cessation of fueling at 1 sec. At approximately 1.4 sec. current penetration reduces the axial q below unity, and the onset of sawtooth transport, modelled by the second term in Equations 3, 6, and 7 above, leads to a flattening of the central profiles of temperature and density. Although the central temperatures reach their equilibrium values fairly soon after the current plateaus at 1.5 sec., the loop voltage is still decreasing due to current penetration and the resulting variation in internal inductance at 2.5 sec., when the RF heating pulse is turned on. For this case the dissipative volt-second consumption during the current rise is approximately 2.5 Wb, and an additional 1.5 Wb is accounted for by the internal poloidal flux.

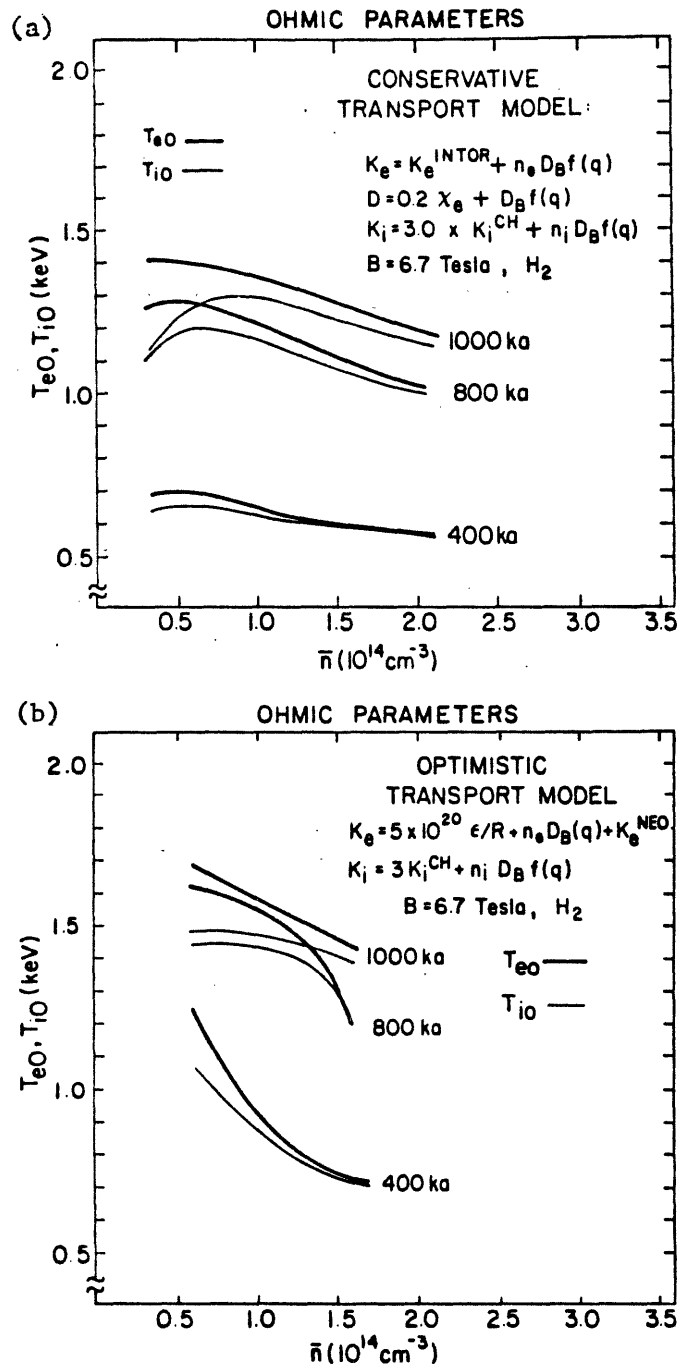


FIGURE 2.2-1 Central electron and ion temperatures for ohmic plasmas assuming (a) INTOR and (b) Neo-Alcator scaling.

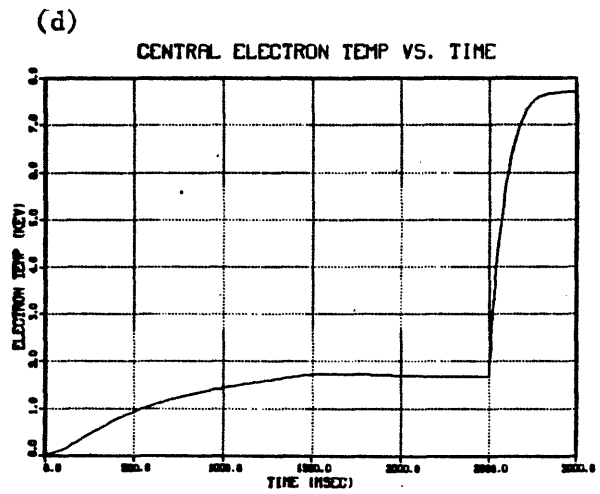
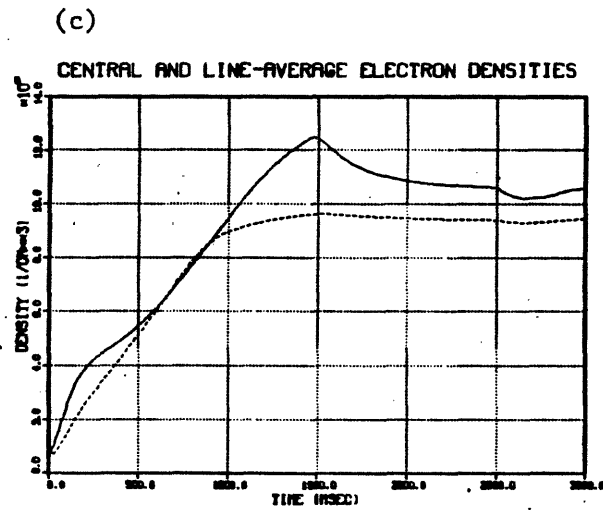
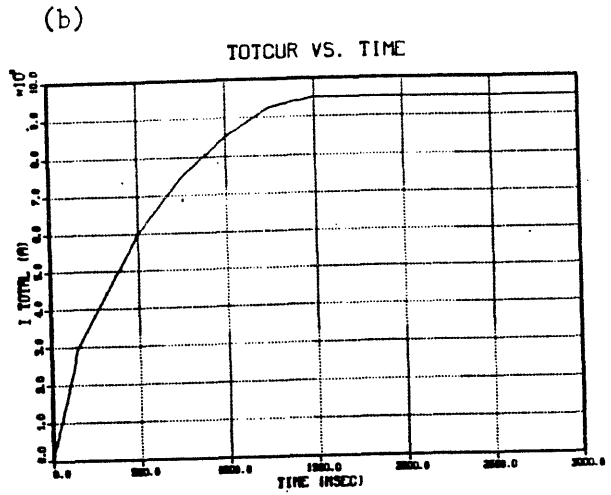
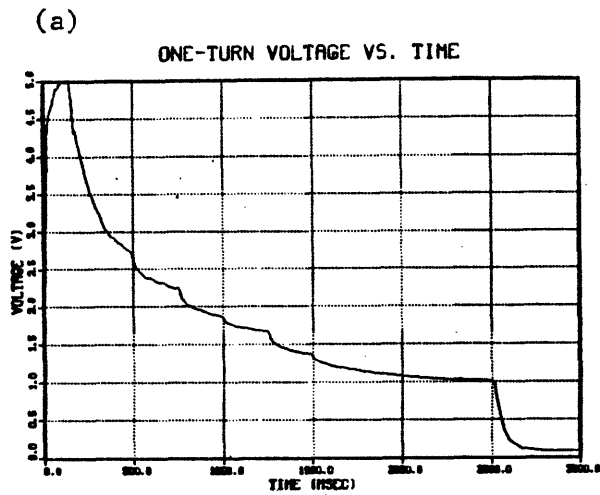


FIGURE 2.2-2 Typical start-up simulation assuming Neo-Alcator transport model. Gas puffing occurs from 0 to 1.0 sec. RF heating begins at 2.5 sec.

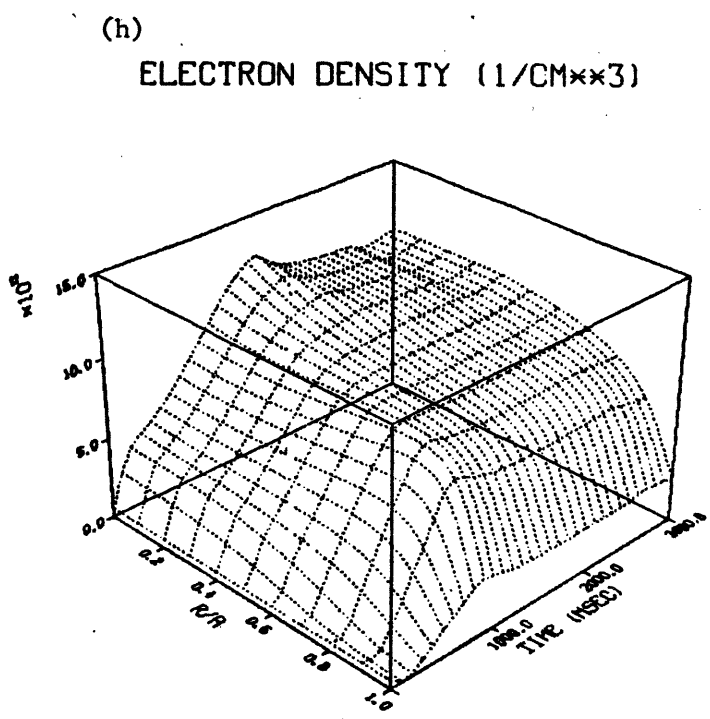
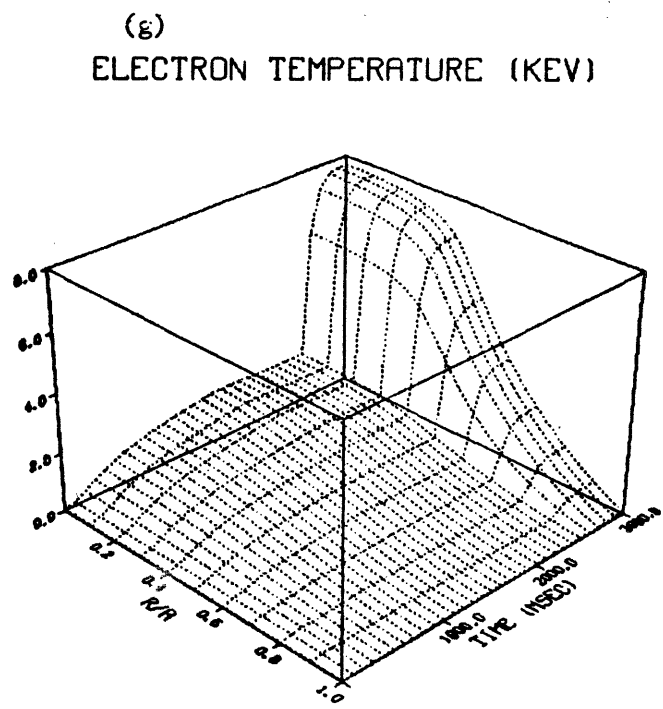
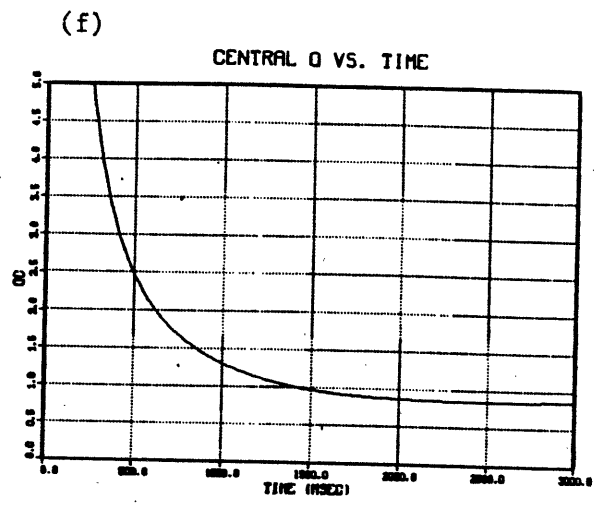
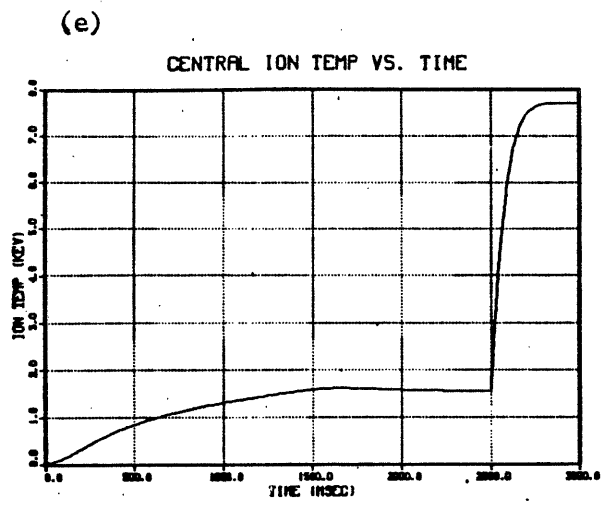


FIGURE 2.2-2 Continued from previous page

2.2.3. High Power Heating Simulations

The Alcator DCT tokamak will use both ion cyclotron (ICRF) and lower hybrid heating (LHH), as well as RF current drive. Detailed calculations and simulations with respect to the physics involved in these processes are described in Sections 2.4 and 2.5 below. In order to evaluate the plasma parameters achievable using the available heating power, we have also performed a series of transport simulations using a simplified power deposition model. Several model transport coefficients have been employed in an effort to take into account the variety of experimental results on existing tokamaks studying auxiliary heating. While the physics involved in these cases is even less well understood than for ohmic plasmas, the range of assumptions included in our study includes the most reasonable extrapolations from present results, and should be sufficient to approximately predict the operating regimes of the new experiment. In addition, while the details of the models chosen may be faulty, they nevertheless are useful in examining, qualitatively, effects such as current penetration and impurity influx, which are expected to be of interest in the operation of long-pulse or steady-state plasmas.

The RF power deposition model used in all of the cases discussed below consists of a simplified input profile, with specified power densities supplied to electrons and ions within a given radius. Following the results of detailed calculations presented below, we have generally taken the power to be absorbed uniformly within $r/a = 0.5$, although some studies have been conducted on the impact of heating off-axis and with different absorption profiles. ICRF power has been assumed to be coupled predominately to majority ions by second harmonic cyclotron

damping with an overall efficiency relative to the power at the source of 60%. RF in the lower hybrid range of frequencies (LHRF), whether for heating or current drive, is expected for our parameters to be absorbed by electrons through Landau damping; we estimate the overall efficiency to be 70-75%. The total CW power available, 4MW of LHRF and 5MW of ICRF, therefore corresponds to 3MW of each frequency deposited in the plasma.

The transport models used in our investigations are taken from analyses of neutral beam injection and ohmically heated plasmas as well as RF heating experiments. The primary differences lie in the assumed form of the electron thermal conductivity. The most pessimistic projections in general follow from the models corresponding to the "L-mode" degraded confinement observed in NBI experiments. We have carried out simulations using two of the expressions for χ_e developed by Kaye and co-workers [2.2-7] to account for experimental results on PDX. The first of these, referred to below as PDX-I, is given by

$$\chi_e = 12.6 r^{1.7} B_p^{-1.8} + D_b f(q) \quad (8)$$

and the second, including a weak density dependence,

$$\chi_e = 7.94 \times 10^6 r^{1.4} B_p^{-1.5} n_e^{-0.4} + D_b f(q) \quad (9)$$

will be referred to as PDX-III. The above expressions are in cgs units except that the poloidal field is given in Tesla. In our application we have included the model sawtooth transport described above, although this term was not included in the PDX work.

Neutral injection experiments in divertor discharges exhibit improved confinement behavior relative to the "L-mode" case referred to above.

While parametric dependences of this improved transport are not known at this time, it is commonly observed that gross confinement times during this "H-mode" operation are approximately equal to those of similar ohmic plasmas, and roughly a factor of two higher than in "L-mode". The relevance of these effects to RF heated plasmas is not presently clear. No intense RF heating experiments have yet been carried out under conditions thought to be conducive to the occurrence of H-mode; in addition, recent experiments on ICRF heating in PLT and LHH in Alcator C do not exhibit as strong a decrease in confinement as might be expected from neutral beam injection. Therefore, in the absence of an explicit expression for H-mode transport coefficients, we have included as one of our models for the RF heating studies the "neo-Alcator" coefficient (3) introduced for the ohmic heating case above.

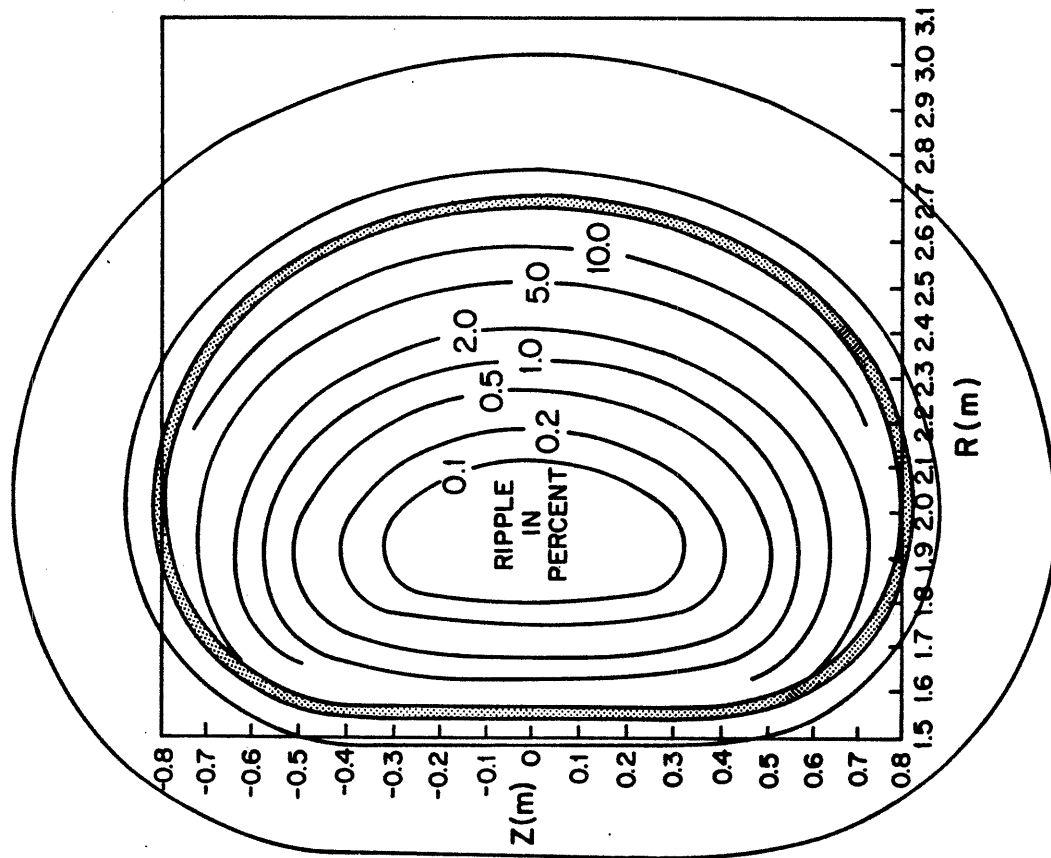
The results of ICRF heating with up to 3 MW of injected power on PLT have been successfully modeled by Hwang [2.2-8] using an electron thermal diffusivity of the form

$$\chi_e = 1.65 \times 10^{17} n_e^{-1} (T_e/T_{e0})^{-0.5} + \chi_{eNC} \quad (10)$$

which has the same density dependence as the INTOR and neo-Alcator scalings. We have compared simulations using this expression with the other three dependences in a number of cases.

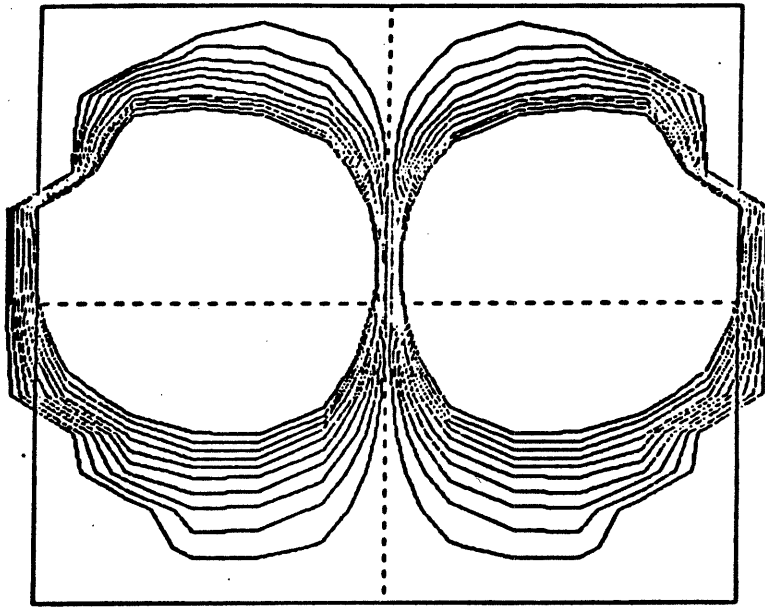
In our consideration of RF heated plasmas, we have retained the same dependences for ion thermal transport and particle diffusion as in the ohmic case, except that terms corresponding to ripple transport [2.2-2, 2.2-9, 2.2-10] have been added to the ion thermal conductivity. Ripple contours for Alcator DCT are shown in Figure 2.2-3a and the corresponding

(a)



(b)

CONTOURS OF α^*



$q = 3$

Isoripple Contours of Toroidal Field

FIGURE 2.2-3 a) Contours of constant ripple.
b) Contours of constant α^* for a circular plasma with $q=3$.

contours of α^* , the ripple trapping parameter [2.2-9], for a circular plasma with $q_a = 3$ are given in Figure 2.2-3b. The on-axis ripple is 0.04% and the largest plasma considered fits within the 2% ripple contour, resulting in little contribution due to the ripple terms for ion temperatures below 9-10 keV.

Simulation results for cases with ICRF heating alone are shown in Figure 2.2-4. Here three of the four transport models mentioned above, neo-Alcator, PDX-I and PLT, have been included. As expected the results for the PDX-I scaling, which was derived from L-mode neutral beam experiments, give the least favorable results in terms of confinement and peak temperatures. The neo-Alcator and PLT expressions result in quite similar scalings with both density and current. At low currents, confinement is limited by ion transport for each of the latter models, while the PDX cases exhibit higher electron losses. All three models yield a roughly linear dependence of global confinement time on plasma current for currents below 1 MA and density about $1.2 \times 10^{14} \text{ cm}^{-3}$, although the underlying mechanisms are different. In the curves representing the neo-Alcator scaling, the central ion and electron temperatures are reduced at the higher currents due to the enlargement of the region dominated by sawtooth transport. For the PDX-I curve, the same effect is reflected in the fact that the central temperatures saturate at the highest current although the global confinement does not.

The plots of confinement time and central temperatures against density for a fixed plasma current of 1 MA in Figure 2.2-5 clearly depict the different dependences of the two models. In each case the ion temperature is seen to be a steeply decreasing function of density, and indeed

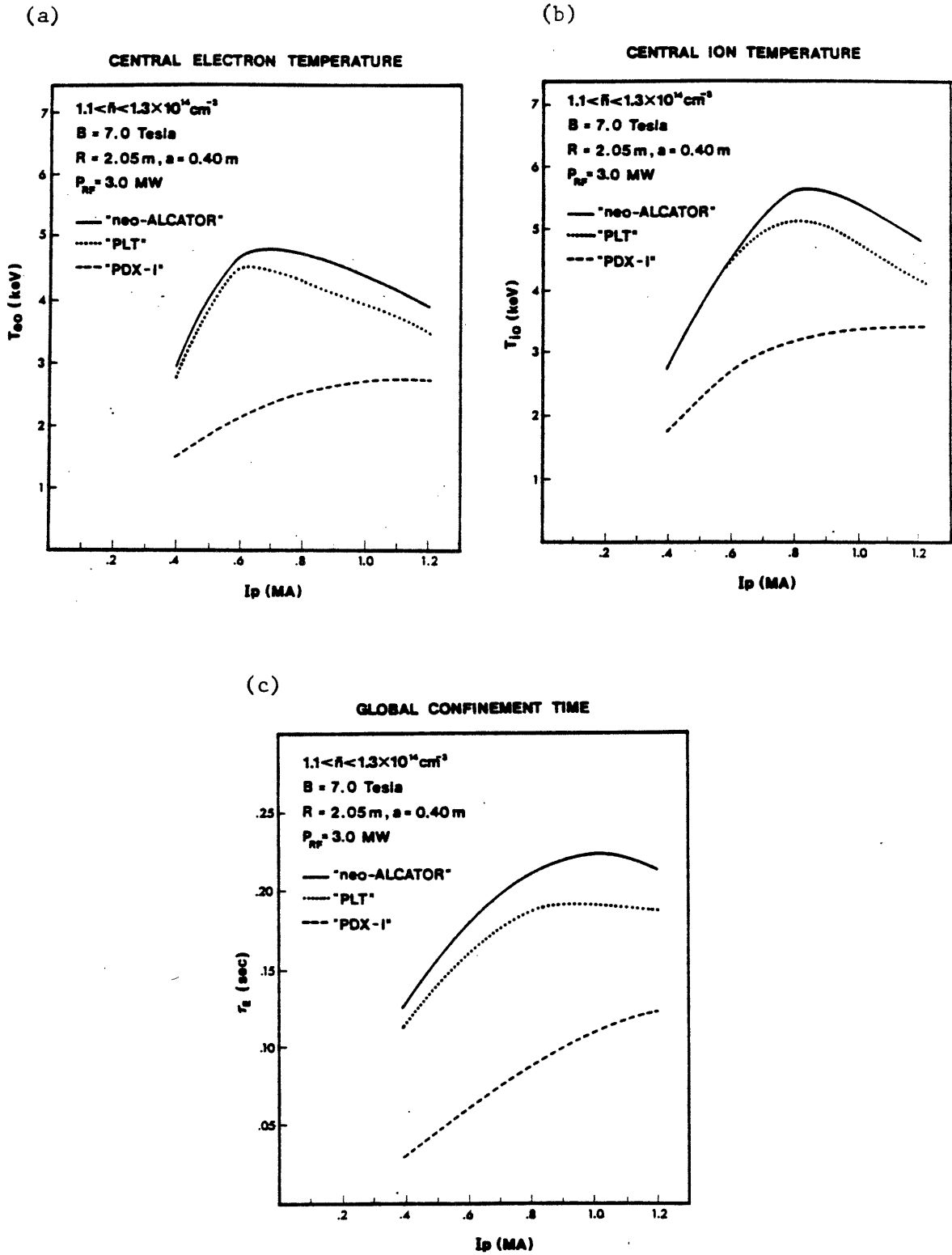


FIGURE 2.2-4 Results of transport simulations with 3.0 MW of ICRF heating shown as a function of plasma current for fixed average density.

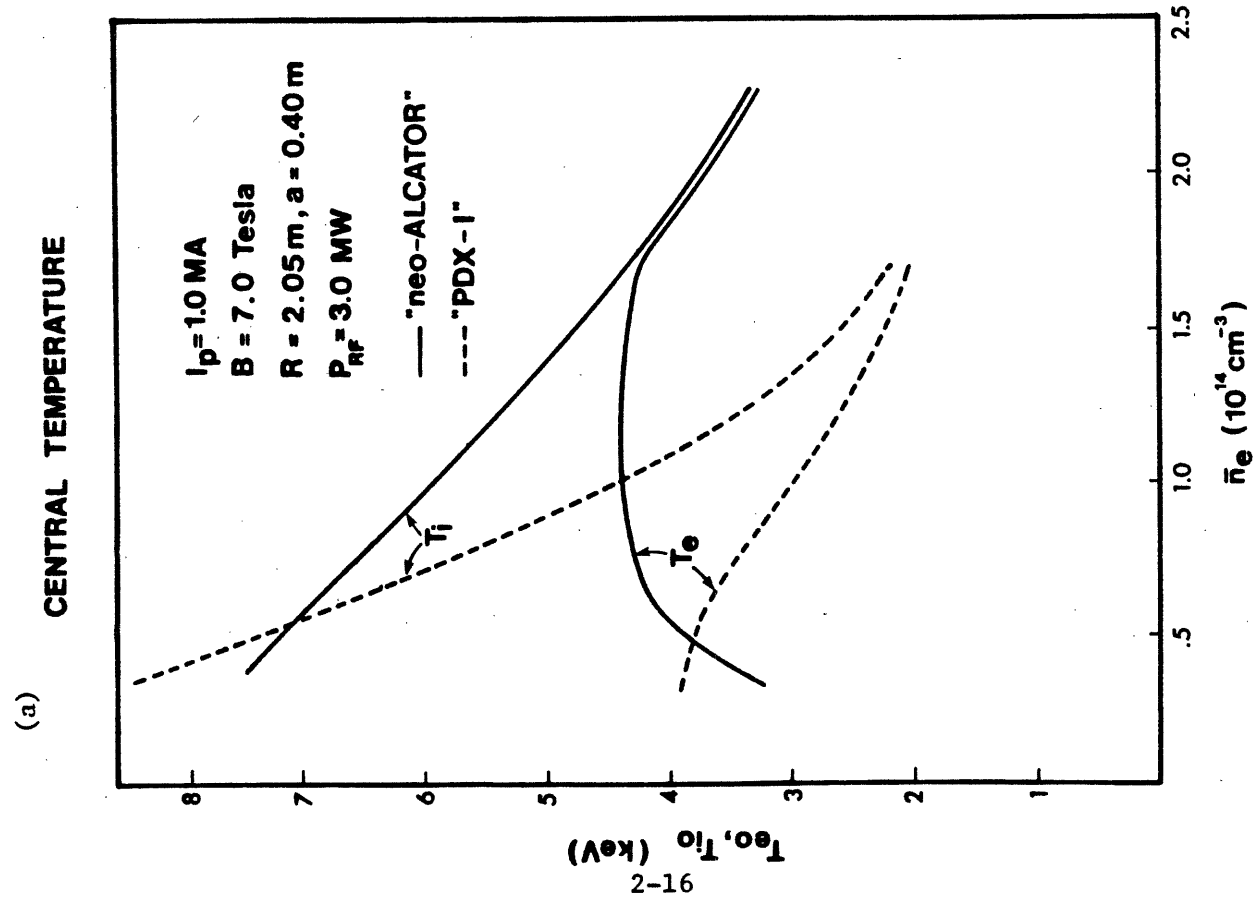
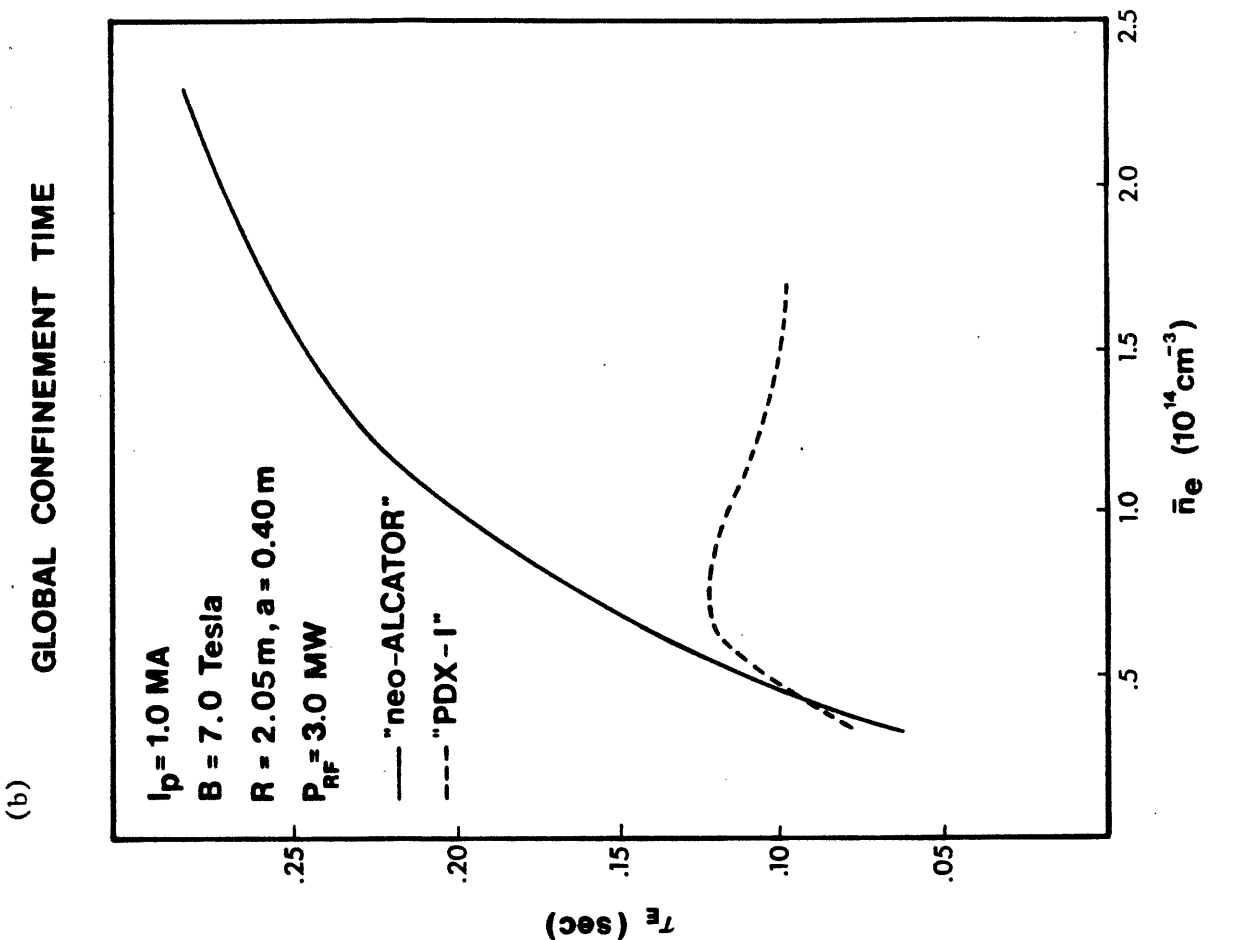


FIGURE 2.2-5 Results of transport simulations with 3.0 MW of ICRF heating shown as a function of density for fixed plasma current.

the values at the lowest densities, near $3 \times 10^{13} \text{ cm}^{-3}$, are similar. At these densities the electrons and ions are nearly decoupled and the central ion temperature depends primarily on the ion transport, which is the same in the two models. As the density is increased, the electron-ion coupling becomes more important and the two sets of curves diverge. For the PDX model the electron temperature is a monotonically decreasing function of density, as expected since χ_e is independent of n_e . For the neo-Alcator model, on the other hand, χ_e decreases with increasing density, with the result that the central temperature rises as the coupling to the ions increases, then levels, and finally decreases at the highest densities, for which the transport is ion dominated and the two species are well coupled. The two species also are closely coupled at these densities in the PDX case, but the electron losses dominate.

Despite the differences in the scaling models considered, it is of interest to note that even for the more pessimistic PDX-I case the absolute parameter values attained in the simulation are satisfactory, and there exist some conditions, particularly at high current and low density, under which the different assumptions lead to similar results. In general we may expect 5 MW of ICRF heating to produce ion temperatures in the range of 4-8 keV and electron temperatures of 2-5 keV over a relatively wide range of currents and densities. Total plasma pressures are 0.5 to 1 atmosphere and inductively driven pulses can be sustained for 30 to 90 seconds. In addition, the increased electron temperature, relative to the ohmic value, should increase the efficiency of RF current drive.

Combined ion and electron heating, and lower hybrid current drive in the presence of ICRF heating will also be carried out as part of the

Alcator DCT program. Simulations of such experiments using the neo-Alcator, PDX-I, and PDX-III models are shown in Figures 2.2-6 through 2.2-8. For a typical electron density of $1.2 \times 10^{14} \text{ cm}^{-3}$, electron and ion temperatures vary from 5 to 9 keV. The corresponding confinement times are between 0.1 and 0.2 seconds and values of $\epsilon\beta_p$ between 0.15 and 0.75, depending on plasma current. As in the ion heating cases, the PDX L-mode models give results similar to the neo-Alcator scaling at the higher currents and lower densities, with PDX-III actually predicting somewhat higher temperatures above 1.2 MA. Inductively driven pulse lengths predicted by the three models are shown in Figure 2.2-9 as functions of plasma current and line average density. Plasma durations greater than one minute are achievable over essentially the entire parameter range of interest, and five minute discharges are feasible under some conditions.

2.2.4. Shaped Plasmas

The ability to produce D-shaped and elongated discharges, including divertor configurations, is an essential feature of the Alcator DCT design. Examples of the device capabilities in this regard are presented in Section 2.3. Simulations of elongated discharges have been carried out using the ONETWO code by solving the one-dimensional transport equations for concentric, elliptical flux surfaces. This technique has been found [2.2-2,2.2-11] to provide a good approximation to results obtained using a 1 1/2-D code in conjunction with an MHD equilibrium solver. The models used for the transport were the same as for the circular geometry presented above. Typical curves for energy confinement time and pulse length vs. current are shown in Figure 2.2-10 for an elliptical plasma

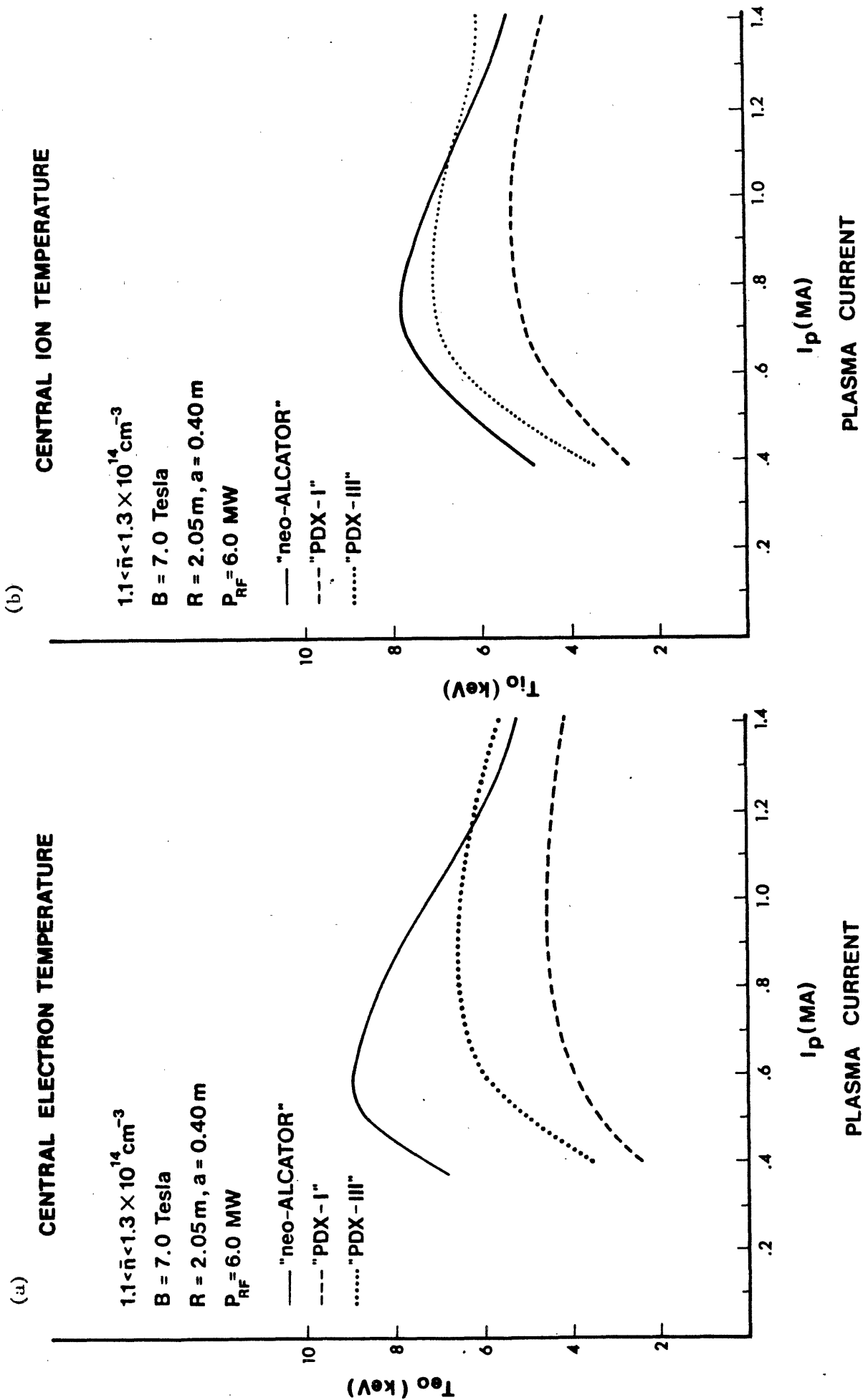


FIGURE 2.2-6 Central temperatures vs. plasma current predicted for 6 MW combined LH and ICRF heating.

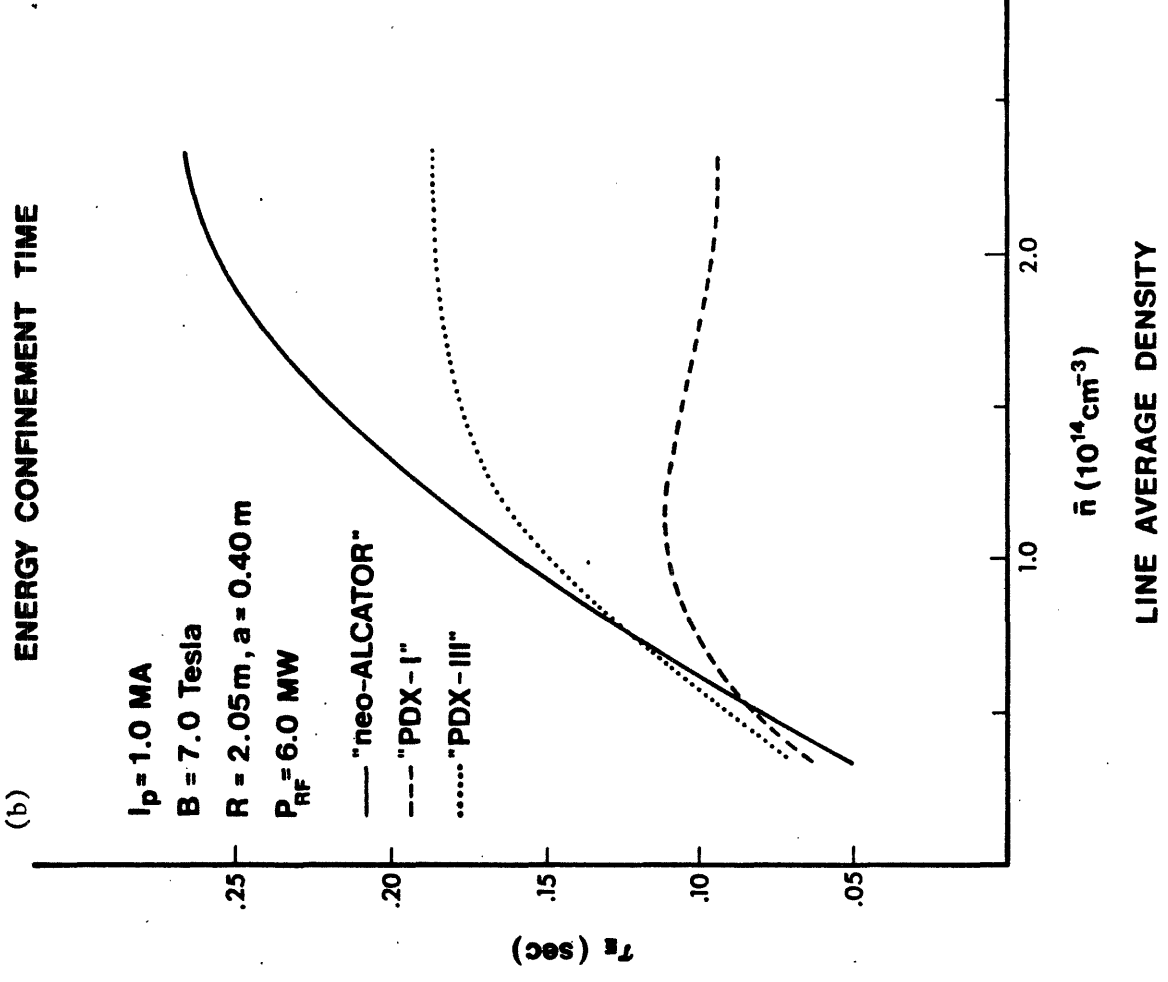
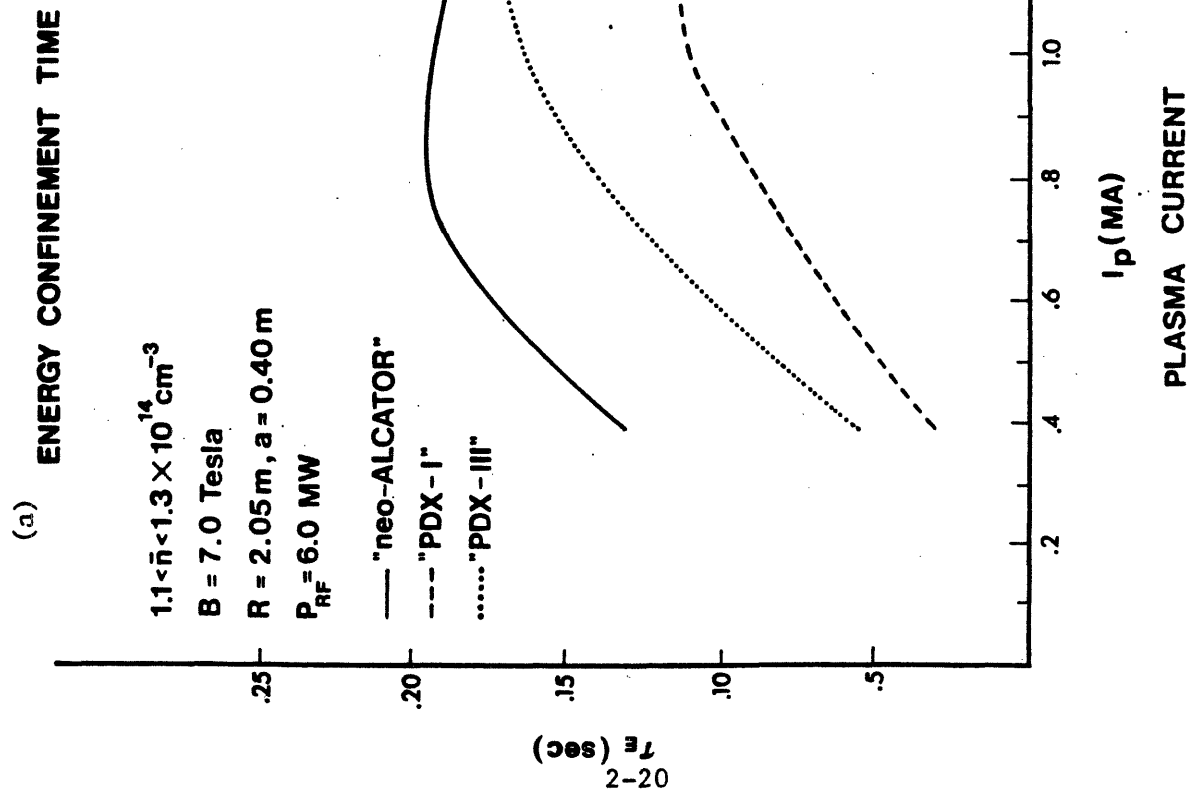


FIGURE 2.2-7 Energy confinement time as a function of plasma current and density with 6MW combined L1I and ICRF heating.

Limiter Safety Factor - q^*

10.0 5.0 4.0 3.0 2.5

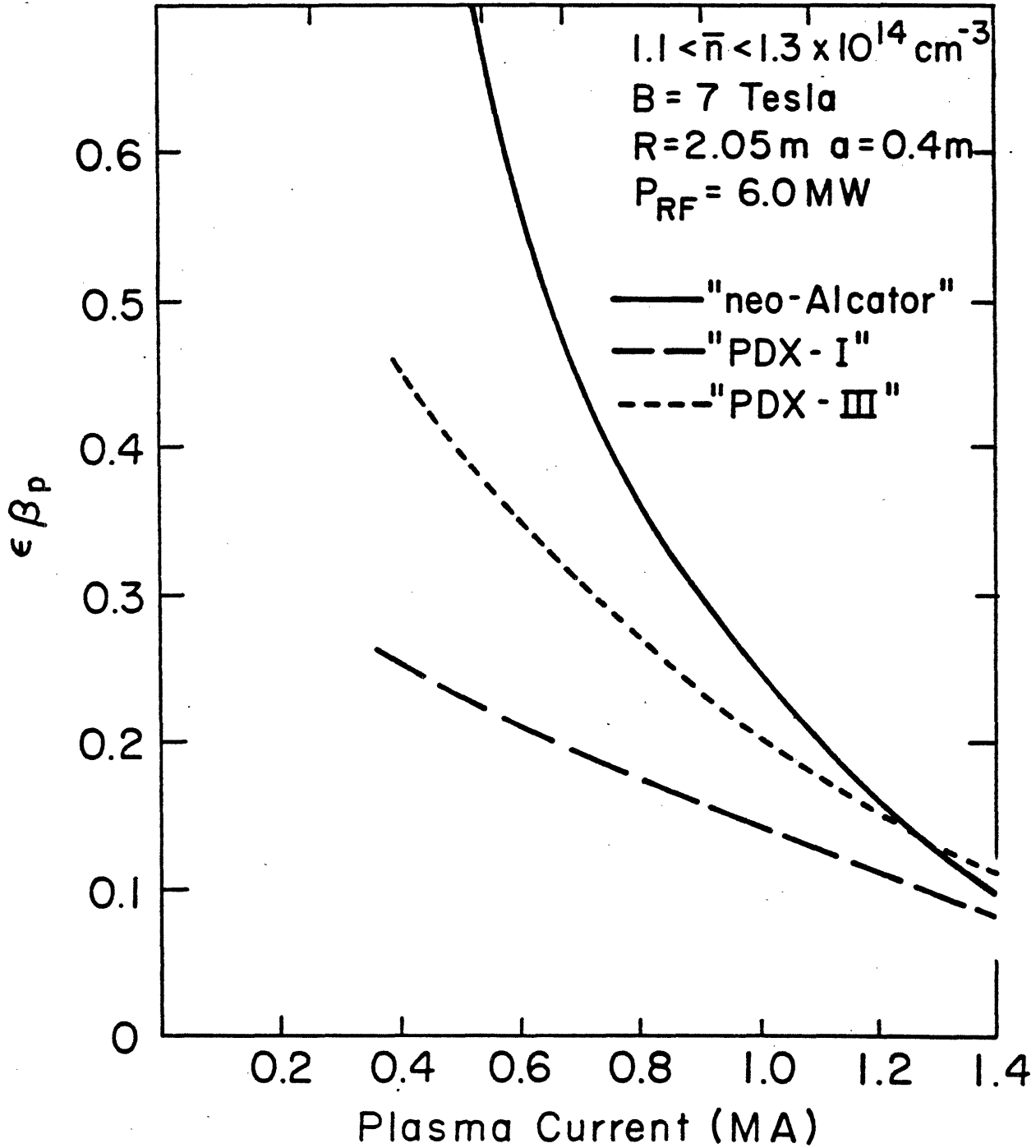


FIGURE 2.2-8 Normalized pressure $\epsilon\beta_p$ as a function of current with 6 MW combined LH and ICRF heating.

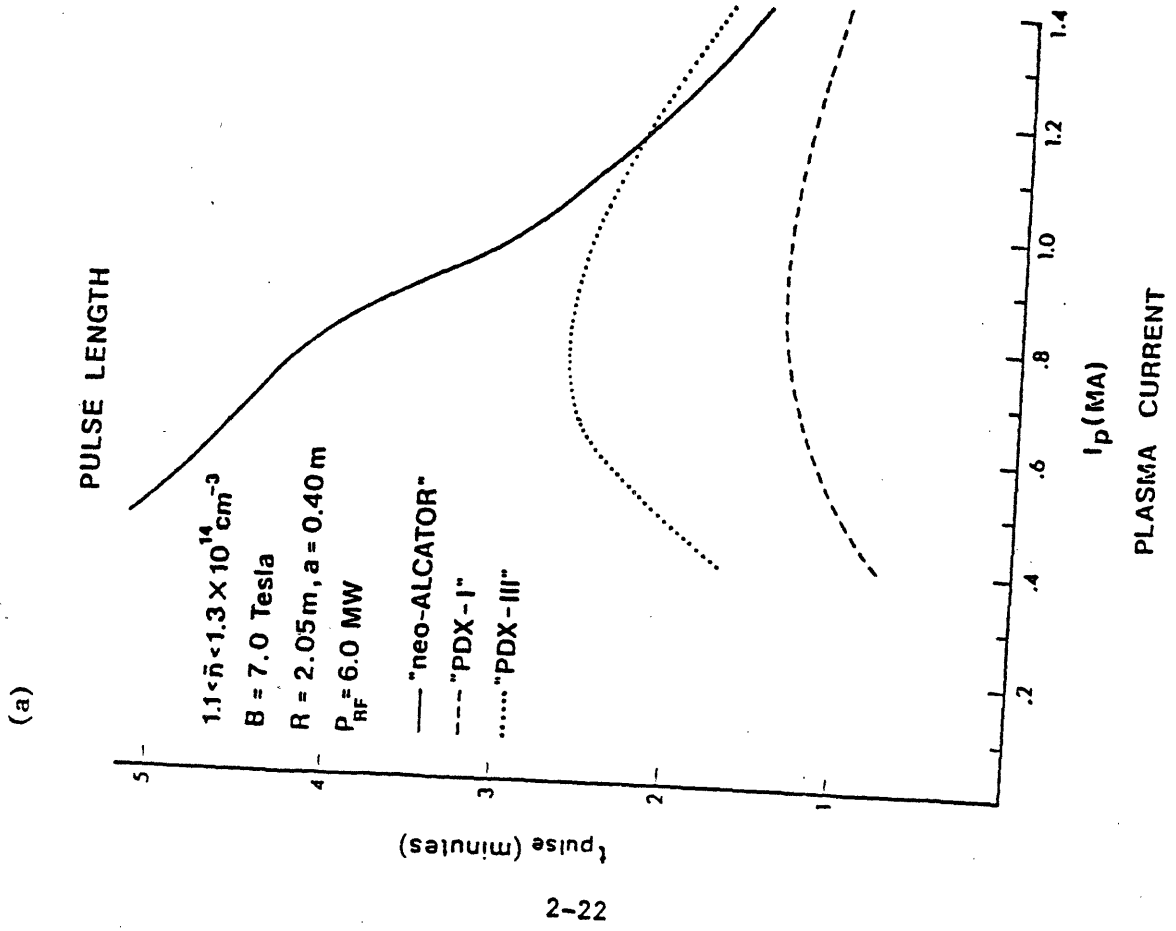
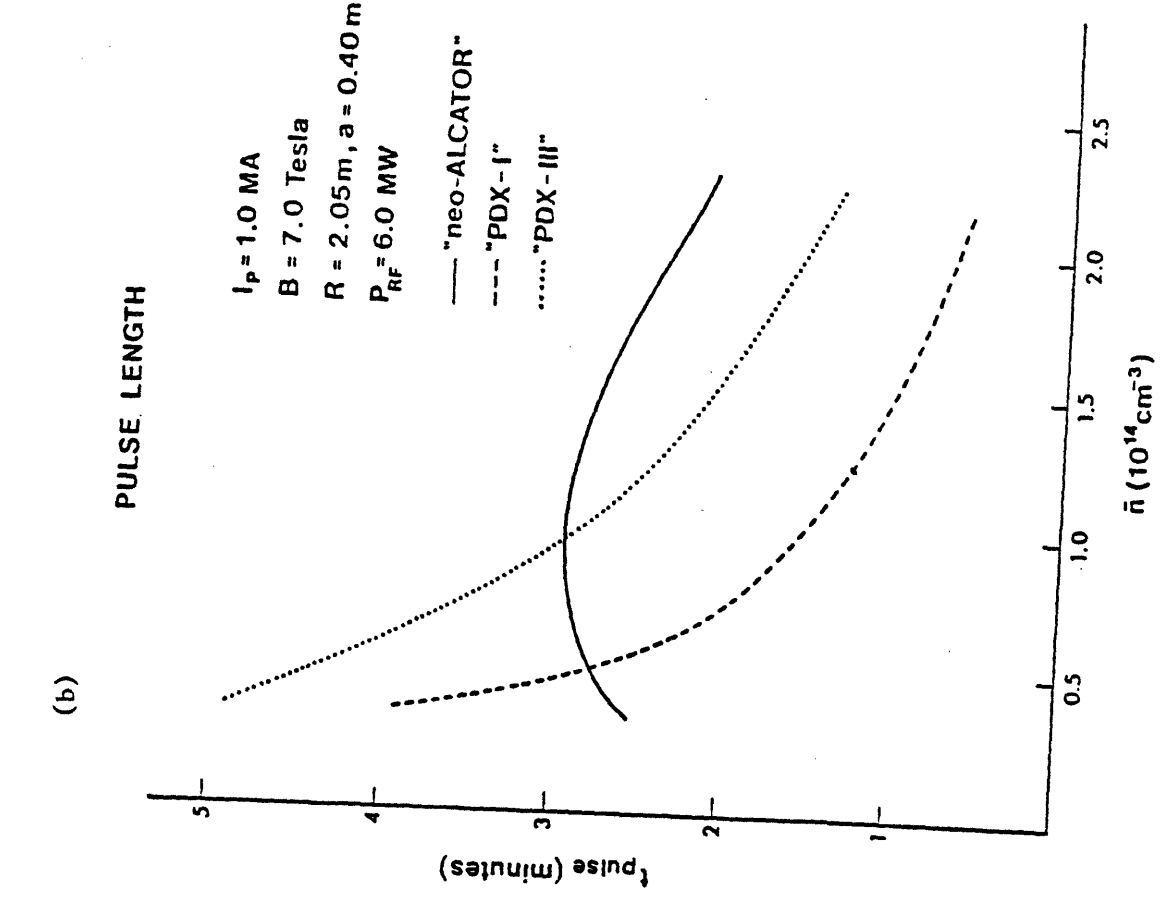


FIGURE 2.2-9 Anticipated inductively driven "flat-top" pulse lengths with 6.0 MW combined LH and ICRF heating.

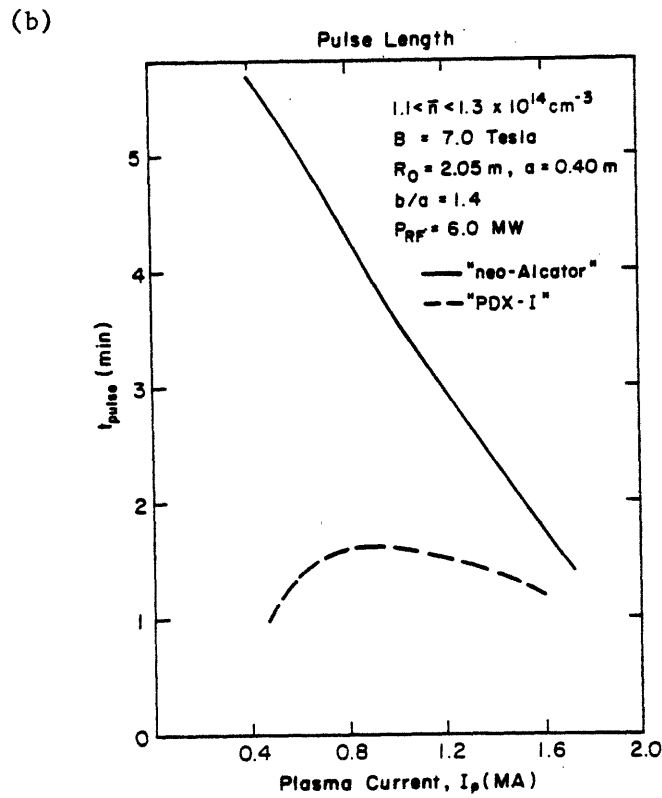
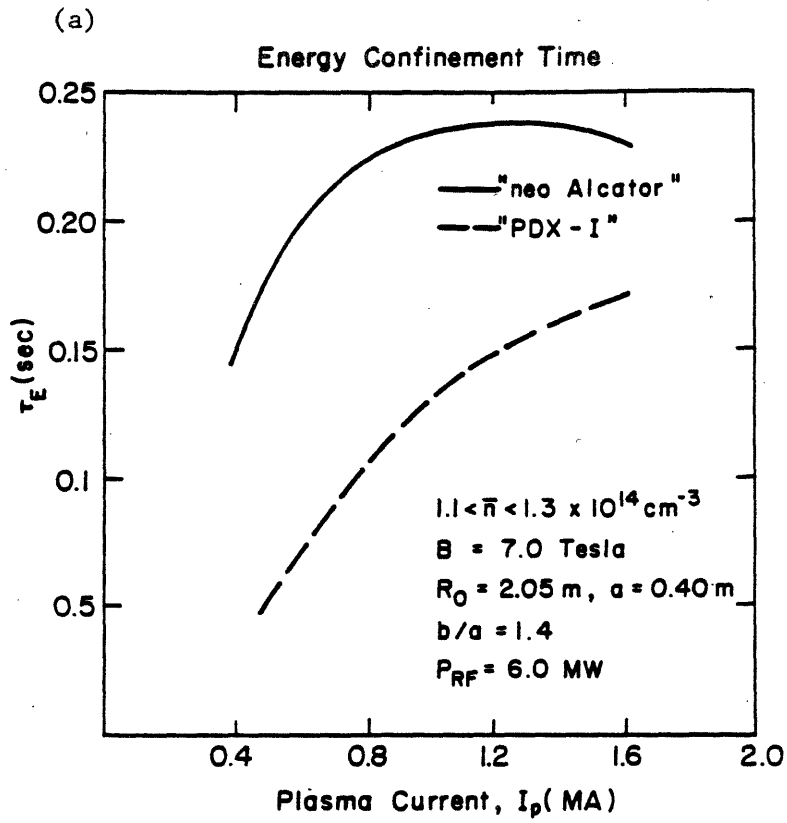


FIGURE 2.2-10 Energy confinement time (a) and inductively driven pulse length (b) for elongated plasmas with 6.0 MW combined LH and ICRF heating.

with an elongation of 1.4. The results are similar to those obtained in the circular case, with somewhat higher confinement times due to the increased volume and larger current capability with a given q . In computing the pulse length, we note that the available flux swing ϕ_{pf} is reduced relative to the circular case by approximately 2.5 Wb due to the flux of the shaping coils; however, this effect is mitigated by the slightly higher temperatures and lower loop voltages predicted by the code, with the result that the pulse lengths are comparable to or slightly longer than in the circular case.

2.2.5. Time Evolution

We have also used the simulation codes to study the temporal evolution of the plasma predicted by the models. In particular, the variation of the current density profile during heating and the associated plasma behavior is an example of a long time scale effect of great interest in quasi-steady state experiments. Some examples of these effects are depicted in Figures 2.2-11 through 2.2-14, in which we consider processes related to sawtooth activity associated with the existence and location of the $q = 1$ surface. The first shows an example of combined LHH and ICRF heating in a 0.9 MA elliptical discharge with an elongation of 1.4. Neo-Alcator scaling has been assumed. The start-up phase is similar to that shown in Figure 2.2-2, with current reaching its plateau value after 1.5 seconds. The RF power is turned on at 2.5 sec and the central electron and ion temperatures respond on a transport time scale, reaching values of 13.5 and 9.5 keV, respectively, within a few tenths of a second. The central current density, however, can evolve only on the resistive time scale, as evidenced by the fact that q_0 drops slowly until about 15

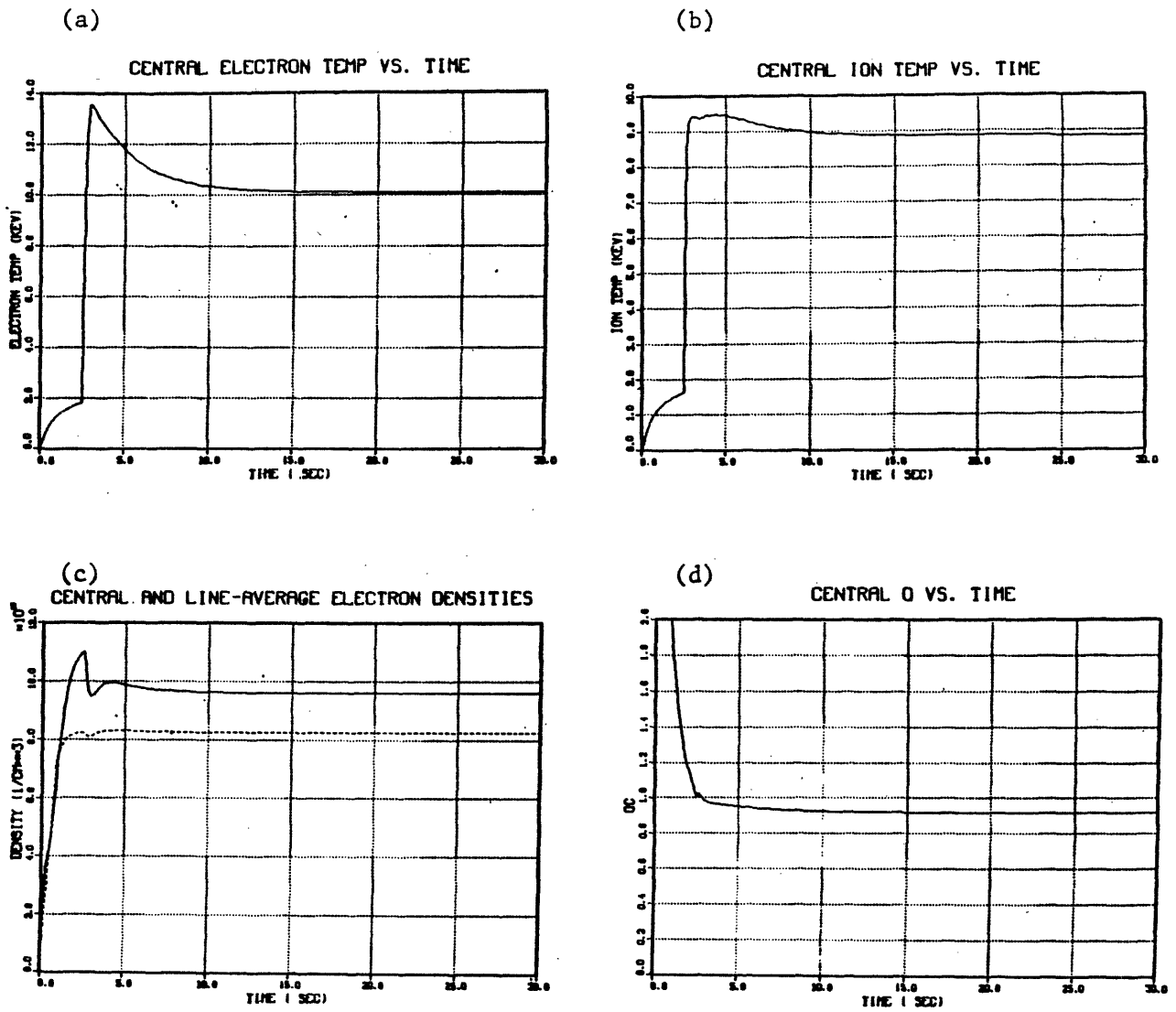
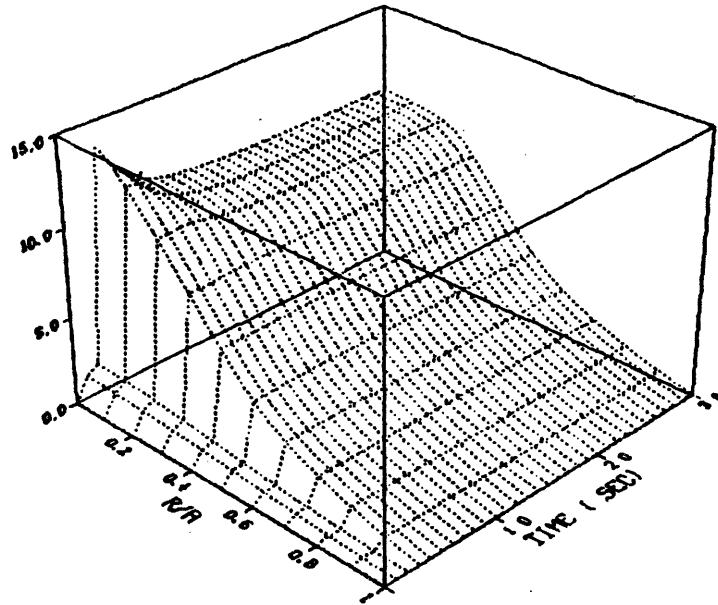


FIGURE 2.2-11 Evolution of RF heated discharges. Start-up phase similar to Figure 2.2-2. Neo-Alcator transport model is assumed. Plasma is elliptical with $b/a = 1.4$, $I_p = 0.92$ MA. 6.0 MW of RF power is absorbed uniformly for $r/a \leq 0.5$.

(c)

ELECTRON TEMPERATURE (KEV)



(d)

CURRENT DENSITY (AMPS/CM**2)

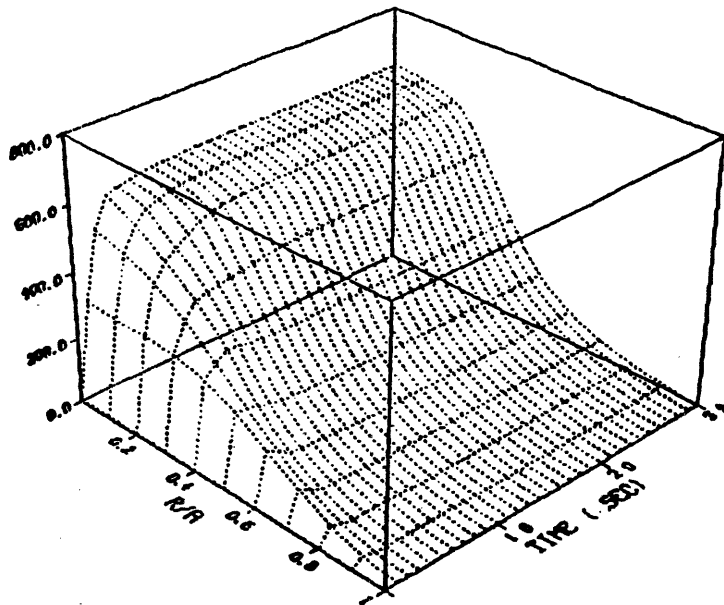


FIGURE 2.2-11 Continued from previous page.

seconds into the shot. As a result of the increased diffusion in the central region caused by the reduction of q_0 and the increase in the size of the $q = 1$ surface, the central electron temperature decreases slowly for over 15 seconds, finally reaching a steady state level 30% below its peak. The ion temperature rises slightly for a few seconds before decaying over a similar time period by about 10%. This is a simple example of a case in which transport effects occur on the much slower resistive time scale.

Even more pronounced effects are observed when the heat deposition is localized off the plasma axis, as in Figure 2.2-12. The target plasma is again elliptical with an elongation of 1.4, and carries a current of 1.2 MA. In this case, however, the RF power is deposited between 0.3 and 0.5 of the minor radius, which at 2.5 sec after discharge initiation lies outside the $q = 1$ surface. Inspection of the trace of the central safety factor as a function of time reveals that q_0 first drops below one during the start-up phase, but rises again shortly after heating commences as the current density becomes slightly hollow. As the j profile continues to evolve, q_0 rises for a few seconds, then drops again, falling below unity for the second time at about 15 sec and reaching its steady-state value between 25 and 30 seconds after start-up. Again the slow evolution of the current density is reflected in the behavior of the temperature and density profiles, with the latter apparently still evolving slowly after thirty seconds.

An example of the importance of subtle profile and timing effects on stability and consequently on transport is illustrated by a comparison of Figure 2.2-12 with the very similar case depicted in Figure 2.2-13; in each

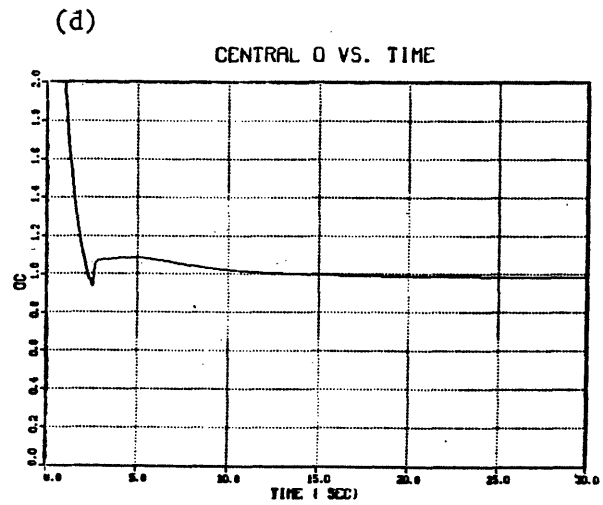
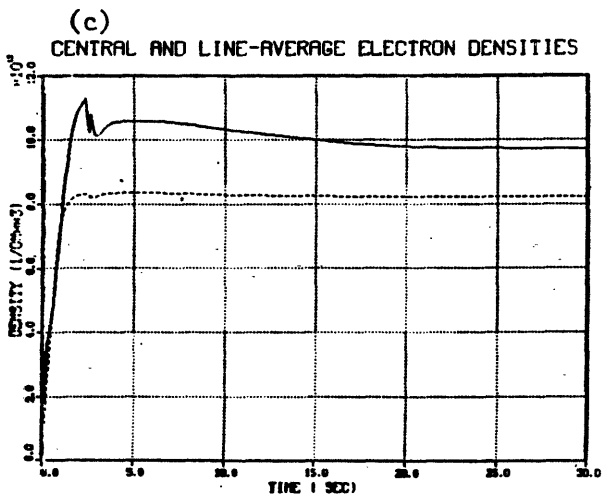
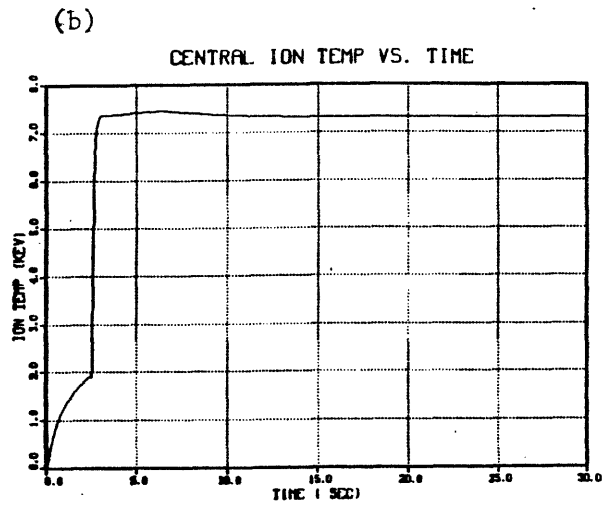
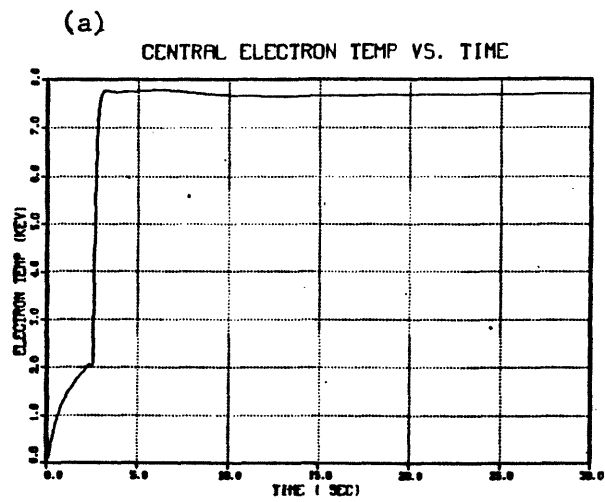
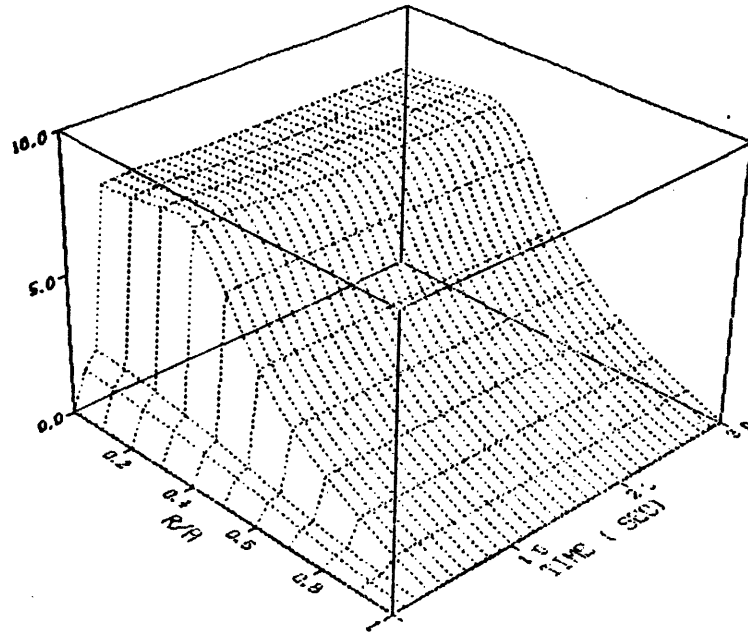


FIGURE 2.2-12 Similar to Figure 2.2-11 except $I_p = 1.2$ MA and RF power is absorbed between $0.3 \leq r/a \leq 0.5$. RF heating begins at 2.5 sec.

(e)

ELECTRON TEMPERATURE (KEV)



(f)

CURRENT DENSITY (AMPS/CM**2)

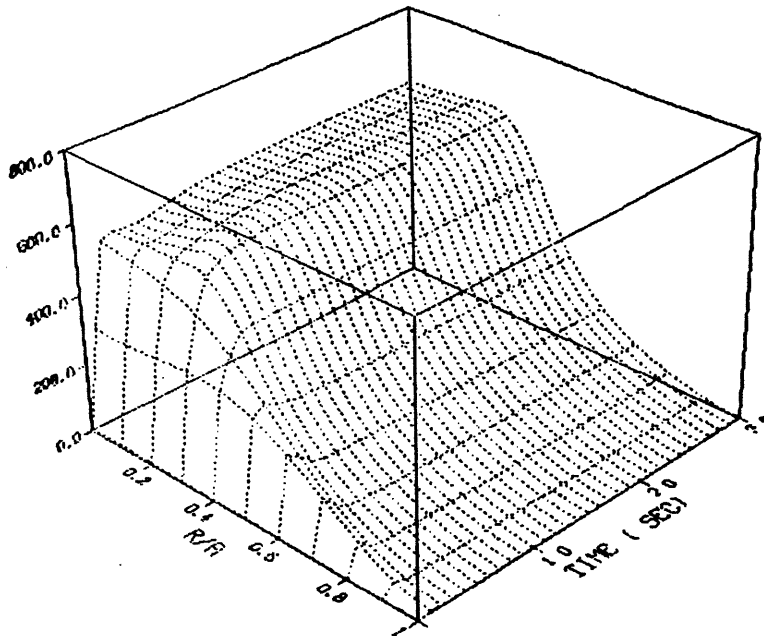


FIGURE 2.2-12 Continued from previous page.

the RF is deposited between 0.3 and 0.5 of the minor radius, and the plasma currents differ by less than 1%. In the latter case, however, the RF power is not turned on until 5 sec after breakdown, by which time the current density profile has stabilized. As a result some of the RF power is deposited inside the $q = 1$ surface and is rapidly transported to the center. Unlike the previous example, the current density profile broadens very slowly during the heating, with q_0 not rising above 1 until 20 sec. The resulting transport effect is seen most clearly on the central density, which undergoes a sharp transition at the time when sawtooth activity no longer balances the inward pinch. As in the previous example, the new configuration continues to evolve until approximately 35 sec.

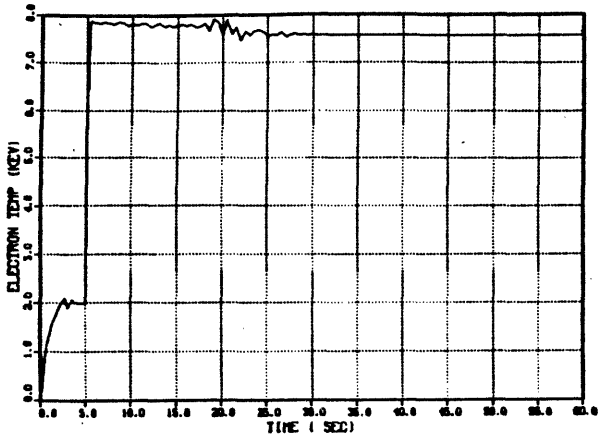
Finally, Figure 2.2-14 presents an example of an attempt to control the current profile to maintain sawtooth activity. The first 25 seconds of this case are identical to that of Figure 2.2-13. Following the abrupt change in central density accompanying the disappearance of the $q = 1$ region, the plasma current is increased by 5%. As a result, the value of q on axis again falls, reaching a new steady state value of 0.96 at about 40 sec.

2.2.6. Summary

Transport simulations indicate that Alcator DCT should operate in regimes suitable for the investigation of problems relevant to tokamak reactors, particularly those related to long-pulse and steady-state operation. Ohmic plasmas with densities between 0.5 and $2.5 \times 10^{14} \text{ cm}^{-3}$, temperatures of 1-2 keV and plasma currents from 400 kA to 1.2 MA can be produced as target plasmas for subsequent RF heating and current drive

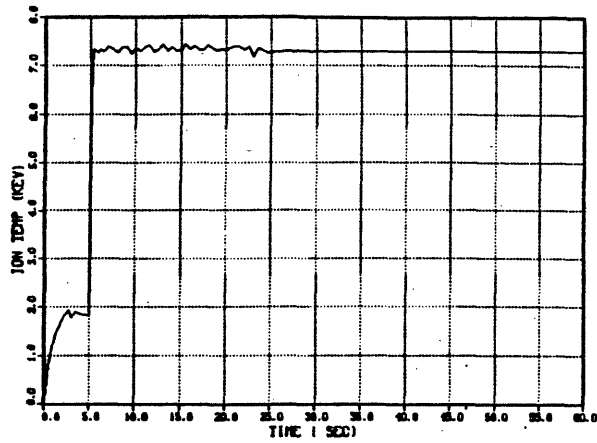
(a)

CENTRAL ELECTRON TEMP VS. TIME



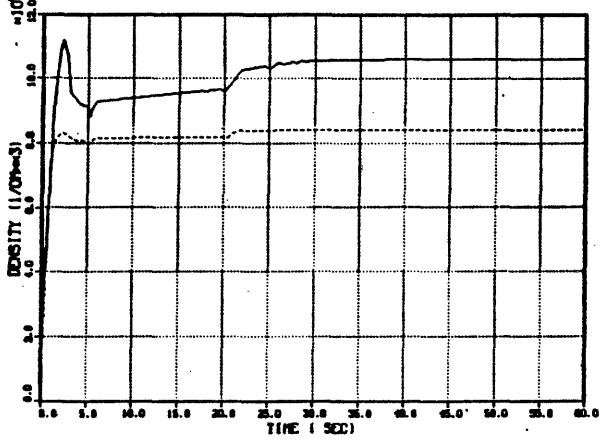
(b)

CENTRAL ION TEMP VS. TIME



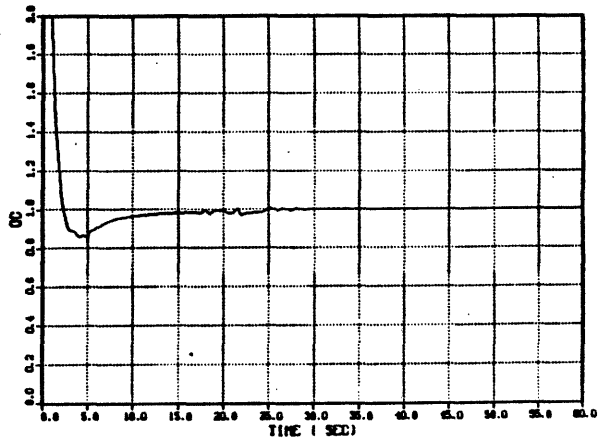
(c)

CENTRAL AND LINE-AVERAGE ELECTRON DENSITIES



(d)

CENTRAL Q VS. TIME



(e)

CURRENT DENSITY (AMPS/CM**2)

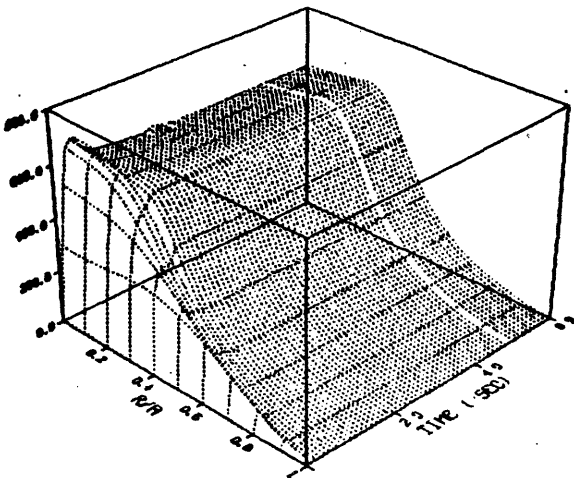
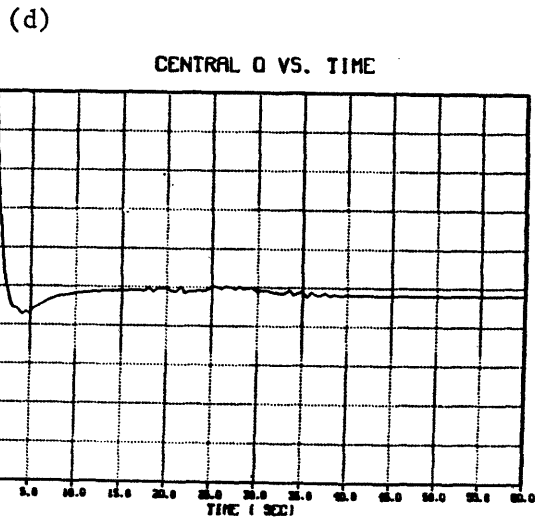
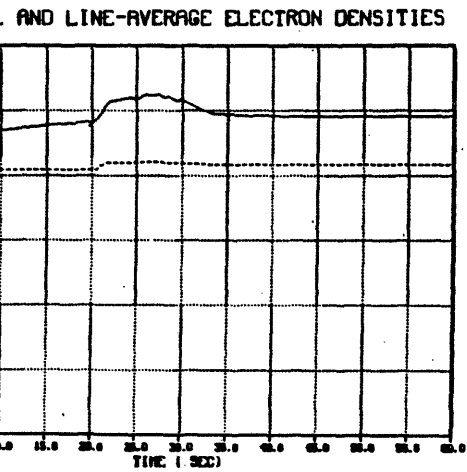
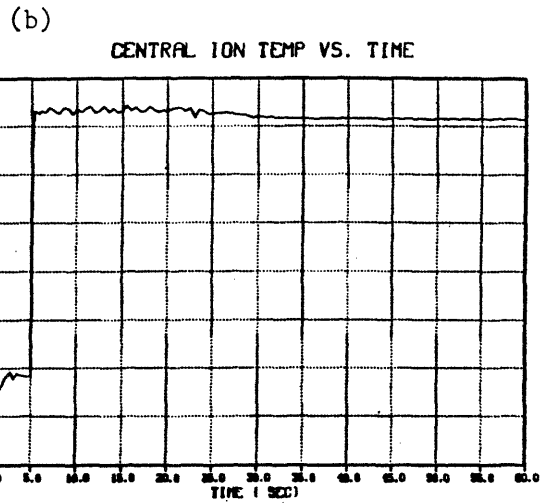
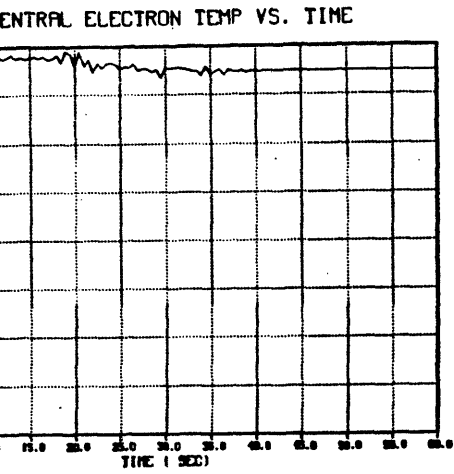


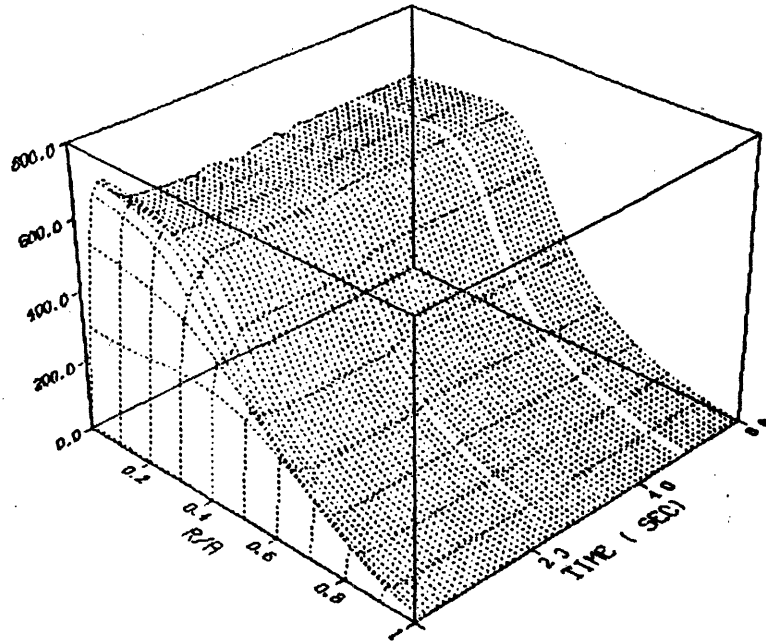
FIGURE 2.2-13 Identical to Figure 2.2-12 except $I_p = 1.19$ MA and RF heating begins at 5.0 sec.



E 2.2-14 Identical to Figure 2.2-13 until 25 sec., at which point I_p is increased from 1.19 MA to 1.25 MA.

(e)

CURRENT DENSITY (AMPS/CM**2)



(f)

TOTCUR VS. TIME

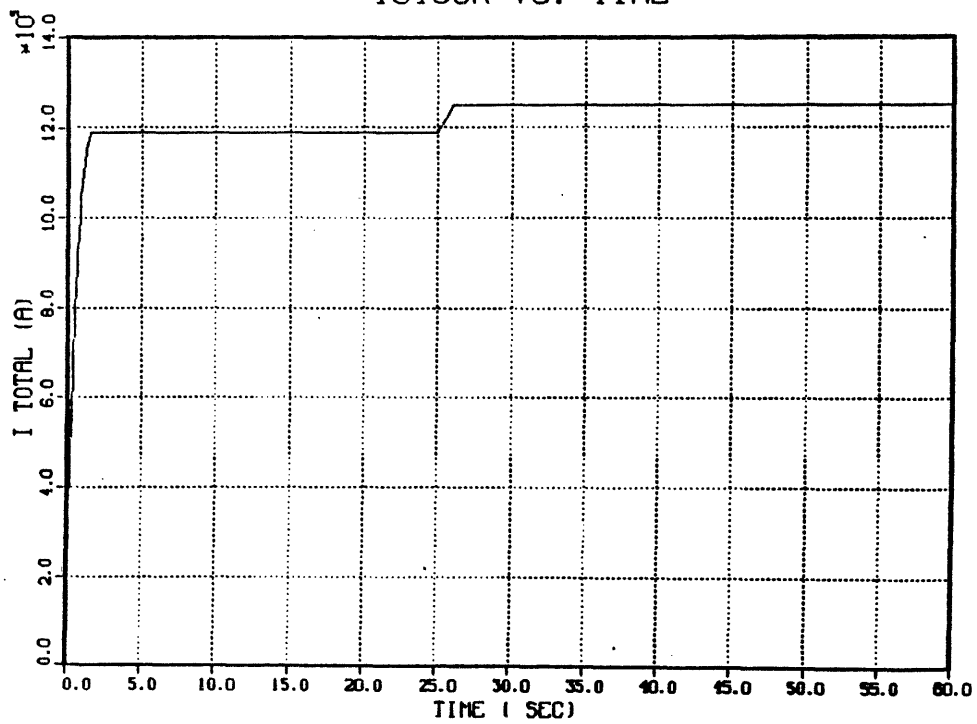


FIGURE 2.2-14 Continued from previous page.

studies. With no additional heating, pulse lengths of 10-30 sec can be obtained. The available RF heating power in the ICRF and LHRF frequency ranges is sufficient to produce discharges with electron and ion temperatures of 5-10 keV and pressures of up to 2 atmospheres. Values of $\epsilon\beta_p$ approaching unity are predicted for the more optimistic scalings, and the most pessimistic assumptions imply $\epsilon\beta_p \gtrsim .25$, corresponding to equilibria with significant "high beta" distortions. Plasma durations of several minutes with inductive current maintenance, or of hours with RF current drive, are anticipated. Time dependent simulations indicate that pulse lengths at least of order one minute will be required for proper study of the evolution and control of current and pressure profiles in these high performance discharges.

A comparison of transport models indicates that the Alcator DCT design provides acceptable performance under a wide variety of assumptions. The large major radius and moderate aspect ratio of the device, which are principally dictated by flux requirements of the OH solenoid, provide an additional advantage under transport models such as neo-Alcator scaling which predict a favorable dependence of confinement on R. The relatively high toroidal field of 7 Tesla permits high current and current density at modest q, which leads to improved performance under assumptions based on "L-mode" transport, such as the PDX scalings. High values of B/R also permit higher density operation, which leads to better confinement under three of the four models considered. Finally, the provision of a poloidal divertor option, primarily included for impurity and particle control and to facilitate heat removal, enhances the probability that more favorable confinement properties, characteristic of H-mode operation, can be achieved. We therefore expect that plasma parameters and pulse lengths

obtained in Alcator DCT will prove suitable for the investigation of long pulse and quasi-steady state phenomena in reactor-like tokamak plasmas.

Acknowledgements

We wish to express our appreciation to C. Singer of PPPL and to W. Pfeiffer and R. Stockdale of GA Technologies for providing us with copies of the BALDUR and ONETWO transport codes and for their assistance in instructing us in the efficient use of these programs.

References

- [2.2-1] D. Post, C. E. Singer, A. M. McKenney, and PPPL Transport Group, "Baldur: A One-Dimensional Plasma Transport Code", TFTR Report #33 (January, 1981).
- [2.2-2] W. W. Pfeiffer, R. H. Davidson, R. L. Miller, and R. E. Waltz, "ONETWO: A Computer Code for Modelling Plasma Transport in Tokamaks" GA-A16178 (Dec. 1980).
- [2.2-3] B. Blackwell, C. L. Fiore, R. Gandy, A. Gondhalekar, R. S. Granetz, M. Greenwald, D. Gwinn, E. Källne, J. Källne, S. E. Kissel, B. Lipschultz, N. G. Loter, E. S. Marmor, S. McCool, D. Overskei, D. S. Pappas, R. R. Parker, R. Petrasso, M. Pickrell, P. A. Politzer, M. Porkolab, P. Pribyl, J. E. Rice, F. Seguin, J. J. Schuss, J. L. Terry, R. Watterson, S. M. Wolfe, "Energy and Impurity Transport in the Alcator C Tokamak", Plasma Physics and Controlled Nuclear Fusion Research 1982 (IAEA 9th International Conference on Plasma Physics and Controlled Fusion Research, Baltimore, September 1982) 1983. IAEA-CN-41/C-4.

- [2.2-4] W. W. Pfeiffer and R. E. Waltz, "Empirical Scaling Laws for Energy Confinement in Ohmically Heated Tokamaks", Nuclear Fusion 19, 51 (1979).
- [2.2-5] R. Hawryluk, "TFTR Experimental Results", unpublished, MIT Plasma Fusion Center Seminar (July, 1983).
- [2.2-6] C. S. Chang and F. L. Hinton, "Effect of Finite Aspect Ratio on the Neoclassical Ion Thermal Conductivity in the Banana Regime", Physics of Fluids 25, 1493 (1982).
- [2.2-7] S. Kaye, unpublished, Transport Analysis Workshop, PPPL, March 2, 1983.
- [2.2-8] D. Q. Hwang, PPPL-1990, Princeton Plasma Physics Laboratory (May 1983).
- [2.2-9] R. J. Goldston and H. H. Towner, "Generalization of Connor and Hastie's Ripple Trapping Coefficient, $G(\alpha)$ ", PPPL-1638R, Princeton Plasma Physics Laboratory (1980).
- [2.2-10] A. H. Boozer, Phys. Fluids 23, 2283 (1980).
- [2.2-11] W. Pfeiffer, private communication.

2.3. MHD Configurations

2.3.1. General Considerations

The sizes and shapes of the Alcator DCT plasmas are set by the objectives of long pulse plasma control, RF heating in relevant plasmas, and the demonstration of realistic and extrapolable magnet systems. These requirements have led to the design of an elongated, dee-shaped vacuum vessel, fitting closely inside the TF coils, which is large enough to accommodate a variety of plasma configurations.

In order to study the long-time behavior of plasmas the provision of some form of divertor is necessary. While the alternative of using a pumped limiter would have many advantages from the reactor viewpoint, it is far from certain that any form of limiter can handle the combined tasks of heat removal, particle removal, impurity control, and boundary control. In view of the need for reliable long pulse operation of Alcator DCT, it would not be prudent to rely solely on limiters. A similar argument may be made with regard to bundle divertors. The study of pumped limiters and other tokamak improvements is, of course, one of the program goals of Alcator DCT.

The second consideration entering into the MHD design of Alcator DCT is the interest in investigation of the interaction between high power RF heating and shaped plasma equilibria, again with emphasis on the long time scale. Therefore, provision must be made for a variety of shapes, both with and without divertors. The analysis and design also includes the time dependent problem of maintaining the plasma position and shape.

2.3.2. Divertor Configurations

Consideration of these requirements (as well as others such as aspect ratio, allowable ripple, ...) have led to the selection of a range of possible equilibrium configurations for Alcator DCT. We have investigated the relative merits of internal coils and external coils for poloidal divertors. There has been considerable practical experience with internal (with respect to the TF coils) coil poloidal divertors. The ASDEX machine is the largest and most recent example of this configuration. The JT-60 device is being built with an internal coil system, with a single null located on the midplane of the torus at the outside. Devices with external coil divertors have not been built, but all of the recent reactor studies which have divertors use this configuration.

In addition to the location of the divertor coils, there is the question of single versus double null systems. While double null poloidal divertors preserve the up-down symmetry of the tokamak, this is done at the expense of devoting a much larger fraction of the volume inside the TF coils to divertor regions. Furthermore, a double null system requires a larger poloidal field coil system, in terms of ampere-turns, ampere-meters, and energy.

We have examined in detail the possible single null, internal coil configurations in Alcator DCT. The particular advantage of internal coils is the small relative size of the coils used. In most configurations (as in present devices) the coil set for an internal coil divertor consists of a triplet, with one coil carrying about half the plasma current in order to create the null. The other coils together carry approximately the same current in the opposite direction. The function

of these coils is to constrict the divertor throat to permit good separation (by means of baffles) between the main plasma and the divertor chamber, and to reduce or eliminate the coupling between the divertor coils and the other PF coils. While these features make the internal coil system very attractive, the associated disadvantages have led us to concentrate our studies on external coil systems. A possible plasma configuration using internal coils is shown in Figure 2.3-1.

The particular disadvantages of the internal coil system are the rather restricted volume that would be available for collector plates and a divertor chamber, the difficulty associated with assembling coils inside the vacuum chamber, the awkward structural supports needed, and the difficulty of obtaining sufficiently elongated plasmas (typically $1.0 < \kappa < 1.2$ can be achieved).

The external coil divertor configuration also has pronounced advantages and disadvantages. This system usually consists of a large single coil located above (or below) the plasma, carrying two to three times the plasma current, which creates the poloidal field null, and an additional coil or set of coils with oppositely directed currents which are needed in order to maintain the vertical equilibrium of the plasma. Since these coils are outside of the TF system, a larger volume is available for plasma. The area available for collection of heat and particles is also increased. The divertor coils assist the PF system in producing high plasma elongation (up to 1.6). There is sufficient space available for structural support. However, for this system, the divertor throat is broad, and the creation of a clearly separated divertor chamber is more difficult. In addition, the large currents required result in large

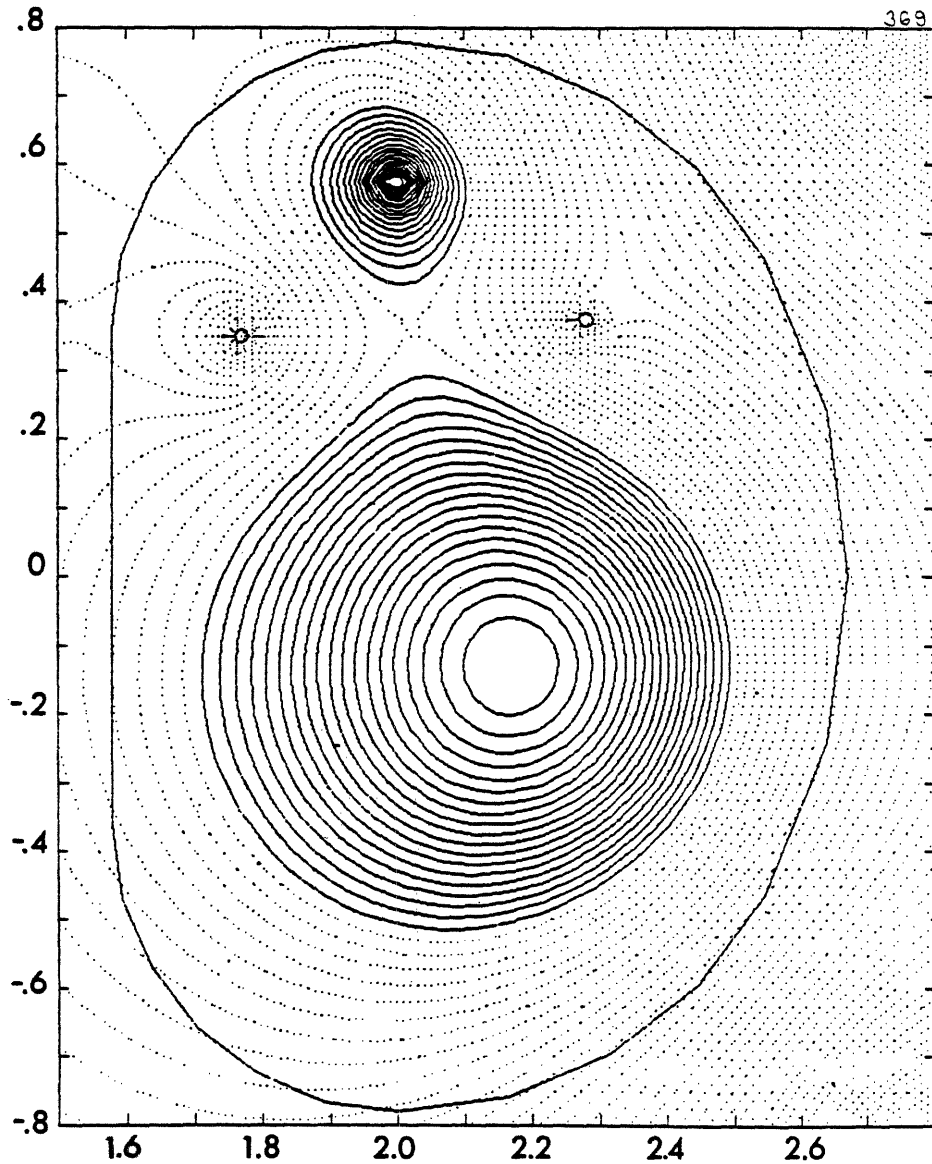


FIGURE 2.3-1 An example of an internal coil divertor configuration. Here and in following figures, the solid lines are equally spaced poloidal flux contours within the plasma, the dashed lines are vacuum flux surfaces. The D-shaped solid line indicates the vacuum vessel wall, the plasma current is 1.0 MA, $\langle \beta \rangle \approx 1\%$, $\beta_p \approx 2$, $\langle a_p \rangle \approx 0.04$. In the divertor cases, the plasma surface is taken at 0.95 of the separatrix flux. In this figure, the main divertor coil carries 400kA and the inner and outer return coils carry -260kA and -140 kA, respectively.

inter-coil forces. Figure 2.3-2 shows the poloidal field coil system designed for INTOR, and illustrates the need for large coils to provide a separatrix.

2.3.3. The Alcator DCT Divertor

The configuration presented here represents a good compromise between these conflicting features. The function of creation of a poloidal field null is shared between the inner PF coil and one of the divertor pair. Thus there is no coil directly above the plasma, and access to the plasma and particularly to the divertor region is maintained. Furthermore, this splitting allows the location of the divertor null to be moved from inside to outside, following changes in the triangularity of the plasma.

An additional advantage of the external coil divertor system is the particularly large volume available for the study of plasma configurations without divertors, as will be needed for studies of pumped (and more exotic) limiters. The possibility of comparison between limited and diverted discharges of essentially the same shape is also attractive. We have set the maximum extent of the Alcator DCT plasma in major radius at 2.42 meters, the position in the mid-plane of the 2% ripple contour. Further, for these studies, the plasma edge was required to be more than 0.1 meter from the vacuum wall at all points, to allow for bumper limiters, and other structures on the walls. These constraints correspond to a maximum plasma width of 0.8 meters, or an aspect ratio of 5, as usually defined. The plasma can, of course, be made wider, by moving the plasma edge into the higher ripple region, but this part of the vacuum chamber

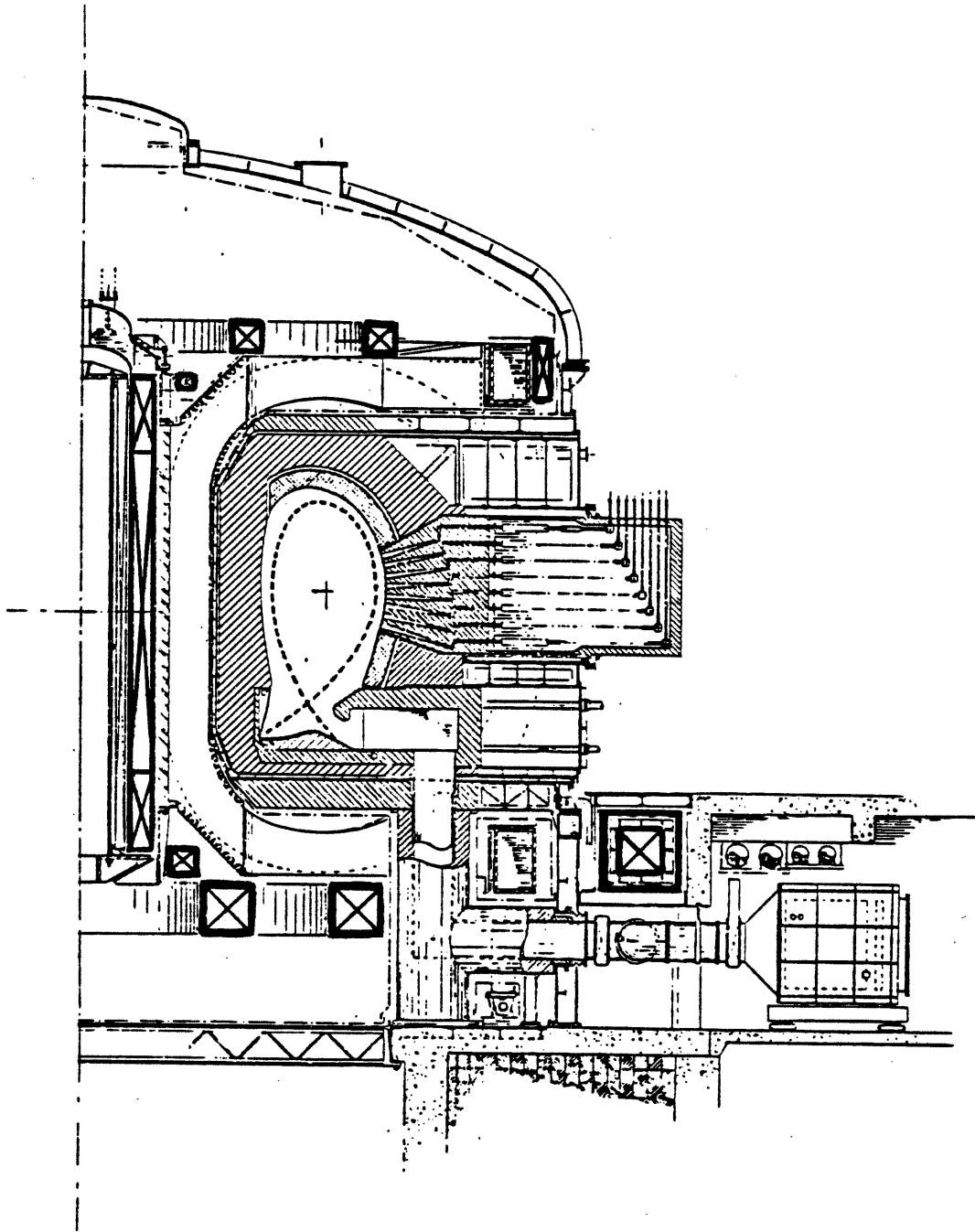


FIGURE 2.3-2 A cross-section of INTOR, showing the poloidal field coil set. Note the large coils at the bottom needed to produce the divertor configuration.

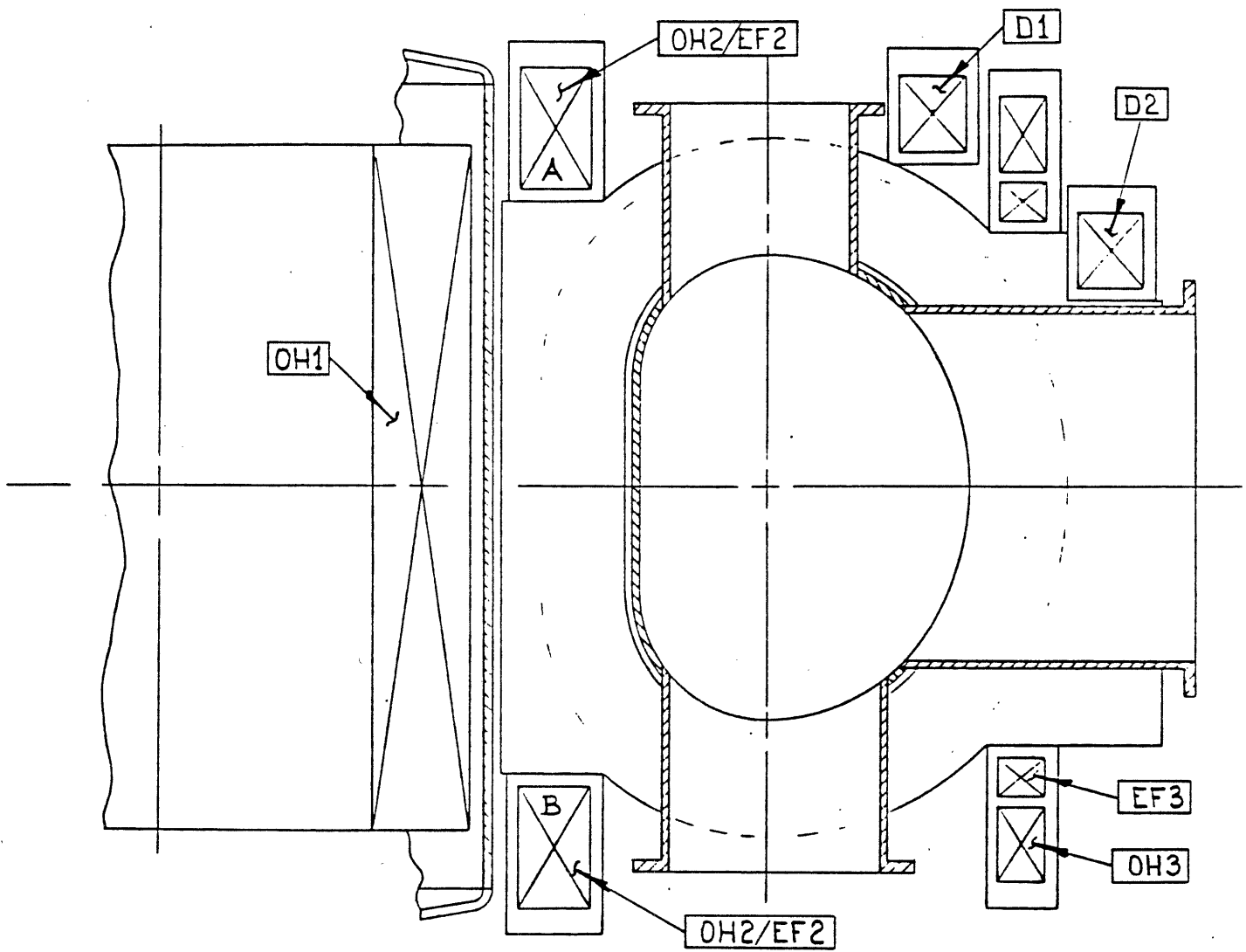


FIGURE 2.3-3 The Alcator DCT poloidal field coil set.

will also be used by the RF antennae.

2.3.4. Plasma Shaping

The simplest plasma configuration possible in Alcator DCT is the 0.40 meter radius circular discharge shown in Figure 2.3-4. For this case, the shaping coils are not energized, and we require only a modest vertical field. By increasing the shaping coil current we obtain the elongated, symmetric shape shown in Figure 2.3-5, which has an elongation of 1.25, and a triangularity of 0.31. Further increasing the currents in coils EF2 causes the triangularity to increase until x-points appear just inside the chamber wall.

In the divertor configurations, the plasma axis is located 0.10 to 0.15 meters below the midplane of the machine in order to provide room for the divertor collectors at the top. The current in coil EF2B and the series opposed pair D1,2 are adjusted to locate the x-point where desired. The other shaping coil, EF2A, is used to control the shape of the other half of the plasma.

2.3.5. Beta Dependent Equilibrium Effects

MHD equilibrium considerations do not seriously limit the achievable beta in Alcator DCT. The configurations shown in Figures 2.3-4,5,6 were computed for $\beta_p \approx 2$, $\langle\beta\rangle \approx 1\%$, and $\beta(0) \approx 3-4\%$. This corresponds to $\langle nT \rangle \approx 6 \times 10^{20} \text{ keV/m}^3$ ($\langle p \rangle = 2 \text{ atm}$) at a toroidal field of 7 Tesla and a plasma current of 1 MA. Figure 2.3-7 shows the variation of magnetic field configuration with beta, and Table 2.3-1 gives the corresponding coil currents. The values of energy content, beta, and $\epsilon\beta_p$ that will be

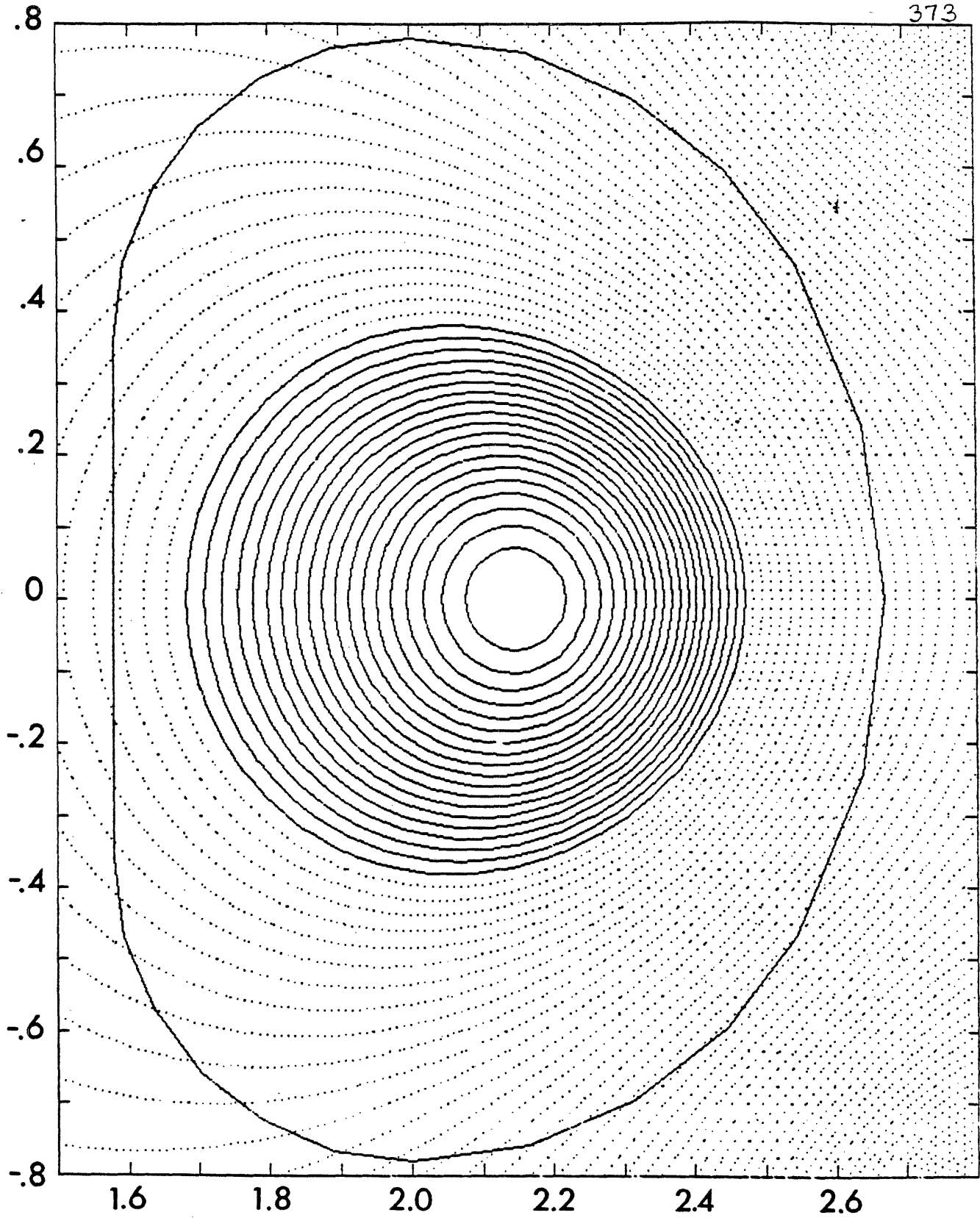


FIGURE 2.3-4 A 0.40m radius circular plasma. The plasma edge is set by a limiter (not shown) placed 0.10 in from the inner wall of the chamber.

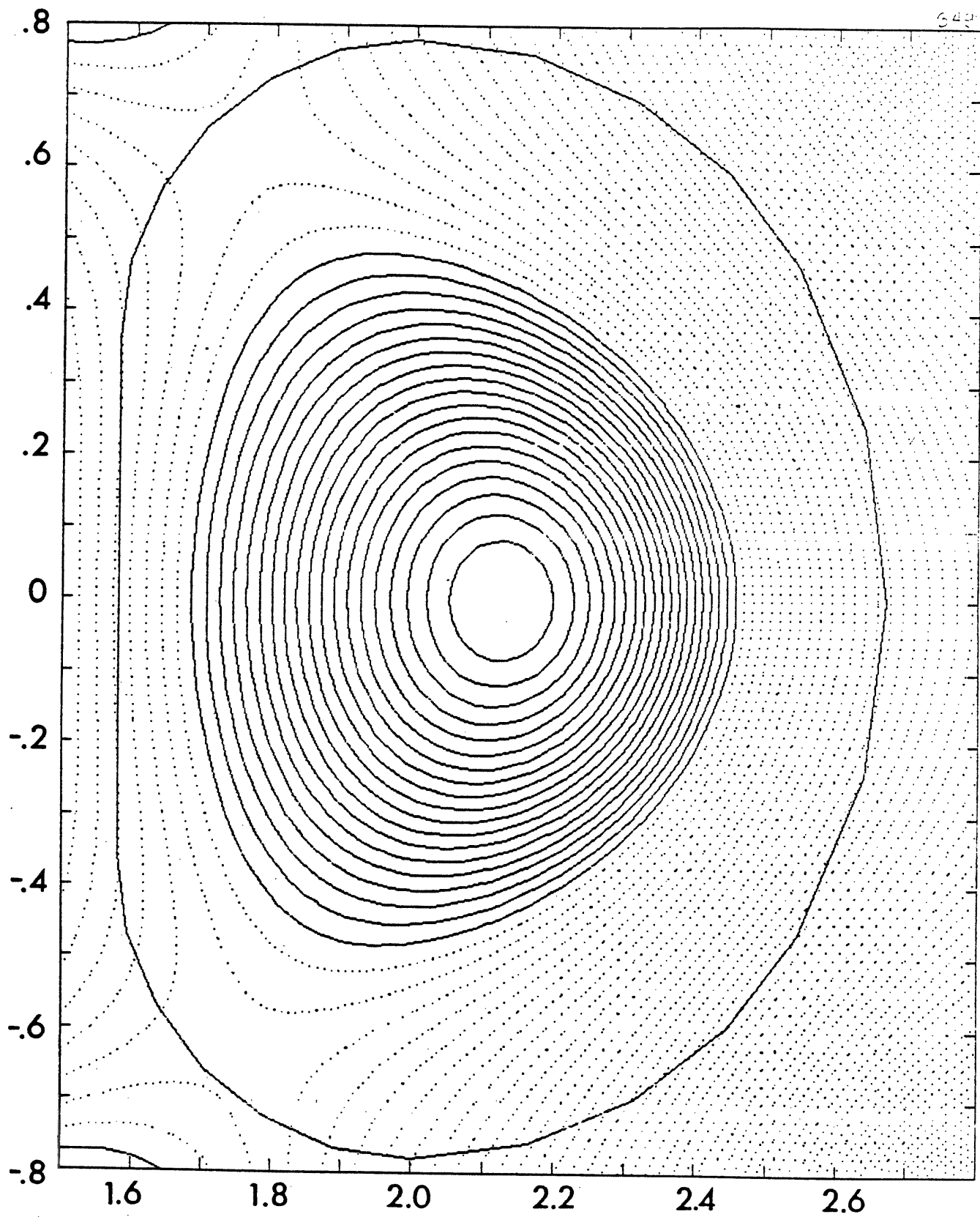


FIGURE 2.3-5 A large (0.44 m average radius) D-shaped plasma; $\kappa = 1.25$, $\delta = 0.31$; current in EF2 = 2.0 MA-T.

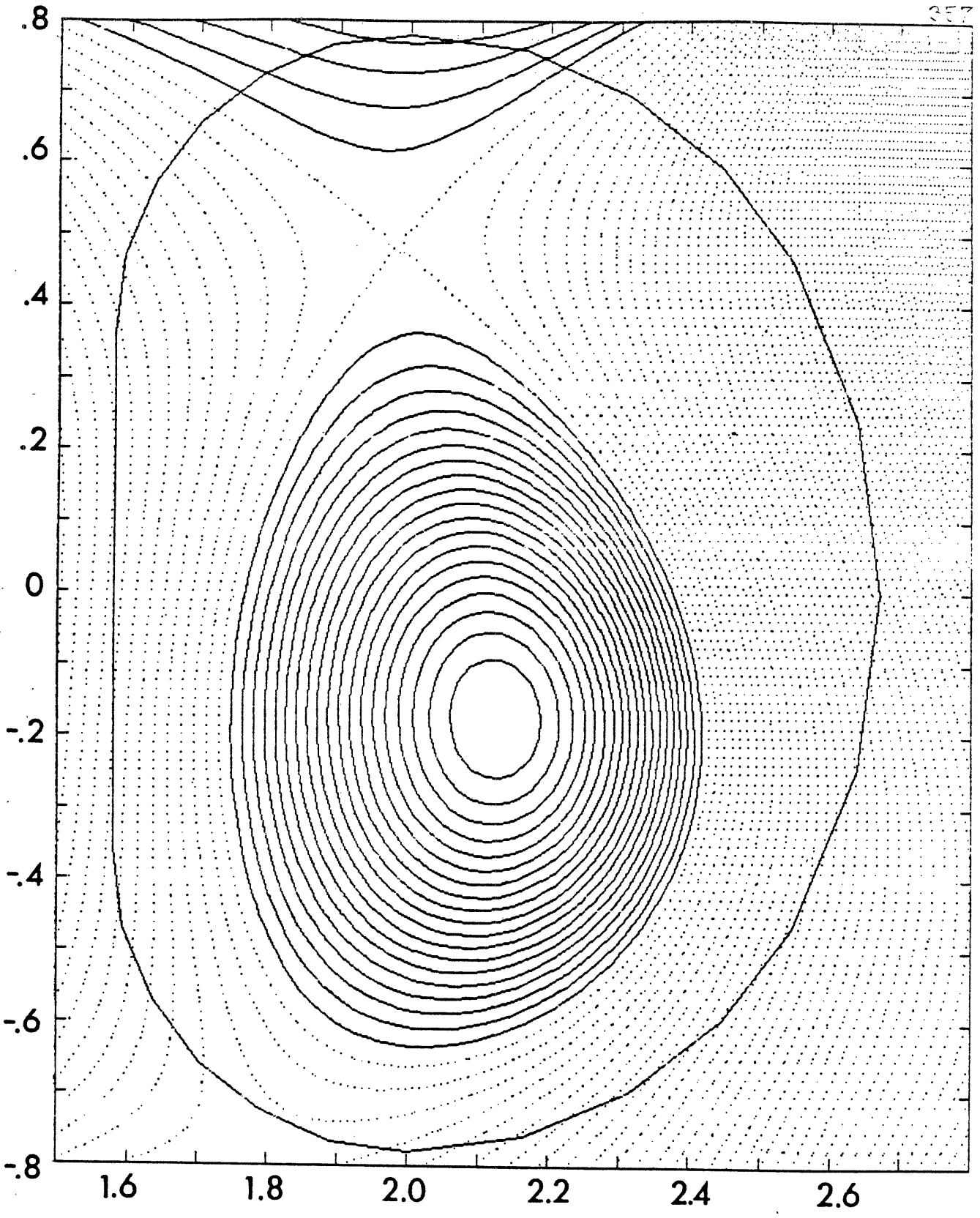


FIGURE 2.3-6 External coil divertor configuration; current in EF2 - 1.6MA,
 current in divertor coils D1 and D2 = ± 1.6 MA; $\kappa = 1.50$,
 $\delta = 0.21$.

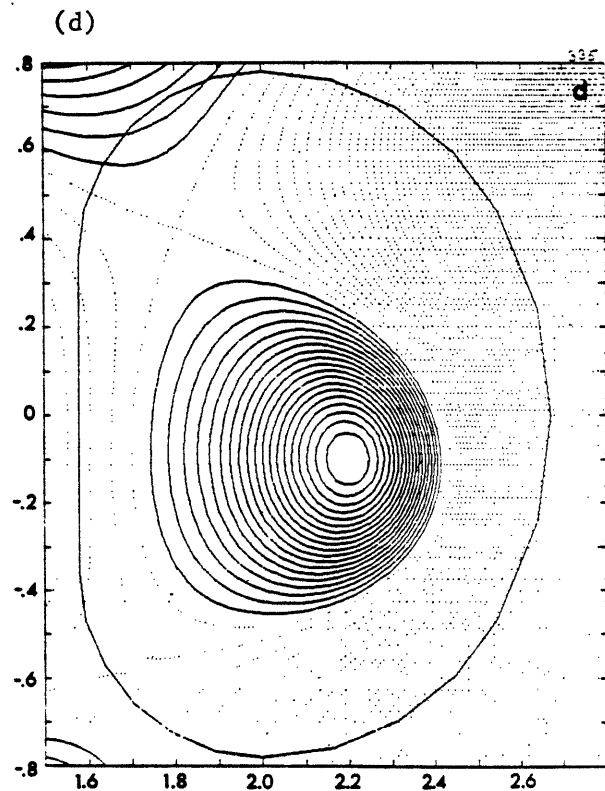
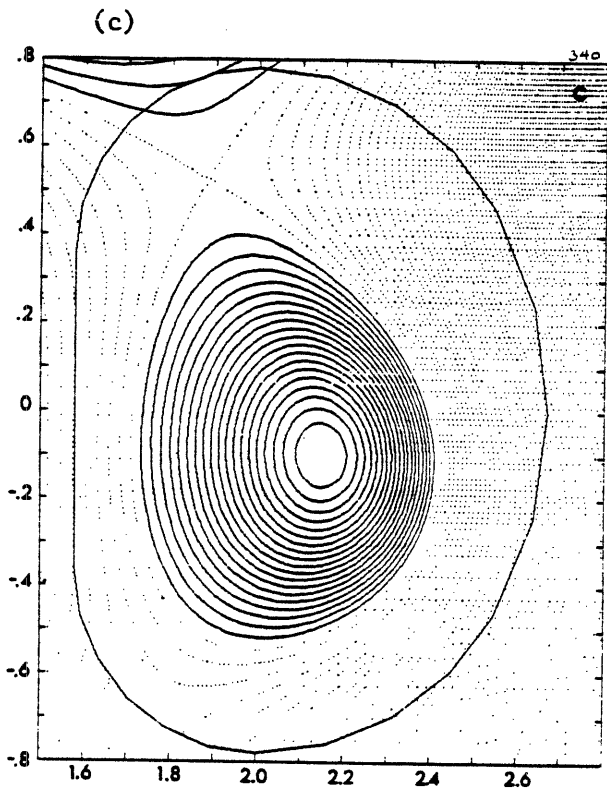
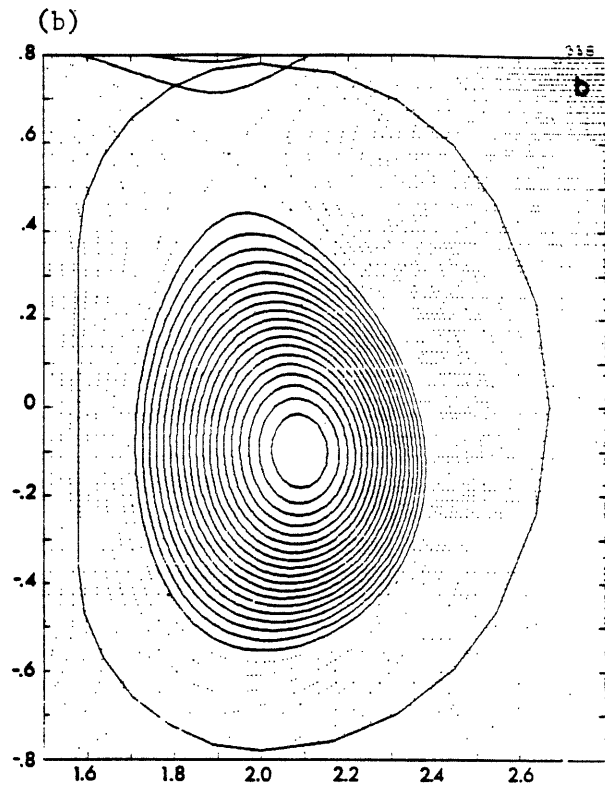
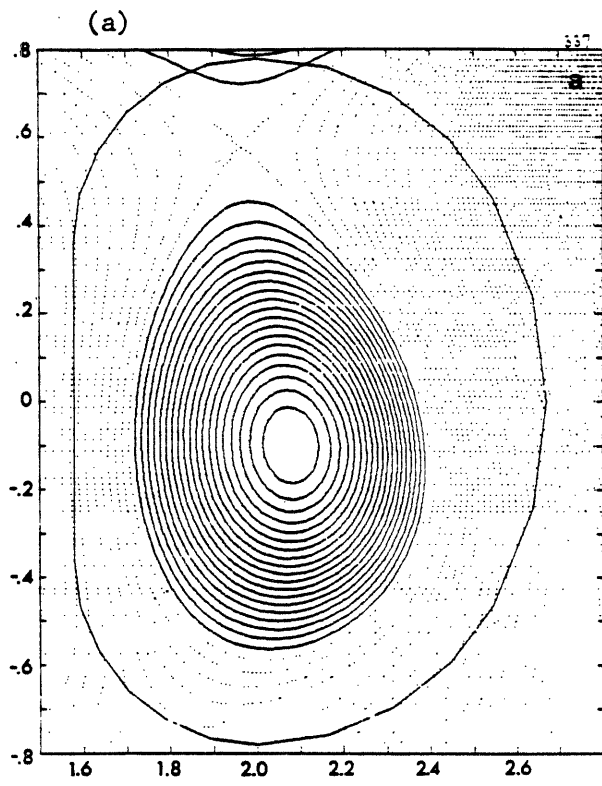


FIGURE 2.3-7 Effect of increasing beta. (a-d) at $\beta_p = 1.02, 1.98, 4.09,$ and 7.33 respectively. Shaping and divertor coil currents fixed at 1.6 MA each. The shift of the magnetic axis with respect to the geometric center of the outer surface is $0.027, 0.042, 0.080, 0.121$ m respectively.

obtained in Alcator DCT are subject to the uncertainties involved in estimation of RF coupling efficiency and of transport and other losses. The equilibrium limit of $\epsilon\beta_p \approx 1$ corresponds roughly to $\langle\beta\rangle > 2.5\%$ and $\beta(0) > 10\%$. This would give $\langle nT \rangle > 15 \times 10^{20}$ keV/m³ at 7 Tesla, or a total energy content of about 5 MJ.

TABLE 2.3-1

Effect of Increasing Beta on EF Coil Current Requirement

Case #	β_p	$\langle\beta\rangle$	I_{lower}^*	I_{upper}
336	0.52	0.25 %	-214 kA	+ 16 kA
337	1.02	0.49	-265	- 37
338	1.98	0.96	-363	-139
340	4.09	2.17	-523	-333
335	7.33	4.70	-809	-641

*Lower and upper refer to the EF3 coils as shown in Figure 2.3-3.

Finite beta effects are clearly seen in these equilibria well before the equilibrium limit is reached. The shift of the plasma axis, and distortion of the plasma surface become significant at $\beta_p \sim 1$. Thus the range of operating parameters envisioned for Alcator DCT fall well within the regime of "finite-beta" equilibria. The use of extreme shaping (i.e., "beans") to achieve very high values of beta is a possible enhancement for Alcator DCT, and is discussed further in the Appendix.

2.3.6. Stability Limits

Although the study of "high beta" phenomena is not a primary objective of the Alcator DCT baseline program, it is interesting and useful to examine the stability limits for this device. The limits for ideal MHD modes, kink and ballooning, are close to the envisioned range of operat-

ing parameters. We have investigated the stability of the Alcator DCT plasmas using the Pest2 code and associated ballooning stability codes. This code does not give exact eigenfunctions, but allows the efficient determination of stability boundaries over a wide parameter range. In order to cope with the perpetual question of internal (fixed plasma boundary) kink modes versus external modes with a wall at infinity, we have considered cases with a wall radius of 0.55 m, the approximate average radius of the Alcator DCT vacuum chamber. Parametric surveys indicate that the shape of the wall has little influence on the low n stability properties, but that its average radius has a strong influence. The choice of $\langle a_{\text{wall}} \rangle / \langle a_{\text{plasma}} \rangle \sim 1.4$ yields an increase in the limiting beta near rational values of q of 50-100% (due to the partial stabilization of the external modes). The range of beta limits for ideal kink modes is roughly 0.8-2.5% depending on the details of choice of pressure and current profiles, the value of q, and the plasma shape. Our studies have concentrated on the n=1 mode, which becomes unstable at the lowest values of beta. The lower values of limiting beta ($\sim 0.8-1.0\%$) are found for high q (~ 4) and peaked pressure profiles. As q is reduced, or the pressure broadens, the beta limit increases. The greatest limits (2.0-2.5%) are obtained for $q \sim 2-2.5$, $p \sim \psi^2$, with an elongation and triangularity of 1.6 and 0.2 respectively. We have also computed the beta limits against ballooning modes for many of these cases. In almost all of the cases the ballooning limit is found to be between 1.0 and 1.3 times the n=1 kink limit.

TABLE 2.3-2

< β > Limits for n=1 Mode

κ (elongation)	δ (triang.)	$q(a)$	$\langle\beta\rangle$ (%)
1.0	0	2.5	1.08
1.0	0	4	0.79
1.0	0	6	0.48
1.3	0	2.5	1.27
1.3	0.2	2.5	1.14
1.6	0	2.5	2.11
1.6	0.2	2.5	2.29

2.3.7. The Vertical (n=0) Instability

A problem associated with the formation of elongated plasmas in tokamaks is that the vacuum equilibrium field required for shaping has negative curvature, resulting in a plasma equilibrium which is unstable to vertical motion. In the absence of any toroidal conductors, this instability has a growth time of the order of the poloidal Alfvén time (typically a microsecond). However, the presence of toroidal conductors, principally the vacuum chamber itself, can increase this growth time by three orders of magnitude (to a millisecond or more). The growth can be further slowed with additional passive conductors. For example, a pair of single turn copper coils may be placed inside the vacuum chamber in the locations shown in Figure 2.3-8. If these are connected in series opposition, they are uncoupled from the rest of the PF system, but couple strongly to vertical motions of the plasma. In order to eliminate the

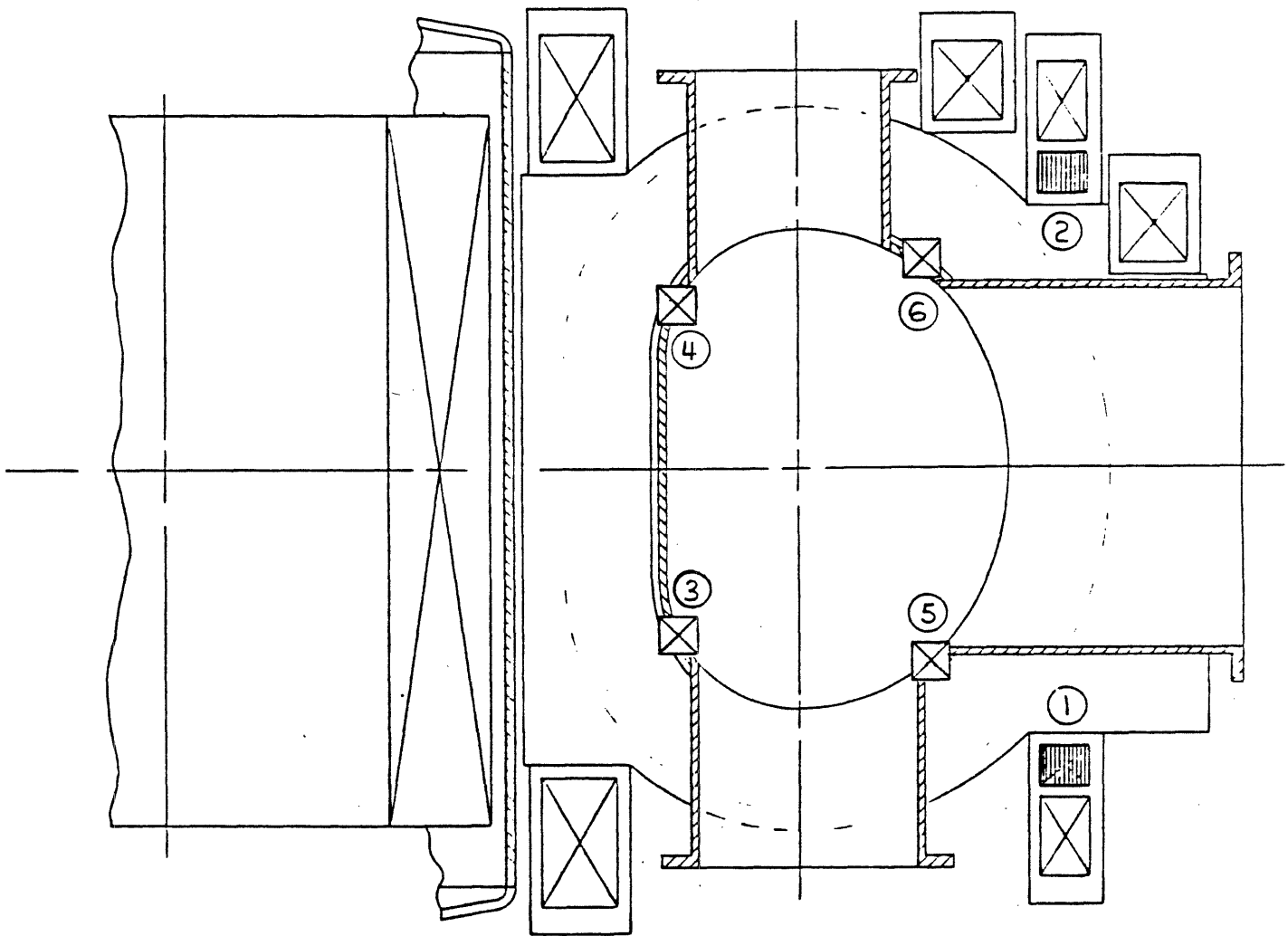


FIGURE 2.3-8 Possible locations for control coils.

instability, an active feedback system is required as well. The power and frequency response required depend on the locations of both the active and passive control coils. Some of the possible configurations are summarized in Table 2.3-3. Figure 2.3-8 shows the locations referred to in the table. Copper coils at locations 3-6 would be installed inside the chamber. Stainless steel coils at these locations simulate the chamber itself. The time constants are in the range of roughly 2-300 msec, and the necessary powers between 20 and 2000 kVA. As most of the possibilities under study are well within the capabilities of existing systems, the selection of a particular control system will depend on the results of further analysis and optimization.

TABLE 2.3-3

Control Coil Parameters

Coil Materials*			Instability growth time (no feedback)
1 & 2	3 & 4	5 & 6	
sc	ss	ss	6 msec
sc	ss	cu	23
sc	cu	ss	79
sc	cu	cu	306

*ss: stainless steel wall
 cu: 100 cm² copper coil
 sc: superconducting

2.4. RF Current Drive

2.4.1. Introduction

The only established technique for RF generation of significant toroidal current in tokamaks is by lower hybrid waves [2.4-1,2]; a detailed

review of this subject has recently been published [2.4-3]. The rapid historical development of LH current drive in recent years is illustrated in Figures 2.4-1 and 2. The physics issues of immediate concern include choice of a suitable frequency; accessibility of the wave spectrum to sufficiently high densities and temperatures; calculation of a "Brambilla spectrum" which will lead into the design of the waveguide array, or grill; current drive efficiency; toroidal ray tracing; and code simulations of current drive and heating. Here we shall discuss each of these relevant physics questions for Alcator DCT parameters.

2.4.2. Frequency Selection

To date frequencies in the range of $f \approx 800$ MHz to 4.6 GHz have been used in different lower hybrid experiments. A summary of some of these experiments is presented in Figure 2.4-3. We see that the frequency determines the operating density in a given device. The efficiency of current generation will depend on $\omega_{pe}^2/\omega_{ce}^2$; the smaller this parameter the larger the efficiency. Hence, efficient current generation at high densities requires a sufficiently high toroidal magnetic field. At present, the highest density current drive operation has been achieved in Alcator C, where RF currents of the order of ~ 200 kA have been driven at average densities of $\bar{n} \approx 8 \times 10^{13}$ cm $^{-3}$, and for short time durations ($t \lesssim 50$ msec) up to densities of $\bar{n} \approx 1 \times 10^{14}$ cm $^{-3}$. In order to achieve these parameters, power levels up to 1 MW were injected [2.4-4]. At such high power levels serious impurity problems arose which should not occur in Alcator DCT because of the divertor action. In any case, we feel that the 4.6 GHz frequency of the 16 cw klystrons presently available should be satisfactory in Alcator DCT to achieve current drive up to

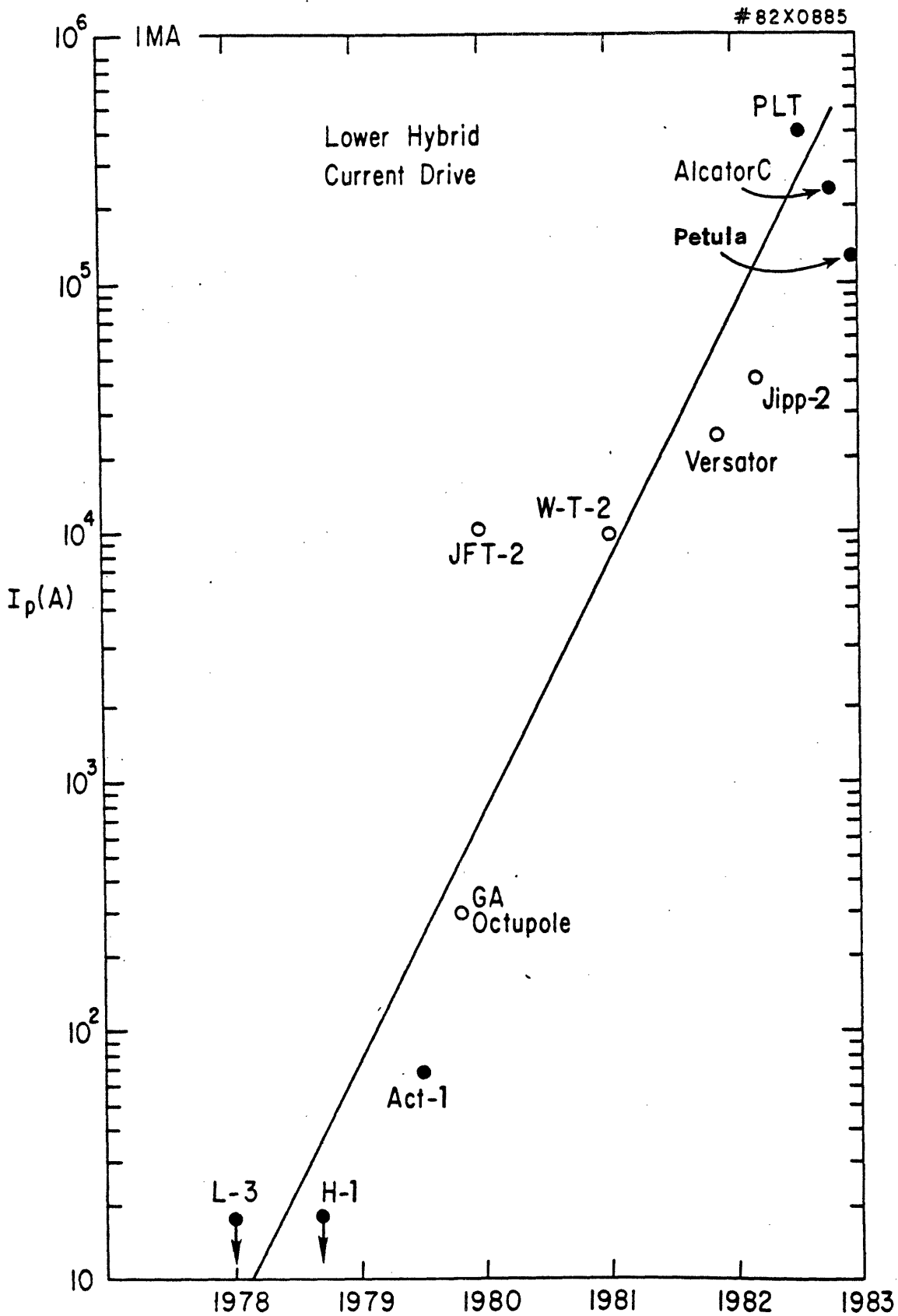


FIGURE 2.4-1 Recent history of lower hybrid current drive experiments: rf current generated versus time [after R. Motley, et al., IAEA Workshop on Current Drive, Culham, England, April, 1983].

CURRENT DRIVE EFFICIENCY

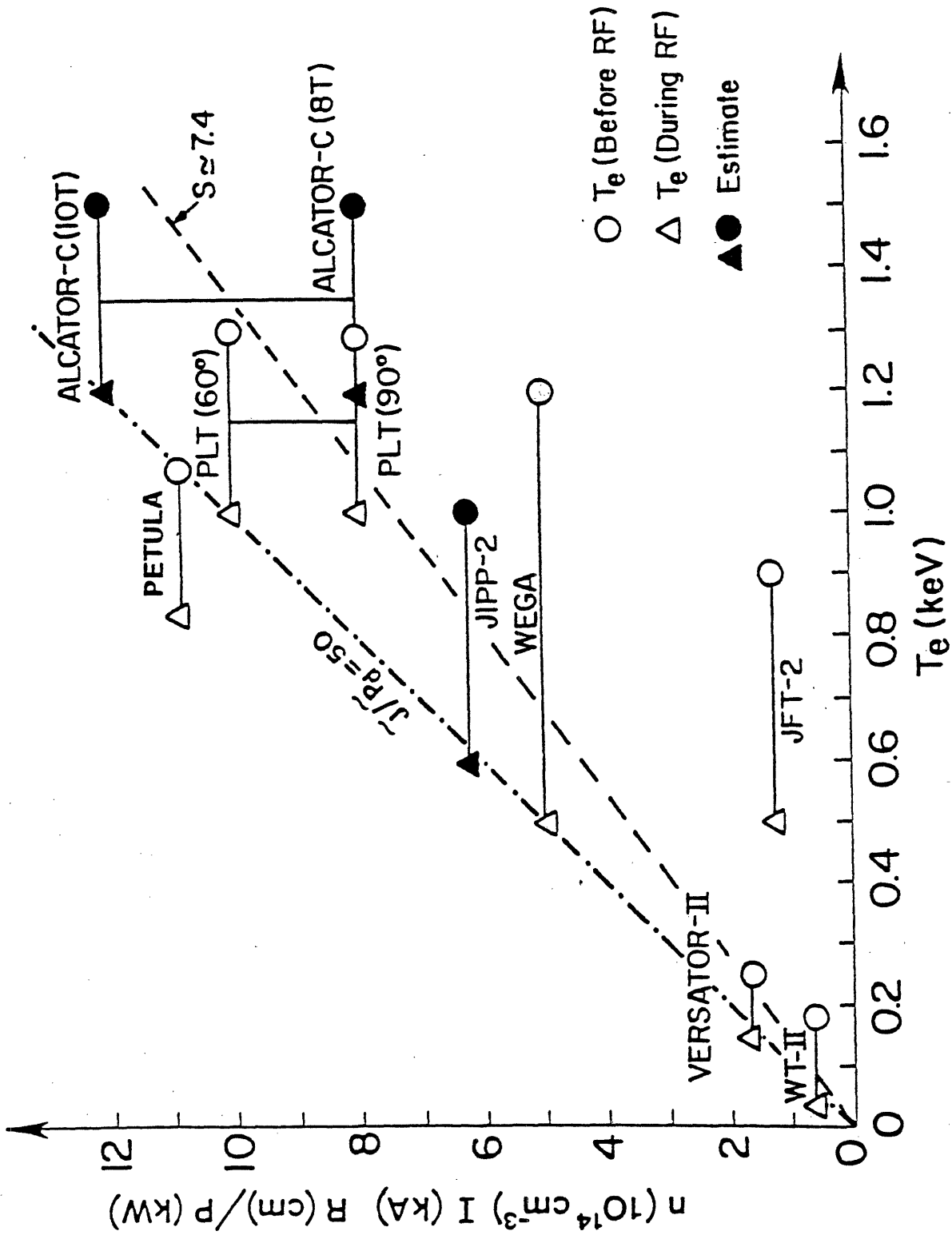


FIGURE 2.4-2 Current drive efficiency in various tokamaks [after M. Porkolab in FED-A Proposal, Oak Ridge National Laboratory . . . , Eds. P. Rutherford and D. Peng, 1983; also Ref. 2.4-3].

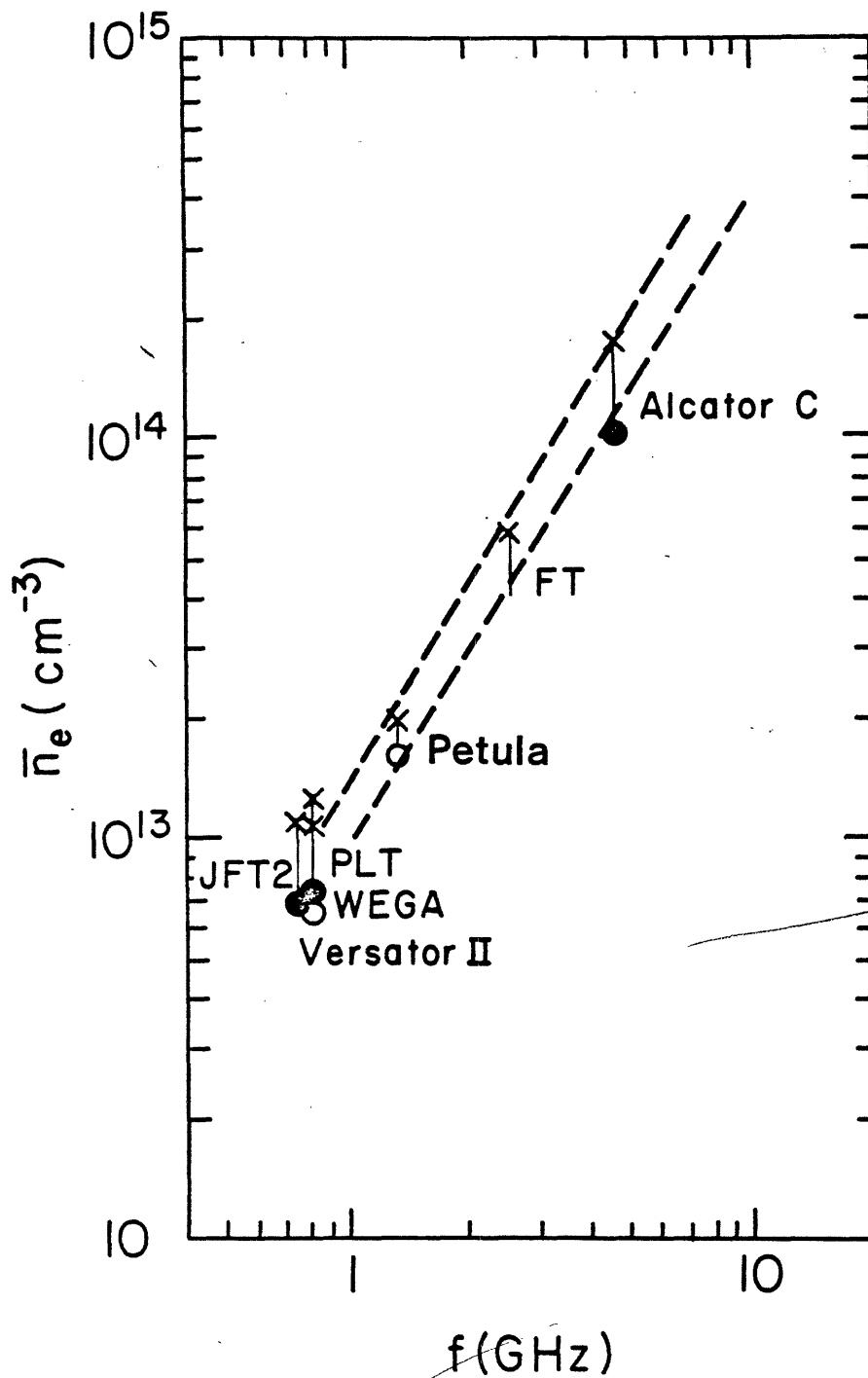


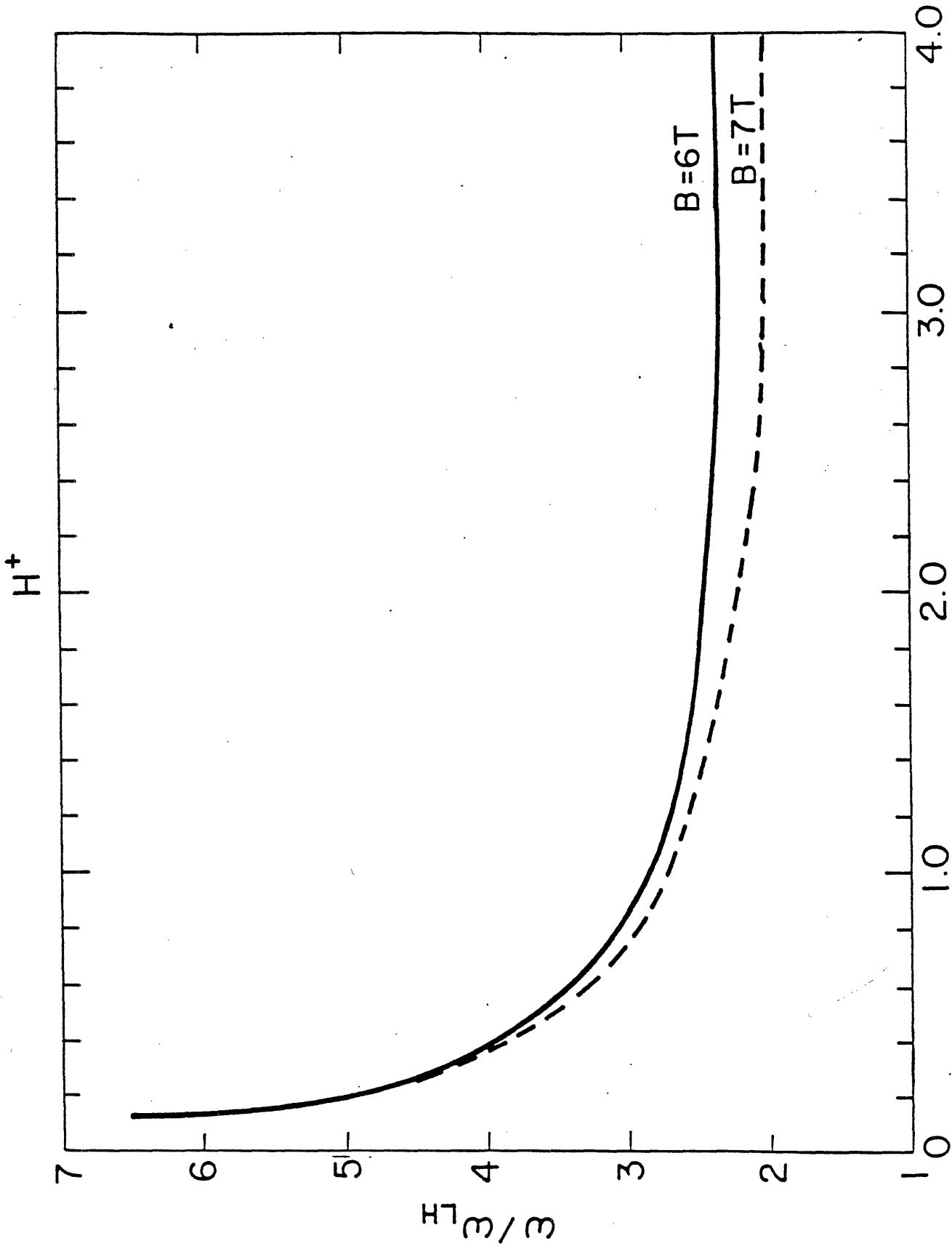
FIGURE 2.4-3 Density "limit" for current drive versus frequency [after F. Santini et al., "Interaction of Lower Hybrid Waves with Fast Electron Tails in FT", IAEA Workshop on Current Drive, Culham, England, 1983]. The dots represent achieved values, and the crosses represent upper limits before ion heating occurs.

densities of $\bar{n} \approx 1 \times 10^{14} \text{ cm}^{-3}$. One of the requirements on the frequency for current drive is that the ratio $\omega/\omega_{\text{LH}}$ should be at least two in order to avoid ion heating. In Figure 2.4-4 we show $\omega/\omega_{\text{LH}}$ for $B = 6 \text{ T}$ and $B = 7 \text{ T}$. We see that at densities $n \lesssim 1.5 \times 10^{14} \text{ cm}^{-3}$ (i.e., $\bar{n} \lesssim 1 \times 10^{14} \text{ cm}^{-3}$) $\omega/\omega_{\text{LH}}(0) \gtrsim 2.5$; at $n(0) \approx 8 \times 10^{13} \text{ cm}^{-3}$ (or $\bar{n} \approx 5.3 \times 10^{13} \text{ cm}^{-3}$) $\omega/\omega_{\text{LH}}(0) \gtrsim 3.0$ at $B = 7 \text{ T}$. Thus, ion heating should not occur either due to linear mode conversion or due to parametric instabilities. We note that at $\bar{n} > 1.4 \times 10^{14} \text{ cm}^{-3}$ parametric instabilities and concomitant ion tail formation are observed in Alcator C, which may lead to absorption of the pump wave on the plasma surface. In addition, in Alcator C at densities $\bar{n} \lesssim 1.4 \times 10^{14} \text{ cm}^{-3}$ at $B \gtrsim 8 \text{ T}$ only electron heating and electron tail formation were observed. Thus, the 4.6 GHz frequency of available klystrons should be acceptable for current drive in Alcator DCT.

2.4.3. Accessibility

The second physics consideration of a lower hybrid current drive system is whether the waves are accessible to the plasma interior. We would like to ensure accessibility of relatively low N_{\parallel} waves since such waves interact with relatively high energy electrons, improving the current drive efficiency. Low N_{\parallel} waves also avoid absorption on the surface by electron Landau damping and collisional damping. The accessibility condition for avoiding mode conversion into the fast wave is given by:

$$N_{\parallel} > \frac{\omega_{\text{pi}}}{\omega} y + \sqrt{1 + \frac{\omega_{\text{pi}}^2}{\omega^2} (y^2 - 1)} \quad (1)$$



n (10^{14} cm^{-3})

FIGURE 2.4-4 ω/ω_{LH} for DCT parameters (hydrogen gas).

where $y^2 = \omega^2 / \omega_{ce} \omega_{ci}$. Absorption by Landau damping is given approximately by

$$N_{\parallel} > 7 / \sqrt{T_e(\text{keV})} \quad \text{for quasi-linear damping} \quad (2a)$$

$$N_{\parallel} > 5.8 / \sqrt{T_e(\text{keV})} \quad \text{for linear Landau damping} \quad (2b)$$

Taking a temperature of $T_e \approx 5$ keV, linear Landau damping occurs for $N_{\parallel} \gtrsim 2.6$, and quasi-linear damping occurs for $N_{\parallel} \gtrsim 3.1$. Using Equation 1 the accessible density as a function of N_{\parallel} is plotted in Figure 2.4-5 for $B = 6$ T and Figure 2.4-6, for $B = 7$ T, both for the case of hydrogen ions. Also shown are the relativistically corrected electron energies with which a wave packet with a given N_{\parallel} interacts and the values of $\omega_{pe}^2 / \omega_{ce}^2$ that are associated with the given density and magnetic field to which a wave packet with a given value of N_{\parallel} is accessible. We see that at $B = 7$ T in hydrogen, $N_{\parallel} \approx 1.45$ is accessible to a density of $n(0) = 1.0 \times 10^{14} \text{ cm}^{-3}$, and this wave packet interacts with electrons of $E \approx 180$ keV energy. On the other hand, if we consider accessibility to a density of $n(0) = 1.5 \times 10^{14} \text{ cm}^{-3}$, the accessible wave packet with $N_{\parallel} \approx 1.56$ resonates only with particles of $E \approx 140$ keV which are more collisional than the 180 keV electrons, and hence require more RF power to drive a given amount of current. Thus, for a given magnetic field and frequency at lower densities a more efficient current drive operation should be achieved. For example, at $n(0) \approx 5 \times 10^{13} \text{ cm}^{-3}$ (or $\bar{n} \approx 3.3 \times 10^{13} \text{ cm}^{-3}$) $N_{\parallel} \approx 1.34$ will interact with electrons of $E \approx 280$ keV which should result in a very efficient RF current production. Based on these results, we propose a Brambilla spectrum with N_{\parallel} 's in the range of $1.3 \lesssim N_{\parallel} \lesssim 3$; the higher values are desirable at the beginning of the RF pulse while the plasma is relatively cool ($T_e \sim 1.5$ keV) and

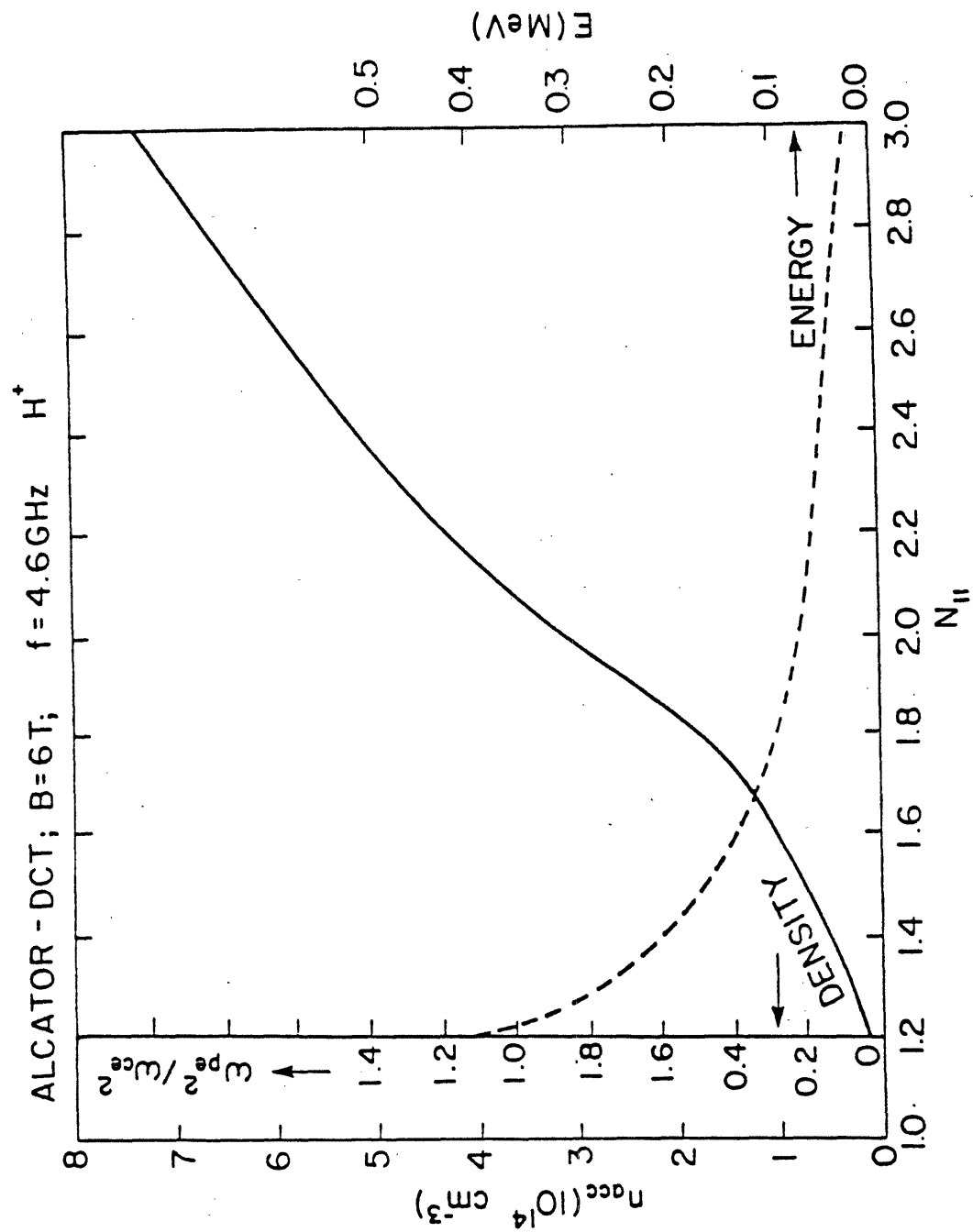


FIGURE 2.4-5 Accessibility density and electron energy versus $N_{||}$. B = 6 T, f = 4.6 GHz, H₂ gas.

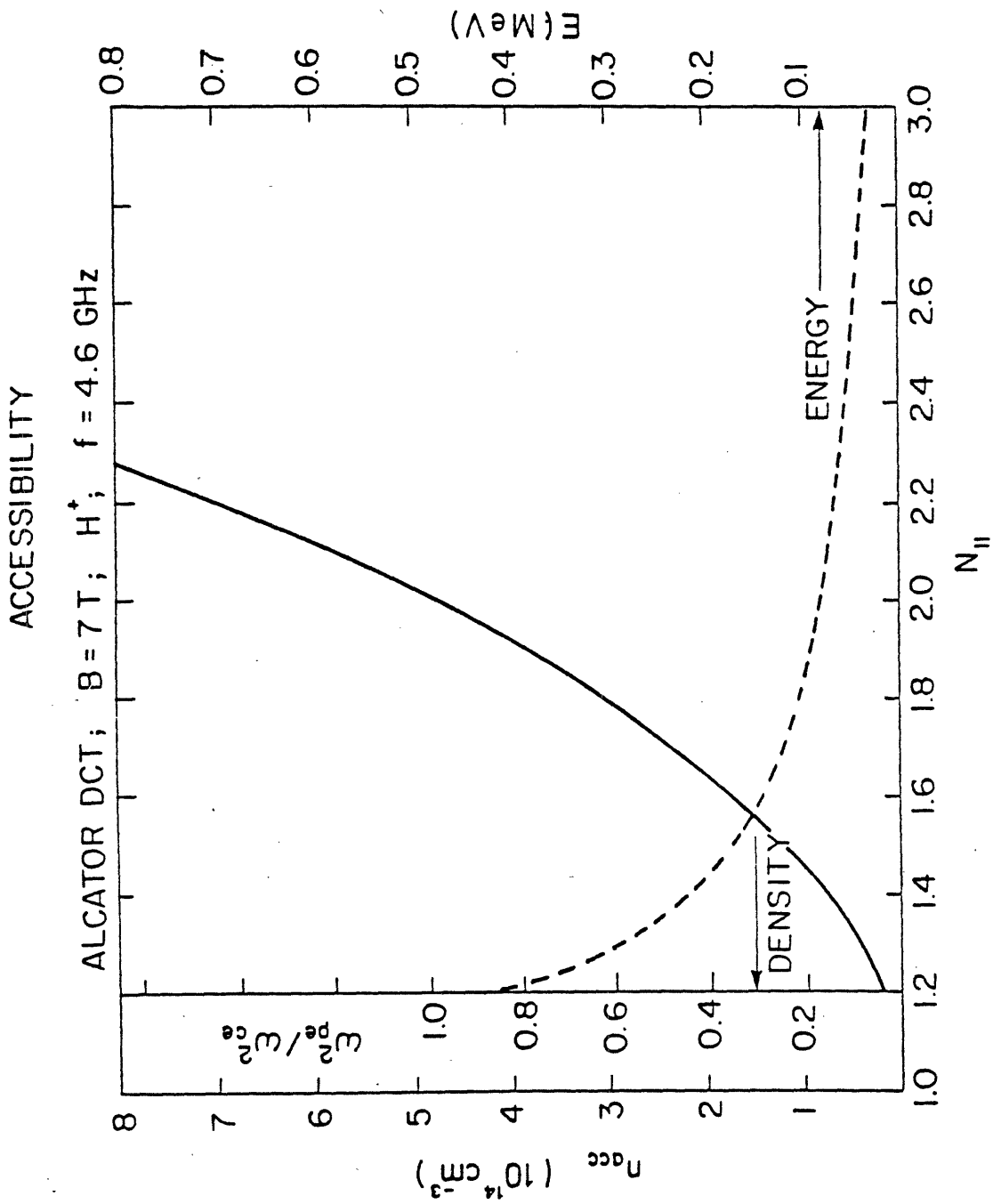


FIGURE 2.4-6 Accessible density and electron energy versus $N_{||}$. B = 7 T, f = 4.6 GHz, H₂ gas.

the lower values are desirable at fully heated plasma conditions.

2.4.4. Brambilla Spectrum

In designing a grill we have to ensure that sufficiently low N_{\parallel} 's are generated to enhance current drive efficiency and that the available ports are filled with waveguides as much as possible so as to occupy the minimum number of ports. Furthermore, the available RF power system should be compatible with the waveguide arrays. The detailed design of the waveguide array will be presented in the section on plasma engineering 3.4. To summarize, we expect 16 waveguides in a given row, and 4 (or at most 6) rows stacked vertically. This would produce a relatively narrow spectrum (considerably narrower than the "ideal" case considered earlier). Nevertheless, we expect that toroidal effects will broaden this spectrum as the rays propagate inward. In general, initially the rays tend to downshift N_{\parallel} and then subsequently upshift N_{\parallel} after the final "bounce" before absorption. The predicted Brambilla spectra for 90° and 180° phasing are shown in Figure 2.4-7. These spectra correspond to 16 waveguides that fit into an Alcator DCT port. We see that at a relative waveguide phasing of 180° the spectrum peaks at $N_{\parallel} \approx \pm 3.2$ and it extends from 1.8 to 3.6. Equal power is contained in the positive and negative components, and a negligible amount of current is expected to be generated. When we consider a relative phasing of 90° , the positive half of the spectrum peaks at $N_{\parallel} \approx 1.66$, and it extends from 1 to 2. There is also a small amount of power ($\sim 10\%$) in the negative half of the spectrum which peaks at $N_{\parallel} \approx -5$; this power is expected to be absorbed near the surface of the plasma column. A relative waveguide phasing of 120° leads to a spectrum which has some components with higher values of $+N_{\parallel}$, as well

Power Spectrum

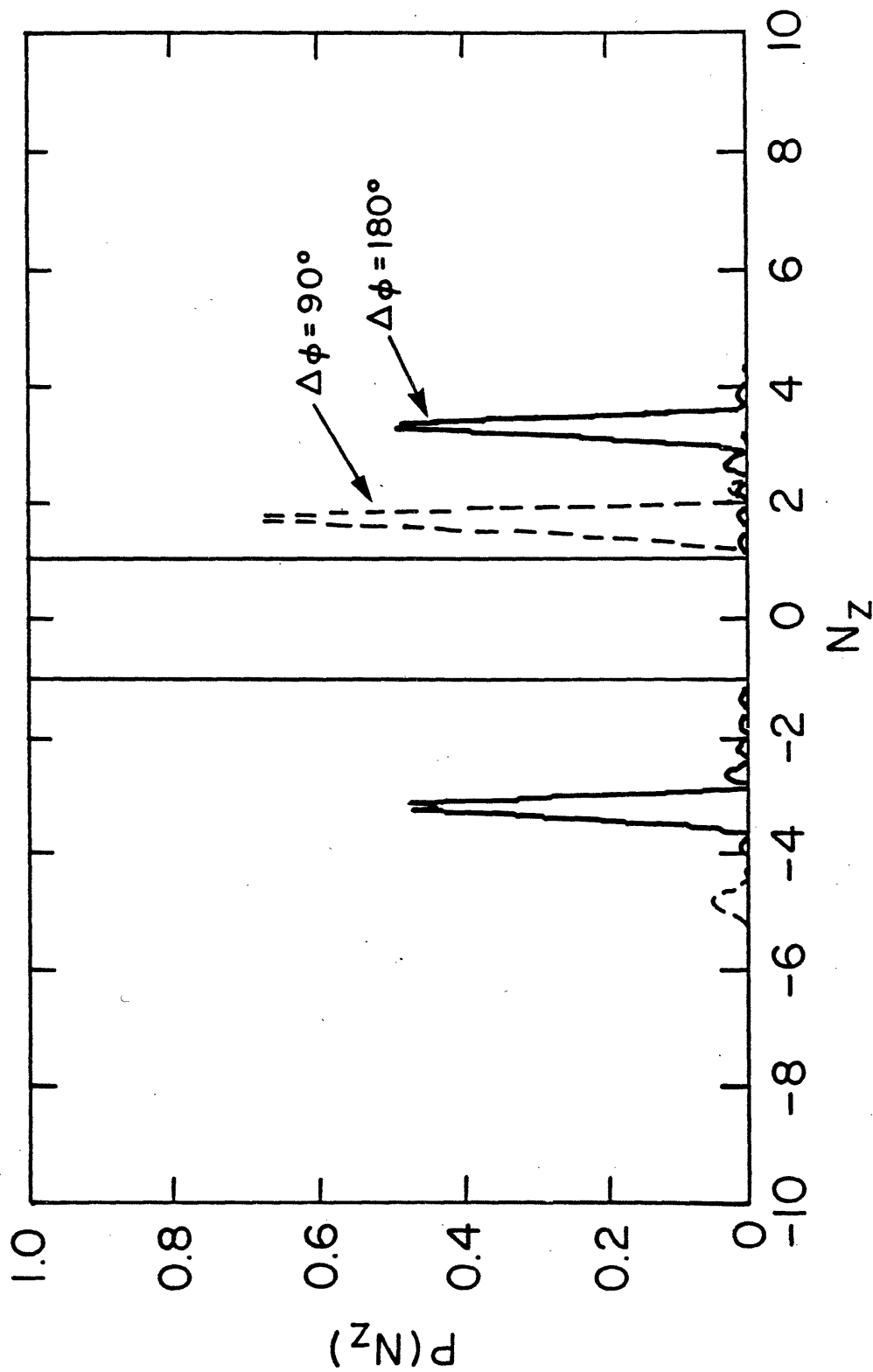


FIGURE 2.4-7 Brambilla spectra for 90° and 180° phasing of the DCT waveguide array: 16 waveguides in a row, the waveguide opening is 0.8 cm, and the separating wall is 0.2 cm.

as 25% of the power being contained in the negative part of the spectrum. Thus, we see that for 90° phasing the present spectrum is excellent for a density of $\bar{n} \lesssim 5 \times 10^{13} \text{ cm}^{-3}$, but that at $\bar{n} \approx 1 \times 10^{14} \text{ cm}^{-3}$ some part of the spectrum may be inaccessible. In that case a narrowing of the waveguide dimensions may be necessary. However, toroidal effects could modify the accessibility, and hence we have to study such effects before settling on final waveguide dimensions. We note that the dimensions used in the present design are similar to those of Alcator C, namely, 0.8 cm waveguide opening and 0.1 cm wall thickness of individual waveguides, leading to 0.2 cm separation of the waveguide openings.

2.4.5. Current Drive Efficiency

One of the key questions is the quantity of toroidal current that may be generated for a given amount of RF power available. This has been calculated by Fisch, and later by Fisch and Karney who used a Fokker-Planck code [2.4-5, 2.4-6]. Assuming an ideal flat power spectrum with $N_{\parallel 2} < N_{\parallel} < N_{\parallel 1}$ which Fisch gave a general formula for current generation which may be written in the following form:

$$\frac{n(10^{14} \text{ cm}^{-3})I(\text{MA})R(\text{m})}{P(\text{MW})} = 0.002 T_e(\text{keV})(\tilde{J}/\tilde{P}_D) \quad (3)$$

where

$$\tilde{J}/\tilde{P}_D = \alpha \langle w^2 \rangle \quad (4)$$

where α is a constant with a value $\alpha \approx 1.4-1.7$, depending on various assumptions and approximations. The normalized mean phase velocity is

defined as

$$\langle w^2 \rangle = \frac{(w_2^2 - w_1^2)}{2 \ln(w_2/w_1)} = \frac{c^2(1 - N_{\parallel 2}^2/N_{\parallel 1}^2)}{2N_{\parallel 2}^2 \frac{T_e}{m_e} \ln(N_{\parallel 1}/N_{\parallel 2})} \quad (5)$$

where $N_{\parallel 1}$ corresponds to the value given by Equation 2a. We note that the dominant factor in the current drive efficiency is $N_{\parallel 2}$, i.e. the minimum accessible N_{\parallel} value defined by Equation 1. Using this relationship, we have estimated the currents expected in Alcator DCT under optimum conditions; namely, we assumed $B = 7.0$ T magnetic field, $n_o/\bar{n} = 1.5$, $P_{abs} = 3.0$ MW, $N_{\parallel 2}$ as determined by accessibility, and $N_{\parallel 1}$ as determined by quasilinear damping rate (i.e., Equation 2a) which will bring a temperature dependence into Equation 5 wherever $N_{\parallel 1}$ occurs). The predictions for densities $\bar{n}_e = 1 \times 10^{14} \text{ cm}^{-3}$ and $\bar{n}_e = 5 \times 10^{13} \text{ cm}^{-3}$ are listed in Table 2.4-1. We see that at a temperature of $T_e = 5$ keV, we expect $I = 490$ kA to be generated at $\bar{n}_e = 1 \times 10^{14} \text{ cm}^{-3}$ and $I = 1.1$ MA at $\bar{n} = 5 \times 10^{13} \text{ cm}^{-3}$. We again note that these are currents generated by an optimized spectrum. In reality a given phased waveguide array will generate less than an optimal amount of current. Hence, we regard the values in Table 2.4-1 as upper limits. More accurate code predictions show that these currents may be generated only at 30% lower density than that assumed here; or, at the densities given in Table 2.4-1 we should expect 30% less current. Given the many approximations, the analytic estimates are surprisingly good when compared with the detailed code calculations of Section 2.4.7.

TABLE 2.4-1

Predictions of the Fisch-Karney Theory for Alcator DCT LH Current Drive

$B = 7.0T; f = 4.6 \text{ GHz}; P_{\text{abs}} = 3.0 \text{ MW}$

<u>$n_e \text{ (cm}^{-3}\text{)}$</u>	<u>$T_e \text{ (keV)}$</u>	<u>$I \text{ (kAmp)}$</u>
1×10^{14}	1	290
	3	400
	5	490
5×10^{13}	1	660
	3	920
	5	1100

2.4.6. Ray Tracing

In order to study the toroidal effects upon the penetration of lower hybrid waves, we have carried out detailed ray tracing calculations. Here we use a parabolic density profile ($n = n_0(1-r^2/a^2)$), $\bar{n} = 2/3 n_0$, $T_{e0} = 3 \text{ keV}$, $T_i = 2.5 \text{ keV}$, $I = 500 \text{ kA}$, $Z_{\text{eff}} = 1$, and hydrogen plasma. In these studies a Shafranov equilibrium is used. (Ray tracing has also been performed in non-Shafranov equilibrium situations). In order to simulate edge absorption, a relatively cold ($T_e = 30 \text{ eV}$, $n_e = 1 \times 10^{13} \text{ cm}^{-3}$) edge plasma halo is also included. The halo density decreases linearly with distance, and its radial extent is 6 cm. Multi-bouncing using specular reflection is allowed for rays that are not absorbed in the first pass and propagate out to the outer edge of the halo plasma. We find that in order to explain the present experimental results in Alcator C and PLT,

such multi-bouncing must be included. In Figures 2.4-8, 2.4-9 we show some examples of ray tracing for Alcator DCT parameters. The results of a rather extensive set of such calculations are summarized in Table 2.4-2 for $n_{e0} = 7.5 \times 10^{13} \text{ cm}^{-3}$, and in Table 2.4-3 for $n_0 = 1.5 \times 10^{14} \text{ cm}^{-3}$. Here $N_{\parallel}^{(0)}$ designates the initial value of N_{\parallel} launched, $N_{\parallel}^{(F)}$ designates the value of N_{\parallel} at the point of absorption, E_e designates the fraction of power absorbed by electrons by Landau damping, $E_e(r)$ gives the radial range where absorption takes place, E_L designates the fraction of power lost in the outer half of the plasma due to collisional absorption, and $E_L(r)$ shows the radial range of the collisional absorption. We find that the accessibility at $n_0 = 7.5 \times 10^{13} \text{ cm}^{-3}$ is good even for low values of N_{\parallel} (~ 1.5 for first pass, 1.3 after multi-passes), but at $n_0 = 1.5 \times 10^{14}$ only $N_{\parallel} > 1.5$ is accessible during the first pass. However, after many passes even lower N_{\parallel} 's, namely, $N_{\parallel}^{(0)} \gtrsim 1.3$ may be accessible.

TABLE 2.4-2

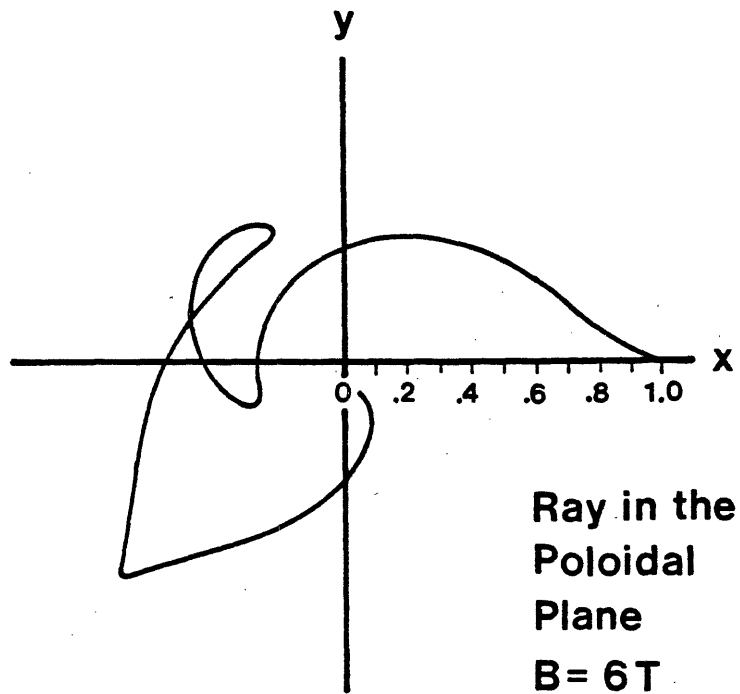
Ray Tracing Results

H^+ PLASMA; $n_{e0} = 7.5 \times 10^{13} \text{ cm}^{-3}$; $B = 7 \text{ T}$; $a = 40 \text{ cm}$

$n_{\parallel}^{(0)}$	$n_{\parallel}^{(F)}$	E_e	$E_e(r)$	E_L	$E_L(r)$
1.3(a)	3.7	94%	$0.15 < r/a < 0.4$	5%	$0.7 < r/a < 1$
1.5(b)	3.2	92%	$0.05 < r/a < 0.3$	7%	$0.7 < r/a < 1$
1.8(c)	3.5	95%	$0.0 < r/a < 0.35$	4%	$0.8 < r/a < 1$
2.0(d)	2.1	0%	---	15%	$0.8 < r/a < 1$
3.0(c)	3.2	98%	$0.05 < r/a < 0.4$	1%	---
4.0(e)	4.3	98%	$0.3 < r/a < 0.55$	1%	---

- (a) Ray not accessible for first π radians of trajectory.
- (b) Initially accessible.
- (c) Damped after 2-3 bounces at edge.
- (d) Ray accessible but never damped (good radial penetration) (if assume linear Landau damping).
- (e) Ray damped on first pass to plasma center.

a]



b]

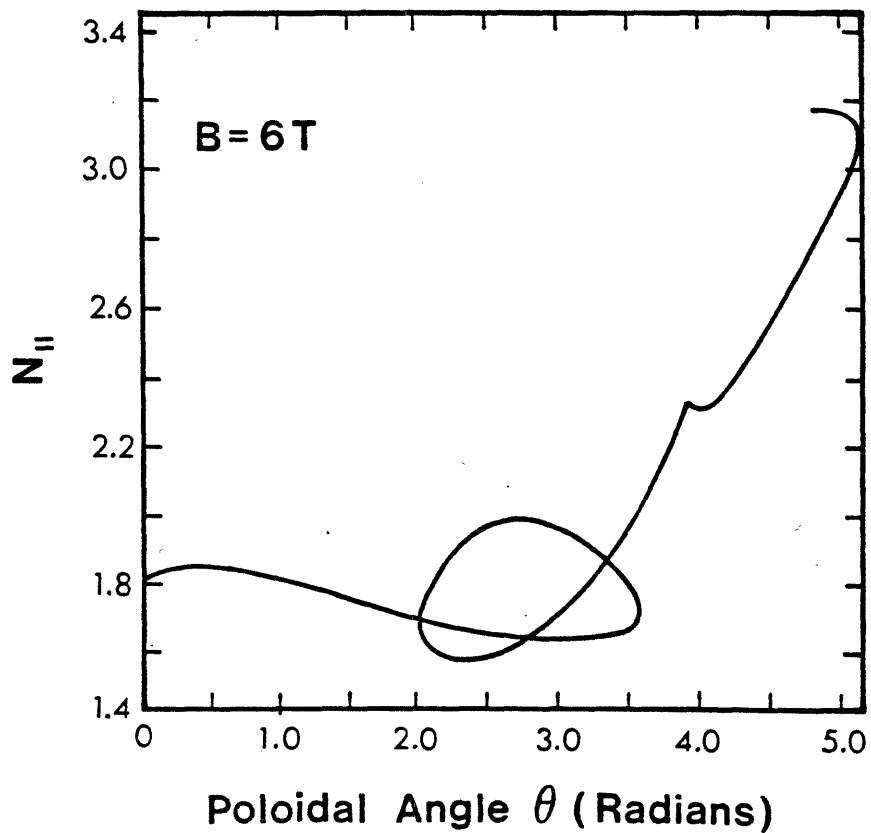
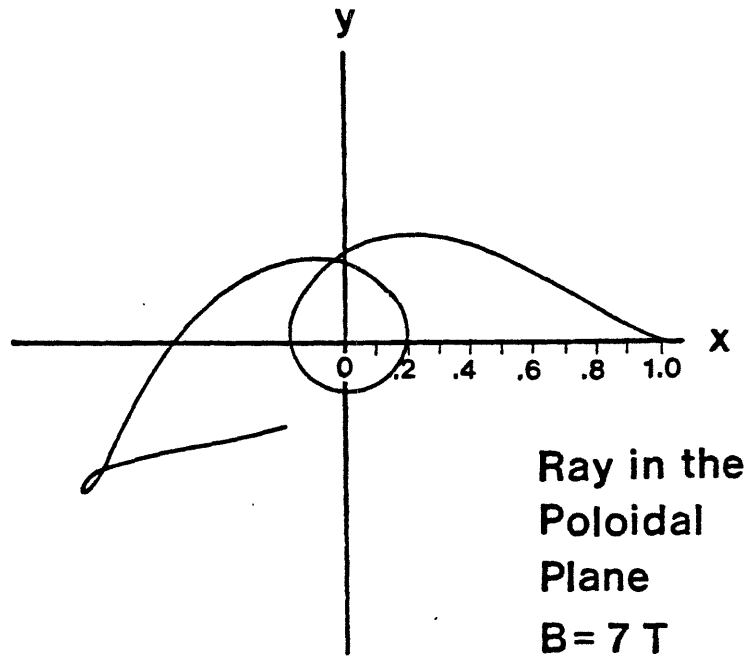


FIGURE 2.4-8 (a) Ray tracing in the poloidal plane; (b) N_{\parallel} versus θ , the poloidal angle. $N_{\parallel}(0) = 1.8$, $B = 6$ T, $n(0) = 7.5 \times 10^{13} \text{ cm}^{-3}$, H_2 gas.

a]



b]

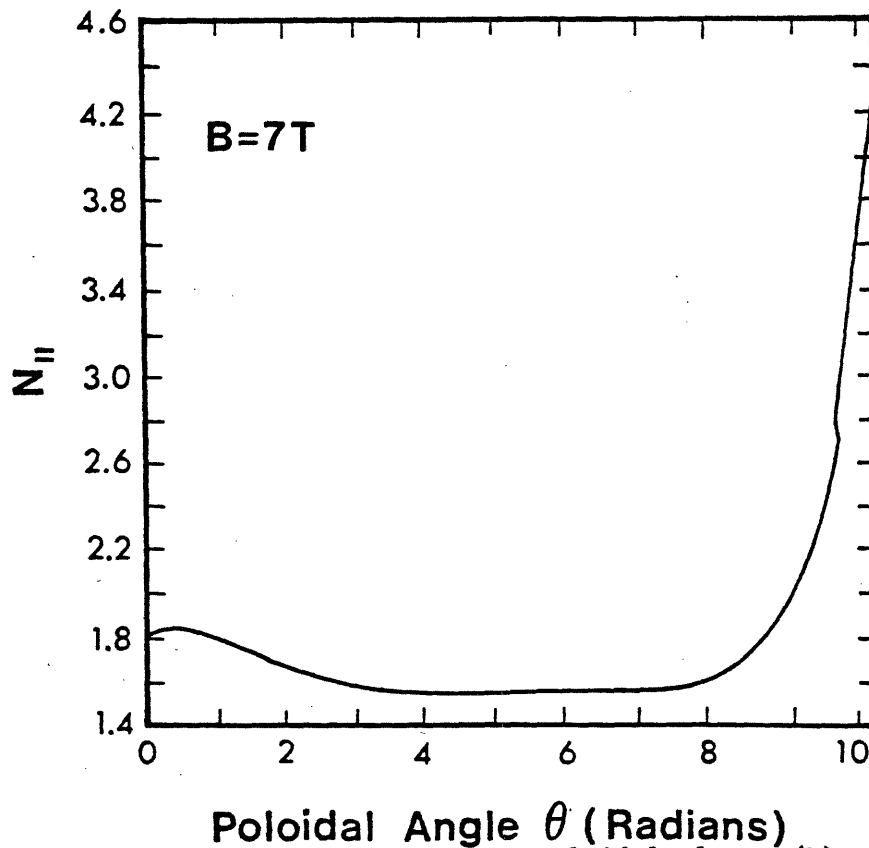


FIGURE 2.4-9 (a) Ray tracing in the poloidal plane; (b) N_{\parallel} versus θ , the poloidal angle. $N_{\parallel}(0) = 1.8$, $B = 7$ T, $n(0) = 1.5 \times 10^{14} \text{ cm}^{-3}$, H_2 gas.

TABLE 2.4-3

Ray Tracing Results

H⁺ PLASMA ; $n_{e0} = 1.5 \times 10^{14} \text{ cm}^{-3}$; $B = 7 \text{ T}$; $a = 40 \text{ cm}$

$n_{\parallel}(0)$	$n_{\parallel}(F)$	E_e	$E_e(r)$	E_L	$E_L(r)$
(a) 1.3	3.4	83%	$0.1 < r/a < 0.35$	17%	$0.7 < r/a < 1$
(a) 1.5	4.0	80%	$0.25 < r/a < 0.4$	19%	$0.6 < r/a < 1$
(b) 1.8	4.2	90%	$0.25 < r/a < 0.5$	9%	$0.7 < r/a < 1$
(c) 2.0	2.7	0%	---	44%	$0.6 < r/a < 1$
(b) 3.0	4.0	93%	$0.0 < r/a < 0.5$	6%	$0.7 < r/a < 1$
(d) 4.0	4.1	96%	$0.3 < r/a < 0.55$	3%	$0.7 < r/a < 1$

(a) Ray inaccessible for first π radian of trajectory

(b) Ray initially accessible (damped after 1 bounce at edge)

(c) Ray accessible but never damped (if assume linear Landau damping)

(d) Ray damped on first pass to plasma center

This result shows that if the divertor can maintain a relatively high edge temperature ($T_e > 50$ eV) we expect negligible collisional surface absorption and eventual ray penetration to the center even at densities $\bar{n} \approx 1.0 \times 10^{14} \text{ cm}^{-3}$. These tables also show good ray penetration for $N_{||} \lesssim 3$ at least for temperatures $T_{e0} \lesssim 3$ keV (assuming linear Landau damping). For higher temperatures, transport code studies will be used to study ray penetration.

2.4.7. Code Simulations

A detailed simulation model has been used to study lower hybrid current drive (LHCD) and lower hybrid heating (LHH) in the Alcator DCT device. The model includes a radial transport code [2.4-7] in conjunction with a one-dimensional Fokker-Planck calculation and a toroidal ray tracing code [2.4-8]. In Figure 2.4-10 we show a block diagram of the combined code package. The code is described in detail in Appendix (A). Here we shall discuss the results of the code. The code was tested by simulating LH current drive in Alcator C and the predictions were compared with the experimental results. The results are shown in Figure 2.4-11. Here the current drive efficiency, $\bar{n}(10^{14} \text{ cm}^{-3})I(\text{kA})/P(\text{kW})$ is plotted as a function of the toroidal magnetic field. We see that the experimentally observed values, which depend on limiter material [2.4-4], span the code predictions at both 8 and 10 Tesla. In general, the currents generated in poco-graphite limited plasmas were 30-40% lower than currents obtained in molybdenum limited plasmas. It is believed that the carbon limiter produces a colder, higher density plasma in the outer layers than molybdenum. On the other hand, at the 1 MW level a decrease in the current after 20-40 msec, accompanied by injection of significant amounts of

BLOCK DIAGRAM OF CODE

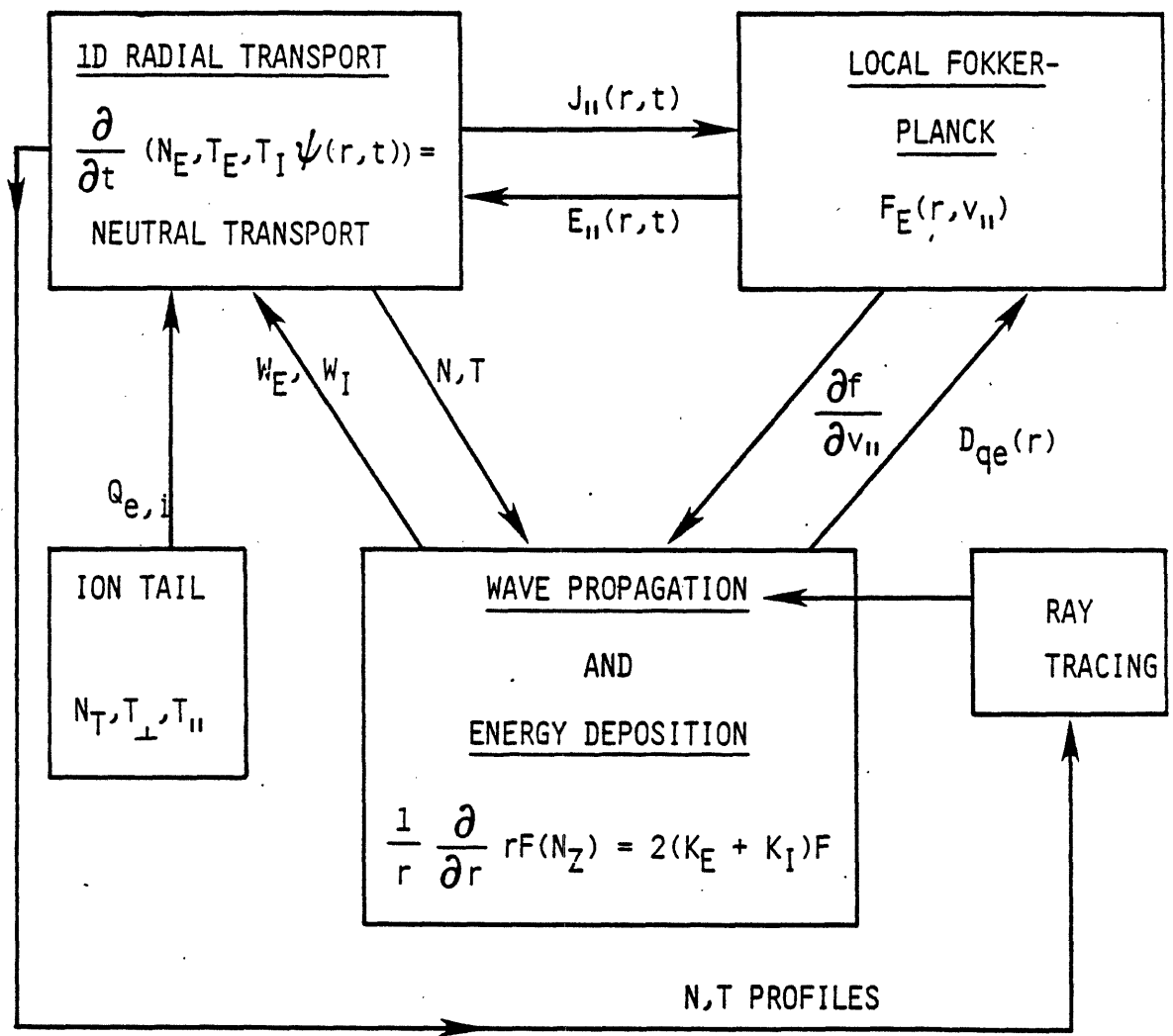


FIGURE 2.4-10 Block diagram of the combined ray tracing transport Fokker-Planck code. See Appendix A for a detailed description of the code.

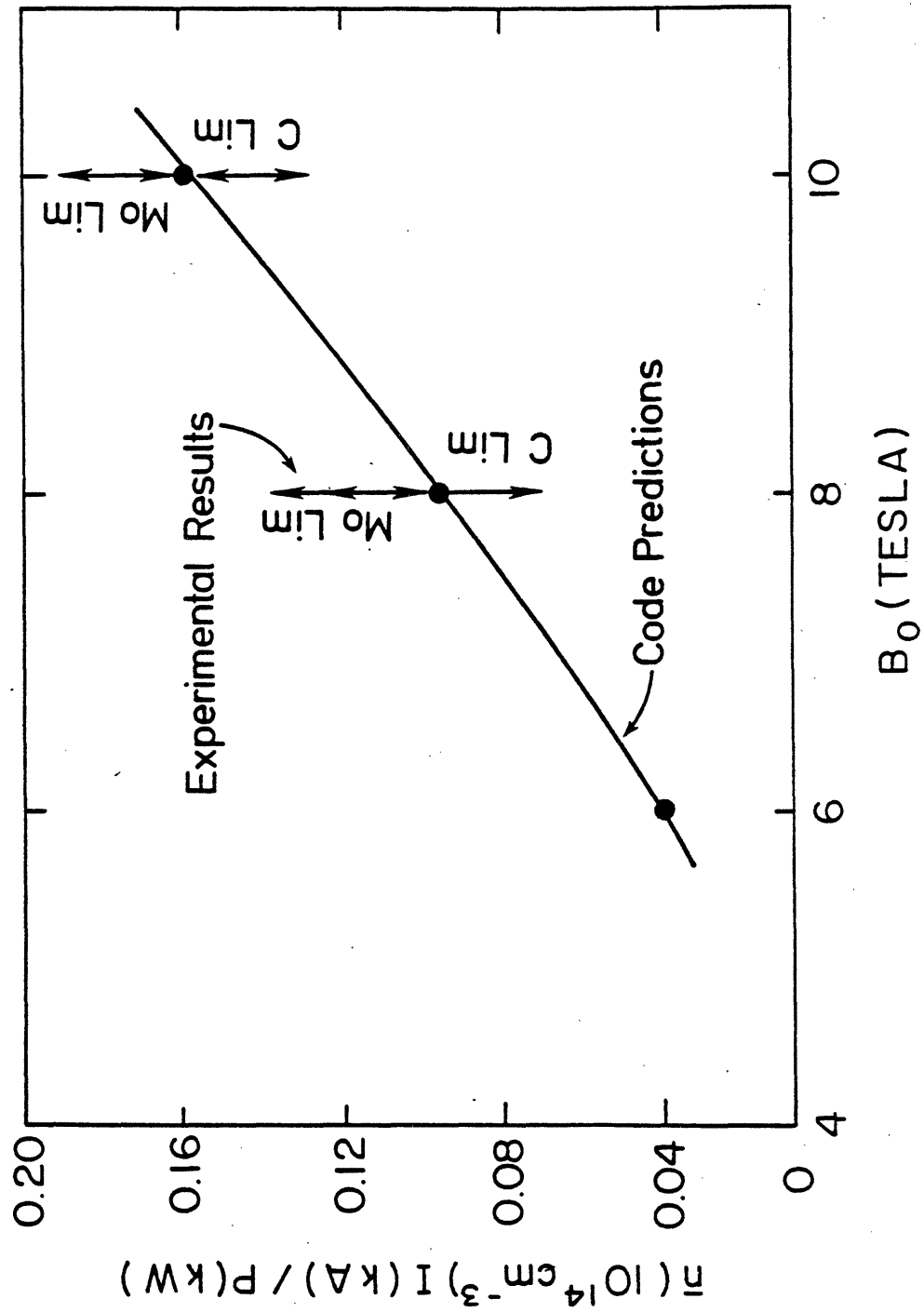


FIGURE 2.4-11 Current drive efficiency versus magnetic field for the Alcator C grill geometry. The code results are shown by the solid line, and the experimental results are indicated by the vertical arrows.

high-Z limiter material (molybdenum) was observed.

For Alcator DCT we have used two Brambilla spectra for current drive studies. The spectrum shown in Figure 2.4-12a and Figure 2.4-7 corresponds to the coupler described in Section 3.4, namely a 16 waveguide coupler with outside guide widths of 1.0 cm. This spectrum peaks at $N_{\parallel} \approx 1.66$. A second idealized spectrum, shown in Figure 2.4-12b was also tested in the code and was found to yield a somewhat better current drive efficiency than the first case. This is due to the fact that this spectrum peaks near $N_{\parallel} \approx 2.0$, and after toroidal broadening it corresponds more closely to the ideal current drive spectrum discussed earlier. However, to produce a grill which would yield a spectrum peaking at $N_{\parallel} \approx 2.0$ would mean reducing the width of the waveguides from the present 1.0 cm and 0.8 cm gap width (assuming we retain the 4.6 GHz klystrons). This is undesirable since it would lead to breakdown at lower power levels. Furthermore, at higher electron temperatures the lower N_{\parallel} spectrum becomes the favored one.

Let us first discuss results associated with the $N_{\parallel}(0) = 1.66$ spectrum. In Figure 2.4-13 we show traces of the electron and the ion temperatures as a function of time. These results are obtained for $P_{\text{rf}}(\text{net}) = 3.0$ MW, $\bar{n} = 7.0 \times 10^{13} \text{ cm}^{-3}$, $n_0 = 1.05 \times 10^{14} \text{ cm}^{-3}$, $Z_{\text{eff}} = 1.2$, $B = 7$ T. We see that $I_{\text{rf}} \approx 420$ kA, $T_{e0} \approx 5.0$ keV, $T_{i0} \approx 3.7$ keV after 220 msec into the discharge (the RF power is injected near $t = 50$ msec). Initially we assume 650 kA of ohmic current. We see that at this density the available RF power is not enough to replace all the ohmic toroidal current. Nevertheless, significant RF current drive is achieved. In Figure 2.4-14a we show a plot of J_{rf} as a function of minor radius. We note that the cur-

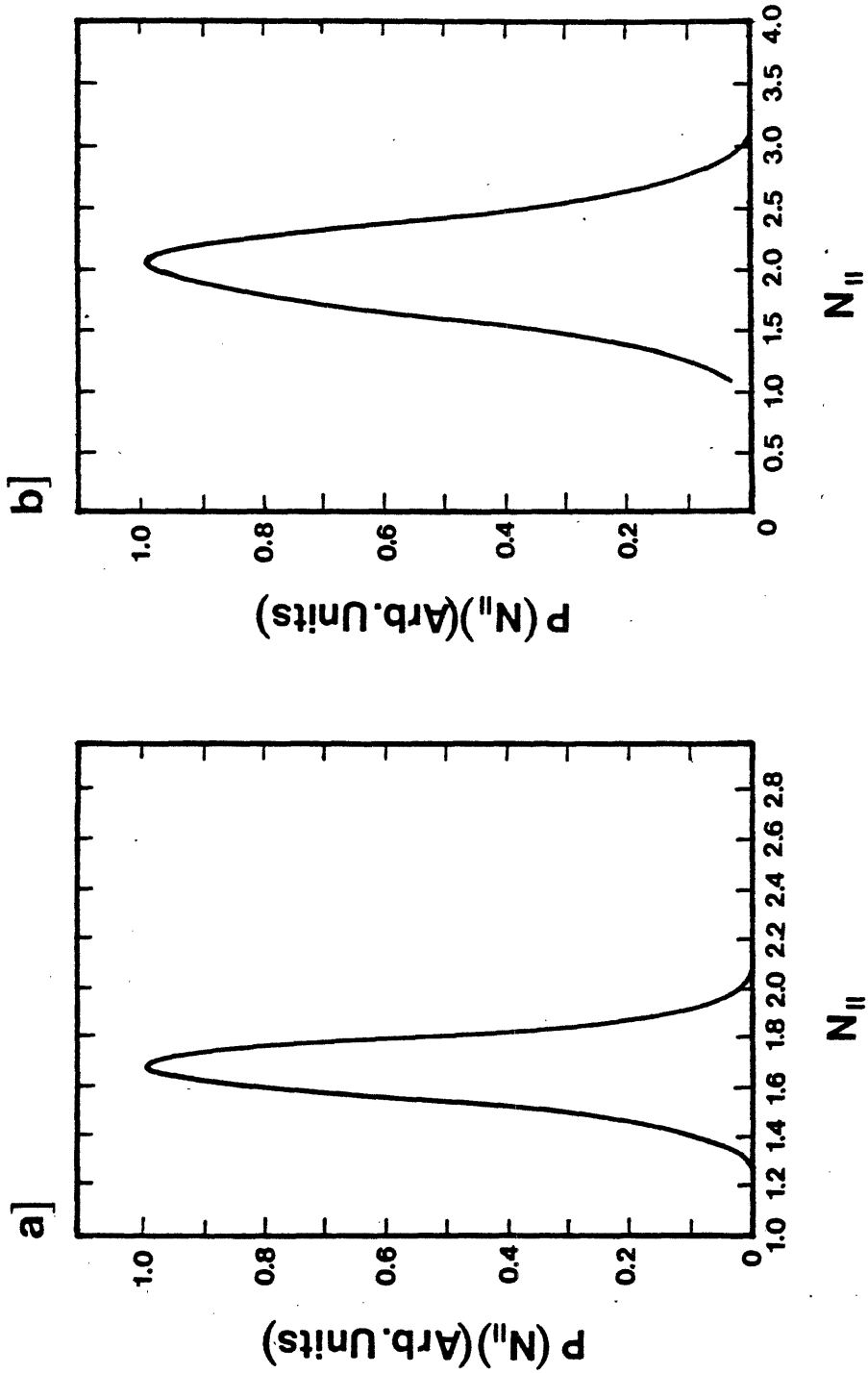


FIGURE 2.4-12 (a) Expanded picture of the DCT 90° Brambilla spectrum; (b) Brambilla spectrum due to an idealized coupler.

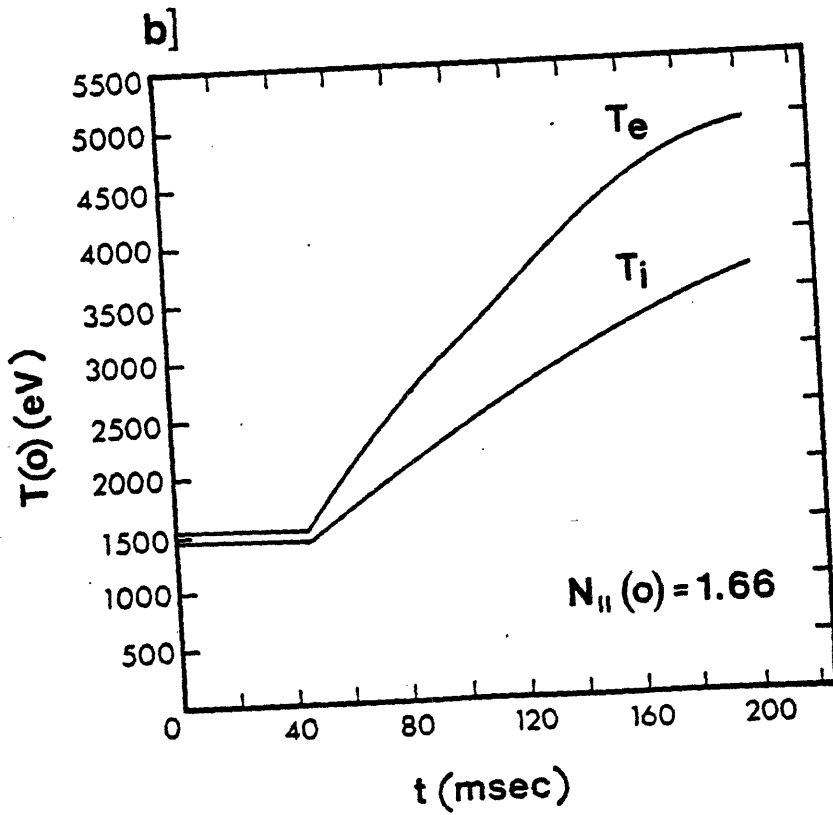
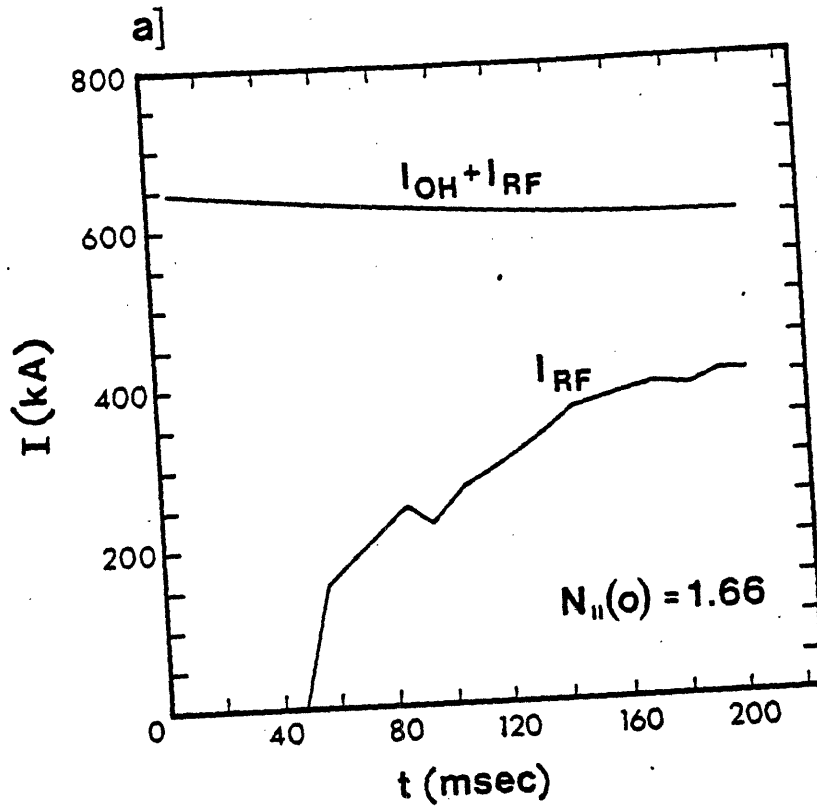


FIGURE 2.4-13 (a) I versus time; (b) T versus time; $N_{||}(o) = 1.66$, DCT spectrum. $\bar{n}_e = 7.0 \times 10^{13} \text{ cm}^{-3}$, $B = 7 \text{ T}$, $P_{RF} = 3.0 \text{ MW}$, $Z_{eff} = 1.2$.

8415

rent generation peaks near $r \approx 7$ cm, and that it is localized to the inner quarter of the minor radius. The power absorption as a function of radius is shown in Figure 2.4-14b. We see that the RF power is also preferentially absorbed in the central quarter of the minor radius, a very positive result. In these code simulations we use $\chi_i = 3 \times \chi_i$ (neoclassic) and χ_e was fixed at the initial ohmic value (which yields a global energy confinement time of $\tau_E = 92$ msec).

In Figure 2.4-15a we show results associated with the more idealized spectrum peaking near $N_{||}(0) = 2.0$. In this case we see that at $t = 220$ msec, $I_{RF} \approx 550$ kA of current is generated. In this case $T_{e0} \approx 4.8$ keV, and $T_{i0} \approx 3.7$ keV at $t = 220$ msec. As shown in Figure 2.4-16 the current density, J_{RF} peaks near $r = 4.0$ cm. Again, the RF power deposition occurs in the central quarter of the minor radius.

In summary, based on detailed code results we find that in Alcator DCT using the available lower hybrid system we can drive up to 0.5 MA of current at a density of $\bar{n} \approx 7 \times 10^{13}$ cm⁻³, and of the order of $I_{RF} \sim 1.1$ MA if we double the available power (see Appendix E). At the same time significant plasma heating is achieved: $T_{e0} \approx 5.0$ keV (7.5 keV) $T_i \approx 3.7$ keV (4.2 keV) for the injected lower hybrid power of $P_{RF} = 3.0$ (6.0) MW. Currents at other densities can be estimated by noting the approximate scaling: $I_{RF} \propto P_{RF}/\bar{n}$.

References

- [2.4-1] M. Porkolab, et al., in Plasma Physics and Contr. Nucl. Fusion Res., 1, 227 (1982) [IAEA, Vienna, 1983].

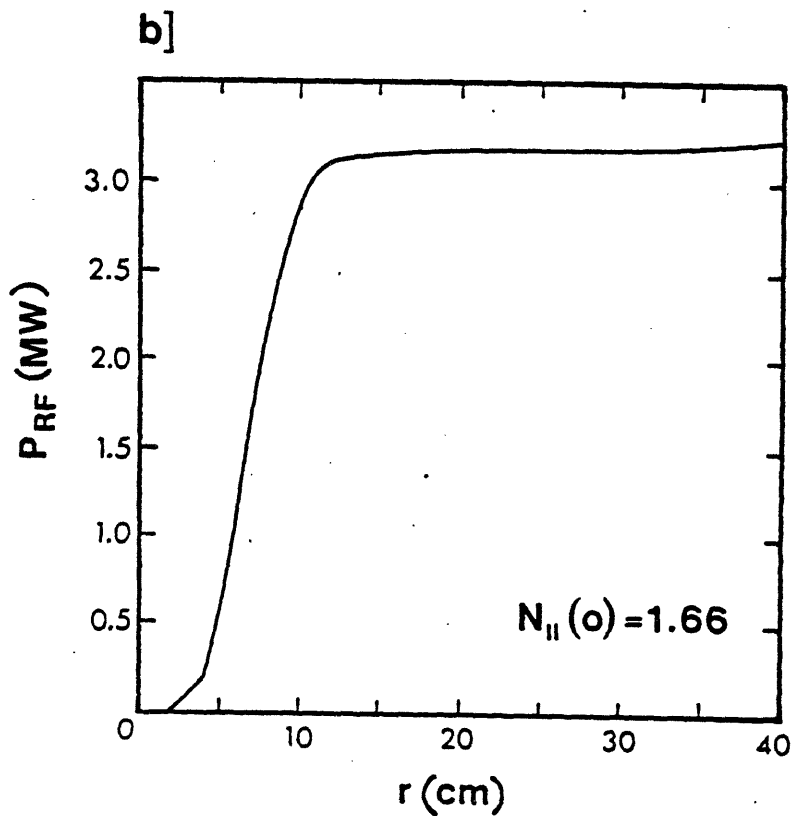
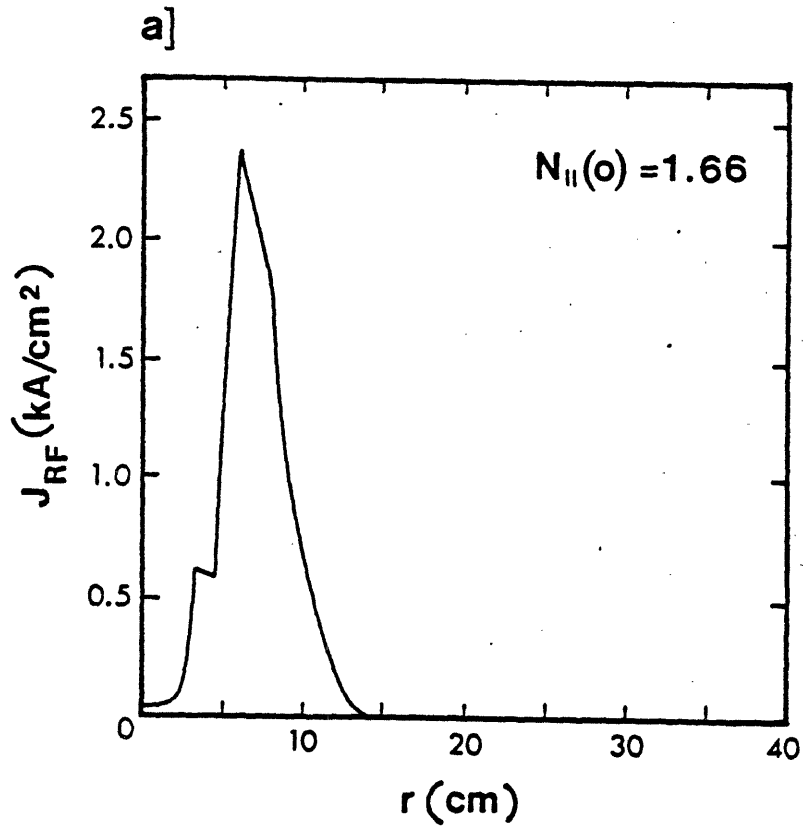


FIGURE 2.4-14 (a) J_{RF} versus radius; (b) P_{RF} versus radius. Same parameters as in Figure 2.4-13. Data taken at $t=200$ msec.

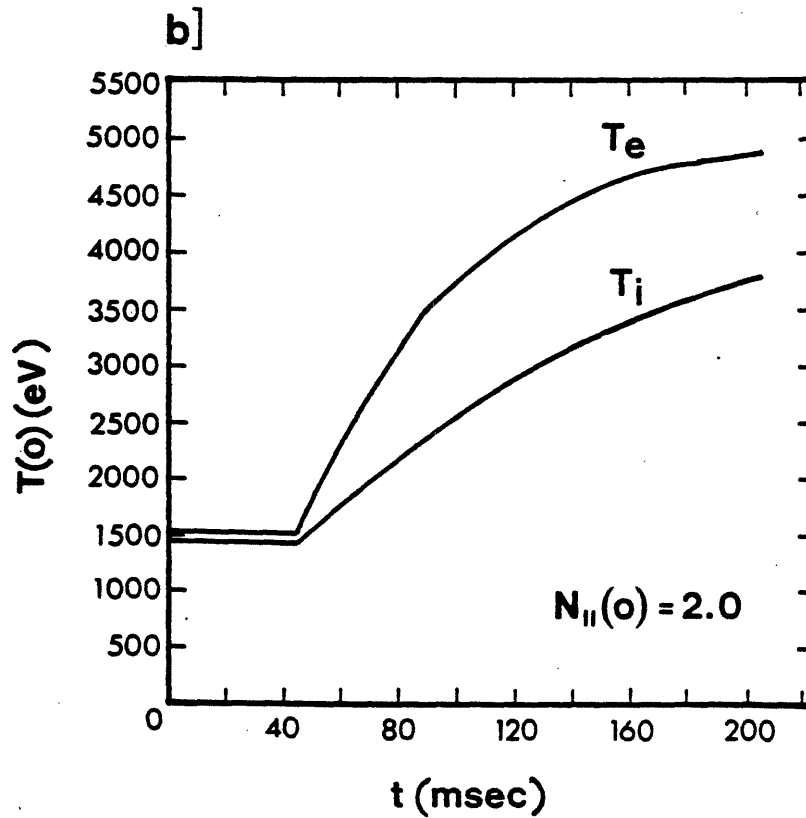
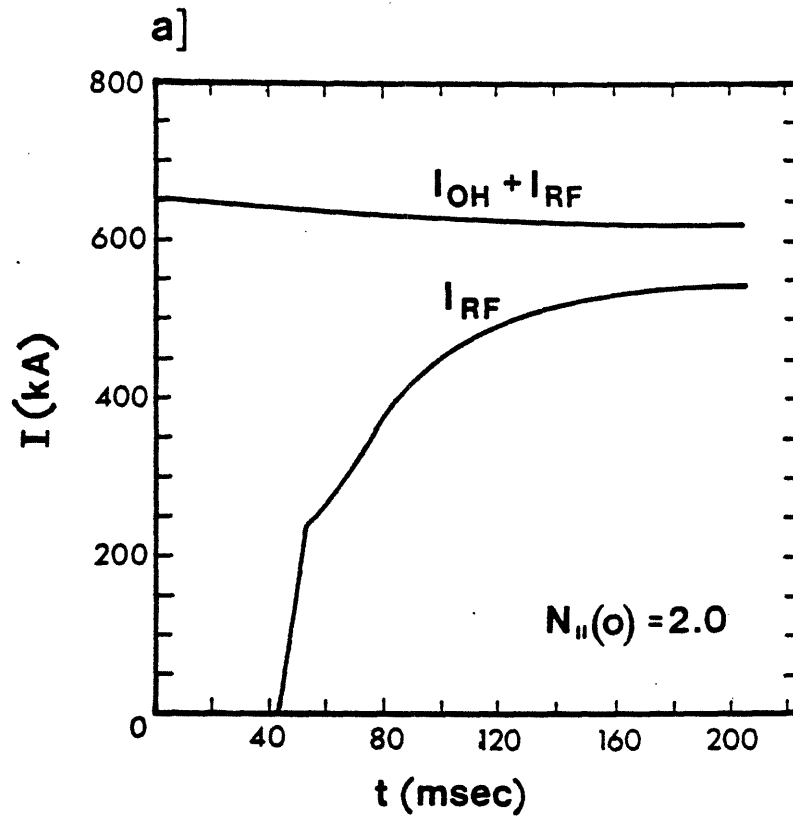


FIGURE 2.4-15 (a) I versus time; (b) T versus time, $N_{||}(0) = 2.0$,
 $\bar{n}_e = 7.0 \times 10^{13} \text{ cm}^{-3}$, $B = 7 \text{ T}$, $P_{RF} = 3.0 \text{ MW}$, $Z_{eff} = 1.2$.

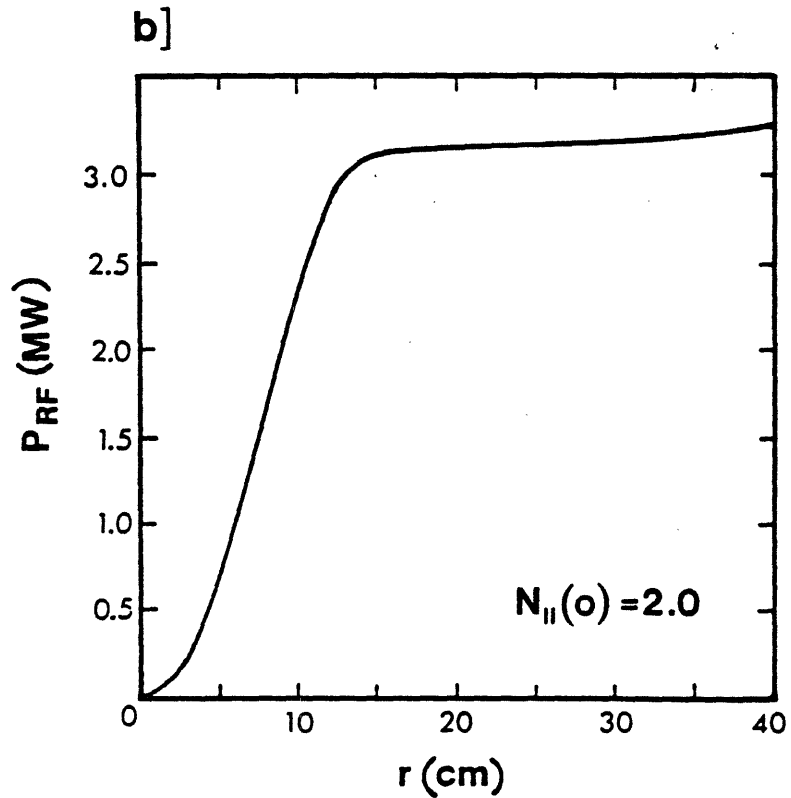
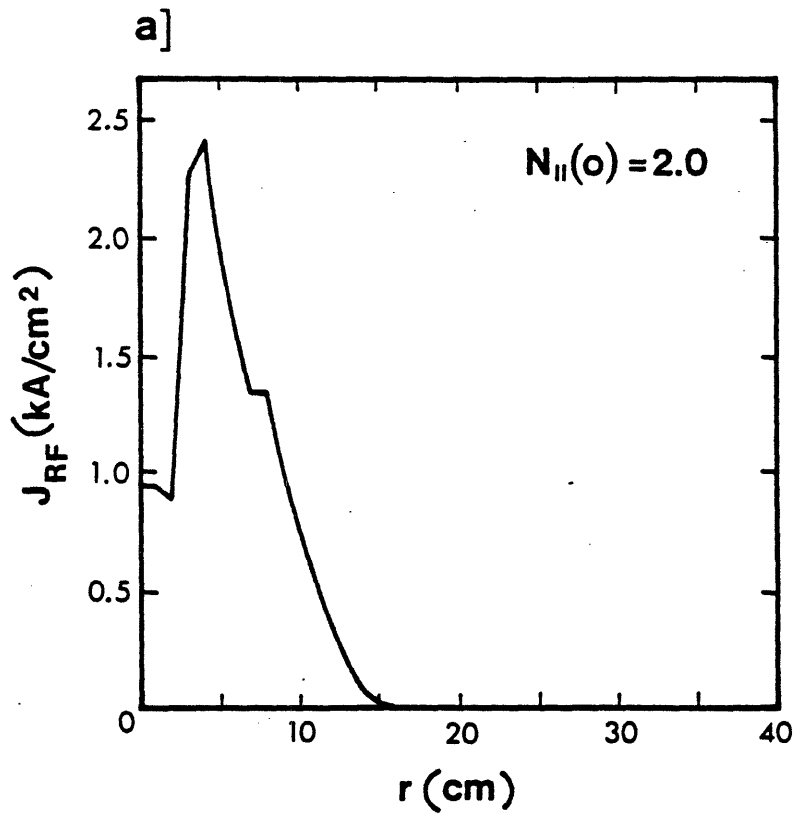


FIGURE 2.4-16 (a) J_{RF} versus radius; (b) P_{RF} versus radius. Same parameters as in Figure 2.4-15a. Data taken at $t=200$ msec.

- [2.4-2] W. Hooke et al., in Plasma Physics and Contr. Nuclear Fusion Res., 1, 232 (1982) [IAEA, Vienna, 1983].
- [2.4-3] M. Porkolab, "Lower Hybrid Experiments, IEEE Minicourse, San Diego, CA, May, 1983 [to be published in Proc. IEEE; also, MIT PFC/CP-83-9, May, 1983].
- [2.4-4] M. Porkolab et al., paper presented at the 11th European Conf. on Contr. Fusion and Plasma Physics, Aachen, West Germany, September 1983 [MIT PFC/CP-83-11].
- [2.4-5] N. J. Fisch, Phys. Rev. Letts. 41, 873 (1973).
- [2.4-6] C. F. Karney and N. J. Fisch, Phys. Fluids 22, 1817 (1979).
- [2.4-7] T. Antonsen, B. Coppi, and R. Englade, Nucl. Fusion 19, 641 (1979).
- [2.4-8] P. T. Bonoli and E. Ott, Phys. Fluids 25, 359 (1982).

2.5. RF Heating

2.5.1. Lower Hybrid Heating

In addition to current drive studies we have examined the possibility of heating an OH supported plasma at an average density of $\bar{n} = 1 \times 10^{14} \text{ cm}^{-3}$. In these studies, which use the same code as the current drive calculations, the phasing of adjacent waveguides is set to 180° . We find that upon injection of $P_{\text{RF}} = 3.0 \text{ MW}$ of RF power the electron temperature saturates at $T_e(0) \approx 3 \text{ keV}$. In a second set of runs we simulate the experimental situation when we start with a relative phasing of 180° and shift to 90° in the middle of the RF pulse, in order to optimize wave penetration at higher temperatures. The results are shown in Figures 2.5-1a,b. In Figure 2.5-1a we show $T_e(0)$ and $T_i(0)$ as a function of time. The RF power is turned on at $t = 50 \text{ msec}$ into the discharge and the relative waveguide phasing is 180° . At time $t = 170 \text{ msec}$ the relative waveguide phasing is shifted to 90° and further heating is achieved. Thus, at 280 milliseconds into the discharge $T_e(0)$ rises above 4.0 keV , and $T_i(0)$ rises above 3.5 keV at a density of $\bar{n} = 1.0 \times 10^{14} \text{ cm}^{-3}$. The radial temperature profiles are shown in Figure 2.5-1b, and in Figure 2.5-2 the radial RF power deposition is depicted. We see that in this case approximately 10% of the power is lost by collisional surface absorption. This is due to the relatively low edge temperature ($T_e(a) = 30 \text{ eV}$, $n(a) = 1.5 \times 10^{13} \text{ cm}^{-3}$) assumed here. Of course, this loss may be reduced to negligible levels if the edge temperatures are sufficiently high ($T_e(a) > 100 \text{ eV}$). The majority of the RF power is deposited in the center of the plasma column.

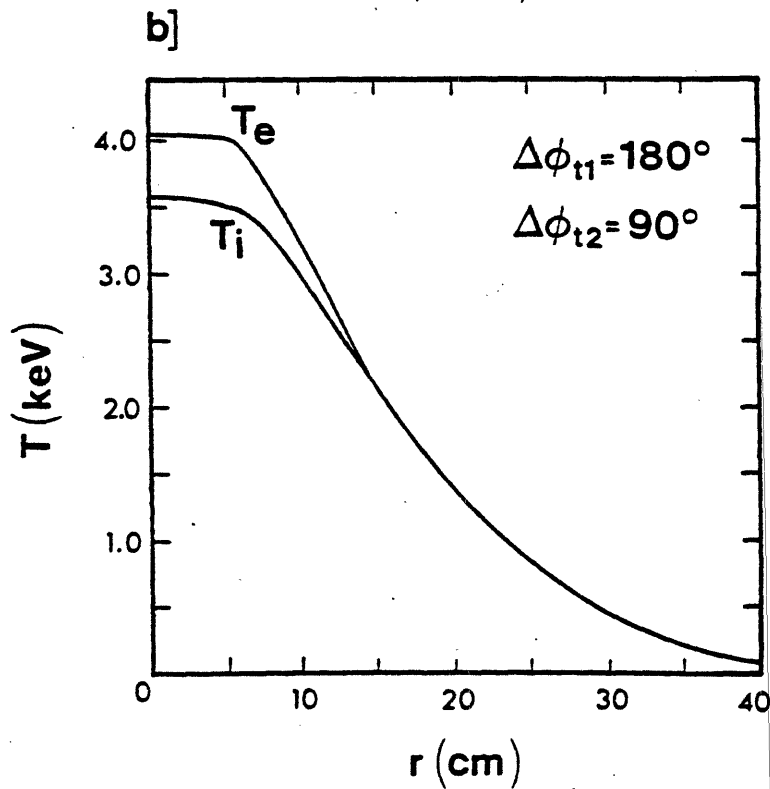
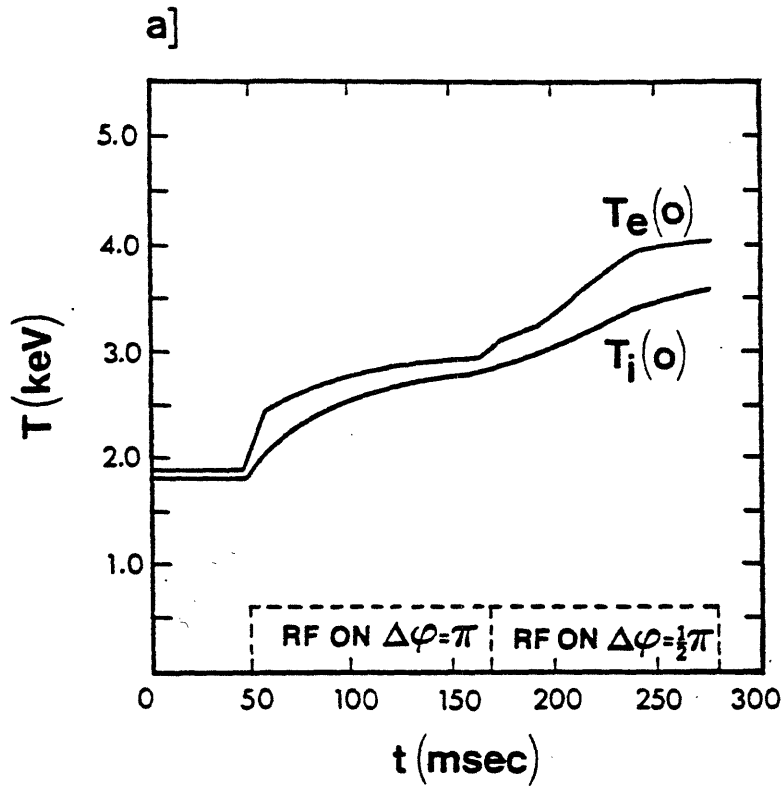


FIGURE 2.5-1 (a) Central temperature versus time. At $t=50$ msec the DCT 180° phased spectrum is turned on; at $t=170$ msec, the phasing is shifted to 90° . $P_{RF} = 3.0$ MW, $\bar{n} = 1.0 \times 10^{14} \text{ cm}^{-3}$, H_2 gas, $B=7.0$ T; (b) radial temperature profiles for the parameters of Figure a $t=280$ msec.

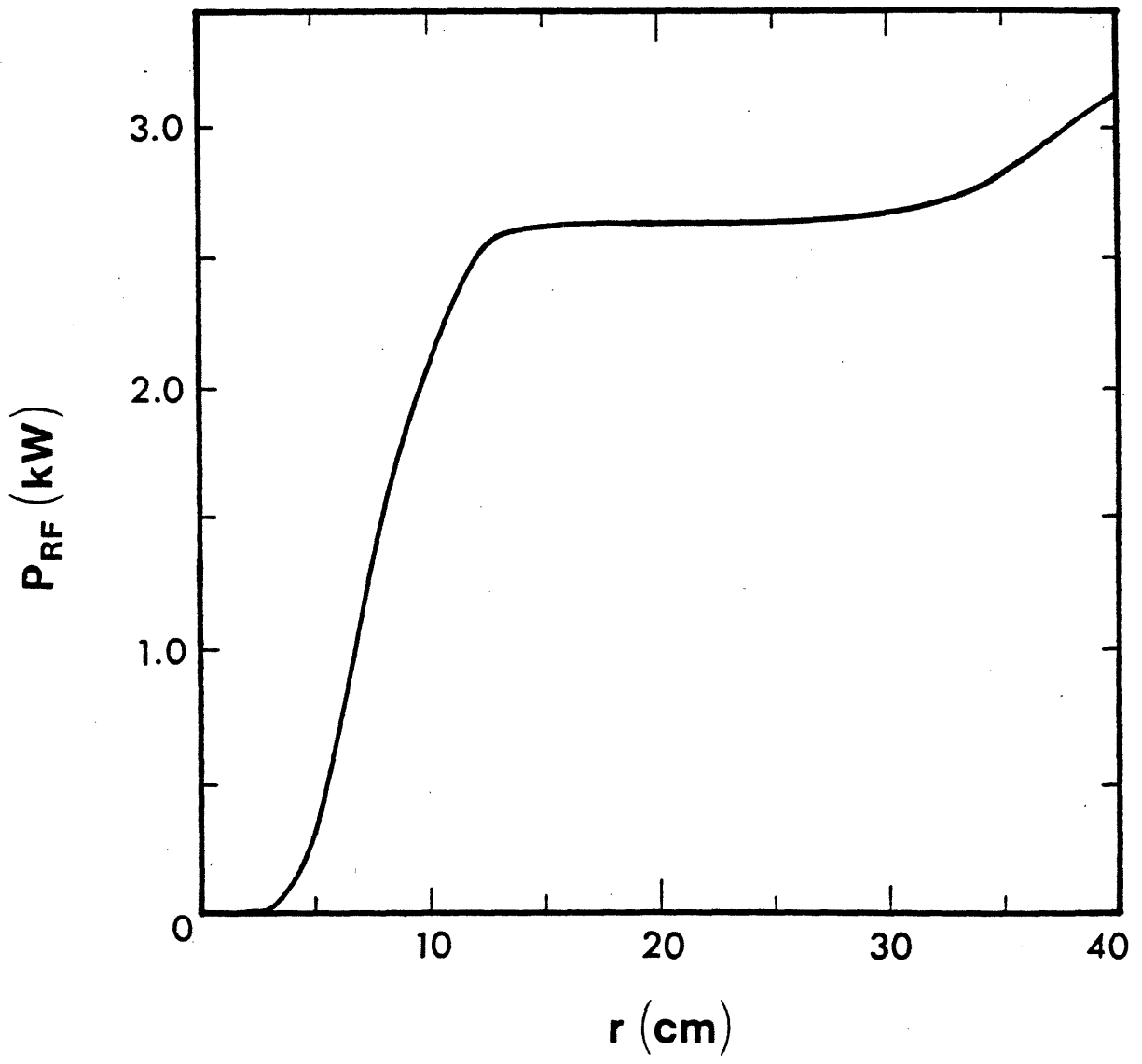


FIGURE 2.5-2 Radial power deposition profiles. Same parameters as in Figure 2.5-1.

2.5.2. ICRF Heating Physics

2.5.2.1. Introduction

Up to 5 MW of RF power in the range 180-215 MHz will be available for heating Alcator DCT. This frequency range corresponds to the second ion harmonic in a pure hydrogen plasma for a toroidal B field on axis of 6-7 Tesla. Both a 1-D full wave slab model and a 2-D in velocity, 0-D in real space, time-dependent Fokker-Planck code have been used to examine second harmonic ICRF heating. The results presented below show that substantial ion absorption should occur, and that the resulting high energy ion tail should be well confined.

2.5.2.2. The Dispersion Relation

Both of our codes incorporate the full 3×3 hot plasma dispersion tensor, accurate to all orders of $k_{\perp}^2 \rho_{ci}^2$ [2.5-1]. We have assumed that a plasma with $n_{i0} = 1.2 \times 10^{14} \text{ cm}^{-3}$ has been ohmically heated to a temperature $T_{i0} = T_{e0} = 1.2 \text{ keV}$ before the RF is turned on. The 1-D dispersion relations for both the fast wave and the Ion Bernstein wave are plotted in Figure 2.5-3. The solid lines correspond to $\text{Re}(k_{\perp}^2)$ and the dashed lines to $\text{Im}(k_{\perp}^2)$. In Figure 2.5-3, $k_{\parallel} = 0.1 \text{ cm}^{-1}$ is assumed to be fixed. For this value of k_{\parallel} we see that the wave propagates out to the plasma edge. The heating zone occurs at the center shown by the peak in the imaginary part of k_{\perp}^2 , and is near the confluence of the Bernstein and fast wave roots.

The fast wave is completely cut off for $k_{\parallel} > 0.7 \text{ cm}^{-1}$ and is evanescent at the plasma edge for $k_{\parallel} > 0.2 \text{ cm}^{-1}$ (assuming an edge density of $1.2 \times 10^{13} \text{ cm}^{-3}$). Optimal coupling to the plasma edge should occur for

$2\omega_{CH}$ DISPERSION RELATION

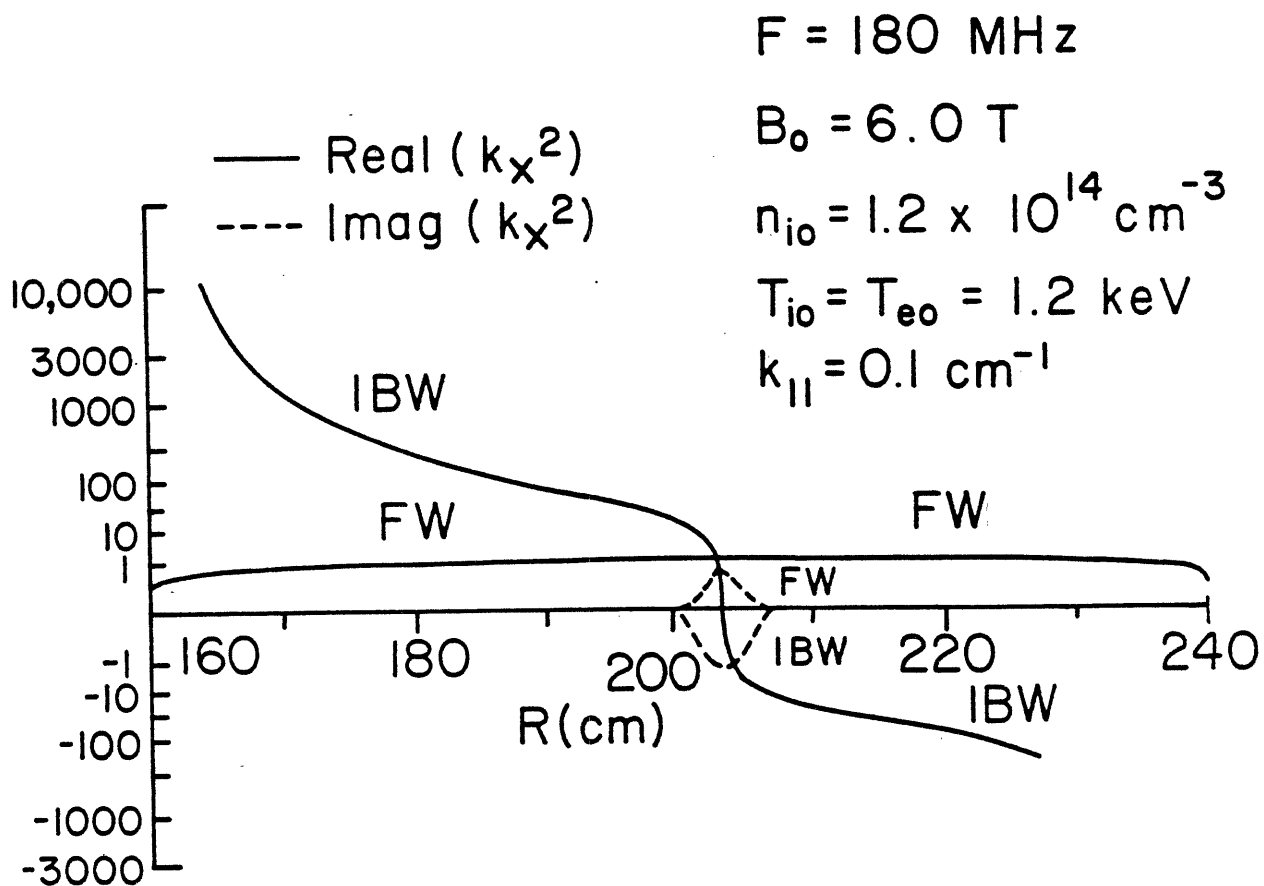


FIGURE 2.5-3 Fast wave and Ion Bernstein wave dispersion relation before RF is applied.

$k_{\parallel} < 0.2 \text{ cm}^{-1}$. For these values of k_{\parallel} , we shall see that strong ion absorption will occur. An antenna 20 cm wide toroidally should launch most of the power in a k_{\parallel} spectrum with $k_{\parallel} < 0.16 \text{ cm}^{-1}$. This antenna, as shown in Section 3.4, will easily fit within a port of Alcator DCT.

2.5.2.3. Predictions of a 1-D Four Wave Slab Model

In this section we determine the amount of absorption occurring within one radial pass, the radial heating deposition, and the species (ions or electrons) which directly absorbs the RF power. The plasma is examined in a rectangular slab geometry, neglecting the poloidal field. We assume that the plasma is uniform in the y (poloidal) and z (toroidal) directions. Density, temperature and magnetic field variations occur in the x (radial) direction only. The geometry is shown in Figure 2.5-4. The plasma is divided into as many as 10,000 thin uniform slabs [2.5-2]. The RF electric field in each slab is given by

$$\underline{E} = \sum_{\ell=1}^4 \underline{E}_{\ell}^0 \exp(ik_{\perp \ell} x) \quad (1)$$

where we have examined mode coupling and power flow between two modes. Two waves are associated with each mode, the waves propagating in the positive and negative x directions. Wave damping occurs within each slab, with k_{\perp} in Equation 1 being complex. The amplitudes \underline{E}_{ℓ}^0 in each slab are found by using electromagnetic boundary conditions (that is tangential E and B fields are continuous) at each slab interface. These conditions yield a set of $4(N-1)$ coupled equations for N slabs. A complete set of equations is obtained when either radiative boundary conditions are used at the edge slabs, or there exists a 2-D (y,z) current

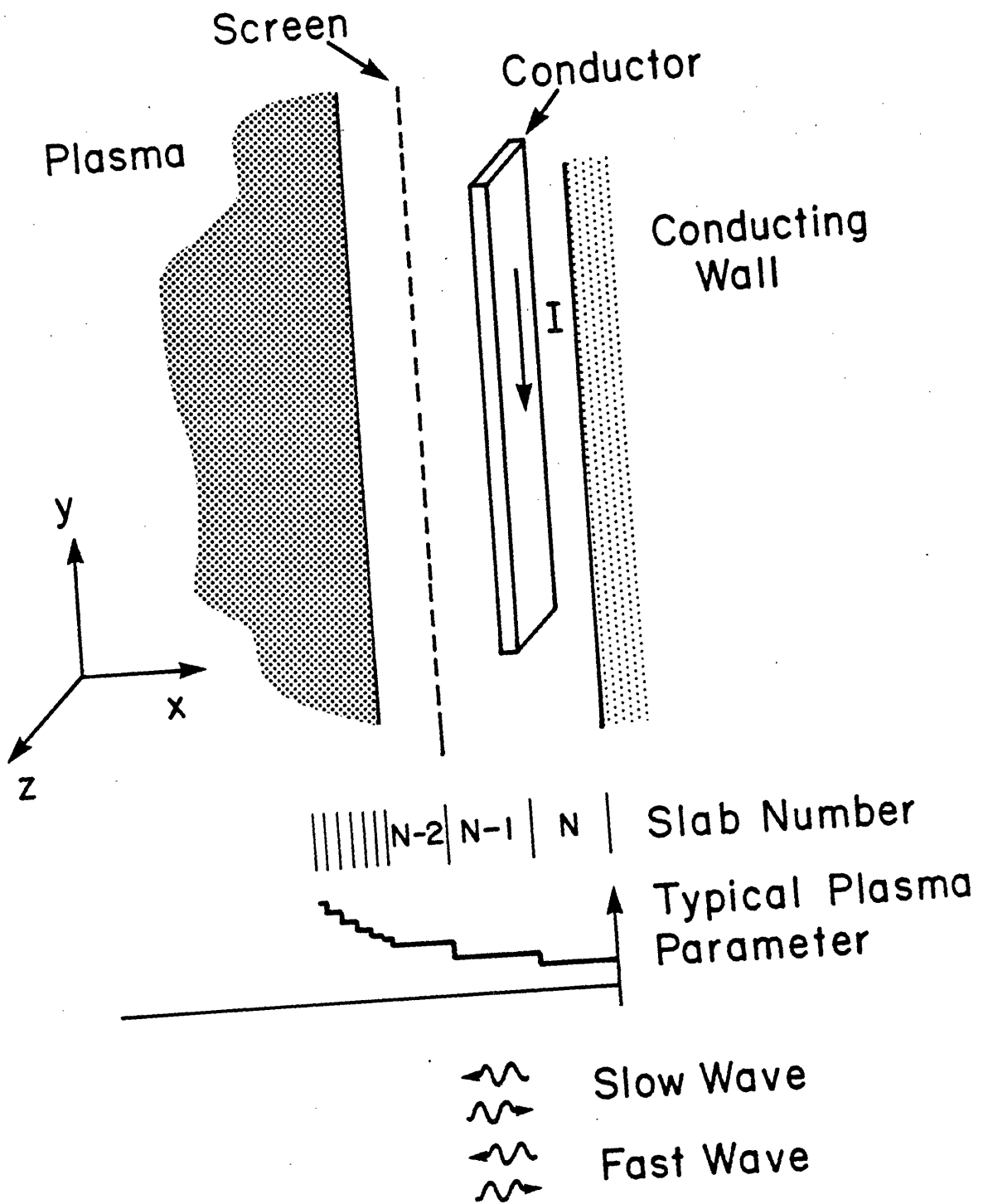


FIGURE 2.5-4 Geometry for the 1-D slab model.

sheet at a slab interface representing the antenna together with metal conducting walls at the plasma edge. We can also include an electrostatic shield when present. The metal wall forces E_y and E_z to vanish at the wall while E_z goes to zero at the shield. The current sheet is represented by a jump in B_z at the appropriate slab interface.

The rather elaborate and computationally time consuming antenna coupling calculations have not been completed for the antenna being designed. For the initial design, we have used the simpler radiative boundary conditions. We assume that only a single value of k_{\parallel} is excited by the antenna and that only an inward propagating fast wave is launched from the low field side. There are no waves launched from the high field side although reflected power coming from either side of the plasma is allowed. The heating zone and the amount of power absorbed within one radial pass can be determined by examining the decrease in the radial Poynting flux. After the RF electric fields have been obtained, the weak damping formula

$$P = \underline{E} \cdot \underline{K} \cdot \underline{A} \cdot \underline{E} \quad (2)$$

determines the fraction of power absorbed by each species. In order to reduce the effect of numerically unstable solutions, a complex band matrix technique is used to solve the set of coupled equations simultaneously. Figure 2.5-5 shows the radial Poynting flux for a low temperature ($T_{i0} = T_{e0} = 1.2$ keV) and a high temperature ($T_{i0} = 5$ keV, $T_{e0} = 3$ keV) Alcator DCT plasma. With our chosen coordinate system, launching power from the low field side results in a negative Poynting flux. The large change in Poynting flux in Figure 2.5-5 occurs at the harmonic of the ion cyclotron

RADIAL POYNTING FLUX

$$B_0 = 6.0 \text{ T} \quad f = 180 \text{ MHz}$$

$$n_{i0} = 1.2 \times 10^{14} \text{ cm}^{-3}$$

$$k_{||} = 0.1 \text{ cm}^{-1}$$

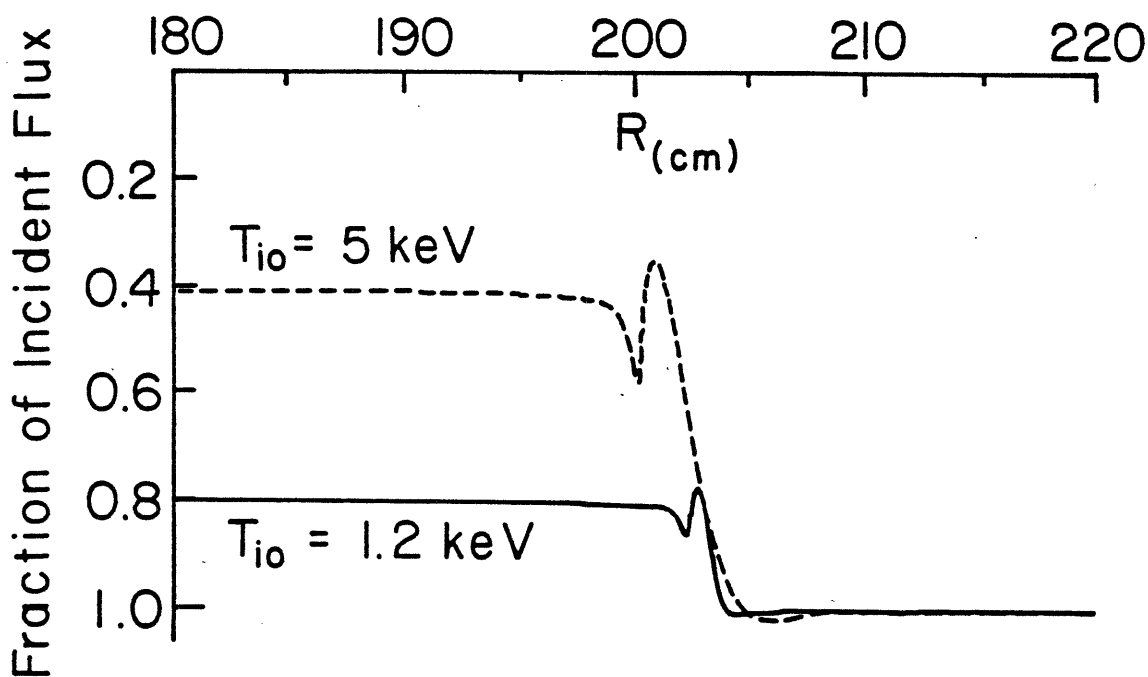


FIGURE 2.5-5 Radial component of the Poynting flux for pre-ICRF ($T_i = T_e = 1.2 \text{ keV}$) and ICRF-heated ($T_i = 5 \text{ keV}$, $T_e = 3 \text{ keV}$) plasma conditions.

resonance, producing strong ion absorption. By taking the ratio of incident Poynting flux to the exiting flux, we see that 20% of the power in the low temperature case, and 60% of power in the high temperature case is absorbed within one pass. Strong ion heating at the center occurs and radial eigenmodes do not dominate the heating. Mode tracking should not be necessary. For moderate values of $k_{\parallel} \approx 0.1 \text{ cm}^{-1}$, little power is mode converted into the Ion Bernstein branch.

2.5.2.4. Predictions of a 2-D Fokker-Planck Code

In the previous section, we have shown that the dominant heating process is second harmonic ion absorption. Stix has shown [2.5-3] that this heating mechanism may produce a large high energy ion component. We have used a 2-D in velocity space, 0-D in real space Fokker-Planck code [2.5-4] to examine this time-dependent ion tail. The Kennel and Engelmann quasi-linear RF operator [2.5-3,4,5] has been written in a compatible form [2.5-6]. In these studies, we have lumped Ohmic heating with charge exchange, radiation and radial transport losses into a global energy loss term

$$\frac{\partial f}{\partial t} = \frac{1}{2v^2} \frac{\partial}{\partial v} v^3 f \quad (4)$$

where (the central) τ_E is typically 100 ms ($a_{RF} = 20 \text{ cm}$, $n_{i0} = 1.5 \times 10^{14} \text{ cm}^{-3}$), derived from 1-D transport simulations (see Section 2.2). Figure 2.5-6 shows the hydrogen distribution function at various times after the RF is turned on, assuming that the RF power is uniformly deposited over a radius (a_{RF}) of 13 cm in a plasma with a density of $1.5 \times 10^{14} \text{ cm}^{-3}$. The simulation is started with Maxwellian distribution functions corresponding

$2\omega_{CH}$ HYDROGEN DISTRIBUTION FUNCTION

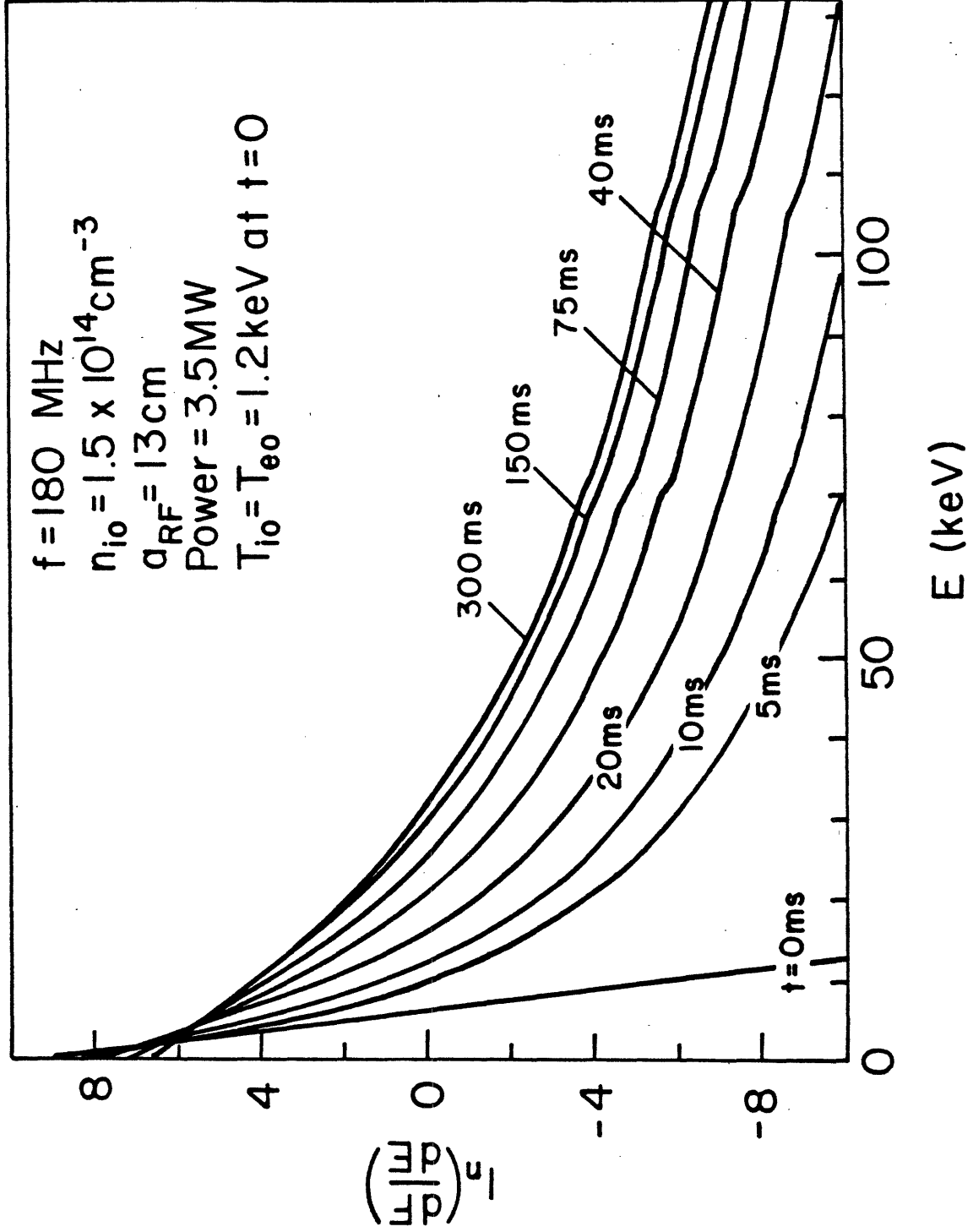


FIGURE 2.5-6 Time evolution of the hydrogen distribution function. ICRF power is applied to an ohmic plasma at $t = 0$.

to the transport equilibrium state before ICRF heating. At the plasma center, the ion distribution approaches an equilibrium after 100 ms. We note that second harmonic heating does not produce a tail with a well-defined temperature, but a smooth transition from the main body to the tail. In Figure 2.5-7 we have taken the second moment of the ion velocity distribution. This figure shows the fraction of energy contained by particles above a given energy. At $t = 300$ ms, less than 0.1% of the ion energy is above 150 keV.

The amount of energy contained in the high energy tail varies with both the plasma density and the assumed RF power deposition. Figure 2.5-9 shows the integrated hydrogen distribution function at the plasma center for a uniform power deposition within radii of 13 cm and 20 cm for different densities. The largest tail is produced in the low density case with a uniform power deposition over half the plasma radius. In this case the fraction of energy in particles above 150 keV is still only 3%. In Figure 2.5-9 we show the energy as a function of radial position for banana orbits which intersect the limiter in Alcator DCT. In the absence of ripple effects, 150 keV particles are well confined out to at least half the plasma radius. Since mechanisms which will decrease the ICRF tail are neglected we can conclude that an ICRF produced high energy ion tail should be well confined in Alcator DCT.

2.5.2.5. Summary of ICRF Physics

We have examined heating Alcator DCT with 3.5 MW of RF power at a frequency of 180 MHz, resulting in second harmonic ion absorption at the plasma center. At the surface little if any mode conversion occurs for

INTEGRATED HYDROGEN ENERGY SPECTRUM

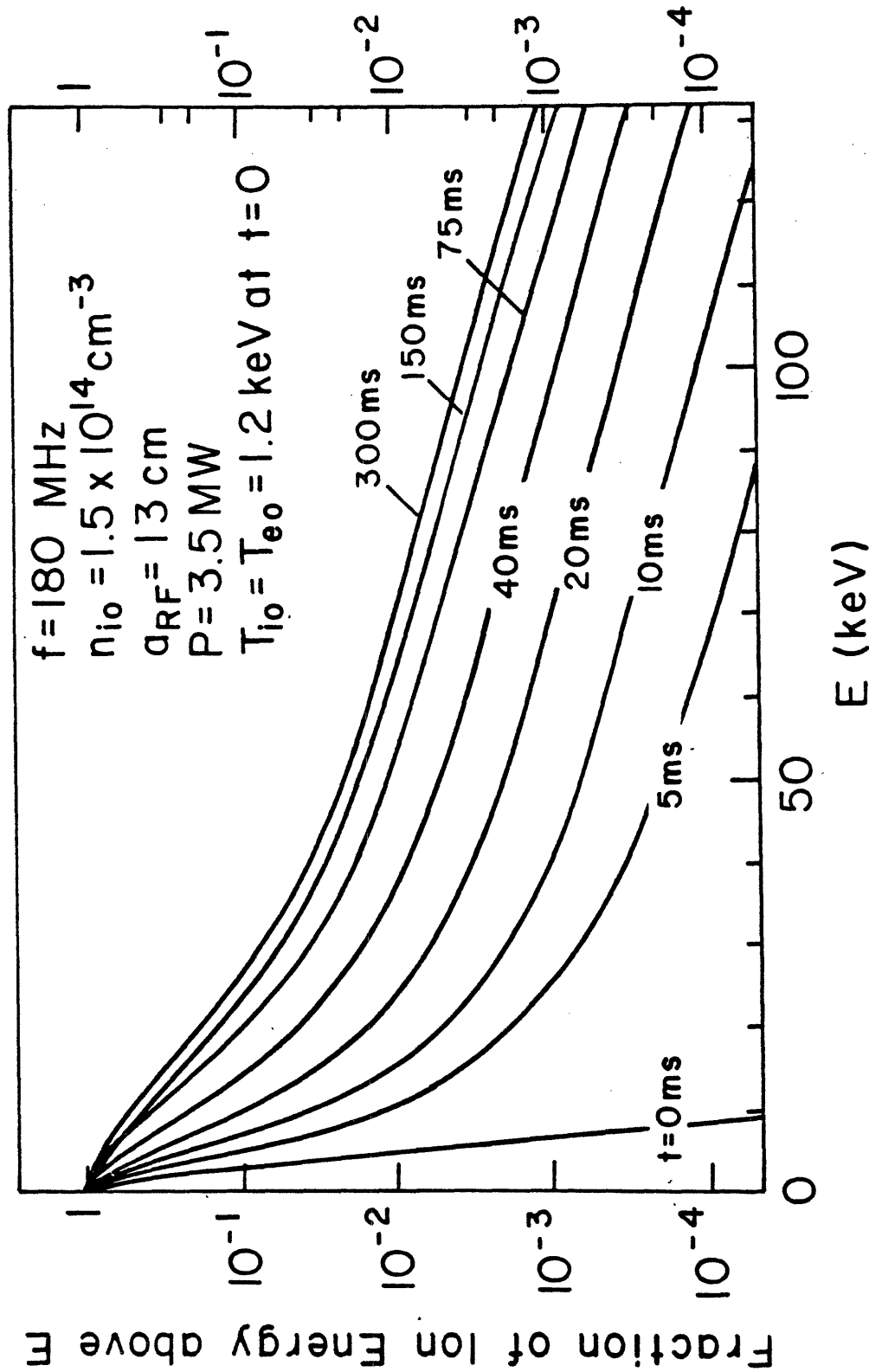


FIGURE 2.5-7 A representation of the time evolution of the second moment of the hydrogen distribution function showing the fraction of the total ion energy above a given energy ("integrated distribution function").

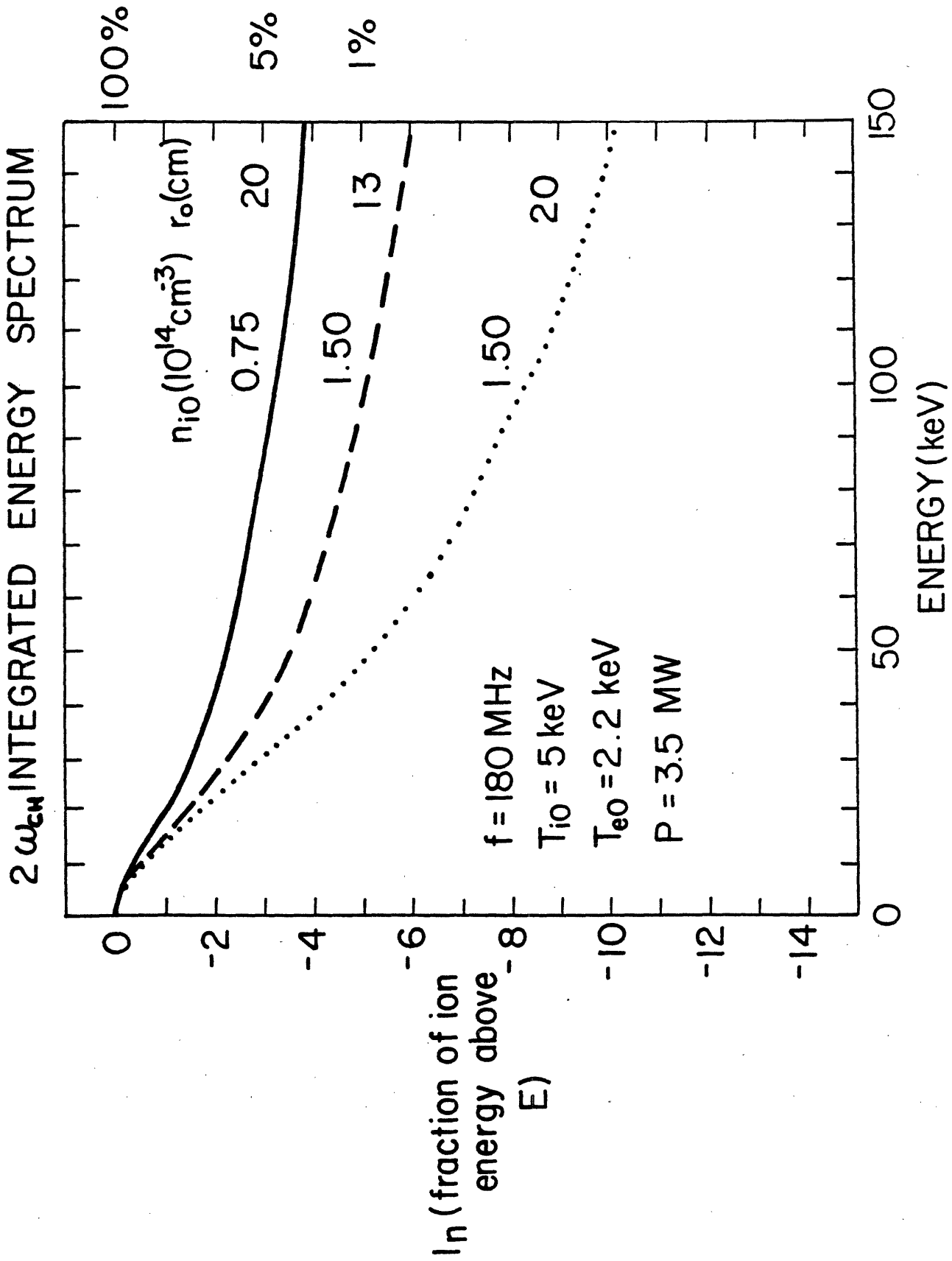


FIGURE 2.5-8 Integrated distribution functions under near-equilibrium conditions, displayed as in Fig. 2.5-7, for different plasma densities and effective ICRF heating radii.

ENERGETIC ION LOSS

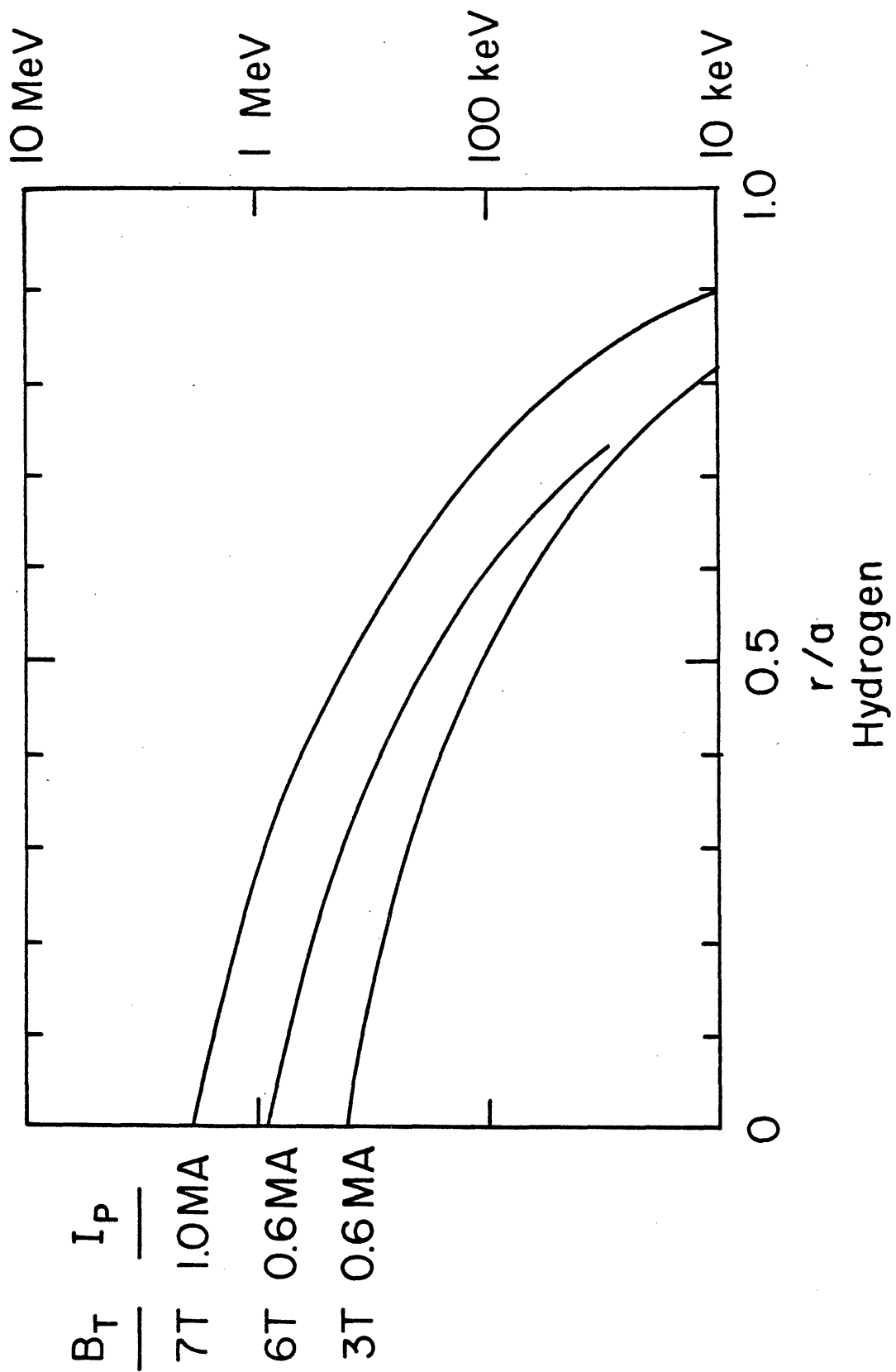


FIGURE 2.5-9 Ion banana loss energy vs radial position for three different plasma conditions. $R = 2$ m, $a = 0.35$ m.

low field side launching of a fast wave for moderate values of $k_{\parallel} \lesssim 0.1 \text{ cm}^{-1}$. The proposed loop coupler will produce a k_{\parallel} spectrum which couples effectively at the plasma edge, propagates to the plasma core and heats ions directly at the second harmonic layer. The single pass absorption should increase with temperature from 20% to 60%.

Fokker-Planck calculations show that at most 3% of the plasma energy will be in ions above 150 keV, well inside the limit of good ion confinement for the central region in Alcator DCT. We therefore conclude that the fast wave at $2\omega_{CH}$ will be an effective auxiliary heating source for Alcator DCT.

References

- [2.5-1] D. G. Swanson, Phys. Fluids 10 (1967) 428, and, S. Ichimaru, Basic Principles of Plasma Physics, A Statistical Approach, W. A. Benjamin Inc., Reading, MA (1973).
- [2.5-2] D. T. Blackfield and B. D. Blackwell, M.I.T. Plasma Fusion Center Report PFC/CP-83-4, February 1983. D. T. Blackfield et al., M.I.T. Plasma Fusion Center Report PFC/RR-81-18, 1981.
- [2.5-3] T. H. Stix, Nucl. Fusion 15 (1975) 737.
- [2.5-4] D. T. Blackfield and J. E. Scharer, Nucl. Fusion 22 (1982) 255.
- [2.5-5] C. I. Kennel and F. Engelmann, Phys. Fluids 9 (1966) 2377.
- [2.5-6] A. A. Mirin, Lawrence Livermore Report UCRL-51615 Rev. 1, February 1975.

CHAPTER 3

PLASMA ENGINEERING

3.1. Introduction

The steady-state maintenance of a reactor-grade plasma necessarily requires solving a number of fusion reactor engineering problems. The field of plasma engineering encompasses those areas of fusion reactor development which are involved with the maintenance and control of the plasma. Specification of the components which interact directly with the plasma depends on an adequate understanding of physical processes and an accurate prediction of plasma behavior. Experimental verification of theoretical plasma models and performance testing of components under reactor relevant conditions are therefore essential. Studies in these areas form an integral part of the Alcator DCT program.

An example of the integration needed in plasma engineering is the design of the collector plates in a divertor. This requires accurate prediction of the plasma transport behavior in the scrape-off layer, knowledge of the surface chemistry and metallurgy of materials, and an understanding of state-of-the-art techniques for control and removal of steady, high level heat fluxes.

In this chapter we will address such plasma-related technology areas. The topics covered include design of systems for steady-state pellet fueling, continuous pumping of particles, heat removal and impurity control, and coupling the RF power needed to heat the plasma and drive current noninductively.

3.2. Pellet Injection

3.2.1. Introduction

Plasma fueling in long-pulse, toroidal fusion devices may be difficult. At present such machines are fueled by a cold gas blanket which surrounds the plasma. In regimes where $n_e \cdot a$ is large, classical processes cannot account for the observed fueling. That is, when the mean free path for neutrals is much less than the minor radius, the Ware pinch is insufficient to produce the observed density rise. Since there is no adequate explanation for this anomalous fueling, it is not possible to extrapolate to reactor conditions. Furthermore, it is possible that the same mechanism which accounts for enhanced fueling is also detrimental to energy confinement. Edge cooling by the cold gas blanket might affect energy transport either in a direct way, or indirectly by altering the current profile in the outer portions of the plasma.

In recent years, experiments on ISX, PDX, and Alcator C have shown that high speed injection of frozen hydrogen pellets is a practical means for raising the density in tokamaks. It is possible to double or triple the plasma density with a single pellet without disruption or unfavorable effects on energy transport. However, so far there has been no demonstration of steady state fueling using pellet injection.

Alcator DCT will provide an ideal test bed for steady state pellet fueling experiments. While global particle confinement times are shorter than discharge times in existing tokamaks, central particle confinement is much better. The Alcator DCT pulse will be many central particle confinement times in length. Furthermore, the pulse time will be longer than the pump-out time for the vacuum system, allowing a true steady-

state regime to be reached. There will be pumped limiters and divertors to control particle exhaust.

In addition to the fueling studies, a pellet injector would allow attainment of plasma regimes which are probably not accessible otherwise. In Alcator C, peak densities approaching $2 \times 10^{21} \text{ m}^{-3}$ have been reached. In general, pellet-fueled plasmas have higher densities and more peaked density profiles than gas fueled ones. The transport properties of these plasmas are of great interest. We also expect plasmas with peaked density profiles to provide a better target for RF heating, since the wave accessibility is improved relative to plasmas with flat profiles and edge collisional absorption is reduced. In this case, one could expect RF power deposition to be more peaked and thus more effective in heating the plasma.

3.2.2. Requirements

We can estimate the fueling requirements for Alcator DCT by multiplying the plasma volume, 6 m^3 by the average density, $1 \times 10^{20} \text{ m}^{-3}$ and dividing by the assumed central particle confinement time, .1 - .2 sec. The result is that $3-6 \times 10^{21}$ particles/sec will be needed to maintain the plasma. We can provide those particles, by injecting 1 mm pellets, each containing 2×10^{20} particles, at the rate of 15 to 30 per second. Each of these pellets would raise the volume averaged density by $3 \times 10^{19} \text{ m}^{-3}$.

For the ohmic plasmas we can calculate the velocity that would be required for 1 mm pellets to penetrate into an Alcator DCT plasma. At $1 \times 10^{20} \text{ m}^{-3}$ we expect central electron temperature in the range 1.4 - 1.7 keV. Using the neutral gas shielding model [3.2-1] we find that at 1000 m/sec

the pellet will penetrate to within .1 m of the magnetic axis, which is almost optimal. At 2000 m/sec the pellet will not be completely ablated before it reaches the axis.

For RF heated plasmas the calculation is more difficult. Not only is the electron temperature much higher (and outside the range over which the shielding model has been tested), there is a significant population of superthermal ions and electrons. Recent experiments on PDX and ISX have shown that energetic ions from the neutral beams increase the pellet ablation rate and reduce the efficiency of pellet fueling. On Alcator C similar results have been found with energetic electron populations present during lower hybrid heating. Increasing the pellet velocity and size will improve the penetration into RF heated discharges.

At present, designs for two different types of injectors, both from ORNL, show promise for application to Alcator DCT. A centrifugal injector has been operating for some time and seems capable of producing the pellet sizes, velocities and repetition rates necessary for Alcator DCT ohmic operation. Further work would be necessary to increase the velocity to that required for the RF heated plasma. An advanced pneumatic injector is under development and should have specifications similar to the centrifugal device.

The problems in fueling RF-heated plasmas by pellets in Alcator DCT are the same as those faced by other large devices. A good deal of communitywide effort has been put into understanding the interaction between the ablating pellet and non-thermal particles. There should be a beneficial interaction between experiments on Alcator DCT and the general program. In this country, pellet injector technology has been developed

primarily at ORNL. We would hope that the M.I.T.-Oak Ridge collaboration which has been so productive on Alcator C would continue on Alcator DCT.

References

[3.2-1] S. L. Milora, J. of Fusion Energy 1, 15 (1981).

3.3. Particle and Impurity Control Techniques

3.3.1. Introduction

A long-pulse machine will need particle pumping to allow control over the plasma density. It will also require techniques for minimizing the generation of impurities due to thermal loading and sputtering, and for preventing their subsequent entrance into the main plasma. The RF power deposited in Alcator DCT causes a high value of heat flux ($\sim .2$ MW/m²) into the plasma edge. This power flux is comparable to values for which large impurity densities are observed during intense auxiliary heating in present day machines (see Appendix D). We conclude that on a long time scale, a simple limiter cannot perform the tasks of impurity and particle control. Alcator DCT will provide a long-pulse test of the two most promising techniques - pumped limiters and poloidal divertors. For the latter option we consider two separate possibilities: an internal poloidal divertor (e.g. PDX [3.3-1], ASDEX [3.3-2]) and an external poloidal divertor (INTOR [3.3-3]). Here internal and external refer to the location of the divertor coils with respect to the TF coils. The designs and parameters for the pumped limiter and the two divertor configurations are presented in the following sections.

3.3.2. Pumped Limiter

Much experimental and theoretical research is presently concerned with the subject of pumped limiters. Although small scale experiments [3.3-4,5,6,7] have produced encouraging results on particle pumping, it is questionable whether pumped limiters will remove particles efficiently on a large scale tokamak without producing an overabundance of impurities. While their ease of construction, compared to the extra coils of divertors, causes pumped limiters to be attractive from an engineering viewpoint, we feel it risky to build a long-pulse, high heat flux tokamak with only this option for impurity control.

Our basic design for a pumped limiter is shown in Figure 3.3-1a. It is fully toroidal with neutralizer plates located under the limiter at 12 of the 24 bottom vertical vacuum vessel ports. Neutrals are therefore created at the entrance of ports through which they can be pumped. The limiter has a single leading edge and is flat to allow for plasma discharges of different shapes, sizes and major radii. For the same reasons, the limiter is movable along a major radius. Approximately 10% of all particles entering the scrape-off layer will pass behind the leading edge and strike the neutralizer plate [3.3-8]. We estimate that between 10 and 50% of the particles striking the plate will then be pumped. Given that each of the vertical ports has a conductance of $\sim 2 \times 10^4$ l/sec, and assuming neutral pressures at the vessel wall will be similar to present results (~ 10 μ torr), we will need $\sim 10,000$ l/sec of steady-state pumping around the torus.

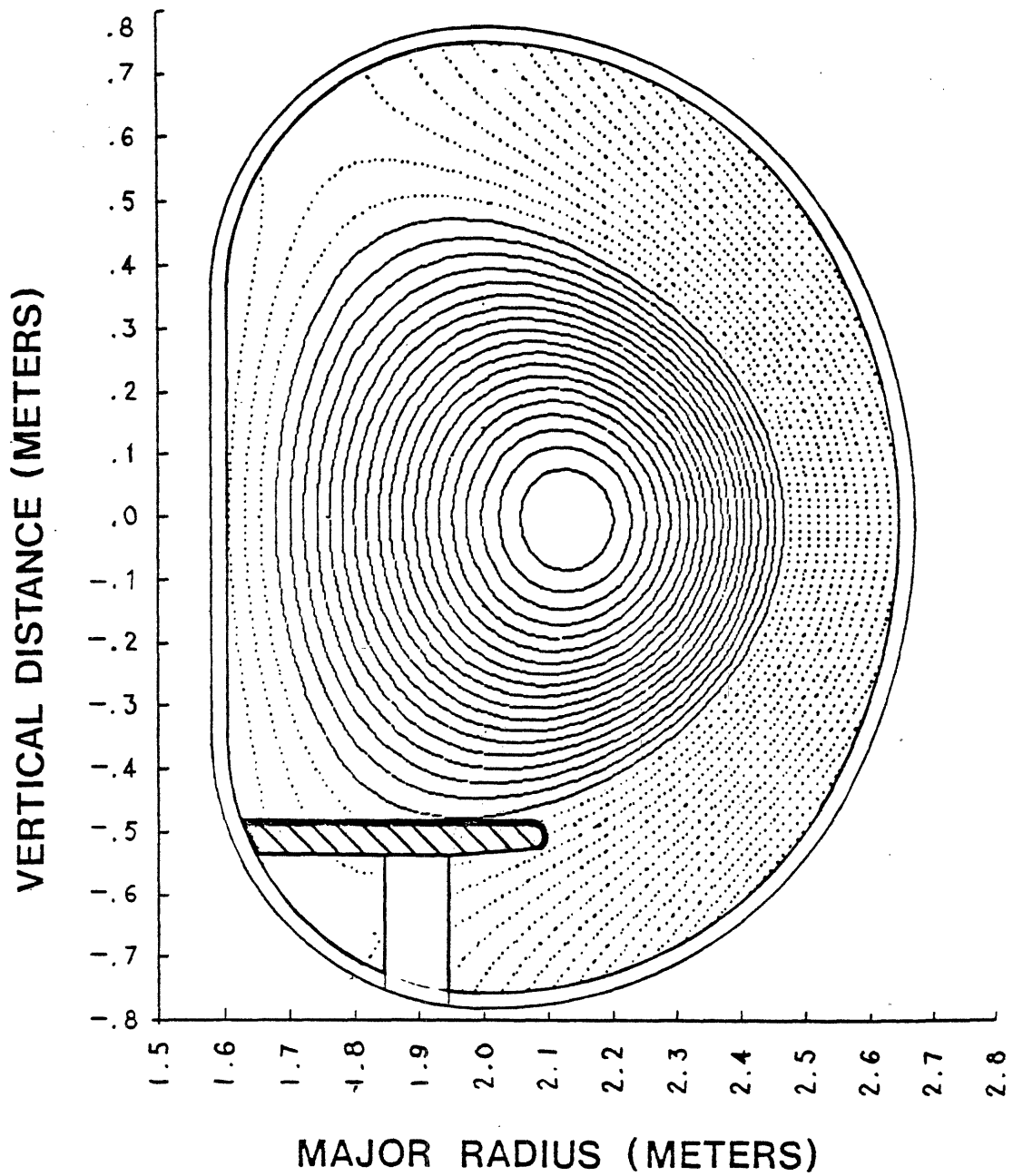


FIGURE 3.3-1a Geometry for Pumped Limiter

3.3.3. Internal Poloidal Divertor

The poloidal divertor produced with internal coils is relatively well understood in comparison to the pumped limiter. The exhaust of particles into the region near the pumping ducts is much more efficient than with a pumped limiter. The impurity generation point is removed from the main plasma edge. Flux multiplication [3.3-9] reduces the average energy per ion and impurity-ion friction causes impurities to accumulate in the divertor chamber [3.3-10]. Because the prototypical poloidal divertor has toroidal neutralizer plates, the fraction of neutrals created there which are subsequently pumped may prove to be less than for a pumped limiter. This could be overcome if some part of the exhaust flux were neutralized on plates localized at pump ports. We are studying this idea.

The coil set for this divertor is a triplet similar to that of ASDEX: a main divertor coil and two matching coils carrying an equal but opposite current. These three coils, which are described in Appendix E, could be superconducting and wound inside the vacuum chamber. The neutralizer plates, covered by coolant-backed tiles, are attached to the main divertor coil. The pair of nulling coils are part of the baffling system defining the divertor chamber (see Figure 3.3-1b). The walls of the divertor chamber and parts of the baffles are also covered with cooled tiles to handle the erosion and absorb the heat load caused by the charge exchange flux. The water coolant for these tiles and the helium for the superconductors are fed through the supports. Further details of these heat removal structures will be given in Section 3.3.7.

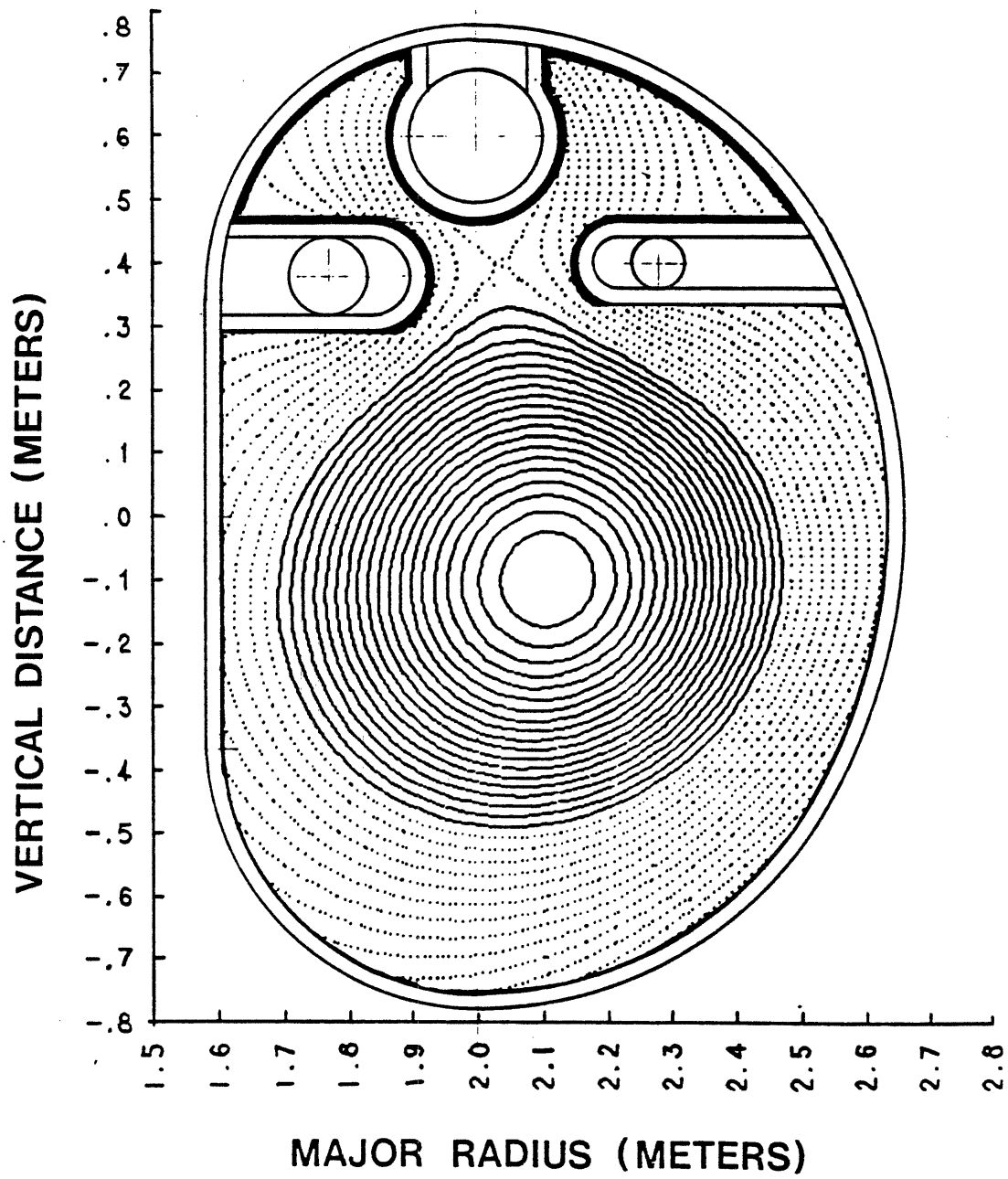


FIGURE 3.3-1b Geometry for Internal Poloidal Divertor

3.3.4. External Poloidal Divertor

The poloidal divertor produced with external coils is not as well understood as the internal poloidal divertor. The only operating device with geometry similar to this class of divertors is the DIII expanded boundary experiment [3.3-11] in which divertor coils link the TF coils. The General Atomic and JAERI teams indicate that the expanded boundary exhibits particle pumping and impurity control similar to the PDX and ASDEX divertors.

The external poloidal divertor throat is much more 'open' than that of the internal divertor. This could lead to a greater leakage of neutral hydrogen and impurities back to the main plasma. On the other hand field lines spread out to a greater extent in the open divertor, allowing easier design of neutralizer plates. When the plasma shape or position is varied, the x-point, and thus the heat flux deposition profile will vary. Our calculations indicate that these variations are less than or of the same order as the λ_E variations discussed below in Section 3.3.5.

We are considering two possible neutralizer plate/baffle configurations for the external divertor. For the first, shown in Figure 3.3-1c, the neutralizer plate is mounted directly on the vacuum vessel wall with the baffles below. In the second configuration, shown in Figure 3.3-1d, the neutralizer plate and baffle are together in the same structure. These two functions are combined because approximately two thirds of the particle flux contacts the plate within several centimeters distance from the separatrix. Any neutral subsequently created there will not have a direct line of sight path back to the main plasma.

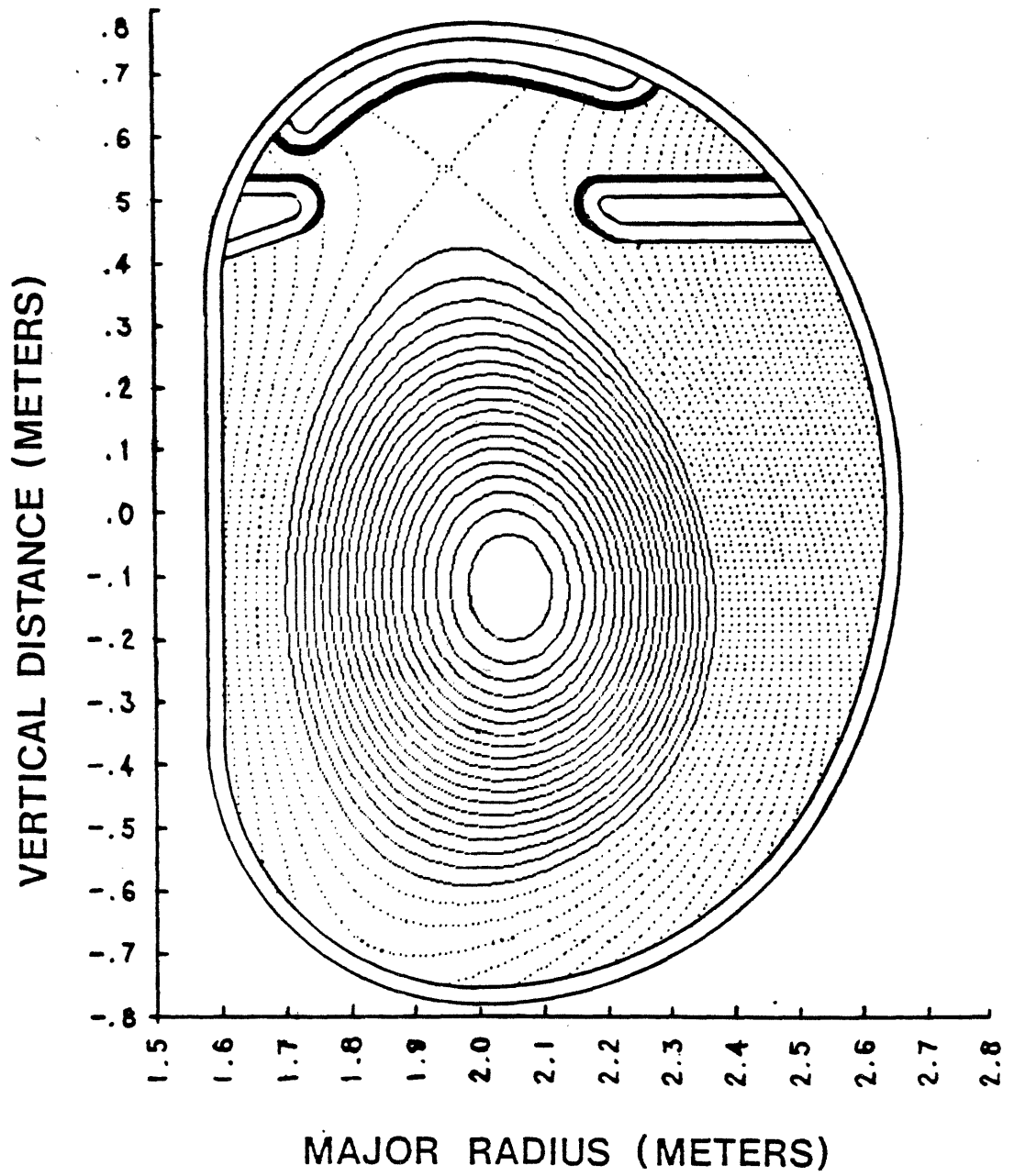


FIGURE 3.3-1c Geometry for External Poloidal Divertor using vacuum vessel wall for mounting neutralizer plate.

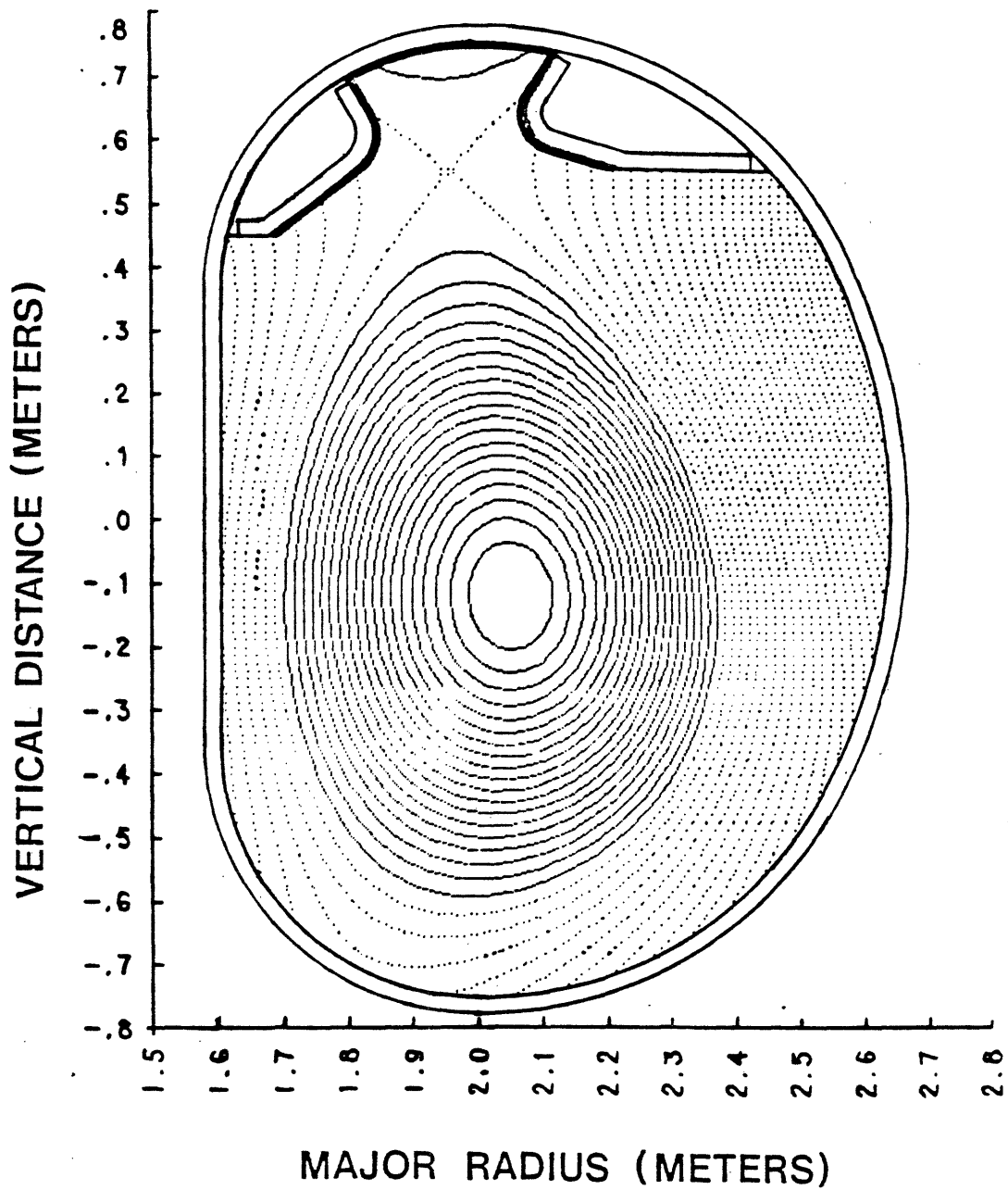


FIGURE 3.3-1d Geometry for External Poloidal Divertor shaped to reduce the heat deposition $< 2\text{MW/m}^2$.

The fact that the first configuration (Figure 3.3-1c) is not an optimized shape results in higher heat loads, although some of this load will be spread out because of perpendicular transport across the separatrix in the 'divertor chamber'. This design appears easier to construct and support than the second (Figure 3.3-1d). It is interesting to note that the heat load results for the configuration shown in Figure 3.3-1d (see next section) imply that one should design for the shortest decay length deemed reasonable. This case is somewhat different from the internal poloidal divertor design, which is quite sensitive to the actual value of the decay length.

3.3.5. Heat Deposition Calculations

To study the heat deposition profiles, we have chosen the extreme case of plasma loading, 10 MW at the plasma edge. The energy decay length in the scrape-off layer, λ_E , estimated by scaling from Alcator C results, is 1.2 cm. We have designed the limiter and divertor plates using this value, and have calculated the resulting heat deposition if λ_E is different by ± 4 mm.

The heat flux parallel to a field line in the scrape-off layer is calculated on the plasma midplane using the above information. The flux surface geometry is given by the output ($\psi(R,Z)$) of an equilibrium code described in Section 2.3. The heat flow is then mapped to the divertor plate or limiter surface assuming constant flow on a flux surface. Knowing $\psi(R,Z)$ we can calculate the vector components of the magnetic field at the plate, and thus the heat deposition. The results for the four different geometries discussed above are shown in Figure 3.3-2.

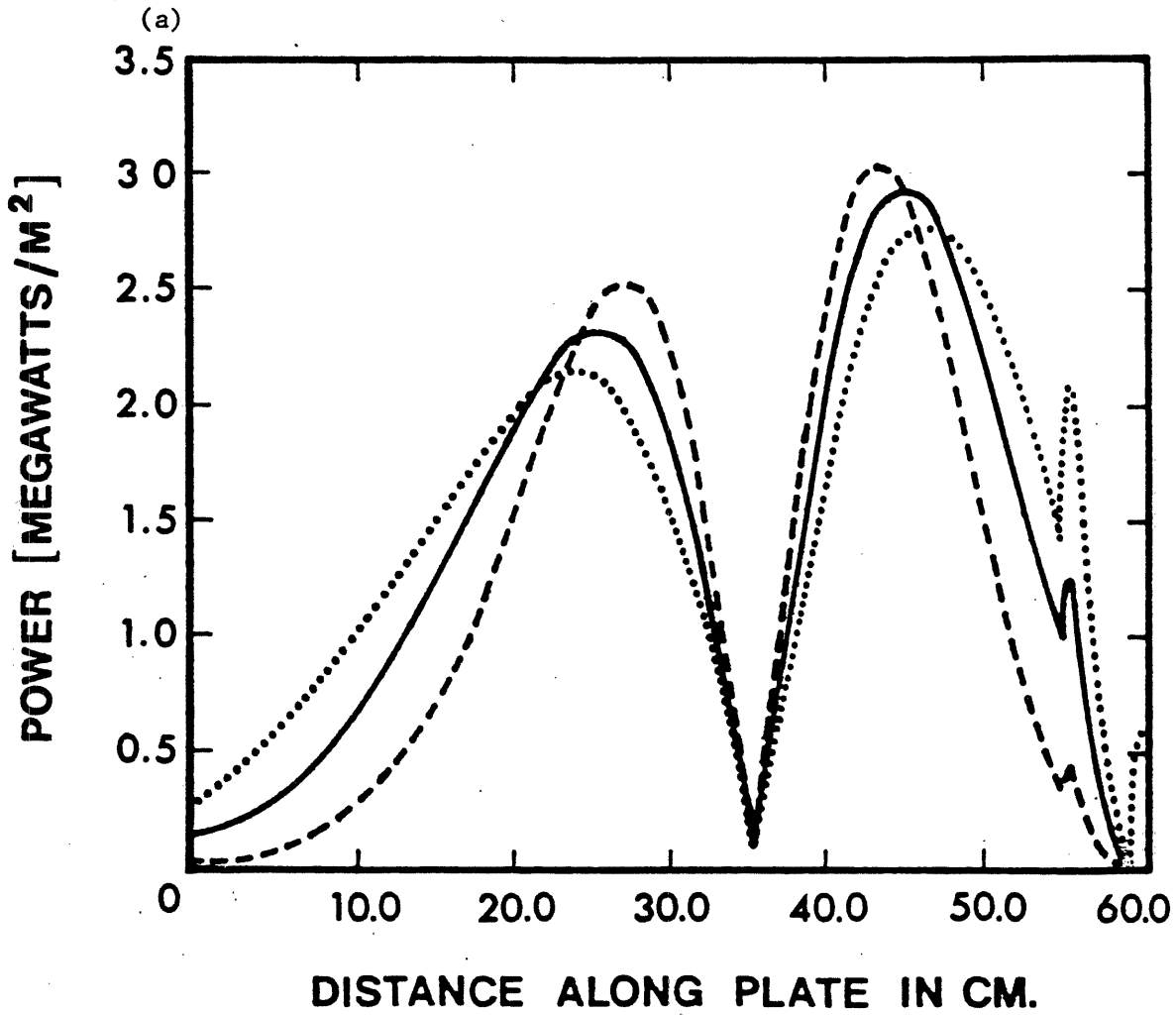


FIGURE 3.3-2a Heat deposition profile for the geometry Figure 3.3-1a. The curves shown are: $\lambda_E = 1.6\text{cm}$ (...); $\lambda_E = 1.2\text{cm}$ (—) and $\lambda_E = .8\text{cm}$ (---).

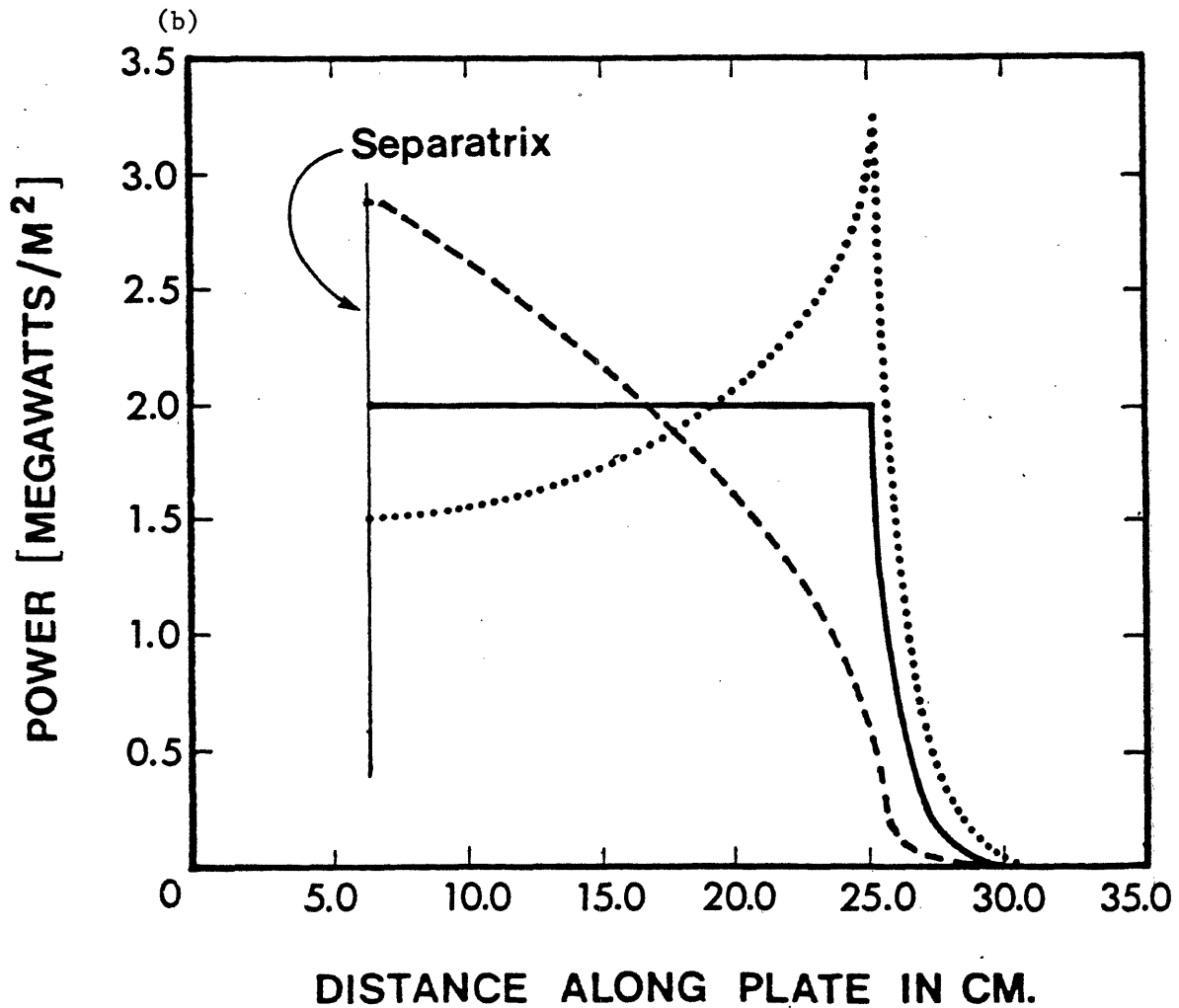


FIGURE 3.3-2b Heat deposition profile for the geometry Figure 3.3-1b. The curves shown are: $\lambda_E = 1.6\text{cm}$ (...); $\lambda_E = 1.2\text{cm}$ (—) and $\lambda_E = .8\text{cm}$ (---). In this case the plates are shaped for $\lambda_E = 1.2\text{cm}$, to force $P_{\text{dep}} < 2\text{MW/m}^2$. Only one plate of two is shown.

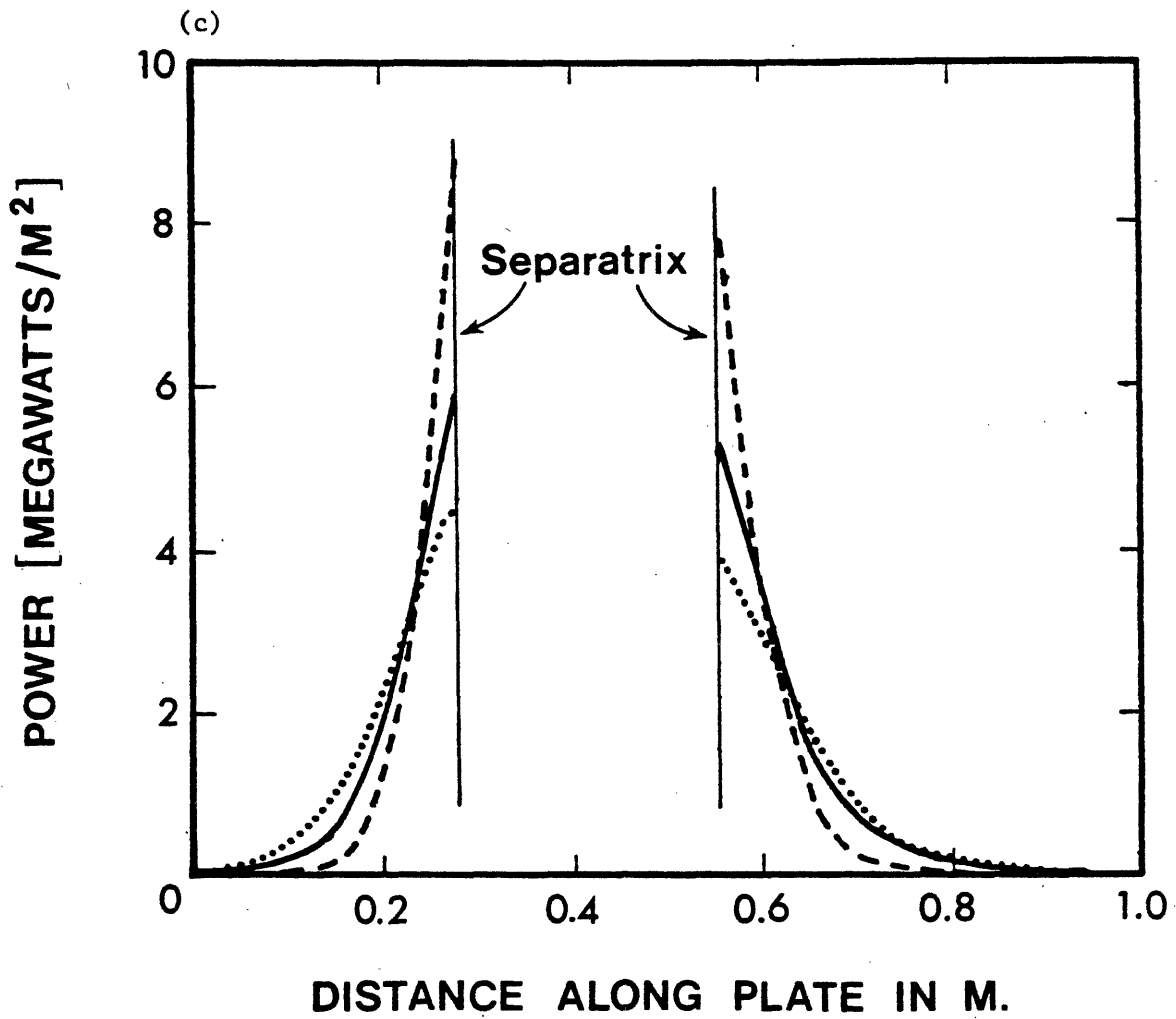


FIGURE 3.3-2c Heat deposition profile for the geometry Figure 3.3-1c. The curves shown are: $\lambda_E = 1.6\text{cm}$ (...); $\lambda_E = 1.2\text{cm}$ (—) and $\lambda_E = .8\text{cm}$ (---).

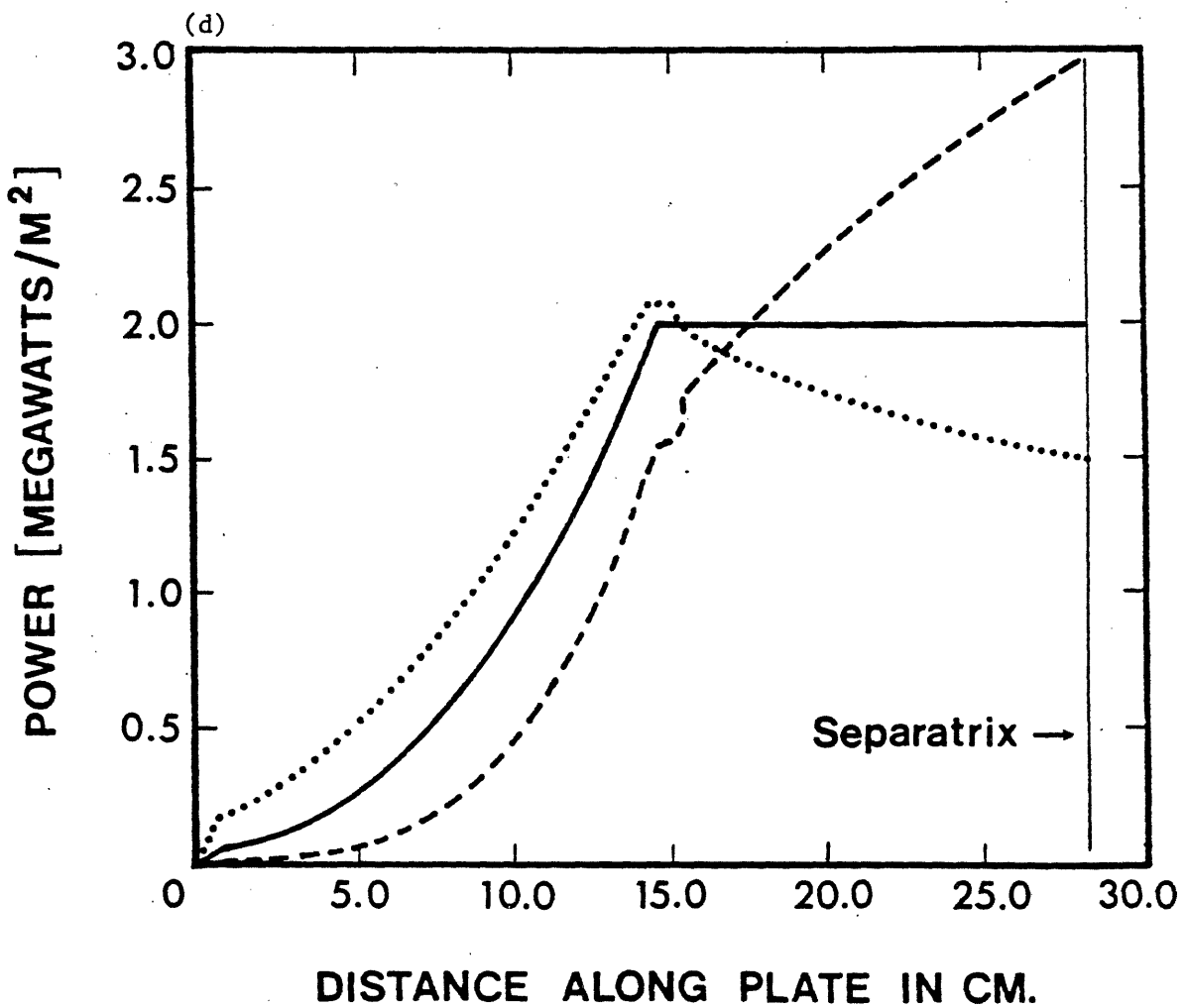


FIGURE 3.3-2d Heat deposition profile for the geometry Figure 3.3-1d. The curves shown are: $\lambda_E = 1.6$ cm (...); $\lambda_E = 1.2$ cm (—) and $\lambda_E = .8$ cm (---). In this case the plates are shaped for $\lambda_E = 1.2$ cm, to force $P_{dep} < 2$ MW/m². Only one plate of two is shown.

For all cases we find the heat loads, and thus the thermally derived impurity sources, to be reactor prototypical. Two of the geometries (Figures 3.3-2b,d) have been optimized for $\lambda_E = 1.2$ cm, limiting the heat load to 2 MW/m^2 . The variation of heat loads with changing λ_E is manageable.

3.3.6. Edge Plasma Parameters

A one-dimensional transport code, described in detail elsewhere [3.3-12], has been used to model the plasma edge. This calculation includes conductive and convective transport processes as well as neutral and impurity sources and sinks. The field line geometry is adaptable to either magnetically or mechanically limited discharges. For this calculation, as for the heat deposition model, we assume that 10 MW of power are deposited uniformly in the plasma scrape-off region. Typical results for the open divertor case are shown in Figure 3.3-3. With variation in the plasma density the flux multiplication effect is seen for all divertor configurations. This effect reduces the average energy carried per ion, which also reduces the sputtering at the divertor plate. Since this model predicts the density and temperature in the divertor chamber, we can calculate an impurity accumulation parameter from impurity momentum balance [3.3-10]. We find this parameter $((1/n_i)(dn_i/dx))^{-1} / (L_{div}/3)$ to be less than 1 over the complete range in edge conditions (Figure 3.3-4).

The parameters for the edge of the main plasma, as opposed to divertor chamber, were roughly similar for all configurations, as the impurity density and power to the edge were kept constant. The edge temperature

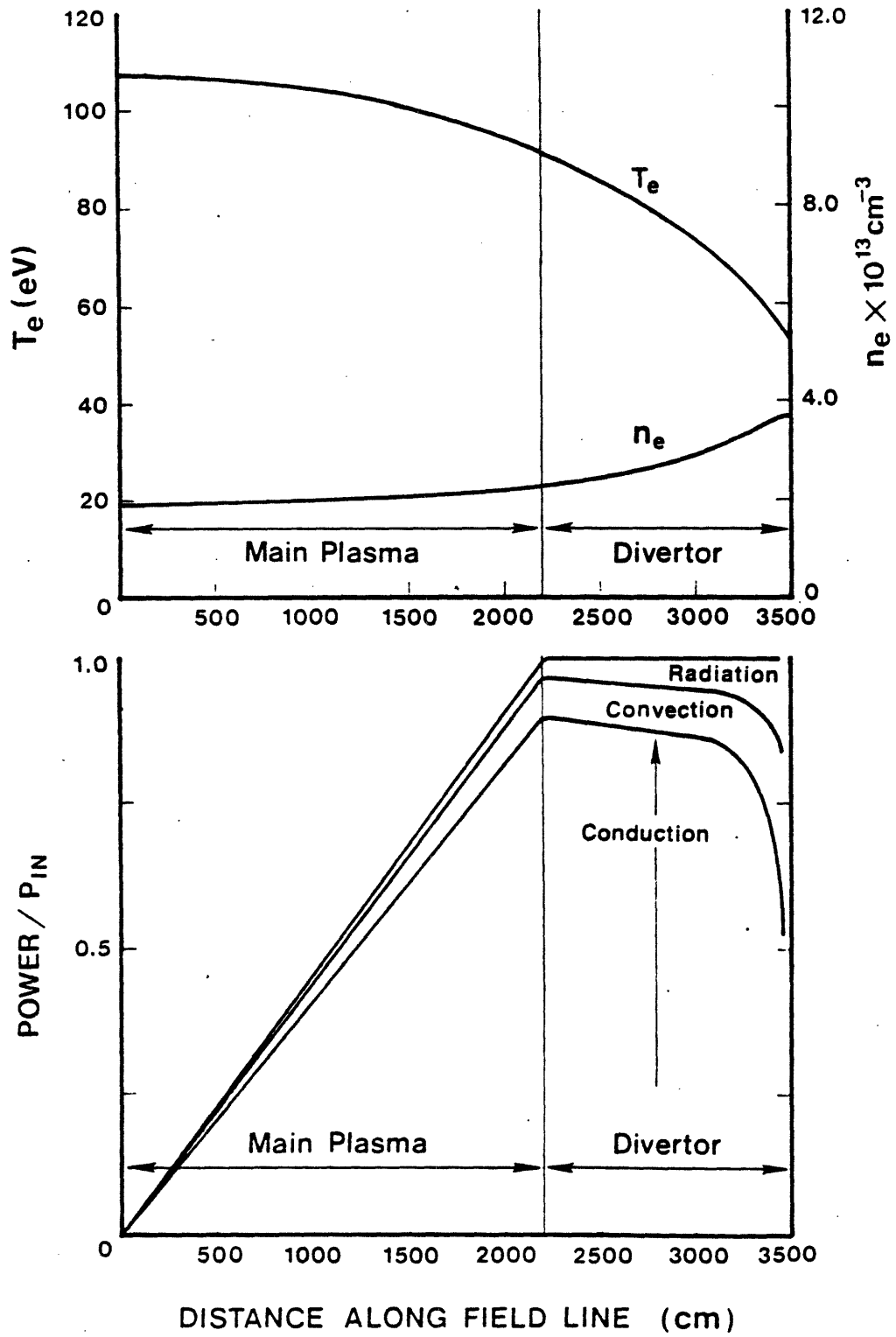


FIGURE 3.3-3 Typical profiles of n_e , T_e , P_{TOT} , P_{COND} , P_{CONV} along a field line for divertor geometry.

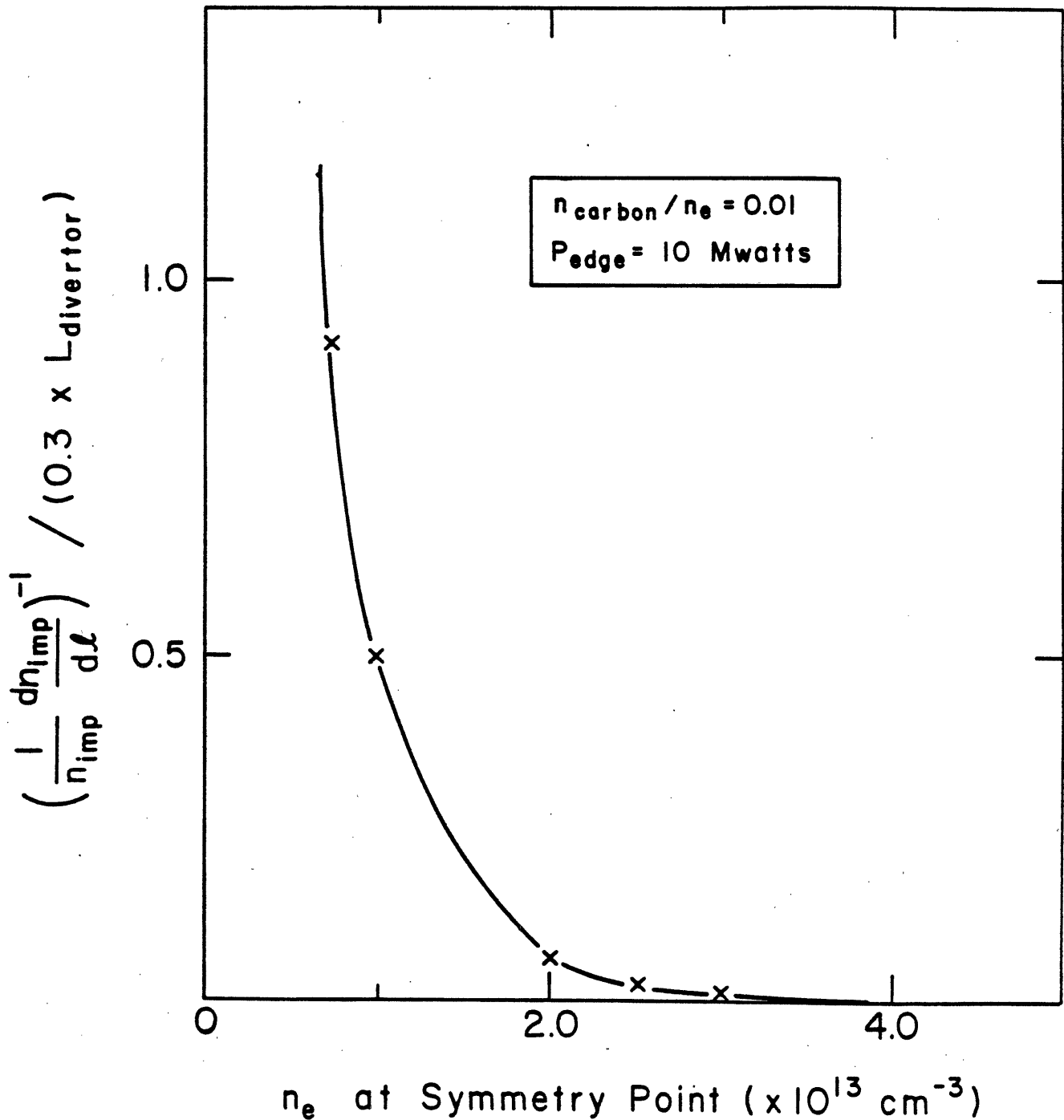


FIGURE 3.3-4 Impurity accumulation parameter vs. edge density. This parameter < 1 indicates that an impurity ion created at the divertor plate will not return to the main chamber.

and electron density ranges were 75 - 100 eV and $.8 - 5 \times 10^{19} \text{ m}^{-3}$ respectively. With these values Alcator DCT would enter a sputtering regime typical of that predicted for reactors. Edge and divertor chamber parameters are summarized in the following table.

TABLE 3.3-1

Plasma Scrape-off Characteristics

P_{EDGE}	10 MW
λ_E	$1.2 \pm .4 \text{ cm}$
n_E	$.8 - 5 \times 10^{13} \text{ cm}^{-3}$
T_e	75 - 150 eV
$P_{\text{in}}/A_{\text{wall}}$.19 MW/m^2
P_{ave} on divertor plate or limiter	2 - 3 MW/m^2
CX power from main plasma	1 MW
Total CX & RAD losses in divertor	.5 - 6 MW
λ_{mfp} (ionization of C)	.5 - 5 cm

3.3.7. Heat Removal Components

The heat removal structures within the vacuum vessel can be characterized by the level of power deposited on them. There are basically three classes as detailed in Table 3.3-2.

TABLE 3.3-2

Classes of Heat Loads

(1) direct plasma contact	2-3 MW/m^2
(2) recycling plasma contact	$\lesssim 1 \text{ MW/m}^2$
(3) radiation/CX from main plasma	.2-.4 MW/m^2

The first level of heat load was described in the previous two sections. It is just the direct heat flow along field lines to the divertor plate or limiter. We are currently considering the INTOR [3.3-3] design for this structure (see Figure 3.3-5). A graphite tile, which contacts the plasma, is brazed to a copper alloy cooled substrate. The brazing method would involve some intermediate layer of a metal, copper pins or copper wool. An alternative would be to use a tile graded in composition from graphite to copper. This would be formed by plasma spray techniques. Plasma-facing surface temperatures have been calculated for different thickness graphite tiles assuming 2 MW/m^2 heat load, 70° C coolant and infinite thermal conductance through the brazing [3.3-8]. These are shown in Table 3.3-3. Further work is needed to determine the efficacy of the different brazing methods described above. Tile lifetime calculations, disruption characteristics, and thermal hydraulics for this class of structures are given in Appendix B.

TABLE 3.3-3

Peak Temperatures ($^\circ\text{C}$) of Pumped Limiter Carbon Tile vs. Thickness

POSITION	Thickness				
	1 mm	2 mm	4 mm	8 mm	12 mm
TOP	131	146	163	216	268
LEADING EDGE	98	106	115	141	166

CONDUCTION COOLED
(POSITIVE CONTACT)

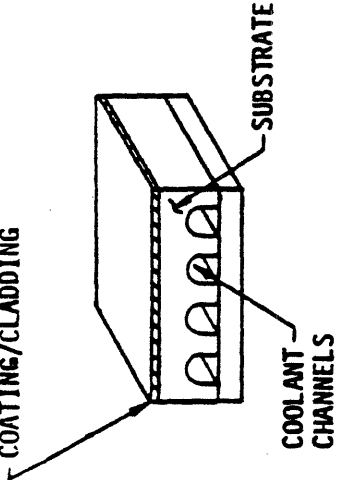
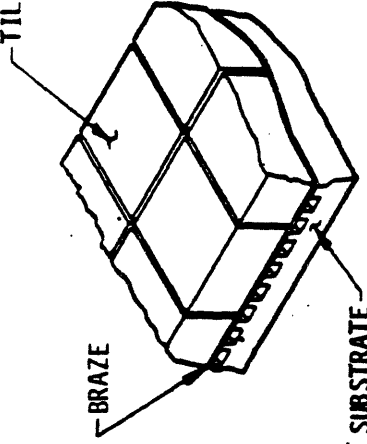
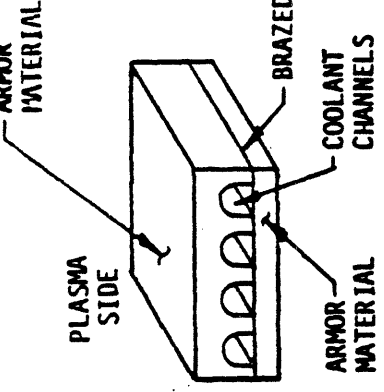
<p>CONCEPT</p>	 <p>COATING/CLADDING</p> <p>SUBSTRATE</p> <p>COOLANT CHANNELS</p>	 <p>TILE</p> <p>BRAZE</p> <p>SUBSTRATE</p>	 <p>ARMOR MATERIAL</p> <p>PLASMA SIDE</p> <p>ARMOR MATERIAL</p> <p>COOLANT CHANNELS</p> <p>BRAZED</p>
	<p>COATING/CLADDING</p>	<p>BRAZED</p>	<p>INTEGRAL COOLANT</p>
<p>PRIMARY CONSIDERATIONS</p>	<p>(SEE APPENDIX A)</p>	<ul style="list-style-type: none"> • HIGH CONDUCTANCE • INTERFACE STRESSES • RADIATION DAMAGE TO BRAZE MATERIAL 	<ul style="list-style-type: none"> • LIMITED TO SPECIFIC MATERIALS • INTERFACE BETWEEN DIFFERENT MATERIALS NOT REQUIRED

FIGURE 3.3-5a Tile mounting design for limiter/divertor plates.

CONDUCTION COOLED
(COMPLIANT LAYER)

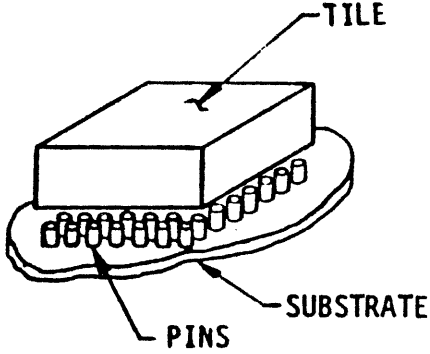
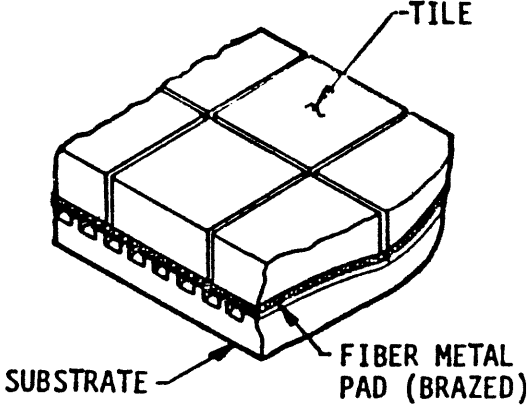
<p>CONCEPT</p>		
	<p>BRAZED PINS</p>	<p>BRAZED COMPLIANT LAYER</p>
<p>PRIMARY CONSIDERATIONS</p>	<ul style="list-style-type: none"> ● LOWER BRAZE STRESSES ● LOWER CONDUCTANCE ● LIMITED TESTING DONE 	<ul style="list-style-type: none"> ● LOW INTERFACE STRESSES ● SIMILAR APPLICATION IN USE AT PRESENT ● RADIATION DAMAGE TO FIBER METAL PAD AND BRAZE ● OUTGASSING & VIRTUAL LEAKS ● LOW THERMAL CONDUCTANCE

FIGURE 3.3-5b Tile mounting design for limiter/divertor plates.

In addition to having the highest heat load, limiters and divertor plates give rise to the second class of heat loads which occurs on adjacent vessel components. This power deposition is due to charge exchange neutrals originating from recycling plasma at the limiter/divertor plate. The structure design for absorption of this power is shown in Figure 3.3-6. What is pictured is again a graphite tile but mounted on a different backing. This cooled structure, manufactured by many companies (e.g., Dean Products), could be either stainless steel or copper depending on the electro-mechanical forces it would experience during a plasma disruption.

An un tiled stainless version of this backing would be used for the bellows cover plates. This structure covers most of the vacuum vessel. A perspective view of this structure and how it could be mounted is shown in Figure 3.3-7. The low heat load for the bellows cover plates would only be due to radiation and charge exchange neutrals emitted from the main plasma.

3.3.8. Heat Removal and Impurity Control Summary

The three configurations we have considered for the long pulse, high heat flux Alcator DCT tokamak are a pumped limiter, internal poloidal divertor and external poloidal divertor. For all three we find the heat flux and sputtering regime to be reactor prototypical. The pumped limiter may adequately pump particles if neutralizer plates localized at pump ports prove successful. However, because the surface is at the main plasma edge, as with simple limiters, we believe pumped limiters are risky with respect to impurity control. Divertors seem more promising

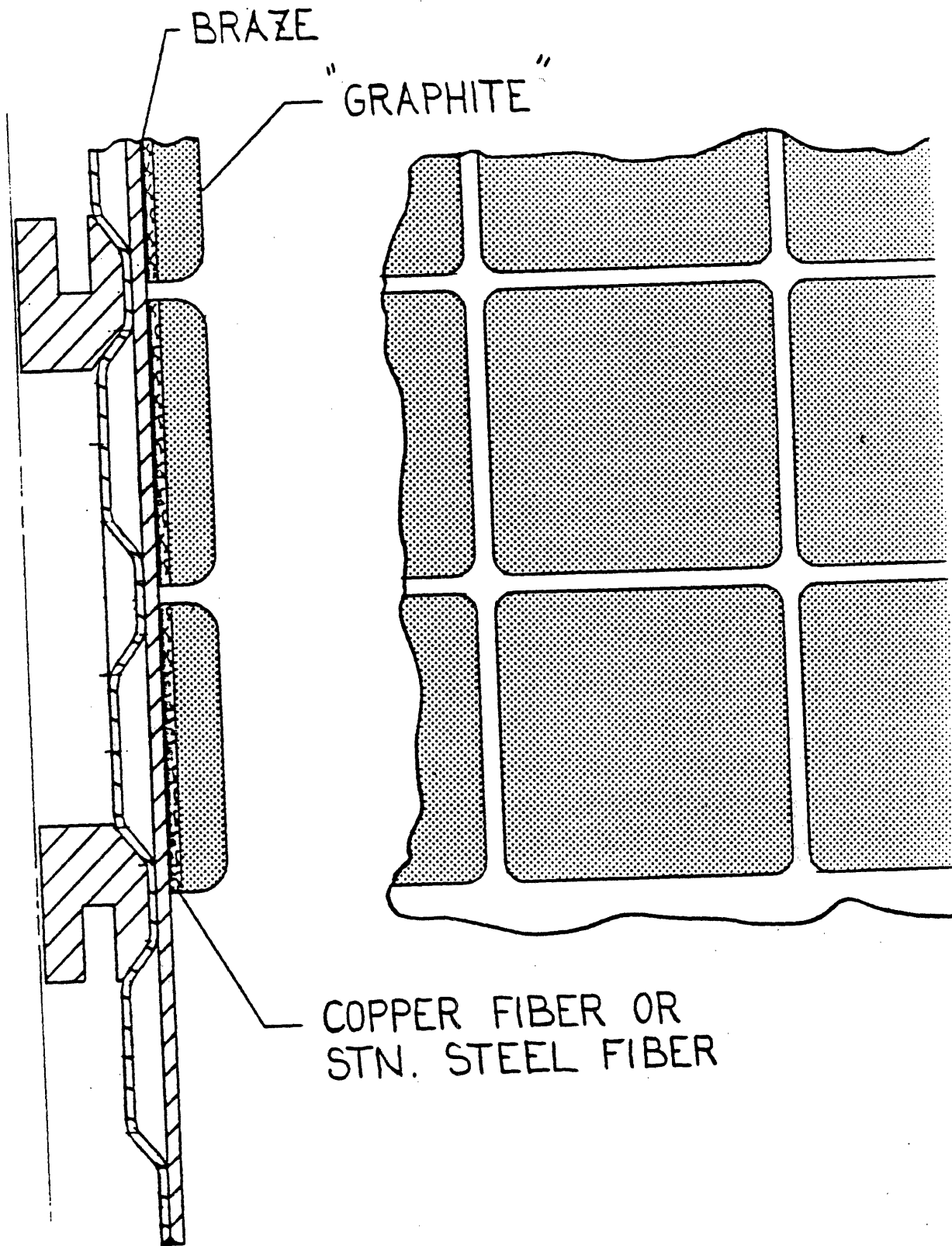


FIGURE 3.3-6 Tile mounting design for bellows cover plates near and far from limiter/divertor plates.

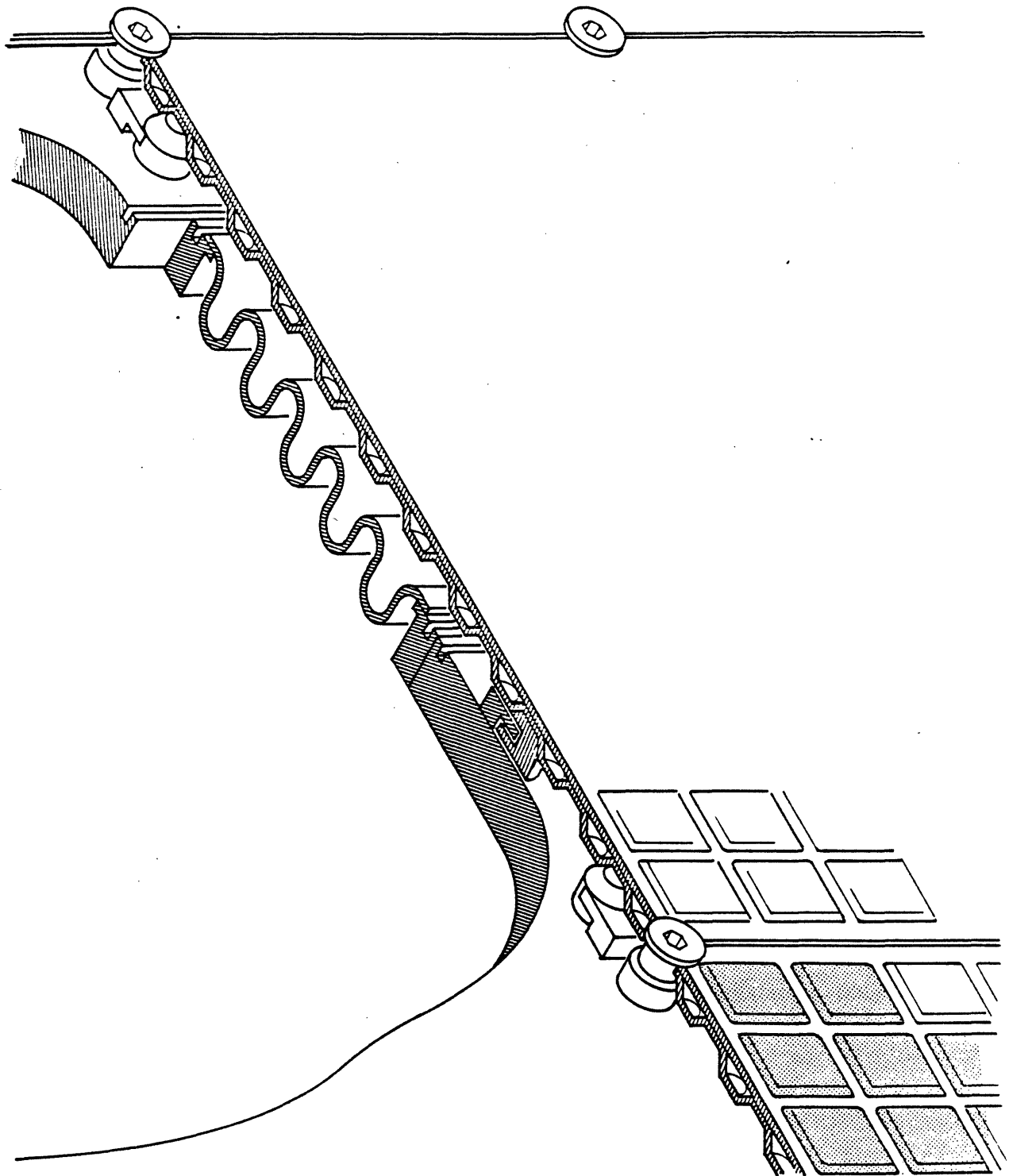


FIGURE 3.3-7 A perspective view of the bellows cover plates.

for several reasons: the heat is spread out due to the length and spreading of field lines; the impurity generation point is removed from the main plasma edge; particle exhaust from the main plasma is more efficient; flux multiplication reduces the average energy per ion, reducing the physical sputtering source; and impurities accumulate in the divertor chamber due to flow of hydrogen ions to the plate. A poloidal divertor is therefore included as part of the Alcator DCT design. We feel that with this impurity control option the possibility of achieving long pulses will be greatly enhanced. In addition, we will retain the pumped limiter design as part of the basic machine, providing a comparison of these two particle and impurity control techniques.

Each divertor option presents some advantages. The internal coil design permits a less 'open' divertor chamber. However, the average field line length is greater for the external coil design (Figure 3.3-8). This is particularly important for the region within one energy decay length of the separatrix ($X/\lambda_E < 1$), which contains 2/3 of the edge heat flow. The additional length enhances two divertor chamber effects. The heat load spreads due to perpendicular transport and an impurity generated at the divertor plate must, after being ionized travel, further to return to the plasma edge. These effects may balance the openness of the external poloidal divertor. From an engineering viewpoint, we found the two configurations roughly equivalent. At present, we are pursuing the external poloidal divertor option because of its greater reactor relevance and promise of effective impurity control. Techniques for winding a superconducting coil inside the chamber are also being studied should the relatively more open divertor prove inadequate.

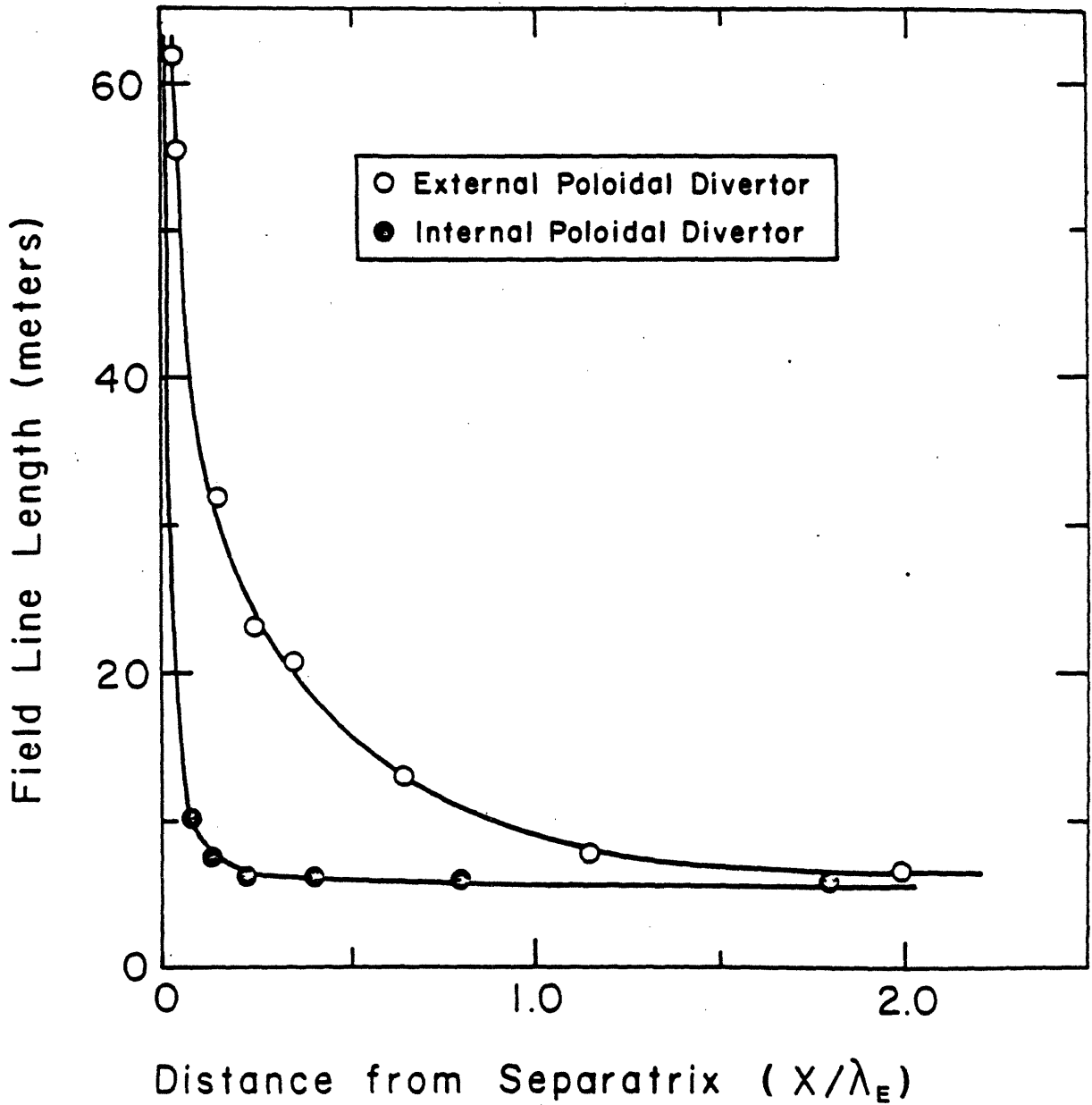


FIGURE 3.3-8 Comparison of field line length vs. X/λ_E on the plasma midplane. The pumped limiter has field line length equal to the asymptotic divertor value for all X .

$$\text{For } X/\lambda_E = 1, \int_0^X = \lambda_E \quad P(\psi(\ell))d\ell = (2/3)P_{IN}.$$

References

- [3.3-1] D. Meade, et al., in Controlled Fusion and Plasma Physics (Proc. 9th European Conf., Oxford, 1979) Vol. 1 (1979) 91.
- [3.3-2] E. Keilhacker, et al., 8th International Conference on Plasma Physics and Controlled Nuclear Fusion Research, Brussels, 1980, Vol. II, p. 351.
- [3.3-3] U. S. FED-INTOR Activity and U.S. Contribution to the International Tokamak Reactor Phase 2-A Workshop.
- [3.3-4] D. Overskei, Phys. Rev. Letters 46, 177 (1982).
- [3.3-5] S. Talmadge, et al., J. Nuclear Fusion 22, 1369, (1982).
- [3.3-6] R. Jacobsen, J. Nuclear Fusion 22, 277 (1982).
- [3.3-7] P. Mioduszewski, J. Nuclear Materials 111 & 112, 253 (1982).
- [3.3-8] J. Brooks, R. Mattis, ANL/FPP/TM-175.
- [3.3-9] M. Petravac, et al., Phys. Rev. Letters, 48, 326 (1982).
- [3.3-10] N. Ohyabu, et al., GA-A16434.
- [3.3-11] M. A. Mahdavi, et al., GA-A16334.
- [3.3-12] B. Lipschultz, to be published as an M.I.T. Plasma Fusion Center Report #PFC/RR-83-25.

3.4. RF Systems and Couplers

3.4.1. Lower Hybrid System

3.4.1.1. General

The lower hybrid system intended for Alcator DCT is already available at M.I.T. where it is being used on Alcator C. It consists of 16 CW Varian klystrons, rated at 0.25 MW each. The tubes are installed on carts in clusters of four, yielding 1 MW of net source power per cart. There are four power supplies, and 16 modulator tubes, one for each klystron. Thus, we have complete control over the DC power source of each klystron. The full power operation of each klystron requires 47 kV at 12.6 A. The power supply/modulator system at present is rated for a 0.5 sec pulsed mode of operation. The harmonic filter and the circulator attached to each klystron are also rated for 0.5 sec pulse duration. Hence, these components will have to be replaced in the CW system. Furthermore, the power supply/modulator units will also require substantial upgrading for a near CW type of operation. The modifications required are straightforward, and will be discussed at some length in the engineering section, including cost estimates.

A schematic of the layout of the RF system for operating a 6×16 waveguide array (i.e., six rows and sixteen columns of waveguides) is shown in Figure 3.4-1. In this layout only one klystron is exhibited. The power is split six ways in case of a 6-row array (or it would be split four ways for a 4-row array). In addition, if we use two couplers on two ports, the power from each klystron would be split two ways before the 16-way split. Thus, the first klystron would be used to power one column of waveguides in all couplers, and additional klystrons would be

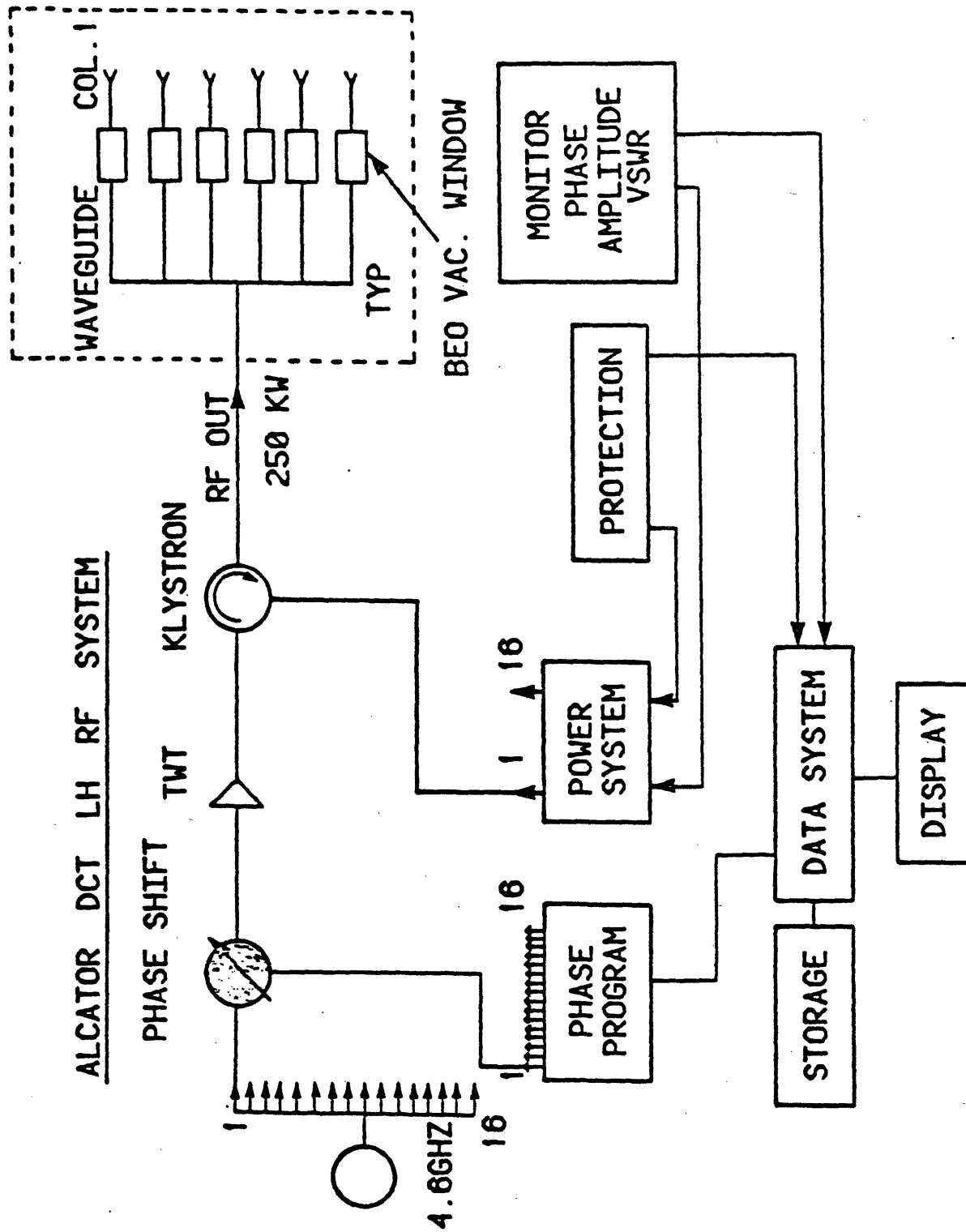


FIGURE 3.4-1 Schematic of the proposed Alcatel DCT Lower hybrid RF system.

used the same way to power adjacent columns. An alternate way to power two couplers is to use two klystron carts (or 8 klystrons) to power one port. This is simply achieved by splitting the power of each klystron two ways, one to power the first column and the other for the ninth column (both of which would be in phase for both 180° and 90° phased operation). We note that our system is provided with the capability of electronic phase control during the duration of the RF pulse (see "Phase Program" in the block diagram). Thus, we can consider a scenario where we start up with 180° phasing of adjacent waveguides for the purposes of heating, and after 50 or 100 msec (for example) switch the phases to 90° for efficient current drive. This phase shifting is achieved within a millisecond (or less) time scale at the low power drive level. The remainder of Figure 3.4-1 is self-explanatory.

3.4.1.2. Lower Hybrid Coupler

The lower hybrid coupler is a phased array of waveguides used extensively in every present day lower hybrid experiment. While there are many versions of this type of coupler, the MIT Alcator C design is by far the most efficient in its capability of handling high power without serious RF breakdown problems. It also enjoys the advantages of utilizing industrial manufacturing procedure (made by Varian Associates). Further, it requires relatively modest "in-house" processing and treatment. The present Alcator C coupler has operated at power levels up to 9.0 kW/cm² (on the windows and in the waveguides) transmitted into the plasma. However, for routine long pulse operation we recommend a maximum power transmission of 5-6 kW/cm² in the waveguides (and on the BeO windows). In the present design BeO windows are brazed into high precision manufactured (wire-EDM)

copper cups which are then brazed into seamless premanufactured 304 stainless steel waveguides. A diagram and a photograph of the present Alcator C 4×4 (16) waveguide coupler is shown in Figures 3.4-2,3. We propose an extension of these techniques to produce several 4×16 (64) arrays (or possibly 6×16 arrays). A schematic of the proposed array is shown in Figures 3.4-4a,b. We note several significant differences between the two couplers. Rather than having a "tongue-groove" joint between the window section and a fan-shaped adaptor section used in the Alcator C design (which was necessitated by the poor access in the Alcator C ports) in Alcator DCT we would bring each individual waveguide to the large port flange and attach it to a subflange with an E-beam weld technique. Water cooling of each window will have to be provided for CW operation. Due to their length, the stainless steel waveguides within the coupler will be silver-plated to reduce RF losses. In addition, minimal cooling may also have to be provided if the power dissipation in the waveguides cannot be reduced to acceptable levels. The size of the waveguides is similar to those used in the present Alcator C arrays (the waveguide width is ~ 5.95 cm as opposed to 5.75 cm in Alcator C). Thus, on the basis of the present Alcator C results we feel that a coupler such as shown here is feasible to fabricate. In fact, Varian has already expressed interest in manufacturing the Alcator DCT couplers.

One question is the number of couplers needed. Assuming a waveguide with open dimensions of $0.8 \times 5.95 = 4.76$ cm², a 64 waveguide array would have an open area of 305 cm². Thus, using two couplers we have a total area of 610 cm². Assuming a net transmitted power of 3.0 MW, the RF power density on the windows and in the waveguide would be 4.9 kW/cm². At present in Alcator C we routinely operate at 6.8 kW/cm², and occasion-

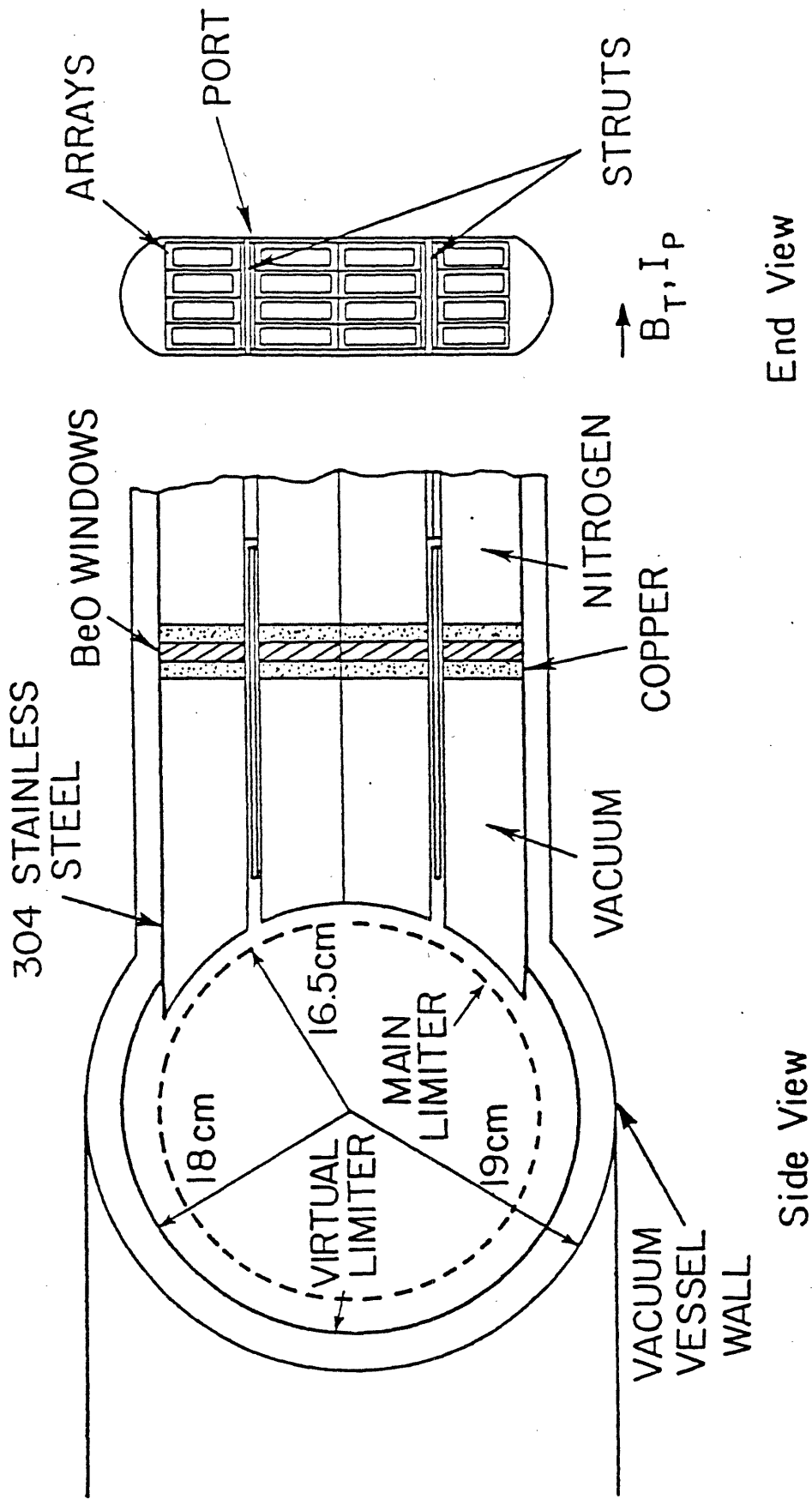
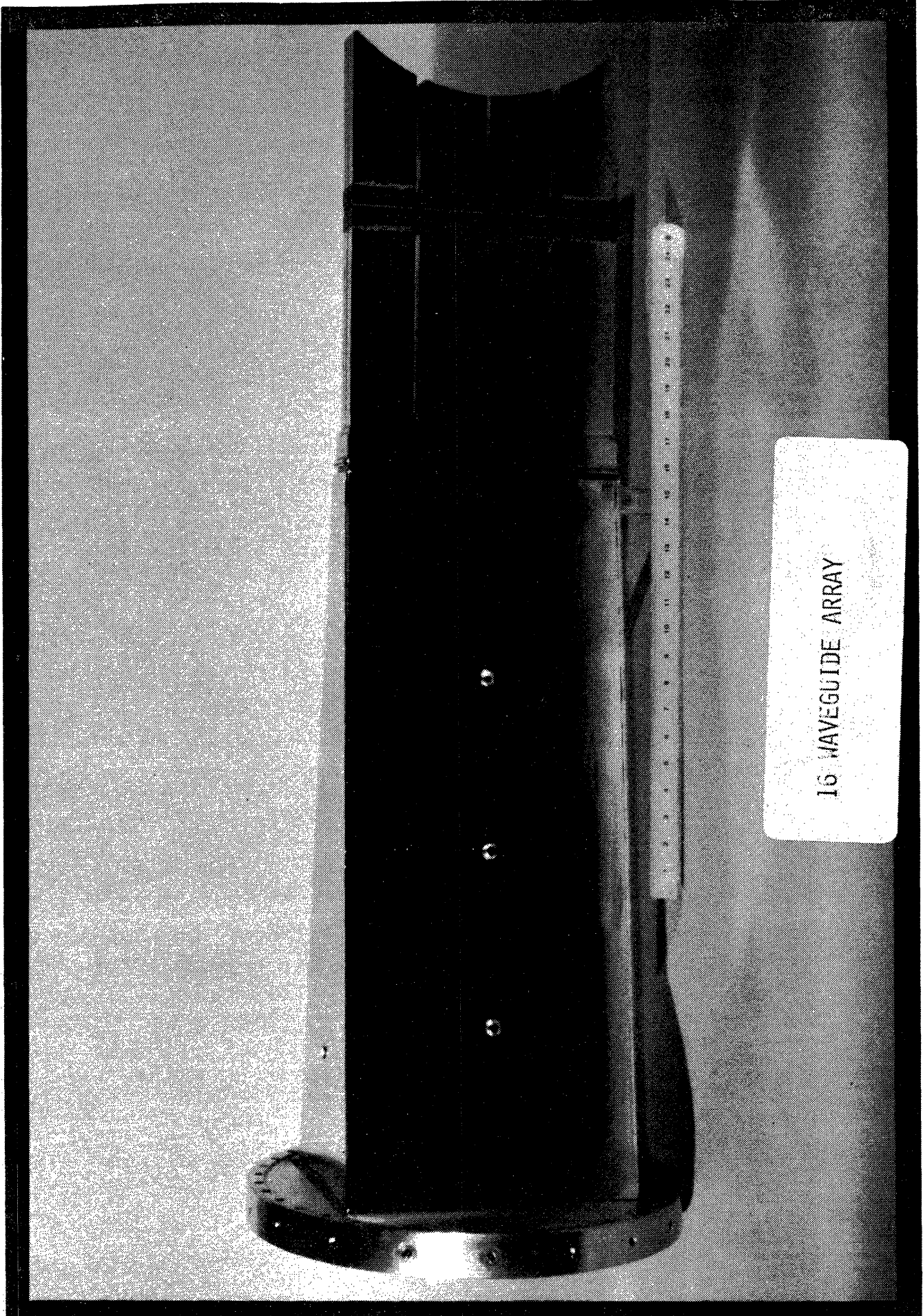
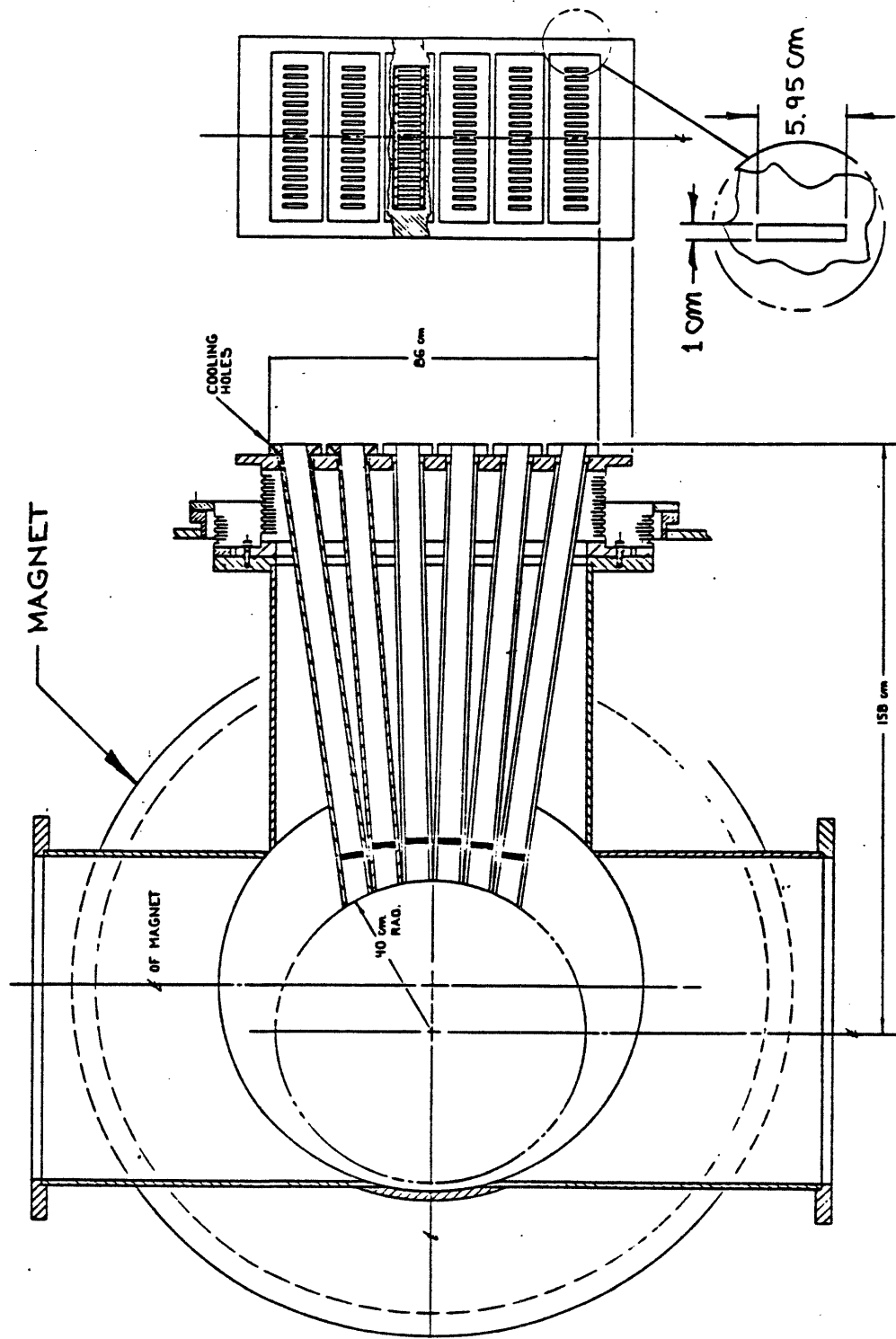


FIGURE 3.4-2 Schematic drawing of the Alcator C 16 waveguide lower hybrid coupler.



16 HAVEGUIDE ARRAY

FIGURE 3.4-3



ELEVATION VIEW

FIGURE 3.4-4a Elevation view of the proposed Alcatraz DCT lower hybrid coupler.

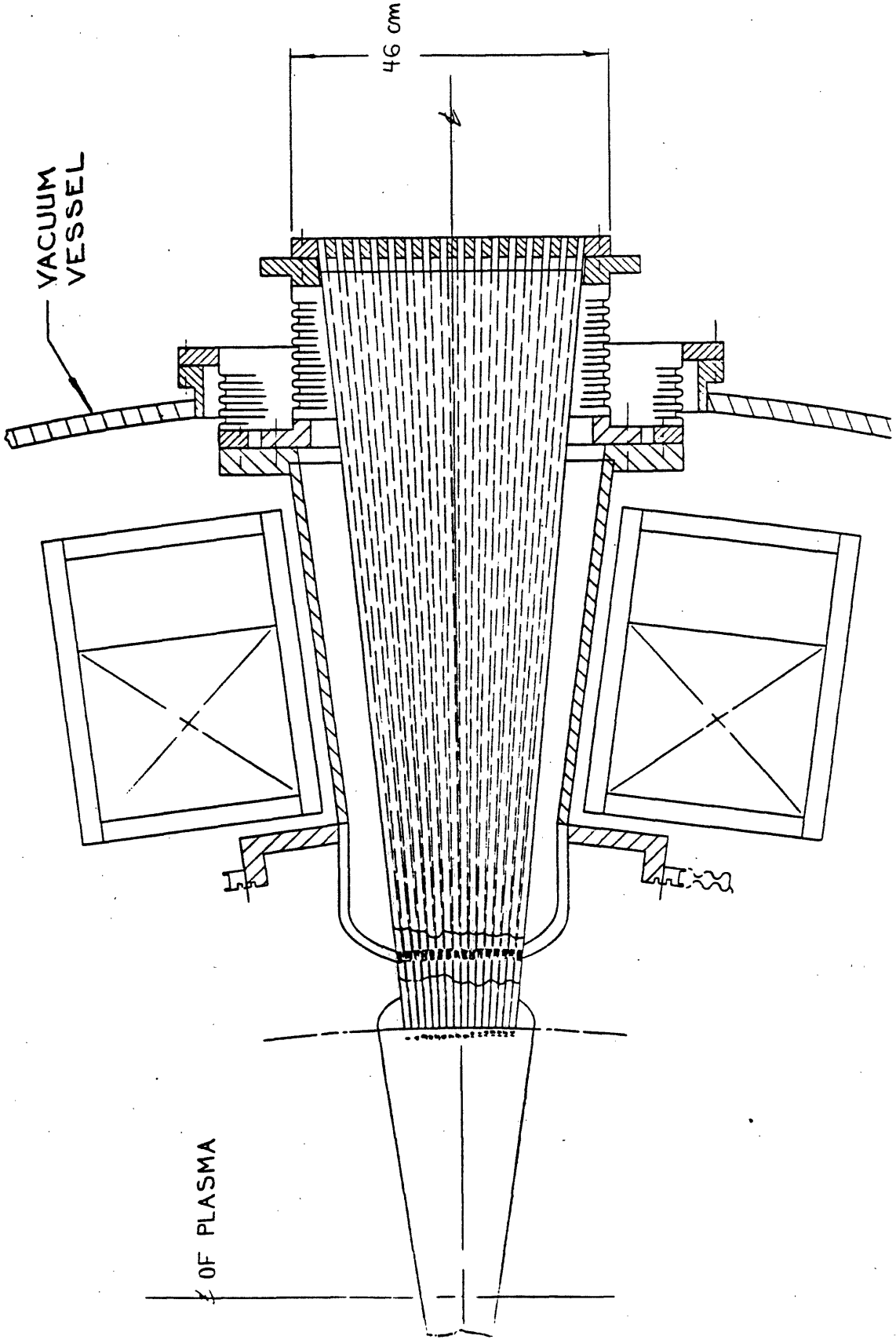


FIGURE 3.4-4b Top view of the proposed Alcatraz DCT lower hybrid coupler.

ally to 9.0 kW/cm^2 . Thus, we feel that two 64 waveguide couplers in Alcator DCT should be satisfactory to handle the power with enough safety margin for CW operation (assuming adequate water cooling). We plan to build at least three couplers, two for operation and one spare. We also note that, an array such as shown in Figure 3.4-4 is repairable if a given row is mounted on a removable subflange as shown. Initial cost estimates are given in the engineering section.

Regarding optimization of coupling to the plasma we note the following: (a) The coupler must be movable by bellows in order to adjust the density at the coupler mouth for minimum reflectivity. At present in Alcator C the total reflectivity of a given 16 array is $R \approx 10\%$ or less when the coupler position is optimized. (b) In order to optimize coupling, the front face of the coupler should conform to the plasma density contour lines. Since we envisage RF current drive operation in plasmas with different surface shapes (circular, D-shaped, diverted,...) we can achieve optimal coupling with individually movable rows of waveguides. Hence we plan to construct the grill with each row of waveguides having its own bellows in order to allow independent motion. In this way, we can obtain good coupling to plasmas with a variety of cross-sections. For further protection of the grill if needed, we could provide additional, water cooled limiters on either side of the waveguide array. These limiters would also permit more direct control of the plasma shape and profile directly in front of the array.

3.4.2. The Alcator DCT ICRF System

3.4.2.1. General

A wide loop antenna has been chosen as the coupler concept for the baseline ICRF design for Alcator DCT. Each antenna is constructed so that it will slide into a horizontal port. The system will consist of five antennas, each rated at 1MW, in five ports of Alcator DCT.

One antenna module consists of a loop 15 cm \times 50 cm (poloidally) above and below the midplane as shown in Figure 3.4-5. The antenna is fed from the ends and terminated in a short at the midplane. Current maxima (voltage minima) occur at the midplane and at the feed point because the length is near a half wavelength, taking into account the reduction in phase velocity caused by the capacitive loading from the shield. The shield consists of horizontal conducting straps surrounding the center conductor.

The antenna width limits k_{\parallel} to $|k_{\parallel}| < 0.15 \text{ cm}^{-1}$, and the evanescent region will limit $|k_{\parallel}|$ to even smaller values, depending on the edge density profile. The single pass absorption is sufficiently high (20-60%) that the radiation resistance of the antenna can be approximated by considering an antenna radiating into a plasma of infinite extent. In addition, the reduced importance of reflections from the wall allows a rectangular slab model to be used, at least for radiation resistance calculations.

We define the lumped radiation resistance of the antenna (R_r) as the resistance which, when placed at the end of a transmission line with the same characteristic impedance as the antenna (Z_a), results in the same

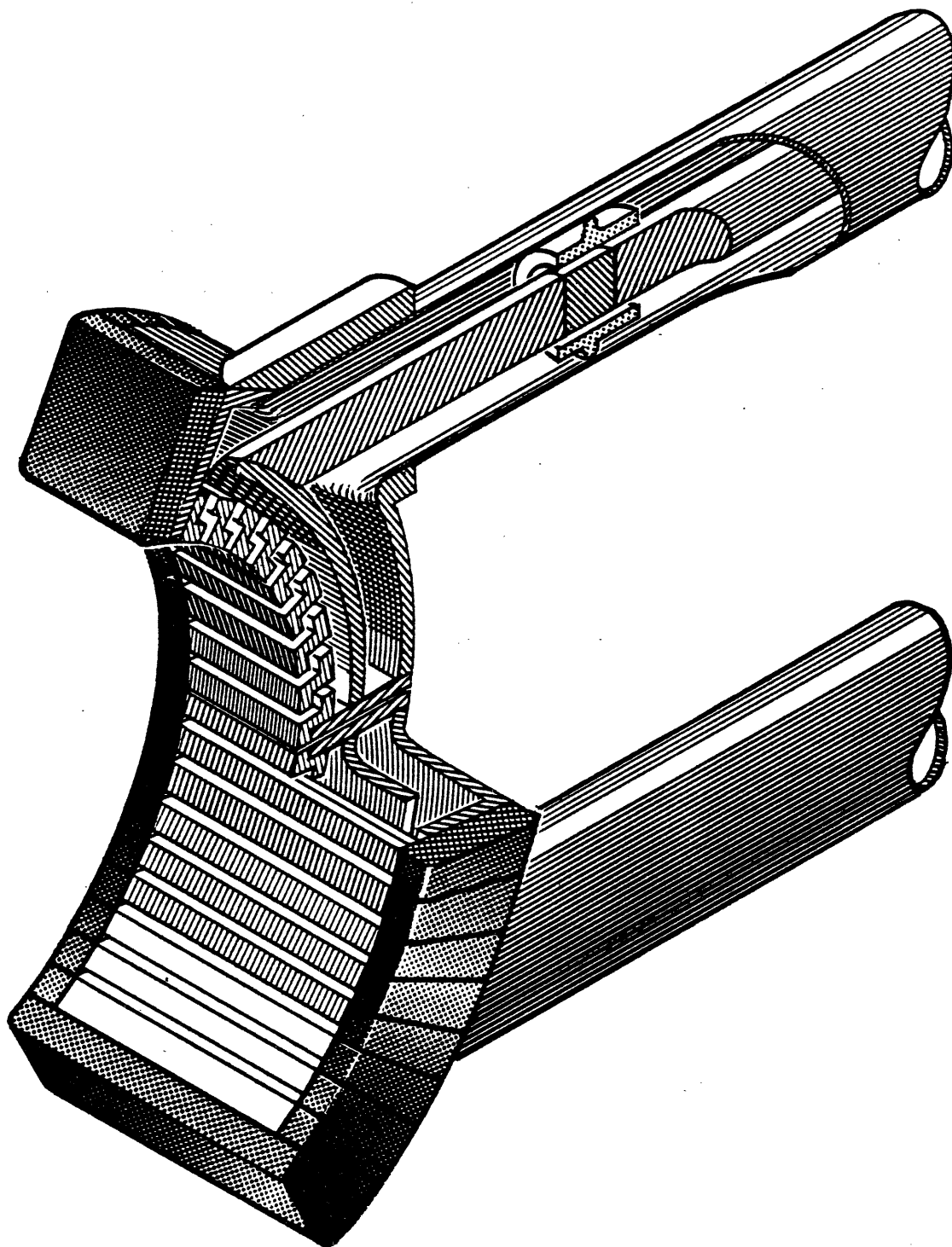


FIGURE 3.4-5 Alcator DCT ICRF antenna concept (1 MW module).

terminal impedance as the antenna. An examination of the scaling of R_r [3.4-1] reveals that while the radiation resistance increases with the length of the antenna, it decreases as the antenna is made wider. The decrease in radiation resistance is compensated by a decrease in the characteristic impedance of the antenna (Z_a) so the standing wave ratio is not degraded. Further, if the impedance of the feed transmission line is matched to Z_a without sacrificing voltage stand-off, the power available to the antenna actually increases with the width of the antenna.

The antenna shown in Figure 3.4-5 has a characteristic impedance of 20 Ohms, and a radiation resistance (R_r) of 2-5 Ohms, depending on the plasma density profile. Separate feeds to the upper and lower elements allow a straightforward connection to the ten sources, and provide for some control of the azimuthal mode number by phasing the elements separately. The individual RF sources can be phased at a low power level (Figure 3.4-6.) With a suitable coupler system, a spectrum of travelling waves can be produced with possible application to ICRF current drive.

3.4.2.2. Tuning and Matching

The RF system block diagram is shown in Figure 3.4-6. A 20 to 50 ohm transformer section precedes the tuning system to keep the mismatch low. It is considerably closer to the machine than the tuning stubs and serves to limit the length of line with a high standing wave ratio. This reduces the possibility of breakdown in the transmission lines and cuts down the losses in the system. Matching is accomplished by a double stub tuner in each feed line. With a spacing of $3\lambda/8$ the range of loads accessible at any given frequency is broad enough to cover most plasma induced

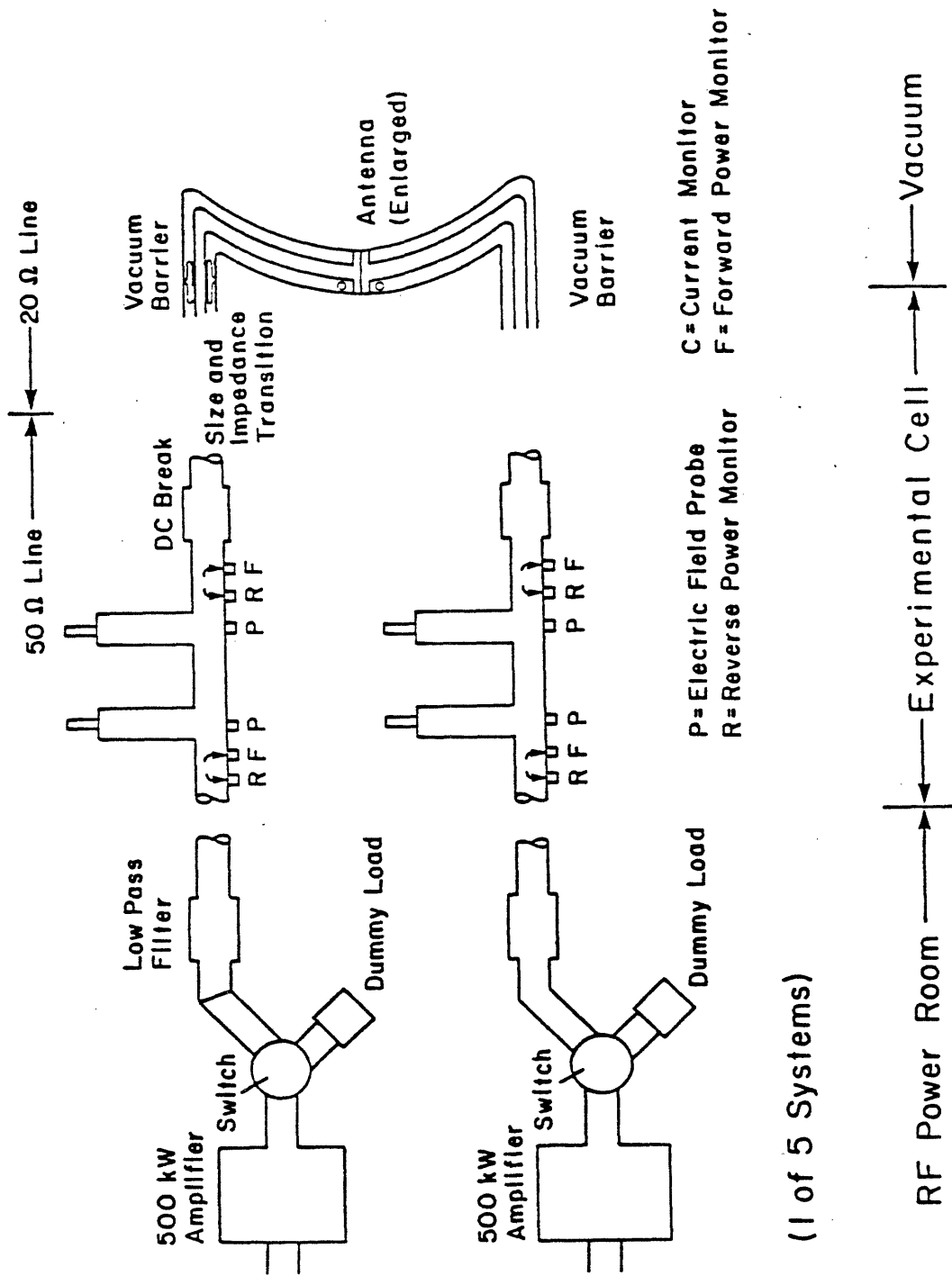


FIGURE 3.4-6 Block diagram of the ICRF tuning and matching system.

load variations. Fixed line sections can be changed to adjust for major loading variations or if the frequency is changed appreciably. The tuning system is diagnosed by reflectometers before and after the tuning stubs, probes at each tuning stub and current monitors in each antenna.

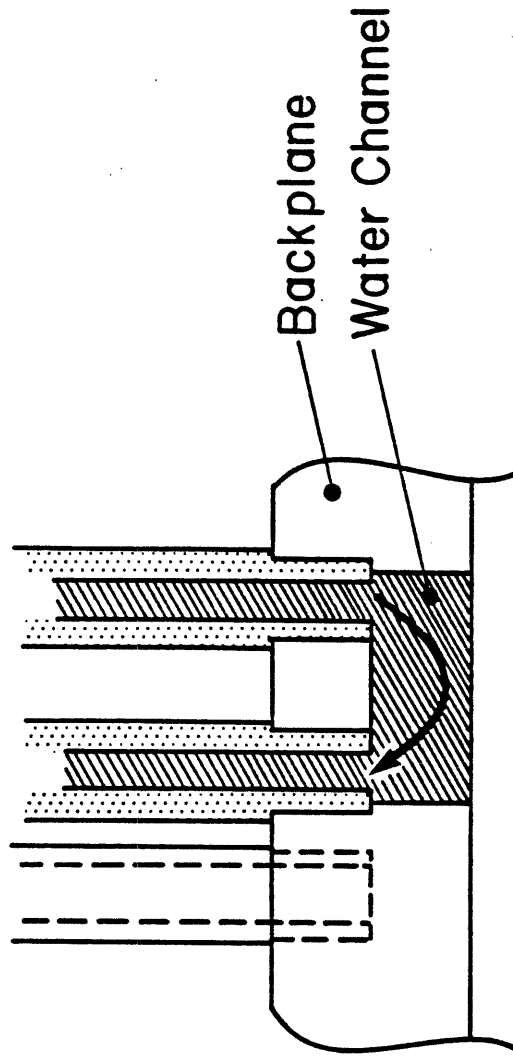
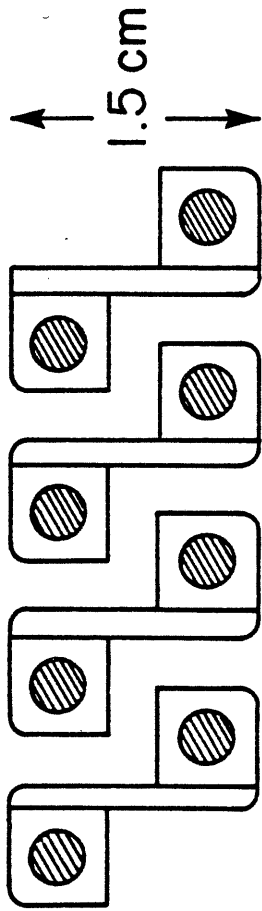
3.4.2.3. Antenna

Both the antenna conductors and the shield are water-cooled, (Figure 3.4-7) to remove power deposited by RF eddy currents and heat flux from the plasma. Table 3.4-1 contains a summary of the heat loads on the antenna components. Each conductor in the shield is also a coolant channel connected in a series-parallel configuration. Coolant tubes run inside the center conductor and along the return conductor. The ceramic vacuum barrier can be cooled from the edge because of the relatively low power deposition in this component.

TABLE 3.4-1

ICRF Antenna Parameters

Frequency	180MHz
Antenna dimensions	
conductor	15cm × 50cm each
shield	20cm × 120cm
RF power density at shield	400W/cm ²
Center Conductor	25kW
Return Conductor	15kW
Shield	30kW RF + 200kW Plasma



Water Cooled Faraday Shield Concept

FIGURE 3.4-7

3.4.2.4. Transmission System

The operation of megawatt-level systems under steady state conditions has some precedents in this frequency range [3.4-2,3]. Manufacturers who have supplied equipment for these projects have indicated that they could supply suitable components. The transmission lines, directional couplers and impedance transformers will have a heat load of approximately 200 Watts per meter concentrated at the center conductor. This represents a 6 kW load per feed line which can be removed by forced dry air (or N₂) circulation within the lines, coupled through a heat exchanger to the central cooling system.

The tuning stubs are water-cooled and the test and reject loads are oil cooled. The five MW cooling capacity required for the test load does not have to be added to the total system capacity because RF power will not be simultaneously deposited in the machine and the test loads.

3.4.2.5. Advanced Coupler Design

Slot antennas are being investigated [3.4-4] as an alternative to conventional ICRF antennas. There are several attractive features to slots:

- flat, all-metal structures -- no protrusions into the vacuum chamber
- k-spectrum couples well to plasma
- radiative nature - antenna does not need to be adjacent to the plasma
- removable units

- good power handling capability

A simple slot antenna in a conducting plane is the dual of an electric dipole and can be called a magnetic dipole. It has the same field pattern as an electric dipole but with the electric and magnetic fields rotated in space by ninety degrees. The simplest method used to excite the slot is a two wire transmission line (or a coaxial cable) connected across the center of the slot as in Figure 3.4-8a. The electric field in the slot has a sinusoidal distribution, peaked at the center, when the slot is approximately one half-wavelength long.

In order to cause the slot to radiate on only one side of the conducting plane, a resonant cavity feed structure can be used, as shown in Figure 3.4-8b. A TE_{101} mode is excited by a probe in the cavity and allowed to radiate out the slot. The cavity is a high Q system which acts as an impedance transformer between the cavity feed and the slot. Therefore, by moving the input probe a match to the ICRF source can be obtained. However, the transformation properties of the cavity rely on a large amount of stored energy in the cavity and this could severely limit the power handling capability of the antenna.

To remove the large amplitude reactive fields, the cavity is replaced by a strip transmission line where the slot is excited by a propagating mode rather than a cavity mode. The impedance of the device is dependent on the geometry of the strip transmission line, and the offset of the transmission line relative to the slot center. Phasing of individual slots is achieved by appropriate slot to slot spacing.

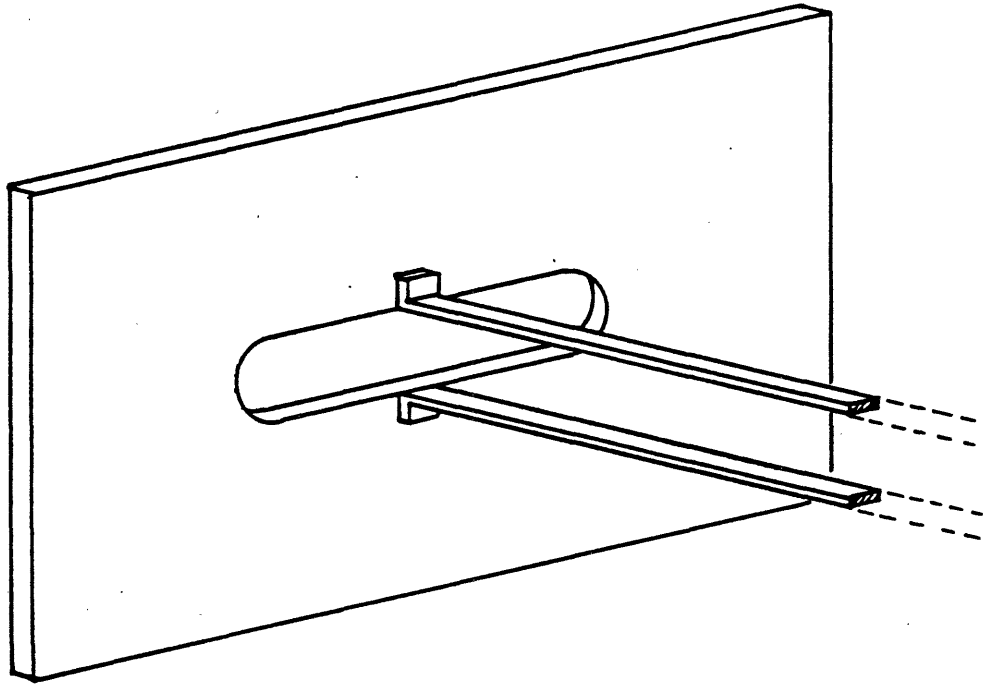


FIGURE 3.4-8a Slot in a flat conducting plane fed by a two-wire line.

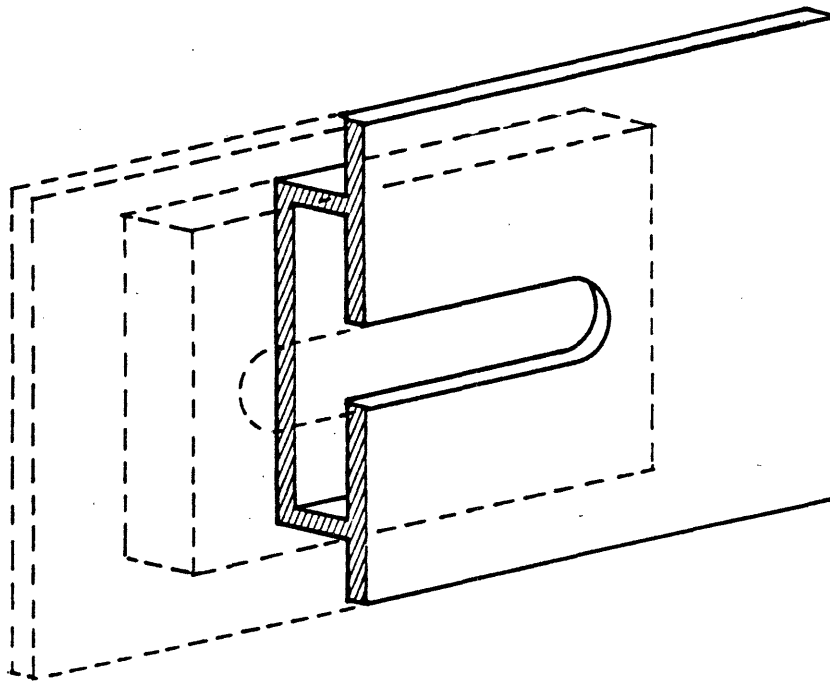


FIGURE 3.4-8b Slot in a flat conducting plane with a cavity feed.

The preliminary characteristics given below are the result of a first attempt at designing a stripline-slot type antenna for Alcator DCT. A single slot array would be 80-90 cm wide and 150-170 cm long. A general schematic of a single unit is shown in Figure 3.4-9. An array could be positioned between two ports or be centered in front of a single horizontal port. Versatile feeding mechanisms allow a center feed through the side port or balanced end feeds from the vertical ports.

Power handling may be estimated following the method used for the ICRF loop antenna. By considering the constraints on the allowable electric fields inside the stripline, one array should be able to handle approximately 1-2 MW. The RF power flux averaged over the antenna surface is 125 W/cm^2 , a value well within the range seen for loop antennas. The power flux will be severely concentrated in the vicinity of the slot so the average surface power flux may be misleading. There is, however, an analogous enhancement for the loop antenna caused by the slots in the Faraday shield, and by the tendency of fields to be concentrated at the edges of a wide loop antenna.

Investigations are under way to determine optimum slot offset, slot to slot spacing, and center conductor position. We plan to investigate increasing the slot width in the expectation that this may decrease the electric field concentration in the slot. The bandwidth of the array will be calculated and measured to provide data on the range of confining magnetic fields (B_0) accessible to a given antenna. Power dissipated in the metal structure will be calculated to determine whether a material of low electrical conductivity, such as stainless steel, can be used for antenna construction. Theoretical studies will focus on coupling from a

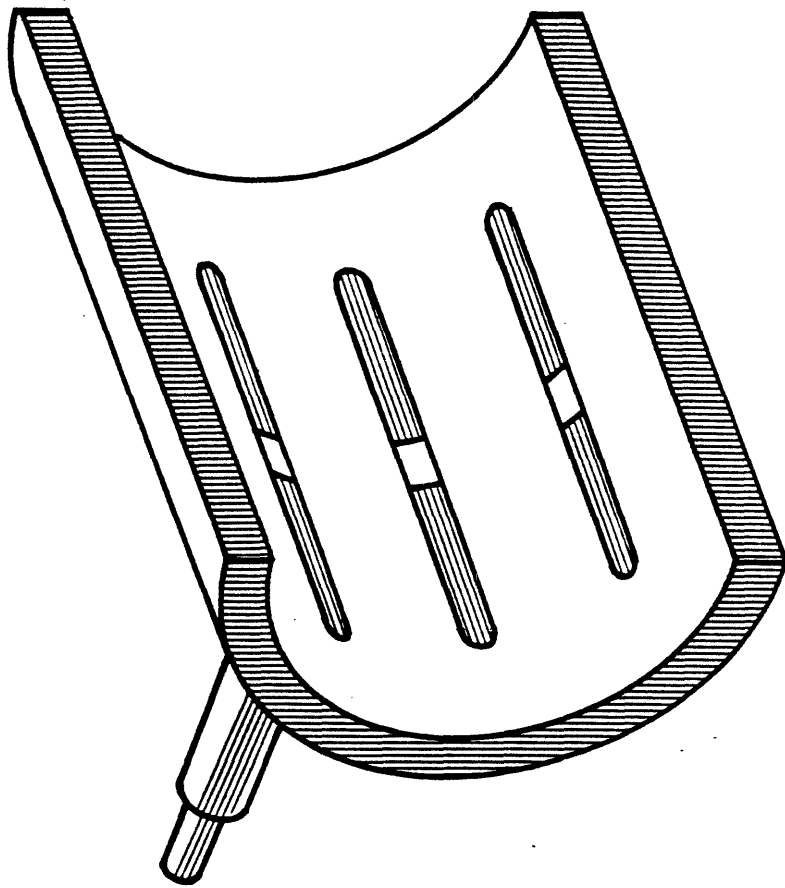


FIGURE 3.4-9 Alcatel DCT slot antenna concept.

slot array to the plasma, initially using cold plasma theory.

The slot antenna ICRF coupler concept shows promise in its power handling and simplicity. We will continue the experimental program to develop this advanced coupler, leading to the construction of a scaled prototype launcher for Alcator DCT.

References

- [3.4-1] D. T. Blackfield, B. D. Blackwell, Numerical Investigation of ICRF Antenna Designs and Heating Schemes for Alcator C, Fifth Topical Conf. on Radio Frequency Plasma Heating Madison, WI 1983.
- [3.4-2] New England Nuclear, 600kW at 205 Mhz
- [3.4-3] FMIT RF system. 600 kW at 80 MHz
- [3.4-4] B. L. Koester, R. R. Parker, B. D. Blackwell, Slot Antennas for ICRF Heating, 1983 IEEE International Conference on Plasma Science, San Diego, California, May 23-25, 1983 (paper #1q1).

CHAPTER 4

ALCATOR DCT POINT DESIGN

4.1. Introduction

The machine follows in the Alcator tradition of a compact high power density, high performance approach, but unlike its predecessor, is dedicated to long pulse issues. The long pulse requirement in a compact device has dictated the use of superconducting magnet technology for both the toroidal and poloidal coil systems.

The machine has a relatively large aspect ratio, more typical of reactors than present-day tokamaks. The larger aspect ratio allows Alcator DCT to have a very large volt-second capacity to ensure long pulses (> 100 s) in the inductively driven mode of operation.

The volt-second capability is sharply sensitive to this aspect ratio. For example, were the major radius to be reduced from 200 cm to 160 cm at fixed plasma size, the flux-change available at a fixed value of peak OH field, would drop by 70% to 10 V-S. The project cost is considerably less sensitive to the major radius, dropping by 15% over this same range. We have, therefore, favored the larger aspect ratio for Alcator DCT which is dedicated to long pulse issues. The 35 volt-second capability of Alcator DCT will be comparable to that of JET despite the compact size of the proposed machine.

The high power density nature of Alcator DCT will place a considerable burden on the first wall and components within the vessel. Solution of these problems will undoubtedly be one of the major technological contributions of the project. The high power nature of the machine led us to

the criterion that the design must provide personnel access to the vessel interior for maintenance and replacement of these components. This, together with a need for tangential access, was one of the principal drivers in choosing a 24 coil design. A minimum of 28 cm of horizontal clearance access is provided, adequate for personnel access.

The machine has "Dee shaped" toroidal field coils, dictated largely by a requirement for elongated plasmas ($\kappa = 1.4$) and a requirement to incorporate a single null poloidal divertor.

The stored energy in the Alcator DCT toroidal field is 550 MJ, which is compared to other experiments in Table 4.4.1. The energy approaches that of Tore Supra and is somewhat larger than the recently tested Mirror Program MFTF Ying-Yang Coil. The poloidal field stores an additional 120 MJ.

TABLE 4.1.1

Energy Storage of Superconducting Fusion Devices

T-7	20 MJ
MFTF Y/Y	400 MJ
DCT	550 MJ
TORE SUPRA	600 MJ
T-15	750 MJ

4.2. Overall Machine Description

An overview and partial plan and elevation view of the point design are shown in Figures 4.2-1, 4.2-2, and 4.2-3.

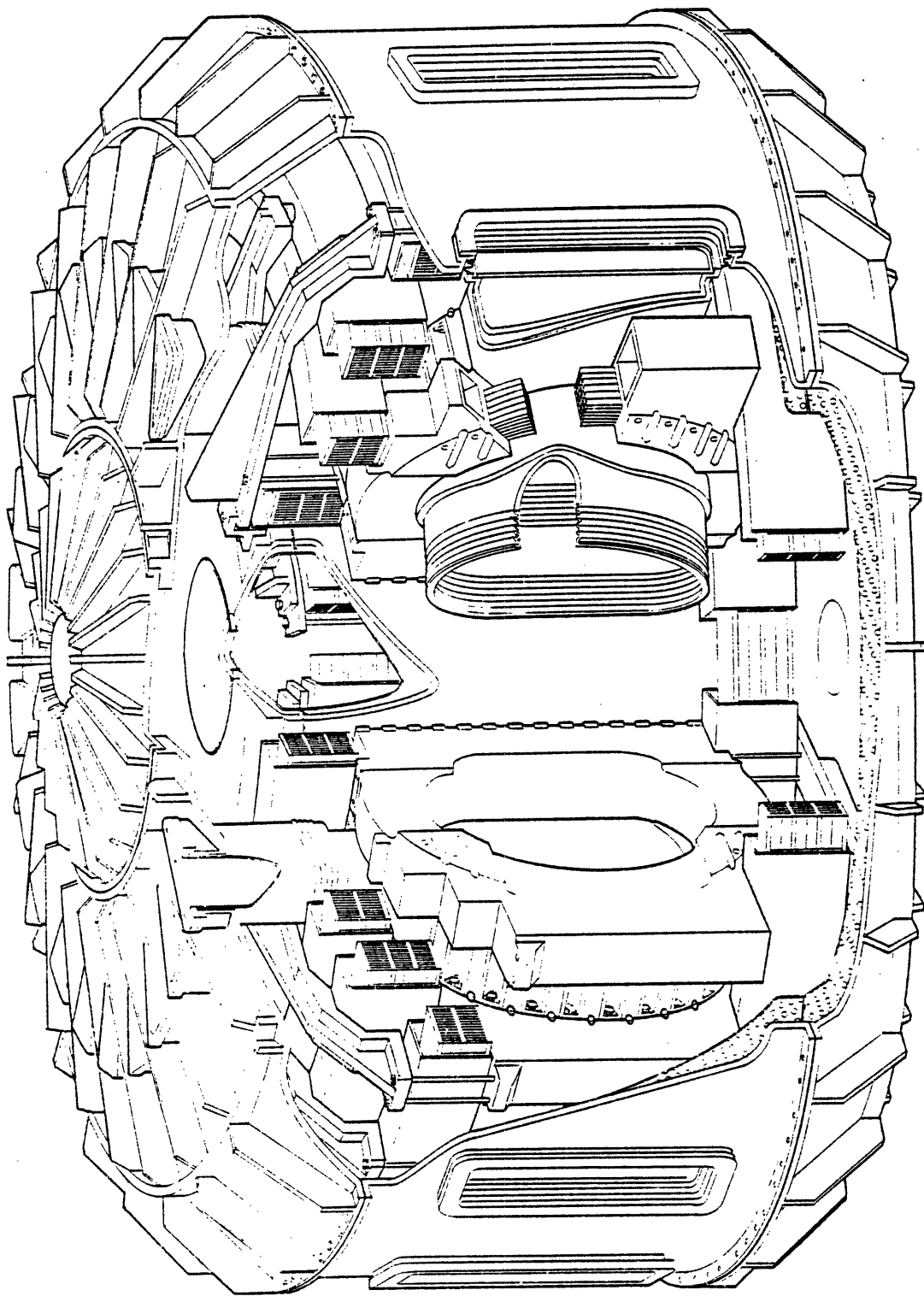


FIGURE 4.2-1 Cut-Away View of Alcatel DCI.

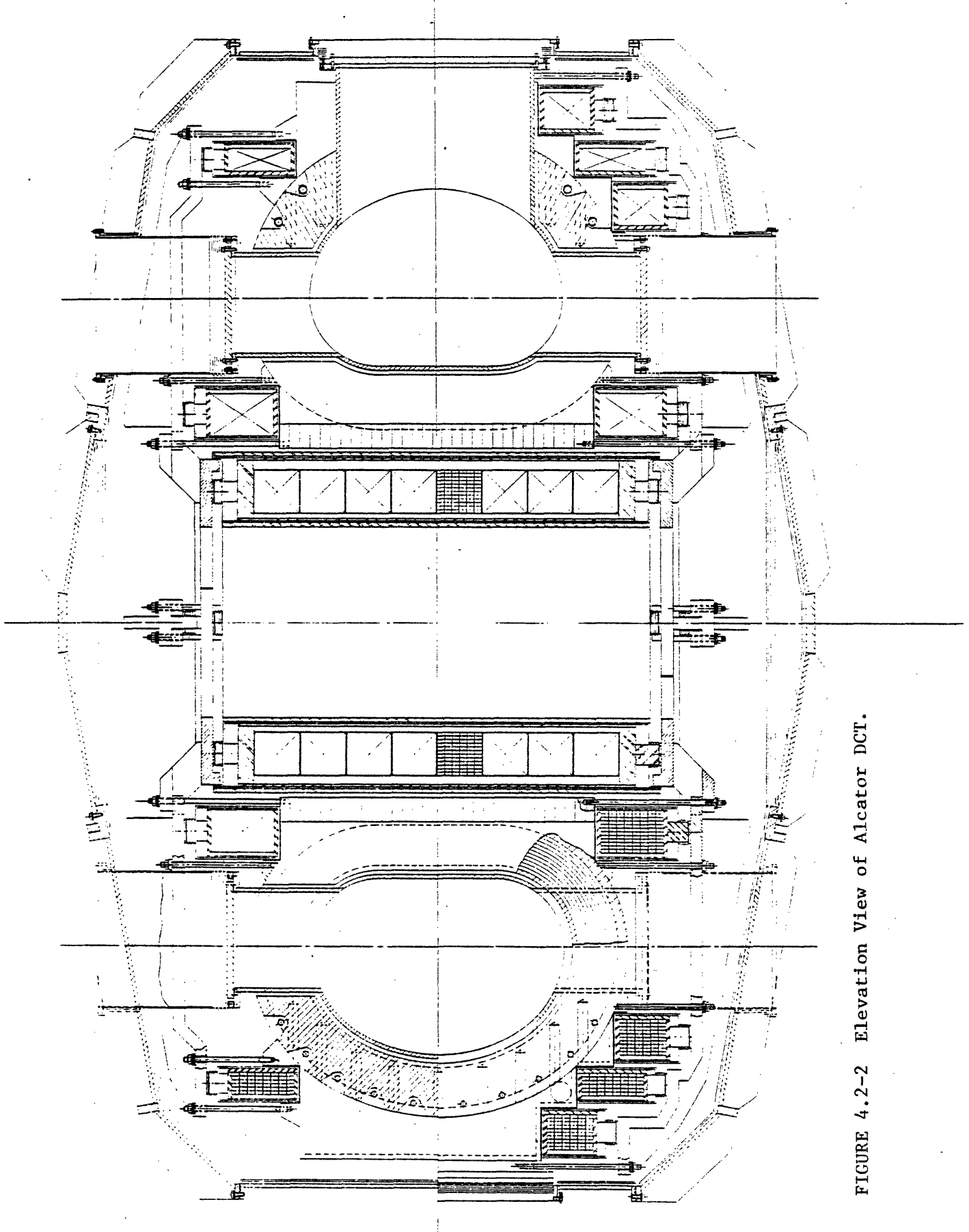


FIGURE 4.2-2 Elevation View of Alcator DCT.

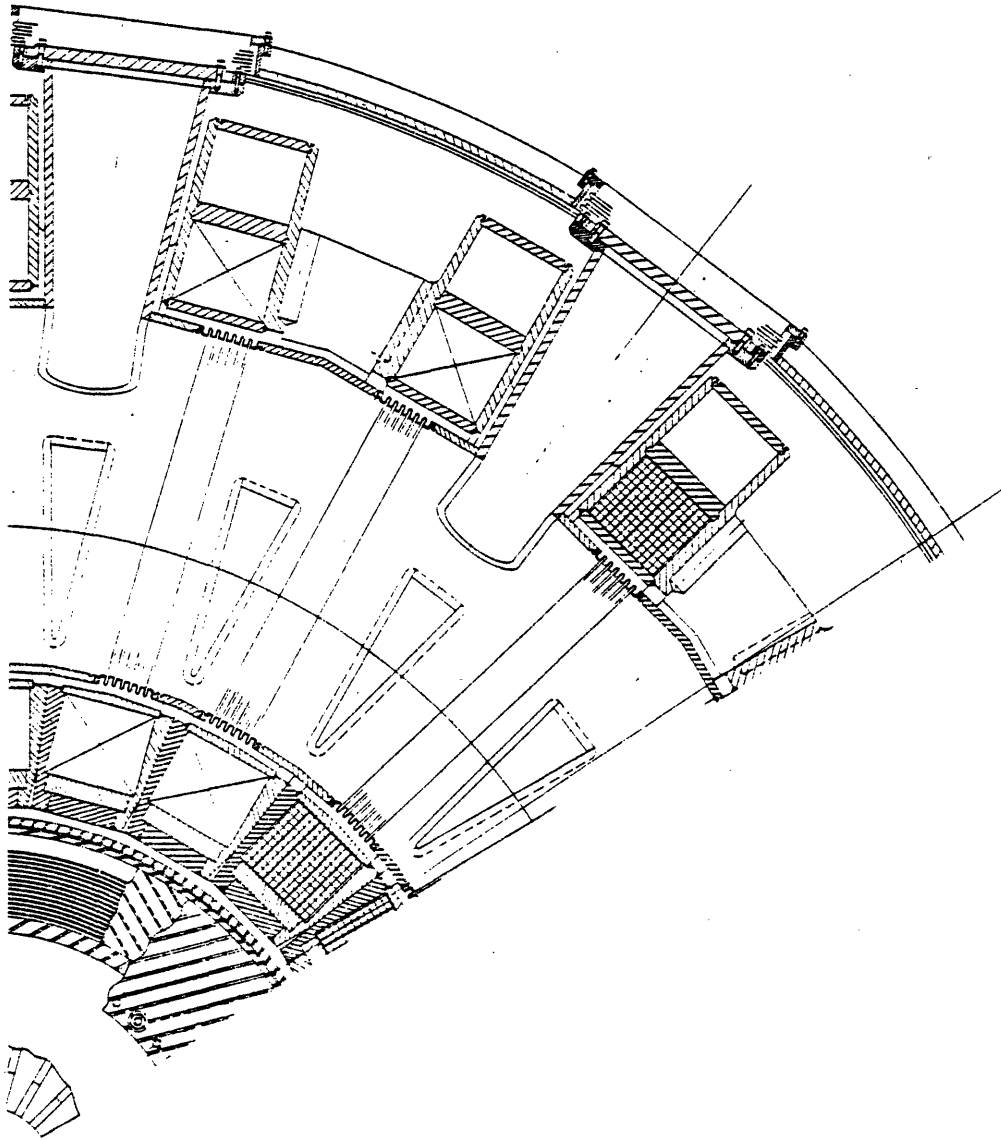


FIGURE 4.2-3a Partial Plan View of Alcator DCT.

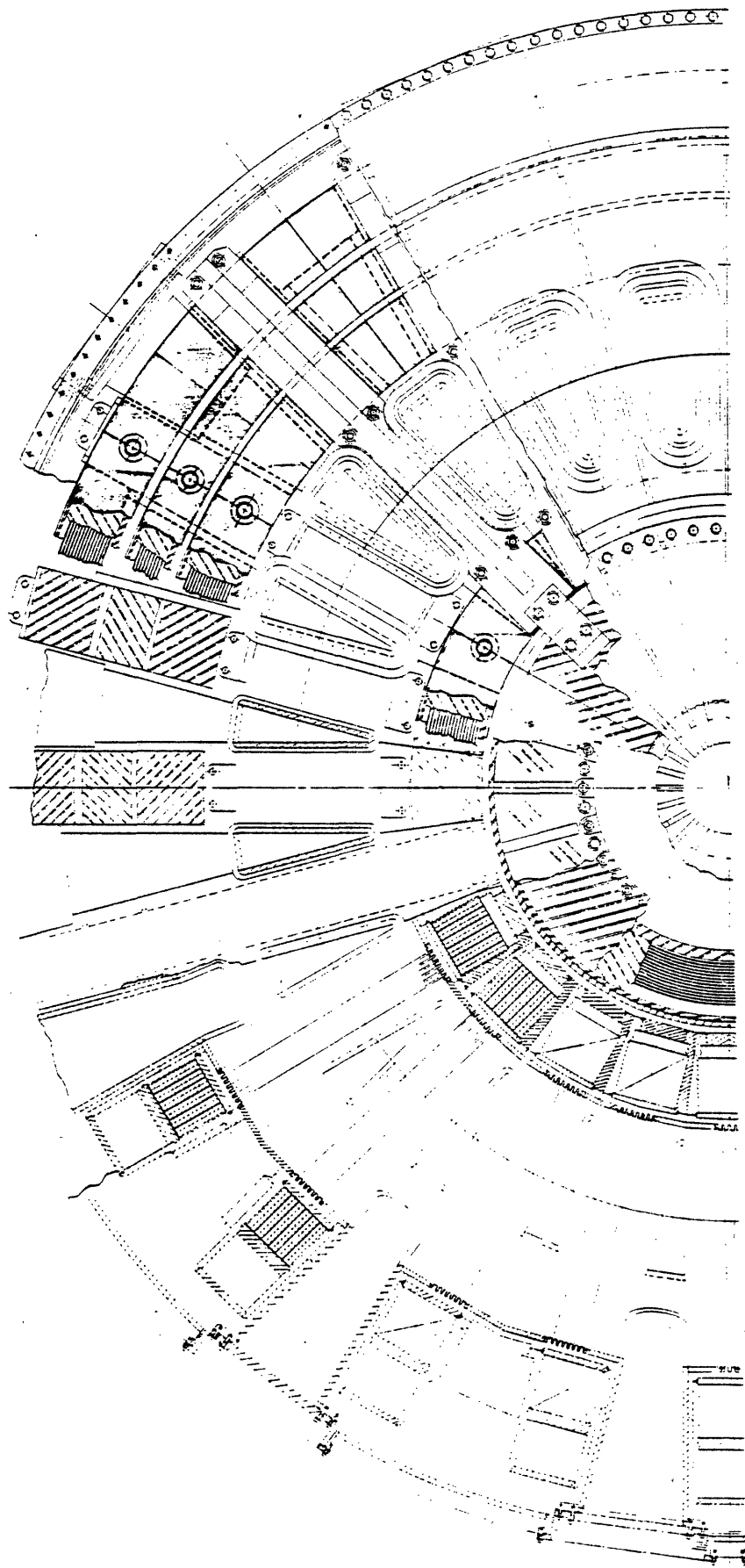


FIGURE 4.2-3b Partial Plan View of Alcator DCT.

The superconducting coil systems are contained in a common vacuum system as is typical of tokamak reactor designs. Each toroidal coil is in a separate heavy-walled cryostat which serves as both a structural support and cryogenic containment vessel. The central OH coil and individual poloidal field coil packages are also contained in individual vessels, although these vessels must be of special construction to increase their toroidal resistance.

The cold mass support is provided from the middle section of the common vacuum section, thus allowing removal of both covers. The middle vacuum section is in turn supported from the floor by out-board legs, much as in Alcator C, as shown in Figure 4.2-4, allowing removal of PF components if required.

The plasma chamber and access ports utilize a second, independent vacuum system, allowing vacuum-break access to the vessel without warmup of the superconducting magnets. Vertical access is provided between every coil, but horizontal access is only provided at every other coil in order to allow for adequate magnetic structure at alternate coils to support the overturning moments. Port location planes containing only vertical access are to be largely devoted to divertor or limiter support, cooling access, and pumping, whereas the planes with both vertical and horizontal ports will be used for heating, current drive and diagnostics. Selected horizontal ports will also be specially constructed to provide tangential diagnostic access as shown in Figure 4.2-5.

The first wall and in-vessel divertor collectors, or limiter components, must be capable of removing large amounts of power at relatively large heat fluxes. The concepts, further described in Section 3.3 are

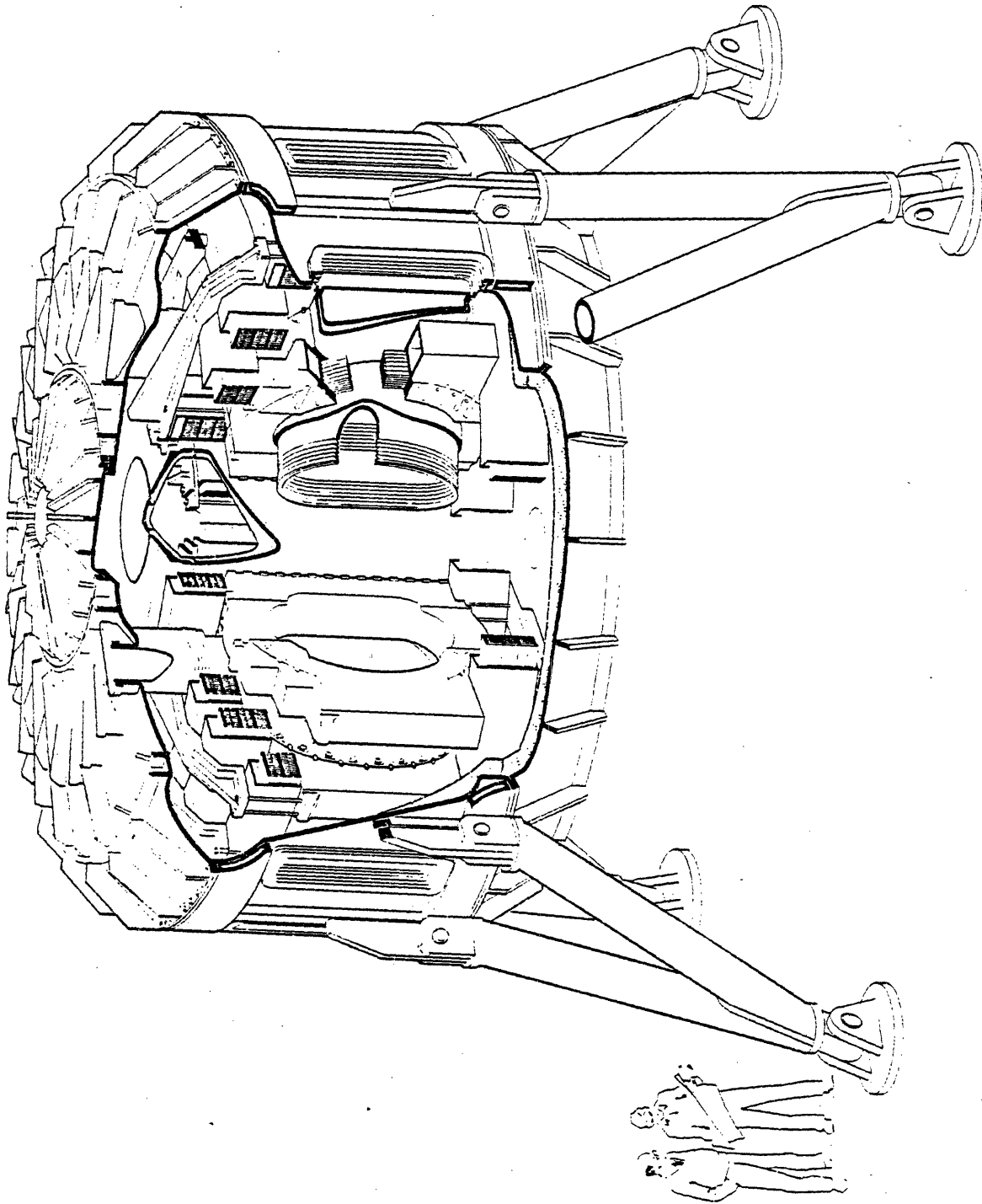


FIGURE 4.2-4a Out-Board Legs Support Concept.

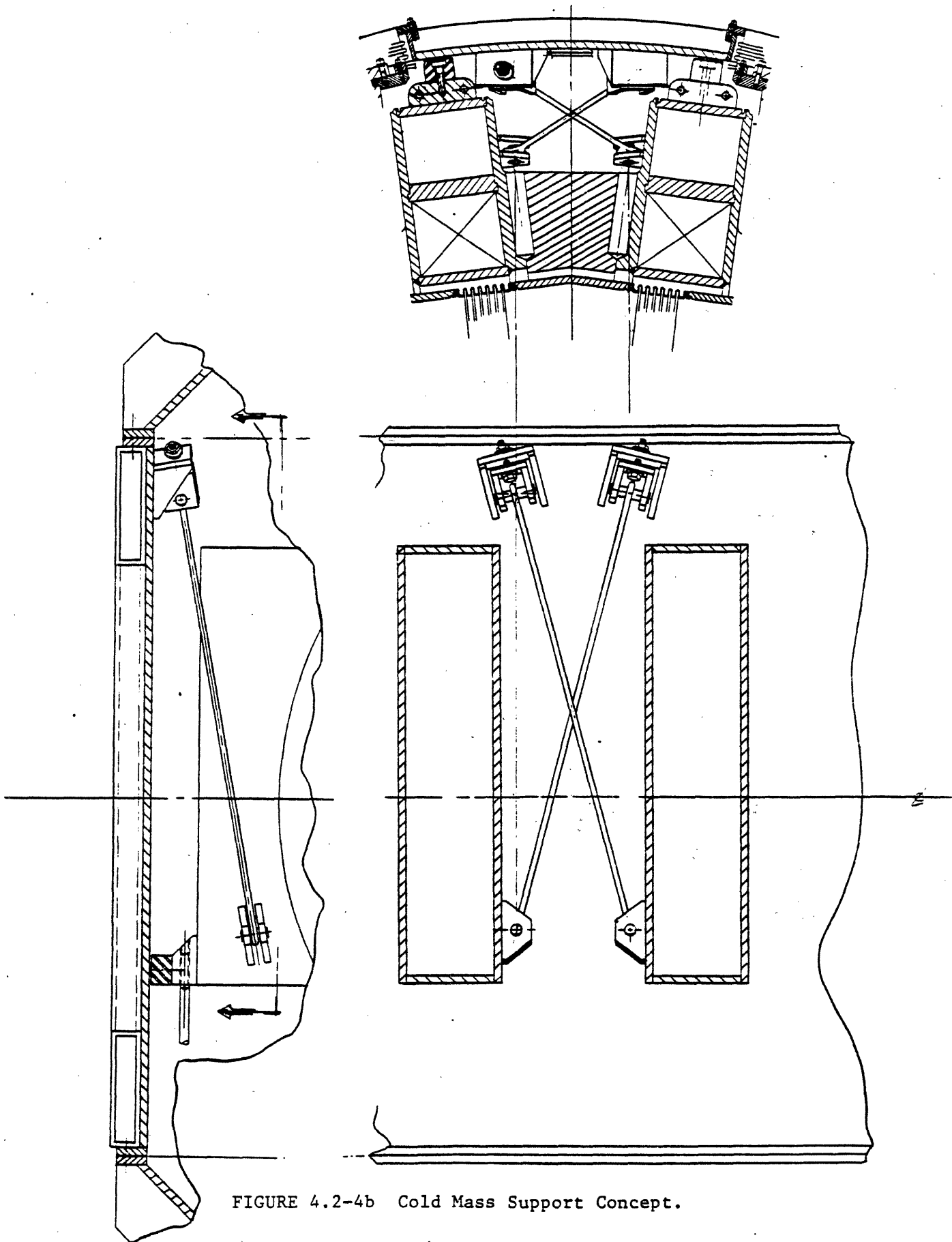


FIGURE 4.2-4b Cold Mass Support Concept.

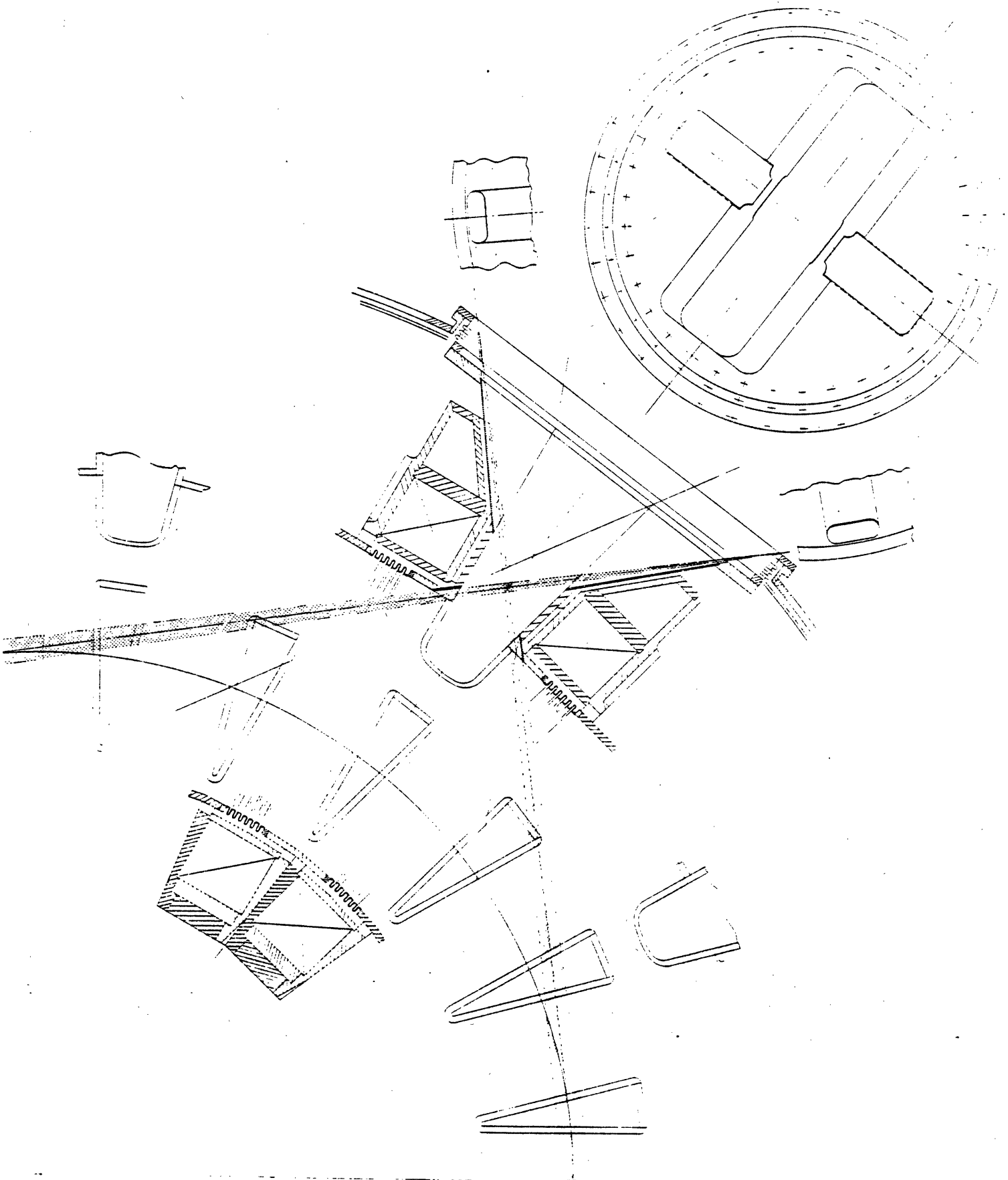


FIGURE 4.2-5 Tangential Access Port Details.

patterned after concepts developed for TFTR, DIII, and some of the near reactor device studies such as FED/INTOR. The uncooled vacuum vessel is made of alternate bellows and heavy wall sections and is entirely shielded by in-vessel water-cooled heat shields (Section 5.2). The heat shields have an average heat flux of approximately 0.2 MW/m^2 .

This heat shield design strategy follows the simple view that the only realistic access to the tokamak first wall is from inside the torus. Components mounted from the inner wall are accessible for repair and modification, whereas cooling from the back side of the vessel is virtually inaccessible.

Approximately 10% of the inner vessel will consist of divertor collector plates or limiters and will see average heat fluxes of approximately 2 MW/m^2 .

Initial assembly of the machine would involve joining of TF coil pair modules by means of an internal weld in the vacuum chamber. The man-rated access to the internal chamber allows the final closure welds to be made from the inside after the torus has been assembled. The replacement of TF coils would require removal of the PF coils, return of the machine to floor level tooling, and cutting of the internal vacuum chamber.

4.3. Magnetic System Concept Selection

4.3.1. Toroidal Field Coils

4.3.1.1. Conductor Choice

The Alcator DCT point design calls for a 7 tesla field on axis resulting in a 10 tesla peak field at the conductor. The only two TF magnet ap-

proaches seriously considered for fields above 8 T are the use of Nb₃Sn at 4.2 K, and the use of NbTi at 1.8 K. Both have been studied FED and INTOR and their advantages and disadvantages debated at some length. In principle, both techniques appear to be extendable to reactor designs. In practice, niobium-tin must carry the disadvantage of maintaining adequate quality control to assure undamaged material properties, and 1.8 K NbTi must carry the disadvantage of a more complex cryogenic system and double case magnet support concept. All four "national" INTOR designs currently use Nb₃Sn approaches.

While both Nb₃Sn and 1.8 NbTi can be extended to reactor operation, operation at 1.8 K will always represent the fundamental disadvantage that energy removal at 1.8 K should require three times the recirculating power required by energy removal at 4.2 K.

We have chosen Nb₃Sn based on its advantages of a simpler requirement on cryogenic systems and a greater energy margin for stability against disturbances, particularly at higher fields. We also note that the United States will have a broader data base in Nb₃Sn than in 1.8 K NbTi because the only one of these two advanced concepts used in LCP will be Nb₃Sn. We therefore contribute directly to that data base.

We have selected an improved version of the niobium-tin conductor used in the Westinghouse LCP coil and in the MIT Livermore test coil. The conductor, described in Table 4.3-1, is pictured in Figure 4.3-1. Twenty-two tonnes of this conductor have been fabricated for the W LCP coil by Airco, an amount equivalent to approximately 40% of the total needed for the entire proposed Alcator DCT. The conductor is a full scale conductor directly usable in next generation large machines.

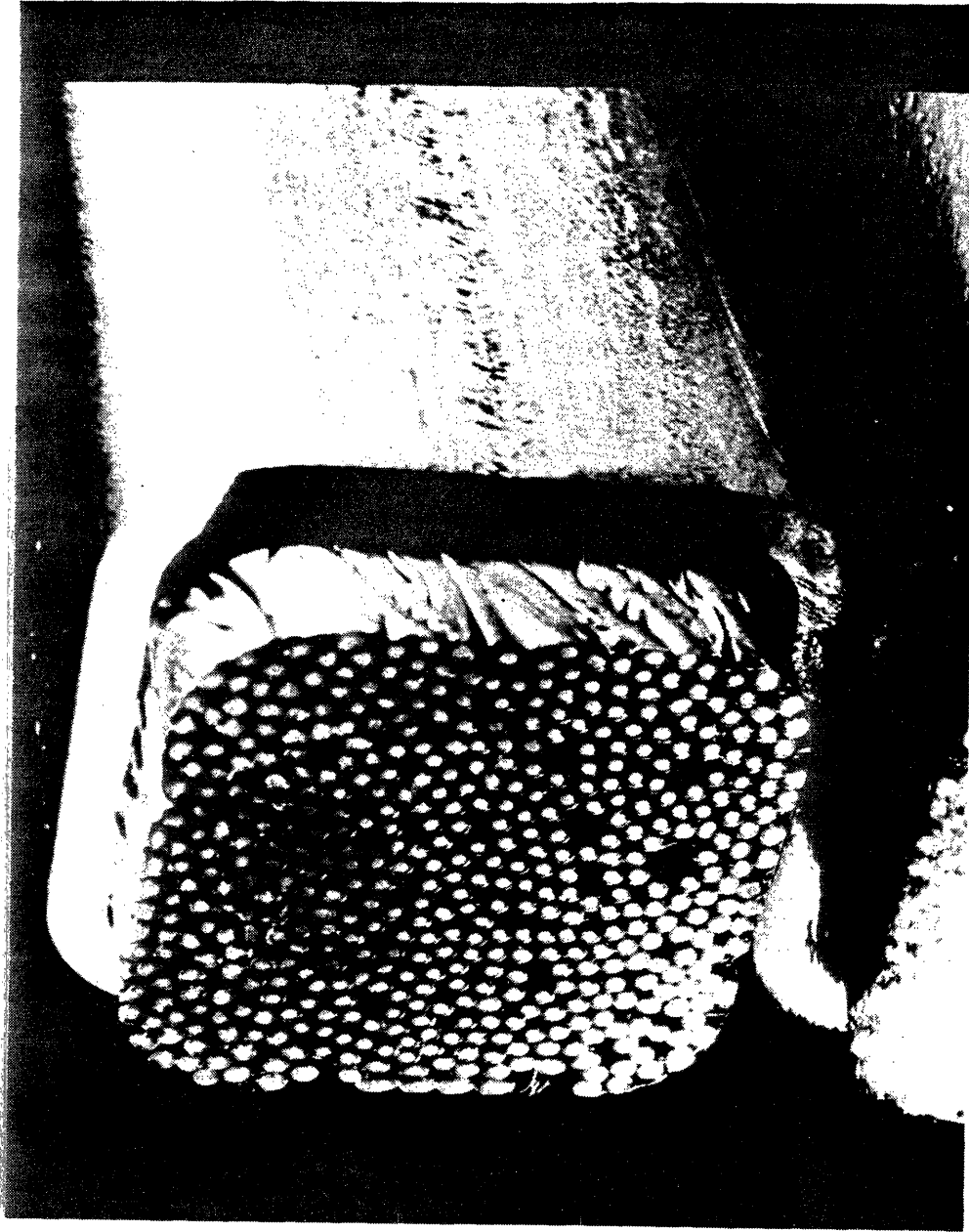


FIGURE 4.3.1A: Nb₃Sn Internally-Cooled-Cabled Superconductor (ICCS) conductor. The cable contains 486 strands which occupy 68% of the area inside the sheath whose thickness is 1.7 mm and outer dimension 21 x 21 mm.

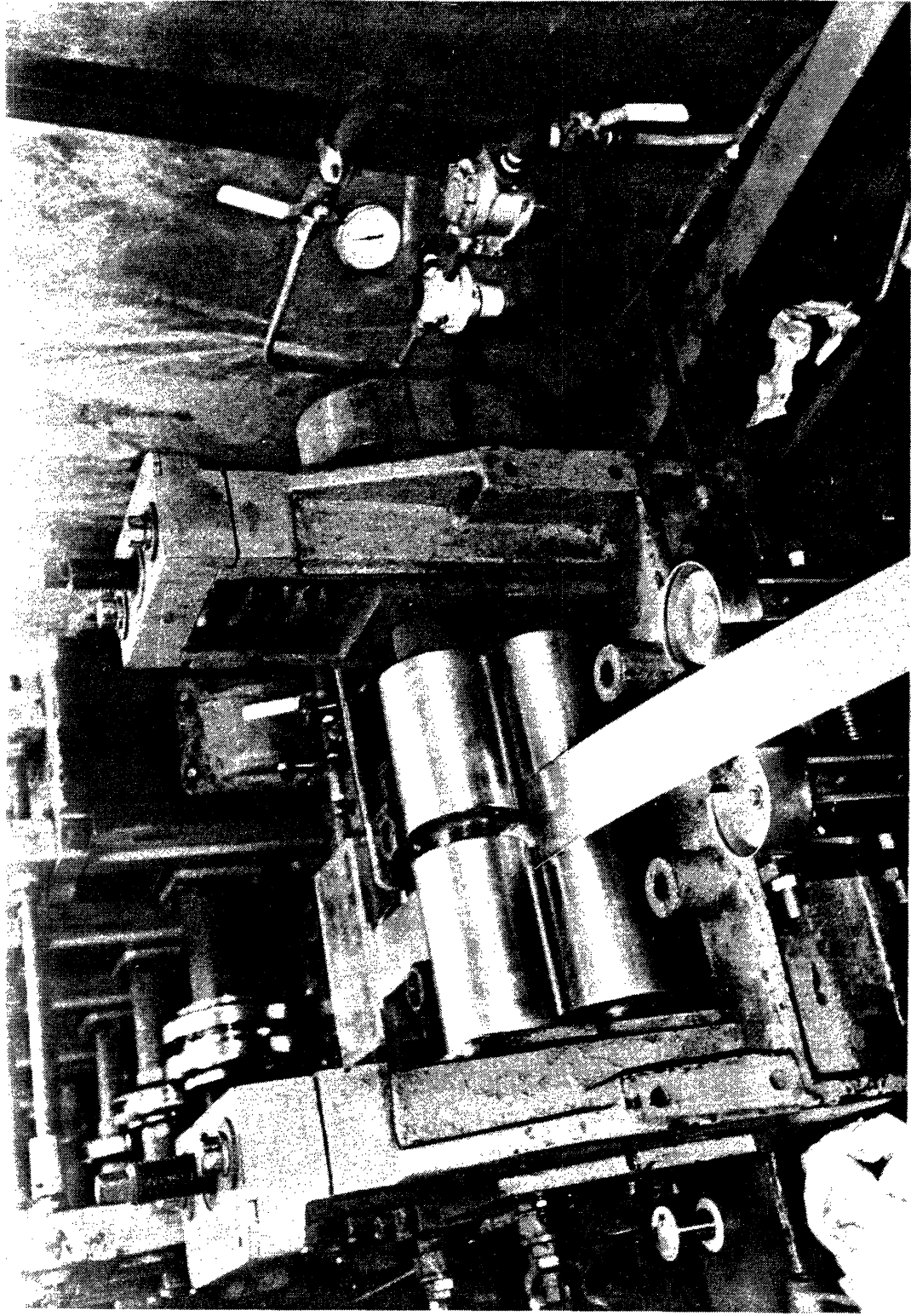


FIGURE 4.3.1B: Airco tube mill used for production of Nb_3Sn ICCS conductor. The operation starts with a continuous sheet of 1.7 mm material which is formed around the cabled conductor, seam welded, and subsequently drawn down and squared-off.

While Alcator DCT will use the full scale Nb₃Sn conductor used in LCP, we have proposed three reactor relevant improvements over the techniques used in LCP. Realization of the following improvements on Alcator DCT will greatly strengthen the Nb₃Sn data base for the next step machines: (1) heat treatment after winding, which will relieve the need for several difficult quality control steps during winding; (2) elimination of the substructure support plates which will lead to a more economical construction; (3) use of pool-boiling helium outside the ground wrap to provide a simple technique for removing average heat loads while static helium internal to the conductor provides a high degree of stability. These points are expanded upon in the next section on winding pack considerations.

TABLE 4.3-1

Alcator DCT TF Conductor*

OVERALL DIMENSION	2.1 × 2.1 cm
SHEATH THICKNESS	1.73 mm
PERCENT VOID	32%
NUMBER OF STRANDS	486
SIZE OF STRANDS	0.7 mm
COPPER AREA	1.19 cm ²
CRITICAL CURRENT (@ 10 tesla)	40 kA
OPERATING CURRENT (@ 10 tesla)	23 kA
I_{op}/I_c	0.58

*Dual Heat Treatment (4 days 700°C, 2 days 730°C) Incoloy Sheath

The M.I.T. 12 Tesla test coil shown in Figure 4.3-2 will serve as a prototype coil for DCT and provide confirmation of the performance of several hundred meters of the full scale conductor at 10 tesla (and above). The prototype coil includes a pulse coil wrapped around the conductor exposed to the highest field, and will be used to confirm stability under simulated disruption conditions.

The energy margin against disruptions and other disturbances, is predicted to be about 500 m J/cm^3 . This margin has been confirmed on subscale conductors utilizing a smaller number of full scale strands, and is very consistent with levels predicted by analytical and numerical models. Disruptions are expected to deposit approximately 50 m J/cm^3 and hence the conductor should have a large margin of safety in this regard.

4.3.1.2. Winding Pack Design

The cross-section of the proposed point design winding pack is shown in Figure 4.3-3. The winding will be constructed from six double pancakes which are 11 layers deep. At 10 tesla peak field, the conductor operating current will be 23 kA, 58% of the critical current at 10 T, 4.2 K and 32% void fraction. Each double pancake will be epoxy impregnated separately and will consist of a single 150 meter length of conductor. We believe that this construction represents one of the principal benefits of the internally cooled conductor, namely the ability to epoxy impregnate the winding. This gives rise to a winding pack of more predictable and higher modulus than a non-impregnated winding, and one with better insulation characteristics.

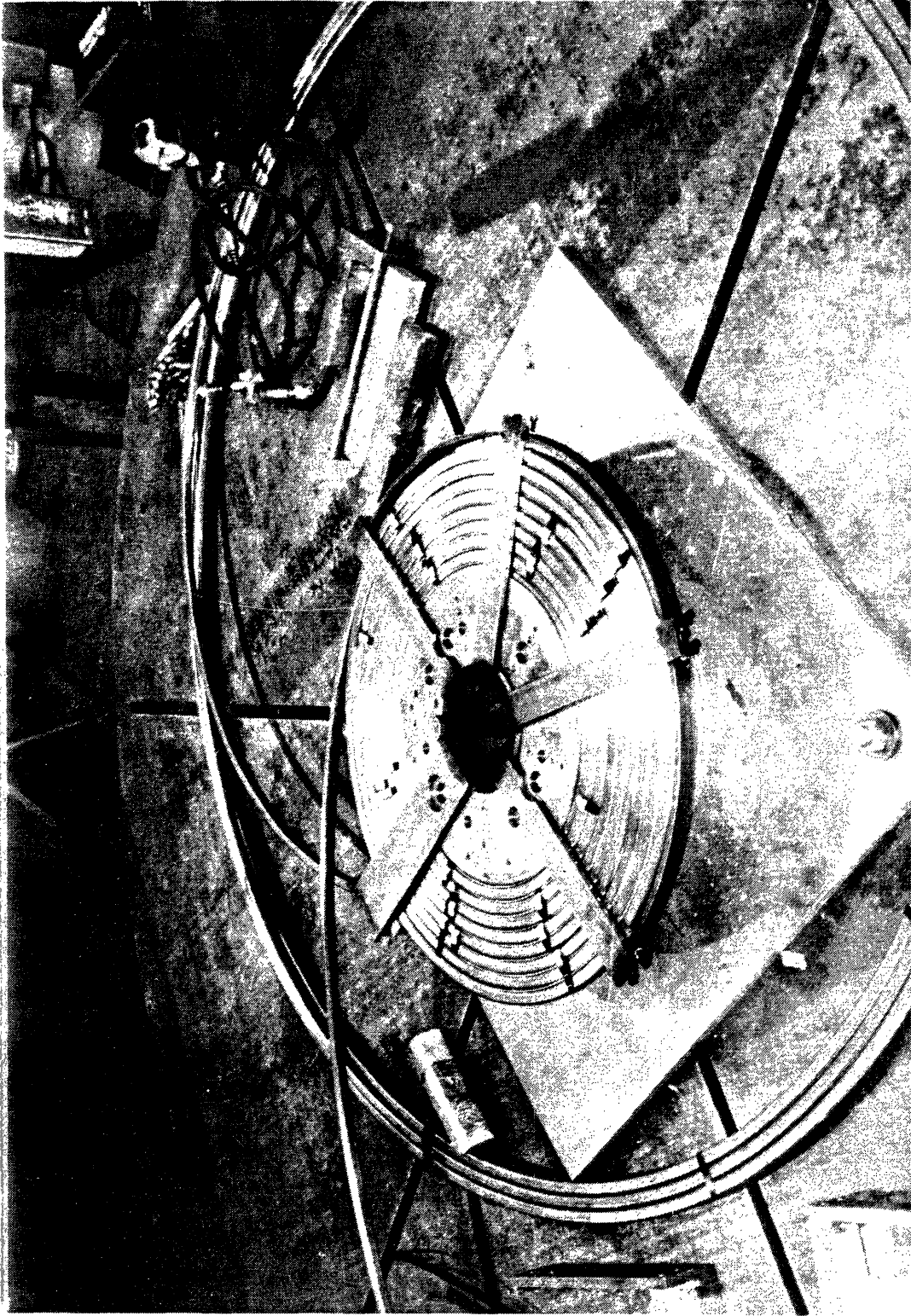


FIGURE 4.3.2: MIT 12 Tesla 40 cm ID coil wound from Nb_3Sn ICCS. The conductor is wound prior to heat-treatment, eliminating the risk of damage to the conductor during winding. The coil is insulated after heat-treatment.

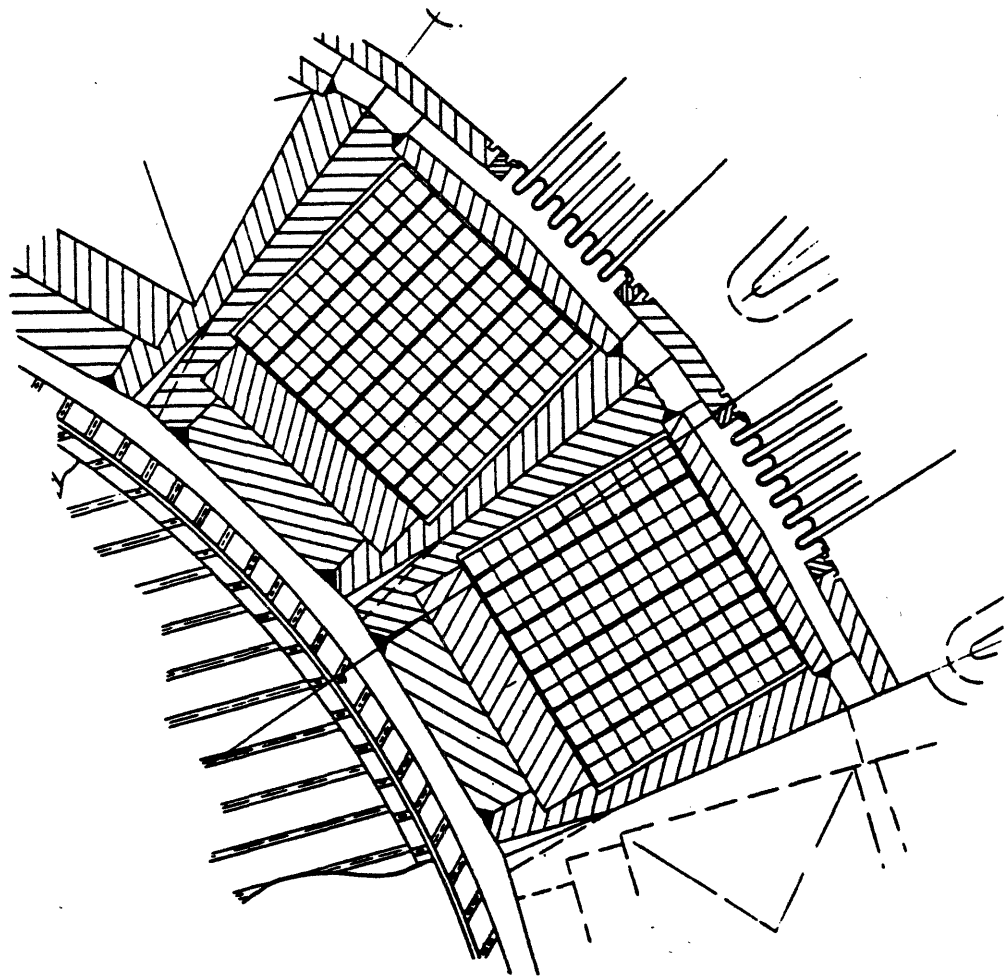


FIGURE 4.3-3 Winding-Pack Cross-Section in Straight Leg of TF Coil.

Non-circular coils present certain specific manufacturing and structural support requirements not found in circular coils. For example, maintaining an adequately high modulus winding in the large radius "straight leg" represents a major manufacturing problem as found by all the LCP manufacturers. Proper support of the radial pressures in the "straight leg" portion represents a structural design problem. With the current design trend toward higher elongations, it is important that near-term coil projects contribute to the solution of these non-circular requirements.

Alcator DCT utilizes an internally cooled conductor in a fully potted winding pack to specifically solve these two non-circular coil problems in a cost effective manner.

The coil current of 2.9 MAT and the peak field of 10 tesla give rise to "worst-place" average radial compression of 50 MPa on the lowest field conductor in the inner leg. Concern that such radial pressures would give rise to excessive stresses in the conductor conduit sheet, gave rise to the Westinghouse LCP concept of grooved support plates into which the conductor was wound. We have performed low cycle mechanical tests on arrays of conductors which have been potted into a support case, and find that radial pressures of 50 MPa can be easily accommodated. The tests indicate that the potting plays a major role in preventing excessive conduit strain. We therefore propose to eliminate the support plates used in the Westinghouse LCP coil, resulting in better overall coil insulation characteristics.

Cable conductors like the Airco conductor can also be questioned from the standpoint of potential transverse loading fatigue of the individual

strands over the short but unsupported spaces in the twisted cable. Calculations do not imply significant strains, but we have undertaken a cable fatigue experiment to be carried out at full field to confirm that the cable is satisfactory in this regard (see Section 9, Research and Development Activities).

The conductor steel conduit is not expected to carry appreciable in-plane tension load in the DCT design, (although it is capable of carrying significant loads). The external coil case is designed to carry the full in-plane load (see Section 4.3.1.3, Structural Approach). The principal function of the conduit is therefore to carry compression loads within the winding pack.

The Airco LCP conductor is not heat treated until it has been jacketed and hence, once formed, the niobium-tin is protected by the steel jacket. The M.I.T. 12 tesla test coil fabrication procedure offers further conductor protection by not heat treating until the coil "pancakes" have been wound. After heat treating, the turns are separated and reinsulated, and the pancakes are then epoxy impregnated. This technique was tested on a full-scale Livermore prototype and eliminates the danger of accidental damage during coil winding, as well as the winding bending strain which can reduce critical current.

This "wind and react" concept is considered an important contribution to future large scale Nb_3Sn technology. The concept allows industrial compatible processes to be utilized during winding without danger of conductor damage, and substitutes the "low technology" requirement of a suitable large furnace.

We propose to epoxy impregnate each double pancake in the winding pack, but not to impregnate the six double pancakes as a single unit. Rather the six pancakes will be assembled with spacers to provide 1.5 mm radial gaps for supplementary external helium cooling. The conductor will be filled with static pressurized helium (supercritical helium) which will provide the stabilization of the conductor against transient disturbances such as startup or disruptions. It has been experimentally and analytically demonstrated at both MIT and ORNL that it is not necessary to circulate the supercritical helium to achieve high levels of stability. Local pressure-driven mass flows provide adequate heat transfer.

While it is not necessary to circulate helium for stability, it is necessary to remove the steady-state average heat load due to disturbances and heat leakage. This could be done by low velocity circulation of the supercritical helium, but a much easier technique is to provide access for atmospheric pressure 4.2 K helium to the faces of the winding pancakes. The conductance of the thermal path, even through the epoxy-glass ground insulation of the pancakes, is sufficient to remove the average heat. This method steady-state cooling allows a significant simplification of the manifolding of the individual pancakes. Each coil will be hydraulically connected as shown in Figure 4.3-4, and will require only one inlet and outlet and 7 pressure relief points. Only the inlet and outlet points need to contain insulated connections to a common manifold, a major simplification over the W LCP coil which must circulate helium through every conductor in parallel.

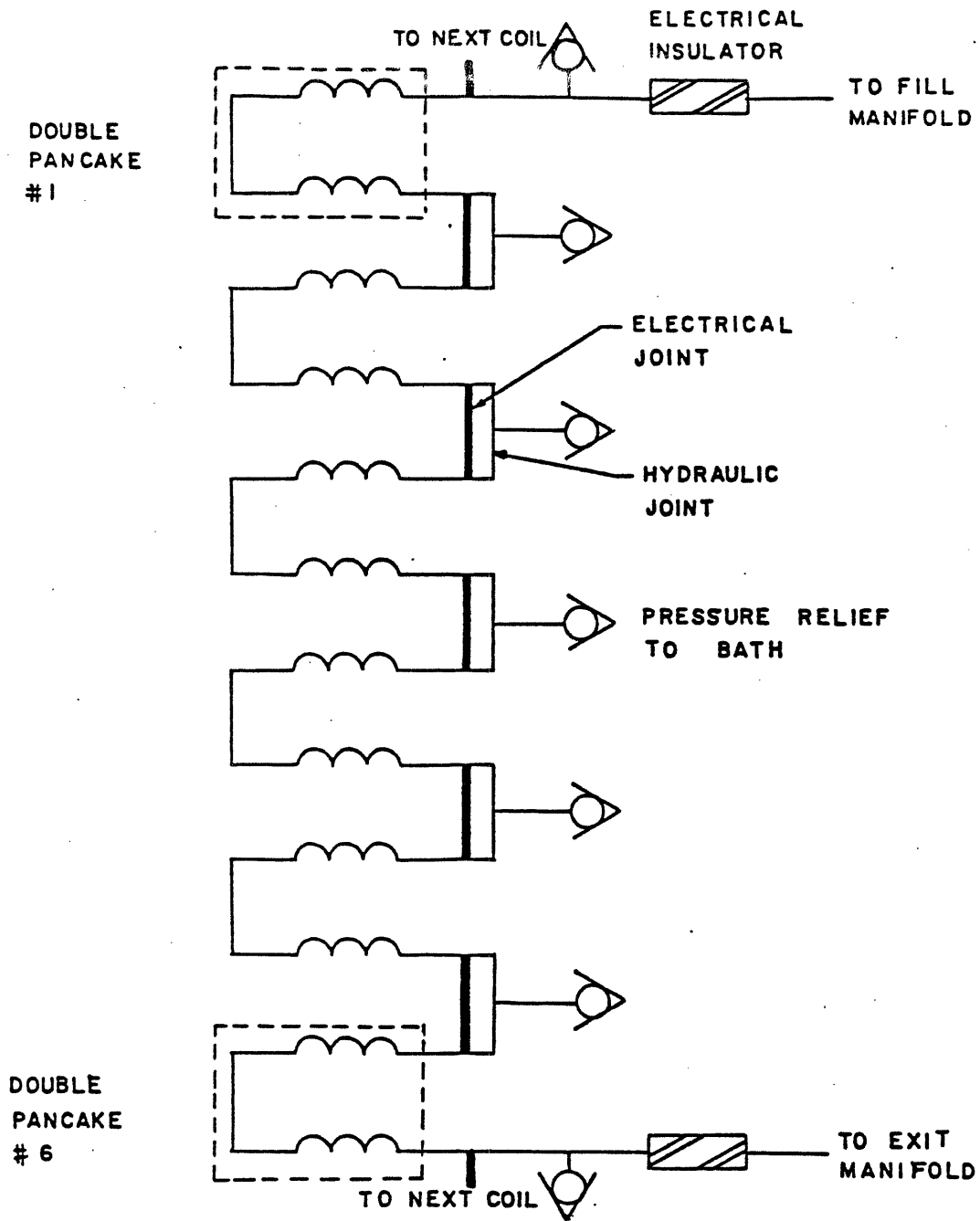


FIGURE 4.3-4 Hydraulic and Electrical Connections for One TF Coil.

4.3.1.3. Structural Approach and Stress Analysis

The overall structural approach chosen for the point design can be discerned from Figures 4.2-1, 4.2-2 and 4.2-3. The winding pack is supported at the outer diameter by the heavy wall case which surrounds it, the case being sufficiently stiff to limit epoxy shear stresses in the winding pack to allowable levels.

The method for supporting the overturning moments is to utilize stiff top-to-bottom elements between every other coil, and to use fasteners and keys on all slip surfaces. These keys would be pins match drilled in adjoining surfaces during fabrication of the cases, or interlocking teeth as shown at the inner wedging region of the coil. The toroidal continuity of the TF case/intercoil support structure must be broken at least once to prevent excessive delay of break-down voltages and EF changes. An appropriate insulated break utilizing G-10 insulation will be inserted in two toroidal locations as suggested by Figure 4.3-5.

Alcator DCT in a single-null divertor configuration experiences a strong nonsymmetric out-of-plane load. This is shown in Figure 4.3-6. The total running load has also been decomposed into a symmetric component and a nonsymmetric component to further illustrate the strong influence of nonsymmetry on loading. This out-of-plane load, together with the inplane load arising from a 7 Tesla field are used in the stress analysis which follows. Stress analysis is currently being carried out through the use of a shell model and through finite-element analysis.

The shell model analysis yielded a poloidal tension stress of 140 MPa at the equator and 77 MPa along the straight leg where the peak out-

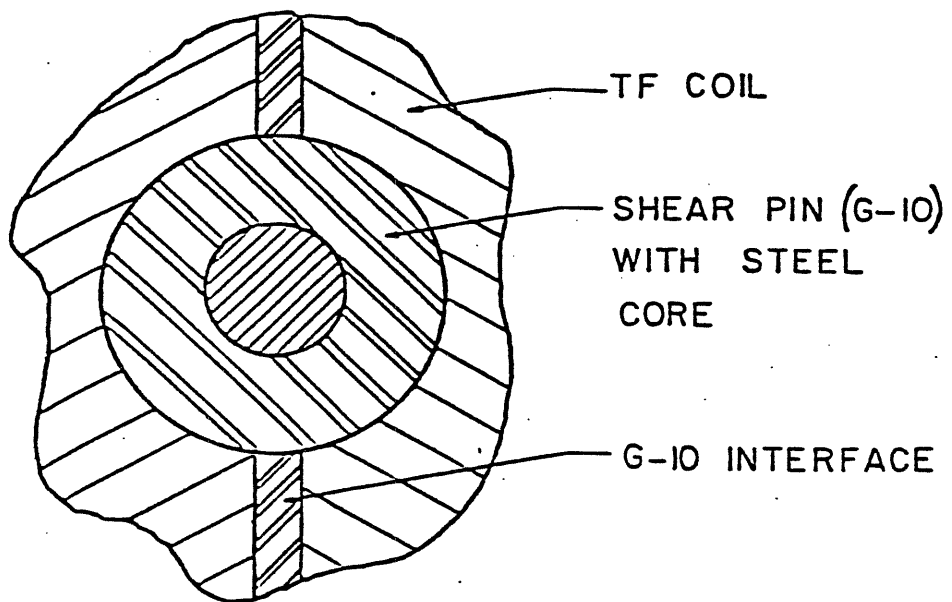


FIGURE 4.3-5 Concept for Insulation Gaps in the TF Intercoil-Structure.

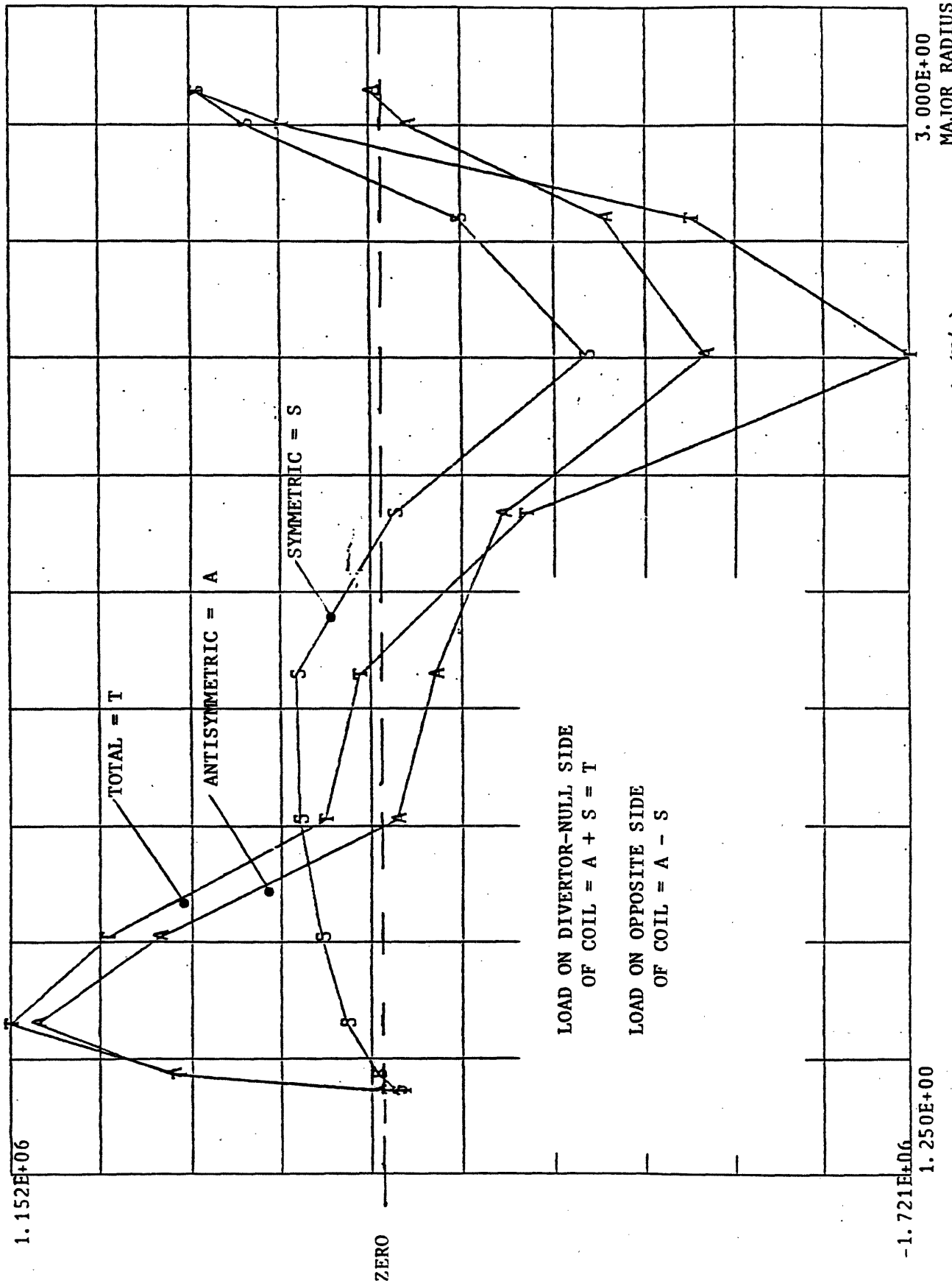


FIGURE 4.3-6a Out of Plane Force Per unit Length (N/m).

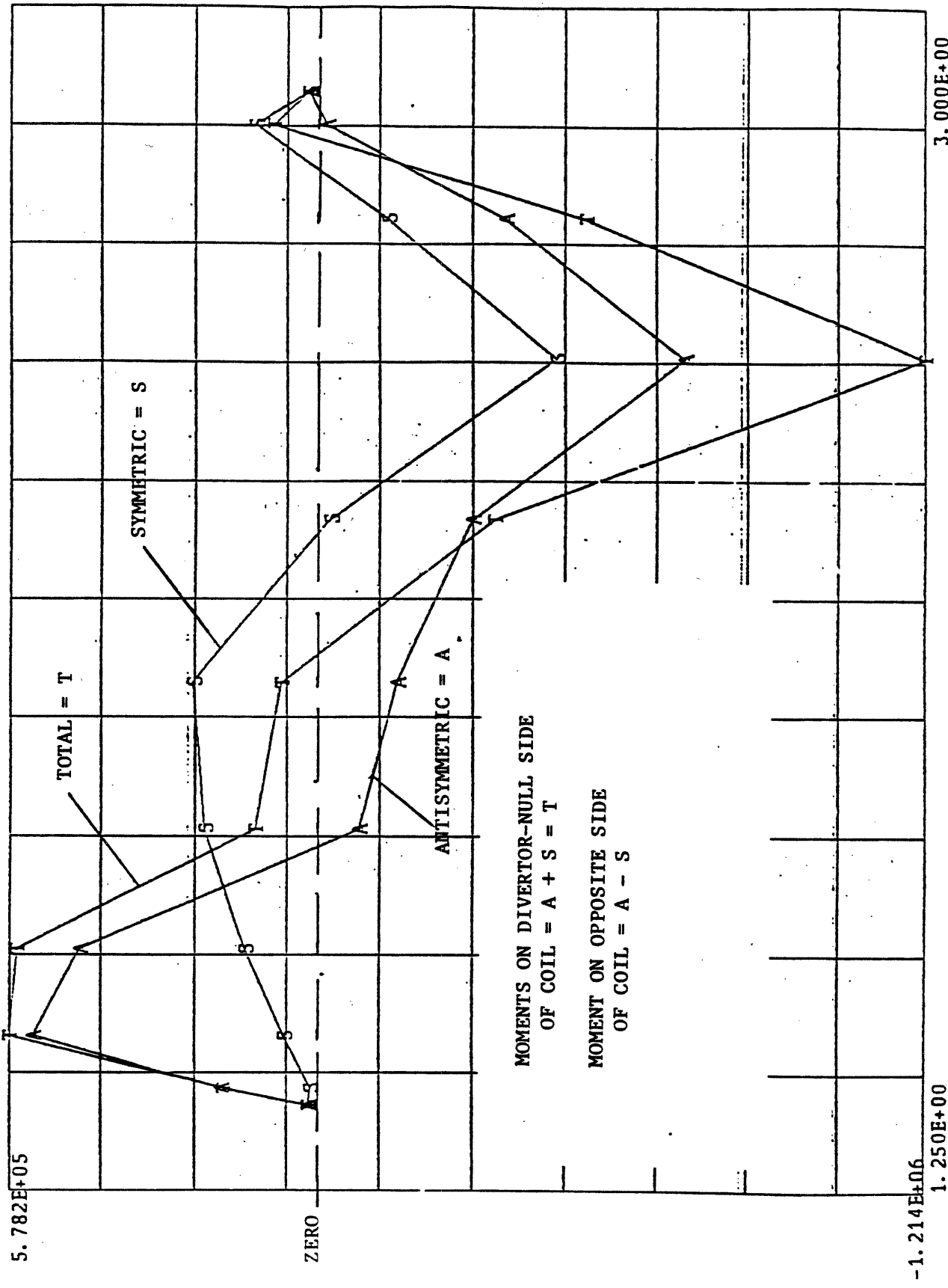


FIGURE 4.3-6b Moment Per Unit Length About Equator on the TF Coil Versus Radius.

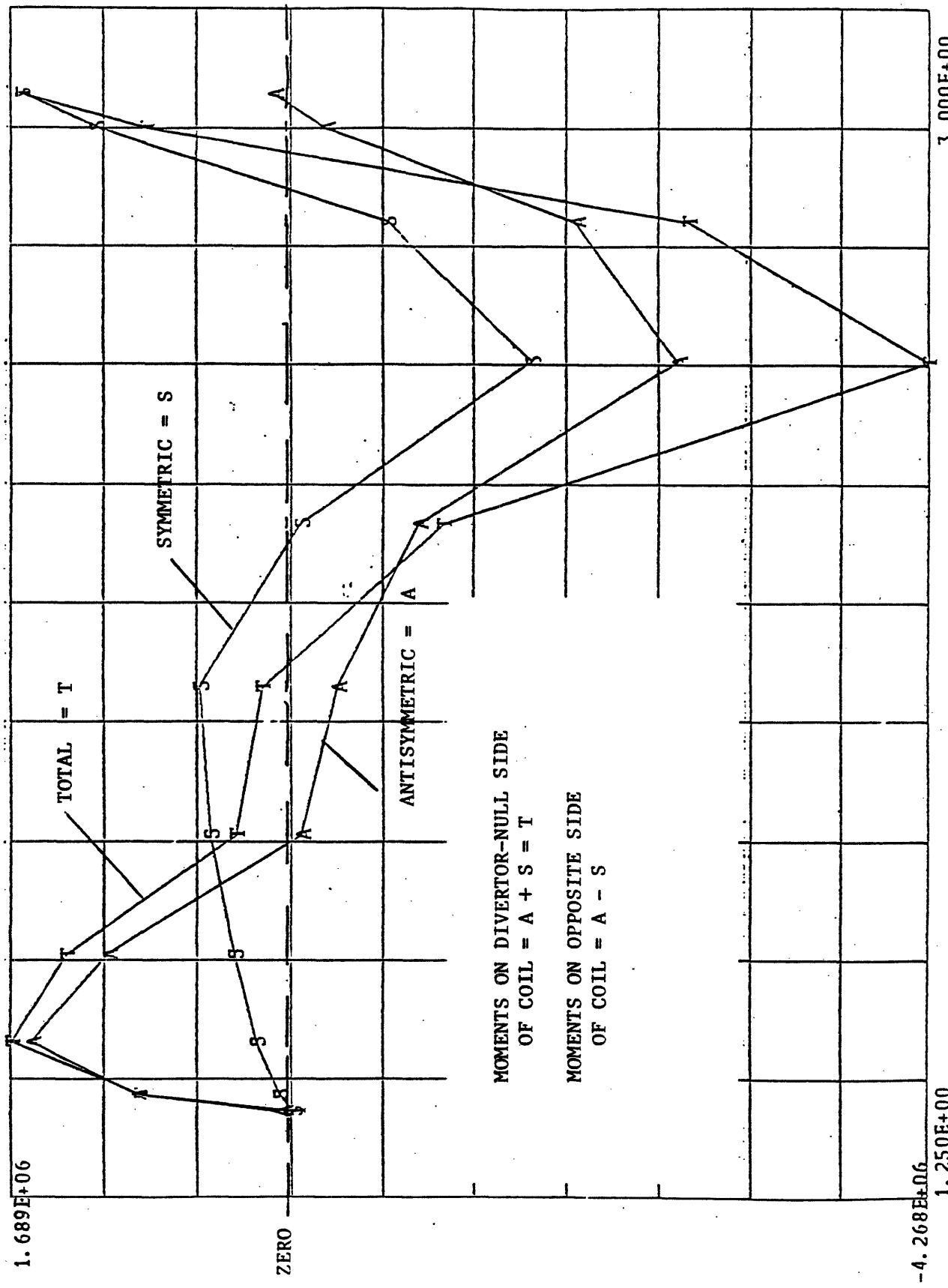


FIGURE 4.3-6c Moment Per Unit Length About Vertical Axis on the TF Coil Versus Radius.

of-plane bending occurs. The toroidal compression values are 159 MPa and 164 MPa in those locations. There also is 95 MPa plate bending stress in the box outer ring (cross-section as in Figure 4.3-7).

If there were no out-of-plane loads, the total applied membrane Tresca stress would be $140 + 159 = 299$ MPa at the equator and $77 + 164 = 241$ MPa at the top of the straight leg where the maximum out-of-plane bending occurs. The bending-plus-membrane values would be $299 + 95 = 394$ MPa at the equator and $241 + 95 = 336$ MPa at the top of the straight leg.

In order to analyze the additional contribution of out-of-plane stresses a calculation was performed using the "space frame theory" and the loads in Figure 4.3-6. The 24 coils were assumed to be rigidly locked together at the top of the straight inner leg due to the pressure of the legs along the inner vertical edge of the case, but were then assumed to be free-standing over the balance of their periphery. The analysis thus did not include the presence of the outer intercoil structure shown in Figure 4.3-8, and hence has a particularly high degree of conservatism.

The "space frame" model is shown in Figure 4.3-9. The problem is to determine the unknown internal force and two moments (f , M_1 , M_2) at the top of the inner leg, which is assumed to act as a rigid wall supporting the remainder of the coil at $R > R_1$. The torques and moments on a typical element are indicated in the figure. A peak bending stress of 81 MPa was found to occur at R_1 . Had the inner-coil structure been included in this analysis, one might expect this number to be reduced by about half.

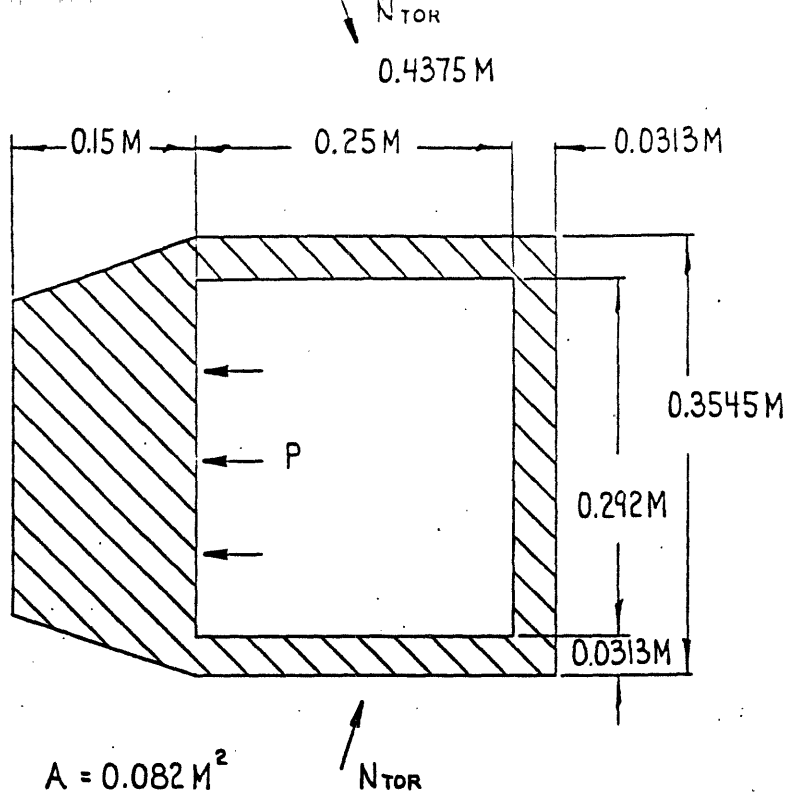


FIGURE 4.3-7

COIL BOX CROSS SECTION AT EQUATOR
INNER LEG

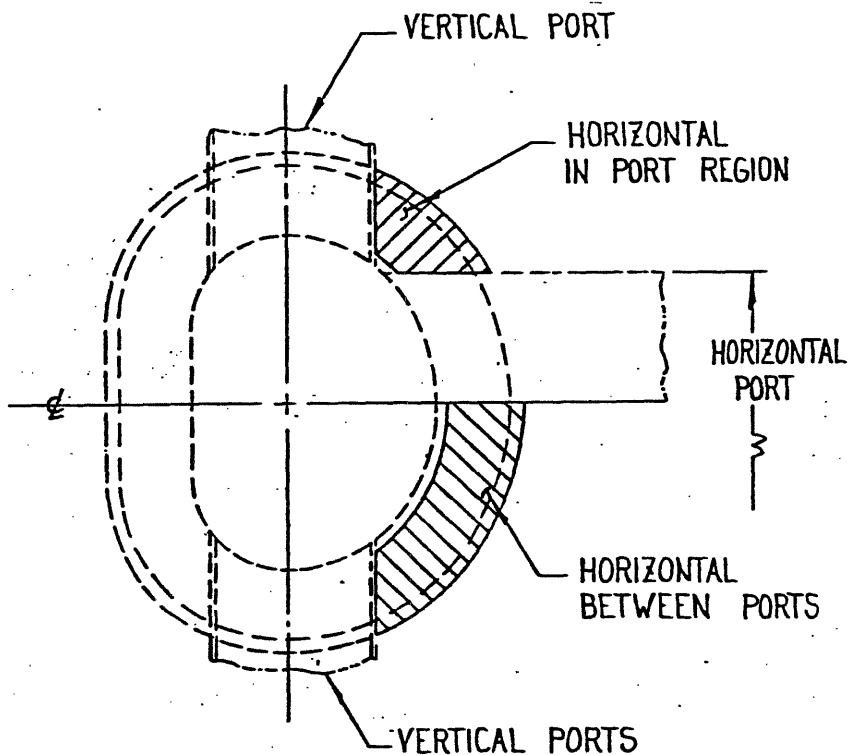
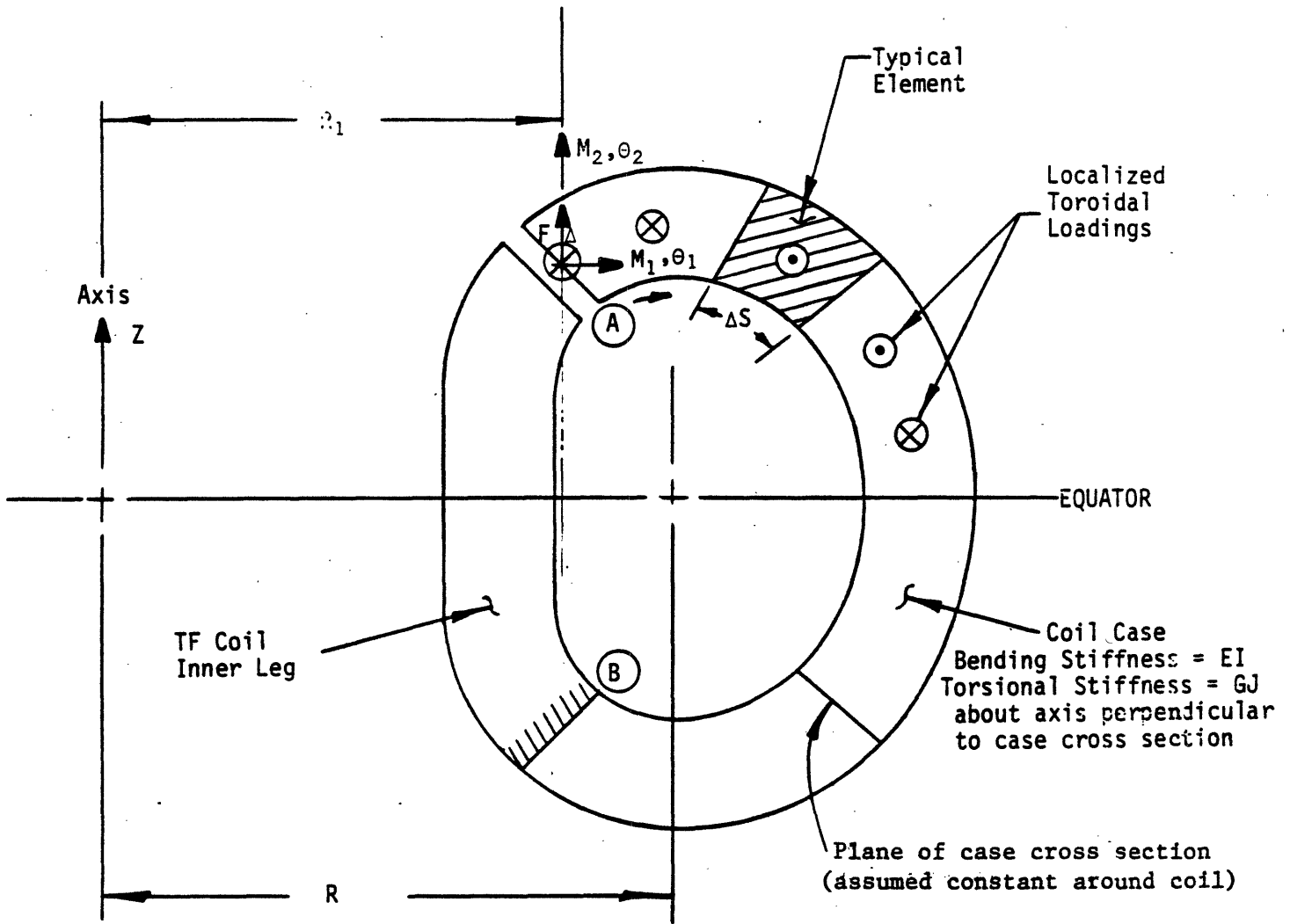


FIGURE 4.3-8

LOCATIONS OF OUTER MATERIAL
STRUCTURES



F , M_1 and M_2 are obtained from the conditions
 $\Delta = \theta_1 = \theta_2 = 0$ at A measured with respect to B.

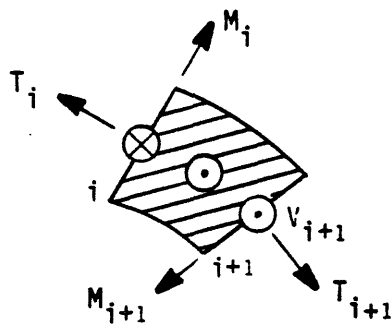


FIGURE 4.3-9 Quasi-Finite Element Model for Analysis of TF Coil Under Toroidally-Directed Forces.

When these stresses from the out-of-plane loads are included, the membrane Tresca values become $299 + 81 = 380$ MPa and $241 + 81 = 322$ MPa at the equator and top of the straight leg, respectively. The membrane plus bending values become $394 + 81 = 475$ MPa and $336 + 81 = 417$ MPa, respectively, at those locations.

In calculating static allowables, we assume a case material of 316 LN whose 4 K ultimate strength is equal to 1656 MPa. The allowable membrane stress was based on 1/3 of the ultimate, or 552 MPa, which also equals 2/3 of the yield (another criterion). Combined membrane plus bending was assumed to have an allowable stress equal to 1.5 times the membrane. The static factors of safety are shown in Table 4.3-2.

TABLE 4.3-2

Static Stress Summary And Corresponding Factors Of Safety*

Location	Total Applied Tresca Stress, Type and Magnitude in MPa	Allowable Stress MPa	Factor of Safety
Equator	Membrane 380	552	1.4
	Membrane Plus Bending 475	828	1.7
Top of Straight Leg	322	552	1.7
	417	828	2.0

* Factor of Safety = Allowable Stress/Applied Stress

We note from the Table that the allowable stress is greater than the applied stress for static loads.

The TF coil is assumed to be subjected to 10^4 TF in-plane load cycles at full field to accommodate start-up/shut-down over a 10 year period. An estimate was made of the case survivability under that condition by a linear elastic fracture mechanics analysis using the Paris equation with $C = 5.2 \times 10^{-12}$, $n = 3.9$ and with a factor of safety of 4 on life. The allowable peak stress was found to be 529 MPa. Compared to a total combined stress cycle of 475 MPa, the factor of safety on stress would be 1.1, and hence more than a factor of 4 on life. This result is conservative, moreover, since only the tension stress perpendicular to an assumed crack should be considered, in accordance with published data.

The out-of-plane component of load, arising from the poloidal fields, can, of course, be expected to experience many more cycles than the in-plane stress which is related to the number of TF field cycles. The out-of-plane contribution to the combined stress is approximately 25%, however, and thus one would have a static load with a superimposed 25% cyclical component. This condition would not be limiting from any practical operating-life point of view.

Some typical results from the shell model are shown in Figure 4.3-10. The finite element models are more accurate, but considerably more cumbersome as illustrated in Figure 4.3-11 which shows part of the model for the Alcator DCT winding pack and case as constructed for us by PPPL. Results are not yet available from the finite element model of the current Alcator DCT point design, but a model of an earlier circular design was particularly useful in examining winding pack interlaminar shear stresses and load

- 1 - Membrane Stress
- 2 - Combined (Membrane + Bending) Stress in Inner Plate
- 3 - Combined (Membrane + Bending) Stress in Outer Plate

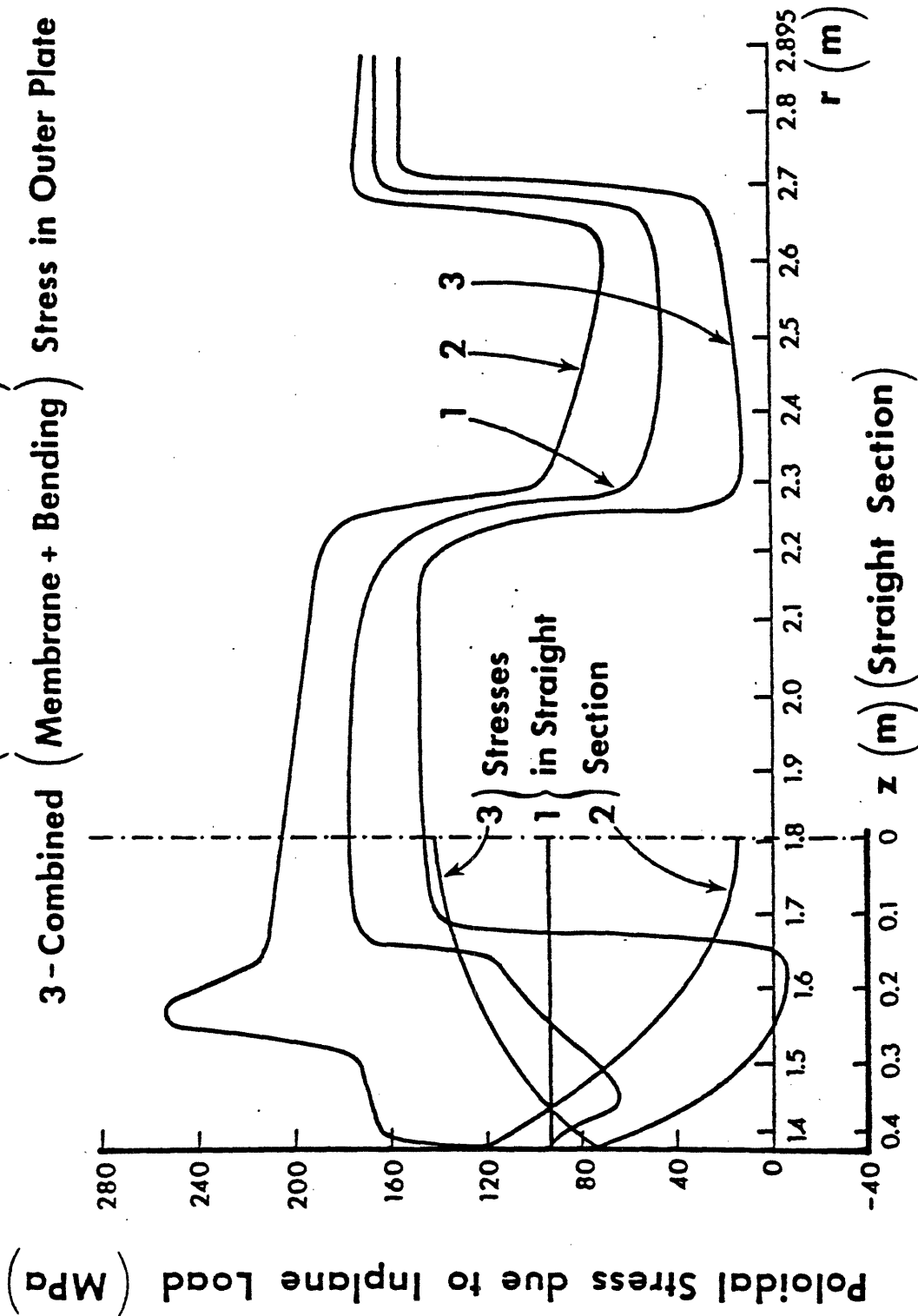


FIGURE 4.3-10a Poloidal Stress Due to Inplane Load as Given by the Shell Model.

- 1 - Membrane Stress
- 2 - Combined (Membrane + Bending) Stress in Inner Plate
- 3 - Combined (Membrane + Bending) Stress in Outer Plate

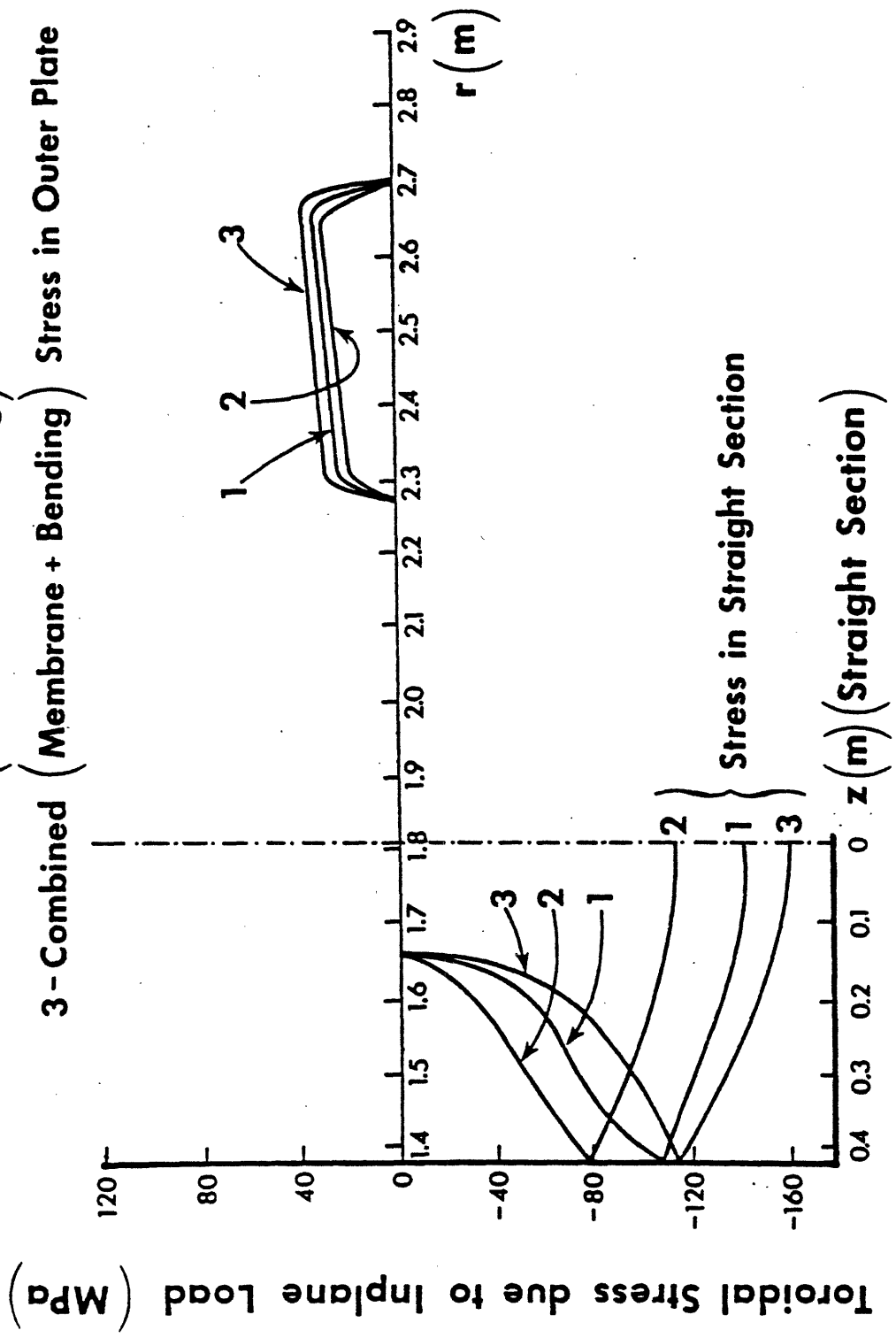
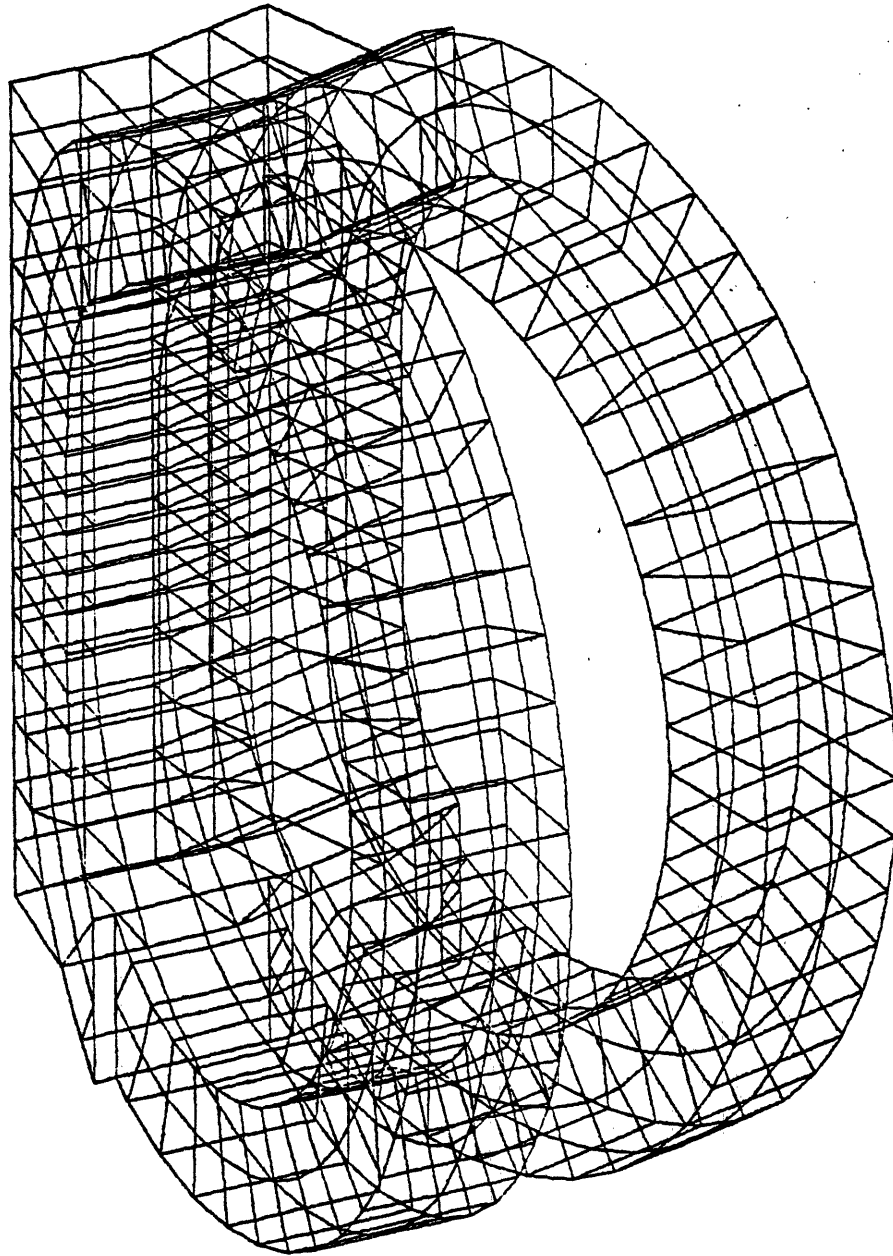


FIGURE 4.3-10b Toroidal Stress Due to Inplane Load as Given by the Shell Model.



ALCATOR FEA - MIT - 7/83
ANALYSIS PERFORMED BY I. J. ZATZ - PPPL
UNDEFORMED SHAPE

FIGURE 4.3-11 Finite-Element Model of Alcator DCT
Case and Intercoil Structure as
Prepared by PPPL.

sharing between the winding pack and case.

4.3.1.4. Protection

While the TF coils are designed to be stable against all disturbances, it is necessary to consider the possibility of a local nonrecovery and, in turn, the requirement to dump the magnetic energy external to the magnet before excessive local heating occurs. Table 4.3-3 lists the peak temperatures which are predicted by the analytical model for the Alcator DCT supercritical-cooled conductor as a function of the dump time constant. The dump time constant is largely a function of the external resistance, and hence of the allowable terminal voltage of the coils and the allowable voltage to ground. The internally cooled coils with full epoxy impregnation are particularly tolerant of voltage during rapid discharge, but warm helium regions (for example near the top of lead stacks) are very poor insulators and can limit voltages unless very careful design is employed.

The peak temperature which can be allowed during a quench has traditionally been an area of uncertainty. Clearly the winding must be protected from temperatures which would damage the superconductor (i.e., approaching heat-treating temperatures of 700 C) but this represents an obvious upper limit. Much lower temperatures, for example, can result in local thermal stresses due to unequal temperature expansion, and can crack epoxy bonds. Traditionally a temperature rise of 100 to 200 K has been generally accepted. For our conductor, this would require a single circuit dump voltage of about ± 2 kV to ground (4 kV terminal to terminal) which is acceptable for an internally cooled, potted winding.

Internally cooled conductors must also protect against over pressure in the conduit as the supercritical helium expands with rising temperature. Simulation of nonrecovery conditions indicated peak pressures in the mid-point of the conduit of approximately 25 atmospheres under the assumption of pressure relief at the end of each double pancake. This pressure is well within the capability of the steel jacket conduit.

Detection of a normal zone within the TF windings is necessary to initiate the protection circuit. We must anticipate that this will be difficult in the tokamak environment, and will require signal processing to distinguish a growing normal zone from induced voltages. Separation of normal zone voltages is one major reason to allow as long as possible before

TABLE 4.3-3

Temperature Rise during Quench¹ as a Function
of Dump Time Constant

Discharge Time Constant ² (s)	Voltage Across 24 coils ³ (kV)	Peak Temperature (K)
8.9	5.38	100
19.3	2.48	300
31.0	1.54	1000

note:

¹ Operating current = 23 kA

² Exponential decay following a delay of 0.2 s at full current before dump start.

³ a) Max voltage to ground is 0.5 times this value if a ground is located between coils 12 and 13.

b) Lower voltage circuit configurations are possible with multiple dump resistors and/or circuits at the expense of complexity;

requiring initiation. Advantage will be taken of nonsymmetry over the 24 symmetric TF coils in signal processing.

It is quite possible that internally cooled conductors will offer a nonelectrical method of quench detection, namely monitoring the internal pressure in the conduit. We might expect a noticeably different pressure rise signature accompanying a spreading normal zone than that due to induced losses. This will be investigated in the 12 Tesla test coil prototype.

Detection of normal zones in the PF coil system will be yet more difficult but again will rely on development of both electrical and non-electrical signal processing techniques.

4.3.2. Poloidal Field System

We propose to use superconducting poloidal field coils on the Alcator DCT machine in order to provide the most economic solution and the maximum capability to run long pulses. Were the PF coils to be copper rather than superconducting for example, they would consume more than 100 MW at full excitation. A similar conclusion has been reached in the TFCD conceptual designs, where even the copper toroidal coil machine option retains a superconducting PF system to limit total power consumption to a more reasonable value. The Alcator DCT will be the first tokamak to use a superconducting poloidal field system.

The Alcator DCT poloidal coil system is shown in Figure 4.3-12, and the coil locations, ampere-turn capability and peak fields given in Table 4.3-4. The proposed coil set is a hybrid system in that any given coil

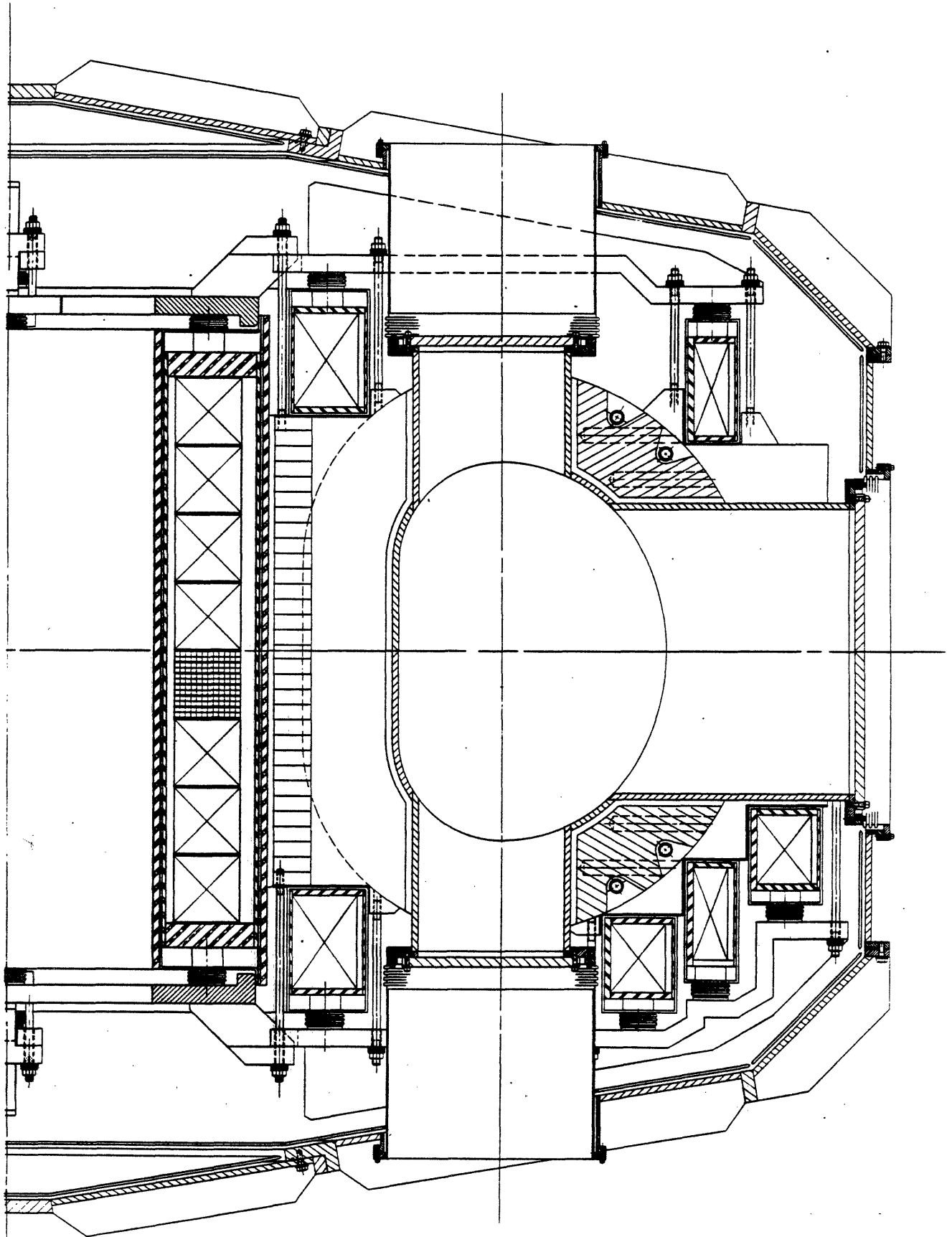


FIGURE 4.3-12 Poloidal Field Coils as Described in Table 4.3-4.

performs multiple functions, for example both an inductive drive and an equilibrium function, or both a divertor and a shaping function. This approach is typical of next-step designs, but is a departure from tokamaks like Alcator in which the inductive drive (OH coils) and equilibrium (EF coils) are independent decoupled systems.

The hybrid approach results in a need for fewer coils (and therefore more available cross-section for any given coil) but can require more sophisticated profiling of currents in any given coil. Specifying the net current-time profile for any given coil can of course, be done by superposition of currents required for an OH function (producing essentially no field in the plasma region) and the shaping and equilibrium currents derived from equilibrium code considerations. The net currents are naturally limited by the coil capabilities (critical current, peak field, coil cross-section, etc.).

Current time profiles for the coil labeled OH2/EF2 are given in Figure 4.3-13 for a typical 1.5 second plasma current ramp. Superimposed on this current profile could also be an initiation plasma breakdown phase, typically lasting 35 milliseconds in which the initial OH component of current might drop by 15%.

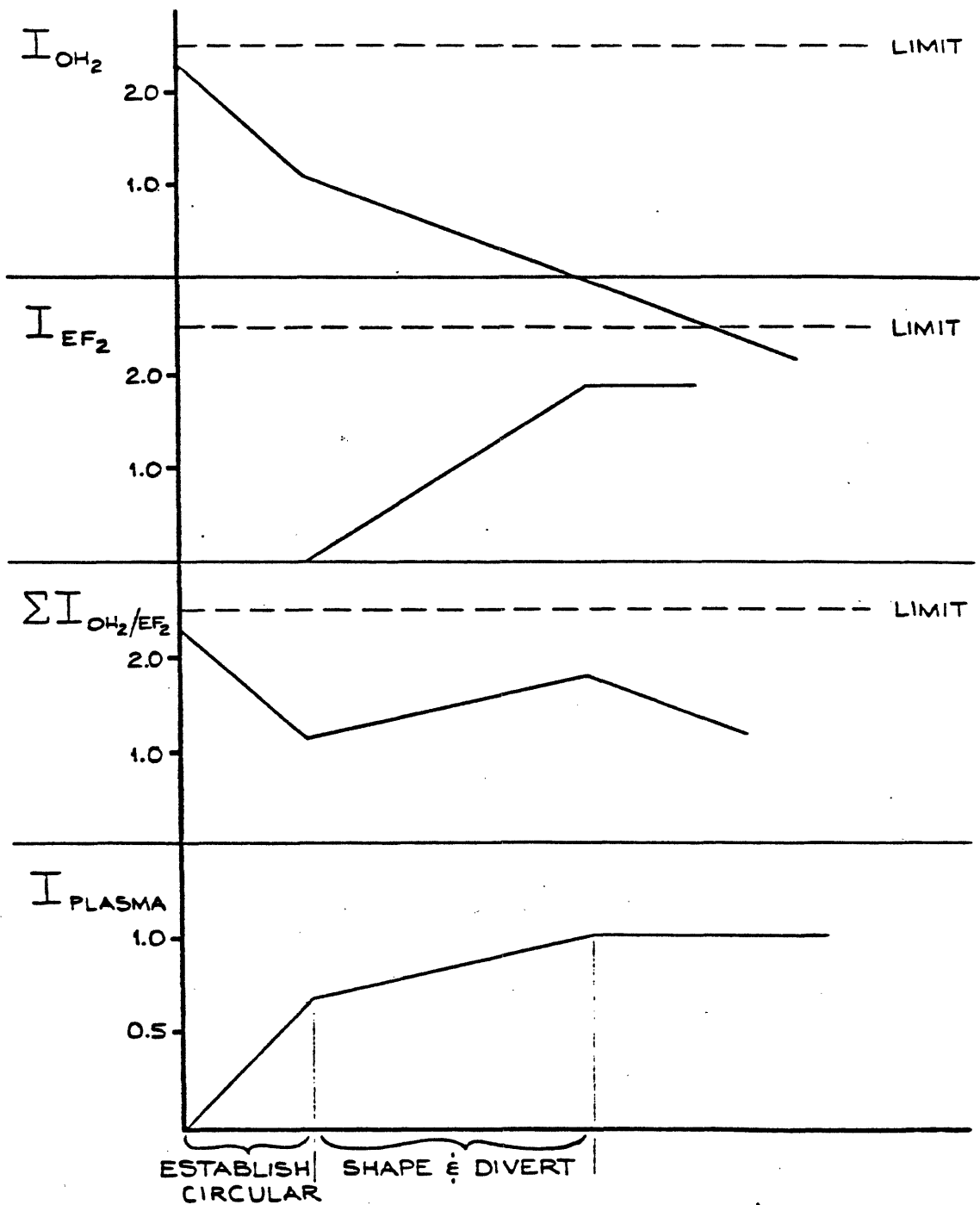


FIGURE 4.3-13a Current Versus Time in OH₂/EF₂ for a Case in which the Initial Plasma is Circular and is Subsequently Shaped and Diverted.

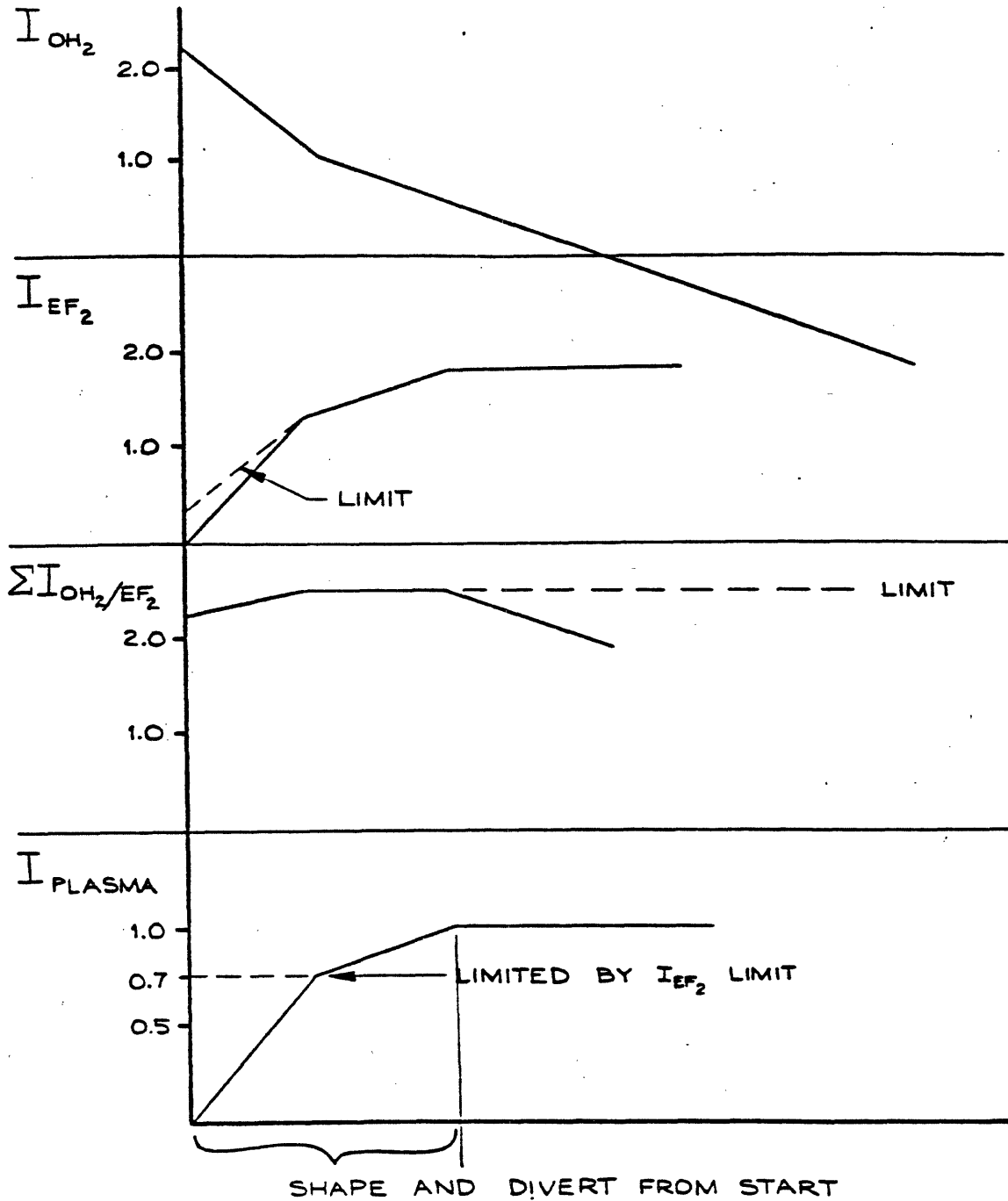


FIGURE 4.3-13b Current Versus Time in OH₂/EF₂ for a Case in which the Plasma is Shaped and Diverted from Startup.

TABLE 4.3-4

Poloidal Field Coils

COIL	COIL#	R1 m	R2 m	Z1 m	Z2 m	NI _{max}	H _{peak} *	N
OH1	1	0.68	0.95	-1.15	1.15	12.6 MA	7 T	252
OH2/EF2 TOP	2	1.17	1.41	1.01	1.39	2.5 MA	4.5 T	50/100 **
OH2/EF2 BOTT	3	1.17	1.41	-1.01	-1.39	2.5 MA		50/100
OH3 TOP	4	2.78	2.92	1.04	1.29	1.0 MA	3.2 T	20
OH3 BOTTOM	5	2.78	2.92	-1.04	1.29	1.0 MA		20
EF3 TOP	6	2.78	2.92	0.89	1.01	0.5 MA	2.3 T	20/40
EF3 BOTTOM	7	2.78	2.92	-0.89	-1.01	0.5 MA		20/40
D1 BOTTOM	8	2.45	2.67	1.12	1.38	1.5 MA	2.1 T	64
D2 BOTTOM	9	3.04	3.26	0.67	0.93	1.5 MA	2.7 T	64

*The peak field is taken as the highest field noted in the normal scenarios which have been investigated.

**Alternate tap connection.

These typical current vs. time profiles would result in field changes and rates of change of field typified by the values in Table 4.3-5.

The PF coils are also exposed to changing fields from disruptions, for example, 0.3 Tesla in 10 milliseconds (where the time constant is determined by the vacuum vessel) is typical.

The field changes outlined above together with control field variations require a reasonably finely divided PF conductor as discussed below.

TABLE 4.3-5

Typical ΔH and \dot{H} in the OHI PF Coil

FUNCTION	FIELD AT START	FIELD AT END	ΔH	INTERVAL	\dot{H}
INITIATION	7 T	5.5 T	1.5 T	35 ms	42 T/S
CURRENT RAMP	5.5 T	1.5 T	4 T	1.5 s	2.7 T/S
FLAT TOP	1.5	-7 T	8.5 T	30 s	0.28 T/S
DISRUPTION	-7 T	-7.5 T	0.5 T	10 ms	50 T/S

4.3.2.1. Conductor Selection

There is generally thought to be a relatively small data base for conductors optimized for poloidal field coil applications. Because of the large field changes and rates of change involved, the conductors are subjected to large losses compared to the toroidal field conductors. Optimized conductors are therefore relatively finely divided (e.g., cables) in order to minimize losses and reduce refrigeration requirements. Most toroidal field conductors (for example, five of six LCP conductors) are not sufficiently divided to qualify as poloidal field conductors. This has given rise to development of several pool-cooled cable conductors for PF application as listed in Table 4.3-6. Such pool-cooled conductors are potential candidates for Alcator DCT as we discuss below, but we believe that internally cooled conductors in the form of the Westinghouse/Airco conductor would make better candidates. That conductor form is sufficiently subdivided and has a large coil manufacturing data base through LCP. While such PF conductors could in fact utilize Nb₃Sn strands as

well, the lower fields typical of the PF coils allow NbTi strands. The internally cooled conductors permit full epoxy impregnation with superior insulation qualities and better control over coil pack mechanical characteristics. By utilizing impregnated coils, superconducting PF coils can share in the large data base for impregnated copper conventional coils. Nonimpregnated pool-cooled cable conductors have a very limited mechanical performance data base, a matter of considerable concern to us.

We propose that Alcator DCT use the Westinghouse/Airco sheath in exact form (although made from 316 LN stainless steel) in order to utilize the Airco tube mill without further development. A PF conductor would typically need to have a copper to superconductor ratio of 5 to 1 to give adequate stability under pulse field conditions and hence would necessarily have a lower overall current density than the Alcator DCT TF conductors. A sheath of the Westinghouse/Airco dimension could carry a cable capable of carrying 12.5 kA, half that of the TF conductor. Nevertheless, the current density is competitive with pool-cooled cable conductors. We would propose to use two or more such conductors wound two-in-hand to build up a suitable total current level (25 kA to 50 kA as discussed below).

TABLE 4.3-6

Poloidal Field Coil Superconductor Data Base

NIOBIUM-TITANIUM CABLES POOL BOILING AT 4.2 K					
MAGNET SYSTEM	DATE	SCALE (MJ)	CURRENT (kA)	FIELD (T)	RAMP TIME (SEC)
ANL	81	3.3	11	6.5	0.4
LASL	CANCELLED	20	50	7	0.5
BONNEVILLE POWER	83	30	5	2.8	0.72*

*Operates at 0.35 Hz; time given is 1/4 period.

Los Alamos National Laboratory has analyzed optimized PF conductors for INTOR, FED, and most recently TFCD. They predict that pool-cooled and internally cooled conductors would give essentially comparable stability and AC loss performance. Given that equality, we would choose internally cooled conductors for what we consider their improved insulation and mechanical properties.

It is not necessary, only desirable, to use the lowest possible loss conductor in a PF application. Provided that the instantaneous loss is not large enough to drive the conductor into a nonrecovery quench situation, the use of a nonoptimized conductor only results in larger refrigeration requirements or a lower duty cycle capability. The Alcator DCT project has access to sufficient nonoptimized superconductor of several types (at an original cost of 4-5 M\$), to wind the entire OH and EF coil systems. One of these conductors was originally manufactured for the canceled large MHD magnet for the Montana CDIF Project. The conductor, shown in Figure

4.3-14, is however, very far from optimum, and requires that the superconducting core be removed from the CDIF conductor, drawn down, and combined with copper strands to form a cable. The superconductor could be used to make the 486 strand cable described in Table 4.3-7 to be used with the Westinghouse/Airco sheath. This cable would be entirely suitable for the larger diameter PF coils with their lower peak fields, and analysis is underway to confirm its adequacy for the central OH coil.

TABLE 4.3-7

Possible ICCS PF Conductors Manufactured

From 20 MJ And CDIF Strands

	20 MJ	CDIF	OPTIMIZED*
SHEATH OD	2.1 × 2.1 cm	2.1 × 2.1 cm	
SHEATH WALL	0.17 cm	0.17 cm	
STRAND DIAMETER	0.2 cm	0.07 cm	0.07
NUMBER OF STRANDS	54	486	
VOID FRACTION	35%	32%	
CU/SC RATIO	5.25:1	6:1	
FILAMENT DIAMETER	22 μ m	35 μ m	8 μ m
CUPRONICKEL BARRIERS	YES	NO	YES
I _{OPERATING}	12.5 kA	12.5 kA	
I _{OP} /I _C @ 7 T	0.7	0.65	0.7
HYDRAULIC PATH	60 m	60 m	

*Characteristics more typical of conductor which would be specified if purchased new.

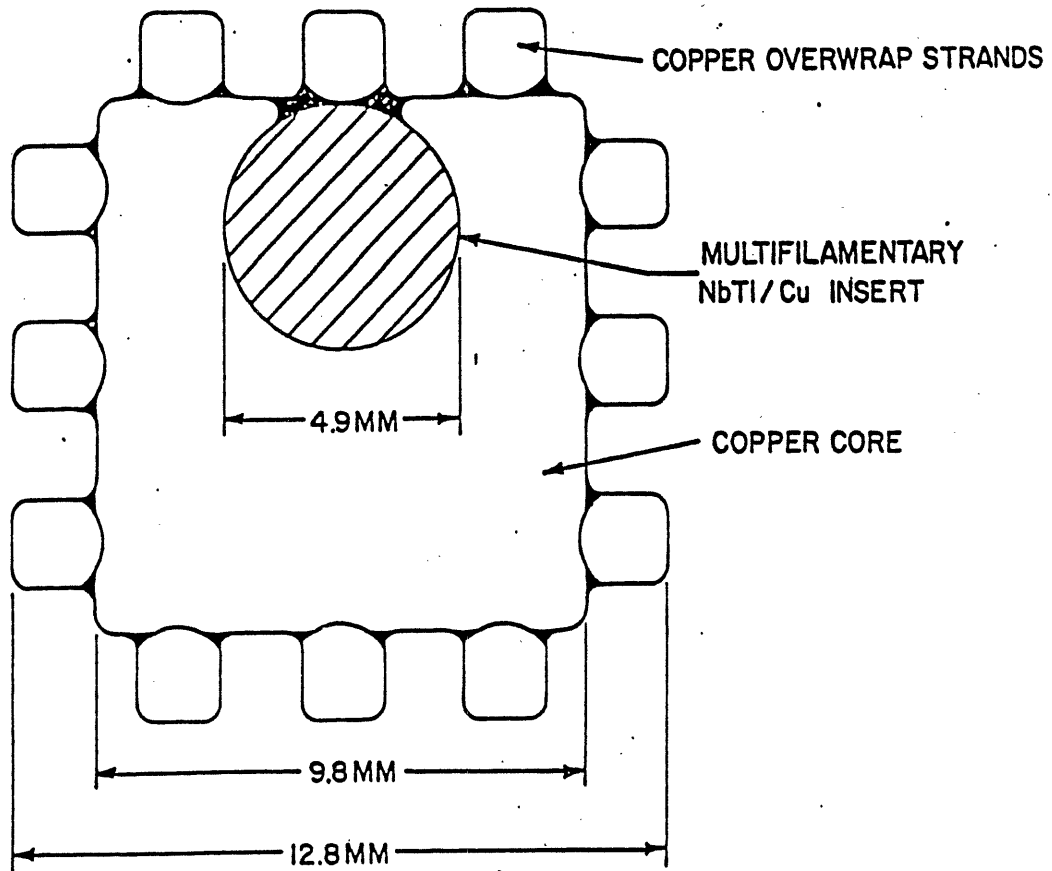


FIGURE 4.3-14 CDIF Conductor from which NbTi/Cu Insert Could be Removed and Redrawn to Form an ICCS Cable.

The project also has potential access to the more highly optimized PF material designed for the Los Alamos/Westinghouse 20 MJ pulse field coil. There is sufficient 20 MJ material to construct half of the central OH coil. That material, which has fine filaments and cupronickel barriers to reduce eddy currents, is complete except for final drawing. The wire cannot however, be drawn below a 2 mm diameter. If used with the Aircro sheath, the material would be used in the form of a 54 strand cable as described in Table 4.3-7. Analysis is underway to confirm that this large strand diameter will be stable in the internal-cooled conductor configuration. A large quantity of fine filament cupronickel shielded wire manufactured for Brookhaven is also available and is currently being studied.

We anticipate utilizing the same indirect cooling technique used in the TF coils to remove the average heat represented by the PF conductor losses. Preliminary analysis indicates that the average generated heat can be removed through an adequate ground plane insulation thicknesses on each double pancake.

Any of the available NbTi materials could also be used to construct a pool-cooled conductor. Such a conductor made from the CDIF material is shown in Figure 4.3-15. This illustrated 25 kA conductor, suggested and designed by the ANL pulse magnet group, would be a nearly optimum conductor and has been cost estimated at a modest fraction of the cost of an entirely new conductor.

Further optimization of PF conductors are possible, largely through the use of smaller superconducting filaments and cupronickel barriers to break-up copper eddy current paths. Use of Nb₃Sn conductors should also

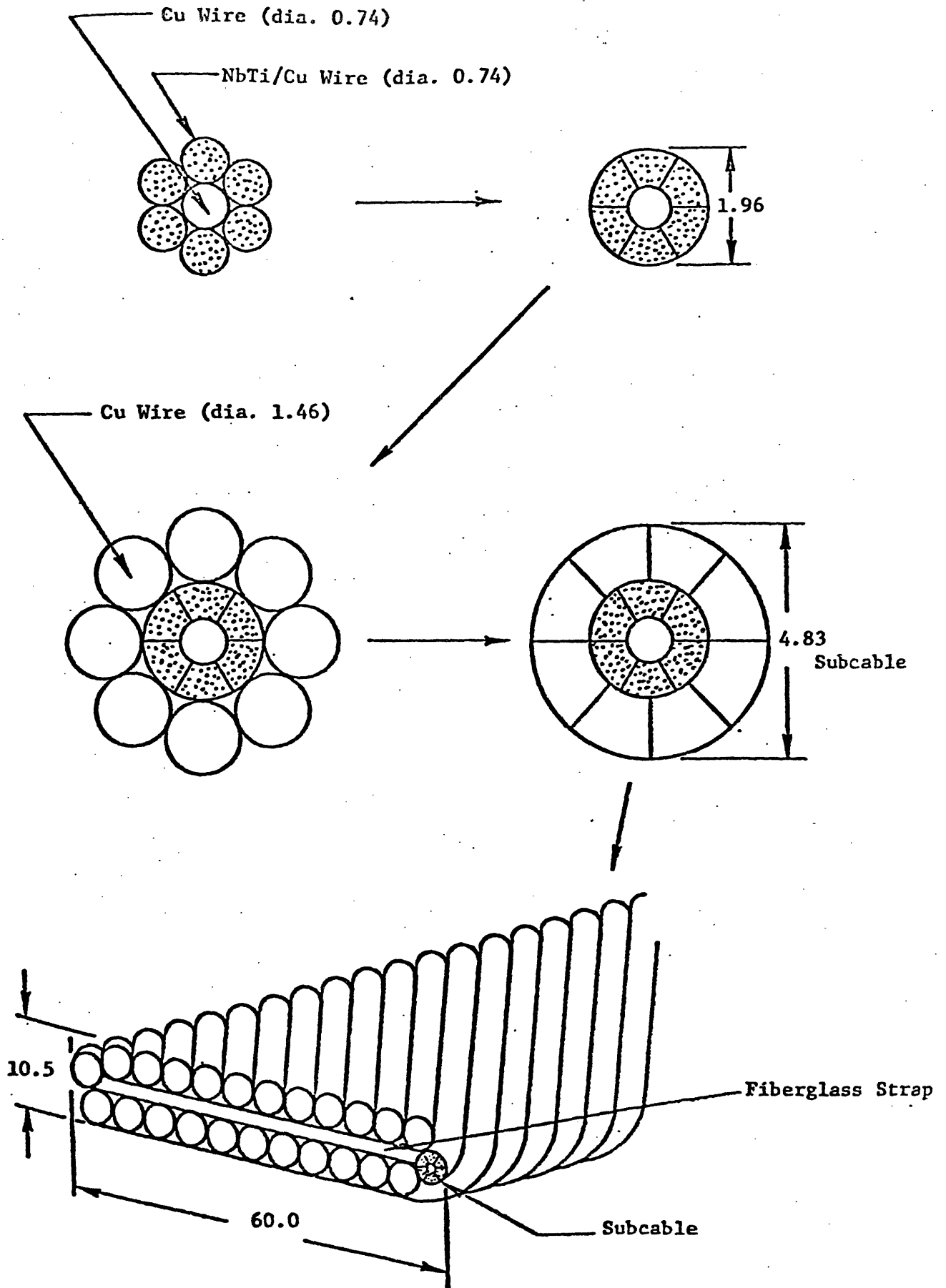


FIGURE 4.3-15 25-kA Cable (Dimensions in mm) Pool-Cooled Conductor Alternate PF Conductor (ANL).

be considered for applications where peak fields and disruption energies exceed the margins available with NbTi. Such optimized conductors are important for TFCD and future reactor applications, and could be tested in Alcator DCT by substitution of certain OH modules with optimized modules.

JAERI has an optimized internally cooled PF conductor under development. Preliminary encouraging discussions have been held concerning the construction of some portion (half) of the DCT central OH transformer as part of the JAERI PF coil development program.

4.3.2.2. Current and Voltage Level Selections

In order to deliver an adequate initiation voltage for startup (see Appendix C) without exceeding a reasonable 20 kV voltage limit the PF coils must operate at the 25 to 50 kA level. This level is also compatible with limiting disruption voltages and is an optimum match to the current level of the existing Alcator C power supplies.

This current level requires that two or more of the proposed 12.5 kA internally cooled conductors be wound-in-hand. Care must be exercised in superconducting parallel circuits to assure current sharing. This would be done by suitable transposition of the conductors as required to balance flux linkages, and by use parasitic series resistances if required.

The inductance matrix for the DCT point design is given in Table 4.3-8. The table has been used to generate the various interaction voltages of interest (Table 4.3-9) under the simplifying assumption of eddy currents flowing only in the central vacuum chamber during disruption.

The influence of eddy currents on startup and control is discussed in Appendix C.

The typical disruption induced voltages given in Table 4.3-9 are calculated for the generally unrealistic case that the power supply across the coil terminals is capable of holding the current in the coil constant.

TABLE 4.3.8

Inductance Matrix For Point Design PF System

COIL#*	COIL#	L OR M (MILLIHENRIES)	COIL#	COIL#	L OR M (MILLIHENRIES)
1	1	53.0	4	4	5.1
1	2	6.9	4	5	0.74
1	3	6.9	4	6	3.9
1	4	2.1	4	7	0.84
1	5	2.1	4	8	9.8
1	6	2.2	4	9	9.4
1	7	2.2	4	10	0.044
1	8	6.9	5	5	5.1
1	9	6.9	5	6	0.84
1	10	0.17	5	7	3.9
2	2	9.4	5	8	2.0
2	3	0.54	5	9	3.2
2	4	1.2	5	10	0.044
2	5	0.5	6	6	5.7
2	6	1.2	6	7	0.94
2	7	0.56	6	8	8.6
2	8	4.6	6	9	11.0
2	9	3.5	6	10	0.05
2	10	0.048	7	7	5.7
3	3	9.5	7	8	2.2
3	4	0.5	7	9	3.6
3	5	1.2	7	10	0.05
3	6	0.56	8	8	43.3
3	7	1.2	8	9	21.4
3	8	1.4	8	10	0.13
3	9	2.0	9	9	56.6
3	10	0.048	9	10	0.16
			10	10	8.2×10^{-3}

* See Table 4.3-4 for coil identification.

TABLE 4.3-9

Examples Of Typical Open Circuit
Induced Voltages

<u>FUNCTION</u>	<u>OPEN CIRCUIT TERMINAL VOLTAGES</u>
OH1 Discharge at 20 kV for Initiation *	OH2 : 2.6 kV OH3 : 0.8 kV
OH1 Charge at 750 V for Flat-top	Plasma: 4.9 V OH2 : 98 V
Plasma Disruption with decay set by 10 msec vacuum wall time constant	OH1 : 16.8 kV OH2 : 4.75 kV OH3 : 4.35 kV D1 : 12.8 kV D2 : 15.8 kV D2-D1 : 2.9 kV

*This discharge voltage would result in a 130 volt loop voltage which would be reduced to approximately half by eddy currents in the vacuum vessel as discussed in Appendix C.

4.3.2.3. PF Coil Loads and Structural Approach

The PF coils as proposed will be wound with internally cooled conductors utilizing the Westinghouse/Airco sheath at an individual conductor current level of 12.5 kA. The coils will be epoxy impregnated. Such a configuration will have adequate steel within the winding pack to support both internal axial compression loads and dilation loads. Typical loads are given in Table 4.3-10a for the start of flat top and in Table 4.3-10b for the end of flat-top. The loads are also averaged over the coil foot-print for vertical loads and over the coil cross-sections for

dilation loads to give an indication of average stresses. The stress levels in the steel conductor conduit would be six times higher than the average for vertical compression and three times higher than the average for tension. The conduit stresses are acceptable compared with allowables. Of interest however, is the fact that several of the PF coils (for example, OH3 and D1 in Table 4.3-10b) experience a negative dilation, and would therefore be subjected to inward buckling if not adequately stiff or supported by the mounts to the TF coils.

The net vertical loads on the PF coils are supported directly to the TF coil cases as shown in Figures 4.2-1, 2 and 3. It will be necessary however, to allow free relative motion along the horizontal plane interface between the PF coils and the TF coils to avoid overstressing the PF coils due to inward motion of the TF coil set under TF field load. This was solved in JT-60, where a similar support concept is used, through the use of low friction pads.

The PF coil cryostats in DCT are not intended to serve a structural role as sufficient steel is included in the winding pack to carry the internal loads, and support from the TF coil cases carries the net vertical forces (and prevents inward buckling in several instances). The cases serve only as helium cryostats and are constructed from a thin metallic shell reinforced with nonmetallics. These cases will need some development (see Chapter 9, RDACS).

TABLE 4.3-10a

PF Coil Loads and Average Stresses

at the End of Flat-Top

	NI (MA)	F_z (MN)	F_z/B^* (MN/m ²)	F_R/A^{**} (MN/m ²)
OH1	- 12.6	- 1.0***	- 0.7	34.2
OH2/EF2 TOP	- 0.55	- 4.0	- 2.06	0.81
OH2/EF2 BOTTOM	- 0.55	+ 3.8	+ 1.96	1.8
OH3 TOP	- 0.74	- 13.2	- 5.3	84
OH3 BOTTOM	- 0.74	+ 2.6	+ 1.04	9.4
EF3 TOP	- 0.21	- 0.83	- 0.33	50.8
EF3 BOTTOM	- 0.07	- 0.75	- 0.3	1.81
D1 TOP	+ 1.5	+ 13.3	+ 3.8	- 58.4
D2 TOP	- 1.5	+10.13	+ 0.03	12.5

*Vertical force divided by coil foot-print area.

**Radial load per unit length divided by coil cross-section.

***This is the net upward load on the whole central transformer due to asymmetry. The attractive loads between the upper and lower half of the transformer are not given here.

TABLE 4.3-10b

PF Coil Loads and Average Stresses

at the Start of Flat-Top

	NI (MA)	F_z (MN)	F_z/B^* (MN/m ²)	$F_R' R/A^{**}$ (MN/m ²)
OH1	+ 2.7	+ 0.22	+ 0.16	6.6
OH2/EF2 TOP	+ 2.5	+ 6.4	- 0.54	38
OH2/EF2 BOTTOM	+ 2.5	+ 7.5	+ 3.9	34
OH3 TOP	+ 0.48	+ 6.6	+ 2.64	- 50.8
OH3 BOTTOM	+ 0.48	+ 0.27	+ 0.1	- 2.5
EF3 TOP	- 0.21	- 4.5	- 1.8	+ 49.4
EF3 BOTTOM	- 0.07	- 0.48	+ 0.19	1.3
D1 TOP	+ 1.5	+ 1.5	+ 0.42	- 2.84
D2 TOP	- 1.5	+ 5.6	- 1.29	38.6

4.3.3. Cryogenic Considerations

4.3.3.1. Design Approaches

There are several factors which complicate cryogenic considerations for the tokamak: (1) nested toroidal components with competition for radial build and access; (2) a need to avoid parasitic closed toroidal low resistance paths; (3) a potential for large pulse losses; and (4) a number of independent coil systems each requiring high current leads. There are, in addition, complications which face any large superconducting system, such as the need to discharge energy rapidly with high voltages between terminals and ground, and the need to manage large inventories of

helium. We comment briefly on the approaches taken in the point design to address some of these complications.

- (a) The magnets are all in a common vacuum and therefore magnets, intercoil supports, and intercoil lead and hydraulic manifolds can all be at a common temperature.
- (b) Each coil is contained in a vacuum tight case which constitutes a helium reservoir. These reservoirs are properly vented and are manifolded to a central external reservoir whose height above the machine is chosen to assure complete filling of the coil reservoirs.
- (c) The internally cooled conductors are filled with a static charge of supercritical helium at 2.5 atmospheres from a central manifold. Each pancake termination contains a pressure relief valve which vents in the coil reservoir. The insulated connections to the main manifold and the pressure reliefs are all located at the top of accessible coil vent stacks to facilitate maintenance.
- (d) The poloidal field coils are contained in high resistance vessels to prevent excessive toroidal current flow. It is proposed to construct the vessel from a thin cryopanel which would be vacuum tight and to provide structural support from either a fiberglass overlay or from a subdivided metallic structure properly gapped and insulated from the liner.
- (e) The outer vacuum vessel containing the coil system will carry a standard liquid nitrogen radiation shield. The space between the TF magnets and the inner vacuum chamber will be insulated

by superinsulation rather than nitrogen panels. This is dictated by the close spacing and the complication of assembly of toroidal shells. The somewhat higher losses are not important when compared with other system losses.

- (f) The interconnections between the TF coils will travel in 10 cm diameter bellows/tube assemblies located above and below the horizontal ports, and connecting the coil interconnection boxes. Only one set of TF leads to room temperature will be supplied.
- (g) It is proposed to bring all TF and PF leads at low temperature to a central lead reservoir located above the machine to facilitate maintenance access to the lead stacks without need to warm up the entire machine. We expect to utilize a thermal disconnect method to disconnect the lead stacks when the machine is not in operation to substantially reduce stand-by helium requirements.

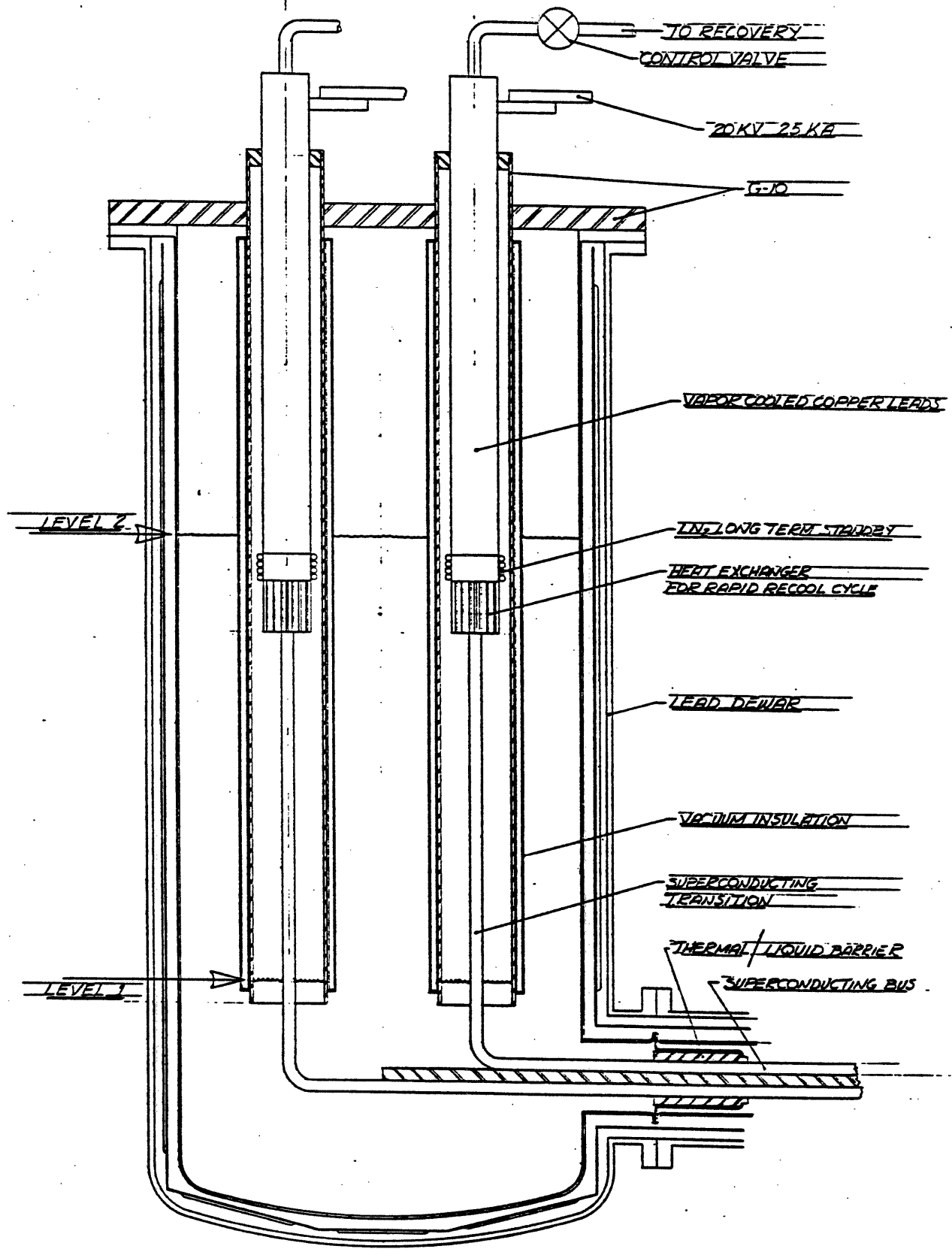
4.3.3.2. Cryogenic Refrigeration System and Loss Inventory

The cryogenic refrigeration system provides cooling for all of the magnets in the system. This system provides the combination of pulsed and steady state operation required by a typical four day series of single shift experiments. The specific refrigeration system design is based on the use of the surplus refrigeration system from the canceled MHD Component Development and Integration Facility (CDIF) as a central liquifier, and the use of two new Fermi Laboratory "Satellite" refrigeration units.

The loss mechanisms causing helium boil-off include pulsed magnetic field losses due to startup, shutdown and plasma disruptions, thermal radiation, conduction through cold mass supports and joint losses. The liquefaction requirements are dominated by the lead losses in the TF and PF system when the machine is at full excitation. Table 4.3-11 lists the individual refrigeration requirements of the system. The cryogenic refrigeration system need not circulate supercritical helium because the internally cooled TF and PF magnets utilize boiling helium at atmospheric pressure for heat removal.

The average entropy generation of the system, and thus the helium and electrical power requirements, would be dominated by helium flow through the 400 kA of total leads if no measures were taken to reduce this requirement by thermal disconnects during stand-by periods. Thermal disconnects, as illustrated in Figure 4.3-16, operate on the principle that the helium level in a lead dewar is varied between an operation level and a stand-by level. Leads of this general concept have been tested, and can alter the lead stand-by loss by a factor of 10, and can cut the overall system refrigeration needs by a factor of three.

The refrigeration system design attempts to utilize the inherent downtime of typical experimental tokamak operation (single shift operation and no runs on weekends), along with the availability of all of the CDIF equipment, in order to achieve significant cost savings. The design permits 600 W of cryogenic losses during each of four daily 8 hour experiments, with 80 discharges a day. It does not require the purchase of an additional CTI-2800, but instead allows the 200 W refrigerator to provide 1,200 W of refrigeration by purchasing two additional heat exchangers and



MODIFICATION OF - - -
 WILSON, CRYOGENICS 1973

FIGURE 4.3-16 Dual Level Current Leads Suitable for Thermal Disconnect of PF Leads.

cold turboexpander that permit stored helium to be utilized effectively. These "satellite" refrigerator units are duplicates of the 24 units used in the Fermi Laboratory "Energy Saver" Project.

TABLE 4.3-11

Cryogenic Refrigeration Load

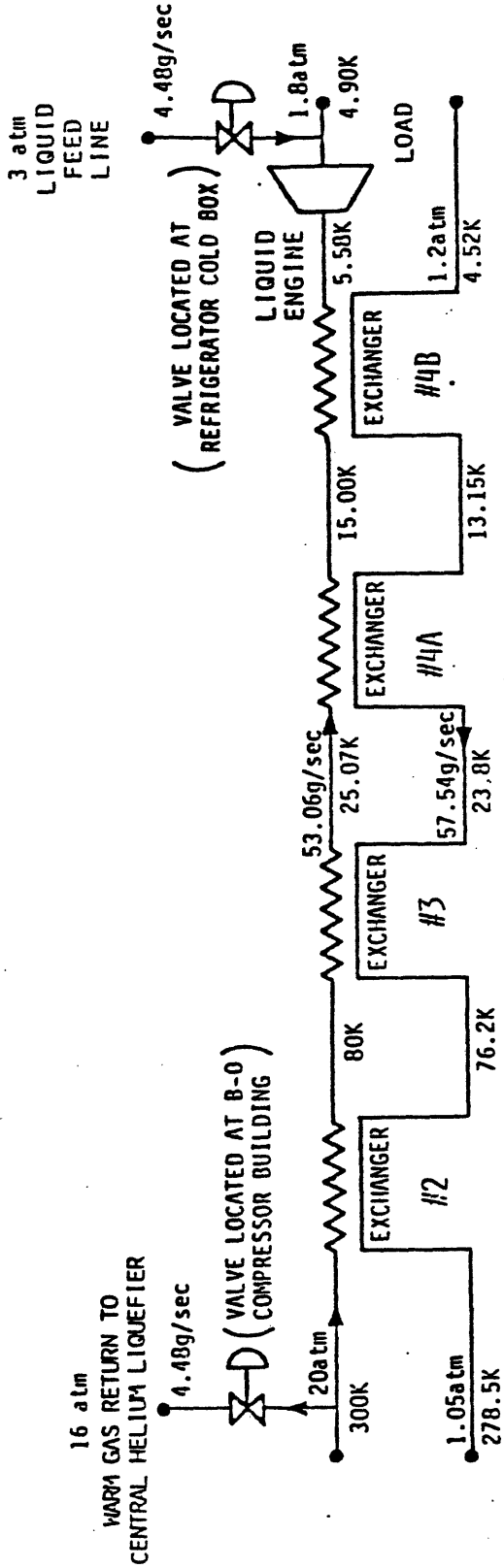
	LOSS/PULSE (kJ)	AVERAGE LOAD (W)
TF PULSED LOSSES	16.7	27.8
PF PULSED LOSSES	143	478
TF LOSSES, DISRUPTION	318	
PF LOSSES, DISRUPTION	1,018	
TF JOINT LOSSES	64.5	108
PF JOINT LOSSES	40	62
COLD MASS SUPPORTS	7.2	12
RADIATION LOSSES	64.2	107
TF LEAD LOSSES	1.4 kg	2.3 g/s
PF LEAD LOSSES	9.8 kg	16.4 g/s

The basic CTI-2800 refrigerator is run continuously as a liquifier, with a capability of generating 10,900 liters of helium per week or of filling the available 4,000 liter storage dewar in two and a half days. During operation of the tokamak, the helium level of the storage dewar is drawn down. If no additional refrigeration were available, it would be necessary to only operate the tokamak every second day. In order to avoid such a severe inconvenience, two "satellite" simplified second re-

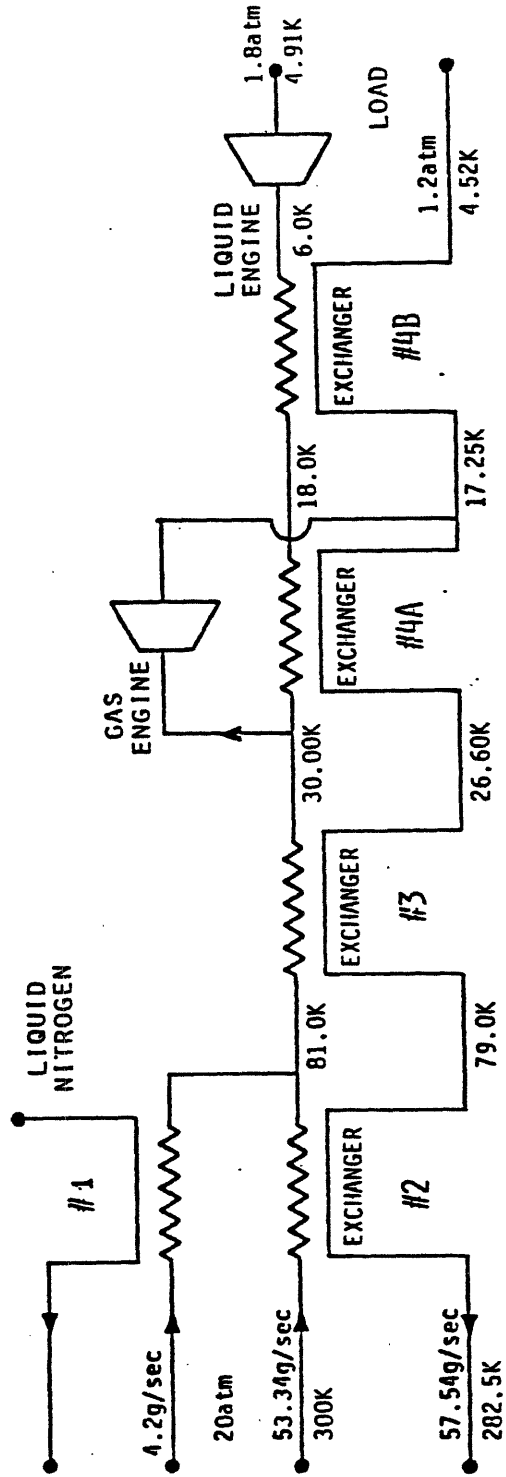
frigerators are constructed, consisting of a room temperature screw compressor (60 g/s, 1-20 atmospheres or 30 g/s, 1/2-20 atmospheres, available from Mycom or Sullair), a 600 W heat exchanger such as those built by Meyer Tool for the Fermi National Accelerator Laboratory, and a cold expansion engine, available from Koch. A simplified circuit diagram of the Fermi satellite is shown in Figure 4.3-17.

With the additional capacity available from the 1,200 W heat exchangers, the following cycle would be typical. In an 8 hour run, the storage dewar is only drawn down by 720 liters. Over a 24 hour period, the storage dewar would be drawn down by 240 liters, and by 1,000 liters over a four consecutive days of runs with no down time. This level is then replenished over the first day of the three day weekend.

When operating under true steady-state conditions, one of the two satellite units would be run as a liquifier. In this steady-state mode, the need is for a steady supply of liquid rather than to handle the uneven gas flows associated with pulse operation. The system as proposed is thus flexible enough to handle pulse mode and true steady-state mode for arbitrarily long operating times.



SATELLITE MODE



REFRIGERATOR, LIQUEFIER & E.D. STANDBY MODE
(refrigerator values illustrated)

FIGURE 4.3-17 FERMI Energy-Saver Satellite Flow Diagram.

CHAPTER 5

VACUUM VESSEL, COOLING SYSTEM and VACUUM PUMPING

5.1. Vacuum Vessel

The Alcator DCT point design vacuum vessel consists of 24 heavy wall stainless steel sections separated by bellows. The bellows serve to control toroidal resistance and to compensate for manufacturing tolerances. The vacuum vessel will not be cooled directly, but will be entirely covered by heat shields as discussed below. This strategy allows maintenance and modification of vessel cooling because the heat shields are removable. The primary vessel, particularly the back side, is essentially unreachable and we are therefore convinced that direct cooling would represent a high risk to operation.

The control of tolerance build-up in the toroidal vessel is particularly worrisome in Alcator DCT where the warm vacuum ports must penetrate through the helium temperature magnet intercoil structure without thermal contact. We would argue that the most feasible way to maintain assured clearance is to isolate the vessel into 24 independent sections separated by bellows, and to support these sections through low thermal loss supports directly from the 24 TF magnets as shown in Figure 5-1. This will assure clearance at each port locating independent of the differential temperature between chamber and magnet, but requires the use of inter-section bellows.

This concept also requires the use of rather stiff chamber elements including the port "towers" which will serve as the support elements. A preliminary design for the chamber sections is shown in Figure 5-2. Typical bellows are shown in Figure 5-3, and were used to obtain costing es-

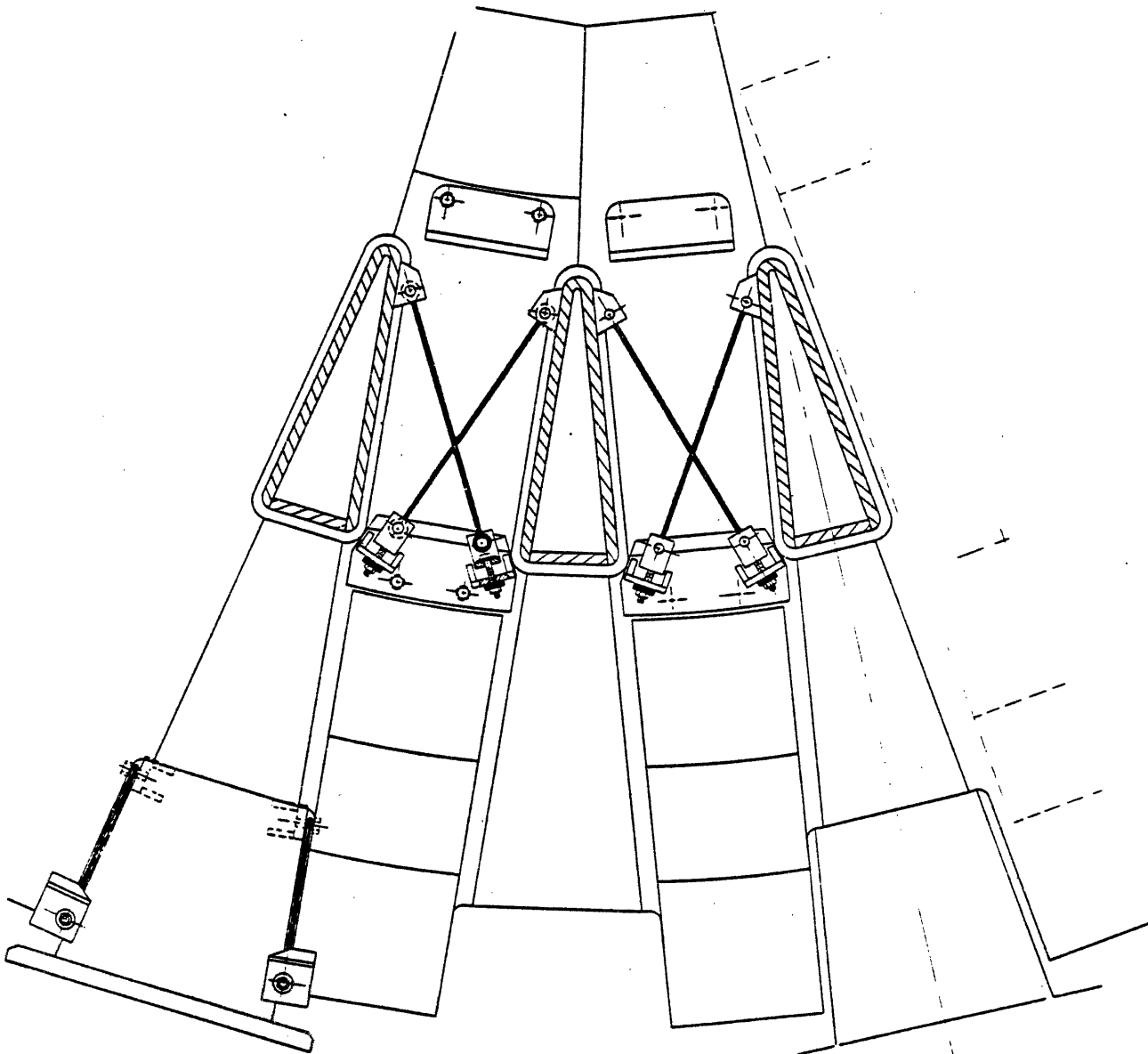


FIGURE 5-1a Plan View Vacuum Chamber Segment Support Concept.
Fiber Cables Support the Chamber from the TF Magnet.

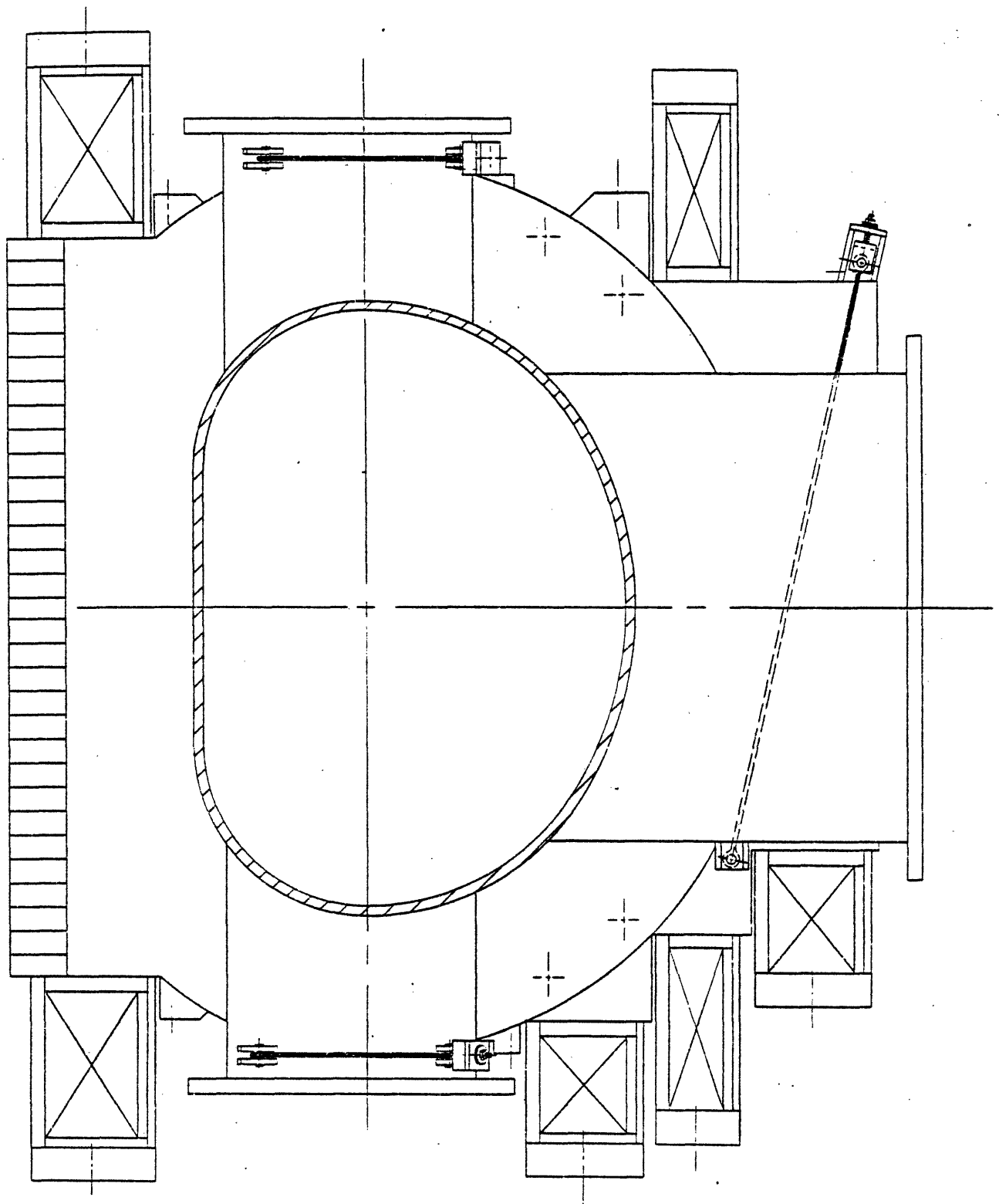


FIGURE 5-1b Elevation View of Chamber Support Concept.

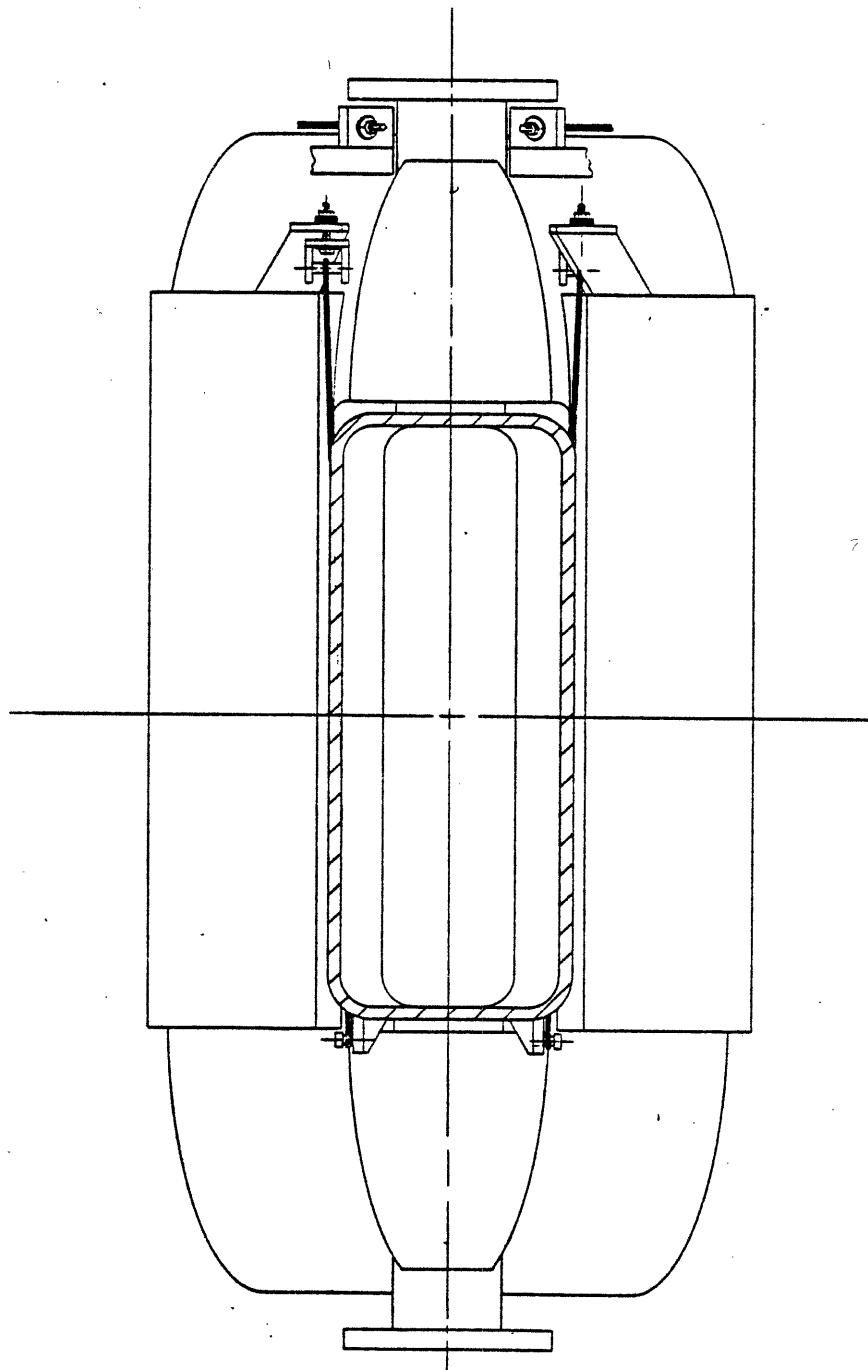
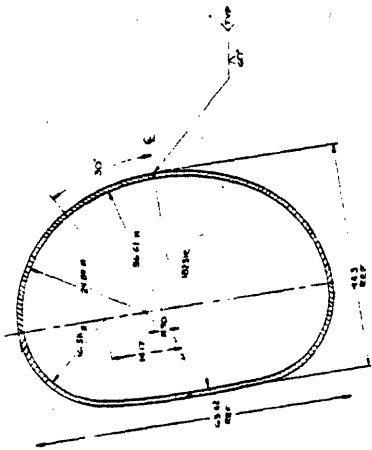
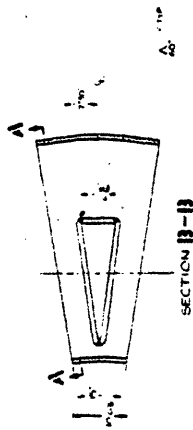
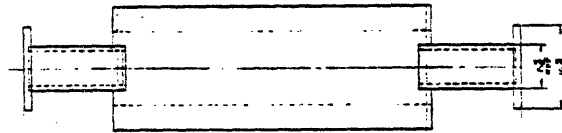


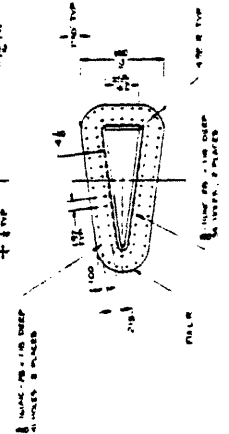
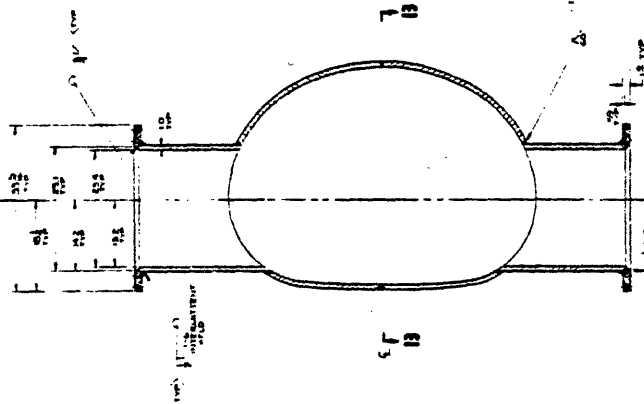
FIGURE 5-1c Vacuum Chamber Segment Supported from the TF Magnet.



SECTION A-A



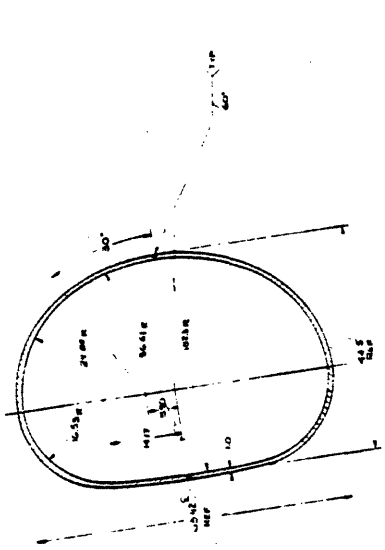
SECTION B-B



NOTES:
 1. MATERIAL: 304-L ST/ST
 2. HELIUM LEAK TEST SHALL NOT SHOW ANY LEAKAGE WITH DETECTOR SET AT A SENSITIVITY OF 1.0E-5 STD 1/100 IN. H₂O
 3. A.D. REQUIRED 12

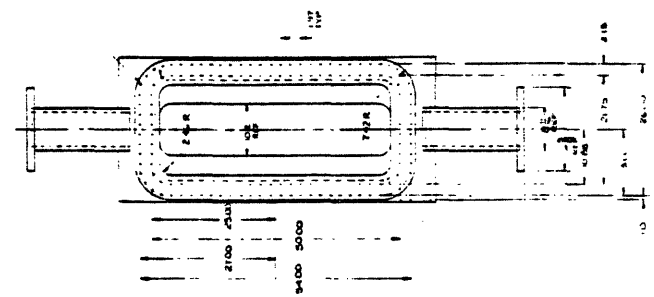
FIGURE 5-2a Two Port Vacuum Chamber Weldment.

CLASSIFICATION	UNCLASSIFIED
CONTROL	UNCONTROLLED
DATE	1980-01-14
BY	DCI-1012
REASON FOR DECLASSIFICATION	CHAMBER WITH VACUUM CHAMBER WITH VACUUM CHAMBER WITH VACUUM
DATE OF DECLASSIFICATION	1980-01-14
BY	DCI-1012

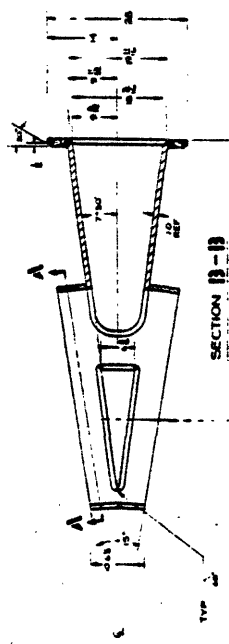


SECTION A-A

1. HOLE, 0.125 IN. DEEP
2. HOLE, 0.125 IN. DEEP



NOTES:
1. UNIT: 304-L ST/ST
2. HELIUM LEAK TEST SHALL NOT SHOW ANY LEAKAGE WITH DETECTOR SENSITIVITY OF 1.00 P.S.F. @ 1.00 IN. H₂O.
3. M.O. ACQUIRED: R



SECTION B-B

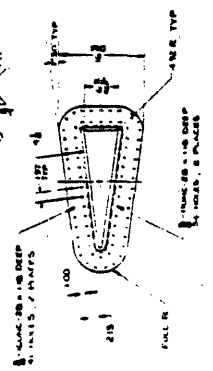
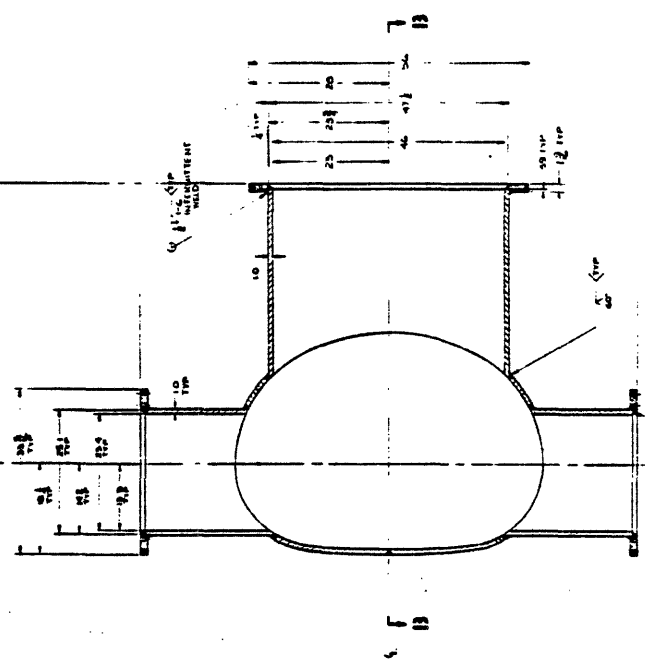
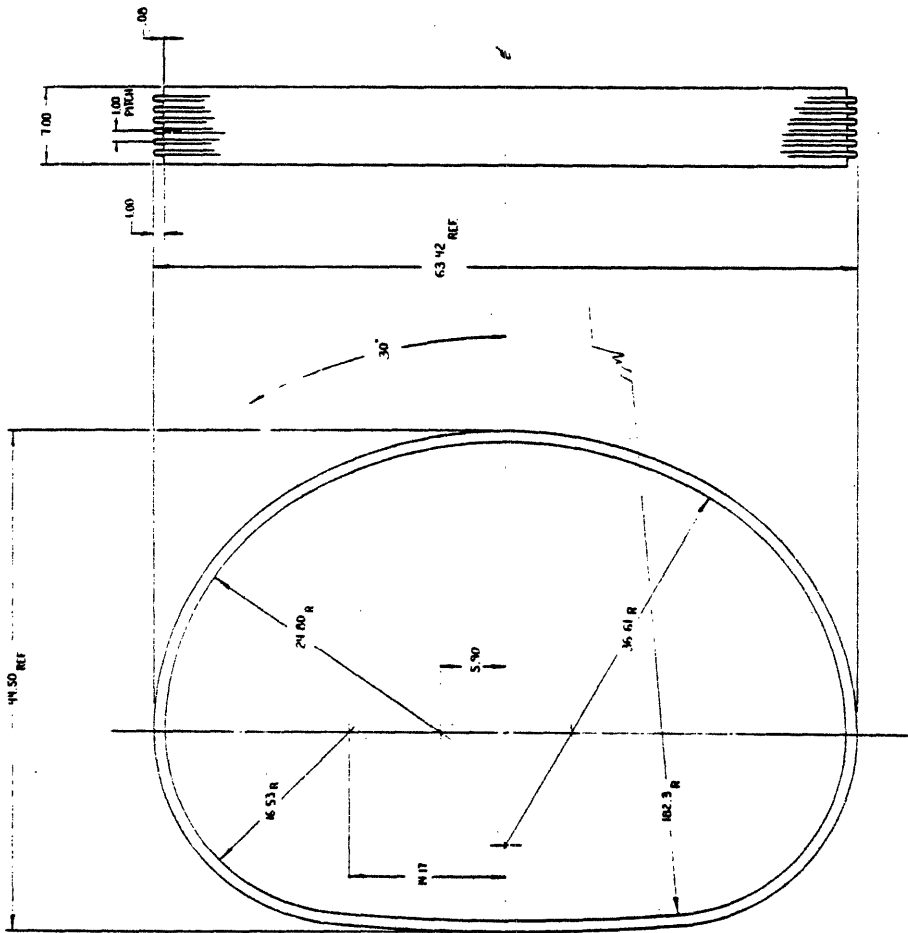


FIGURE 5-2b Three Port Vacuum Chamber Weldment.

PROJECT	DATE	DESIGNED BY	APPROVED BY
VACUUM CHAMBER WITH HELIUM LEAK TEST SENSITIVITY OF 1.00 P.S.F. @ 1.00 IN. H ₂ O.			
MASSACHUSETTS INSTITUTE OF TECHNOLOGY			
DEPARTMENT OF AERONAUTICS AND ASTRONAUTICS			
300 MASSACHUSETTS AVENUE			
CAMBRIDGE, MASSACHUSETTS 02139			

REV.	DESCRIPTION	REV. DATE	APP'D



MATL - 304-L SS, STL
 NO REQ D - 24

FIGURE 5-3 Vacuum Chamber Bellows.

PLASMA FUSION CENTER MASSACHUSETTS INSTITUTE OF TECHNOLOGY		DCT VACUUM CHAMBER BELLOW	
REV.	DATE	REV.	DATE
1	9/23/67	1	10/10/67
2	10/10/67	2	10/10/67
3	10/10/67	3	10/10/67
4	10/10/67	4	10/10/67
5	10/10/67	5	10/10/67
6	10/10/67	6	10/10/67
7	10/10/67	7	10/10/67
8	10/10/67	8	10/10/67
9	10/10/67	9	10/10/67
10	10/10/67	10	10/10/67
11	10/10/67	11	10/10/67
12	10/10/67	12	10/10/67
13	10/10/67	13	10/10/67
14	10/10/67	14	10/10/67
15	10/10/67	15	10/10/67
16	10/10/67	16	10/10/67
17	10/10/67	17	10/10/67
18	10/10/67	18	10/10/67
19	10/10/67	19	10/10/67
20	10/10/67	20	10/10/67

timates and confirm manufacturing feasibility.

An elementary stress analysis has been performed on the vessel. The vacuum vessel was assumed to be a toroidal shell interrupted by the vertical and horizontal ports. It also was assumed to operate at 300 K. At that temperature, typical strength values for stainless steels are 275 MPa for yield and 552 MPa for ultimate. The design value would be 184 MPa (2/3 yield or 1/3 ultimate) for membrane loading alone and 275 MPa for membrane plus bending.

Views of the vessel arrangement are shown on Figure 5-4. The twenty four vertical ports enter at ab and a'b. The twelve horizontal ports enter at bb'.

The loading consists of an atmospheric component, either internal or external, resulting from loss of vacuum either outside or inside the vessel. A plasma distribution pressure of approximately one atmosphere (see Appendix C) was found to peak along the equator (point c) and to fall away to negligibly small values azimuthally beyond a and a'. Conservatively, however, the disruption pressure was assumed to be one atmosphere acting either inward or outward. Consequently, the design pressures were chosen at 0.1 MPa along abb'a and 0.2 MPa aca'.

The toroidal band in the zone aca' was analyzed for ring buckling resistance. From the data on Figure 5-5, $p_{cr} = 13$ MPa which provides a factor of safety against buckling of $13/0.2 = 65$. The applied toroidal stress, $p_{1HR/A} = 13$ MPa, is negligibly small compared to 2/3 yield.

The outer region was considered to be a set of ringlike segments of poloidal extent abb'a (Figure 5-4) with toroidal extent d_e between the

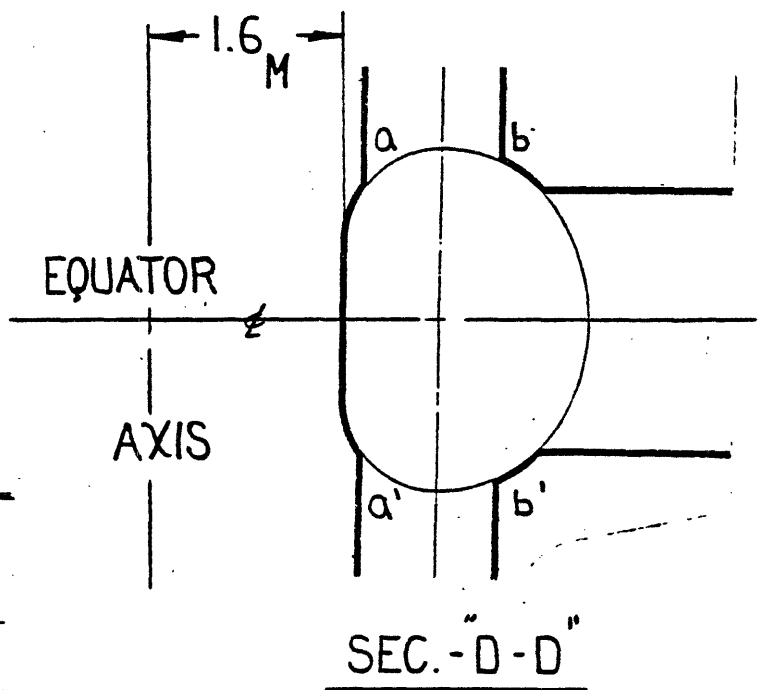
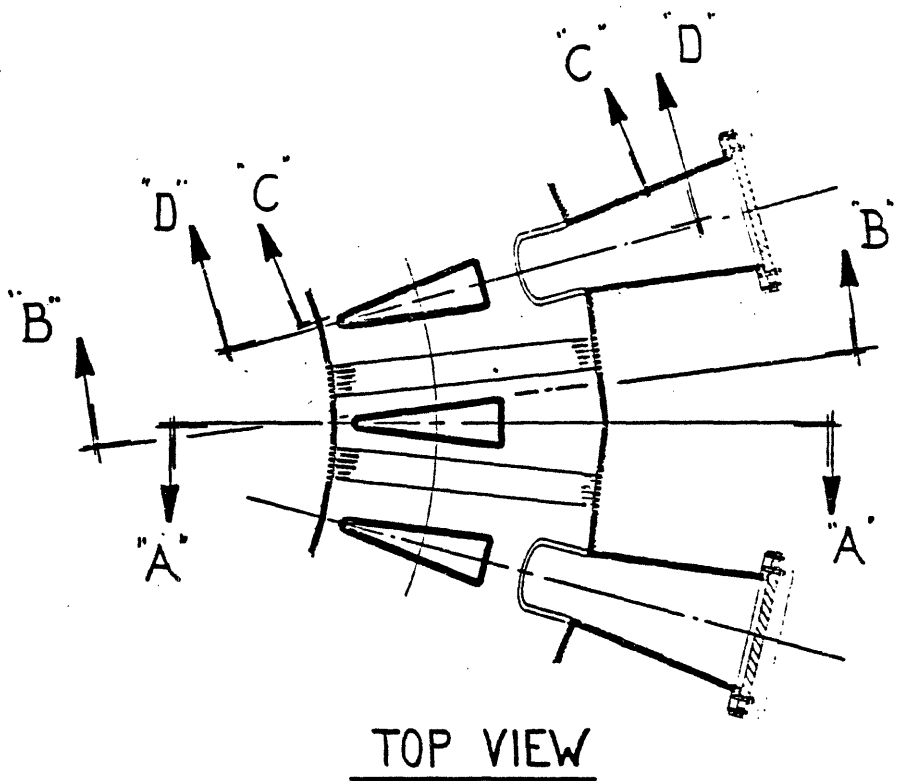
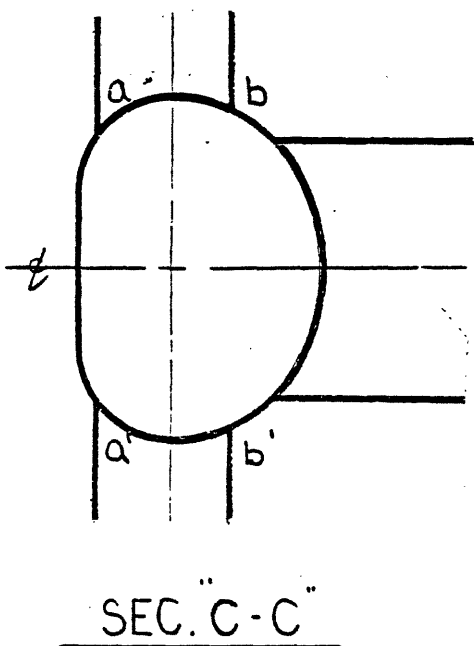
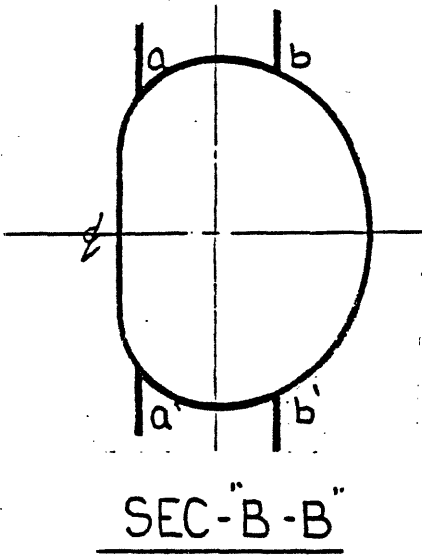
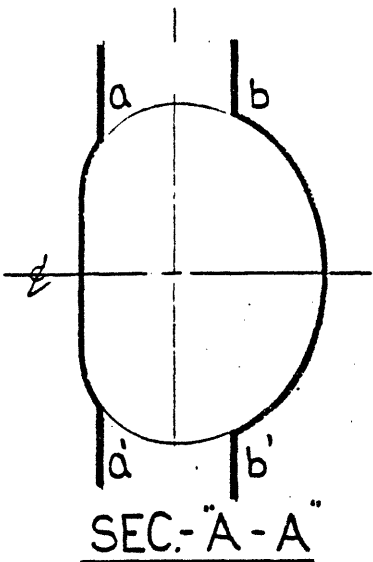


FIGURE 5-4

VIEW OF INNER VACUUM VESSEL

horizontal and vertical ports and extent ee' across a vertical port. The radial pressure creates arch action combined with bending. However, the analysis was simplified by considering the outer regions (between b and b') to be flat plates clamped at b and b' by the vertical plates of the vertical ports. There also is shear restraint from the vertical sides of the horizontal ports, which we neglected.

The bending stress is 135 MPa. The safety factor would be 2.0. In addition, the vertical port shear restraints could increase the safety factor by as much as 50 percent, according to an elementary estimate.

The buckling safety factor would be high for this region if the pressure were to be external.

5.2. Vessel Cooling System

The vessel will be cooled by heat shield elements supported from the vessel wall as indicated in Figure 5-5. These shields, further discussed in Section 3.2, must be supported against electromagnetic forces which can apply severe loading conditions. The point design calls for three shield elements in each of 24 segments. We propose to mount the segments entirely from the back-side as indicated in Figure 5-6 where "cee-like" attachments on the panels engage mating pieces on the chamber. The panel is then locked against disengagement by edge pins. This attachment technique allows limited relative motion in the toroidal and poloidal direction to accommodate differential expansion, but does not allow radial motion under electromagnetic loads.

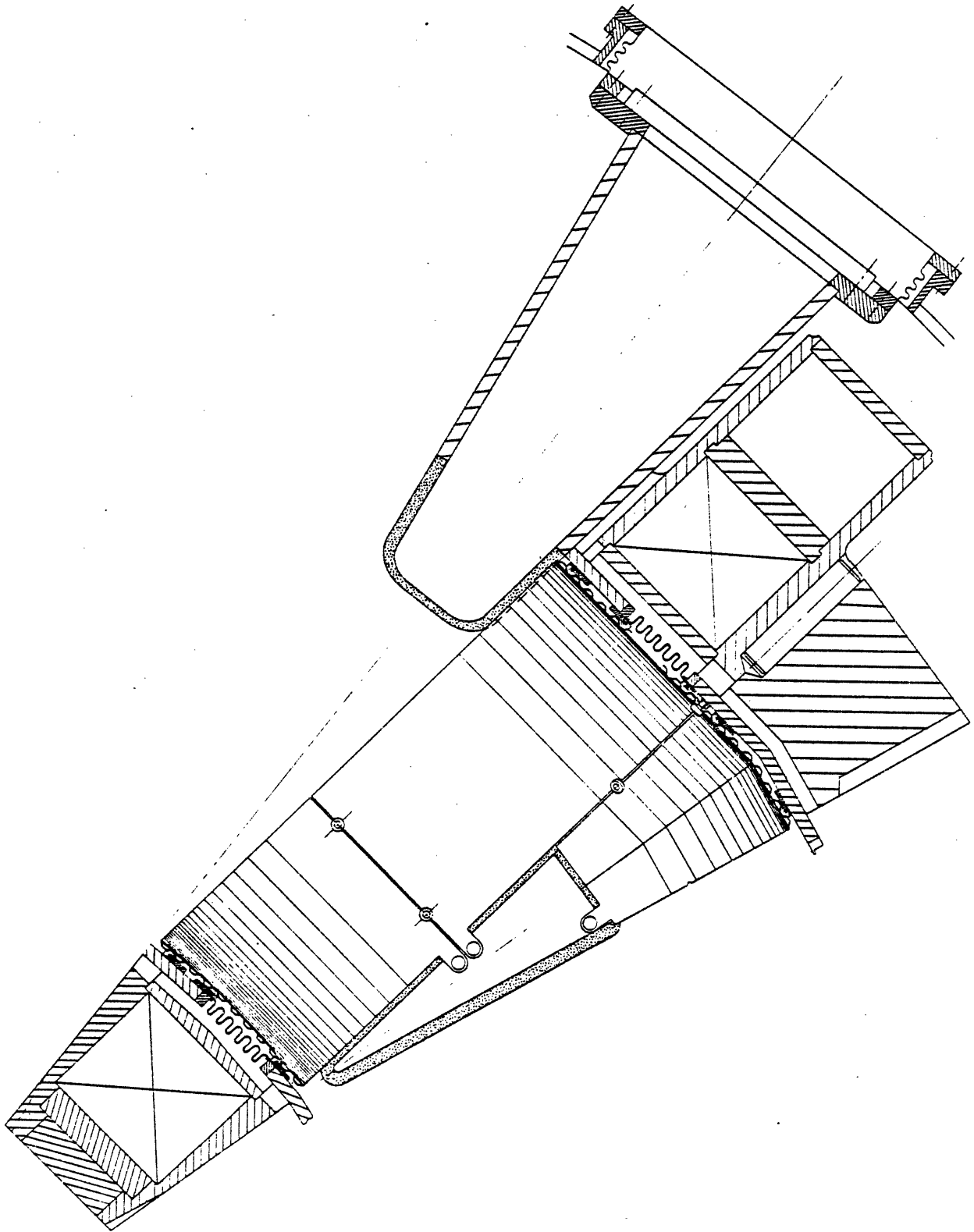


FIGURE 5-5 Water-Cooled Heat Shields to Protect DCT Vacuum Vessel.

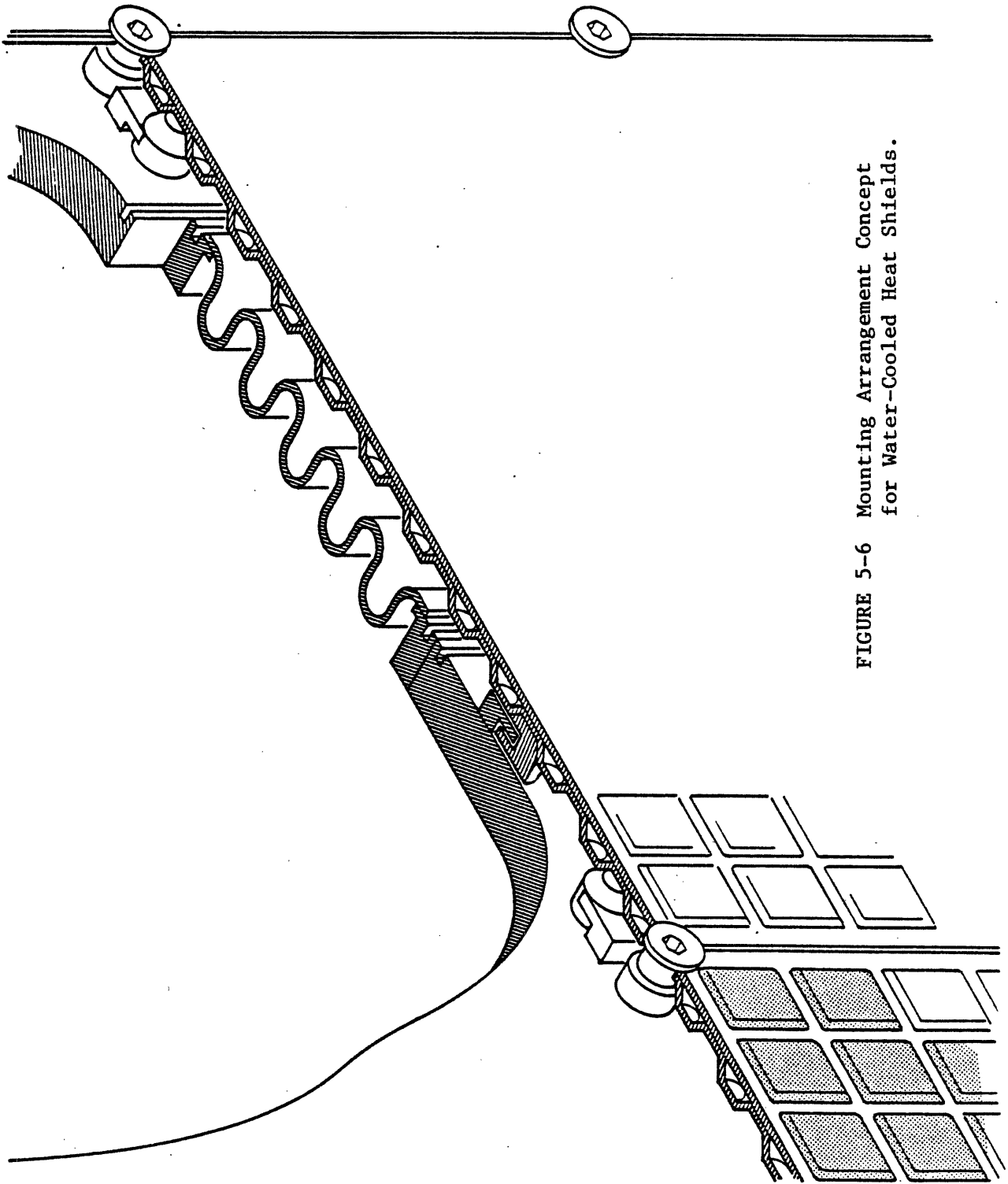


FIGURE 5-6 Mounting Arrangement Concept for Water-Cooled Heat Shields.

The heat shield elements must bridge the bellows in each section. As in common in all such bellows cover strategies there are two design options: either the shield can be electrically isolated at one edge, letting the toroidal resistance be controlled by the bellows, or it can be electrically attached and be part of the electromagnetic path. Electrical isolation is difficult to achieve with mechanical reliability. On the other hand, nonisolated elements require increased support (because of toroidal currents during disruption), and decrease the vessel resistance. If low-voltage start-up strategies are developed, we will undoubtedly elect to mechanically attach the shields without electrical isolation. If isolation is required, we would adopt strategies similar to those used on the TFTR bellows covers.

The proposed heat shields would be constructed from stainless steel and be similar to the widely used liquid nitrogen cooling panels. Typical material thicknesses would be 1.5 mm for the back surface and 2.5 mm for the front surface. Average heat fluxes (except immediately flanking the limiter or collector areas) is expected to be 0.2 MW/m^2 . We propose to use a nucleate pool boiling strategy for cooling the panels, namely to let the panel operate near 100°C , but to flow sufficient water to prevent bulk boiling. This widely used technique provides very good local heat transfer through local boiling without requiring large velocity flows. A flow of 120 liters/minute divided between the three shield elements in each of 24 segments is sufficient to prevent bulk boiling.

The total in-vessel cooling system must reject about 10 MW of heat on a steady-state basis. This must be added to the inefficiency of the RF heating system, for a total of approximately 20 MW steady-state

heat rejection in the baseline case. The Alcator DCT site is fortunate in having access to the river water cooling system installed by the Francis Bitter National Magnet Laboratory in the early 1960's. At that time a pair of 36 inch pipes were run 1,500 feet to the river passing under Memorial Drive. That line has a capacity with present pumps of 30 MW, of which the Magnet Laboratory uses approximately 10. The river water would be circulated through the secondary side of clean water heat-exchangers associated with the various cooling circuits. These new heat exchangers (which are relatively inexpensive) would be purchased for the project to avoid interference with the Magnet Laboratory clean water cooling system.

5.3. Vessel Vacuum Pumping System

Vessel pumping requirements are approximately 10,000 l/sec, with the major emphasis on pumping in the divertor collector area. The conductance through the vertical ports directly behind the collector area is large compared to this requirement (20,000 l/sec per port) and does not represent a limit. Turbo-molecular pumps are the primary candidates for vessel pumping.

CHAPTER 6

ALCATOR DCT DIAGNOSTICS

6.1. Introduction

In planning for the diagnosis of the Alcator DCT, we intend to draw heavily on the existing expertise and equipment which form an integral part of the present Alcator C effort. Several unique diagnostics, which will contribute greatly to an understanding of the behavior of Alcator DCT plasmas are presently in use on Alcator C, and at the same time, new techniques are being studied and refined for use both on Alcator C and then on Alcator DCT. Furthermore, we have identified diagnostic areas which require special attention on Alcator DCT owing to its long pulse nature. These latter include the measurement of plasma current, position and shape, all of which may require new techniques when pulse lengths of minutes or hours are contemplated. In the following sections, we first examine in detail the diagnostics which are presently available within the Alcator C program, have been proven on Alcator C, and can in a very straightforward manner be transferred to Alcator DCT. A discussion of the status of diagnostics which are presently being developed in conjunction with the Alcator C program follows. Finally, we examine the special needs which result from long-pulse/steady-state operation.

6.2. Fully Developed Diagnostic Systems

6.2.1. Multi-point Ruby Thomson Scattering

The existing Alcator C system can be used, with only very minor modifications, to measure spatial profiles of T_e and n_e on Alcator DCT. Accuracy of $\pm 5\%$ for T_e and $\pm 10\%$ for n_e can be realized. Because of the

excellent access on Alcator DCT, collection solid angle can be increased, and stray light levels reduced, so that it is reasonable to expect good signal to noise with n_e as low as $5 \times 10^{12} \text{ cm}^{-3}$. Single shot profiles at a minimum of six spatial positions are provided and more positions can be added at low cost. For the diagnosis of long pulse discharges, the laser is capable of a repetition rate of up to 4 pulses per minute.

6.2.2. Infrared Density Interferometer

The present system consists of a five chord methyl alcohol laser interferometer (119 μ), which will be well suited to the expected ranges of density for Alcator DCT. The system can in principle run steady-state, although it may be necessary to introduce a collinear He-Ne laser to compensate for long term drifts. An upgrade of the system to provide more chords can be realized at reasonable cost, and this possibility is presently being investigated.

6.2.3. Electron Cyclotron Emission

The electron cyclotron emission diagnostics now in use on Alcator C should adapt in a straightforward manner to Alcator DCT. The diagnostic system consists of three parts: 1) an adjustable Fabry-Perot interferometer to monitor continuously the central electron temperature; 2) a fast scanning Fabry-Perot interferometer to give T_e profiles every 2 msec with 2 cm resolution; 3) a Michelson interferometer which gives complete emission spectra over the range $50 \text{ GHz} < \nu < 1000 \text{ GHz}$. For non-circular discharges, the chord being viewed by the scanning Fabry-Perot interferometer can be swept with a vibrating mirror to give complete two

dimensional electron temperature profiles.

6.2.4. Neutral Particle Energy Analysis

There are presently two neutral particle energy and mass analyzers in use on Alcator C. A ten channel analyzer measures particles in the range $500 \text{ eV} < E < 40 \text{ keV}$ and is a routine ion temperature diagnostic on Alcator C. A second, five channel system, has been modified so that it views in the vertical direction. Both systems are mechanically scannable. Ion temperature time histories and profiles can in this way be measured. Minor modifications to the 10 channel system's support structure should allow for complete vertical scans in 1 to 2 seconds during quasi-steady-state plasma conditions.

6.2.5. Neutron Diagnostics

Operation at full plasma parameters in pure deuterium will not be routine for Alcator DCT. It will be possible, however, to run with modest deuterium seeding of hydrogen plasmas, and valuable diagnostic information about the ion temperature can be gained from the subsequent neutron production. The following equipment is presently available from Alcator C experiments: 1) a very high resolution ^3He spectrometer to measure the energy distribution of neutrons produced, yielding a direct measure of the ion energy distribution function; 2) a BF_3 long counter array to measure total neutron flux; 3) a Ne^{213} moderately high resolution neutron spectrometer to measure 14 MeV neutron spectra as well as 2.5 MeV spectra (from D-T and D-D reactions respectively); 4) a horizontally viewing, movable, borated water collimator which, in conjunction with one or more

of the above detector systems, can be used to provide spatially resolved neutron production rate information from which both parallel and perpendicular ion energy distribution information can be inferred. At modest cost, a multichannel vertically viewing collimator can be designed to provide continuous time behavior of the ion temperature profile. These diagnostic systems will also be used to study non-fusion neutrons arising from energetic (multi-MeV) electrons through electrodisintegration and photoneutron processes. These studies will be performed on both hydrogen and deuterium plasmas, and can provide information about energetic electron populations in ohmic and RF current driven discharges.

6.2.6. Visible and UV Spectroscopy

6.2.6.1. Survey of Intrinsic Impurity Levels

Because of the long pulse nature of Alcator DCT, the monitoring of impurity levels is extremely important. In order to achieve routine surveys of impurity levels in Alcator DCT, the rather complete set of instrumentation presently operating on Alcator C will be utilized. This set includes: a 1.5 meter visible and near UV time resolving spectrograph (2200 Å to 7000 Å) which can be used to observe the time histories of up to 15 lines simultaneously; an 0.125 meter far UV monochromator (1200 Å to 2300 Å) used mainly to monitor emission from low Z impurities and neutral and molecular hydrogen; an 0.2 meter extreme UV monochromator (400 Å to 1500 Å) which can monitor the low Z impurities as well as intermediate charge states of the heavier metallic impurities such as Fe and Mo which could be present; a 1 meter grazing incidence monochromator (40 Å to 600 Å) mainly used to monitor higher ionization stages of the metallic impurities; a 2.2 meter grazing incidence, time resolving spectrograph

(18 Å to 600 Å) which can monitor any 40 Å section within its spectral range, having 4 msec time and 0.5 Å spectral resolution; and finally visible continuum monitors which basically measure chordal integrals of $n_e^2 \times Z_{\text{eff}}/\sqrt{T_e}$, thus providing a direct measurement of total plasma impurity levels. The presently operating continuum instruments include 2 single channel systems, and a 20 channel imaging array.

6.2.6.2. Doppler Broadening and Shifts

Measurement of the Doppler broadening of far UV lines from both intrinsic and injected impurities can be used to infer ion temperature profiles. A high resolution, multichannel detector, with sensitivity from 1200 Å to 3000 Å, is presently being built by the group headed by H. W. Moos at Johns Hopkins University. It is expected that this new detector system will be tested on an existing 1 meter normal incidence vacuum instrument, which has previously been used on Alcator C with a vibrating mirror and single detector to measure Doppler widths. The new combination will yield Doppler profile measurements of single impurity lines with a time resolution of about 4 msec. This instrumentation can also be used to measure shifts in the energies due to bulk plasma rotation.

6.2.7. X-ray Diagnostics

6.2.7.1. Spectroscopic

The measurement of X-rays provides information concerning the electron distribution function (from both the hard and soft continua), impurity concentrations (from $\Delta n = 1$ impurity line strengths in medium and high Z impurities) and the ion temperature (from Doppler broadening

line emission). If the electron distribution function is Maxwellian, the electron temperature can be determined. Populations of RF induced non-thermal electrons, as well as run-away electron production, can also be monitored via the resulting medium and hard X-ray emissions. Systems presently in service on Alcator C include: two Si(Li) pulse height detectors ($500 \text{ eV} < h\nu < 10 \text{ keV}$, 200 eV resolution); an HgI_2 pulse height detector ($5 \text{ keV} < h\nu < 100 \text{ keV}$, 500 eV resolution); a flat crystal monochromator ($1 \text{ keV} < h\nu < 8 \text{ keV}$, 50 eV resolution); an 8 channel, collimated NaI detector system ($10 \text{ keV} < h\nu < 500 \text{ keV}$, 1 keV resolution); a compact curved crystal time resolving spectrometer for measuring Doppler widths ($2000 \text{ eV} < h\nu < 3500 \text{ eV}$, 0.5 eV resolution); a multi-chord collimated NaI detector array to measure hard X-rays produced at the walls and limiter/divertor plate structures ($0.5 \text{ MeV} < h\nu < 20 \text{ MeV}$).

6.2.7.2. Broad Band Diode Arrays

An X-ray tomography diagnostic is feasible for Alcator DCT. Much of the work which is required to develop such a device is being carried on at the present time for a prototype experiment on Alcator C. This includes circuitry design, materials processing (i.e., the brazing of beryllium to stainless steel), and development of better computer reconstruction algorithms. In addition, after the prototype is installed on Alcator C, other potential problems such as detector noise and channel cross talk will be addressed.

The most desirable configuration for such an instrument would consist of about 400 detectors arranged on 50 array chips and encased in a ring-shaped stainless steel housing that would surround the plasma at one

toroidal location. The ring should fit just inside the vacuum chamber wall in the shadow of the limiter structure and would not necessarily have to take up significant port access space. (It could be shifted sideways after insertion.)

The bremsstrahlung emission from a Alcator DCT plasma will deposit roughly the same amount of power on the X-ray detector surfaces as an Alcator C discharge. (The longer path length and higher temperature are offset by the somewhat lower density.) Therefore, we can use the same type and size detectors and apertures, and even the same circuitry.

In addition to the tomography diagnostic, we will probably want a few small detector arrays at different toroidal locations to check on toroidal asymmetry and toroidal mode numbers of instabilities. Three such arrays presently exist, and have been implemented on Alcator C. With various filters, these arrays have also been used to study the details of the transport of injected, trace impurities on Alcator C, and it is anticipated that this work would continue on Alcator DCT.

6.2.8. Bolometry

In the attempt to understand the overall power balance and the contribution that radiation makes in the various regimes of operation on Alcator DCT, bolometric measurements of total power radiated to the walls will play an important role. The present bolometric array on Alcator C has 16 collimated channels, covering approximately 30 cm. The detectors are discrete thermistors. Without modification, this array could be used to view approximately one half of the Alcator DCT plasma at a time. The addition of a scanning mechanism will allow access to the entire profile in one dimension.

6.2.9. CO₂ Scattering

CO₂ laser scattering has been demonstrated to provide an important diagnostic capability during lower hybrid heating and current drive experiments on Alcator C. In addition, this technique can be used to study the low frequency edge fluctuations which have been shown to influence the propagation of driven lower hybrid waves. The device presently operational on Alcator C is a CW diagnostic for which longer machine pulses can be readily accommodated. A machine pulse which is long enough that a quasi steady-state is reached for at least five seconds would permit determination of the N_{||} spectrum of the driven lower hybrid wave during a single discharge.

6.2.10. Edge Plasma and Wall Diagnostics

Since one of the main goals of the Alcator DCT device will be to examine impurity generation and heat and particle removal at walls and limiter/divertor plate structures, detailed analysis of the limiter shadow and divertor plasma properties will be very important. Much attention has been paid to edge plasma and material interaction issues on Alcator C, and as a result, a substantial number of edge probes (Langmuir type) and their associated instrumentation have been developed. There have also been numerous studies performed with limiters and probes instrumented with thermocouples. As a result, the expertise exists within the Alcator group to design and carry out similar studies on Alcator DCT. These studies, coupled with the extensive spectroscopic techniques available, as described in 6.2.6, should yield an excellent understanding of the edge plasma and its interactions with the material structures of the limiter, first wall, and divertor plates.

6.3. Diagnostic Systems In Development

In a number of areas, diagnostic development continues, both for near term use on Alcator C, as well as for Alcator DCT. The main areas of research are as follows.

6.3.1. Nd:YAG Thomson Scattering

A quasi-continuous Thomson scattering diagnostic based on a repetitively Q-switched Nd:YAG laser is now under development for installation on Alcator C. This system will measure T_e and n_e at a single spatial point, at a minimum repetition rate of 50 Hz for periods of up to eight seconds. Additional spatial points have been allowed for in the optical and detection system design. This capability would permit profiles of T_e and n_e to be monitored as functions of time on a single discharge. No such diagnostic with the unique combination of short averaging time (the laser pulse width of 20 nsec), quasi-continuous time resolution (the interpulse period of 20 msec), and the ability to determine an entire profile currently exists. Operation of the diagnostic at lower pulse rates for very long Alcator DCT pulses should not be difficult.

6.3.2. CO₂ Dual Wavelength Interferometer

An interferometer system utilizing the CO₂ line, in combination with the visible He-Ne line to measure vibrational fringe shifts, is being considered. A line average density of $1 \times 10^{14} \text{ cm}^{-3}$ and minor radius of 40 cm correspond to 0.5 fringes at the CO₂ wavelength. Such a device could provide spatial resolution of 1-2 cm over a large number of parallel chords. In addition, such a system would be very useful for monitoring

the large increments in density caused by the injection of frozen hydrogen pellets.

6.3.3. Neutral Particle Analyzer

A new neutral particle analyzer is needed to accommodate several research needs. The energy measurement capability should be expanded to 80 keV to be compatible with the ICRF experiments. Simultaneous dual mass resolution is also desirable for the RF experiments, as well as for pellet injection and H-D isotope exchange studies. Such an analyzer would be designed so that it could be used in a fast mode for studying transient phenomena on MHD time scales.

6.3.4. Diagnostic Neutral Beam

A diagnostic neutral beam would aid the spatial resolution of the charge exchange diagnostics, as well as providing a source of neutrals for spectroscopic measurements of charge exchanged impurity ions. In order to penetrate the relatively large, dense DCT plasma, a beam energy of about 50 keV would be required.

6.3.5. Time of Flight Low Energy Neutral Spectrometer

A time of flight analyzer for studying the energy and density of the edge neutrals is desirable for Alcator DCT. The long pulse length with associated pump out and recycling problems make this an interesting diagnostic for this plasma. The current Princeton design can resolve particle energies as low as 12 eV and as high as 2000 eV. Such a system is presently being constructed for use on Alcator C.

6.3.6. X-ray Spectroscopy

i) A multi-channel flat crystal array is under development which will allow examination of the detailed time development of electron temperature. This should prove to be useful in the study of such plasma phenomena as internal disruptions, as well as providing another temperature measurement which can be used for true steady-state operation.

ii) A multi-channel system to measure radial profiles of ion temperature through impurity line Doppler widths is under development. The system will be a straightforward extrapolation of the single channel compact curved crystal instrument which is currently in use.

iii) A rotating flat crystal instrument, which will provide a complete spectrum between 1 Å and 10 Å every 8 msec is also being developed. This device will allow convenient survey monitoring of impurity lines due to elements from Al through Mo which could occur in the plasma.

6.3.7. Infrared Surface Temperature Measurements

In order better to understand the interaction between the plasma and either limiter or divertor plate structures, it will be necessary to monitor surface as well as bulk temperature increases. We are presently investigating various infrared imaging systems to accomplish the first of these goals, and anticipate that one or more of the commercially available systems will be a part of the initial Alcator DCT diagnostics package.

6.3.8. Charged Fusion Product Measurements

A proton spectrometer is being developed for measuring the energy spectrum of 3 MeV protons arising from D-D reactions. The system, consisting of collimated Si(Li) detectors, will provide information on the ion energy distribution function. The instrument will also yield valuable, spatially resolved, information about the confinement of energetic charged particles.

6.4. Special Steady-State Diagnostics Issues

Certain conventional plasma diagnostics may not be adequate for the diagnosis of very long pulse discharges. In particular, any technique using time derivatives of physical quantities as the basis of the measurement may run into trouble. Examples include external loops to detect plasma position and plasma current. It appears unlikely that conventional systems can be designed to measure, for example, very slow changes in plasma current over a period of many minutes or hours. While a complete set of conventional external loops and coils are included as part of the Alcator DCT design, we are presently investigating several alternative methods, particularly for the measurement of plasma current and position. Plasma position and shape could, in principle, be monitored in real time with X-ray arrays, visible plasma-TV imaging, and/or the density interferometer array. Novel solutions to problems associated with the external loops include the possibilities of using arrays of Hall probes, superconducting loops, or fiber optic loops which can measure $\int \vec{B} \cdot d\vec{\ell}$ through the Faraday rotation effect. All of these approaches are being investigated in detail, and the final choices have not been made at this time.

6.5. Summary

The diagnostic systems described in this chapter are summarized in Tables 6.5-1 and 6.5-2. Table 6.5-1 enumerates the systems which are presently fully developed and have operated successfully on Alcator C. Similarly, Table 6.5-2 lists those diagnostics which are presently in development for use both on Alcator C and then on DCT, as well as those special techniques which are being investigated as solutions to the special long pulse diagnostic problems which are anticipated for DCT.

TABLE 6.5-1

Fully Developed Diagnostic Systems

<u>Technique</u>	<u>Measured Parameters</u>	<u>Features</u>
1. Ruby Thomson Scattering	$T_e(r); n_e(r)$	Minimum of 6 spatial points, 4 pulses per minute
2. FIR Density Interferometry	$n_e(r,t)$	$\lambda = 119 \mu\text{m}$, 5 spatial points
3. Electron Cyclotron Emission:		
a) Adjustable Fabry-Perot	$T_e(r, t)$	Measures time history at single spatial point. Complete T_e radial profile every 2 msec. Covers $50 \text{ GHz} < \nu < 1000 \text{ GHz}$
b) Fast scanning Fabry-Perot	$T_e(r,t)$	
c) Michelson Interferometer	Emission Spectra	
4. Neutral Particle Energy Analysis	$T_i(r,t)$; Ion Distribution Function	Two systems in operation
5. Neutron Diagnostics		
a) ^3He Spectrometer	$T_i(r=0,t)$	Total Neutron Flux
b) BF_3 Long Counter Array	Total Neutron Flux	
c) Ne^{213} Spectrometer	Energy Spectra of both D-D and D-T produced neutrons	
d) Borated Water Collimator	$T_i(r)$	
6. Visible and UV Spectroscopy		
a) 1.5 Meter Visible Near UV Time Resolving Spectrograph	Line Emission	$2200\text{\AA} < \lambda < 7000\text{\AA}$ with 15 lines viewed simultaneously
b) 0.125 Meter Far UV Monochromator	Line Emission	$1200\text{\AA} < \lambda < 2300\text{\AA}$
c) 0.2 Meter Extreme UV Monochromator	Line Emission	$400\text{\AA} < \lambda < 1500\text{\AA}$
d) 1.0 Meter Grazing Incidence Monochromator	Line Emission	$40\text{\AA} < \lambda < 600\text{\AA}$
e) 2.2 Meter Grazing Incidence Time Resolving Spectrograph	Line Emission	Covers any 40\AA slice between 18\AA and 600\AA , with 4 msec time and 0.5\AA spectral resolution.
f) Visible continuum monitors	$n_e^2 \times Z_{\text{eff}}/\sqrt{T_e}$	20 channel imaging array and 2 single chord systems presently operating.

TABLE 6.5-1 Cont'd.

Fully Developed Diagnostic Systems

<u>Technique</u>	<u>Measured Parameters</u>	<u>Features</u>
7. X-ray Diagnostics		
a) Two Si(Li) Pulse Height Analysis Systems	$T_e(r, t)$	500 eV < $h\nu$ < 10 keV, 200 eV energy and 50 msec time resolution
b) HgI ₂ Pulse Height System	$T_e(r, t)$; Electron tails	5 keV < $h\nu$ < 100 keV, 500 eV resolution
c) Flat crystal monochromator	Line and Continuum Emission	1 keV < $h\nu$ < 8 keV, 50 eV resolution
d) NaI Multichannel Pulse Height System	Spatially Resolved X-ray Spectra; RF Induced Electron Tails	10 keV < $h\nu$ < 500 keV, 1 keV resolution, 8 channel collimated system
e) Compact Curved Crystal Time Resolving Spectrograph	$T_i(r, t)$; $T_e(r, t)$; $n_o(r, t)$	2 keV < $h\nu$ < 3.5 keV, 0.5 eV resolution. Measures Doppler broadening of impurity lines.
f) NaI Array	Hard x-rays produced at walls and limiter/divertor plate structures	0.5 MeV < $h\nu$ < 20 MeV spatially resolved
g) Broad Band Diode Arrays	Plasma position and shape; MHD activity; impurity transport	Fully two-dimensional tomographic reconstructions are feasible.
8. Bolometry	Total radiated plus charge exchange power from plasma	16 channel, spatially resolved
9. CO ₂ scattering	Fluctuations; Driven lower hybrid waves	
10. Langmuir Probes	Edge temperature and density profiles	Poloidal and radial scanning capability with multi-probe arrays.

TABLE 6.5-2

Diagnostic Systems In Development

<u>Technique</u>	<u>Measured Parameters</u>	<u>Features</u>
1. Nd:YAG Thomson Scattering	$T_e(r,t); n_e(r,t)$	50 Hz repetition rate
2. CO ₂ Dual Wavelength Interferometry	$n_e(r,t)$	Multi-chord, CW operation. Able easily to follow density rise with pellet injection.
3. Neutral Particle Energy Analysis	$T_i(r,t);$ ICRF produced ion tails.	Extended energy range (to 80 keV); simultaneous dual mass resolution.
4. Diagnostic Neutral Beam	$T_i(r,t);$ Impurity density profiles	Improved spatial resolution for charge-exchange measurements; central T_i from broadening of impurity lines populated by charge-exchange recombination.
5. Time of Flight Low Energy Neutral Spectroscopy	Edge T_i and neutral density	10 eV < E < 2000 eV
6. UV Doppler Broadening Spectroscopy	$T_i(r,t)$	1200Å < λ < 3000Å, multi-channel system to yield line profile every 4 msec.
7. X-ray Diagnostics		
a) Multi-channel flat crystal spectrograph	$T_e(r,t)$	1 msec time resolution
b) Multi-chord curved crystal spectrograph	$T_i(r,t)$	Measure up to 10 chords simultaneously
c) Rotating flat crystal spectrograph	Line and continuum emission	1Å < λ < 10Å, scan every 8 msec
8. Infrared Surface Temperature Measurements	Limiters/divertor plate surface temperatures	
9. Collimated Si(Li) Detectors	Production rate and Confinement of D-D produced 3 MeV protons	

TABLE 6.5-2 Cont'd.

Diagnostic Systems in Development

<u>Technique</u>	<u>Measured Parameters</u>	<u>Features</u>
10. Special Long Pulse Diagnostics		
a) Hall Probe Arrays	Plasma current; Position;	
b) Superconducting Loops	Shape; $\beta_p + \ell_i/2$	
c) Fiber Optic Loops (Faraday Effect)		

CHAPTER 7

DATA ACQUISITION and CONTROL

7.1. Data Handling

The end product of any experiment is a set of analyzed data. In the case of magnetic fusion experiments this data set is enormous. For Alcator C, 1 - 2 megabytes of raw data are acquired per shot; approximately 100 megabytes are accumulated per day. For a long-pulse/steady-state experiment such as Alcator DCT, it is more useful to express computational requirements by the average rate, megabytes/hour rather than megabytes/shot. We plan to handle 20-30 megabytes/hour. To be useful this data must be efficiently acquired, stored, displayed and analyzed.

There are substantial advantages in having data available for analysis immediately after a shot, and in completing preliminary processing between shots. Operational parameters can be adjusted in response to the results and machine performance can be more quickly optimized. In addition, systematic parameter scans can be carried out more efficiently. In the case of very long pulse and quasi-steady-state operation, some quantity of data must be analyzed and displayed in real time. In all cases, the physics staff can work most effectively when data is made available quickly.

Real time operations represent a new regime for tokamak data systems. At present, data is archived and an adequate level of analysis is performed in the 5 minute period between shots. However, the real-time capacity of such a system is smaller by the duty factor, (of the order of 10^{-3}). Thus we would have to reduce the data rate by almost a factor of 1000 to allow the present system to keep up. Since we cannot expand our cap-

abilities by three orders of magnitude, we propose to handle the real time problems by a modest increase in processing power, a substantial reduction in the data rate for real time processing, and a system designed for good performance and flexibility. The mix of real-time and between shot work loads will not be known until we gain operational experience with a long pulse device. The overall goal is to maximize system throughput with the finite hardware and personnel resources available.

7.1.1. System Description

Figure 7-1 shows a schematic of the proposed Alcator DCT data acquisition system. The interface to individual plasma diagnostics is through CAMAC modules. Some front-end intelligence may be provided in the CAMAC crates. These crates communicate with the computer system over a fast serial link. In the diagram, two computers are dedicated to data acquisition and two to analysis. There is a back-end storage network to facilitate rapid data sharing. The computers also communicate over a local area network which also links the data acquisition system through the PFC VAX to the MFE computational facility. A smaller diagnostic development system, with its own CAMAC loop, is provided to allow off-line development of diagnostic hardware and software. Display stations provide rapid presentation of raw or slightly processed data. Users access the analysis computers through the local network. Work stations for local graphics processing may be provided to off-load those tasks from the main computers.

The architecture shown in the figure offers many advantages. Each of the computers is of the same type, although not necessarily the same

DCT DATA ACQUISITION SYSTEM

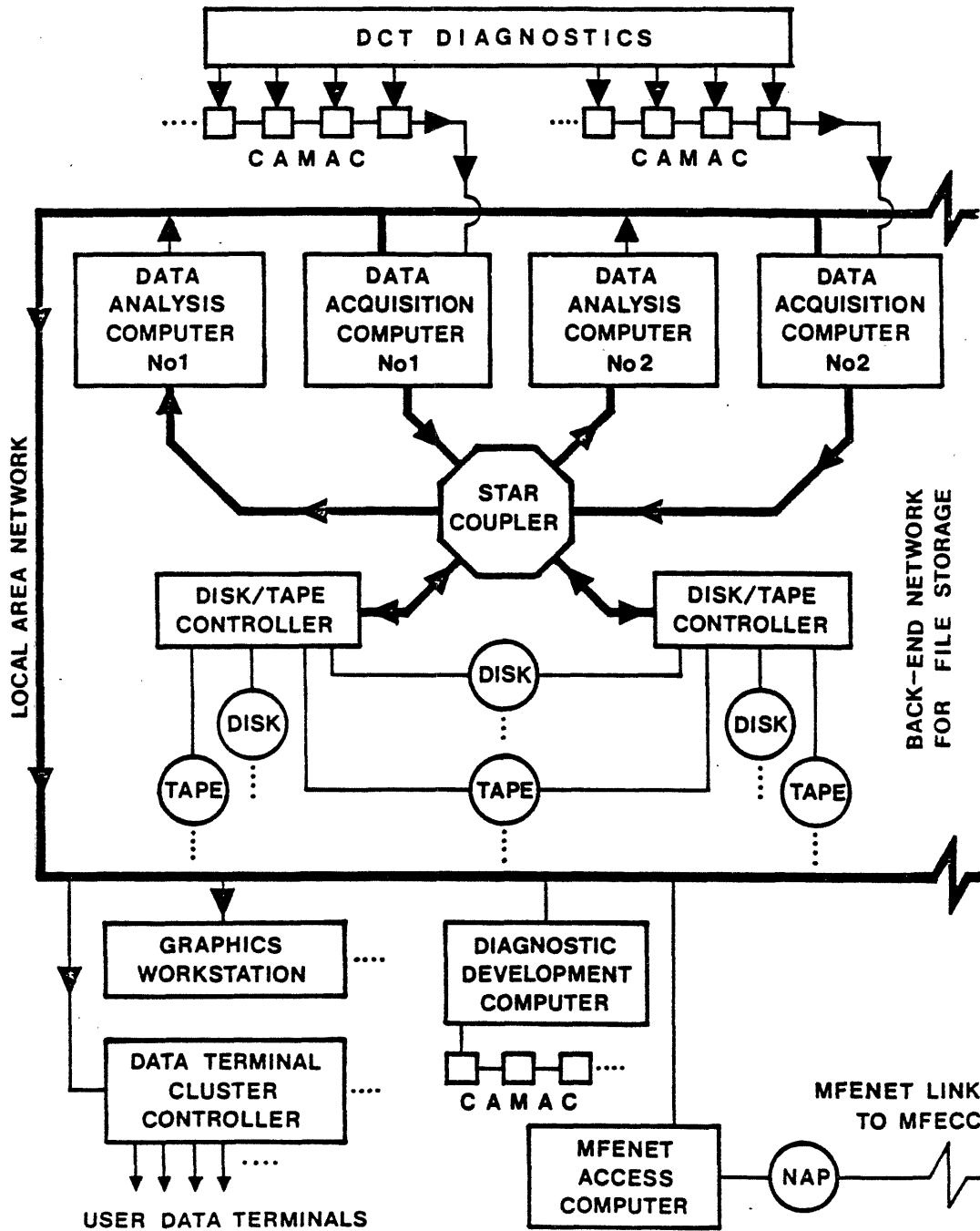


FIGURE 7-1

model, and each runs the same operating system. This simplifies software development, eases hardware and software maintenance and provides a level of redundancy. Similarly, communications links are standardized. The CAMAC and serial highway are intrinsically standard and modular. The back-end storage allows acquired data to be immediately available for full analysis. Often, distributed processing systems trade their processing problems for communications problems. With much diagnostic data, information from several sources must be combined for analysis. With the system we propose, the data base for all diagnostic data is unified, eliminating the communications difficulties. With a single data base we can maximize the storage at a single node, allowing us to keep data on line longer. Finally, the modular nature of the structure allows for easy development and growth.

7.1.2. Data Acquisition Hardware - CAMAC

The Alcatraz DCT data acquisition system utilizes CAMAC hardware much like that used in the Alcatraz C experiment. CAMAC, an acronym for Computer Automated Measurement And Control, is an internationally accepted interface standard offering increased system flexibility, reduced hardware and software efforts, and increased system longevity. CAMAC modules are available to perform a wide variety of tasks: A/D, D/A, scalars, digital interfaces, clocks, display interfaces, terminal interfaces, etc. The standardization to CAMAC allows a standard interface to the computer system with great savings in software development time.

The link from CAMAC crates to the computer is over a serial highway interface. The serial highway signal is carried by fiber optics at rates

up to 50 MBaud. The fiber optic provides high-voltage isolation. The highway structure simplifies wiring in the experimental cell. One or two fiber optic cables circumnavigate the cell and connect all data acquisition hardware. Expansion is modular and easily accomplished.

7.1.3. Computers

We require computational bandwidth approximately three times that of the VAX-11/780 computer presently supporting the Alcatraz C experiment. To that end, we propose the acquisition of additional computers that can handle an aggregate load twice that of the VAX-11/780 to be added to the existing system.

The determination that the requirements are equivalent to three VAX-11/780's is based on our experience on Alcatraz C. The present system is already saturated; we cannot acquire more data, display more data, or analyze more data than is presently handled. We have an uncomfortable load during run time. The system is heavily utilized into the late evening for interactive data analysis, and on through the night for CPU-intensive batch jobs. For the Alcatraz DCT system, we predict a substantial increase in the data to be acquired and analyzed. However, we can and must impose more realistic limits on this growth. Even with an increase in the number of experimenters, we cannot manage more than two to three times the data presently handled, and will be limited to about 20 - 30 megabytes per hour.

We propose a division of responsibility among three or more computers. The data acquisition is best handled on a computer separate from that which handles the data analysis, as long as an efficient

communications path is available for data transfer from one to the other. Our experience shows that the data acquisition computer can be considerably smaller than the data analysis computer. An additional machine is required for development of new diagnostic interfaces and their software support, in an "offline" mode that will not conflict with the experimental schedule. This diagnostic development computer may be small and relatively inexpensive. Specifically, analysis will require the equivalent of a VAX-11/782, data acquisition a VAX-11/750, and diagnostic development a VAX-11/730.

7.1.4. Back-End Network

It is the "back-end network" for file storage that makes the use of separate computers for data acquisition and for data analysis efficient. Disk storage and magtape archival facilities are shared among multiple computers via the back-end network. As at MFECC, each computer has access to the shared file storage devices.

The back-end network also facilitates growth. Compatible peripherals and computers can be added to the network without serious impact on the ongoing experiment. If the data acquisition computer proves to have inadequate bandwidth, a second data acquisition computer might be added to the configuration painlessly. Replacement of a computer with a larger system often involves a great deal of effort and much downtime.

The back-end network should allow us to add the existing Alcatraz C VAX-11/780 to this configuration to increase the data analysis capacity, accessing the same database on the same storage devices as the other computers. Without the back-end network, the use of two separate compu-

ters to analyze and modify the same database is quite inefficient, often leading to the decision to replace those two computers with one larger system.

The total disk storage capacity of this back-end network should be on the order of three gigabytes. The present disk storage capacity of the Alcatraz C VAX-11/780 is approximately one gigabyte. The additional requirement is equivalent to four Winchester disk drives, each with a capacity on the order of half a gigabyte in a 10.5 inch high rack-mounted module. The target for data storage capacity here is to allow online disk access for only the most recent months' data. Access to older data will require recovery from the archive tapes. If video disk technology were to mature during the lifetime of the machine, it could be incorporated into the archive system.

7.1.5. Local Area Network

The Local Area Network (LAN) is not a new concept, although the versatility of these networks is constantly improving. The computers supporting the Alcatraz Experiment, the Tara Tandem Mirror Experiment, and access to the MFE Network for the Plasma Fusion Center community should soon be connected together via an Ethernet LAN. We expect to connect the Alcatraz DCT computers to this same network.

It is this network that provides the communications path between the analysis computers and the MFECC via the MFENET access computer and NAP. The diagnostic development computer communicates with the other computers via this network, also. Although this computer is not connected to the back-end network, the LAN provides access to all of the files

available through that back-end network.

When a data terminal is connected directly to one of the computers on the LAN, that terminal can be "logged in" to any other computer on the network and used as if connected directly to the latter computer. However, such use imposes an unnecessary burden on the first computer just to handle the communications. In the future, we would hope to make use of data terminal cluster controllers, inexpensive boxes that support up to eight data terminals and connect directly to the LAN for communication with any of the associated computers. Graphics work stations can also be connected directly to the network instead of to a specific computer when such work stations might benefit from access to multiple computers. Network overhead is an important consideration here. When any terminal's function is primarily related to a specific computer, it will still be appropriate to use a direct connection.

7.1.6. Data Display System

The Alcatraz DCT data system includes several experimenter display stations to provide graphical display of data acquired during a shot. These display stations contain high resolution color graphics monitors with suitable input devices (i.e., keyboard, pushbutton panel, track ball, joy stick, or mouse) to enable the experimenter to call up various displays.

Some of these display stations, dedicated to displaying unprocessed shot data, are tied directly into one or more of the data acquisition computers providing fast, highly specialized displays. Other similar display stations are provided for displaying processed data as well as

unprocessed data from any of the computers in the network. These more general displays do not require the immediate response characteristics of the former stations.

7.1.7. Data System Software

A software system to efficiently store and retrieve raw data as well as the results of numerous analysis programs must be included in the project. The data base management system provides data sorting, query language, report generators, and form processing. Tools to provide these services should be in place well before the start up of the machine to avoid the duplication of effort which occurs when each experimenter develops his/her own applications software.

The data system software is comprised of purchased software packages to the extent they are available to handle data manipulation, statistical analyses, plotting and display, reports and networking between the multiple computers. The use of purchased software reduces the development and support requirements that would exist if the software were predominantly developed in-house. Unfortunately, no single package or collection of software products provides the functionality required. Several man-years of effort is required to provide such a system. The resultant data system will be a blend of purchased and locally developed software integrated into a user friendly and efficient data system, allowing the experimenters to spend more time analyzing the content of the data and less time worrying about where or how the data is stored.

7.2. Automated Control System

The interface between man and machine for Alcatraz DCT is a programmable controller (PC). Commercial systems are available which can replace much of the customized, hard-wired control system used for Alcatraz C. The PC is a micro-computer with a modest amount of memory and interfaces to switch contacts, relays, motor starters, thermo-couples, etc. Programming is accomplished with a standard video terminal. Operational control can be through a terminal with touch-panel display, trackball, or light pen. Alternately, standard switches and knobs can be read by the PC which will perform a function (if allowed by the stored control program) and drive a pilot light to indicate what it has done. Some link between control system and the data acquisition computers is provided to log the control sequence and machine parameters with the data acquired for each shot.

The advantages of automated control over a hardwired system are considerable. First, there is a substantial savings in time and money. Commercial PC's are relatively inexpensive because they are produced in large numbers. Much of the hard-wiring is replaced by programmable logic; there will be lower labor costs. The control configuration is modular, which should shorten the installation time. PC's are rugged and reliable. They are often installed in factories and production facilities where the environmental control is minimal. Because the control functions are programmed, PC's offer versatility and flexibility. System documentation is excellent. After any modifications, hard copies of the control flow diagrams can be produced and distributed. Maintenance and system growth are eased by the good documentation and the modular nature of the system.

For Alcator DCT it is straightforward to automate power supply controls, vacuum systems, liner temperature control, cryogenic systems, gas injection systems, RF systems and some diagnostic subsystems. Redundant programmed and hard-wired safety interlocks would be included.

Fast programming and sequencing on a time scale much faster than 1 second are difficult with currently available PC's. Typically timing must be controlled to better than .1 msec and programming for the poloidal fields or gas injection must have resolution of a few msec. A separate CAMAC system could be used for these functions. CAMAC modules with these capabilities are already available. This solution has the disadvantage of splitting the control functions between two systems. We will vigorously pursue alternatives which meet the functional requirements and allow for an integrated control system.

Considerable effort will be put into the human controller interface. Safe and efficient operation of Alcator DCT depends on clearly displaying the system status and in providing a good mechanism for quickly and accurately entering control parameters. The programmable logic of the PC can help by alerting operators to problems and by preventing controls from being set outside of programmed limits.

CHAPTER 8

FACILITIES

8.1. Siting and Building Layout

8.1.1. Overall Site Description

The Alcator DCT will be located in the east side of the Nabisco Laboratory. The Tara tandem mirror experiment is on the west side. Figure 8.1-1 gives an overview of the proposed modifications to the Nabisco site. The square footage of various areas are given in Table 8.1-1.

We propose to retain the front portion of the large "garage" area, only leveling the floor with a new slab. The internal space within the existing one and two story Nabisco building will also be retained, and will be up-graded for use as control room and support areas.

The rear portion of the garage will be demolished in order to construct an experimental cell approximately 90 × 90 feet overall. The roof area above the new cell will be enclosed to provide a power equipment room. The cell area will be served by a 20 ton crane, large enough to lift the heaviest subsystem component.

The east side of the Nabisco site is flanked by the 220 MVA alternator and the main switch yard. The rectifier units and RF modulators, currently in the basement of the Magnet Laboratory, will be relocated into the remaining garage area, and an enclosure located on the roof of the new cell. It is considerably less expensive to relocate the equipment than to construct bus systems to the new site.

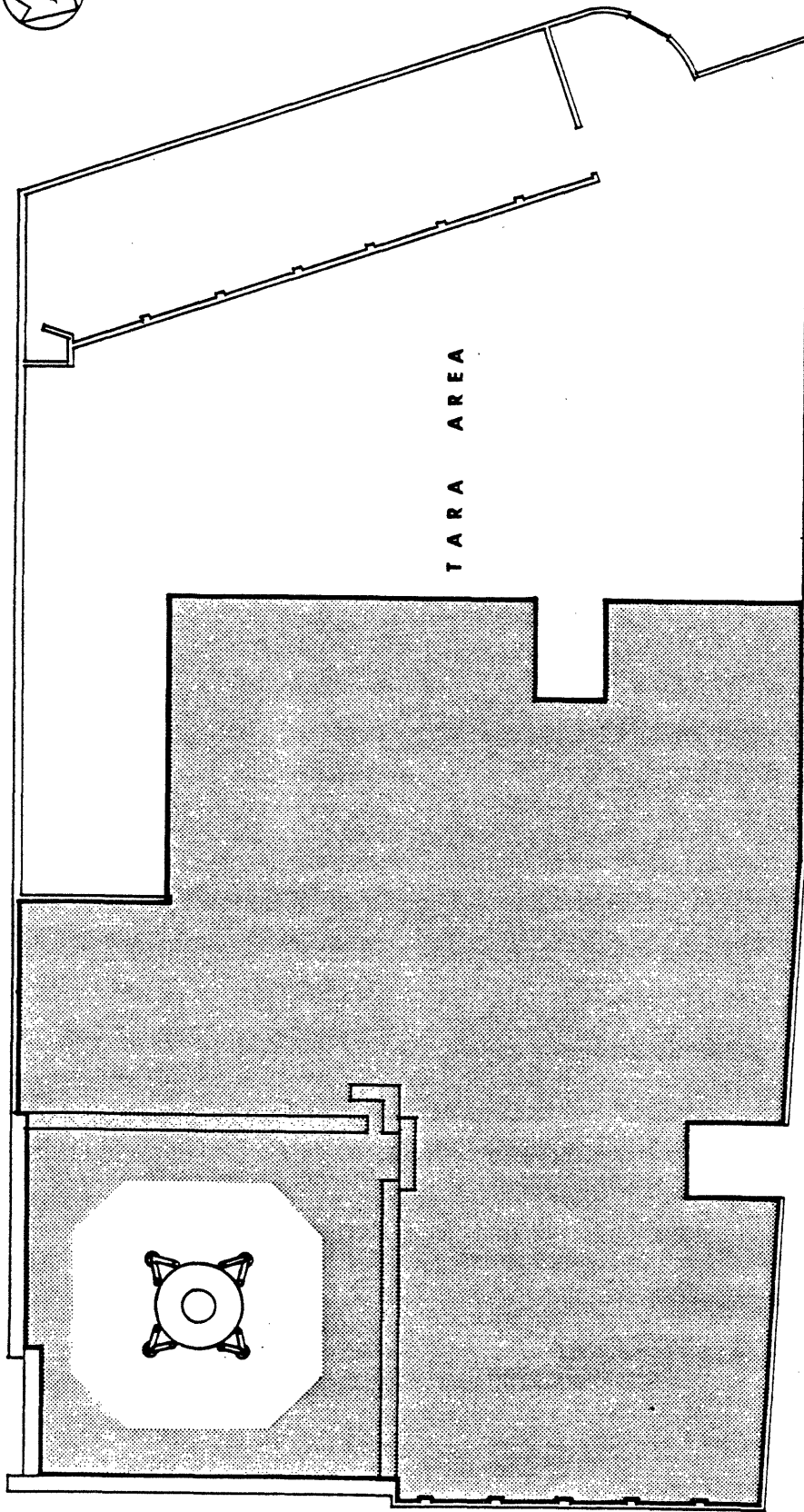


FIGURE 8.1-1 Overview of the DCT Experimental Cell, Power and Support Areas in the Nabisco Laboratory.

8.1.2. Shielding Requirements of the Experimental Cell

In order to operate Alcator DCT with deuterium, consideration must be given to biological shielding, to activation of material within the machine and the experimental area, and to the tritium generation by thermonuclear reactions.

Preliminary shielding studies have been done using both the ANISN transport code and the MCNP Monte-Carlo code. The results of these calculations indicate that limited operation in deuterium will be made possible by housing the DCT in a shielding cell.

Figure 8.1-2 shows the concrete biological shield thickness required as a function of the number of seconds per day of running time at full performance Alcator DCT parameters (8 keV, $n = 10^{14} \text{ cm}^{-3}$). A reasonable compromise would be to add 0.9 meters to the minimum 0.6 meter required for construction of such high walls, and to add a 1.0 meter roof. This requires incremental construction cost of approximately \$400 K, and allows 1000 seconds per day of deuterium operation at full machine parameters. These thicknesses are consistent with shield dimensions chosen by Tore-Supra and Asdex-Upgrade.

Activation of materials within the cell, particularly within the machine are also of consideration in such a high performance long pulse machine. We have examined the number of seconds of operation required to activate typical structural materials at various distances from the machine to a level such that they could not be safely handled after a 24 hour cool-down. Even at the first wall, the operating times for such an activation level are longer than the limits set by the 1.5 meter

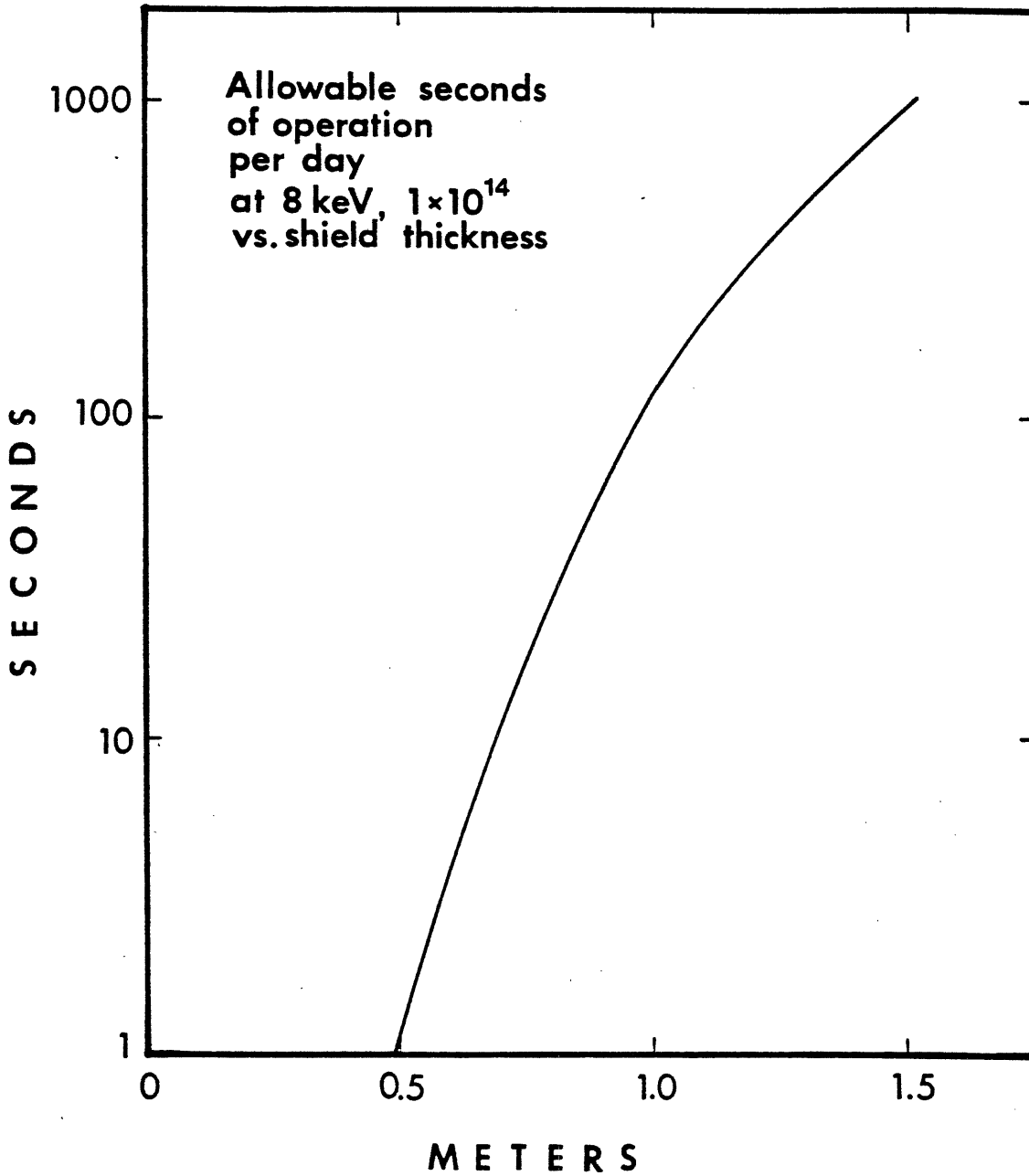


FIGURE 8.1-2 Allowable Seconds of Full Operation Per Day in Deuterium as a Function of Experimental Cell Concrete Wall Thickness.

biological shielding.

Tritium will be produced via the proton branch of D-D reaction. This will require the discharge from vacuum systems to be diluted with air to permissible tritium concentration levels and vented out an exhaust system.

8.1.3. Experimental Cell and Power Equipment Area Description

The experimental cell as shown in Figure 8.1-3 is 90 × 90 feet square and excavated to the standard basement level of the surrounding buildings. Water-table considerations make it uneconomical to go deeper. The cell will have two removable platform levels as shown, served by permanent balconies and by the two-axis crane. A clear horizontal width of 20 feet from the machine is allowed.

The power room above the cell shown in Figure 8.1-3 will contain the cryogenic equipment and the magnet power supplies, including all the relocated Alcator C TF and OH supplies, which will be used to supply the Alcator DCT OH and EF systems.

The cell will have a moveable-block access door at the rear for delivery of major subsystem components, and a smaller rolling access door at the front for diagnostic and heating equipment access.

The single story remaining garage area will be largely used for RF transmitters and modulators. The present 4 MW of LH and 5 MW of ICRH are schematically shown in this area.

8.1.4. Support Areas

Figure 8.1-3 shows the control area, data acquisition and general preparation areas immediately flanking the cell and power areas. These will be completed in a manner similar to the Tara facility.

Also shown are additional preparation laboratories in the "common facilities" area flanking the Tara Laboratories. This area will include common machine shops, vacuum shop and electronic shop areas, and will be commonly managed and supported.

TABLE 8.1-1

Experimental Areas

<u>FUNCTION</u>	<u>SQUARE FOOTAGE</u>
Experimental Cell	8,100
Roof Power Room	9,600
RF Surplus Area	6,800
Control Room	3,400
Computer	2,100
Support Labs	5,400
Common Shop Areas	7,700

8.2. Power Systems

8.2.1. Prime Power

Present prime power (13.8 kV AC) at the PFC site consists of a 225 MVA alternator with over 200 MJ available stored energy and a 750 MCM cable tie to the Cambridge system. The power capabilities of that cable are given in Table 8.2-1. It is basically rated as a 13 MVA steady-state cable with higher power ratings for limited duty cycles as indicated in Table 8.2-1.

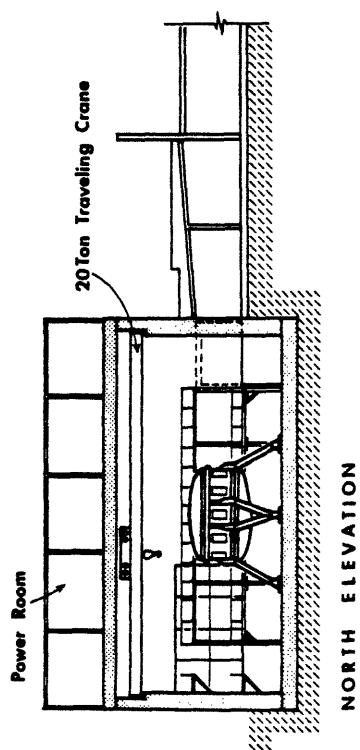
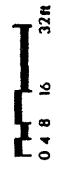
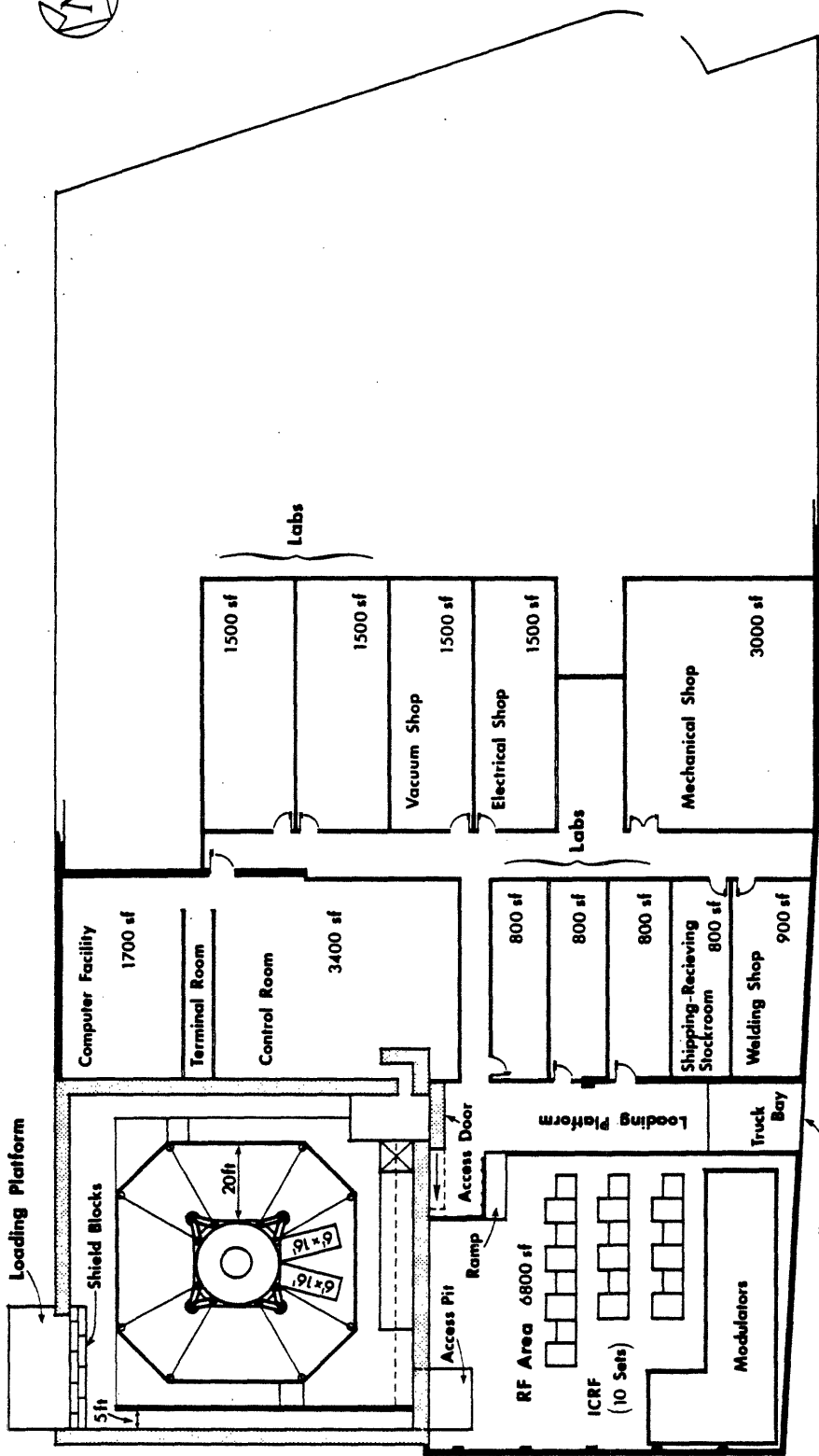


FIGURE 8.1-3 Detail of Experimental Cell, Power, and Support Areas.

Cambridge Electric currently limits the PFC to a peak short duration pulse load of 20 MVA on top of a 10 MVA steady-state load based on their desire to avoid "flicker" on their system. Larger slow low-duty cycle loads as limited by the cable thermal capacity would presumably be permitted.

The PFC is not the only user of the present tie line, the Magnet Laboratory being the major "steady-state" load. The Magnet Laboratory draws up to 10 MW for periods of several hours, and generally operates for approximately 12 hours per day, 5 days per week. The Tara Project draws up to 20 MVA in 4 second pulses at 5 minute intervals. It would be necessary to coordinate the DCT operation with the other users of this line to prevent overloading the cable.

There are several strategies for relieving the current prime power limitations. The lowest cost option is to lay a 1500 MCM cable parallel to the present cable, tripling the steady capacity. The next lowest cost option would be to install a used 20 MVA gas turbine peaking unit, of which a number are available. A third alternative is to install a 115 kV substation tapping into the new 115 kV line which will be coming into the nearby Blackstone plant in the next few years. This line will be "stiffer" and avoid the flicker problem of the low voltage lines.

The cost of the parallel cable option has been included in the baseline cost estimate (see Section 10.).

TABLE 8.2-1

13.8 kV 750 Mcm Cable Capacity

Steady-state	13 MVA
5 Min On	
50 Min Off	18 MVA
60 Sec On	
600 Sec Off	26 MVA

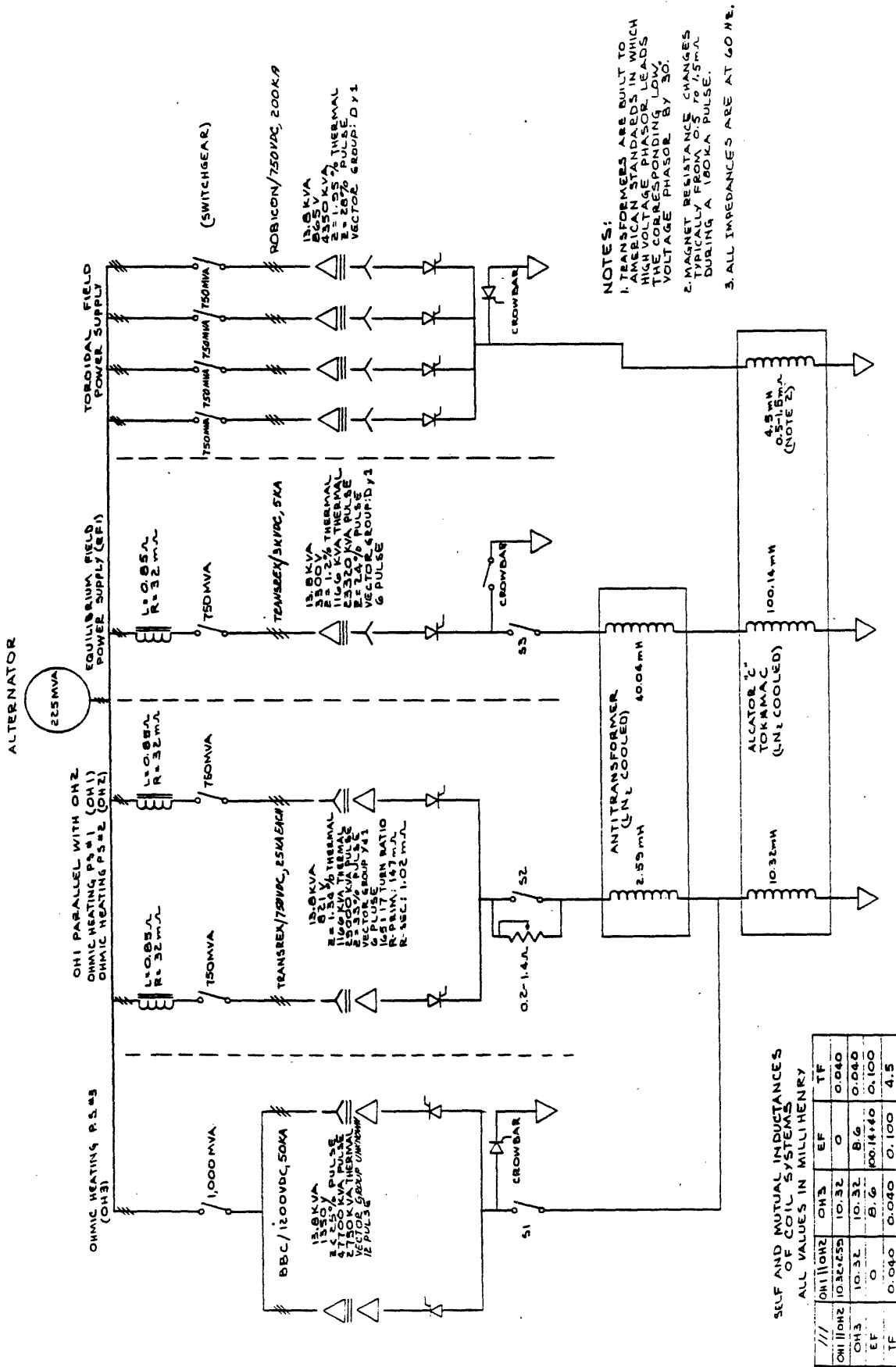
8.2.2. Magnet Power Supplies

Alcator DCT will utilize superconducting coils of high current capacity. The TF coil will operate at 25 kA and the various PF coils at either 50 kA or 25 kA levels. While essentially no voltage is required for steady-state operation (i.e., RF current drive), voltage is required during ramp up of fields, during inductive drive operation, and for control purposes. To drive OH1 at a rate consistent with providing 5 volts loop-voltage for example, requires 750 volts.

We propose to use the various high current supplies from Alcator C to supply the PF systems but to purchase new steady-state supplies for charging the OH system and for powering the TF magnets, where there are only modest voltage requirements.

There are eight major power supply units currently in use on Alcator C as shown in Figure 8.2-1, with a combined rating of nearly 300 MVA. These supplies are rated for an equivalent square wave pulse time of 20 seconds, but must be de-rated for longer pulses as shown in Table 8.2-2.

It is evident from Table 8.2-2 that the major limitation for truly long-pulse operation (greater than one minute) lies with the power supply



SELF AND MUTUAL INDUPTANCES OF COIL SYSTEMS
ALL VALUES IN MILLIHENRY

	OH1	OH2	OH3	EF	TF
OH1/OH2	10.32	10.32	0	0.040	
OH1/EF	10.32	8.6	0.040	0.100	
OH1/TF	0	8.6	100.14/60	0.100	4.5
EF/TF	0.040	0.040	0.100	4.5	

FIGURE 8.2-1 Overall Circuit Diagram of the Present Alcator C Magnet Power.

transformers and not the rectifiers. We note however, that there are really two modes of operation of the PF system, namely pulse times consistent with inductive drive, (nominally > 100 seconds) and true steady-state, associated with RF current drive. The power supplies and coil connections would be configured differently for these two modes, allowing steady-state operation even under the limitations of the present supplies. To accommodate this dual mode we propose to rewind some of the present transformers to provide low voltage continuous rated taps and to provide steady-state cooling. Costs for these rewinds have been included. Typical power supply/coil assignments are shown in Table 8.2-3. The PF coils are wound from basic 12.5 kA conductors wound 2 in hand for 25 kA operation (and 2 pancakes in parallel for 50 kA operation) and can be reconnected i.e., tap changed, to favor low currents for steady-state operation.

TABLE 8.2-2

Long-Pulse Rating of Present Supplies

POWER SUPPLY	20 SECOND RATING	60 SECOND RATING	300 SECOND RATING	CONTINUOUS RATING	
				RECTIFIERS	TRANSFORMERS
Robicon 1,2,3,4 750 VOLT	50,000 A	22,500	15,000	25,000	5,000
Transrex 1,2 750 VOLT	25,000 A	11,250	7,500	12,500	2,500
BBC-1 1,500 VOLT	50,000 A	22,500	15,000	25,000	5,000
Transrex 3 3,000 VOLT/ 1,500 VOLT	5,000 A/ 10,000 A	2,250/ 4,500	1,500/ 3,000	2,500/ 5,000	500/ 1,000

TABLE 8.2-3

Typical Coil Power Supply Assignments

COIL	POWER SUPPLY ASSIGNMENT	
	60 SECOND PULSE	CONTINUOUS OPERATION*
OH1	New Low Voltage Supply (+ SWING) Robicon 2, 3 (- SWING)	New Low Voltage Supply
OH2/EF2	BBC-1	BBC-1
OH3	SERIES WITH OH1	SERIES WITH OH1
EF3 TOP	Transrex 1	Robicon 1, 2
EF3 BOTTOM	Transrex 2	Robicon 3, 4
D1 - D2	Robicon 4	Transrex 1, 2

* Assumes OH initiation plus RF current ramp and coils connected in maximum number of turns mode.

8.2.3. RF Power System

The baseline Alcator DCT proposes to convert the present 4 MW of lower hybrid equipment to steady-state capability, and to bring the existing FPS-17 radar transmitter units into operation with 5 MW of steady-state capability. The overall system diagrams for the two systems are shown in Figures 8.2-2 and 8.2-3.

8.2.3.1. Lower Hybrid System

The 4 megawatt, 4.6 GHz RF system is composed of 4 clusters with 4 klystrons per cluster. While the 4 megawatt system is in-house, the

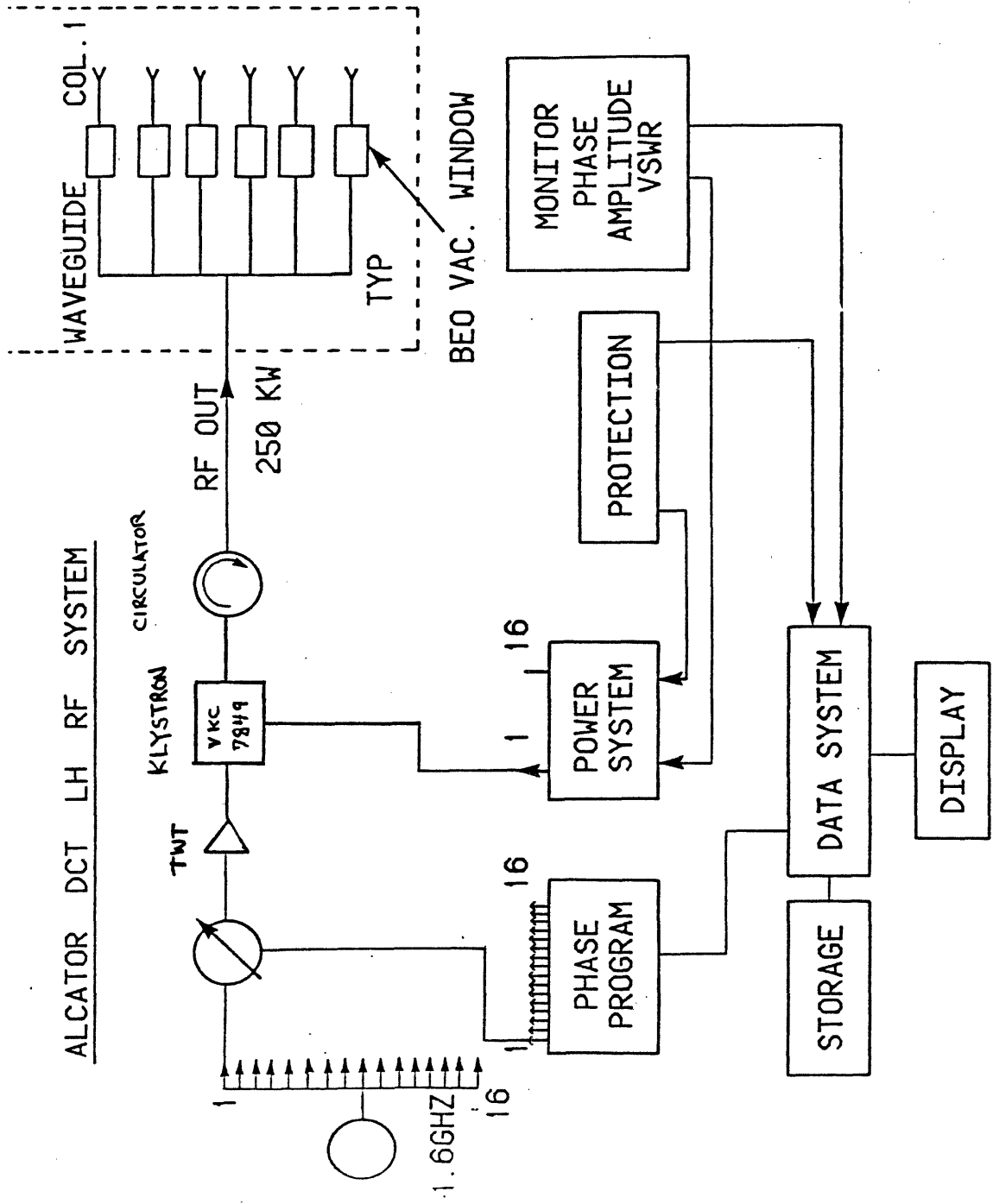


FIGURE 8.2-2 Block Diagram Alcatraz DCT Lower Hybrid RF System.

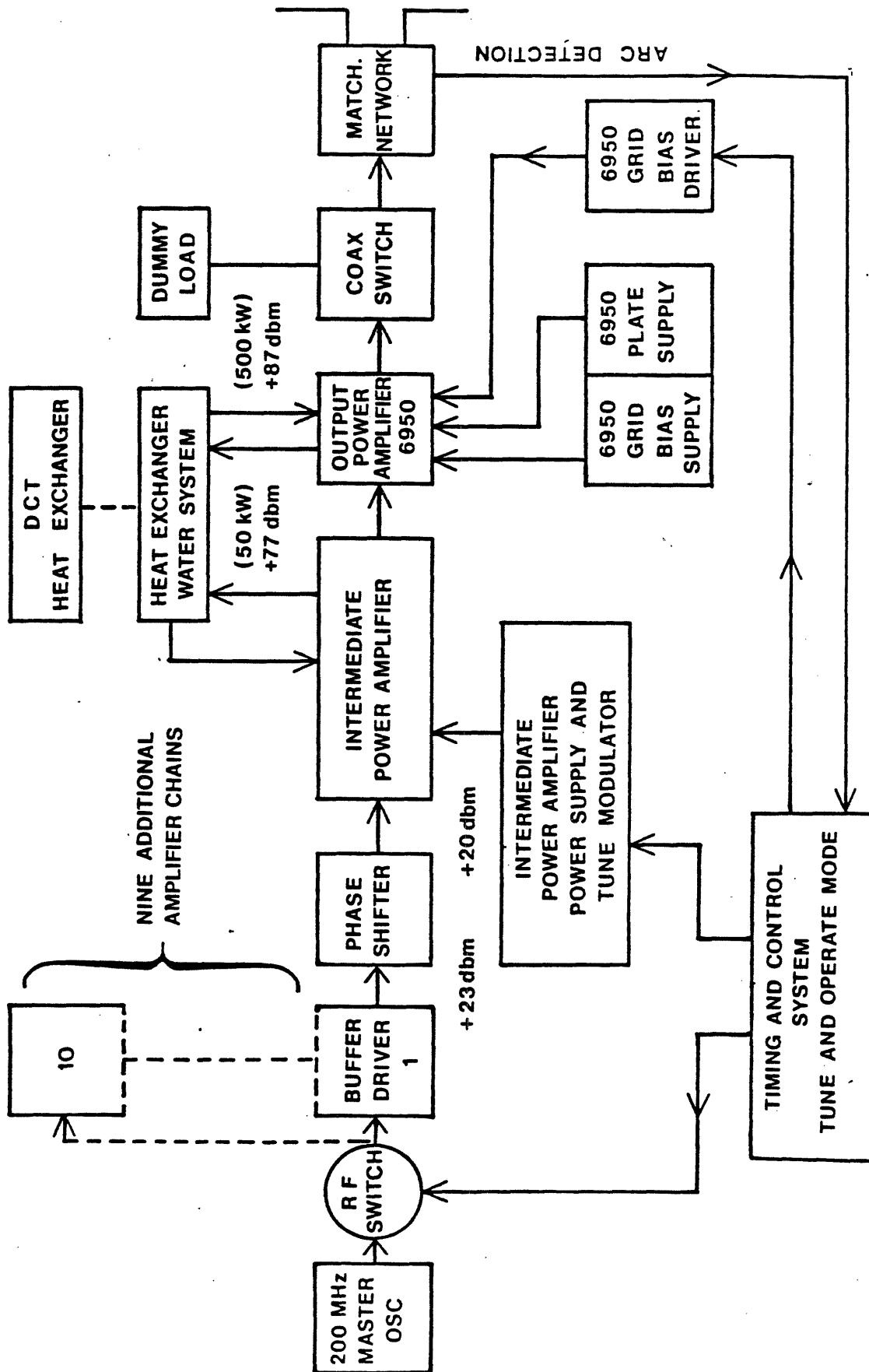


FIGURE 8.2-3 ICRF - 5 MW CHAIN

present system is limited to a 0.5 second pulse every 5 minutes. The average power limitations are due to the power supply cooling limit, the 250 kW circulators, the harmonic filters and some of the elements in the pulse power modulators.

New circulators will need to be purchased and the harmonic filters will need to be replaced. The pulse power modulators will need some resistor and water flow changes; the transformer/rectifiers will need new transformers and a heat exchanger installed on each of 3 of the transformer/rectifiers. The fourth transformer/rectifier, a General Electric power supply, is equipped with heat exchangers and circulator pumps.

To prevent excessive primary current in the 13.8 kV lines when the systems are turned off (or crowbarred), a series inductor capable of handling the 64 amps possible RMS current will be installed in each of the transformer/rectifier high voltage lines.

The pulse power modulators will be moved to the Alcator DCT area. The high voltage cables and the control cables will be rerun with some cabling replaced.

The cost of these modifications are discussed in Section 10.

8.2.3.2. ICRF

A 5 megawatt, 200 MHz RF system would be comprised of 10 amplifier chains of 500 kilowatts. Each amplifier chain consists of a buffer-driver stage, a phase shifter, an intermediate power amplifier supplying 50 kilowatts to a 500 kilowatt output amplifier.

The output power amplifiers are out of the FPS-17 radar system acquired by the U.S. Department of Energy and assigned to M.I.T. for use in ICRF heating. Only minor modifications will be required for these power amplifiers. We have 13 new and 20 used RCA 6950 power amplifier tubes.

The intermediate power amplifiers will be standard television transmitter design and capable of operating, with a mechanical tuning change, at 90 MHz or 200 MHz. The power supply to support the intermediate power amplifier will contain the necessary bias supplies and bias modulators to allow for tune and test.

The output power amplifier will have, with the plate power supply, the necessary grid bias and grid bias modulator for tune and test. A master oscillator and RF switch will drive buffer amplifiers and phase shifters for the 10 amplifier chains. A unit tuning and control system allows a simple set of commands to be sent out for tune, operate or inhibit in the case of arc or over current faults.

A heat exchanger which will handle 500 kW of heat per amplifier chain for a total of 5 MW will need to be implemented. Each amplifier chain will have a holding tank and deionizer column. At least 2 megohm centimeter water will need to be maintained.

The cost of these modifications is discussed in Section 10.

CHAPTER 9

DCT RESEARCH AND DEVELOPMENT ACTIVITIES (RDAC)

Alcator DCT will be the first superconducting TF coil tokamak in the U.S. program, and the first tokamak in the world program to utilize superconducting PF coils. In addition, it will be the first potentially steady-state device with reactor level heat fluxes. These three factors alone make the device a state-of-the-art undertaking. To build the device in a near-term time scale at a reasonable and predictable cost, we must take maximum advantage of existing concepts and hardware.

At the same time, we must keep in mind that the concepts chosen will become, in turn, those with the largest data base for the next steps in the program, and therefore should be extrapolatable.

As an example of this dual requirement, we have chosen Nb₃Sn internally cooled TF conductor because it has a manufacturing data base through the Westinghouse/Airco LCP coil, a performance data base through LCP RDAC's and the MIT 12 Tesla program, and can be extrapolated for the next generation devices.

We have similarly tried to choose PF concepts which are a reasonable balance between the currently available data base (which is unfortunately much smaller than the TF data base) and concepts which we consider extrapolatable. To take a maximum advantage of previous pulse coil R & D, we plan to utilize wire produced for the cancelled 20 MJ pulse coil project in the critical portions of the PF system, but we plan to use internally cooled conductors which we consider most appropriate for extrapolation.

The detailed considerations of conductor selection are discussed in Section 4.0, Alcator DCT Point Design Description.

The Alcator DCT project carries certain specific RDAC items as listed below. It could not, however, stand alone without D and T programs such as the high-heat-flux, first wall, blanket and shield, plasma wall interactions, 12 Tesla program, and a broad range of their analytical and component development programs. It will be clearly handicapped by the current lack of a D and T program in pulse field development.

TABLE 9.1

Specific Project RDAC Items

1. TF ICCS cable strand-insulation development
2. TF conductor process improvement
3. ICCS mechanical tests
4. Dummy TF pancake winding
5. PF conductor reprocess development
6. PF conductor stability tests
7. PF module stability test
8. PF lead development
9. PF cryostat development
10. Prototype tile procurement

1. TF ICCS Cable Strand-Insulation Development

The original Westinghouse/Airco LCP Conductor was to have a strand-to-strand sulfide insulation to reduce ac losses. The process was developed by Westinghouse, but eliminated from the final conductor to re-

duce cost and because it proved not to be needed to meet LCP pulse-loss specifications nor to prevent sintering of the strands during heat treatment. We propose to reexamine the possibility of utilizing strand insulation and have discussed a development program with Airco for a less costly chemical process.

2. TF Conductor Process Improvement

Recent developments in the M.I.T. 12 Tesla program have resulted in major potential performance improvements in the Westinghouse/Airco Nb₃Sn conductor. Sub-scale conductors have been used to demonstrate that a two-stage heat treatment can result in a dramatic increase in critical current of the strands used in the Westinghouse/Airco conductor principally by reducing the strain sensitivity which currently degrades their performance when encapsulated inside the steel jacket. The steel jacket shrinks more than the Nb₃Sn during the cycle from 700° C reaction to helium temperature, placing the Nb₃Sn under strong compression, previously strongly reducing the critical current. Recent tests have further shown that when an Incoloy 903 sheath is used rather than the currently used JBK-75 stainless steel, the current density reduction effect essentially disappears. These two combined effects result in an improvement of 50% in critical current.

RDAC money has been identified to allow Airco to confirm the ability of the tube-mill to process Incoloy sheet, and to make modifications as required.

Performance of full scale conductor will be confirmed in the M.I.T. 12 Tesla prototype coil.

3. ICCS Mechanical Tests

Three areas require further testing:

- A) The mechanical properties of welded Incoloy following the Nb₃Sn activation cycle must be confirmed at low temperature. This work has been discussed with Teledyne Corporation.
- B) The mechanical properties of arrays of ICCS conductors in winding pack mock-ups will be further confirmed. Preliminary tests at LN₂ temperatures recently carried out at Man Labs indicate comfortable safety margins against radial compression loads for the ICCS conductor when they are epoxy impregnated into a confining case. These tests are in contrast to non-potted tests carried out by Westinghouse for LCP.
- C) The fatigue properties of Nb₃Sn cables compacted in conduit will be tested in sub-size conductors. A 27 strand conductor of void fraction comparable to the full cable will be tested by alternating current direction at least 10,000 times in a fixed background field provided by a Bitter magnet. This test, now in preparation, should be completed early in FY84.

4. Dummy TF Pancake Winding

One TF pancake will be wound from dummy ICCS material in order to develop tooling, heat-treatment control and insulation techniques. A similar procedure was utilized in the 12 Tesla program and resulted in a number of process improvements. A quotation has been obtained for this work at Everson Electric.

5. PF Conductor Reprocess Development

Current plans call for the use of both 20MJ pulse program wire and CDIF MHD program magnet wire in constructing the PF conductors. In both cases the wire requires additional processing. The 20 MJ wire must be drawn to final size and insulated. The CDIF wire must be removed from the copper monolith into which it is soldered and then redrawn to smaller size. A small development program is proposed to process short pieces of both materials, and has been discussed with IGC.

6. PF Conductor Stability Tests

There is an unfortunately small data base for conductors suitable for PF coil use. This is particularly true for internally cooled conductors, with the sole experience being at JAERI in Japan. We propose to fabricate sub-size conductors made from both the 20 MJ and CDIF conductors and test them in small stability coils. This procedure has been developed by the M.I.T. 12 Tesla group. They wind small (10 cm) diameter coils and place them in a Bitter magnet 12 Tesla background field, and apply a strong pulse field to inductively drive the samples non-superconducting. This is an ideal set-up for testing PF conductors, which can be tested in the same apparatus.

7. PF Module Stability Test

We propose to wind two 40 cm ID double pancake modules which will be tested in the split-coil pulse field test facility at ANL. One module will use 20 MJ wire, the other CDIF wire. These tests will constitute prototype testing of the full-scale DCT conductors.

A proposal has been received from ANL to conduct these tests. The coils will be wound at Everson Electric and the ICCS conductors sheathed at Airco. Tooling developed for the 12 Tesla program can be used for coil winding.

8. PF Lead Development

The PF system will utilize a number of high current (25 KA) high voltage (20 kV) leads. In order to limit the stand-by helium losses to a reasonable level it will be necessary to utilize leads in which the helium level can be altered between a running level and a low loss stand-by level. Smaller leads of this nature were developed by the Rutherford Laboratory in the early 1970's, but have not seen use at higher currents or in other applications. Such leads can reduce consumption by a factor of ten.

There is also limited experience with high voltage leads (LANL, KfK). Since there will be 8 pairs of leads which must have high reliability, we consider it appropriate to develop a prototype. The work will be carried out at M.I.T.

9. PF Cryostat Development

PF cryostats must exhibit high electrical resistivity to avoid excessive toroidal path short circuits, and to avoid excessive losses during PF field changes. Past studies have identified this area as one requiring development, either towards nonmetallic cryostats or metal cryostats with reliable electrical breaks. We propose to avoid the uncertainties associated with both these approaches by utilizing a relatively thin metallic cryostat reinforced by nonmetallics. We propose to construct a suitable

mock-up for mechanical testing at LN₂ temperature.

10. Prototype Protective Tile Procurement

In the area of high heat-flux components, we propose to use a developed stainless steel heat shield over the majority of the wall. There are, however, no currently proven tiles or tile attachment concepts capable of steady-state heat removal.

We do not propose to develop steady-state rated protective tiles within the Alcator DCT project, but rather to depend on the developments which will be taking place in the U.S. (and in other countries) in high heat flux component development programs. We urge those programs to develop a generic tile, perhaps 5 cm × 5 cm and to develop a suitable attachment concept. Alcator DCT (and other machines) could then adopt such tiles to their particular requirements (tile thickness, etc.).

We have set aside RDAC funds toward prototype tile procurement to be leveraged through the high heat flux component program.

CHAPTER 10

COST, SCHEDULE AND PROJECT MANAGEMENT

10.1. Cost

Costs have been estimated for the base line Alcator DCT in two categories: (1) fabricated and purchased components, and (2) composite labor costs associated with engineering, installation and program management. Component costs have been estimated using unit costs derived from other recent projects at MIT and elsewhere in the community, and from cost estimates or quotations received from industry on selected components. Composite labor costs for installation have been estimated by totaling individual task (work breakdown structure) time estimates. Design, supervision, and project management has been estimated based on M.I.T. project experience in Alcator C, Tara, and various superconducting magnet projects.

10.1.1. Costing Basis for Fabricated and Purchased Components

Table 10-1 gives a summary of Alcator DCT component costs which were derived as described in this section.

TABLE 10-1

Fabricated and Purchased Component Cost Summary

TF MAGNET

WIRE	\$ 7.35 M	
CABLE/SHEATH/TERM	1.82	
WINDING	0.95	
STRUCTURE	2.38	
	<u>12.5</u>	<u>\$12.5 M</u>

PF MAGNET

CONDUCTOR	0.375	
ICCS FAB	1.175	
WINDING	0.95	
CASES	0.5	
	<u>3.0</u>	<u>\$ 3.0 M</u>

MAGNET CRYOSTAT

VESSEL	1.05	
LN ₂ PANELS	0.1	
SEALS	0.25	
LEGS	0.3	
	<u>1.7</u>	<u>\$ 1.7 M</u>

REFRIGERATION

SATELLITES	0.7	
CDIF INST./MOD	0.1	
LEAD ASSEMBLIES	0.4	
	<u>1.2</u>	<u>\$ 1.2 M</u>

TORUS

24 SECTORS AND FLANGES	0.825	
BELLOWS	0.075	
SEALS	0.250	
VACUUM STATIONS	0.250	
	<u>1.4</u>	<u>\$ 1.4 M</u>

LIMITERS/HEAT SHIELD

HEAT SHIELD	0.2	
COLLECTORS	0.6	
HEAT EXCHANGERS	0.5	
	<u>1.3</u>	<u>\$ 1.3 M</u>

SITE MODIFICATIONS

EXPERIMENTAL CELL	2.2	
SUPPORT AND POWER AREAS	2.0	
	<u>4.2</u>	<u>\$ 4.2 M</u>

FACILITIES

PRIME POWER CABLE	0.75	
TF SUPPLY/PROTECTION	0.5	
PF SUPPLY/BUS SYSTEM	1.3	
CONTROL	0.50	
DATA COMPUTERS	1.5	
CAMAC HARDWARE	0.25	
	<u>4.8</u>	<u>\$ 4.8 M</u>

RF MODIFICATIONS

LH POWER TRAIN	1.6	
ANTENNA/TRANS	2.25	
ICRH POWER TRAIN	3.1	
ANTENNA/TRANS/CONTROL	1.25	
	<u>8.2</u>	<u>\$ 8.2 M</u>

R & D ACTIVITIES (RDACS)

\$0.65 M

TOTAL

\$38.95 M

10.1.1.1. Toroidal Field Coils and Intercoil Structure

Conductor (18,000 Meters for 24 Coils and One Spare)

Airco has quoted to us a quantity of 12,340 m (based on an earlier design) of the identical bronze process wire used in LCP for which they have a reasonable manufacturing basis. They also quoted on cabling, sheathing and terminations as per their LCP experience.

We have extrapolated these quotations to the longer required lengths to obtain a cost estimate. We have substituted the sheath material cost of Incoloy 903 for the JBK-75 sheath used by Airco.

We have also explored the cost of applying sulphide insulation to the wire to reduce the losses under ramped fields and disruptions. The process developed at Westinghouse would be transferred to Airco. If we elect to insulate, Airco estimates a cost increment of \$250 K. We have included this cost below:

Wire	\$7,350 K
Insulation	250 K
Cabling	280 K
Sheath	560 K
Tube Mill	440 K
Terminations	290 K
	<u>\$9,170 K</u>

This conductor will operate at 23 kA, 57% of critical current, and the cost per kiloampere-meter of conductor would therefore be approximately \$22.

Coil Winding

Everson Electric has wound our 12 Tesla prototype coil and is therefore familiar with handling the steel-sheathed conductor. They have

quoted on production of the coil. Airco has quoted on the activation of the pancakes after winding (and before insulating).

Winding tooling	\$ 50 K
Winding	390 K
Activation	100 K
Epoxy tooling	80 K
Epoxy Impregnation/ insulation	330 K
	<hr/>
	\$950 K

The winding pack weight of all 24 coils is about 50×10^3 kg, and therefore the above represents a winding cost of approximately \$20/kgm.

Coil Cases and Intercoil Structure

We have obtained quotations or industrial estimates on all elements of the cases and intercoil structure. General Dynamics estimated the cost of welding the cases based on their LCP experience. We have obtained quotations on machining the side plates and intercoil wedges. We have quotations on rolling the outer heavy Dee-shaped rings, and have estimated the inner ring and nose pieces based on these quotations.

Side plates	\$1,130 K
Outer rings	300 K
Inner rings	100 K
Nose pieces	130 K
Case welding	500 K
Intercoil wedges	220 K
	<hr/>
	\$2,380 K

The total weight of these components is 130×10^3 kg, and the unit cost is therefore approximately \$18/kg.

TF Unit Cost Comparison

Unit costs based on the Alcator DCT TF coil cost estimate are compared below with approximate unit costs from selected projects.

	WINDING PACK COST	STRUCTURE COST	OVERALL COST
ALCATOR DCT	\$200/kg	\$18/kg	\$75/kg
MFTF SOLENOIDS			48/kg
MFTF Y/Y	138/kg	18/kg	54/kg
CFFF (MHD)			60/kg
TFTR (COPPER)			69/kg

10.1.1.2. Poloidal Field Coils and PF Cryostats

Conductor

The base line Alcator DCT proposal is based on utilizing existing basic superconductor from the CDIF MHD Project and from the 20 MJ Pulse Coil Project. We propose in both cases to process the superconductor into appropriate wire, cable it, and utilize it in internally cooled conductor form utilizing the Airco tube mill.

The PF ampere-meter requirement is approximately half the TF requirement. Because of the lower overall current density in the PF coils however, a nearly equal conductor length is required for the PF, namely 16,000 meters. There is more than enough superconductor available from CDIF and the 20 MJ project to meet this requirement.

We have obtained estimates from IGC for reprocessing the surplus conductor, as they were the original fabricator. We have used Airco estimates for tube mill operation and cabling based on the TF conductor quotations. We have assumed 304 stainless steel for the conduit.

To utilize the CDIF conductor the core must be removed from the built-up conductor in about two-thirds of the conductor. It would then be cleaned and redrawn to 0.7 mm. The 20 MJ wire only requires drawing to final size.

Conductor reprocessing	\$ 250 K
New copper wire	125 K
Cabling/insulation	260 K
Sheathing	140 K
Tube mill	415 K
Terminations	360 K
	<hr/>
	\$1550 K

Winding

The wind cost is based on the TF winding cost of similar lengths of conductor and is taken at \$950 K or about \$20/kg.

PF Cryostats

The base line concept for the PF cryostats is to utilize a relatively thin metallic vacuum tight cryostat and to reinforce it with nonmetallic structures to support the vacuum loads.

We have estimated the costs based on the use of commercial stainless steel LN₂ paneling (for example Dean Products) for the vacuum vessel. We have estimated the nonmetallic overlay based on the costs of constructing the Alcator C nonmetal dewars, utilizing a square footage basis for comparison. We have also included 9×10^3 kgms of nonmetallic materials using \$12/kg in accordance with MHD cost studies by A. M. Hatch. Stainless steel structural tie-down cross-beams are included at \$14/kg.

Metal panels	\$135 K
Nonmetallic materials	115 K
Nonmetallic overlay Construction	150 K
Stainless structural tie-downs	<u>100 K</u>
	\$500 K

10.1.1.3. Magnet Vacuum Cryostat

The TF and PF magnets are contained in a single vacuum cryostat. The vessel weight is 75×10^3 kg of stainless steel. We have estimated the cost based on a \$14/kg unit weight of large vessels utilized by A. M. Hatch in his extensive study of an ETF scale MHD magnet and recent experience with the CDIF and CFFF medium scale MHD magnets.

The liquid nitrogen panels were based on a \$100/ft² basis from LLL and TARA cryopanel experience. The cost of seals and hardware was based on \$4 K per port opening.

The cost of the outer support legs, which weigh 35×10^3 kg was based on the assumption that half the weight would require little fabrication (i.e., tubular elements) and the rest would be fabricated at \$14/kg.

Vessel	\$1050 K
LN ₂ Panels	100 K
Port seals	250 K
Support legs	<u>300 K</u>
	\$1700 K

10.1.1.4. Refrigeration

The Alcator DCT base line proposal is based on the use of the CDIF 2800 refrigerator system surplus from the Montana CDIF Project as a

liquifier, and on the use of two Fermi energy saver type satellite units as reliquifier, refrigerators. The CDIF system is complete with screw compressors, purifiers and medium pressure gas storage.

There have been 24 Fermi type units built for the energy saver, and a substantial manufacturing cost base exists. They were purchased as components (cold box, compressors, heat exchangers) and assembled at Fermi. We would utilize the same sources of equipment.

The TF and PF coils will be connected by superconducting bus to external "lead dewars" where the transition to room temperature bus will be accomplished. The costing is based on experience in the 12 Tesla Program and in the MHD Magnet Technology Program.

Energy Saver Satellites	\$ 700 K
CDIF inst/mods	100 K
Lead assemblies	400 K
	<u>\$1200 K</u>

10.1.1.5. Vacuum Chamber Torus and Vacuum Pumping

The vacuum torus will be constructed of 24 heavy walled sectors separated by bellows. Cooling will be done through heat shields. We have obtained quotations from Metal Bellows for the bellows in order to establish the feasibility of fabrication. Metal Bellows fabricated the Alcator C vacuum chamber.

We have estimated the 33×10^3 kg chamber costs (including port covers) using a \$25/kg unit cost, versus \$14/kg unit costs used for the large magnet chamber to reflect the increased difficulty of shaping the Dee-sections and the port towers. Rolling of the Dee-sections has been

established through the quotation on rolling the Dee outer support rings in the TF case. Seals and hardware have been estimated at \$4 K/port opening.

We have not included the cost of modifications to the blank port covers specialized for diagnostics, (i.e., windows, probe interlocks, RF feed-through etc.). These are included with the RF system or are considered part of diagnostics and not costed as part of the base machine.

Vacuum pumping is based on 10,000 ℓ /sec of turbo-molecular pumps.

Vessel sections with port covers	\$ 825 K
Bellows	75 K
Seals	250 K
Vacuum stations	250 K
	<u>\$1400 K</u>

10.1.1.6. Collector Plates and Heat Shields

The majority of the vacuum chamber will be covered by 50 m² of heat shields which we propose to construct from sandwich panels similar to those used for LN₂ cryopanel. We have based a cost estimate on a base cost of \$100/ft² from the neutral beam experience, and have taken a multiplier of 4 to account for the special vessel fastener requirements and for the necessary use of smaller units constructed with reasonable accuracy.

The cooling system for the heat shields and limiters will utilize the "river water system" brought to the Magnet Laboratory, and will need to purchase only heat exchangers, clean water pumps, and demineralizers. Costing for this equipment is based on the TARA cooling system costs.

The divertor collector plates occupy approximately 7.5 m². We have costed the collectors on the assumption that there would be 48 panels consisting of a water-cooled substrate with poco-graphite tiles attached by brazing. We have allowed cost for pre-processing the tiles to provide a suitable transition region between the graphite and the substrate.

Primary Collectors:

Tile material 3000 × 5 cm × 5 cm × 1 cm	\$ 25 K
Tile machining 3000 × \$50	150 K
Tile transition 3000 × \$50	150 K
Brazing	25 K
Substrate panels @ \$100/kg	100 K
Panel attachments 50 × \$2 K	100 K
Cooling attachments	50 K
	<u>\$ 600 K</u>
Heat shields	200 K
Heat exchangers, etc.	500 K
	<u>\$1300 K</u>

10.1.1.7. Site Modifications

The proposed site work would renovate the front half of the existing Nabisco garage to use as an RF power room and would construct a new experimental cell in place of the rear garage section. Control room, computer area and staging laboratories would be located inside the present Nabisco building much as in the Tara Project.

Site costing is based on the Tara project in which a new experimental cell was constructed and the balance of the space obtained by renovating the West side of the Nabisco building.

New cell 8100 ft ² @ \$270/ft ²	\$2200 K
Control, computer, staging labs @ \$88/ft ²	1000 K
Cell roof power room @ \$30/ft ²	300 K
Garage area RF @ \$50/ft ²	350 K
Shop and support labs @ \$88/ft ²	350 K
	<u>\$4200 K</u>

10.1.1.8. Power and Control

The Alcator DCT machine will utilize all existing Alcator magnet power supplies for the poloidal field system. Transformers will be rewound and the supplies will be relocated to the roof-power room of the new cell.

Two new low voltage power supplies will be purchased for the TF magnets and for charging the OH system, along with appropriate protective breakers and energy dump resistors. Additional dump resistors will also be purchased for the PF systems, but sufficient breakers exist as part of the current Alcator C PF system.

In order to run in a true steady state mode, an additional AC cable must be installed paralleling the present cable. The cost of this installation has been estimated by Cambridge Electric.

Control costs are scaled from the Tara Project and are based on commercial control (Gould Electric) equipment being installed for Tara.

Data acquisition costs are also included although they could equally well be included with diagnostics under the base program. Costs are based on Vax equipment with Camac interfaces.

Prime power cable and switch gear	\$ 750 K
TF supply/protection	500 K
New PF and modification of Alcatraz supplies	1300 K
Controls	500 K
Data acquisition computers*	1500 K
Camac	250 K
	<u>\$4800 K</u>

*Detailed breakdown costs available

10.1.1.9. RF Modifications

Lower Hybrid Modifications

Alcatraz DCT will utilize the 4 MW LH equipment from the Alcatraz C Project suitably modified for steady state operation. New launchers will be provided in order to obtain a superior spectrum taking advantage of the wider ports. The modulators and tubes will be moved to the new site, but the power supplies will remain in the present out-door location.

Launcher estimates are based on present Alcatraz C experience and discussions with Varian.

Power Train Modifications

Circulators	\$ 850 K
Harmonic filters	130 K
Modulator modifications	140 K
Transformer/rectifier modifications	240 K
Control cable replacement	80 K
Inductors	120 K
Relocation	40 K
	<u>\$1600 K</u>

Launchers

3 Launchers (one spare)	2250 K
-------------------------	--------

ICRH Modifications

Alcator DCT will use the FPS-17 radar equipment presently at MIT to supply 5 MW steady state ICRH heating (8 MW, 10 seconds). There are 10 transmitter units and a large number of spare power tubes. One of the units is currently installed on Alcator C, the remaining units are in storage at M.I.T.

Power Train Modifications

Oscillator, RF switch, buffer, phase shifter	\$ 45 K
Intermediate power amplifier	1250 K
Modifications to HPA	70 K
HPA plate supply	1250 K
Grid bias supply, grid modulator	50 K
Timing and control	100 K
Heat exchanger	100 K
Coax switches	60 K
Dummy loads	65 K
Relocation	75 K
Transmission line cooling	35 K
	<u>\$3100 K</u>

Antenna/Transmission

Transmission line	240 K
Tuners	115 K
Tuning control	30 K
Data system	10 K
LP filters	80 K
Antennas	400 K
Vacuum barriers	25 K
Reflectometers	20 K
DC breaks	100 K
Dryers	30 K
Arc control	200 K
	<u>\$1250 K</u>

10.1.1.10. Alcator DCT Research and Development Activities (RDACS)

The Alcator DCT Project carries certain specific RDAC items as listed below. It could not however, stand alone without D and T programs such as the high-heat-flux, first wall, blanket and shield, plasma wall interactions, 12 Tesla Program, and a broad range of other analytical and component development programs. It will be clearly handicapped by the current lack of a D and T program in pulse field development.

SPECIFIC PROJECT RDAC ITEMS

	<u>FABRICATED AND PURCHASED COMPONENT COST*</u>
1. TF ICCS cable strand insulation development	50 K
2. TF conductor process improvement	50 K
3. ICCS mechanical tests	50 K
4. Dummy TF pancake winding	50 K
5. PF conductor reprocess development	50 K
6. PF conductor stability tests	25 K
7. PF module stability test	200 K
8. PF lead development	50 K
9. PF cryostat development	25 K
10. Prototype tile development	100 K
	<u>\$650 K</u>

*Not including the fractional time of Alcator DCT engineers associated with these R and D activities nor the personnel costs associated with D and T programs through which this work might be carried out.

10.1.2. Composite Labor Costs for Engineering, Installation and Project Management

Table 10-2 indicates the estimated support personnel required to carry out the specific assembly installation tasks identified. Each task estimate was built-up from an estimate of subtasks, the largest of which is broken down in Table 10-3 to illustrate the level of detail used.

Table 10-4 is an estimate of the design and supervision staff personnel requirements. This has been developed by assessing in which specific areas the Alcator engineering group would need to be supplemented, by identifying specific individuals to take responsibility for tasks, and by identifying any new hires required. The majority of the augmented Alcator staff would be drawn from the present Alcator DCT preconceptual group, and from nonfusion engineering activities.

We consider this level of engineering the minimum consistent with a project of this advanced nature. We will need to make maximum use of engineering assistance from other fusion laboratories in carrying out specific analyses at our request, and to minimize the risks through frequent reviews and independent analyses.

The cost of supplying the manning listed in Table 10-2 and 10-4 is given in Table 10-5, and is based on a composite cost of \$92.5 K/engineering man-year, \$69 K/assistant engineer man-year, and \$55 K/support personnel man-year.

TABLE 10-2

Assembly and Installation Support Personnel Summary

TASK	MAN-YEARS
R & D	2.5
TF MAGNET/CHAMBER SEGMENT ASSEMBLY	14*
PF COIL SUBASSEMBLIES	2.5
SEGMENT INTEGRATION	2.5
IN-VESSEL COMPONENT INSTALLATION	2.0
VACUUM PUMPING SYSTEM	1.0
PF ASSEMBLY	1.0
MAIN VACUUM TANK ASSEMBLY	2.0
INTERCONNECTIONS	5
REFRIGERATION	4
POWER SUPPLY INSTALLATION	2.5
CONTROLS	4.0
RF POWER	4.0
	<hr/>
	47

*See Table 10-3 for breakdown.

TABLE 10-3

TF Magnet/Chamber Segment Assembly Breakdown

SUBTASK	PEOPLE × DAYS PER UNIT
RECEIVE & QA	2 × 5
PREPARE/COLD TEST MAGNETS	4 × 15*
CLEAN ELEMENTS	2 × 5
ASSEMBLE CHAMBER SEGMENT/LEAK CHECK	2 × 5
SUPERINSULATION	1 × 10
FIT-UP MAGNET/INTERCOIL/CHAMBER	4 × 10
	<hr/>
	140 per unit**
	140 × 25
	<hr/>
	250 = 14.0 MY

*Parallel operation

**Series time 35 days = 2 months; 25 units in 12 months requires 4 parallel assembly operations plus 2 coil test crews for overlap of cold test preparation, and cold test.

TABLE 10-4

Engineering Personnel

	MAN YEARS
ENGINEERS	65
ENGINEERING ASSISTANTS	31

TABLE 10-5

Personnel Cost as Specified by Table 10-2 and 10-4

ENGINEERING	\$8150 K
TECHNICAL SUPPORT	<u>2585 K</u>
	\$10,735 K

10.2. Schedule

The construction and assembly schedule for Alcator DCT given in Figure 10.1 would lead to engineering check out at the end of FY87 and the start of physics operation at the beginning of FY88. We consider this four year schedule a reasonable compromise from the three and a half year project time we could achieve with an optimum cash flow in the early years. Further reduction of early year costs could stretch the construction program beyond four years, which we believe would not be in the best interest of the overall fusion program. The funding profile which accompanies this schedule is discussed in Section 10.3.

One accommodation which has been made to smooth out the cost profile has been to construct the site in two phases. The first phase would construct the power room in the front half of the garage, and the experimental cell. The second phase would develop the support areas. This early phase would be necessary to accommodate sub-assembly construction and long term rebuilding of the ICRH equipment. Delay of the support areas is not an attractive option, however, as it will undoubtedly compromise startup.

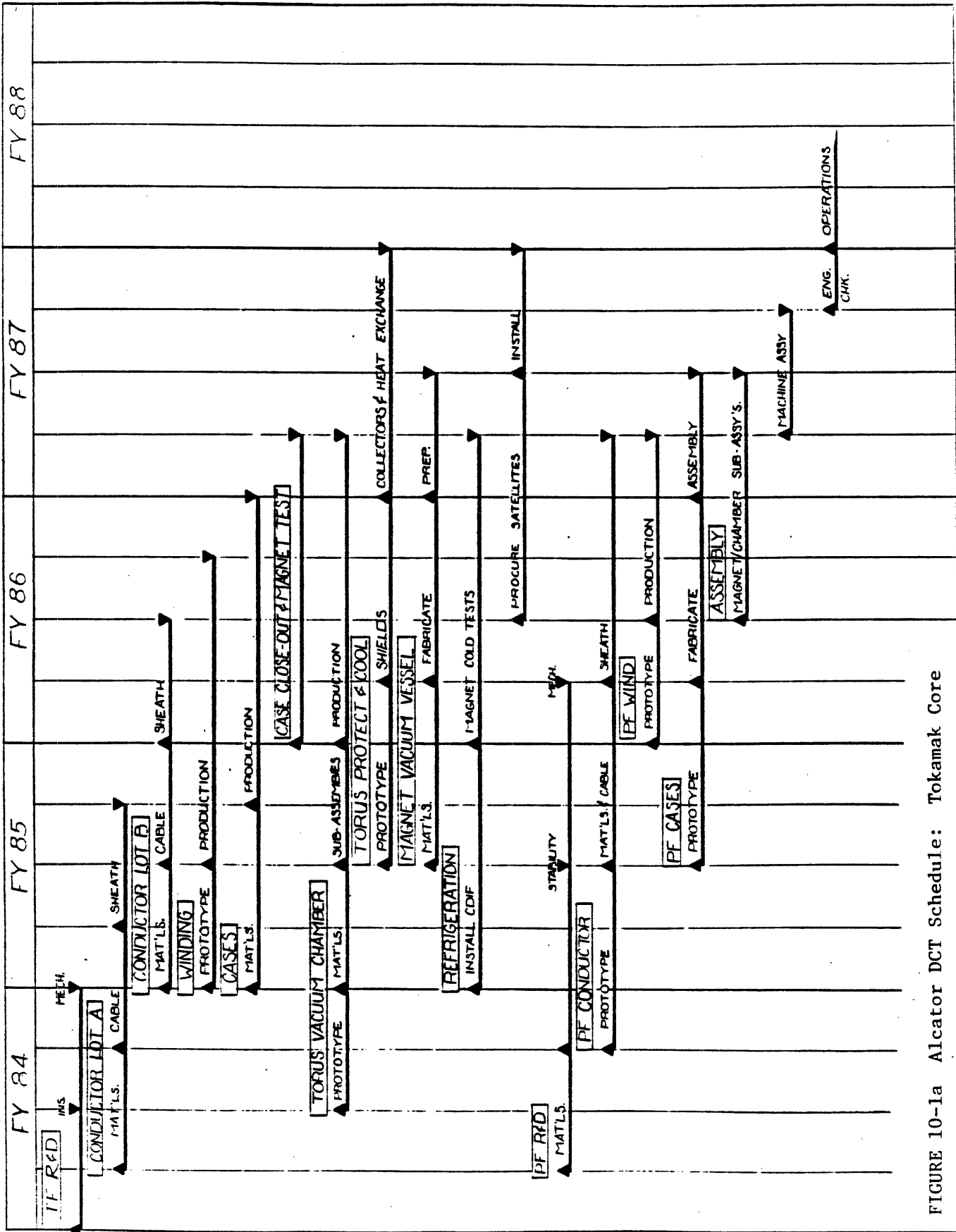


FIGURE 10-1a Alcator DCT Schedule: Tokamak Core

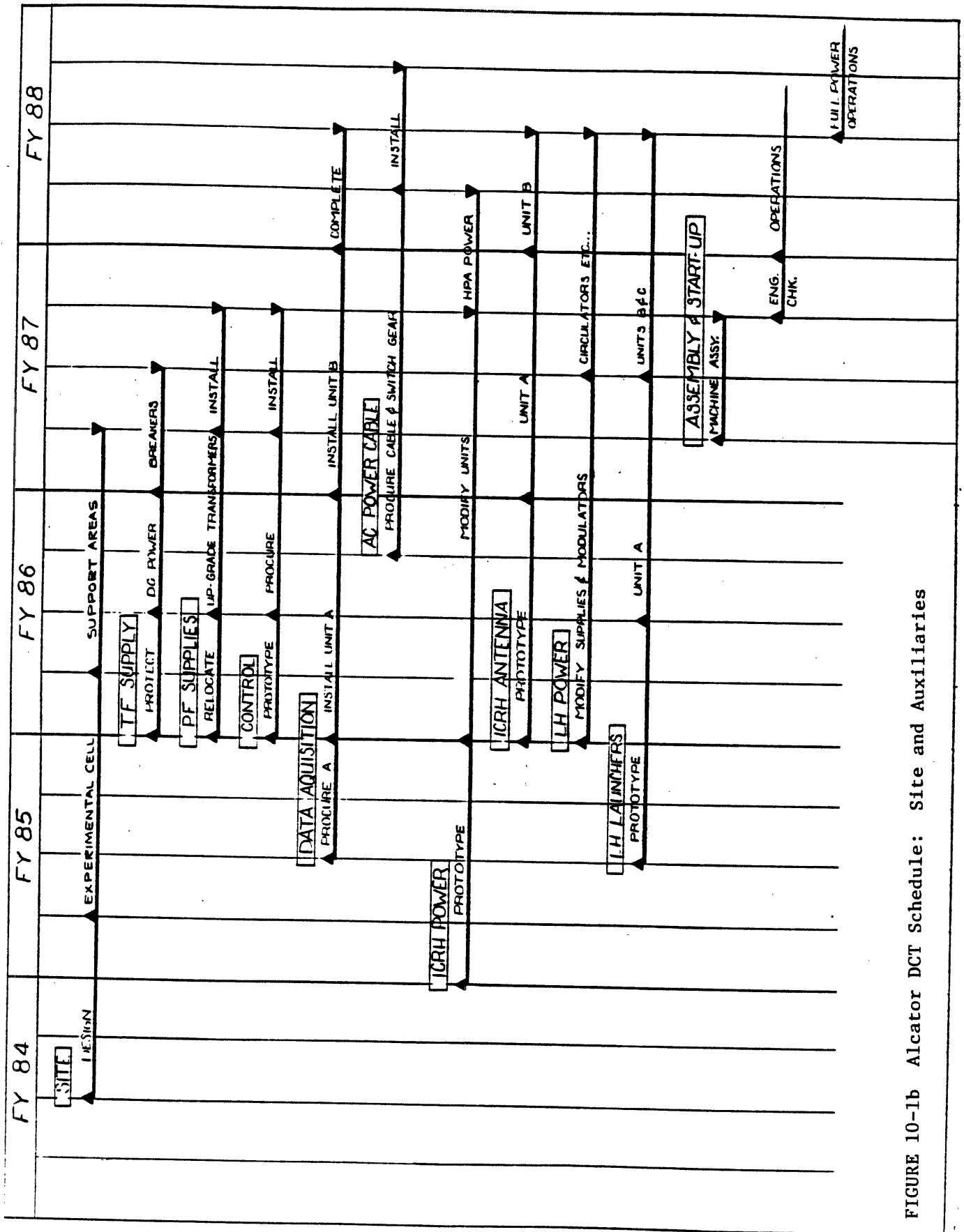


FIGURE 10-1b Alcatraz DCT Schedule: Site and Auxiliaries

A second major accommodation to smooth the cost profile has been the shifting of power supply modification and data computers toward the end of the project. This shift will certainly also have an impact on the rate of ramp-up of effective operations, and it also does not make maximum effective use of manpower early in the project.

Unattractive as they may be, these accommodations represent the only options for shifting substantial costs.

10.3. Funding Profiles

The summary funding profile for Alcator DCT consistent with the schedule given in Figure 10-1, is given in Table 10-6. The peak construction year is FY86 when \$14.785M will be spent. The detailed fabricated and purchased component cost profile is given in Table 10-7.

It is necessary to view these cost profiles in the context of the proposed overall base toroidal confinement program at M.I.T. We show such a proposed overall profile in Table 10-8. We have assumed a base program throughout the FY84-87 construction period which would be level at the FY83 level of \$10M through FY85, and would then rise gradually to \$16M in FY88 consistent with operation of the larger machine. We have analyzed what major fraction of that base program could be devoted to construction either through the use of the present Alcator engineering group or through savings resulting from the phase-back of Alcator C operations. Table 10-8 assumes essentially full operation of Alcator C through FY84 with a phase-back beginning early in FY85.

Table 10-8 shows that we have allocated approximately \$28M of this base program over the FY84-88 construction and startup period, thus requiring an incremental cost above that base program of \$21M spread over four years. We suggest that this incremental cost be identified as the Major Device Fabrication (MDF).

During the phase-back period, all engineering personnel would be devoted to construction of the new machine. A reduced physics group under the base program, would participate in design and development, anticipate and prepare certain diagnostics, and prepare the data acquisition system. A number of the Alcator physics personnel will work on Tara and other fusion experiments during the phased-back period.

It is clear from Table 10-8 that a very major fraction of the base program will be devoted to machine construction in FY85, 86 and 87. The minimum level of the remaining program would be approximately \$3M in FY86, the absolute minimum level consistent with preparing for the new machine.

TABLE 10-6

Summary Construction Cost Profile for October FY88 Startup

	TOTAL	FY84	FY85	FY86	FY87	FY88
COMPONENT COST	\$38.95 M	2.80	9.1	11.85	11.1	4.1
LABOR COST	<u>\$10.735 M</u>	<u>1.9</u>	<u>2.7</u>	<u>2.935</u>	<u>2.7</u>	<u>0.5</u>
TOTAL	\$49.685 M	4.7	11.8	14.785	13.8	4.6

TABLE 10-7

Fabricated And Purchased Component Cost Profile

	FY84	FY85	FY86	FY87	FY88	TOTAL
TF CONDUCTOR A	2.00	2.585				
B		2.065	2.52			9.170
WINDING		0.4	0.55			0.950
CASES		1.0	1.0	0.38		2.380
VAC CHAMBER	0.2	0.48	0.57	0.15		1.4
MAG VESSEL		0.4	0.5	0.8		1.7
PROTECT/COOL		0.1	0.35	0.65	0.2	1.3
REFRIGERATION		0.1	0.15	0.95		1.2
PF CONDUCTOR	0.25	0.45	0.55	0.3		1.550
PF WIND			0.6	0.35		0.95
PF CASES		0.1	0.2	0.2		0.5
SITE	0.1	0.7	1.8	1.6		4.2
TF SUPPLY			0.2	0.3		0.5
PF SUPPLY			0.30	0.45	0.55	1.3
CONTROL			0.25	0.25		0.5
DATA ACQ			0.5	0.75	0.5	1.75
AC CABLE				0.2	0.55	0.75
ICRH POWER		0.3	0.5	1.5	0.8	3.10
ICRH ANTENNA			0.25	0.5	0.5	1.25
LH POWER			0.5	0.50	0.6	1.6
LH ANTENNA		0.1	0.5	1.25	0.4	2.25
R & D	0.25	0.3	0.1			0.65
TOTAL	2.8	9.1	11.85	11.1	4.1	38.95

TABLE 10-8

Base Operating Program with Machine Construction

	FY84	FY85	FY86	FY87	FY88	TOTAL
ALCATOR BASE OPERATING PROGRAM	\$10M	10	11	14	16	
MACHINE COST	4.7	11.8	14.785	13.8	4.6	49.685
MACHINE COST INCLUDED IN BASE PROGRAM	1.7	4.8	7.785	9.8	4.6	28.685
INCREMENTAL COST ABOVE BASE PROGRAM	3.0	7.0	7.0	4.0	-	21
TOTAL BASE COST PLUS INCREMENTAL	\$13M	17	18.0	18.0	16	

10.4. Project Management

We propose to organize the Alcator DCT project following guidelines similar to those developed between M.I.T., OFE and CORO for the TARA project. That project was approximately one third the size of the Alcator DCT project and is being carried out on time and on budget over a 2 1/2 year period.

10.4.1. Management Plan

A formal management plan would be written within the first three months of the project and will be negotiated with OFE. The TARA management plan provides a useful model and has the following elements:

- 1.0 Introduction - Describe the purpose and scope of the management plan.
- 2.0 Objectives - Describe the major technical, schedule, and cost objectives of the project. Include descriptions of, and definition of the boundaries between, MDF, site preparation, and base program. Define the completion of the MDF.
- 3.0 Performance Criteria - Define the performance criteria for each major subsystem (i.e., the subsystem performance requirements in terms of engineering parameters rather than the experimental physics objectives of the overall system).
- 4.0 Organization - Define the project organization. Include PFC organization, relationship to OSP, PFO, subcontractors, and DOE (OFE, Field Office, and Procurement). Describe the responsibilities of all parties, identify key personnel, and describe the staffing plan for the project.
- 5.0 Work Plan - Describe the major subsystems, including subsystem design description which relate project performance requirements to design parameters. Describe what is going to be done and how it will be accomplished, in accordance with the WBS. Discuss quality assurance and quality control for each subsystem.
- 6.0 Schedule - Provide a summary schedule for the project using form DOE 535 (Milestone Schedule and Status Report), based on detailed logic diagrams. Include a log of major milestones which ties into the summary schedule. Indicate the critical path(s).
- 7.0 Cost Plan - Provide a summary cost plan. Provide time-phased cost details by WBS. Include costs, commitments, and need for funds as a function of time.

- 8.0 Manpower Plan - Provide a summary manpower plan with time-phased manpower details by WBS.
- 9.0 Management Systems - Describe the systems that will be used to manage the cost, schedule, and technical performance of the project. Include funds for management and control.
- 10.0 Documentation and Reporting Plan - Briefly summarize all project documentation including content, frequency of issue, distribution, and responsibility for preparation, review, and approval.
- 11.0 Procurement Plan - Discuss the acquisition strategy for the project. Identify and discuss anticipated major subcontracts, including scope of work, planned award date, estimated cost, need for DOE approval, and potential contractors. Identify the need for long-lead procurements. Discuss plans for Government-furnished and M.I.T.-furnished equipment and facilities.
- 12.0 Test Plan - Discuss the rationale for all tests planned for the project. Relate the test effort to the project's technical risks, operational issues and concepts, performance criteria, and system availability. Include component, subsystem, integrated system, and operational tests.
- 13.0 Change Control Plan - Define the need and the procedures for approval of changes to the technical, schedule, and cost baselines.
- 14.0 Environmental, Safety, and Health Plan - Describe the plan for ensuring compliance with ES&H requirements.
- 15.0 Work Breakdown Structure - Provide a three-level WBS for the project.
- 16.0 Logic Diagram - Provide a logic diagram (activity net) for each major subsystem.

17.0 Management Plan Approval - Provide a signature page for M.I.T. and DOE approval of the management plan.

10.4.2. Project Organization

We proposed to organize the overall Alcator DCT project as shown in Figure 10-2. R. Parker and B. Montgomery will serve as co-project leaders as they did for Alcator C.

The project managers will be advised by a Review Board which will be chosen to reflect a broad input from inside and outside M.I.T.

The project office would be responsible for monitoring financial affairs, for contracting, and for reporting.

An independent quality assurance function is shown to monitor all technical activities reporting to the project managers. It is our intention to staff this position with an individual such as one with experience in the nuclear construction industry, and to give him broad responsibility for assuring independent review and analysis of design specifications, fabrication, acceptance and installation of major components and systems.

The project is shown as divided into two main branches, a project physics branch, and a project engineering branch. This reflects our strong view of the need for a project oriented, interactive contribution from physics as well as engineering.

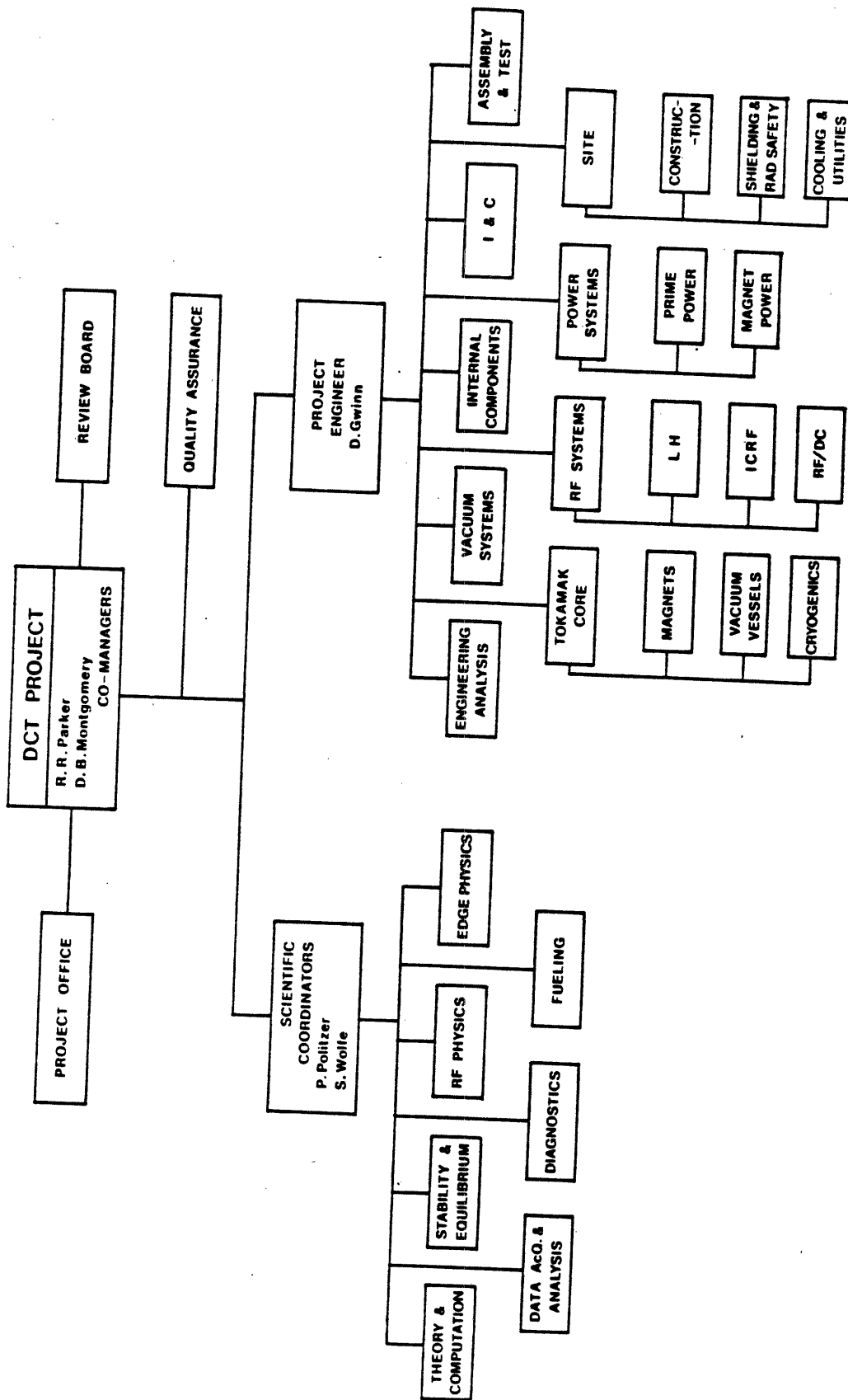


FIGURE 10-2 Alcatraz DCT Project Organization

APPENDIX A

DESCRIPTION of the LOWER HYBRID CURRENT DRIVE CODE

The transport code solves conservation equations for the time evolution of the bulk plasma quantities $\psi(r)$, $T_e(r)$, and $T_i(r)$, where $\partial\psi/\partial r = B_\theta(r)$. The plasma density $N(r)$ and the toroidal field B_0 are held constant in time. The ion conductivity is assumed to be three times the neo-classical value [A-1] and the electron thermal conductivity is taken to be of the form [A-2] $\lambda_e = \lambda_e^0(T_e = T_e^0)$. Here

$$\lambda_e^0 = B_\theta(r) Z_{ef}^{0.4} (a / (r N^{0.8} T_{em_i}^{0.2}))$$

and T_e^0 is the electron temperature at the instant before the RF is turned on. Net RF source terms for the electron and ion energy densities are obtained from quantities calculated in the ray tracing and Fokker-Planck code blocks. The stream function ψ is used as a dependent variable because the externally imposed boundary condition in the simulated experiments involves impressed voltage rather than total plasma current.

The parallel electron distribution function $f_e(V_\parallel)$ is found by solving at each plasma radius a relativistic one-dimensional Fokker-Planck equation written as,

$$\begin{aligned} \frac{\partial f_e}{\partial t} = \frac{1}{\gamma^3} \left\{ - \frac{eE_\parallel}{m_e} \frac{\partial f_e}{\partial V_\parallel} + \frac{\partial}{\partial V_\parallel} \frac{1}{\gamma^3} D_{q\parallel}(V_\parallel) \frac{\partial f}{\partial V_\parallel} \right. \\ \left. + \frac{\partial}{\partial V_\parallel} \nu(V_\parallel) \left[V_\parallel f_e + \frac{1}{\gamma^3} \left(\frac{1}{2} v_e^2 + \frac{\overline{v_1^2 - v_e^2}}{2(2+Z_{eff})} (1+Z_{eff}) \right) \right] \right. \\ \left. \times \frac{\partial f_e}{\partial V_\parallel} \right\} + \Gamma \delta(V_\parallel) \left\{ - f_e(V_\parallel) / \tau_L = 0. \right. \end{aligned}$$

Here $D_{q\ell}$ is an appropriately averaged quasilinear diffusion coefficient for electrons on a magnetic surface that is calculated by the ray tracing code, $\nu(V_{\parallel})$ is an effective collision frequency, τ_L is a loss rate for electrons (important at high velocities), $\Gamma\delta(V_{\parallel})$ is a source of particles at low velocity which balances the loss of electrons, and E_{\parallel} is the DC electric field. For phase velocities below those corresponding to the region of power of LH waves, $\overline{V_1^2}$ is inferred from numerical simulations of Wiley and Hinton [A-3]. For phase velocities which lie in the region of RF power, $\overline{V_1^2}$ is assumed to be $\sim 5V_e^2 Z_{\text{eff}}^{0.4}$ [A-4]. τ_L is taken to be 100 msec. The RF current density and the energy loss rate due to the escape of plateau electrons are found by taking appropriate moments of $f_e - f_e(D_{q\ell}) = 0$.

The wave propagation is modelled using the ray equations $\frac{dx}{dt} = -(\partial D / \partial \underline{k}) / (\partial D / \partial \omega)$ and $\frac{dk}{dt} = (\partial D / \partial \underline{x}) / (\partial D / \partial \omega)$, where t is time along a ray trajectory, $\underline{x} = (r, \theta, \phi)$ are the usual toroidal coordinates, $\underline{k} = (k_r, k_{\theta}, k_{\phi})$ are the canonically conjugate momenta, and $D(\underline{x}, \underline{k}, \omega) = 0$ is the LH dispersion relation including electromagnetic and warm plasma effects. The Brambilla power spectrum launched at the plasma edge is discretized into 26 components. An axisymmetric toroidal equilibrium is constructed using Shafranov's aspect ratio expansion, where the zeroth order equilibrium is given by the quantities N , T_e , T_i , B_{θ} , and B_0 of the transport code. Resonant wave damping is calculated using the quasilinear electron distribution outlined above and assuming a Maxwellian distribution function for the ions. Nonresonant absorption due to electron-ion Coulomb collisions is also calculated. A rate equation for the power deposition that incorporates these damping mechanisms is integrated simultaneously with the ray equations and rays are followed until they

are completely absorbed. RF power deposition is found by summing ray losses in 40 radial zones. The quasilinear diffusion coefficient $D_{q\parallel}$ is calculated by appropriately summing ray amplitudes for multiple passes through a magnetic surface, taking into account the strong variation of $k_{\parallel} = \underline{k} \cdot \underline{B} / |\underline{B}|$ along a ray trajectory due to the ϕ dependence of the dispersion relation and the r dependence of B_{θ} [A-5].

References

- [A-1] F. L. Hinton and R. D. Hazeltine, Rev. Mod. Phys. 48, 239 (1976).
- [A-2] B. Coppi, Comm. Plasma Phys. Cont. Fusion 1, 1 (1982).
- [A-3] J. C. Wiley and F. L. Hinton, Phys. Fluids 23, 921 (1980).
- [A-4] C. F. F. Karney and N. J. Fisch, Phys. Fluids 22, 1817 (1979).
- [A-5] P. T. Bonoli and E. Ott, Phys. Fluids 25, 359 (1982).

APPENDIX B

HEAT LOAD ANALYSIS

This Appendix includes a brief summation of several different analyses of the primary heat load surface. Further material is available in "Pumped Limiter Study for Alcator DCT" (ANL/FPP/TM-175) on the following subjects: heat and particle loads; erosion/redeposition; disruption characteristics; fatigue lifetime of limiter heat sink; surface material comparisons; and lifetime analysis.

B.1. Thermal Hydraulics of the Collector Plate

The structure receiving the primary heat load for Alcator DCT is assumed to remove the total steady-state input power of 10 MW. Allowing a maximum temperature rise of 30° C in the coolant requires that it flow at a rate of 80 kg/sec. Dividing this flow equally among 12 modules yields 6.6 kg/sec/module. The dimensions of each module are .6 × 1.0 meters. Therefore the average heat flux is 1.38 MW/m².

The cooling tubes for such a 'pad' could consist of a series run of 4.0 cm diameter cooling tubes. Given a flow rate of 6.6 kg/sec we find that the water flow velocity is 5 m/sec. For the above conditions, in addition to a water temperature of 75° C, the Reynolds number would be 5.4×10^5 . The pressure drop for twelve such tubes plus 180° bends is 31 psi.

To calculate the heat transfer coefficient we use the McAdam correlation for heat transfer in turbulent flow. The value of h determined is 2.1×10^4 W/m² °C. With an assumed temperature difference of 100°C

between the tube wall and the bulk fluid, the necessary area for heat transfer is 0.4 m^2 . Twelve 1.0 meter long tubes on 5 cm centers would form an array equal in width to the module. Each tube would have to provide 3.0 cm of active perimeter ($\sim 90^\circ$). This would be achievable with any reasonably thick tile covering. We have calculated front surface temperatures assuming perfect heat conductance between the back surface of the graphite tile and the coolant channel wall. These values are shown in Figure B-1. The parameters discussed above are summarized in the following table.

TABLE B-1

Pumped Limiter/Divertor Plate

CONTINUOUS TOROIDAL LIMITER/DIVERTOR PLATE

TOTAL POWER (MW)	10.0
TOTAL AREA (m^2)	7.5
AVERAGE FLUX (W/cm^2)	138
PEAK FLUX (W/cm^2)	200
TOTAL COOLANT FLOW (kg/s)	80
ΔT_{WATER} ($^\circ\text{C}$)	30
COOLANT TUBE DIA. (cm)	4.0
HEAT TRANSFER COEFF. ($\text{W}/\text{cm}^2 \text{ }^\circ\text{C}$)	2.1
REYNOLDS NUMBER	5.4×10^5
PRANDTL NUMBER (at 75°C)	2.5
FLOW VELOCITY (m/s)	5.1
PRESSURE DROP (Pascals) [psi]	2.1×10^5 [31]

T at surface vs. thickness (POCO graphite)

k (W/cm deg C) = $6.00E-01$ q (W/cm**2) = 138

emissivity = $8.00E-01$ h (W/cm**2 deg K) = 2.1

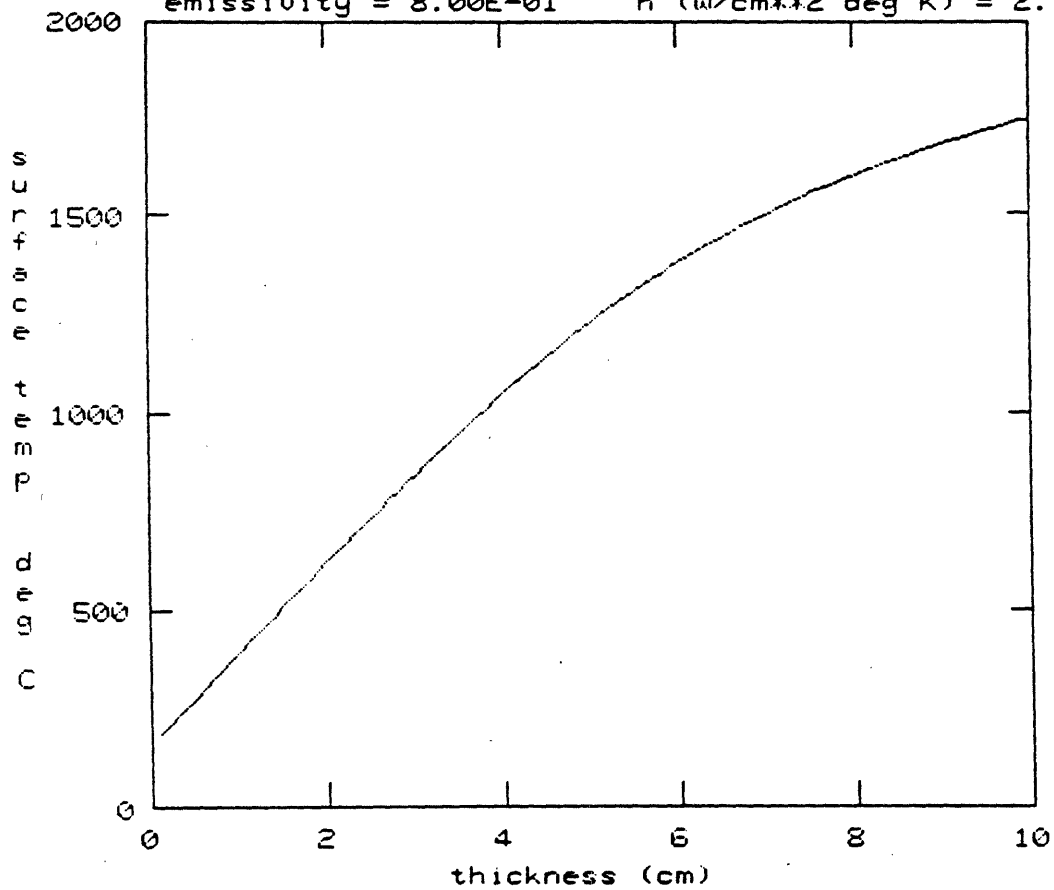


FIGURE B-1 Surface temperature vs. thickness of a graphite block.

B.2. Disruption Characteristics and Lifetime Analysis

Disruption heat loads can be a significant erosion mechanism for the primary heat loading surface. We assume that the plasma thermal energy is deposited in the same profiles as the normal deposition described in Section 3.3. The magnetic energy will be deposited uniformly over the vacuum chamber. The time scales over which these loads are deposited are 1 ms and 5 ms respectively. Results are summarized in the following table.

TABLE B-2

Disruption Characteristics

Thermal Quench

Time	1 ms
Energy to limiter	1 MJ
Limiter area	7.5 m ²
Average energy density	13.3 J/cm ²
Disruption peaking factor	2.5

Current Quench

Time	5 ms
Energy to limiter (50%) and walls (50%)	2 MJ
Average limiter deposition	13.3 J/cm ²
Average wall deposition	1.67 J/cm ²
Peaking factor	2.5

The erosion rates due to disruptions is dependent on several factors: the initial temperature of the surface; the uniformity of the melted layer; the structure of the surface (redeposited, previously melted,

etc.); and the quantity of melt layer lost. Calculations of disruption melt layer thickness for INTOR assumed a 500 J/cm^2 , 5 ms deposition with an initial temperature of 300° C . The melted layer was 28μ /disruption. For Alcator DCT, on the other hand, we have assumed $\sim 30 \text{ J/cm}^2$ peak load over 1 ms. This should lead to much lower erosion rates.

The lifetime analysis will then be dominated by the sputtering and redeposition rates. Calculations by Argonne indicate a net difference between those two rates of 1-2 cm/year. This estimate is highly dependent on the physics of the scrapeoff layer. One goal of the Alcator C program is to understand these processes in order to predict such numbers for a reactor.

APPENDIX C
EDDY CURRENT EFFECTS

C.1. Disruption Induced Eddy Currents

A finite element model has been constructed to estimate some of the electromagnetic effects of a plasma disruption in an Alcator DCT scale device. The model is shown in Figure C-1 and is based on the dimensions of an earlier Alcator DCT concept. It utilized a set of 36 TF coils with a circular vessel cross-section. The model uses: (1) a circular plasma with two uniform λ_j current density regions; (2) three OH coils; (3) two EF coils; (4) a continuous inner shell; (5) an outer shell with continuous sections which are shaded and interrupted sections for port access; and (6) a vacuum vessel with inboard and outboard segments which are continuous while other sections are discontinuous. Cases have been run where the outboard segment has either no net current, or net current with stainless steel and/or copper to consider conditions where a continuous segment of enhanced conductivity may be necessary for passive stabilization purposes.

Whether or not a section is toroidally continuous, and can thus carry a net current through an R-Z plane, has a significant effect on its time constant and ability to delay the collapse of the plasma flux following a disruption. Several different cases were run to illustrate these effects and are discussed in this section. Specifically they consisted of:

- Case a - no net current in cross-hatched regions in Figure C-1 or in outboard segment.
- Case b - net current allowed in all shells including cross-hatched regions in Figure C-1.

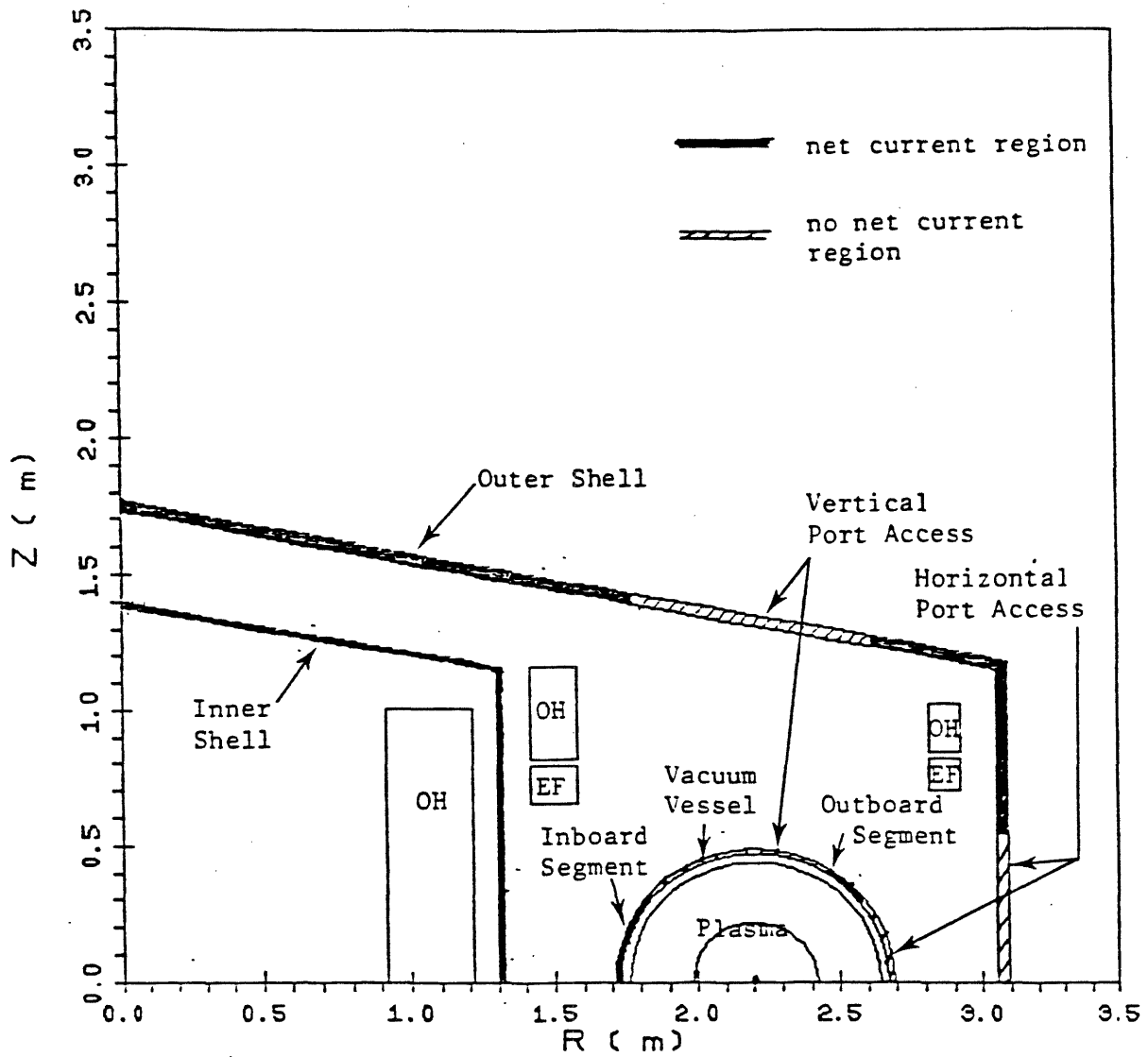


FIGURE C-1 Major Components of the Finite Element Model

Case c - model as in Figure C-1 with outboard segment consisting of toroidally continuous stainless steel.

Case d - model as in Figure C-1 with outboard segment consisting of toroidally continuous copper.

The model utilized a 10^6 A plasma which decayed linearly to zero current in 5 ms and the shell characteristics outlined in Table C.1-1. The model is axially symmetric. Therefore, sections such as those between access ports are modeled as no-net-current regions to force current return, and with a thickness or resistivity adjustment to account for the added current path length for saddle currents which do not occur explicitly in the model. Copper was added in parallel to the stainless steel in the cross-hatched regions of the vacuum vessel to enhance conductivity as a possible stabilizing mechanism.

The field lines produced by the plasma in the steady-state are shown in Figure C-2. As the plasma current decays, those field lines which link shells induce eddy currents which tend to retard the decay of the plasma flux. Figures C-3 and C-4 show field line patterns for two of the four cases at the same instant of time, 10 msec after the start of the plasma decay (disruption). In both cases the plasma current is zero at 10 msec. Regions where strong eddy currents have been induced are indicated by a strong kink in the field lines as they pass through the current carrying region because, on this scale, the current causes an effective discontinuity in the tangential component of the field.

In Figure C-3, the diffusion of field lines is retarded primarily by the net current carrying region in the outer corner of the outer shell.

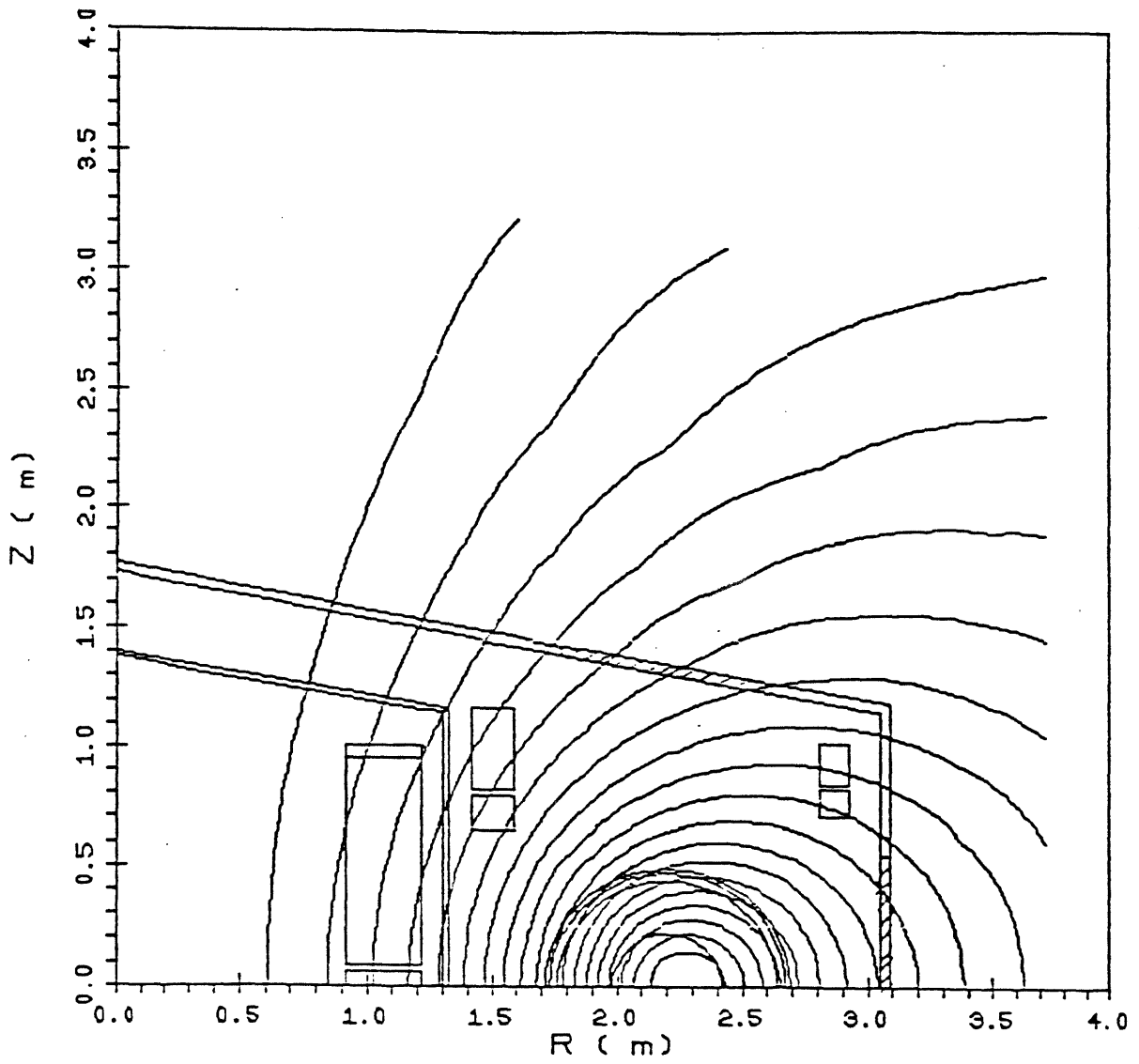
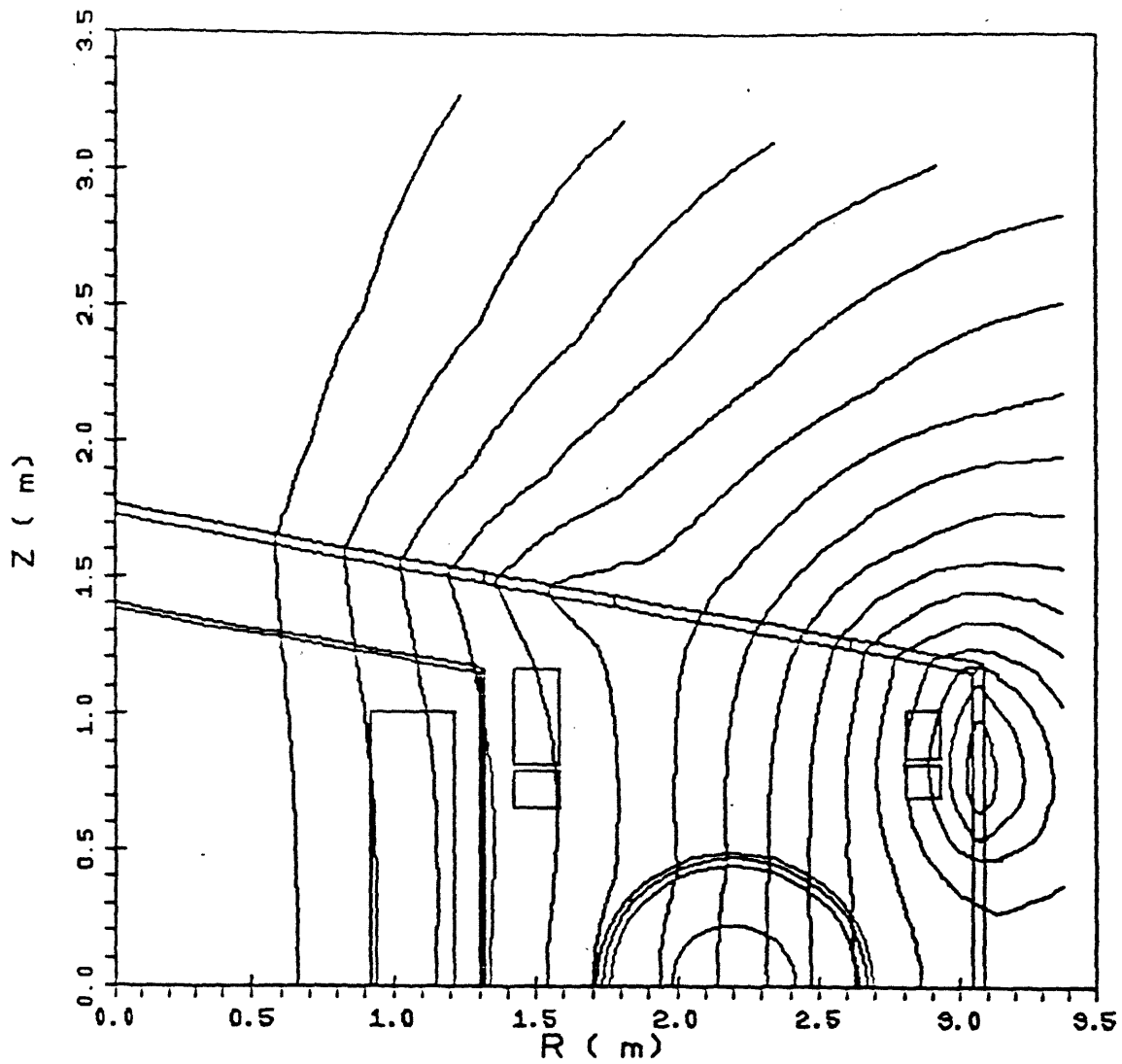
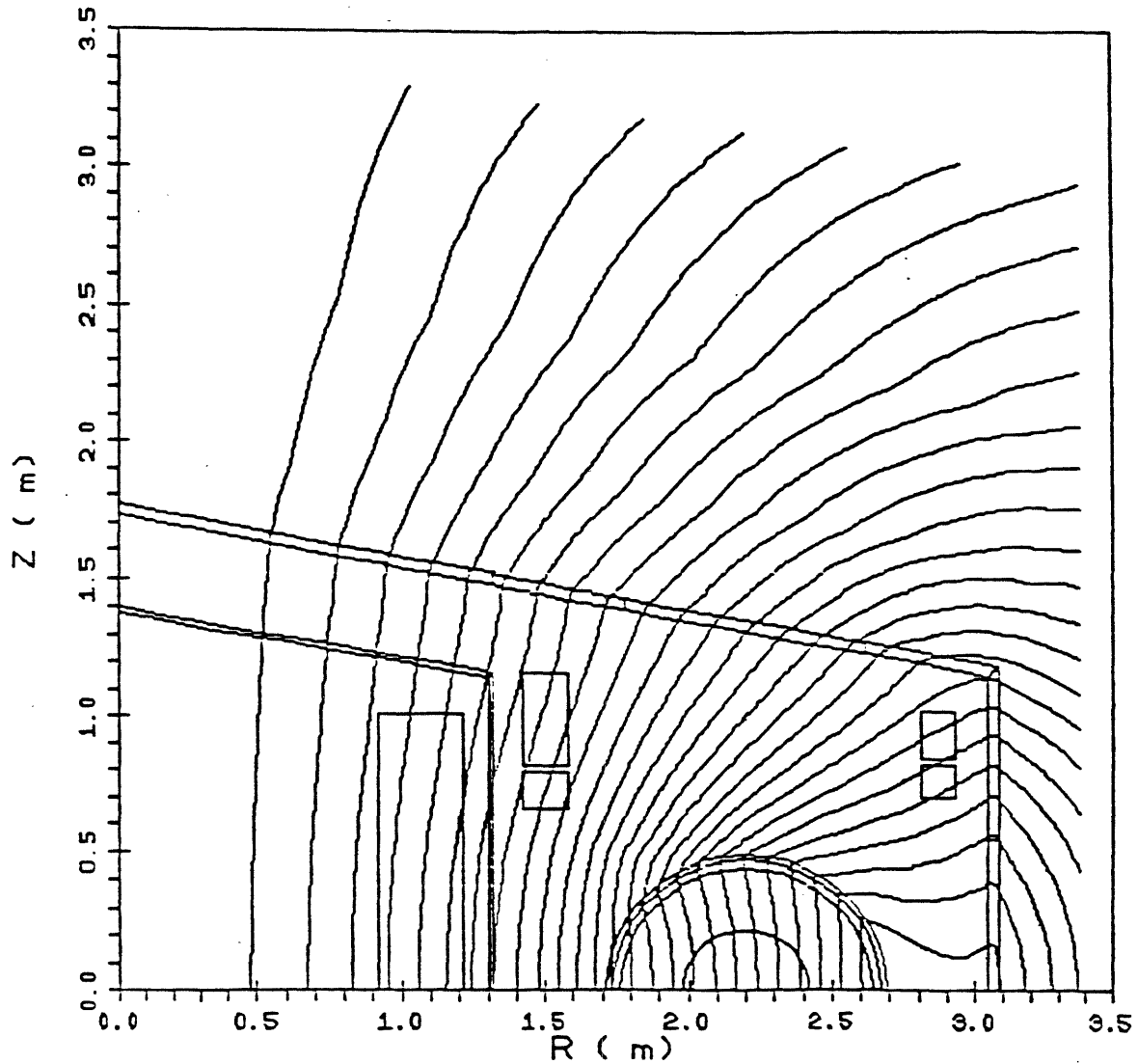


FIGURE C-2 Steady State Field Lines Produced by the Plasma



CONTOURS OF CONSTANT r_A

FIGURE C-3 Field Lines 10 ms after Plasma Disruption for Case "a," no Net Current in Cross-Hatched Sections or in Outboard Segment (Figure 3.1). Eddy Currents Induced Primarily in Outer Shell Net Current Regions and in Inboard Segment.



CONTOURS OF CONSTANT r_A

FIGURE C-4. Field Lines 10 ms after Plasma Disruption for Case b, Net Current in all Shells. Eddy Currents Primarily Induced throughout the Vacuum Vessel and Outer Shell.

TABLE C.1-1

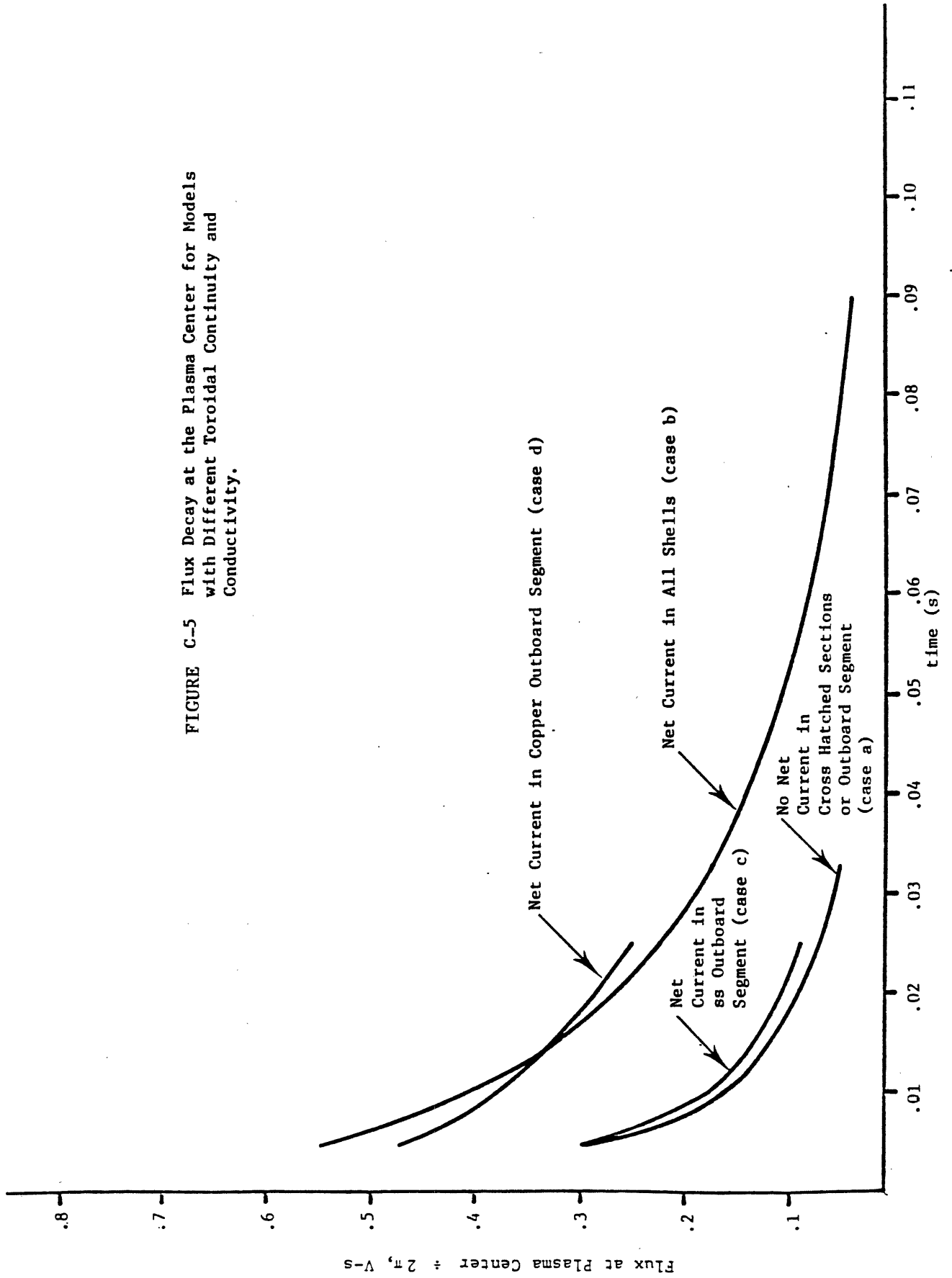
Shell Characteristics for Finite Element Model in Figure C-1

REGION	CONSTRUCTION
1. Inner Shell	0.15 cm thick stainless steel at 4.2 K; toroidally continuous
2. Outer shell, top & outer corner	2.5 cm thick stainless steel at 300 K; toroidally continuous
3. Outer shell, vertical port access	2.5 cm thick stainless steel at 300 K; plates subtend $\sim 5^\circ$ out of $\sim 10^\circ$ between port centers
4. Outer shell horizontal port access	2.5 cm thick stainless steel at 300 K; plates subtend $\sim 12^\circ$ out of $\sim 20^\circ$ between port centers
5. Vacuum vessel inboard segment	2.5 cm thick stainless steel at 300 K in series with two parallel bellows 0.1 cm thick and equivalent length = twice actual; plates occupy $\sim 1/4$ of periphery; bellows occupy $\sim 3/4$
6. Vacuum vessel vertical and horizontal port access	2.5 cm thick stainless steel at 300 K in series with two parallel bellows 0.1 cm thick and equivalent length = twice actual; plates occupy $\sim 1/4$ of periphery; bellows occupy $\sim 1/4$ of periphery; ports $\sim 1/2$ of periphery; stainless in parallel with ~ 0.33 cm equivalent thickness of copper for passive stabilization

Figure C-4 is markedly different because net current is allowed to flow in all shell sections. As a result, the entire vacuum vessel carries strong eddy currents and the increased field line density relative to the first case shows that the flux decay time is substantially slower.

The flux decay in time is a function of position. For illustrative purposes, it is shown in Figure C-5 for the four cases, for a contour

FIGURE C-5 Flux Decay at the Plasma Center for Models with Different Toroidal Continuity and Conductivity.



through the plasma center, and can be used to envision the typical time for eddy current decay. Strictly speaking, the process is not described by a single time constant because eddy currents at different positions do not necessarily decay at the same rate. For comparison purposes, however, the times at which the flux in Figure C-5 decays to e^{-1} and to e^{-2} of its initial value are as follows:

TABLE C.1-2

"Time Constant" for Flux Decay in Figure C-5

CASE	CONDITION	e^{-1} TIME (ms)	e^{-2} TIME (ms)
a	No net current in cross-hatch sections or out-board segment	< 5	11
		< 5	11
b	Net current in all shells	11	41
c	Net current in ss out-board	< 5	12
d	Net current in Cu out-board	10	~ 52

The eddy currents induced in the shells interact with their own fields and with the applied fields from the OH and EF coils to produce electromagnetic loads on the shells. Locally this load can have components normal and tangential to the shell surface. These may be expressed as normal and shear pressures, respectively, where each represents a local force per unit shell surface area (i.e., the local force density component may be found if desired by dividing these pressures by the shell thickness). The normal and shear pressure distributions were computed for the three shells for the four cases: a, b, c and d discussed earlier. The distributions of normal and shear pressure in the vacuum

vessel for case b (net current in all shells) are shown in Figures C-6 and C-7.

Load distribution and magnitudes vary considerably between cases. A summary of the extreme load magnitudes for each case and the location is given in Table C.1-3. Loads were calculated assuming that the disruption occurred when the OH coils were at the end of their negative swing and the EF coils were on. Although load magnitudes are generally modest, they require review because of their non-uniform distribution. The loads given illustrate typical levels and distributions, but not necessarily the worst case since other points in the PF coil current scenario have not yet been considered. The model will also be up-dated to reflect the noncircular aspects of the current design.

TABLE C.1-3

Summary of Extreme Local Loads for Each Case

CASE	MAX NORMAL PRESSURE		LOCATION	MAX SHEAR PRESSURE		LOCATION
	(N/m ²)	(psi)		(N/m ²)	(psi)	
a	1.3×10^5	18.9	Outer shell at corner	-8.3×10^4	-12.0	Outer shell top near port
b	-6×10^4	-8.70	Vacuum vessel out-board	-4.6×10^4	-6.67	Outer shell top near port
c	1.1×10^5	15.9	Outer shell at corner	-7.7×10^4	-11.0	Outer shell top near port
d	-3×10^5	-43.5*	Vacuum vessel out-board	3.7×10^5	-53.6*	Vacuum vessel out-board

*High localized pressure on copper stabilization loop or coil.

Case_5_Pn_vacvessel

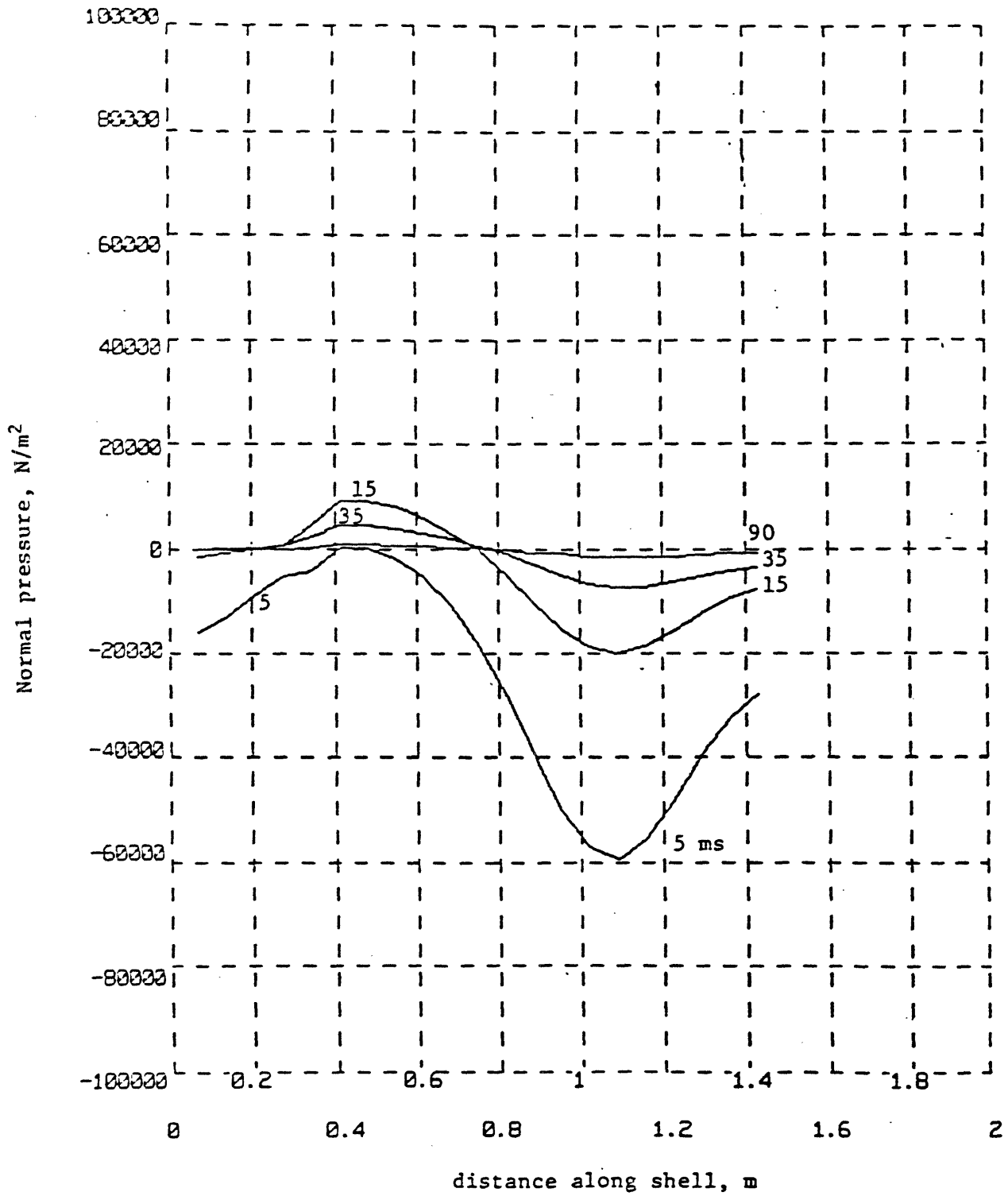


FIGURE C-6 Normal Pressure on Vacuum Vessel for Case b.

Case_5_Ps_vacvessel

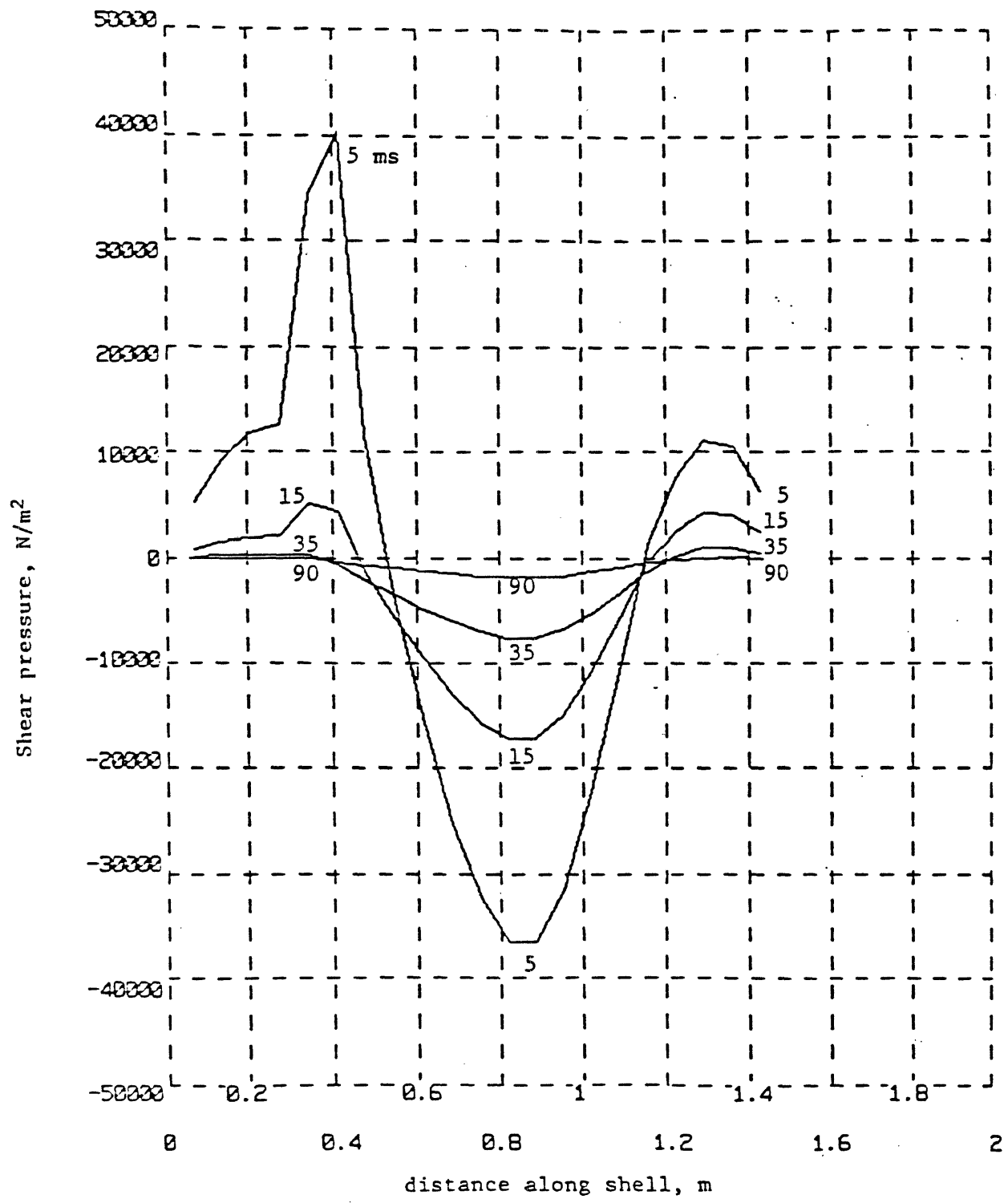


FIGURE C-7 Shear Pressure on Vacuum Vessel for Case b.

C.2. Start-up Induced Eddy Currents

The finite element model described in the previous section was also used to estimate the delay of flux penetration into the vacuum vessel during the OH system swing. The OH coil field line pattern before the swing starts is shown in Figure C-8.

The voltage induced in the plasma would appear as soon as the OH ramp begins and would be ≈ 123 V for a ramp to zero current in 0.117 sec if eddy current effects were not present. The effect of the eddy currents is to delay the flux change and, in turn, the voltage at the plasma. The voltage vs. time for two cases is shown in Figure C-9. Both use the finite element model described earlier. The upper trace (shorter time constant) corresponds to Case a described earlier and the other trace to Case d. Case a does not allow net current flow in the cross-hatched sections (port access) in Figure C-1 or in the outboard segment whereas Case d uses a copper outboard segment as may be required for enhanced passive stabilization. The plasma loop voltage 5 msec after the start of the OH ramp-down is only half the value which would be available if the eddy currents were not present. As discussed in Section 4.3.2.2, this ramp-down rate represents the 20 kV voltage limit at a 50 kA OH current level and, therefore, Figure C-9 represents the maximum feasible voltages available. We consider the voltage at 5 msec to be adequate for unassisted plasma breakdown.

Figure C-10 shows typical induced currents in the vacuum vessel during OH ramp-down.

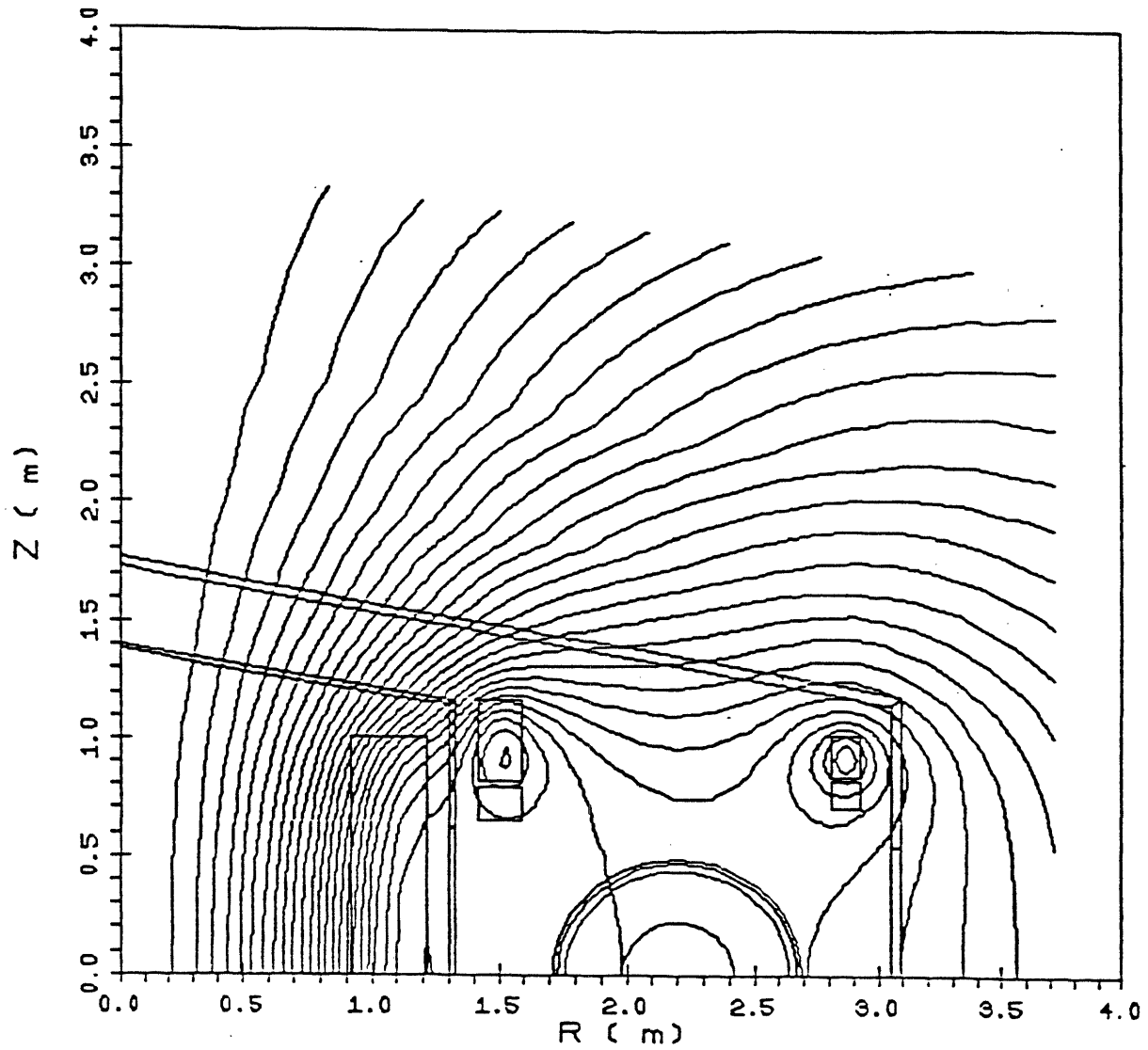


FIGURE C-8 Steady State Field Lines from the OH Coil System.

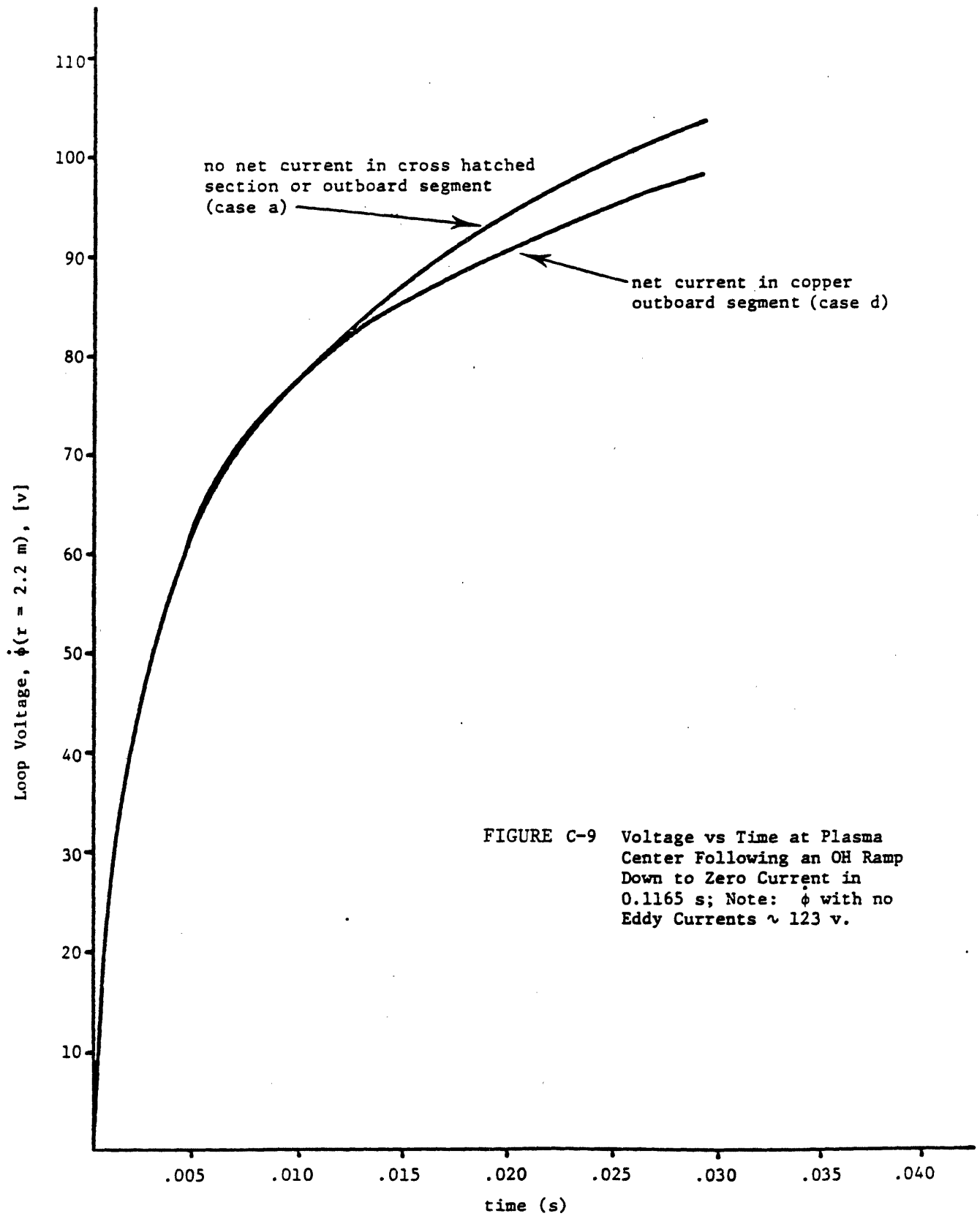


FIGURE C-9 Voltage vs Time at Plasma Center Following an OH Ramp Down to Zero Current in 0.1165 s; Note: $\dot{\phi}$ with no Eddy Currents $\sim 123 \text{ v}$.

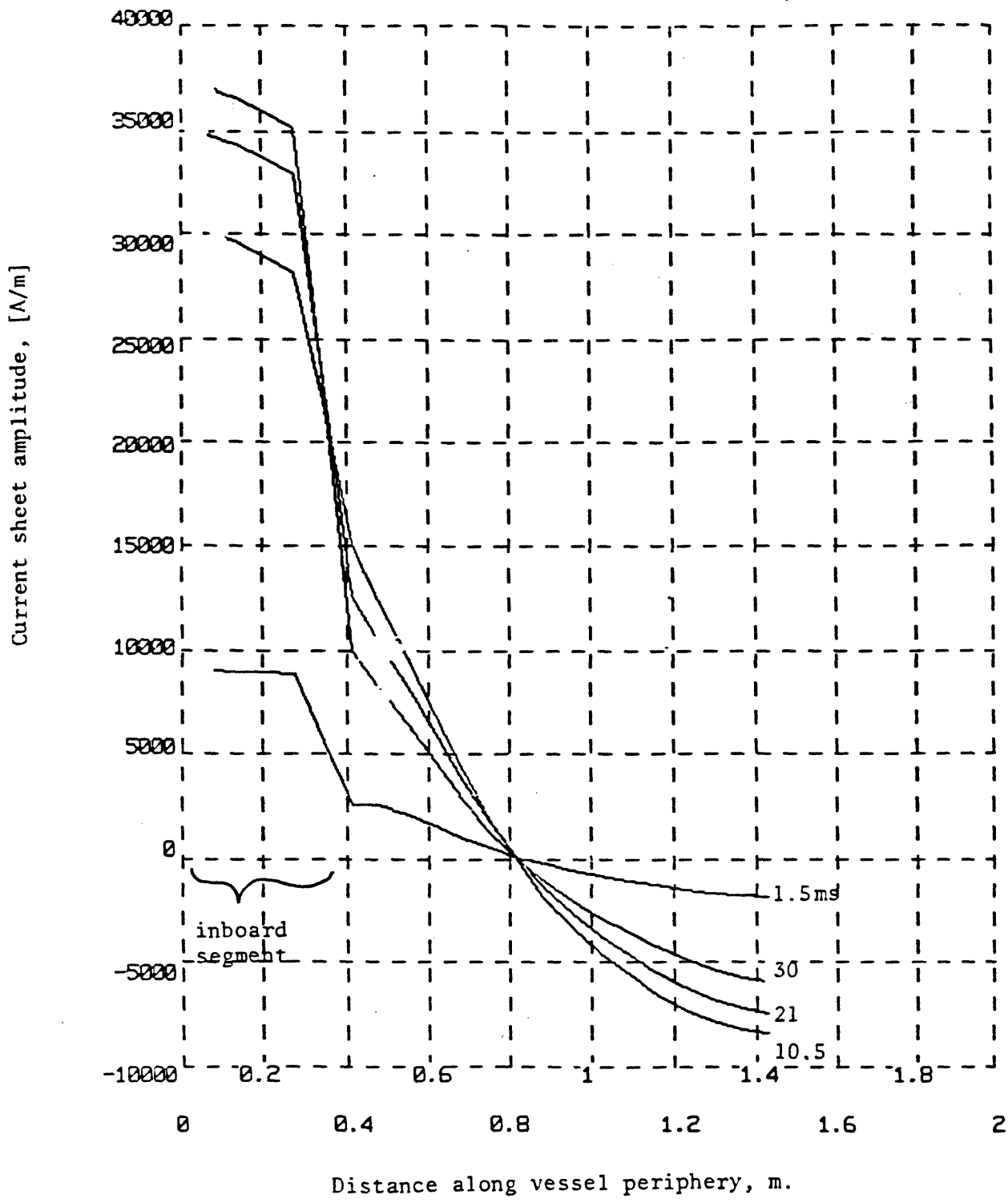


FIGURE C-10 Induced Current in the Vacuum Vessel vs Distance Around Periphery Measured from the Inboard Side for Case a during OH Rampdown.

APPENDIX D

HIGH POWER RF INDUCED IMPURITY GENERATION in TOKAMAK EXPERIMENTS

D.1. Introduction

Impurities play a role in the development of nearly all tokamak discharges. However, through the application of various techniques, including discharge cleaning (both glow and pulsed), baking and gettering, and through judicious choices of limiter design and materials [D-1], it has been generally possible to run these devices over wide parameter ranges with only minor perturbations of plasma resistivity and power balance caused by impurities. This is especially true in the case of ohmically heated discharges. As auxiliary input powers, particularly from various forms of RF, reach levels of 1 MW or greater, certain presently operating devices begin to see strong impurity effects once again. Examples include ICRF heating on TFR [D-2], Alfvén wave heating on TCA [D-3] and lower hybrid heating and current drive on Alcator C [D-4,5]. In this appendix, we examine some of these results, and gauge their consequences with regard to the problems of impurity control on Alcator DCT.

D.2. TFR

The time histories of a typical set of plasma parameters from an ICRF heating case on the TFR device is shown in Figure D-1. [D-2] After about 30 msec into the RF pulse, the electron and ion temperatures stop rising and subsequently decrease for the duration of the RF. This cooling is attributed to radiation from nickel impurities whose influx increases greatly after the RF power is injected. Figure D-2 shows a series of radiated power profiles derived from bolometric measurements. By 40 msec

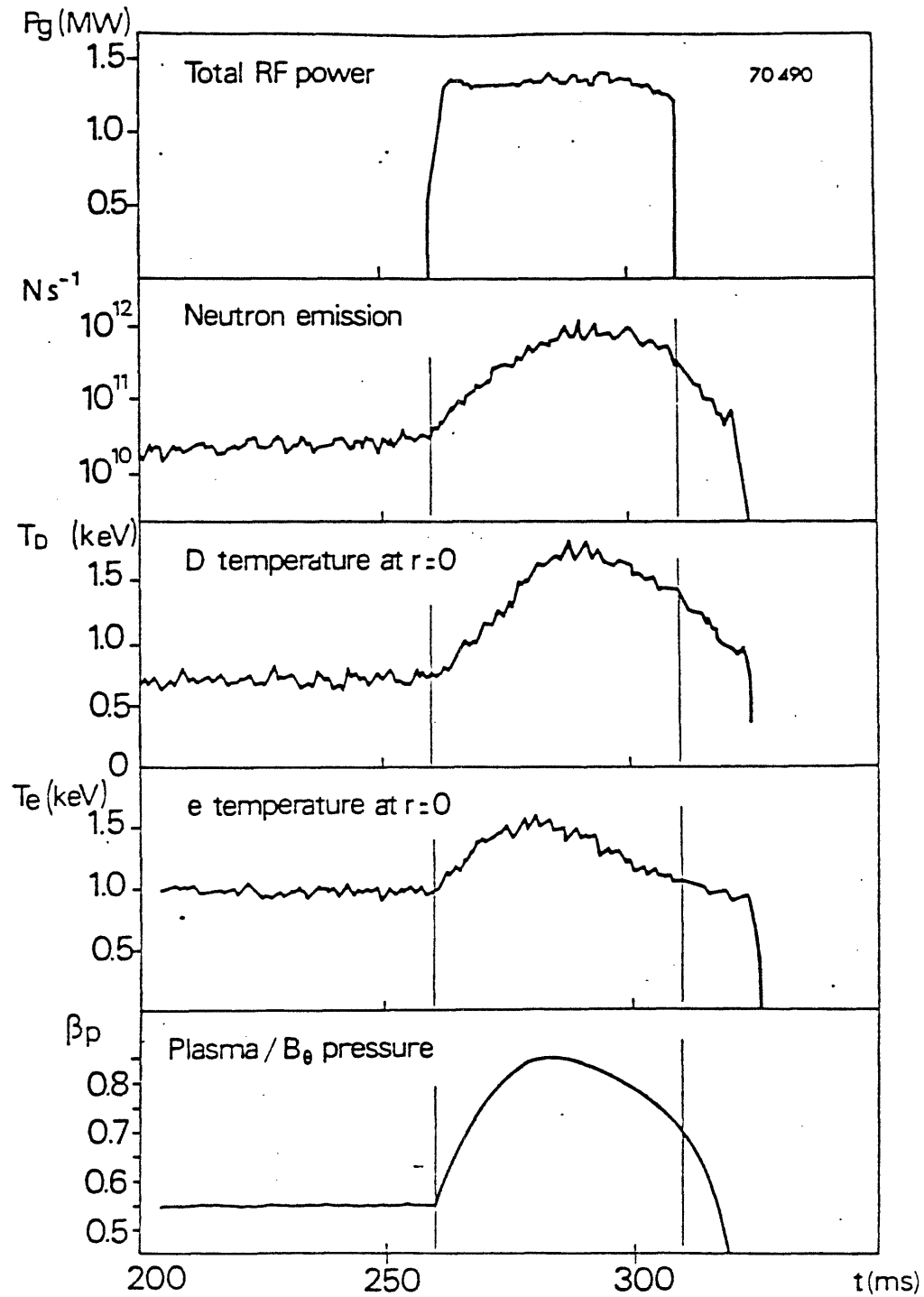


FIGURE D-1 Time histories of various plasma parameters for a typical ICRF discharge in the TFR tokamak.

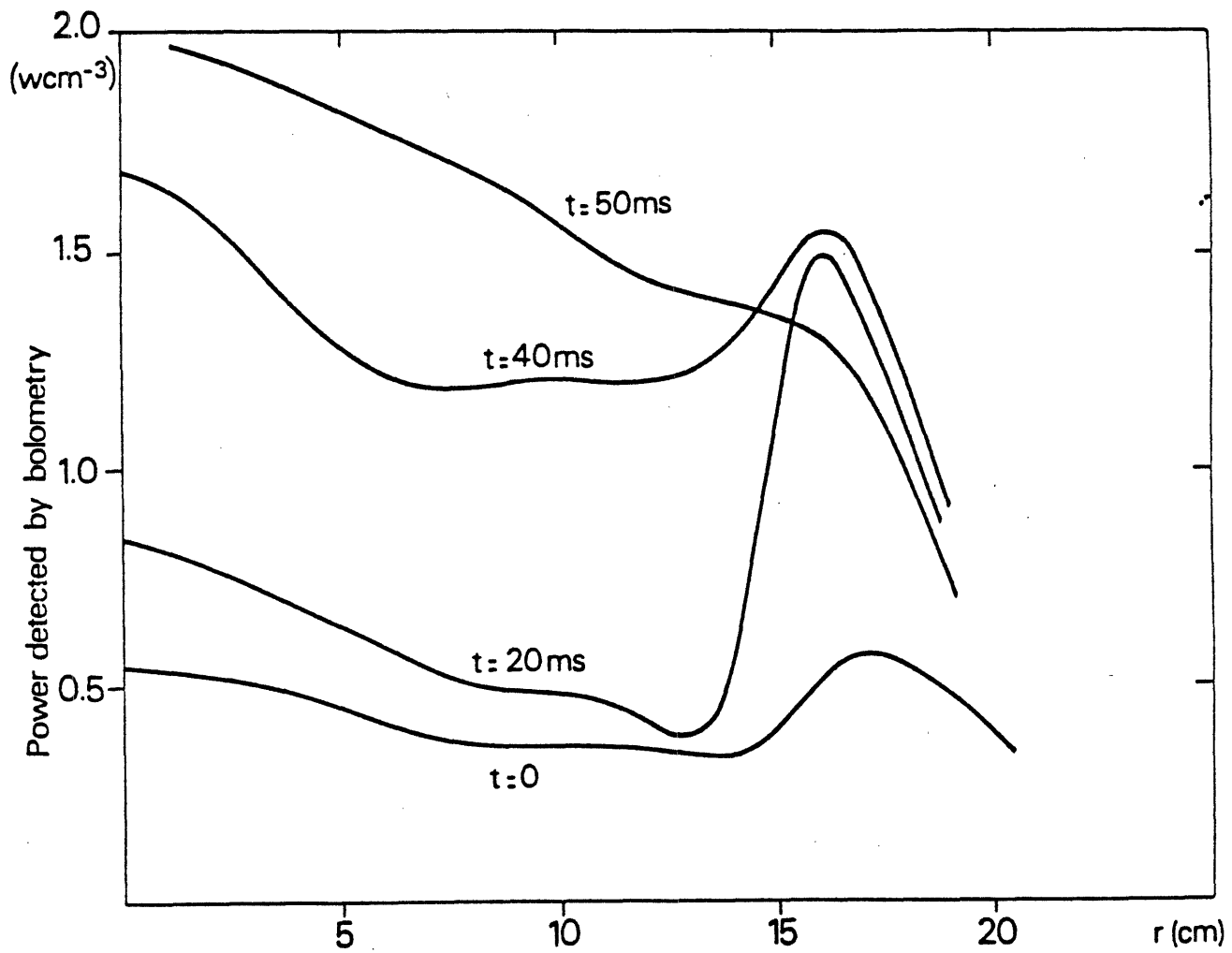


FIGURE D-2 Bolometric profiles of radiated power at various times after the start of RF injection from the shot of Figure D-1.

(after the RF comes on) essentially all of the input power is being radiated away. When the input RF power is increased beyond 1.5 MW, the plasma is terminated by a major disruption after less than 50 msec. In these experiments, the walls, limiters and antenna structures were all constructed of Inconel, so that the main source of the nickel could not be determined. More recent experiments [D-6] indicate that the Faraday shield and the limiters appear to be roughly equal contributors to the impurity influx.

D.3. Alcator C

Experiments are presently underway on the Alcator C tokamak to study current drive and heating using lower hybrid RF at $\nu = 4.6$ GHz [D-4,5]. To date, up to 1 MW of power has been coupled into the plasma. Experiments using limiters composed of molybdenum, silicon-carbide coated graphite, and bare graphite have been performed.

The time histories of various plasma parameters during a typical LHRF heating discharge with Mo limiters are shown in Figure D-3. In this case the total forward RF power coupled into the vacuum chamber (P_{RF}) was 950 kW. The central chord brightness at $\lambda = 75$ Å is indicative of Mo behavior in the plasma. This wavelength is in the center of a pseudo-continuum [D-7] which includes lines from many ionization states, up to MoXXX, and this emission is predominantly from the regions of the plasma where $500 \text{ eV} < T_e < 1500 \text{ eV}$ [D-8]. This signal is thus a good indicator of the time history of the Mo density, provided that the electron density and temperature are not changing significantly. It is clear from Figure D-3 that there is a large increase in the Mo level in the plasma during

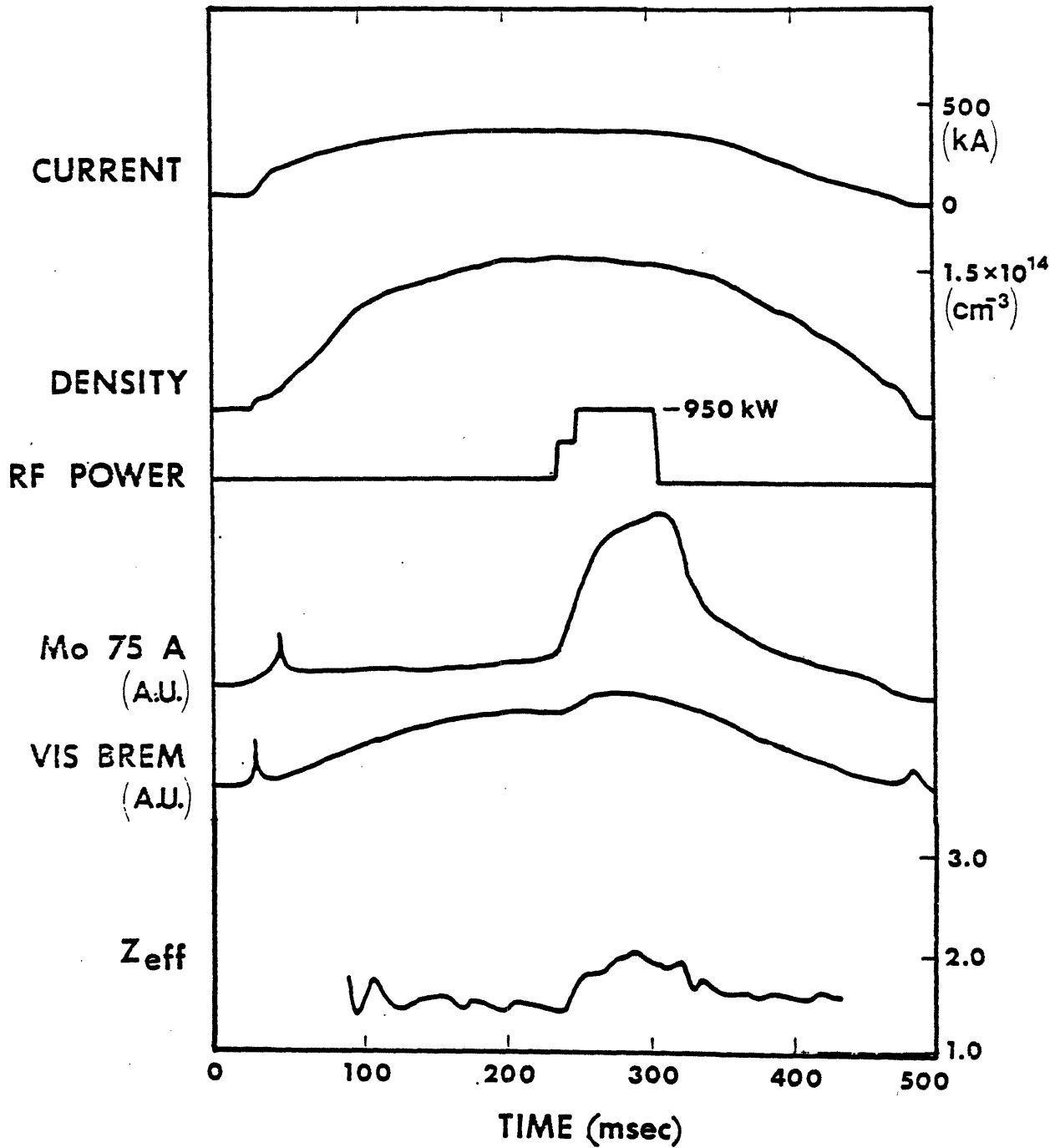


FIGURE D-3 Time histories of various plasma parameters for a typical Alcator C heating discharge with molybdenum limiters. In this case, the peak parameters are $I_p = 400$ kA, $\bar{n}_e = 1.6 \times 10^{14} \text{ cm}^{-3}$, $P_{RF} = 950$ kW, $B_T = 9.3$ T.

the RF pulse. The fifth trace in Figure D-3 shows the brightness at $\lambda = 5360 \text{ \AA}$, which is due mainly to free-free bremsstrahlung. Since the emissivity is proportional to $n_e^2 Z_{\text{eff}}^2 / \sqrt{T_e}$, it can be used to infer a "line-averaged" Z_{eff} [D-9], which is shown as the last trace in the figure. It can be seen that before the RF power is injected, $Z_{\text{eff}} = 1.5$. The enhancement over 1 is due mostly to carbon in the plasma, which is the dominant low Z impurity.

During the RF pulse, with the Mo limiters, the C levels do not change significantly, and we infer that the change in Z_{eff} is due almost entirely to the increased molybdenum. It is thus possible to calculate the absolute Mo density in the plasma. Although bolometric measurements of total radiated power were not available during these experiments, using the cooling rate formalism of Post et al. [D-10], the resulting radiated power loss from the plasma due to the molybdenum can be estimated. Assuming that $n_{\text{Mo}}(r)/n_e(r) = \text{constant}$, the result is that about 1 MW is radiated away. It must be pointed out that there are large uncertainties in this calculation. In particular, the cooling rates, according to the authors of Reference D-10, are only accurate to about a factor of 2. A direct comparison between the brightness at 75 \AA and bolometric measurements has been made, in non-RF discharges [D-11]. In these cases, the cooling rate model, combined with the Z_{eff} measurement, predicted central radiated power densities which were 25% higher than was actually observed. Using these observations as a "calibration" for the technique would imply that $\sim 0.8 \text{ MW}$ is radiated during the RF case examined here. The resultant heating is modest, with T_e increasing by about 400 eV and T_i by about 200 eV.

In order to reduce the levels of high Z (Mo) impurities in the LHRF heated plasmas, the Mo limiters were replaced with limiters utilizing coated graphite blocks. The coatings are chemical vapor deposited silicon carbide, with a coating thickness of about 100 micron. The blocks were baked in vacuum to a temperature of 900° C after coating and before being installed in the tokamak. Mo levels with these limiters decreased by about a factor of 20 to 30 when compared to similar ohmic discharges with the Mo limiters. During the LHRF heating, only small increases in the Mo level were seen (< 30%). However, both Si and C levels are seen to increase substantially. Figure D-4 shows the time development of several plasma parameters with $P_{RF} = 850$ kW and the SiC limiters. Along with the increases of Si and C influx, as evidenced by line radiation from ionization states near the edge of the plasma, strong increases of Z_{eff} are also seen. Figure D-4 shows the Z_{eff} time history for this discharge, and there is clearly a much larger perturbation to this parameter than was the case with the Mo limiters. Although Z_{eff} increases substantially, the electron temperature also goes up, and the net ohmic input power is not greatly increased (< 15%). T_e in this case, as inferred from both soft X-rays and Thomson scattering, increases from 2000 eV before the RF, to about 3000 eV during the heating pulse. The time history of the ion temperature is also shown in Figure D-4, with T_i almost doubling during the heating. It thus appears that the central radiation problem has been largely alleviated, allowing for the good heating. However, plasma purity has been seriously compromised. The increase of Z_{eff} is a very non-linear function of P_{RF} . Figure D-5 shows the results of a power scan with fixed n_e , I_p , and B_t . Below about 500 kW, little or no effect is seen. As the power level approaches 1 MW, the change in Z_{eff} is seen to

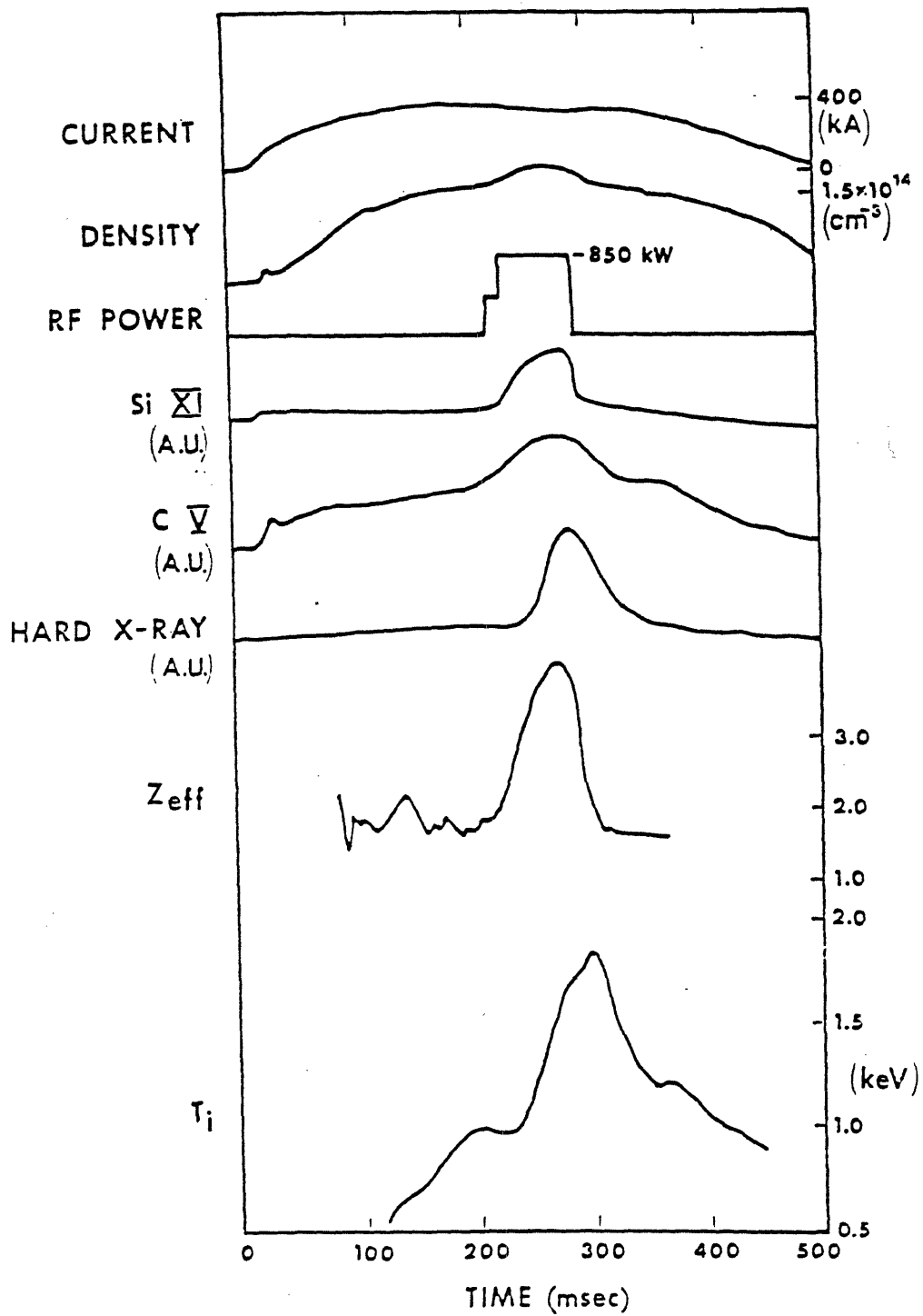


FIGURE D-4 Typical heating discharge with silicon carbide coated graphite limiters: $I_p = 400$ kA, $\bar{n}_e = 1.7 \times 10^{14}$ cm⁻³, $P_{RF} = 850$ kW, $B_T = 9.3$ T.

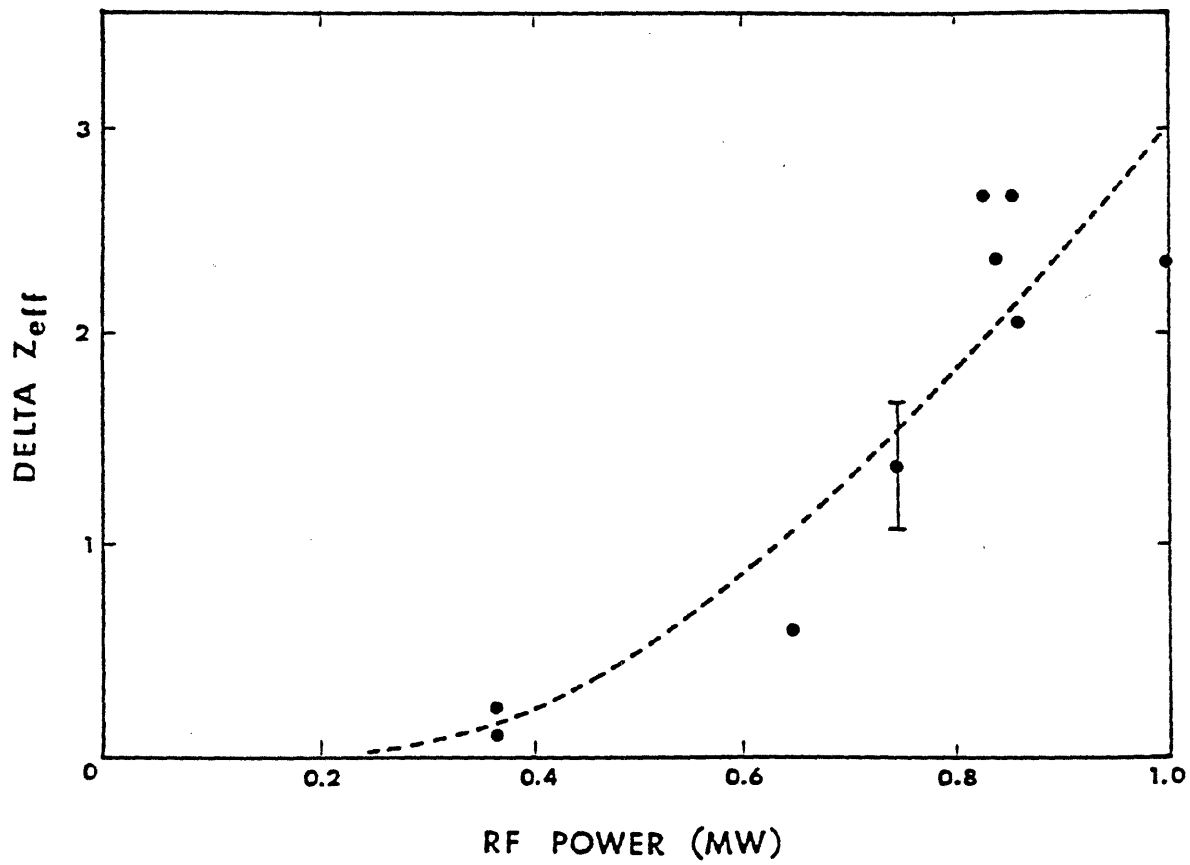


FIGURE D-5 Power scan for ΔZ_{eff} vs. P_{RF} with SiC limiters.

increase sharply.

One of the main effects which the LHRF has on the plasma is to produce a population of non-thermal electrons, with energies in the range of 20 keV to over 300 keV. Figure D-6 shows typical X-ray spectra, with and without the RF (Mo limiter, $P_{RF} = 500$ kW). At $P_{RF} = 900$ kW, estimates indicate that the fractional population of these non-thermal electrons is on the order of 10^{-3} . Since they have energies of 10 or more times the thermal, if these electrons are relatively poorly confined, they could account for a significant energy loss from the plasma. Furthermore, they might be expected to be scraped off in a small poloidal portion of the limiters, due to the small outward shift of their drift surfaces relative to the flux surfaces. Post-mortem examination of the SiC coated limiters indicates that there is indeed much damage in a poloidally localized region of the limiters near the outside mid-plane. The total area affected is about 5 cm^2 . If, in fact, 100 kW or more is carried out of the plasma by the non-thermal electrons, the resulting power loading ($\geq 20 \text{ kW/cm}^2$) would be sufficient to give rise to rapid surface melting (for Mo or SiC) or sublimation (graphite). This then might be the major cause of the impurity generation in these experiments.

D.4. PLT

ICRF heating results from the PLT device have been more favorable [D-12]. At the 1 MW level, metal densities are seen to double, but do not dominate the discharge characteristics, with less than 15% of the central input power being radiated away. The total radiated power in these cases scaled linearly with input power up to 3 MW, so that the fractional radia-

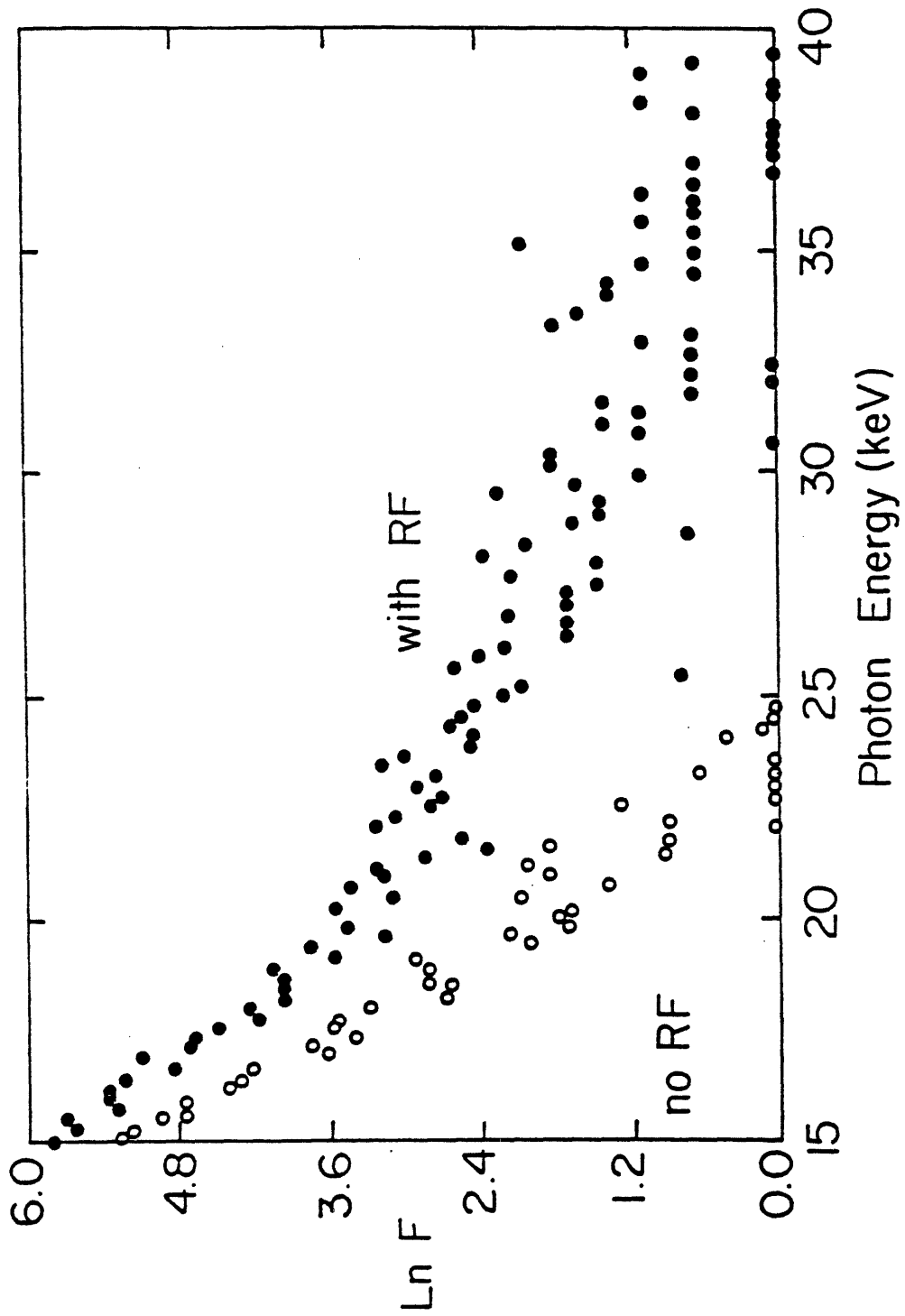


FIGURE D-6 X-ray spectra, with and without the RF.

ted power was roughly constant. In order to compare these results with those of the other high power RF experiments, it is useful to examine the surface power loadings in each case. Table D.4-1 gives such a comparison, where the power flux is simply the surface area of the plasma divided into the total RF input power. Note that PLT is a factor of two lower than TFR, while Alcator C falls between the two cases. The comparable number for Alcator DCT, with 7 MW of RF power, is about the same as that on Alcator C.

Conclusions

All of the experimental results described in this Appendix were obtained on tokamaks using mechanical limiters to define the plasma edge. In light of these results, we feel that the operation of a long pulse, intensely RF heated and current driven high density tokamak using only limiters to handle particle and heat flows could be an extremely high risk venture. Although there have been, to date, no high power RF experiments on devices using poloidal divertors, the results from neutral beam injection on PDX [D-13] clearly indicate a decrease of plasma contamination when divertor operation is compared to limiter operation. The poloidal divertor, as discussed in the main body of this proposal, has therefore been included as the primary impurity control option in the design of Alcator DCT.

TABLE D.4-1

<u>DEVICE</u>	<u>POWER (MW)</u>	<u>AREA (cm²)</u>	<u>POWER FLUX (W/cm²)</u>
ALCATOR C	1	4.2×10^4	23
TFR	2	7.1×10^4	28
PLT	3	2.2×10^5	14
ALCATOR DCT	7	3.2×10^5	22
REACTOR			> 50

References

- [D-1] G. M. McCracken and P. E. Stott, Nucl. Fusion 19 (1979) 889, and references therein.
- [D-2] Equipe TFR, "ICRF Results on TFR at Megawatt Power Levels", Report EUR-CEA-FC-1108, July 1981.
- [D-3] M. F. Stamp, A. Pochelon, N. J. Peacock, J. B. Lister, B. Joye, H. Gordon, "A Spectroscopic Survey of the TCA Tokamak with and without Low-Frequency RF Heating", Report LRP 220/83, February 1983.
- [D-4] M. Porkolab, et. al., "Lower Hybrid Current Drive and Heating Experiments at the 1 MW Level in Alcator C," Proceedings of the Fifth Topical Conference on Radio Frequency Plasma Heating, Madison, Wisconsin, 1983; and, M. Porkolab, et. al., 9th Int. Conf. on Plasma Res. and Contr. Nucl. Fus. Res., Baltimore, U.S.A., 1982, IAEA-CN-41/C-4.
- [D-5] E. Marmor, et. al., "Impurity Generation During Intense Lower Hybrid Heating Experiments on the Alcator C Tokamak," " PFC/JA-83-37 (1983) to be published in J. of Nucl. Mater.
- [D-6] J. Adam, Invited paper, 11th European Conference on Controlled Fusion and Plasma Physics, Aachen, W. Germany, September, 1983.
- [D-7] W. L. Hodge, J. Castracane, H. W. Moos and E. S. Marmor, J. Quant. Spectrosc. Radiat. Transfer 27 (1982) 493.
- [D-8] James Castracane, "Grazing Incidence EUV Study of the Alcator Tokamaks", Johns Hopkins University Ph.D. thesis (1981), unpublished.
- [D-9] M. E. Foord, E. S. Marmor, and J. L. Terry, Rev. Sci. Instrum. 53 (1982) 1407.
- [D-10] D. E. Post, R. V. Jensen, C. B. Tarter, W. H. Grasberger and W. A. Lokke, Atomic Data and Nucl. Tables 20 (1977) 397.
- [D-11] M. M. Pickrell, "The Role of Radiation on the Power Balance of the Alcator C Tokamak," MIT Report PFC/RR-82-30, 1982.
- [D-12] D. Q. Hwang, J. C. Hosea, H. R. Thompson, J. R. Wilson, et. al., "Experimental Results and Transport Simulations of ICRF Heating in PLT", Proceedings of Fifth Topical Conference on Radio Frequency Plasma Heating, Madison, Wisconsin, 1983.
- [D-13] R. J. Fonck, et al., Princeton Plasma Physics Laboratory, report PPPL-1932, 1982.

APPENDIX E
ENHANCEMENTS

The facility described thus far in this proposal represents the baseline version of Alcator DCT. In this Appendix to the proposal, we describe some of the enhancements, improvements, or up-grades which are possible. These are directed toward improving the performance of the device, through increases in the heating power by the addition of alternative RF systems, or via changes in the plasma configuration.

E.1. RF Systems

Here we consider enhanced performance scenarios for Alcator DCT by upgrading the lower hybrid and the ICRF power systems, by introducing a lower frequency, high power ICRF system, and by introducing an ECRH system. We shall discuss each of these in turn.

E.1.1. Enhanced Lower Hybrid Current Drive System

In order to raise the RF driven current to 1 MA, we have performed code calculations where the RF power was increased from 3 MW to 6 MW (or 8 MW at the source). We retained the same frequency and spectrum as before (i.e., $N_{\parallel}(0) = 1.66$) and obtained excellent results. In Figure E.1-1a we show the current generated by 6.0 MW of net LH power incident upon the plasma. We see that 100 msec after RF power injection at $\bar{n} = 7.0 \times 10^{13} \text{ cm}^{-3}$ the RF driven current would rise above 1.1 MA. At the same time, as shown in Figure E.1-1b, T_{e0} would rise to 7.5 keV, and T_{i0} would rise to 4.2 keV (assuming no additional RF power, such as ICRF). In the present case we find that J_{RF} would peak near $r \approx 10 \text{ cm}$, and P_{RF} would be

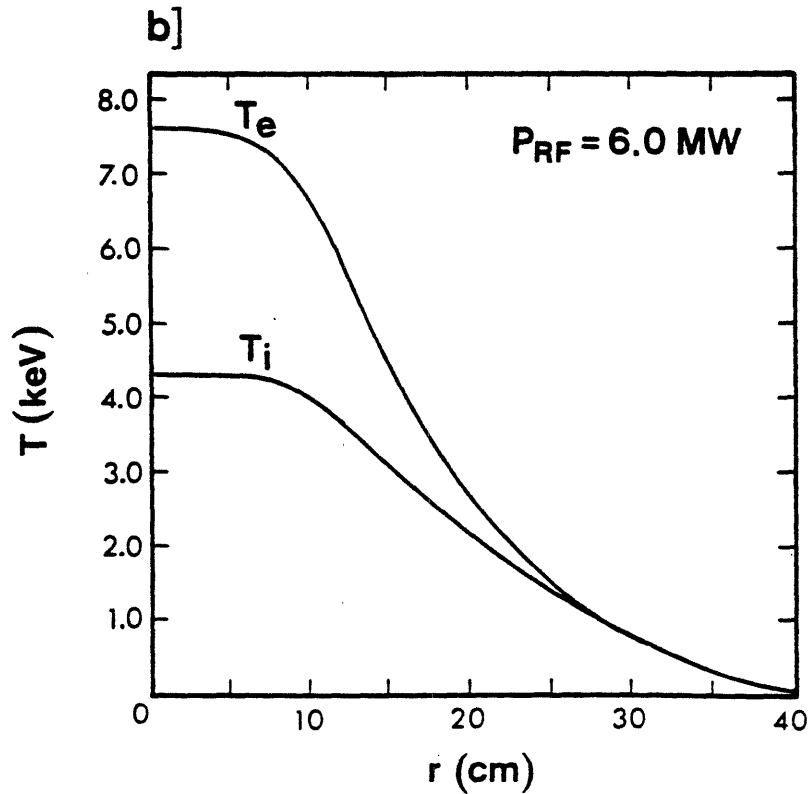
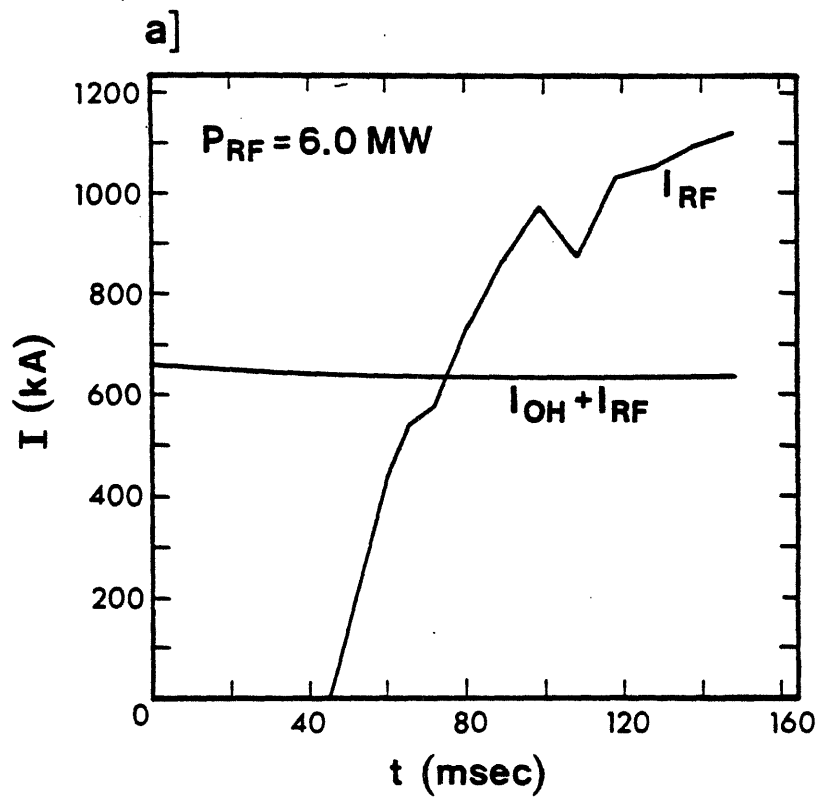


FIGURE E.1-1 Performance with 6.0 MW absorbed lower-hybrid power. a) RF-induced and total current vs. time; b) radial temperature profiles.

deposited in the region $0 \lesssim r \lesssim 15$ cm, again demonstrating excellent central power deposition.

By adding 3.5 MW ICRF power we would expect that the temperatures would rise to the 10 keV level. Thus, we would expect a very high performance, long-pulse tokamak. Furthermore, other "advanced" current drive schemes, such as the fast (Alfvén) wave and whistler wave current drive concepts could be tested at such high temperatures.

E.1.2. Enhanced ICRF Systems

The ICRF systems could be upgraded two ways: (a) double the ICRF power at 186 MHz from 5 MW to 10 MW, and thus increase the ion temperature toward the 10 keV level; (b) acquire a lower-frequency ICRF system to carry out 2nd harmonic heating experiments in hydrogen at $B = 3 - 4$ Tesla ($f \approx 90 - 120$ MHz) or use a 45 - 60 MHz system for minority H^+ heating, or 30 - 45 MHz system for He^3 minority heating. The purpose of these "low magnetic field" experiments would be to carry out high beta plasma physics experiments, possibly with shaped plasmas. We expect that approximately 10 MW of power may be needed for such experiments. We propose to use the "national ICRF facility" that is in the planning stage at the present time. Given the large number of ports in Alcator DCT, we do not foresee any problem in delivering 10 MW of power into the device.

E.1.3. ECRH Option

We would like to propose to study ECRH start-up combined with lower hybrid current drive in an upgraded version of DCT. This would allow an OH-free start-up of a high density, high magnetic field tokamak. To do

this at 7.0 Tesla, 196 GHz gyrotrons would be necessary. A 140 GHz short pulse gyrotron has already been developed at M.I.T. by R. Temkin and co-workers, and it is ready for development into a longer-pulse tube. We would like to see such a developmental work commence as soon as possible. As a follow-up, a higher frequency ($f \sim 180\text{--}200$ GHz) gyrotron developmental work would result in providing the necessary tube for Alcator DCT. While the power necessary for start-up in a combined ECRH-LH current drive scenario is not yet known, we could test the concept in Alcator C if the 140 GHz long pulse tube were developed. We expect that a total ECRH power of one megawatt should be satisfactory when combined with the available lower hybrid current drive system.

E.2. Beta Enhancement with Extreme Shaping

One of several possibilities being studied for eventual enhancement of the Alcator DCT device is a program for the investigation of the extremely shaped plasma configurations referred to as "beans". There has recently been a significant renewal of interest in these indented plasma shapes, because of the prospect of attaining MHD stable, high beta equilibria. It may even be possible to operate in the "second" stability regime, with beta above the range of ballooning mode instability. This is now an area of active research, and the PBX experiment is being assembled at PPPL to study the problems involved in producing high beta, bean-shaped plasmas. We have considered some of the problems involved in modification of Alcator DCT to enable the creation and study of these configurations.

In order to produce the required indentation of the inner surface of the plasma, it appears to be necessary to place a coil on the midplane of the tokamak, very close to the inner edge of the plasma (see Figure E.2-1). With the proposed Alcator DCT coil configuration, the installation of this "pusher" coil inside the vacuum chamber would be the only structural modification needed. The considerations involved in the installation of internal coils are discussed in Appendix E.3 of this proposal. Both copper and superconducting coil types have been examined. The current required in the pusher coil is approximately half of the plasma current, or about 500 kA in Alcator DCT. This is well within the capabilities of the Alcator DCT power systems. In addition to the pusher coil, the central (near the midplane) section of the OH solenoid would have to be operated independent of the OH system. However, the current requirements do not exceed the present design capacity of this coil.

The plasma parameters which might be achievable with an indented, bean-shaped configuration in Alcator DCT have not been examined in detail. Even the general range of values depends on the results of shape control, confinement, and heating studies now beginning on the PBX experiment. One point worth noting is that, compared to other devices, the somewhat larger aspect ratio of Alcator DCT results in a narrowing of the unstable range of beta values (to ballooning modes), and might make it possible to explore experimentally the stability boundaries at more relevant plasma parameters.

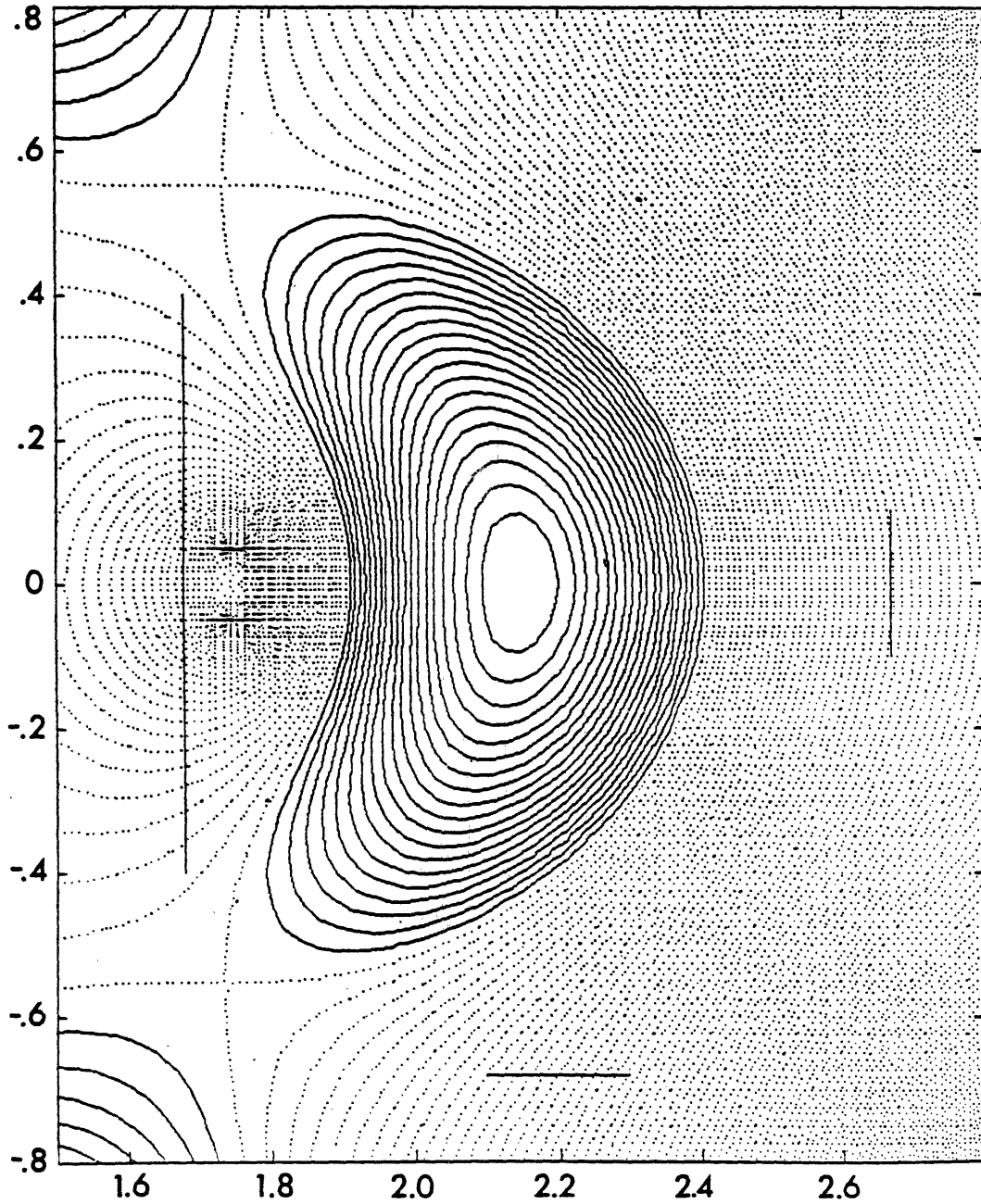


FIGURE E.2-1 Bean-shaped plasma; $B_{T0} = 3$ T, $I_p = 1.0$ MA; $q(a) = 2.0$; $\langle a_p \rangle = 0.38$ m; $b/a = 1.7$; $d/2a = 0.19$. The pusher coil, located inside the vacuum chamber, carries 500 kA.

E.3. Internal Coils for Divertors and Shaping

As part of the point design trade-off studies we have considered the use of internal coils to form a poloidal divertor or to provide advanced shaping such as "bean" shapes.

The ampere-turn requirements and coil positions for a typical internal coil single null divertor are given in Table E.3-1. It is clear that the ampere-turn requirements of internal coils are substantially less (400 kA versus 1,500 kA) than external coils. We did not find, however, that their substitution would substantially reduce out-of-plane loads on the TF magnets, as those loads are dominated by the external shaping coils.

Poloidal divertors have traditionally used coils inside the vacuum chamber, as in PDX and Asdex, for example. However, such linked coils present the obvious dilemma of machine assembly. We have examined the Asdex and JT-60 internal coils as representatives of reasonable mechanical joint designs. Both suffer, however, from a much increased heating load in the joint area. This is not of prime importance for short pulse machines where the conductor temperature is controlled by heat capacity, but is of great importance for a steady-state machine.

TABLE E.3-1

Internal Triplet Divertor

COIL	MAJOR RADIUS (m)	HEIGHT ABOVE MIDLINE (m)	NI (MA)
D1	1.77	0.38	- 0.26
D2	2.00	0.60	+ 0.40
D3	2.28	0.40	- 0.14

We have, therefore, examined a wind-in-place strategy similar to that proposed for SLPX and a form-in-place as proposed for the PLT rework. Machines of the scale of Alcator DCT which readily allow personnel access to the interior, can utilize such a strategy. A suitable copper winding crosssection for 400 kA is shown in Figure E.3-1, and would have an outer jacket diameter of 18.5 cm. The steady-state triplet divertor set of Table E.3-1 wound as in Figure E.3-1, would consume 6 MW of power and require 128 parallel water passages carrying a total of 1,600ℓ / minute of coolant. Clearly manifolding such a flow in a confined space would be very difficult.

If one considers wind-in-place strategy, one can also actually consider winding a superconducting coil. Figure E.3-2 shows such a coil wound from Nb₃Sn ICCS conductor. This conductor would be pre-heat-treated as with the LCP Westinghouse material, rather than post-heat-treated as in the Alcator DCT TF coils. The 400 kA internal coil would contain 250 meters of Nb₃Sn conductor (one-third the material in one TF coil), and would have the same overall jacket dimension of 18.5 cm diameter (overall

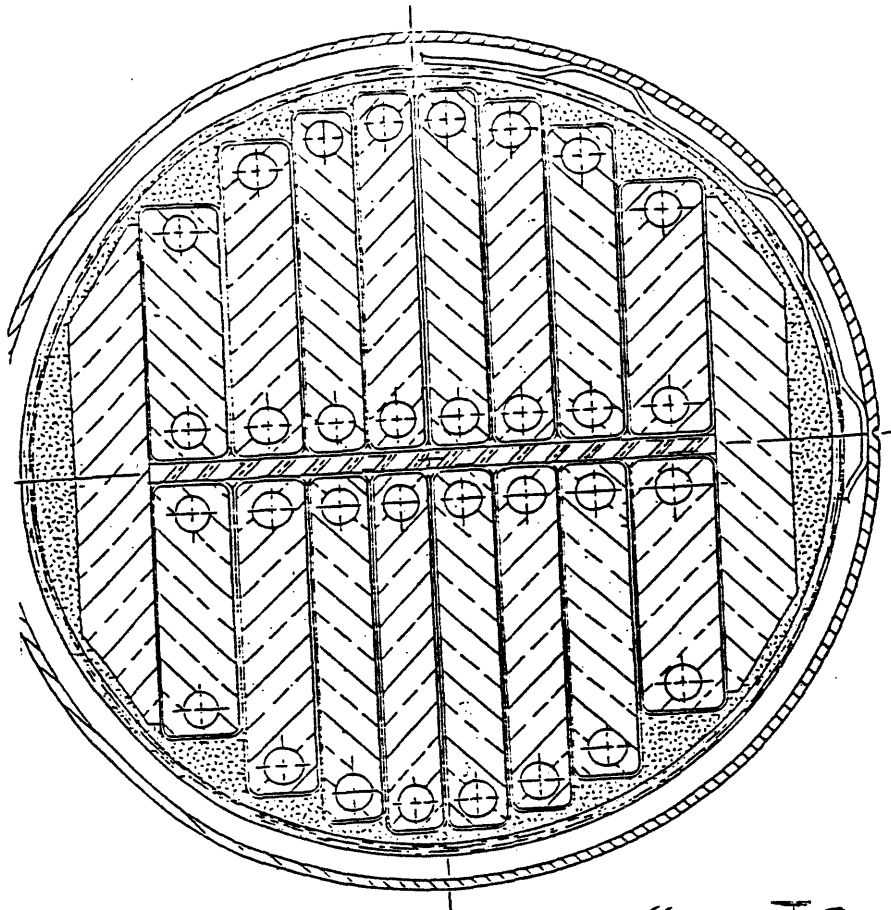


FIGURE E.3-1 Resistive Internal Coil Concept with Hollow-Conductor Copper.

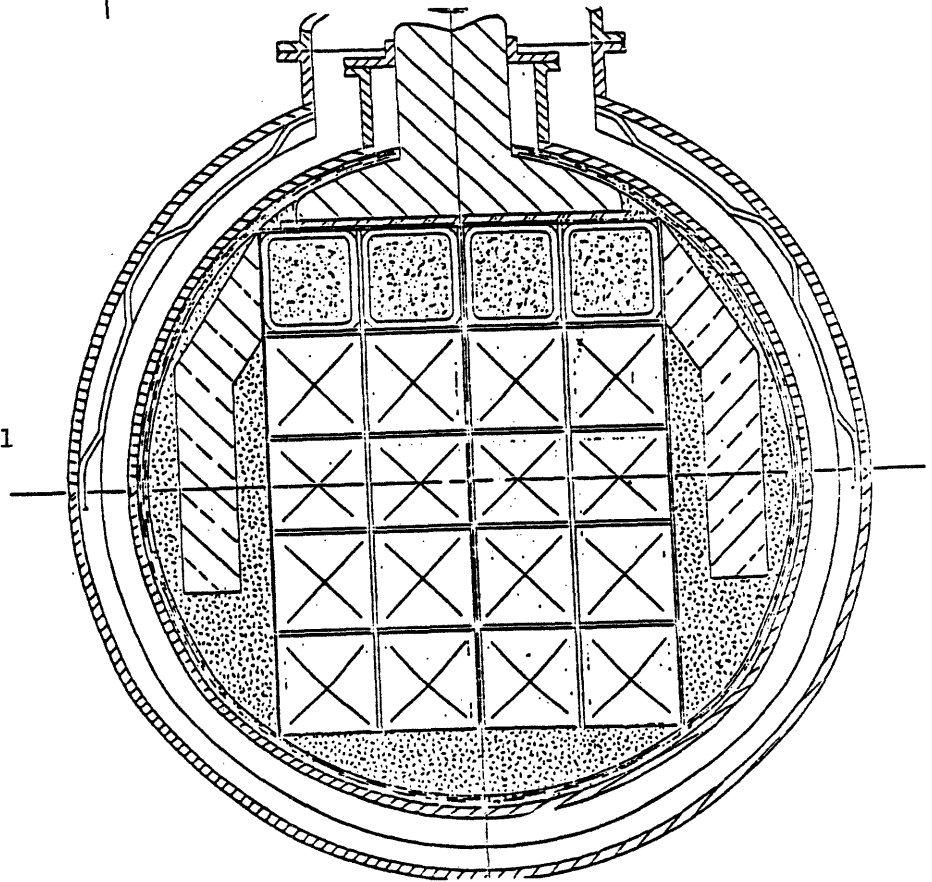


FIGURE E.3-2 Superconducting Internal Coil Concept with Nb_3Sn ICCS Conductor

current density 1.5×10^3 A/cm²).

A further major advantage of a wind-in-place strategy is the opportunity to consider retro-fitting internal coils after the machine has been constructed. Such a retro-fit might be utilized effectively for example, to provide advanced bean-shaped plasmas should a future high priority arise for such shaping. The bean-shaped plasma example shown in Figure E.2-1 would require an internal equatorial current of one half the plasma current (i.e., 500 kA for a 1,000 kA plasma). That example also requires a smaller reverse current in the region of the OH transformer, and would be accomplished by altering the current in the central modules.

We do not currently anticipate including internal coils for shaping or divertors in the baseline Alcator DCT construction. We are considering, however, the possible use of internal passive or active coils for position control.

APPENDIX F
REACTOR RELEVANCE

Alcator DCT is a long pulse, superconducting tokamak with relatively large aspect ratio and magnetic field. It has the capability of achieving true steady state operation by means of lower hybrid current drive. Clearly, at the primary level of sophistication a superconducting tokamak with long pulse and steady state capabilities is directly relevant to the mainline tokamak reactor concept as perceived by the fusion community for a number of years. At the next level, in view of the differences in the range of operation and the design philosophy between Alcator DCT and the current generation of large tokamaks (e.g., TFTR, JET, Doublet Big D) it is of legitimate concern to ascertain whether this device bridges the gap toward reactor relevant tokamaks or seeks an isolated corner of parameter space to achieve a special subset of performance criteria.

Alcator DCT has been designed to either operate directly in, or more closely approach, the regime of reactor interest with respect to all major reactor parameters accessible to the experiment: (1) Magnetic Field, (2) Aspect Ratio, (3) β , (4) Long Pulse and (5) Current Drive. Of particular concern are the relatively larger aspect ratio and higher magnetic field which appear to go against the "conventional wisdom" of several years ago. To a certain extent it was this "conventional wisdom" that led to the current generation of low field, low aspect ratio tokamaks. However, reactor studies carried out over the past several years indicate that low field, low aspect ratio may not be the optimum direction to follow. These studies indicate that higher field, larger aspect ratio are at least as desirable if not more so.

This question as well as the other relevant issues are discussed below.

F.1. Magnetic Field

There are two issues regarding the magnetic field. First, regardless of whether a low or high aspect ratio device is used, recent reactor design studies have shown the need for relatively higher values of the magnetic field at the coil [F-1,2]. One obvious reason for this is that high field lowers the required βA ($A \equiv R_0/a$). Table F.1-1 shows how the magnetic field at the coil has increased in recent reactor designs [F-1]. Note that the magnetic field at the coil in the more recent Demo-commercial tokamak designs (HFCTR, NUMAK, STARFIRE) has increased substantially from that in earlier designs and typically is on the order of 11 T. Thus, the Alcator DCT design value of 10 T is quite close to the regime of interest. Furthermore, a crucial issue in the magnetic technology program is directly addressed in that Alcator DCT will be the first tokamak to utilize Nb_3Sn superconducting magnets.

The second issue concerns the magnetic field at the plasma itself. While $B_0 = 7$ T for Alcator DCT is considerably higher than that in TFTR, JET, or Doublet Big D, this value is actually much closer to what would be expected in a reactor since a reactor will likely have a larger aspect ratio than most current experiments. See Discussion (F.2). For example, for fixed $B_c = 11$ T, blanket and shield thickness $b = 1.5$ m, and minor plasma radius $a = 2$ m, the magnetic field at the plasma for a device with aspect ratio $A = 5$ is $B_0 = 7.2$ T. For a device with $A = 3$ the field is only 4.6 T. Thus, once one realizes that reactor aspect ratios may be larger than those anticipated several years ago, the value of $B_0 = 7$ T in

Alcator DCT is directly in the regime of reactor interest.

F.2. Aspect Ratio

Although there are a number of potential advantages for operating at relatively large aspect ratio (e.g., higher field at the plasma for a given field at the magnet, capability of very long ohmic pulses for long pulse reactors, improved transport because of weaker toroidal effects, ease of maintenance), the overriding reason for low aspect ratio has been the achievement of high β ; that is, if the maximum β scales as $\beta \sim 1/A$ and if high β is required in a reactor, then clearly one should operate at as low an aspect ratio as technologically feasible.

Recent studies [F-3,4,5] have shown that this reasoning is fallacious. Since β is defined in terms of B_0 , the magnetic field at the plasma, β is indeed increased for low aspect ratio at fixed B_0 . However, the technological limit is not on B_0 , but on B_c , the field at the coil. As the aspect ratio decreases, B_0 becomes progressively smaller than B_c . Thus, at fixed B_c one should not try to operate at the lowest possible aspect ratio. There is a unique optimum aspect ratio balancing the A scaling of β with the $1/R$ scaling of the toroidal field. Reactor studies show that this optimum occurs when $A \sim 4-5$. A particular calculation illustrated in Figure F-1 demonstrates the dependence of the field at the coil, B_c vs aspect ratio for fixed plasma pressure and minor radius [F-3]. Note the optimum in the aspect ratio. A simple analytical calculation which minimizes Volume/Power, a direct measure of the nuclear island cost, and then determines the aspect ratio to minimize the required βA shows there is also an optimum value of

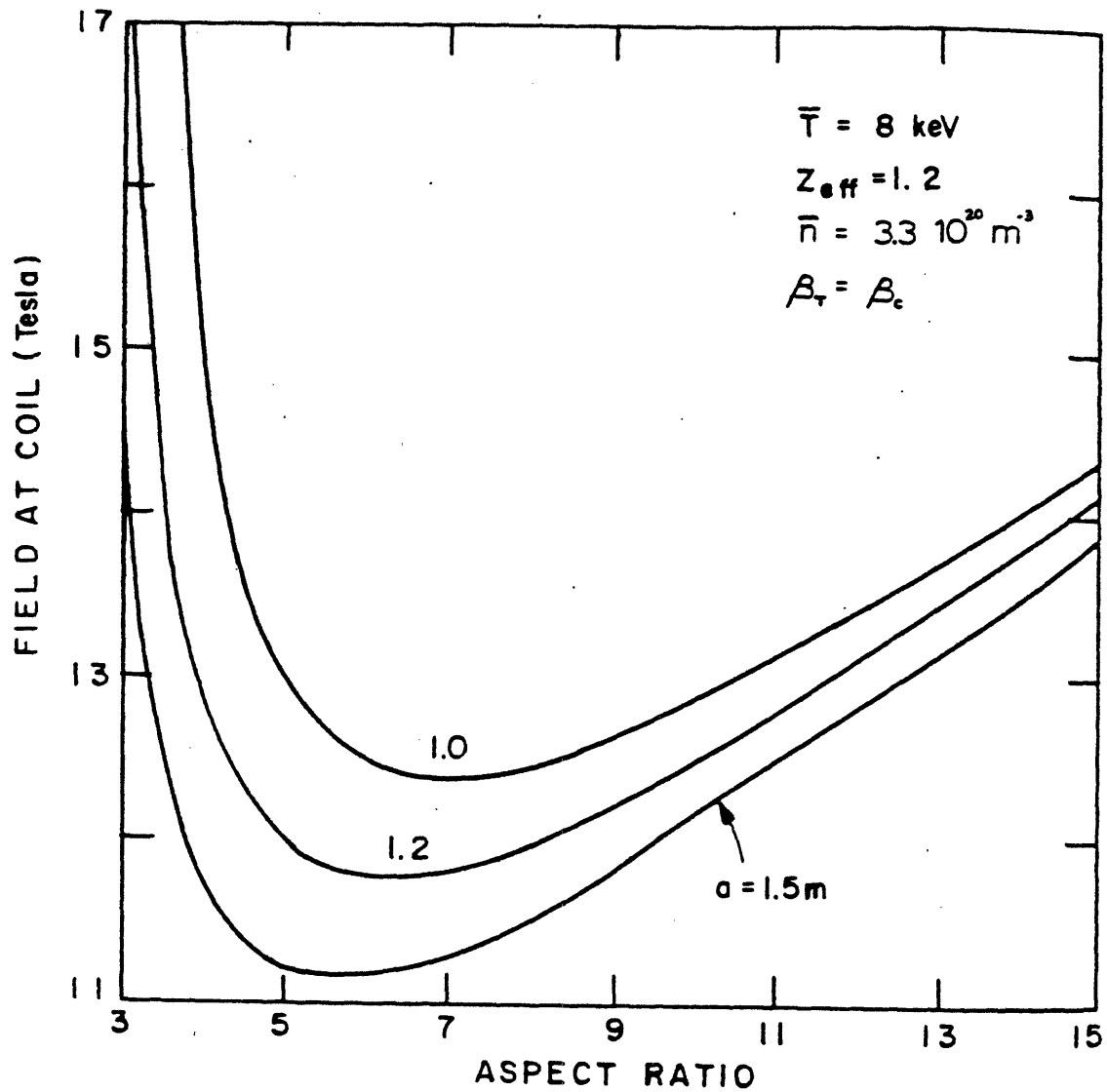


FIGURE F-1 B_c vs. A for fixed pressure and minor radius indicating optimum aspect ratio. The distance from the plasma edge to the TF coil is 1.3 m. It is assumed that $\beta = 1/A$.

A given by [F-5]

$$A = 3 \left[1 + \frac{e^{1/2}b}{b + d} \right]$$

where e is the elongation, b is the distance between the first wall and the inside of the coil (i.e., the thickness of the blanket and shield) and d is the distance from the inside of the first coil to the "edge" of the reactor (i.e., the thickness of the toroidal coil, transformer and supporting structure). Note that the optimized A depends only on the geometry of the reactor and not on B_c or β . For typical values, $e = 1.6$, $b = 1.5$ m, $d = 1.5$ m one finds $A = 4.9$ which is consistent with the more exact numerical studies. Thus, the aspect ratio of Alctor DCT is directly in the regime of reactor interest.

F.3. Beta

Until recently it was thought that the most desirable tokamak reactors would operate at "as high a β as possible". If lower β 's were used, this would imply higher toroidal fields leading to a greatly increased reactor cost. This argument is also somewhat fallacious. Operation at relatively moderate values of β does not significantly increase the cost of a reactor with superconducting magnets since in most designs the magnet cost is less than 20% of the total plant cost. For the HFCTR Demonstration reactor design which used a higher field (7.4 T on axis) and lower β ($\beta = 4.5\%$) than earlier designs, it was found that the cost/kWe was less than 10% higher than that of the high β ($\beta = 10\%$) ORNL Demonstration reactor [F-3]. Furthermore, operation at moderately high fields and moderate values of β ($\beta < 5\%$) reduces the requirements for the equilibrium

field system and can eliminate the need for vertical stability control. Simplification of the EF system could facilitate maintenance [F-6] and increase reactor reliability. To decide what values of β are reactor relevant, one can adopt the point of view that high β is difficult to achieve because of MHD physics issues, and that this is a critical limitation in the reactor design. One can then design an optimized reactor by choosing the aspect ratio so as to minimize the required βA . (Note that the MHD limitations are not on β but on βA). It is this procedure which gave rise to Equation 1. The corresponding minimized RMS averaged βA is given by [F-5]

$$\beta A = 91\mu_0 \left(\frac{T^2}{W_T \overline{\sigma v}} \right)^{1/2} \left(\frac{1 + e^2}{2e} \right)^{1/4} \frac{P_W^{1/2} [1 + e^{1/2} b / (b + d)]}{B_C^2 (b + d)^{1/2}} \quad (2)$$

where $W_T = 20$ MeV and P_W is the wall loading which must be as large as technologically possible to minimize the cost. Once P_W is set, the minimum required β is obtained by operating at the highest possible field, at the minimum of the $T^2 / \overline{\sigma v}$ curve (i.e., $T \approx 13.3$ keV) and at the aspect ratio given by Equation 1. For $P_W = 2$ MW/m², $B_C = 10$ T, $T = 13.3$ keV, $e = 1.6$, $b = 1.5$ m and $d = 1.5$ m it follows that

$$\beta A = 9.9 P_W^{1/2} / B_C^2 = .13 \quad (3)$$

with P_W in MW/m² and B_C in T. Setting $A = 5$ yields $\beta \approx 2.6\%$.

Thus, the ideal model, consistent with the more detailed studies, shows that the combination of larger aspect ratio and large fields substantially reduces the required β from that anticipated in the early designs. Note that as far as the reactor design is concerned there is no real

distinction whether the required β_A is obtained by either high β_p/A , low q or a combination thereof.

F.4. Long Pulse Capability

If the use of lower hybrid waves or some other form of noninductive current drive is not sufficiently efficient for steady-state operation, tokamak reactors could be operated in a long pulse mode. In this case current drive might still be used for startup, shutdown, and profile control. Long pulse reactor design is facilitated by use of a high performance OH transformer. A design concept has recently been developed for an ultra long pulse tokamak reactor (ULTR) which can provide 24 hour pulses with inductive drive [F-6]. The purpose of this design was to determine the pulse length capability of a reasonable size reactor where the design is optimized to get maximum use of the OH drive. The ULTR concept uses a 10 T OH transformer which is double swung. The device has a major radius of 9.7 m and an aspect ratio of 4.9. The principles used in the ULTR design can be applied to a device which is approximately the size of STARFIRE with a pulse length of 4 hours. The substantial OH drive capability of Alcator DCT is prototypical of these very long pulse reactor designs.

F.5. Lower Hybrid Current Drive

The efficiency of lower hybrid drive increases with increasing wave velocity. However, the allowed wave velocity is limited by accessibility. For fixed plasma density (and hence fusion power at a fixed temperature) operation at higher field allows penetration at a lower value of the parallel index of refraction, n_z , and a higher value of wave velocity. Figure

F-2 shows a calculation of the effect of n_z upon Q , the ratio of fusion power to RF power needed to drive the current [F-7]. Figure F-3 shows how Q then depends upon plasma beta (and hence upon magnetic field) through the accessibility requirement.

Table F.5-1 gives illustrative parameters for a high field reactor using steady state current drive with lower hybrid waves [F-7]. These parameters are an extrapolation of the HFCTR Demonstration reactor design [F-3]. In contrast to the STARFIRE reactor design where hollow current profiles were used because of wave penetration limits, high values of Q were obtained with parabolic current profiles.

Alcator DCT provides an excellent test of the viability of lower hybrid current drive as a mechanism for achieving steady state operation in a parameter range of direct interest to tokamak reactors.

References

- [F-1] C. C. Baker, Proceedings of IEEE 69, 917 (1981).
- [F-2] G. Kulcinski, IAEA Workshop on Tokamak Reactor Design, Tokyo, October 1981, private communication.
- [F-3] D. R. Cohn et al., M.I.T. Plasma Fusion Center Report RR-79-2, 1979.
- [F-4] W. R. Spears and J. A. Wesson, Nucl. Fusion 20, 1525 (1980).
- [F-5] J. P. Freidberg and J. A. Wesson, to be published.
- [F-6] L. Bromberg, D. R. Cohn and J. E. C. Williams, Journal of Fusion Energy 3, 63 (1983).

[F-7] S. Y. Yuen, D. Kaplan and D. R. Cohn, Nucl. Fusion 20, 1980; S. Y. Yuen, J. H. Schultz, D. Kaplan and D. Cohn, M.I.T. Plasma Fusion Center Report RR-79-22 (1979).

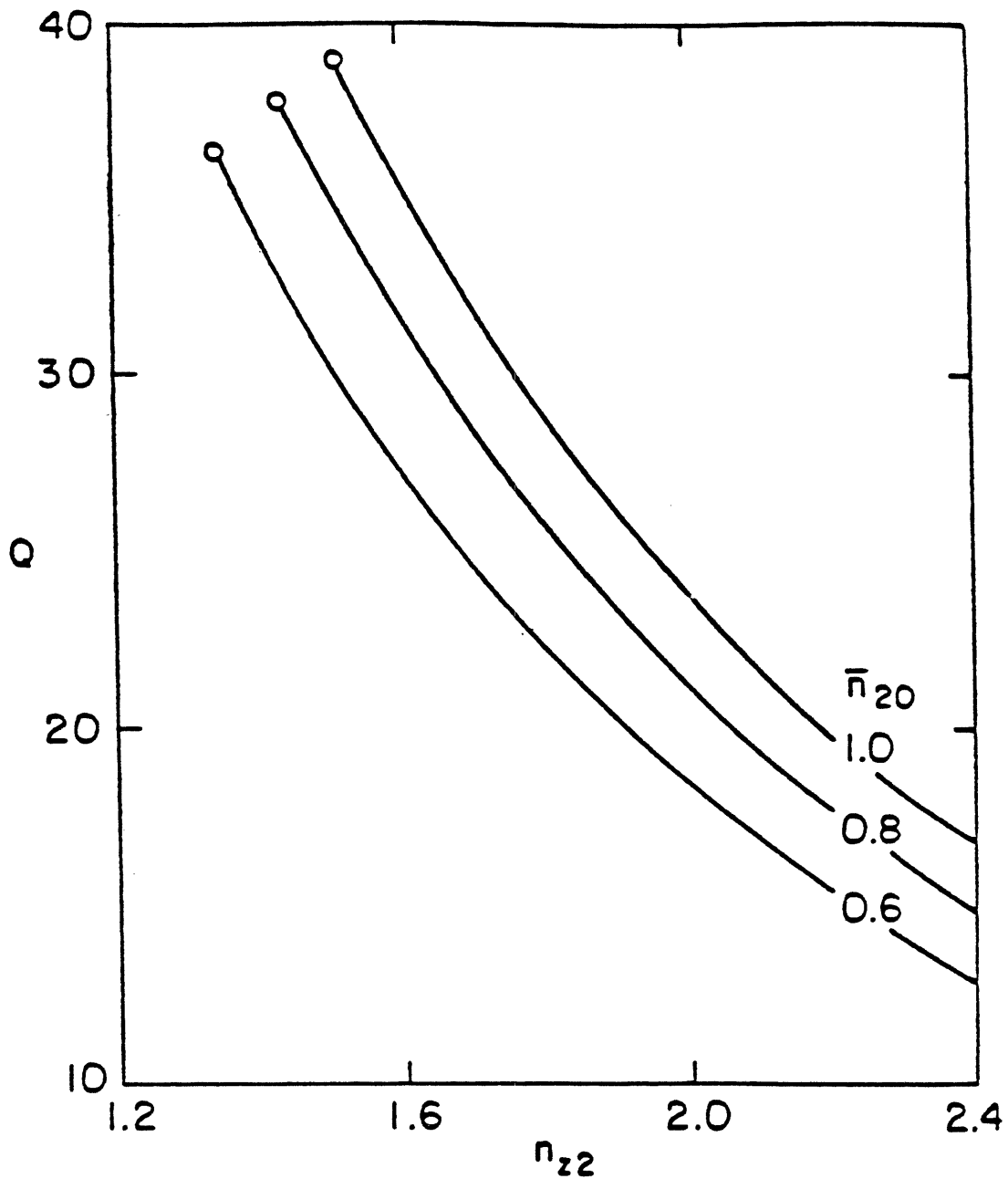


FIGURE F-2 Fusion to RF power ratio as a function of parallel index of refraction. The circles mark the minimum n_z allowed by accessibility condition. [$R = 6$ m, $A = 5$, $B_0 = 7.5$ T, $T_e = 15$ keV, $n_e = n_{e0} (1 - \rho^3)$, $T = T_0 (1 - \rho^2)$, $J = J_0 (1 - \rho^2)$ where $\rho = r/a$]

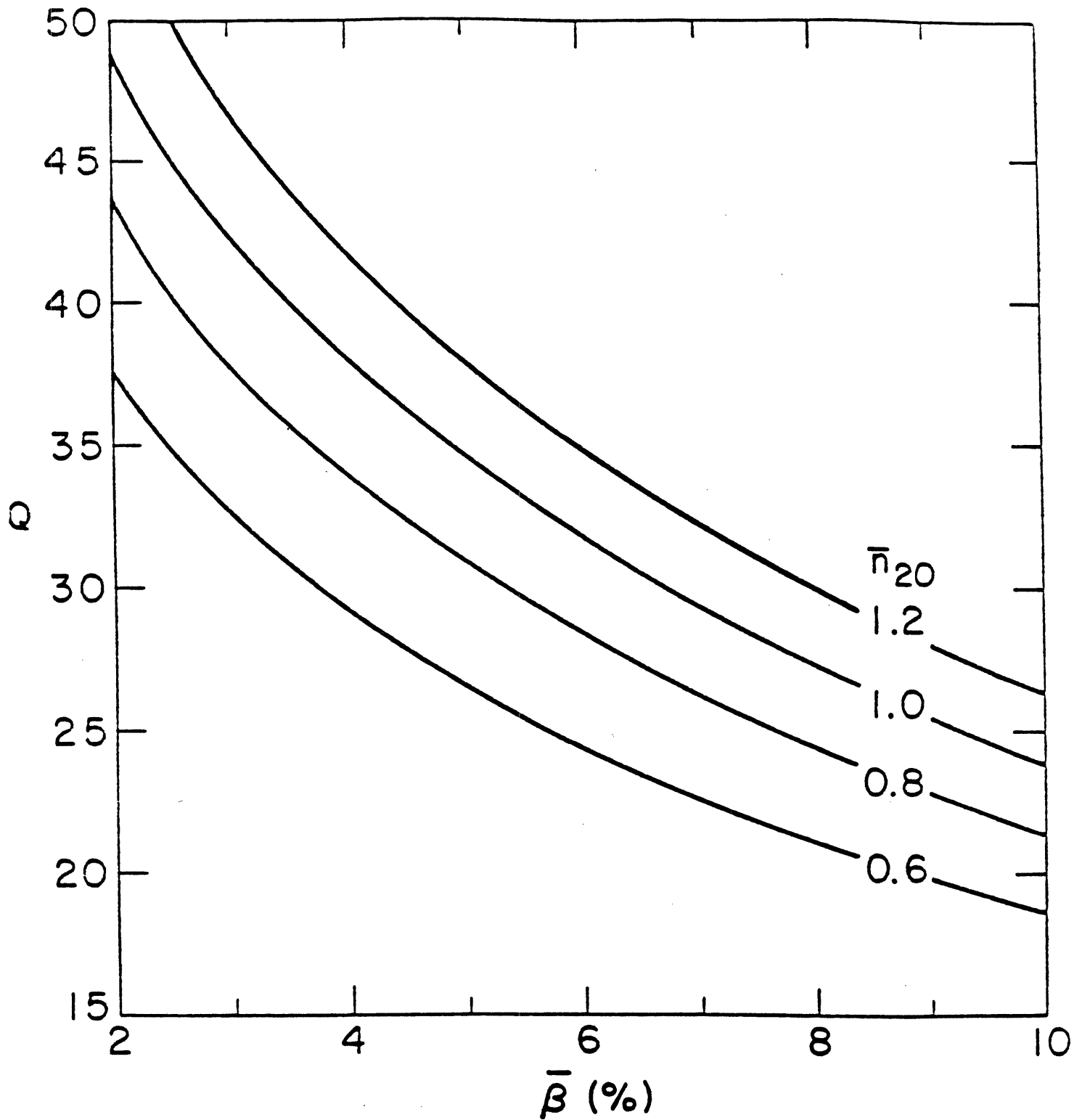


FIGURE F-3 Fusion to RF power ratio versus averaged toroidal beta for several plasma densities. [$R = 6$ m, $A = 5$, $\omega = 2\omega_{LH}(0)$, $\bar{T}_e = 15$ keV, $\bar{T}_i = 22$ keV, $n_e = n_{e0} (1 - \rho^3)$, $T = T_0 (1 - \rho^2)$, $\bar{J} = J_0 (1 - \rho^2)$ where ($\rho = r/a$)].

TABLE F.1-1

Summary of Major Parameters for Some Selected Tokamak Reactor Studies

(from Ref. [F-1])

Parameter	UWMAK-1	UWMAK-III	ORNL DEMO	HFCTR	NUWMAK	STARFIRE
R(m)	13	8	6.2	6	5.2	7.0
a(m)	5	2.5	1.5	1.2	1.1	1.94
P _{th} (MW)	5000	5000	2150	2470	2300	4000
P _n (MW/m ²)	1.25	2.0	2.7	3.4	4.0	3.6
B _{T,max} (T)		8.7	7.1	13.1	11.9	11.1
(β)(%)	5.2	5.8	10.0	4.0	6.0	6.7
I _p (MA)	21	16	3.9	6.7	7.2	10.1
e	1.0	2.0	1.6	1.5	1.6	1.6